JOURNAL OF APPLIED PHYSICS

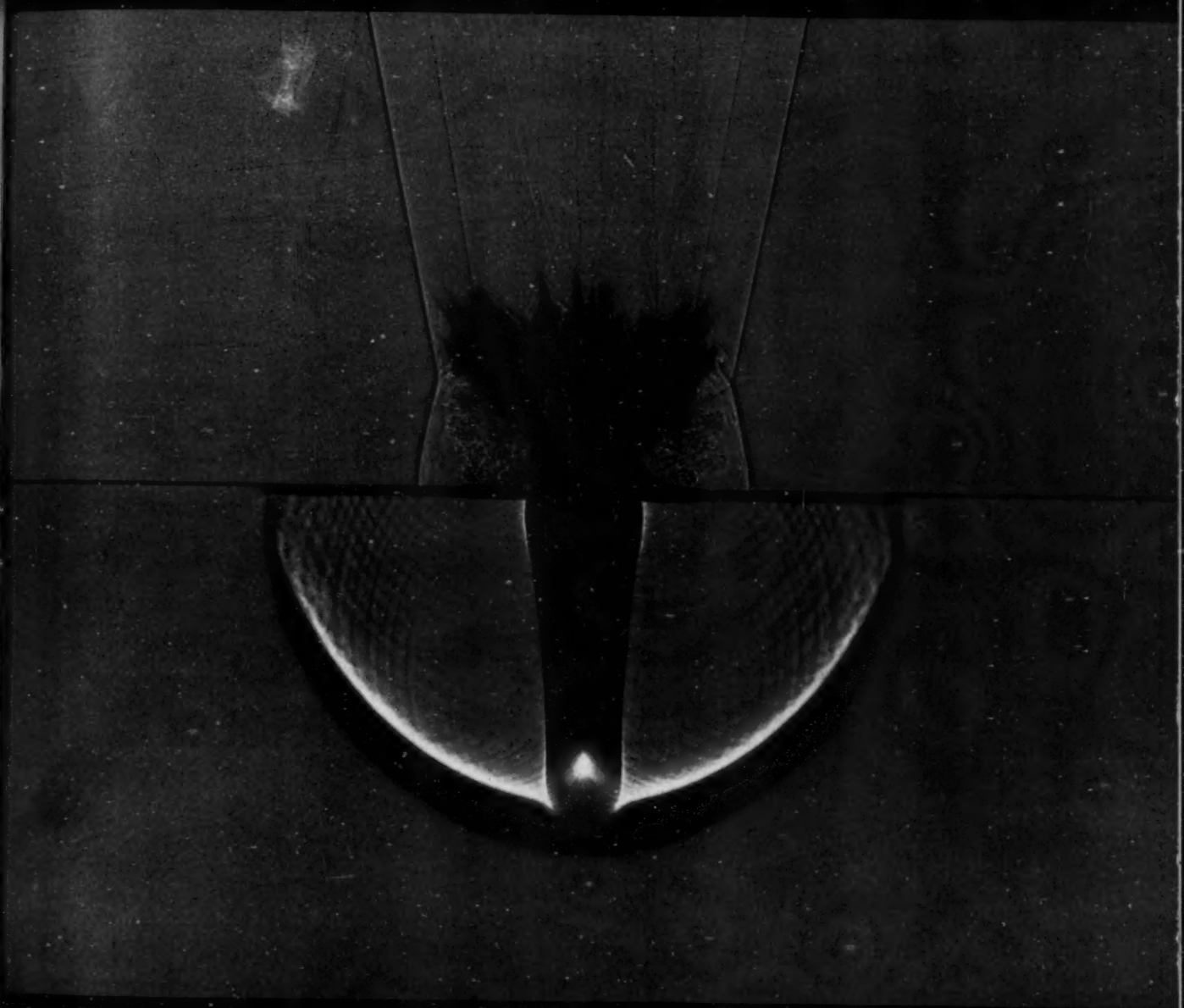

JOURNAL OF APPLIED PHYSICS

Vol. 21, No. 12 DECEMBER, 1950

In This Issue

		Page
Electron Microscopy of Wet Biological Tissues by Replica Techniques	Irwin W. Fischbein	1199
Magneto-Ionic Triple Splitting of Ionospheric Waves	O. E. H. Rydbeck	1205
Equivalent Circuit for the Transmission of Plane Elastic Waves through a Plate at Oblique Incidence	William T. Thomson	1215
Gas Evolution in Liquids and Cavitation	P. H. Schweitzer and V. G. Szebehely	1218
Electrical Conductivity Method for Measuring Self-Diffusion of Metals	J. H. Dedrick and G. C. Kuczynski	1224
Simple Interferometric Test for Conical Flow	J. H. Giese, F. D. Bennett, and V. E. Bergdolt	1226
Theory of Collinear Antennas	Ronold King	1232
Beam Oscillations in an F-M Cyclotron	T. Teichmann	1251
On the Theory of Dislocations	John Lee Bogdanoff	1258
Microwave Study of the High Pressure Arc	J. D. Cobine, E. P. Cleary, and W. C. Gray	1264
Relationship between Resistance and Temperature of Thermistors	G. Bosson, F. Gutmann, and L. M. Simmons	1267
High Intensity Short Duration Spark Light Source	J. A. Fitzpatrick, J. C. Hubbard, and W. J. Thaler	1269
Emissivity Changes of Thoria Cathodes	O. A. Weinreich	1272
Techniques for Measuring the Dynamic Characteristics of a Low Pressure Discharge	Bentley T. Barnes and Stephen Eros	1275
On the Radiation Patterns of Dielectric Rods of Circular Cross Section—the $TM_{0,1}$ Mode	C. W. Horton, F. C. Karal, Jr., and C. M. McKinney	1279
Precision Determination of the Lattice Constants of Zinc Oxide	R. B. Heller, J. McGannon, and A. H. Weber	1283
Virtual Mass of a Sphere Entering Water Vertically	Albert May and Jean C. Woodhull	1285
Plastic Flow of Platinum Wires	R. P. Carreker, Jr.	1289
Effect of Magnetic Field on the Breakdown of Gases at Microwave Frequencies	Benjamin Lax, W. P. Allis, and Sanborn C. Brown	1297
Quantum Limits of the Electrostatic Image Force Theory	R. G. Sachs and D. L. Dexter	1304
Production of 2537 Radiation and the Role of Metastable Atoms in an Argon-Mercury Discharge	Carl Kenty	1309
Vibrational Relaxation Times in Gases	Wayland Griffith	1319
Numerical Determination of Fundamental Modes	Donald A. Flanders and George Shortley	1326
Determination of Eigenvalues Using a Generalized Laplace Transform	Morris D. Friedman	1333
Letters to the Editor:		
Comment on "Relationship between Gough-Joule Coefficients and Moduli of Vulcanized Rubbers"	M. Mooney	1338
Approximation Method for the Determination of the Elastic Constants of Cubic Single Crystals	J. R. Neighbours and Charles S. Smith	1338
Coefficient of Self-Diffusion of Copper	G. Cohen and G. C. Kuczynski	1339
Erratum: Transonic Potential Flow of a Compressible Fluid	W. R. Sears	1340
Erratum: Separation of Gases by Fractional Permeation through Membranes	Sol Weller and Waldo A. Steiner	1340
Deformations and Stresses in Bourdon Tubes	R. A. Clark and E. Reissner	1340
Shadowgrams of Spherical Missiles Entering Water at Supersonic Speeds	J. H. McMillen, R. L. Kramer, and D. E. Allmand	1341
Author Index to Volume 21		1343
Subject Index to Volume 21		1349
Index to Advertisers		xxxii

BOARD OF EDITORS

Elmer Hutchisson,
Editor

Earle C. Gregg,
Assistant Editor

Associate Editors
Howard H. Aiken
James Hillier
W. James Lyons
Philip Morrison
Eric Reissner
Raymond J. Seeger
Frederick Seitz
Charles S. Smith

Publication of the

American Institute of Physics

OFFICERS
George R. Harrison,
Chairman
George B. Pegram,
Treasurer

GOVERNING BOARD
J. W. Beams
C. Paul Boner
Wallace R. Brode
W. F. Fair, Jr.
J. B. Fisk
G. P. Harnwell
George R. Harrison
W. V. Houston
Rudolph Kingslake
Paul Kirkpatrick
Paul E. Klopsteg
F. W. Loomis
Philip M. Morse
J. R. Oppenheimer
George B. Pegram
Harold K. Schilling
Francis G. Slack
John C. Steinberg

Consultant on Printing
Melvin Loos

ADMINISTRATIVE STAFF
Henry A. Barton,
Director
Wallace Waterfall,
Executive Secretary
Theodore Vorburger,
Assistant Treasurer and Comptroller
Ruth F. Bryans,
Publication Manager
Betty H. Goodfriend,
Assistant Secretary
Eileen B. Neuberger,
Circulation Manager

The Journal of Applied Physics, published monthly at Prince and Lemon Sts., Lancaster, Pa., is devoted to physics in its role as the science basic to other natural sciences and to the arts and industries. Previous to 1937 this publication was known as Physics. The Journal of Applied Physics publishes editorials and reviews, as well as technical papers of applied physics. Articles appearing in it are indexed regularly, according to their field, by Physics Abstracts, Chemical Abstracts, Engineering Index, Inc., Industrial Arts Index, etc.

Manuscripts should be submitted to Elmer Hutchisson, Editor, Case Institute of Technology, Cleveland 6, Ohio. Unless otherwise stated, submission of a manuscript is a representation that it has been neither copyrighted, published, nor submitted for publication elsewhere. The authors' institutions are requested to pay a **publication charge** of $8 per page which, if honored, entitles them to 100 reprints without further charge. Instructions will be sent with galley proofs.

Subscriptions, renewals, and orders for back numbers should be addressed to the American Institute of Physics, 57 East 55 Street, New York 22, New York.

Subscription Price	U.S. and Canada	Elsewhere
To members and associate members of the American Institute of Physics	$10.00	$11.00
To all others	12.00	13.00

Back Number Prices

Yearly back number rate when complete year is available: $10.00. Single copies: $1.00 each.

Changes of address should be sent to the American Institute of Physics; **corrected proofs** should be sent to the Publication Manager, American Institute of Physics. **Advertising rates** supplied on request. Orders, advertising copy, and cuts should be sent to the American Institute of Physics.

Entered as second class matter January 22, 1937, at the Post Office at Lancaster, Pennsylvania, under the Act of March 3, 1879. Accepted for mailing at the special rate of postage provided for in paragraph (d-2), section 34.40, P. L. & R. of 1948, authorized May 2, 1932.

Journal
of
Applied Physics

Volume 21, Number 12 December, 1950

Electron Microscopy of Wet Biological Tissues by Replica Techniques*

IRWIN W. FISCHBEIN
School of Forestry, University of California, Berkeley, California
(Received April 20, 1950)

The study of wet biological tissues *in situ* using the electron microscope was made possible by modifying existing replica techniques and developing a new wet replication method. The shortcomings of existing replica techniques are discussed and the modifications necessitated are described.

Replicas of wet tissues were produced in extremely thin polystyrene films which could be observed directly in the electron microscope; however, superior results were obtained by preparing silica replicas from the replicated polystyrene films. A modified two-replica silica method proved satisfactory but the three-replica silica method developed was preferable. Electron micrographs of wet wood fiber surfaces used to illustrate these techniques reveal new data concerning submicroscopic cell wall structure.

The problem of interpreting replicas of partially degraded and disorganized materials is illustrated and discussed briefly.

INTRODUCTION

THE successful application of a replica method for the electron microscopy of wet biological structures has not been reported although several replica techniques for dry organic materials have been described.[1–4] While some features of cell wall organization have been revealed by the application of replica methods to dry plant fibers, results in general have been quite unsatisfactory.[1,2] This was the experience in the present study after a survey of existing replica techniques. Failure to obtain satisfactory replicas was attributed in part to the plant tissue being thoroughly dry before embedding took place because plant cell walls are saturated with water in the natural state. Furthermore, it was reasoned that micellar systems in the swollen state would reveal more of their submicroscopic structural arrangement since the microinterstices are distended with water. Therefore, it was necessary to develop an effective wet replication method and at the same time to modify certain aspects of existing replica techniques.

SHORTCOMINGS OF EXISTING REPLICA TECHNIQUES

Gold-shadowed replicas of dry wood fiber surfaces formed by embedding with heat and pressure in thin polystyrene films,[3] or by casting thin films from Collodion[4] and Formvar[5] solutions, failed to show adequate fine structure and contrast. The exact reason for the thin-film replicas failing to show the desired fine structure and contrast is not clear. It may be due in part to improper gold-shadowing technique since varying the thin-film thickness did not affect the contrast conditions.

Because of the excellent contrast generally obtainable with silica replicas, the low pressure silica replica method developed by Barnes, Burton and Scott for the study of organic surfaces was tried.[1] In applying this method, the tissue surface was completely desiccated before replication took place. In addition, excessive destruction of the silica replica occurred during the washing procedure. This probably resulted from the prolonged and vigorous washing necessary for the complete dissolution of the 1-mil polystyrene film specified in the method. In the cases where intact replica film areas were obtained and observed in the electron microscope, the silica replicas failed to show

* From a Ph.D. dissertation submitted in Biophysics at the University of California (January, 1950).

[1] Barnes, Burton, and Scott, J. App. Phys. **16**, 730 (1945).

[2] S. F. Kern, J. Polymer Sci. **1**, 259 (1946).

[3] M. Swerdlow and G. S. Seeman, Bur. Standards J. Res. **41**, 231 (1948), RP1921.

[4] C. W. Hock, Textile Res. J. **18**, 366 (1948).

[5] V. J. Schaefer, J. App. Phys. **13**, 427 (1942).

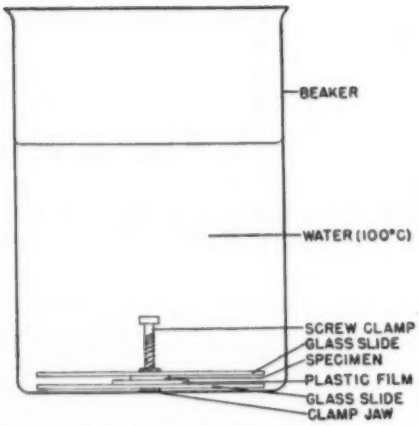

FIG. 1. Sandwiched replica unit with pressure applied submerged in a beaker of hot distilled water for wet replication.

the degree of fine structure to be expected but the contrast conditions were excellent.

The problem of desiccation of the specimen during replication was obviated by the introduction of a new wet replication method. The excessive destruction of the silica replicas during washing was circumvented by the use of extremely thin polystyrene films in the washing procedure and by the introduction of a different solvent and washing apparatus.

Certain shortcomings of the modified two-replica silica method developed in this study were overcome by the use of a third replica. The resulting three-replica silica method was found to be superior from the standpoint of ease of manipulation and of revealing fine structure.

THE WET REPLICATION METHOD

Satisfactory replicas of wood microtome sections, wood fibers, cambial cells and bacterial cells in the wet state were obtained by the following method:

1. The wet object to be replicated is placed on the replicating plastic which is sandwiched between two clean glass microscope slides. A few drops of distilled water are placed on the object before applying the upper glass slide.

2. Pressure is applied directly over the object by means of a medium-sized pinch clamp or Hoffman screw clamp.

3. The sandwiched unit with the pressure applied is completely submerged in a beaker of distilled water at 100°C. (See Fig. 1.) The correct amount of pressure to be applied by the screw clamp is readily attainable in a few trials. When too much pressure is applied, the glass slides crack during heating. The correct pressure is slightly less than that which will cause the glass slides to crack. If a medium-sized pinch clamp is used, this problem does not arise; however, the screw clamp is much easier to manipulate and gives more uniform pressure. The unit remains in the boiling water for approximately 7 minutes when polystyrene or polyethylene are the replicating plastics. The unit is then removed and allowed to cool to room temperature before releasing the pressure clamp.

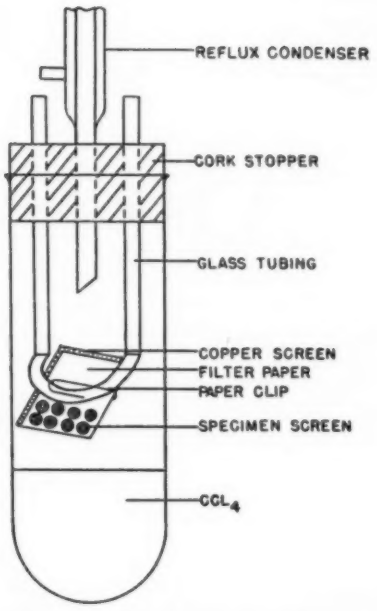

FIG. 2. Apparatus used to wash the polystyrene film from the silica replicas by solvent condensation.

4. The object is allowed to dry and is removed from the plastic replica by mechanical stripping with a tweezer or with a readily adhering pressure sensitive tape.

Although only the use of polystyrene and polyethylene are described in this paper for the initial replica, any plastic with a similar softening point and resistance to water absorption could be used.

A thin-film polystyrene replica made by the wet method in a polystyrene film cast on a glass slide from a 1 percent polystyrene solution in benzene showed more fine structure when gold-shadowed than one made by the dry method. However, the contrast and fine structure observed were much less than that obtainable by the silica methods.

MODIFIED TWO-REPLICA SILICA METHOD

The standard two-replica silica method[6] was modified in the following manner in order to obtain satisfactory silica replicas of wet tissues:

1. An extremely tenuous film is obtained on a clean glass microscope slide by dipping the slide into a 1 percent solution of polystyrene in benzene and allowing the slide to dry while held in a vertical position on a piece of paper toweling. A replica is produced in this thin film by the wet replication method.

2. The thin-film replica is cut into $\frac{1}{8}$-inch squares on the microscope slide with a scalpel or sharp knife and the replica squares are floated from the slide onto a

[6] C. H. Gerould, J. App. Phys. 18, 333 (1947).

water surface by slowly inserting the glass slide at a low angle into a dish of distilled water. The floating replica squares are lifted from the water surface by raising the specimen screens up under them. The specimen screens are then placed on a piece of paper toweling so that the polystyrene film will be pulled down tight and flat on the screen as the water is imbibed by the paper. These thin-film replicas are ready for silica evaporation. (If it is desired, a suitable metal such as gold, chromium, or uranium can be used to shadowcast this replica[7] which can then be observed directly in the electron microscope.)

3. The thin-film replicas mounted on specimen screens are placed in a high vacuum chamber directly above a tightly wound 15° cone-shaped coil filament of 20-mil tungsten wire for silica evaporation. The turns of the tungsten coil must be close together to prevent excess evaporation of the silica through the sides and bottom of the coil. The quantity of silica (2–3 mg) to be evaporated can be conveniently measured into the coil with a micropipette calibrated to deliver the correct volume of Ludox.† The specimen screens are supported in the inverted position above the coil with a piece of transparent cellulose adhesive tape mounted on a glass slide with the adhesive side exposed. Specimen screens readily stick to the tape when pressed lightly against the adhesive surface with a forceps. Transparent adhesive tape used in this manner is a convenient way to carry, catalogue, and store finished specimen screens.

4. After silica evaporation, the double replica mounted on the specimen screen is placed in the washing apparatus shown in Fig. 2. The specimen screens rest on the filter paper square (Whatman No. 1) and are washed gently in a liquid film formed by the condensing vapors after the filter paper is saturated. The washing time and rate are determined empirically and the heating is accomplished by means of a water bath. Only the solvent vapors which condense on the water-cooled glass condensing tube wet the filter paper. The reflux condenser is placed in the system to prevent the danger of a closed system.

After the washing schedule has been established, many finished specimen screens contain a large number of squares covered by the clean intact silica replicas. Carbon tetrachloride was superior to ethyl bromide as the washing agent in this apparatus. This may be due to the fact that carbon tetrachloride does not swell the polystyrene before dissolving it and that the washing can be more readily controlled because carbon tetrachloride is not as volatile as ethyl bromide. After the washing is completed, the filter paper is allowed to dry before the specimen screens are removed to be placed on the adhesive-taped glass slides. These clean silica replicas are ready for observation in the electron microscope.

[7] R. C. Williams and R. C. Backus, J. App. Phys. **20**, 98 (1949).
† Ludox, 30 percent colloidal silica solution in water. Technical Grade. DuPont de Nemours Company, Baltimore, Md.

The completely clean silica replicas prepared in this manner do not display the fragility reported by Heinmets.[8] They can be observed at maximum intensities in the RCA Type EMB and EMU scopes without excessive destruction. However, since the silica films are extremely thin, maximum intensities are not necessary for careful examination. Figure 3 shows a silica replica, made in this manner, of the lumen wall surface of a tracheid of ponderosa pine which has been partially disrupted by drastic chemical treatment. Distinct fibrils which have resulted from this chemical action can be seen grading down to the limit of resolution of the instrument.

Although this method is entirely satisfactory as far as the structures revealed are concerned, the manipulation of thin-film replicas formed by pressure embedding is quite difficult. Many excellent areas are repeatedly lost during the removal of the replicated object from the thin-film polystyrene and also when the thin-film squares are floated onto the water surface. Furthermore, uniform embedding in the thin polystyrene film is very difficult because the film cast from the 1 percent solution is extremely tenuous. The result of this is that the areas most deeply embedded and, therefore, best

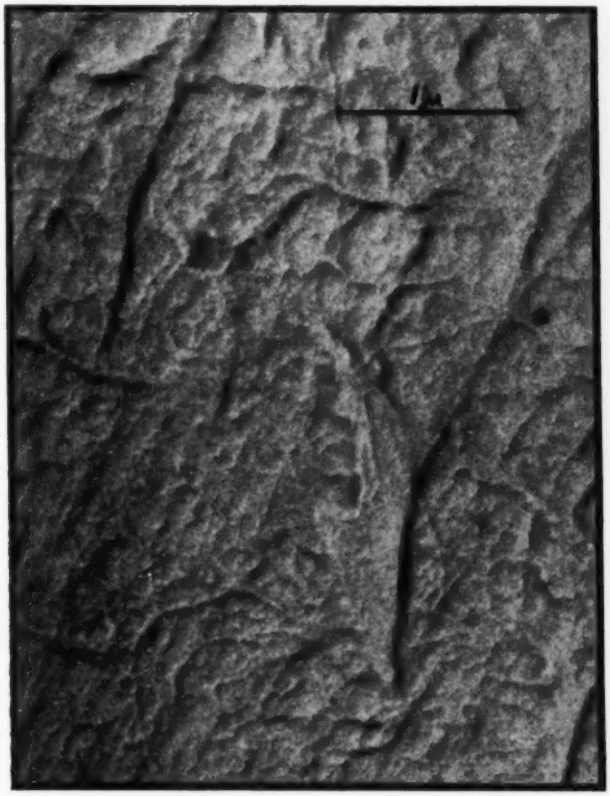

FIG. 3. Surface of the inner layer of the secondary wall of a ponderosa pine fiber after vigorous chemical treatment, showing disorganization of the fibrillar orientation. Silica replica made by the modified two-replica silica method in which the first step is a polystyrene replica of the wet tissue. ×24,000.

[8] F. Heinmets, J. App. Phys. **20**, 384 (1949).

for revealing fine structure are also the most fragile. In an effort to overcome these difficulties, another method was developed in which an extra replication step was introduced. This resulted in simpler, surer manipulation and in a deeper replica of better contrast.

THE THREE-REPLICA SILICA METHOD

The three-replica silica method is a combination of the advantages of a deep replica with adequate embedding and a uniform thin-film replica with ease in washing away the polystyrene.

The steps in the preparation of the final silica replica are as follows:

1. A 4-mils thick film of polyethylene 1-inch square is used for the initial replica, with the wet object replicated in the manner described under the wet replication method.

2. The polyethylene film, after the object has been replicated, is glued to a glass slide with ordinary mucilage. After the mucilage has dried, the object is removed from the polyethylene by teasing it out with tweezers or by stripping it with pressure sensitive tape.

3. The slide with the replicated polyethylene glued to it is immersed in a coplin jar of a 1 percent solution of polystyrene in benzene. The solution is allowed to dry while the slide is held in a vertical position on a piece of paper toweling. This produces a thin, uniform polystyrene film on the replicated polyethylene sheet.

4. The thin-film polystyrene replica is stripped from the polyethylene replica by backing the polystyrene with a thick layer of a 20 percent solution of gelatin in water.[9] After the gelatin has dried, the thin-film polystyrene replica is removed with the gelatin when it is flaked off.

5. The gelatin with the thin polystyrene replica adhering to it is cut into $\frac{1}{8}$-inch squares which are placed gelatin side down into a Syracuse watch glass of hot distilled water. The gelatin dissolves, leaving the small replica squares floating on the water surface with the replica side up. These are then transferred to a large dish of distilled water by means of a piece of 80-mesh screen.

6. The thin-film replicas are lifted from the water surface on the specimen screens which are placed on a piece of paper toweling and allowed to dry. The dry replicas are placed in the vacuum chamber for silica evaporation.

7. The polystyrene is removed by reflux washing in the washing apparatus, and the clean silica films on the specimen screens are ready for electron microscopy.

An example of the results obtainable by this method is shown in Fig. 4 which is a replica of the inner layer of the secondary wall of a redwood tracheid. The low slope of fibrillar orientation of this layer of the wall adjoining the lumen is clearly discernible. This condition of low fibrillar slope in the inner layer of the secondary wall has been observed in all normal coniferous tracheids examined and although this condition had been previously postulated, this is the first time it has been directly demonstrated.

An area from Fig. 4 is shown in Fig. 5 at a higher magnification which makes visible markings on the fibrils. These markings which appear at approximately right angles to the direction of fibrillar orientation may be the result of an alternation of areas with diminishing and increasing crystallinity. The protuberances appearing along the oriented ridges are not necessarily perfect crystalline aggregates. Rather, they can be areas with a greater degree of crystallinity than the intervening areas. If this is the case, it would support the theory put forth by Roseveare and coworkers[10] suggesting that a mechanism exists in crystallizing high polymeric systems for the systematic arrangement of the crystalline aggregates to produce a super-lattice of crystallites. This would explain the fact that in fibrillar cellulose systems planes of weakness are found to exist at right angles to the prevailing direction of fibrillar orientation.[11] The redwood microtome section from which this replica was made was not treated chemically and this is

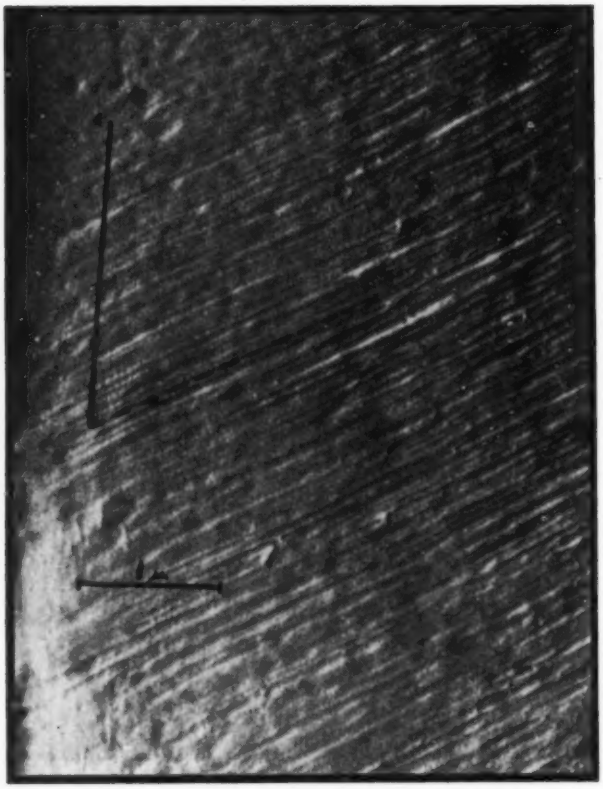

FIG. 4. Surface of the inner layer of the secondary wall of a redwood tracheid without any previous chemical treatment, showing the low slope of fibrillar orientation. The solid line denotes the fiber axis; the dashed line indicates the fibril axis. Silica replica made by the three-replica silica method in which the first step is a polyethylene replica of the wet tissue. ×18,500.

[9] V. J. Schaefer, Phys. Rev. **63**, 495 (1942).
[10] Roseveare, Waller, and Wilson, Textile Res. J. **18**, 114 (1948).
[11] I. W. Bailey, Bull. Torrey Bot. Club **66**, 201 (1939).

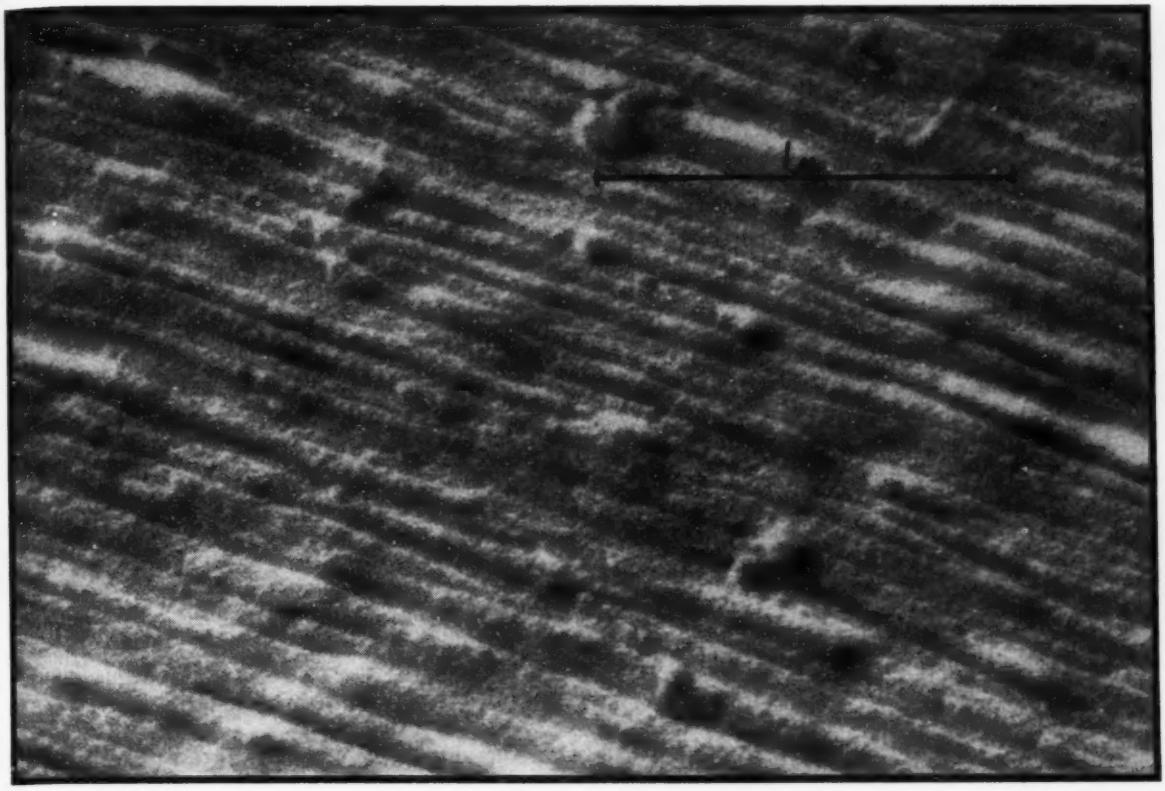

FIG. 5. An area from Fig. 4 highly magnified (×55,000), showing distinct markings on the fibrils.

the first time an unaltered, water-saturated plant fiber wall has been shown by means of the electron microscope.

A replica of a cross section of the walls of ponderosa pine tracheids is shown in Fig. 6. This cross section (20-microns thick) was partially delignified by a holocellulose method before replication took place. The light places in the cross section are areas where lignin has been removed. The striae crossing the wall are due to knife tears produced during sectioning. The middle lamella region consists of the light colored irregular areas, where maximum lignin removal has occurred, separating the walls of adjacent cells.

At the beginning of this study it was assumed that a direct replica method in which the initial replica would be observed in the electron microscope would be preferable to any method in which additional replicas were introduced before the final replica for observation. However, this assumption proved to be incorrect and the three-replica silica method is unquestionably preferable to any other method attempted in this study. Although the three-replica silica method appears to be quite complicated, it is actually possible for an experienced technician to produce a large number of excellent silica replicas in a relatively short time. For example, in this study as many as 50 specimen screens with a large number of observable areas of intact silica replicas could be prepared in a 2-day period.

FIG. 6. Cross section of the walls of partially delignified ponderosa pine fibers. Portions of the walls and lumina of three adjoining cells is shown. Silica replica produced by the three-replica silica method. ×4500.

FIG. 7. Bordered pit of ponderosa pine fiber which has undergone drastic chemical treatment showing fibrils reoriented radially around the pit aperture by the replicating procedure. Silica replica produced by the three-replica silica method. ×4000.

FIG. 8. Bordered pit of ponderosa pine fiber which has undergone very mild chemical treatment showing the true circular fibrillar orientation of the cellulose around the pit aperture. Silica replica produced by the three-replica silica method. ×10,000.

Using the three-replica silica method, it has been possible to use the electron microscope to study the submicroscopic structural relationships of the layers and markings of the secondary cell wall of coniferous tracheids. A later paper will discuss the results of this study.

INTERPRETATION OF REPLICAS

The interpretation of replicas of partially degraded and disorganized materials is a serious problem. In Fig. 7 is shown a replica of a bordered pit in the outer layer of the secondary wall of a fiber produced by a drastic maceration method. Fibrils with an apparent radial orientation around the pit aperture can be seen. These radially oriented fibrils were pulled into this position during the replication process. This interpretation is correct since the bordered pit in this same layer from a replica of a fiber produced by a mild maceration method shown in Fig. 8 displays circular rather than radial orientation around the pit aperture. This is in agreement with the accepted interpretation of bordered pit structure in this layer.

Loosely aggregated substances can be disorganized and reoriented by replicating pressures and, therefore, replicas of such materials should be interpreted with caution.

The author is indebted to Dr. Robert A. Cockrell of the School of Forestry and to Dr. William N. Takahashi of the College of Agriculture, University of California, for their helpful suggestions during the course of the study.

Magneto-Ionic Triple Splitting of Ionospheric Waves

O. E. H. Rydbeck
Research Laboratory of Electronics, Chalmers University of Technology, Gothenburg, Sweden
(Received November 28, 1949)

In recent years reports have appeared from various ionospheric observatories concerning the appearance of a third magneto-ionic component or a so-called z trace. The phenomenon has also been called magneto-ionic triple splitting. After having recorded a number of such triple splits at the new Kiruna observatory, we became very interested in the problem as a whole. The entire matter was examined theoretically and as a result it has been possible to show that strong coupling often exists between the ordinary and z components as a critical level. It has further been possible to show that the z wave becomes strongly excited when the collisional frequency ν approaches the critical collisional frequency ν_c of Appleton and Builder. When ν is larger than ν_c the o echo rapidly disappears and only the z and x components remain (if ν_c is sufficiently small, *i.e.* at very high latitudes). A useful expression for the transmission coefficient of the $o-z$ wave has been derived.

INTRODUCTION

TRIPLE splitting of ionospheric waves or rays was reported in 1933 by Eckersley.[1] A few years later, in 1935 and 1936, Toshniwal[2] and Harang[3] reported similar phenomena. This interesting matter did not attract much attention until after the war the chain of recording ionospheric observatories had been greatly increased. According to Meek,[4] triple splitting was observed in Canada in 1943 when the Churchill ionosphere station commenced operation. Since then the phenomenon was observed frequently at other Canadian stations as well. In Hobart, Tasmania, in 1946, Newstead observed F_2 triple splitting.[5] Seaton, reporting from College, Alaska, in 1947, presents a record of F_2 triple splitting[6] and discusses the possible mechanism of excitation of the third or z component of the downcoming wave. Further, Gipps, Gipps, and Venton at Brisbane[7] as late as August, 1948 describe a ray trace which appears to have the characteristics of the z component. It is significant that all the reports mentioned come from places of high or fairly high geomagnetic latitude.

At the Kiruna Ionospheric and Wave Propagation Observatory, which started regular recording on October 1, 1948,[8] a large number of triple splits have been recorded both in the E and the F regions. As far as is known to us, E triple splitting has only been reported earlier by Meek.[4] The fairly frequent occurrence of ionospheric triple splitting at Kiruna has made us particularly interested in the phenomenon. The purpose of the present note is to make a preliminary investigation of the excitation and properties of this interesting z component of the wave.

THEORETICAL CONSIDERATIONS

In his treatise, "On the propagation of radio waves,"[9] the author has described the coupled wave equations governing the propagation of the ordinary and extraordinary waves in a plane inhomogeneous ionosphere. With the symbols used in that work[9] and the assumption that the electron density varies in the phase propagation or z direction only these equations become

$$\frac{d^2\Pi_1}{dz^2}+(k_0^2\epsilon_1+\psi^2)\Pi_1=-\pi_2\frac{d\psi}{dz}-2\frac{d\Pi_2}{dz}\cdot\psi, \qquad (1)$$

$$\frac{d^2\Pi_2}{dz^2}+(k_0^2\epsilon_2+\psi^2)\Pi_2=-\pi_1\frac{d\psi}{dz}-2\frac{d\Pi_1}{dz}\cdot\psi. \qquad (2)$$

The values of ϵ_1 and ϵ_2 are given by the Appleton-Hartree formula,[10] $k_0=2\pi/\lambda_0$ (where λ_0 is the vacuum wave-length), and ψ is a coupling coefficient. One further has (if the time factor is $e^{-j\omega t}$)

$$\psi=-\frac{j}{2}\cdot\frac{d(v^2)}{dz}\cdot\frac{\delta_c}{(v^2-ja_1)(v^2+ja_2)}, \qquad (3)$$

with

$$\left.\begin{aligned}a_1&=\delta_c+\delta,\\ \text{and}\qquad a_2&=\delta_c-\delta.\end{aligned}\right\} \qquad (4)$$

In these formulas

$$\delta=\nu/\omega, \qquad (5)$$

where ν is the frequency of collision and $\omega=2\pi\cdot f$, the wave angular frequency, is a loss angle measure of the medium. The critical loss angle is

$$\delta_c=\nu_c/\omega, \qquad (6)$$

where ν_c is the critical collisional frequency of Appleton-

[1] T. L. Eckersley, "Discussion of the ionosphere," Proc. Roy. Soc. **A141**, 710 (1933).
[2] G. R. Toshniwal, "Threefold magneto-ionic splitting of the radio echoes reflected from the ionosphere," Nature **135**, 471 (1935).
[3] L. Harang, "Vertical movements of air in the upper atmosphere," Terr. Mag. and Atmos. Elec. **41**, 160 (1936).
[4] J. H. Meek, "Triple splitting of ionospheric rays," Nature **161**, 597 (1948).
[5] G. Newstead, "Triple magneto ionic splitting of rays reflected from the F_2 region," Nature **161**, 312 (1948).
[6] S. L. Seaton, "Magnetoionic multiple refraction at high latitudes," Proc. I.R.E. **36**, 450 (1948).
[7] Gipps, Gipps, and Venton, "Note on night-time phenomena in the F_2 region at Brisbane," J. Council Sci. Ind. Research **21**, 215 (1948).
[8] O. E. H. Rydbeck, "The Ionospheric and Radio Wave Propagation Observatory at Kiruna, 67°50′ N, 20°14.5′ E," Tellus **1**, No. 4 (1949).
[9] O. E. H. Rydbeck, 1944. "On the propagation of radio waves," Trans. Chalmers University of Technology, No. 34.
[10] E. V. Appleton, "Wireless studies of the ionosphere," Inst. Elec. Eng. **71** (1932).

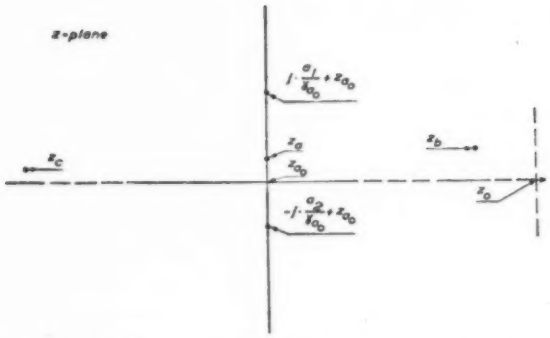

FIG. 1. Showing the location of the zero of n^2 and the poles of ψ in the z plane.

Builder,[11] *viz.*,

$$\nu_c = \tfrac{1}{2} \cdot (\sin^2\theta/\cos\theta) \cdot \omega_H, \tag{7}$$

and θ is the angle between the z axis and the direction of the terrestrial magnetic field. Further $\omega_H = 2\pi \cdot f_H$ is the angular frequency of gyration of the free electron in this field, and

$$\nu^2 = (\omega_c^2/\omega^2) - 1, \tag{8}$$

where ω_c is the ordinary wave critical angular frequency of the electron density level in question. For a parabolic layer formed between $z = z_0 - \Delta h$ and $z = z_0 + \Delta h$, for example, one would have

$$\omega_c^2 = \omega_{cm}^2\{1 - [(z - z_0)/\Delta h]^2\}, \tag{9}$$

where ω_{cm} is the ordinary wave critical angular frequency of the layer.

In the wave equations (1) and (2) we assume that index (1) denotes the ordinary or o component and index (2) the "unusual" z component.

For the unperturbed o wave functions we use the following approximations*

$$\Pi_1^{0(1)} = (\pi W_1/2n_1)^{\frac{1}{2}} \exp(\pm j\pi/6) \cdot H_{1/3}^{(2)}(W_1), \tag{10}$$

where $n_1 = (\epsilon_1)^{\frac{1}{2}}$ is the index of refraction of the o mode and W_1 the phase integral

$$W_1 = \int_{z_a}^{z} k_0 n_1 dz = W_1(z_a, z). \tag{11}$$

It is important to note that z_a is the location of the zero of ϵ_1, i.e., the branch point of n_1. When we have losses, this point (or points) lie in the complex z plane.

Assuming that to the left of the layer $n_1 = e^{-j\pi}$, $\Pi_1^{0(1)}$ apparently represents a wave incident upon the layer. Neglecting the possible formation of a z wave we see that the coefficient of reflection, at the lower boundary $z_0 - \Delta h$, becomes

$$R \cong \exp[j \cdot 2\{W_1(z_a, z_0 - \Delta h) - \pi/4\}] \tag{12}$$

if the layer is not very thin and $\omega \neq \omega_{cm}$.

For the unperturbed z wave functions we use similar wave functions denoted $\Pi_2^{0(1)}$ with

$$W_2 = \int_{z_b}^{z} k_0 n_2 dz = W_2(z_b, z), \tag{13}$$

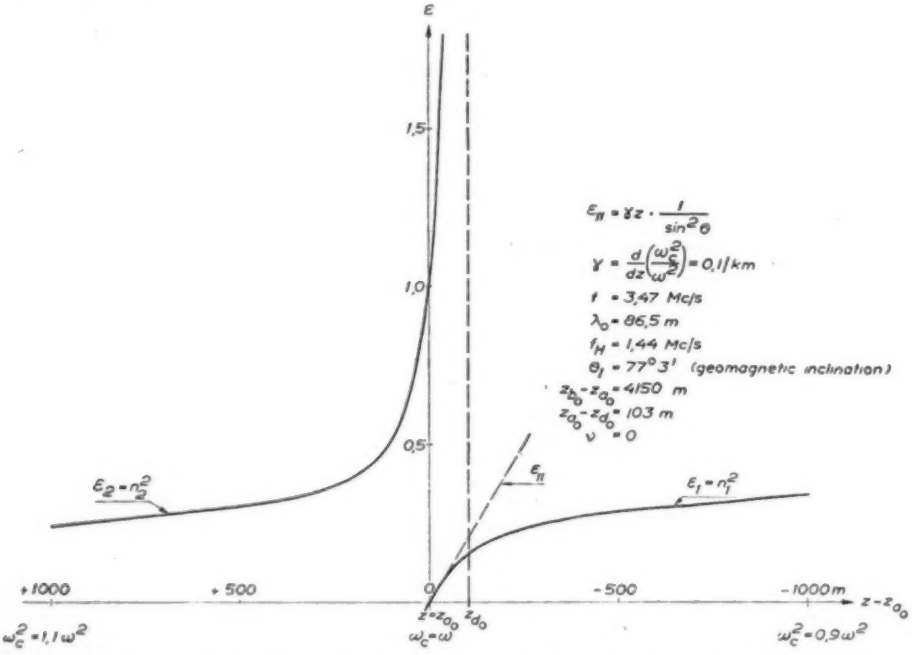

FIG. 2. Index of refraction in the neighborhood of $\omega_c = \omega$ when $\nu = 0$. *Note.* $|\epsilon_2| = \infty$ for $z = z_d$, at which point (branch point of Rai)

$$\frac{\omega_c^2}{\omega^2} = \frac{1 + j\delta}{1 + \dfrac{y^2 \sin^2\theta}{(1 + j\delta)^2 - y^2}}.$$

[11] E. V. Appleton and G. Builder, "The ionosphere as a doubly refracting medium," Proc. Phys. Soc. **45** (1933).

* Generally sufficiently accurate except in the neighborhood of a second zero of ϵ_1. When two zeros come very close (not of immediate interest in this connection) parabolic wave functions have to be used. See O. E. H. Rydbeck, "On the propagation of waves in an inhomogeneous medium," Report No. 7 from the Research Laboratory of Electronics. Trans. Chalmers University of Technology **74**, 23 (1948).

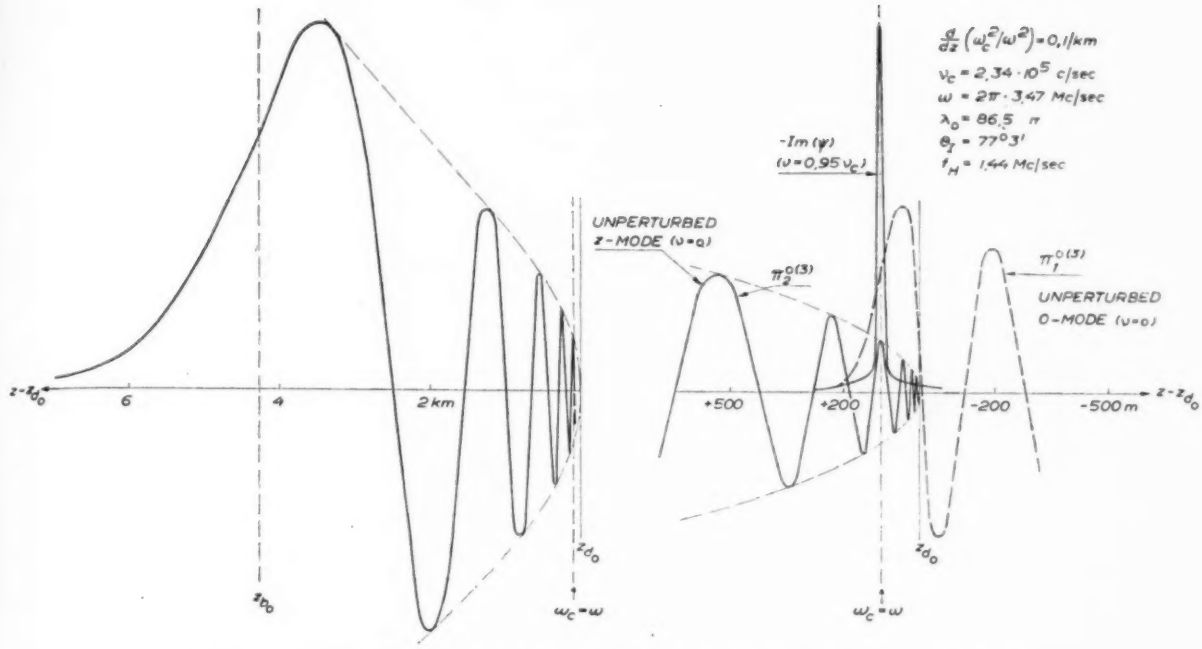

FIG. 3. The coupling coefficient and the unperturbed wave functions in the interaction region.

where z_b is the position of the appropriate ϵ_2 zero. A fundamental question apparently is to study the behavior of n_1 and n_2 in the z plane. To this question we will return briefly after first having studied the nature of the coupling coefficient.

Denoting by $z=z_{a0}$ the interaction level where $\omega_c^2=\omega^2$ (also branch point of n_1 when $\nu=0$), we use the following approximation in the neighborhood of this level, *viz.*,

$$v^2=\left\{\frac{d}{dz}\left(\frac{\omega_c^2}{\omega^2}\right)\right\}_{z_{a0}}(z-z_{a0})=\gamma_{a0}(z-z_{a0}). \tag{14}$$

Under these circumstances we have

$$\psi=-\frac{j}{2}\cdot\frac{\delta_c/\gamma_{a0}}{\{(z-z_{a0})-ja_1/\gamma_{a0}\}\{(z-z_{a0})+ja_2/\gamma_{a0}\}}. \tag{15}$$

It is extremely interesting, from an interaction point of view to find, that

$$\int_{-\infty}^{+\infty}\psi dz=\begin{cases}0, & \nu>\nu_c\\ -j\pi/2, & \nu<\nu_c\end{cases}. \tag{16}$$

Returning now to the question of the refractive index, we find it convenient to use the following form of the Appleton-Hartree formula, *viz.*,

$$n_1^2=1-\frac{(v^2+1)(-v^2+j\delta)}{(1+j\delta)(-v^2+j\delta)-\cos\theta\cdot y\{\delta_c^2+(-v^2+j\delta)^2\}^{\frac{1}{2}}}. \tag{17}$$

One easily verifies that n_1^2 is zero for $v^2=j\delta$, and n_2^2 zero for $v^2=\pm y+j\delta$, where $y=\omega_H/\omega$. Thus, even considering the losses the zeros of n_1^2 and n_2^2 are independent of θ.

Denoting by z_c the position of the n_2^2 zero corresponding to $v^2=-y+j\delta$, we find for the parabolic layer

$$z_a\cong z_0-\Delta h\left[1-\left(\frac{\omega}{\omega_{cm}}\right)^2\right]^{\frac{1}{2}}+j\frac{\delta\cdot\Delta h}{2}\cdot\frac{\omega/\omega_{cm}}{[(\omega_{cm}/\omega)^2-1]^{\frac{1}{2}}}(\omega^2<\omega_{cm}^2), \tag{18a}$$

$$z_b\cong z_0-\Delta h\left[1-\left(\frac{\omega}{\omega_{cmz}}\right)^2\right]^{\frac{1}{2}}+j\cdot\frac{\delta\Delta h}{2}\cdot\frac{\omega^2/\omega_{cm}^2}{[1-(\omega/\omega_{cmz})^2]^{\frac{1}{2}}}\quad[\omega^2<\omega_{cmz}^2=\omega_{cm}^2/(1+y)], \tag{18b}$$

and

$$z_c\cong z_0-\Delta h[1-(\omega/\omega_{cmz})^2]^{\frac{1}{2}}+j\frac{\delta\Delta h}{2}\cdot\frac{\omega^2/\omega_{cm}^2}{[1-(\omega/\omega_{cmz})^2]^{\frac{1}{2}}}\quad[\omega^2<\omega_{cmz}^2=\omega_{cm}^2/(1-y)]. \tag{18c}$$

Thus,

$$\mathrm{Im}(z_b)>\mathrm{Im}(z_a)>\mathrm{Im}(z_c).$$

It is especially interesting to find that

$$\mathrm{Im}(z_a)=(a_1-a_2)/2\gamma_{a0}, \tag{19}$$

$$\frac{1}{\gamma_{a0}}=\frac{\Delta h}{2}\cdot\frac{\omega/\omega_{cm}}{[\omega_{cm}^2/\omega^2-1]^{\frac{1}{2}}}.$$

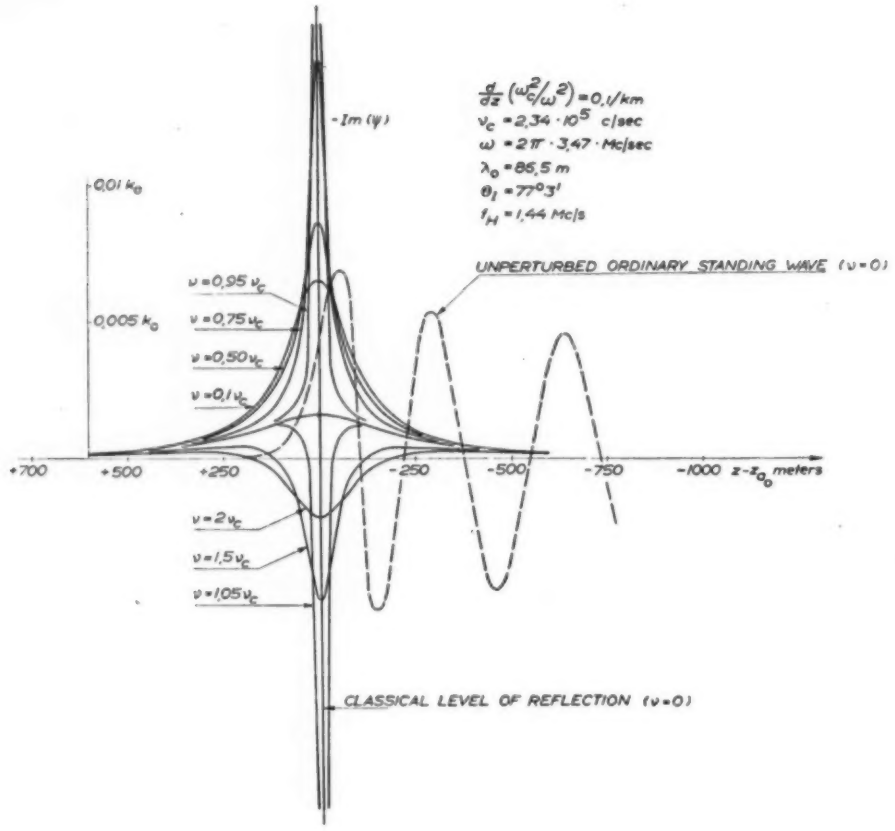

FIG. 4. Demonstrating the nature of $-\mathrm{Im}(\psi)$.

As $\mathrm{Re}(z_a)=z_{a0}$ this means that the zero of n_1^2 is located midway between the poles $ja_1/\gamma_{a0}+z_{a0}$ and $-ja_2/\gamma_{a0}+z_{a0}$ of ψ. The situation is depicted in Fig. 1.

It is further interesting to note that

$$(n_2)_{z=z_a}=1 \tag{20}$$

and that at the poles $n_1=n_2$.

We have in Fig. 2 plotted the variation of ϵ_1 and ϵ_2 for $\nu=0$, a normal electron density gradient and geomagnetic conditions of the Kiruna observatory. The unperturbed standing wave functions,

$$\Pi_1^{0(3)}=\Pi_1^{0(1)}+\Pi_1^{0(2)} \quad \text{and} \quad \Pi_2^{0(3)}=\Pi_2^{0(1)}+\Pi_2^{0(2)},$$

corresponding to these ϵ-variations are shown in Fig. 3 for $\nu=0$ together with $-\mathrm{Im}(\psi)$ for $\nu=0.95\nu_c$. This figure demonstrates that the coupling actually takes place within a very narrow region of a few hundred meters effective extension.

It is of particular interest in this connexion to demonstrate the peculiar nature of ψ for various ν-values. The variation of the important component $-\mathrm{Im}(\psi)$ is therefore depicted in Fig. 4 from which it is easy to understand that the "interaction integral" (16) is zero when $\nu>\nu_c$.

Let us next study the first-order approximations to solutions of the excited z waves, running up and down between z_d and z_b. Introducing

$$\xi_1^{(1)}(z)=-\Pi_1^{0(1)}\cdot\frac{d\psi}{dz}-2\cdot\frac{d\Pi_1^{0(1)}}{dz}\cdot\psi, \text{ etc.,} \tag{21}$$

we find the first-order z wave approximations

$$\Pi_2^{(1)}=-\Pi_2^{0(1)}\cdot\frac{1}{w_2^0}\cdot\int_{b_1}^{z}\Pi_2^{0(2)}(\xi_1^{(1)}+\xi_1^{(2)})dz \tag{22}$$

and

$$\Pi_2^{(2)}=\Pi_2^{0(2)}\cdot\frac{1}{w_2^0}\cdot\int_{b_2}^{z}\Pi_2^{0(1)}(\xi_1^{(1)}+\xi_1^{(2)})dz. \tag{23}$$

Here b_1 and b_2 are lower and upper boundaries of the effective interaction region. Further, w_2^0 is the Wronskian of the pair $\Pi_2^{0(1)}$, $\Pi_2^{0(2)}$. With our form of functions $w_2^0=j\cdot2k_0$.

Of practical interest for the moment only is to study $\Pi_2^{(1)}$ when $z>b_2$ and $\Pi_2^{(2)}$ when $z<b_1$, i.e., we are not going to study in detail how the Π_2-functions build up within the interaction zone.

At first sight it appears as if one of the two terms of (21) would complicate the treatments of the interaction integrals (22) and (23). On the contrary one finds, after partial integration, that the presence of both these terms makes it possible to analyze the interaction integrals fairly simply.

We thus find for $z>b_2$:†

$$\Pi_2^{(1)}=-\Pi_2^{0(1)}\cdot\frac{1}{w_2{}^0}\cdot\int_{b_1}^{b_2}\left\{\Pi_1{}^{0(2)}\cdot\Pi_2{}^{0(2)}\left(\frac{\Pi_1{}^{0(2)'}}{\Pi_1{}^{0(2)}}-\frac{\Pi_2{}^{0(2)'}}{\Pi_2{}^{0(2)}}\right)\psi+\Pi_1{}^{0(1)}\cdot\Pi_2{}^{0(2)}\left(\frac{\Pi_1{}^{0(1)'}}{\Pi_1{}^{0(1)}}-\frac{\Pi_2{}^{0(2)'}}{\Pi_2{}^{0(2)}}\right)\psi\right\}dz, \quad (24)$$

and similarly for $z<b_1$

$$\Pi_2^{(2)}=\Pi_2^{0(2)}\cdot\frac{1}{w_2{}^0}\times\int_{b_2}^{b_1}\left\{\Pi_1{}^{0(2)}\cdot\Pi_2{}^{0(1)}\left(\frac{\Pi_1{}^{0(2)'}}{\Pi_1{}^{0(2)}}-\frac{\Pi_2{}^{0(1)'}}{\Pi_2{}^{0(1)}}\right)\psi+\Pi_1{}^{0(1)}\cdot\Pi_2{}^{0(1)}\left(\frac{\Pi_1{}^{0(1)'}}{\Pi_1{}^{0(1)}}-\frac{\Pi_2{}^{0(1)'}}{\Pi_2{}^{0(1)}}\right)\psi\right\}dz. \quad (25)$$

We are of course principally interested in Eq. (24) which yields the amplitude of the wave propagating toward z_b. As far as the interaction integral is concerned replacing b_1 by $-\infty$ and b_2 by $+\infty$ does not appreciably affect its value if b_1 and b_2 are well outside the main interaction zone. We thus write

$$\underset{z>b_1}{\Pi_2^{(1)}}=-\Pi_2^{0(1)}\cdot\frac{1}{w_2{}^0}\cdot J_2^{(1)}(b_1,b_2)\cong-\Pi_2^{0(1)}\cdot\frac{1}{w_2{}^0}\cdot J_2^{(1)}(-\infty,+\infty). \quad (24a)$$

If the path of integration is displaced to encircle the pole z_2 of ψ, it is possible to show that the dominant contribution to $J_2^{(1)}$ actually comes from the pole. This pole also is a branch point of n_1 and n_2 (though not a zero point), and in the first order approximation we may still use the approximate wave functions (10).

We have already mentioned that at the ψ-poles $n_1=n_2$. The distance between the poles and z_a, δ_c/γ_{a0}, is quite large. For the locality in question (Kiruna) $\nu_c\cong 2.1\cdot 10^5$ sec.$^{-1}$ and with the gradient chosen this distance is greater than about 100 meters. The amplitude of W_1 at the poles therefore will be at least of the order 3, the corresponding phase angle with the chosen orientation somewhere between $-\pi/2$ and $-3\pi/4$ at $z_{a0}+j\cdot a_1/\gamma_{a0}$ and between $+\pi/2$ and $+3\pi/4$ at $z_{a0}-ja_2/\gamma_{a0}$. For $W_2[z_{a0},\pm j\cdot(a_2'/\gamma_{a0})+z_{a0}]$ the amplitude is about three times as large with phase angles approximately $\mp\pi/2$. We can therefore use the asymp-

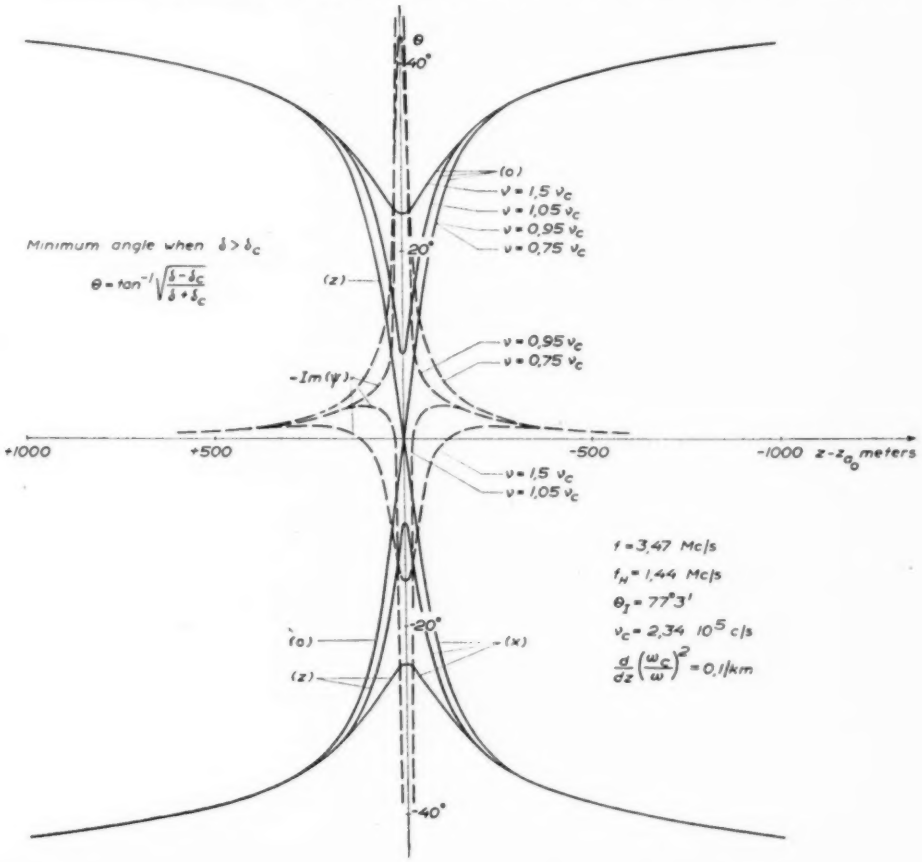

FIG. 5. Depicting the variation in polarization in the coupling region.

† *Note.* $\Pi_1{}^{0(2)'}=d\Pi_1{}^{0(2)}/dz$, etc.

totic representation of the Hankel functions at the poles and as there $n_1=n_2$ we infer that the first term of $J_2^{(1)}$ practically disappears (the parenthesis tends to zero). Moreover, $|\Pi_1^{0(2)}|\ll|\Pi_1^{0(1)}|$ at the lower pole. It can therefore safely be said that the first term of $J_2^{(1)}$ does not contribute to its value. We have thus shown that only the "incident" wave function produces the z wave proceeding in the same direction. This is only virtual as the $\Pi_1^{0(2)}$ function must be present to make the integral converge over the path. Also from a physical point of view $\Pi_1^{0(1)}$ cannot be present without $\Pi_1^{0(2)}$.

For the $\Pi_2^{(2)}$-component the result is similar. This time, however, we have to evaluate the residue at $z_{a0}+j\cdot a_1/\gamma_{a0}$ as the wave function products are bounded only in the upper half-plane. Virtually only the "reflected" wave function $\Pi_1^{0(2)}$ contributes to the residue and therefore to the $\Pi_2^{(2)}$-component.

As at the pole

$$\frac{\Pi_1^{0(1)\prime}}{\Pi_1^{0(1)}}-\frac{\Pi_2^{0(2)\prime}}{\Pi_2^{0(2)}}\cong 2\cdot jk_0\cdot n_{\text{pole}},$$

we find

$$\underset{z>b_2}{\Pi_2^{(1)}(z)}\cong\Pi_2^{0(1)}\cdot\exp\left[-j\left\{W_1\left(z_{a0},-j\cdot\frac{a_2}{\gamma_{a0}}+z_{a0}\right)-W_2\left(z_{a0},-j\frac{a_2}{\gamma_{a0}}+z_{a0}\right)\right\}\right]\cdot\pi/2\,\exp(-j\pi/2).$$

Actually we should have started with unit amplitude value of the wave incident at $z=z_0-\Delta h$. The $\Pi_1^{0(1)}(z)$ wave function of the interaction integral therefore should have been replaced by $\Pi_1^{0(1)}(z)/\Pi_1^{0(1)}(z_0-\Delta h)$. Denoting the pole positions by z_1 and z_2, respectively, and introducing this scaled-down wave function we find, if $z>b_2$ but $z\neq z_b$ that

$$\Pi_2^{(1)}(z)\cong\frac{\pi}{2}\cdot\frac{1}{(n_2)^{\frac{1}{2}}}\cdot\exp[j\{W_1(z_{a0},z_0-\Delta h)+W_2(z,z_{a0})\}]\cdot\exp[j\{W_2(z_{a0},z_2)-W_1(z_{a0},z_2)-\pi/2\}]. \quad (26)$$

As the first exponential is the straight phase integral up to z (though with exchanged refractive index after the z wave "takes over") we are led to introduce the first order transmission coefficient T^+ of direction into the layer, *viz.*,

$$T^+\cong(\pi/2)\cdot\exp[j\{W_2(z_{a0},z_2)-W_1(z_{a0},z_2)-\pi/2\}]. \quad \nu<\nu_c. \quad (27)$$

As

$$z_2-z_{a0}=-j\frac{\delta_c-\delta}{\gamma_{a0}}=-j\frac{\nu_c-\nu}{\omega}\cdot\frac{\Delta h}{2}\cdot\frac{\omega/\omega_{cm}}{[(\omega_{cm}^2/\omega^2)-1]^{\frac{1}{2}}},$$

we see that as ν approaches ν_c, $|T^+|$ approaches $\pi/2$.

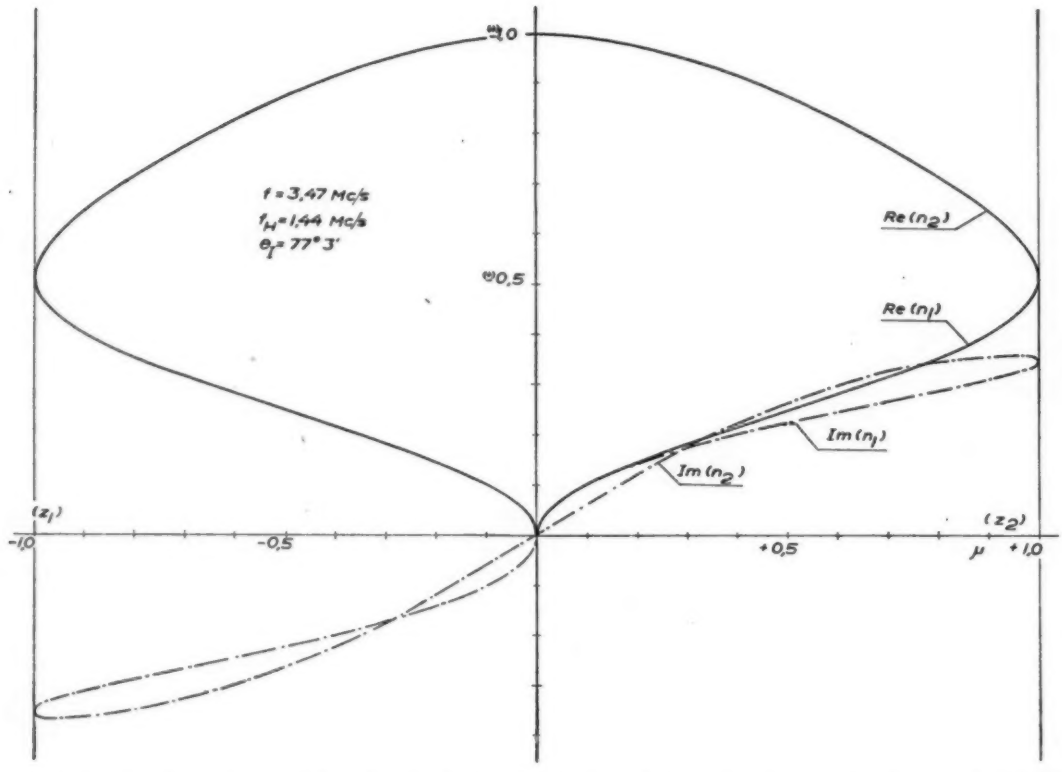

FIG. 6. Showing the variation of the refractive indices for the O^- and Z^- modes along the imaginary axis, joining the ψ-poles Z_1 and Z_2. $[\mu=-(\nu^2-j\delta)/j\delta_c.]$

This indicates very strong coupling, as indeed one would expect. When, namely, ν approaches ν_c the mathematical reflection point, z_a, comes farther and farther away from the interaction point z_{a0}. The interaction pole, z_2, at the same time comes closer and closer to the interaction point and more and more of the incident wave energy is transformed into the z wave. Finally there appears to be complete transformation. However, when the coupling becomes so strong, our first-order approximations cannot be accurate enough. However, if approximations of higher order are also considered, one finds that as ν approaches ν_c the amplitude factor $\pi/2$ of T^+ effectively is reduced to 1.[12] For practical calculations we therefore put

$$T^+\cong\exp[j\{W_2(z_{a0}, z_2)-W_1(z_{a0}, z_2)-\pi/2\}]. \quad \nu\leq\nu_c. \quad (27a)$$

It is obvious that as ν becomes larger than ν_c, z_2 moves into the upper half-plane, and thus in the first-order approximation

$$T^+=0, \quad \nu>\nu_c. \quad (27b)$$

How can this result be explained physically? Let us look at Fig. 5 where we have depicted the polarization of the o and x (z) components as functions of distance in the neighborhood of $\omega_c^2=\omega^2$. The polarization curves only cross each other when $\nu\leqslant\nu_c$ (compare the earlier results of Mary Taylor[13]) and at the level $\omega_c^2=\omega^2$ where the o and z components have the same polarization, in this case plane. At this level the main coupling must occur.

We have further plotted $-\mathrm{Im}(\psi)$ as a function of distance in Fig. 5 in order to show how rapidly the polarization varies through the coupling range when $\nu\lesssim\nu_c$. When ν approaches ν_c the coupling becomes very strong in a narrow region where the difference in polarization is quite small.

As n_1 and n_2 represent the same quantity in different Riemann-surfaces, the cuts joining these surfaces run from z_1 and z_2, say to respectively $v^2=\pm j\infty$. If $\pi_2^{0(1)}$ is "carried" through the cut from the n_2 to the n_1 plane, one immediately infers that along the axis of reals ($z<z_{a0}$) it represents an o wave in the latter plane, traveling in the same direction as $\pi_1^{0(1)}$. Obviously the transformation coefficient, in this geometrical interpretation, becomes

$$T_{0z}\cong\exp[j\{W_2(z_{a0}, z_2)-W_1(z_{a0}, z_2)\}]. \quad \nu\leq\nu_c. \quad (27c)$$

When $\nu>\nu_c$ the axis of reals runs through the cut and the o wave automatically transforms into a z wave, *i.e.* we have longitudinal transmission. Therefore

$$T_{0z}\cong 1, \quad \nu\geq\nu_c \quad (28)$$

which, of course, in no way contradicts the result (27b) of the coupling theory.

[12] O. E. H. Rydbeck, "Magneto ionic triple splitting," Trans. Chalmers University of Technology (in press).

[13] Mary Taylor, "The Appleton-Hartree formula and dispersion curves for the propagation of electromagnetic waves through an ionized medium in the presence of an external magnetic field, Parts I and II." Proc. Phys. Soc. **45** (1933) and **46** (1934).

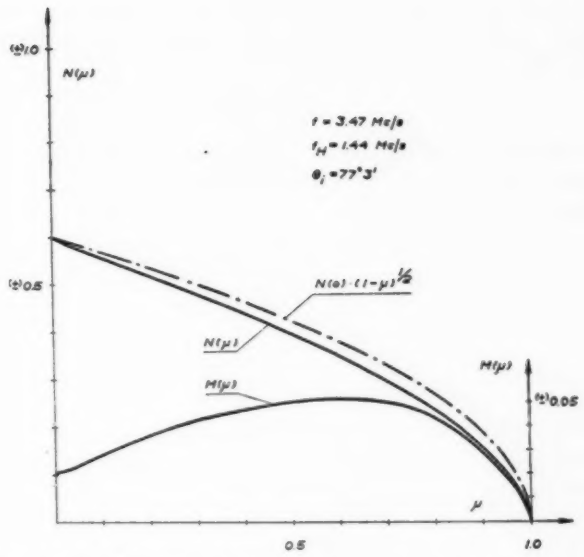

FIG. 7. Depicting the variation of $N(\mu)$ and $M(\mu)$ along the axis of the ψ-poles. [$\mu=-(v^2-j\delta)/j\delta_c$.]

Thus according to both the coupling theory and the geometrical interpretation one approximately has

$$\left.\begin{aligned} R_z\cong\exp[j\cdot 2\{W_1(z_{a0}, z_0-\Delta h) \\ +W_2(z_b, z_{a0})-\pi/4\}\cdot(T_{0z})^2, \ \nu\leq\nu_c \end{aligned}\right\}$$

and

$$\left.\begin{aligned} R_z\cong\exp[j\cdot 2\{W_1(z_b, z_0-\Delta h)-\pi/4\}]. \quad \nu\geq\nu_c \end{aligned}\right\} \quad (29)$$

When $\nu>\nu_c$, R_0 rapidly becomes smaller and only the z and x components are recorded (if ν_c is sufficiently small).

Finally it should be mentioned that a detailed study of the connection relation between the wave functions in the n_1 and n_2 planes shows that theoretically an infinite (but highly attenuated) group of waves are running up and down between the principal branch points.[12]

However, one should not be led to believe that transmission conditions as a whole are optimal for the z wave when $\nu\cong\nu_c$. The regular path attenuation naturally becomes quite considerable unless ν_c is fairly low as at high latitudes.

The ratio between the two reflection coefficients becomes ($\nu\leq\nu_c$)

$$R_z/R_0\cong\exp[j\cdot 2\{W_2(z_{b0}, z_{a0})+W_2(z_b, z_{b0}) \\ -W_1(z_a, z_{a0})\}]. \quad (T_{0z})^2. \quad (30)$$

Assuming $W_2(z_b, z_{b0})$ roughly equal to $W_1(z_a, z_{a0})$, a reasonable assumption when $\nu<\nu_c$, we infer from (30) that the probability of observing both the o wave and the z wave must increase when we approach such regions where ν is small and $|T|^2$ large. Let us therefore next study how $|T|^2$ varies with the collisional frequency.

As

$$T_{0z}\cong\exp\left[j\left\{k_0\int_{z_{a0}}^{z_2}(n_2-n_1)dz-(\pi/2)\right\}\right]. \quad \nu<\nu_c. \quad (27a)$$

It is of particular interest to plot n_2-n_1 from z_2 to z_{a0} (and then to z_1) along the axis between the ψ-poles. To that end we introduce

$$-v^2+j\delta=\mp j\mu\delta_c,$$

where the upper sign denotes the direction from z_a to z_1 and μ runs from 0 to 1. We then obtain the two simple expressions

$$n_1^2=\frac{1-(1-\mu^2)^{\frac{1}{2}}+\frac{1}{2}\mu^2\cdot\tan^2\theta}{1-(1-\mu^2)^{\frac{1}{2}}-[j\mu(1+j\delta)/y\cos\theta]}, \quad (31)$$

$$n_2^2=\frac{1+(1-\mu^2)^{\frac{1}{2}}+\frac{1}{2}\mu^2\cdot\tan^2\theta}{1+(1-\mu^2)^{\frac{1}{2}}-[j\mu(1+j\delta)/y\cos\theta]} \quad (32)$$

where it is no serious neglect to drop $j\delta$. It is therefore a comparatively simple matter to plot the variation of n_2 and n_1 along the axis between the poles. The result is shown in Fig 6. We immediately note that the difference between $\mathrm{Im}(n_2)$ and $\mathrm{Im}(n_1)$ always is very small indicating a practically negligible phase change.

Equation (27a) can be written

$$T_{0z}\cong\exp\left[-j\left\{k_0\delta_c(1-\mu)M(\mu)/\gamma_{a0}-\frac{\pi}{2}\right\}-k_0\delta_c(1-\mu)N(\mu)/\gamma_{a0}\right], \quad (33)$$

where $\mu=\nu/\nu_c$,

$$N(\mu)=\frac{1}{1-\mu}\int_\mu^1\{\mathrm{Re}(n_2)-\mathrm{Re}(n_1)\}d\mu \quad (34)$$

and

$$M(\mu)=\frac{1}{1-\mu}\int_\mu^1\{\mathrm{Im}(n_2)-\mathrm{Im}(n_1)\}d\mu. \quad (35)$$

We also have with very good accuracy

$$T_{0z}^2\cong\exp[-2k_0\delta_c(1-\mu)|N(\mu)|/\gamma_{a0}], \quad (36)$$

as at least for $|\mu|<1$, $|M(\mu)|<0.05$ (for the y and θ-values chosen). This is demonstrated by Fig. 7. The magnitude of $M(\mu)$ always is very small which indicates negligible net phase shift.

It is very interesting to note that $N(\mu)$, for the geomagnetic values chosen, is represented quite well by $N(0)(1-\mu)^{\frac{1}{2}}$. From (36) we finally obtain the practically useful formula

$$T_{0z}^2\cong\exp\left[-\frac{\nu_c\cdot\Delta h}{c_0}\left(1-\frac{\nu}{\nu_c}\right)^{\frac{1}{2}}|N(0)|\cdot\frac{\omega/\omega_{cm}}{(\omega_{cm}^2/\omega^2-1)^{\frac{1}{2}}}\right]. \quad \nu\leq\nu_c \quad (37)$$

$$(\omega<\omega_{cm})$$

Figure 8 illustrates this result for typical E layer values and Kiruna geomagnetic conditions.

The critical collisional frequency, ν_c, increases rapidly with decreasing geomagnetic latitude as shown in Fig. 9. For comparison a height scale corresponding to the daylight ν-values has also been introduced in order to show the relative position of the ionized layer.

It is thus clear from what has been said and, again, from the nature of relation (37) that $o-z-o$ E trans-

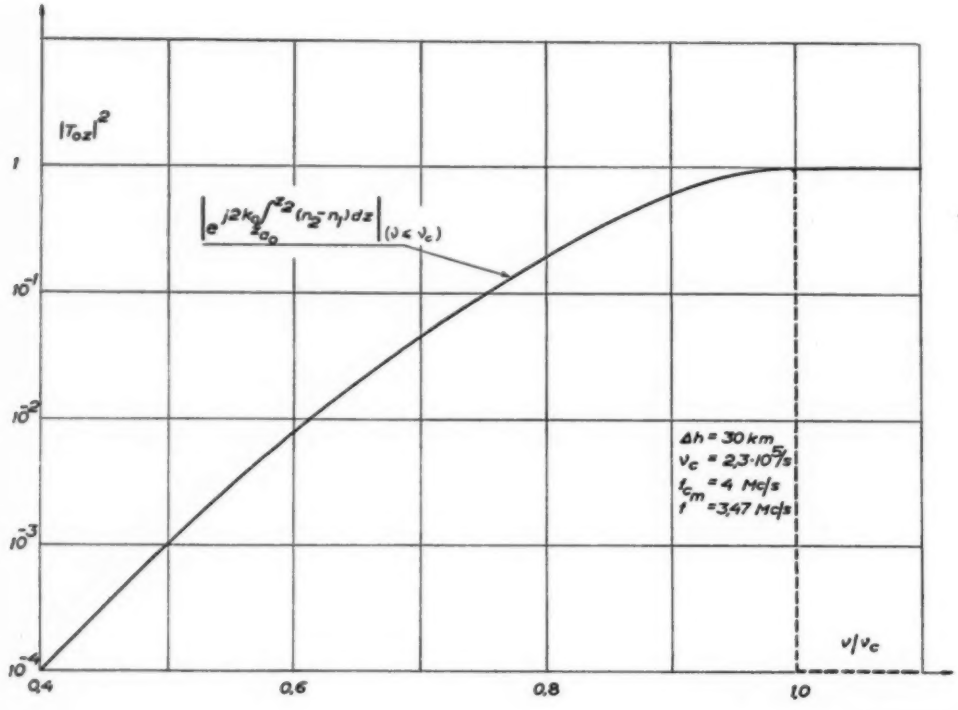

FIG. 8. The total transmission coefficient as a function of ν.

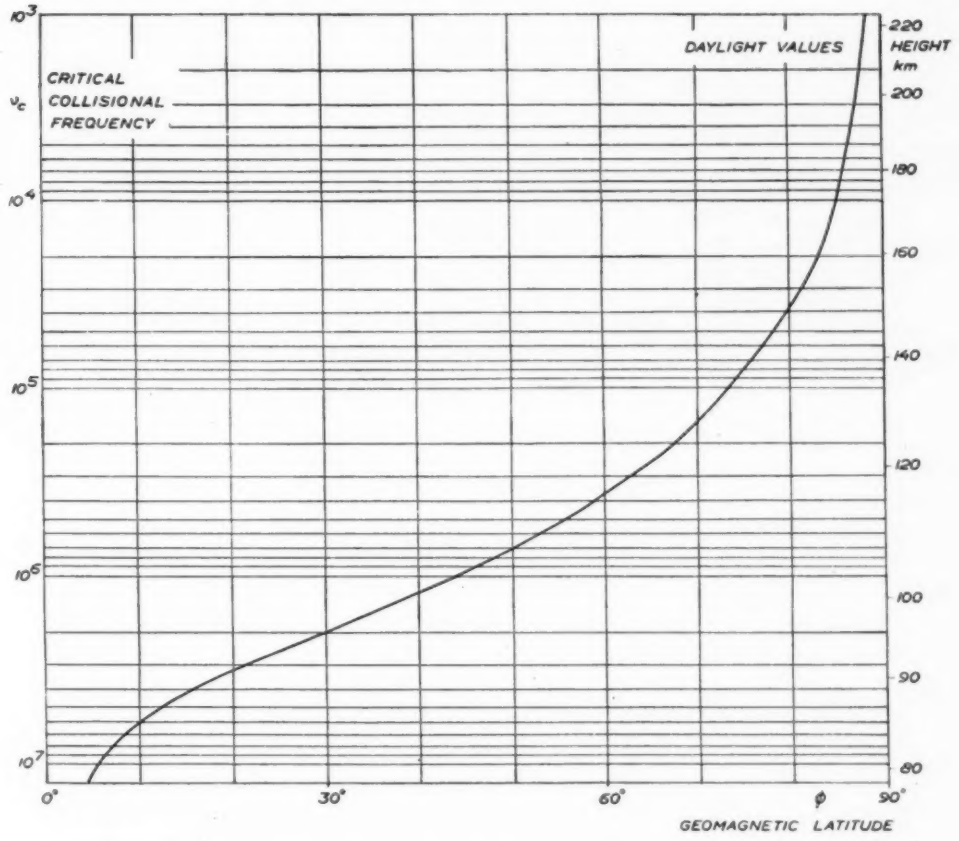

FIG. 9. The variation of critical collisional frequency with geomagnetic latitude.

mission of appreciable strength only is possible at high latitudes, preferably above 70°N or below 70°S. This is in full accord with experimental facts, both others' and our own.

EXPERIMENTAL RESULTS

It appears from Fig. 9 that at Kiruna, for example,[8] where the geomagnetic latitude is about 65°, triple splitting cannot occur with great strength much below about 120 km but that it must occur with considerable intensity slightly above that height. This is in complete agreement with our experience. We record triple penetration of the E layer almost regularly and in Fig. 10 is shown one of the typical records obtained with the new 16-kw panoramic recorder.[14] It is interesting to note that on this occasion, as so many times before, the $o-z-o$ component is almost as strong as the o component. One notes the characteristic fact that $o-z-o$ wave reflected from the F_2 layer disappears when the o wave penetrates the E layer. The reason for this is clear, both physically and from (37). This feature of the z trace has already been reported by Meek.[4] Actually the z trace is much delayed and absorbed when the o wave begins to penetrate.

It is clear both from the form of relation (37) and from Fig. 9 that at Kiruna, for example, T^2 is considerably smaller for the $o-z-o$ wave in the F_2 layer. However, on account of the small ν and therefore low attenuation on the whole, the z trace can be seen on F_2 records although usually not as frequently as near the lower critical ν_c-level. Figure 11 is a clear-cut sample of F_2 triple splitting recorded recently at Kiruna.

Figure 12 finally shows another characteristic example of E layer triple splitting which again shows that the z trace disappears near f_{E0}.

The present investigation has shown that with respect to the o and z waves when $\nu < \nu_c$ the layers of the iono-

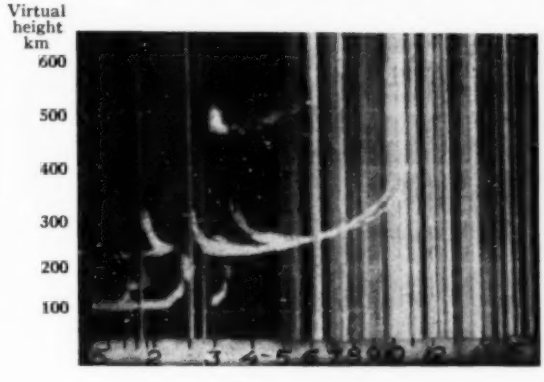

FIG. 10. Panoramic Kiruna recording of ionospheric magnetic ionic triple splitting at the E level. (April 3, 1949; 1543 GMT.)

[14] R. Lindquist, "A 16-kw panoramic ionospheric recorder," Trans. Chalmers University of Technology (in press).

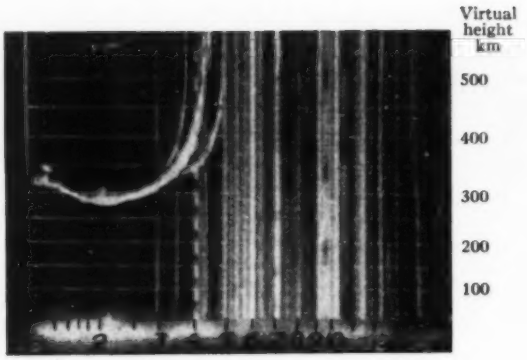

FIG. 11. Magneto-ionic F_2 triple splitting recorded at Kiruna. (October 6, 1949; 0442 GMT.)

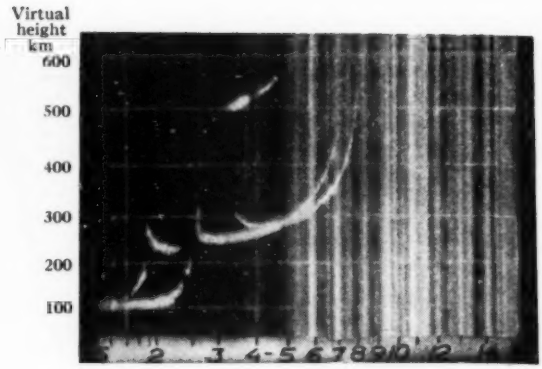

FIG. 12. Further example of E magneto-ionic triple splitting. (April 25, 1949; 1640 GMT.)

sphere act as if they constituted coupled transmission lines. The "ordinary" line runs from $z_0 \pm \Delta h$ to $\pm z_{a0}$ the "z" line from $\pm z_{a0}$ to $\pm z_{b0}$, or from $+z_{a0}$ to $-z_{a0}$ when the $o-z-o$ wave penetrates. It is not possible to detect any difference in polarization between the o and $o-z-o$ waves outside the layers. There they are, in fact, both ordinary waves.

ACKNOWLEDGMENTS

The support of the National Research Boards for the Technical and Natural Sciences made this investigation possible. The author's thanks are also due, and are cordially extended, to S. Forsgren, E.E., who has been responsible for the preparation of the various graphs presented in this communication.

The Equivalent Circuit for the Transmission of Plane Elastic Waves through a Plate at Oblique Incidence

WILLIAM T. THOMSON
University of Wisconsin, Madison, Wisconsin
(Received April 20, 1950)

Equations are developed for the transmission of a plane elastic wave through a plate at oblique incidence with unequal fluid medium on each side of the plate. The plate transmitting both the dilatation and shear wave is reduced to a simple equivalent circuit with impedances which are functions of the incidence angle.

INTRODUCTION

THE transmission of plane elastic waves through a stratified solid medium at oblique incidence was recently treated by the author.[1] When the solid medium is reduced to a single plate surrounded by a fluid medium, the problem is somewhat simplified. The latter case has been studied by Reissner,[2] and Smyth and Lindsay.[3] Reissner's equation for transmission is conveniently expressed in terms of two factors M and N which are also used in this paper.

To make the problem more general, the fluid on each side of the plate will be assumed to be different. This, however, has no effect on the equivalent circuit, other than that of altering the terminal conditions.

Nomenclature

The symbols used are identical to those of reference 1 with few additions.

Δ', Δ'' = progressive and reflected dilatation in solid.
ω', ω'' = progressive and reflected rotations in solid.
c_Δ = velocity of dilatation wave in solid.
c_ω = velocity of rotation or shear wave in solid.
c_0 = velocity of propagation in first fluid medium.
c_2 = velocity of propagation in second fluid medium.
ρ = density of plate.
ρ_0, ρ_2 = density of fluid mediums.
p = angular frequency in radians per sec.
l, m, n = direction cosines of normal to advancing wave with respect to x, y, z axis.
σ = normal stress perpendicular to xy plane.
τ = shearing stress in xy plane.
ζ = particle velocity in z direction.
d = thickness of plate.
λ_Δ = wave-length of dilatational wave in plate.
$P=(pn_\Delta d)/c_\Delta$.
$Q=\dfrac{pn_\omega d}{c_\omega}$.
φ', φ'', φ''' = incident, reflected, and transmitted wave amplitudes in fluid.
θ_0 = angle of incidence.

$$F=\left(\frac{\cos\theta_0}{\rho_0 c_0}\right)\left(\frac{\rho c_\Delta}{\cos\theta_\Delta}\right)\left(\frac{\cos^2 2\theta_\omega}{\sin P}\right)$$

$$G=\left(\frac{\cos\theta_0}{\rho_0 c_0}\right)\left(\frac{\rho c_\omega}{\cos\theta_\omega}\right)\left(\frac{\sin^2 2\theta_\omega}{\sin Q}\right)$$

Same coefficients as those of Reissner's paper, reference 2, but rearranged in symmetric form.

$N=F+G$.
$M=F\cos P+G\cos Q$.

[1] W. T. Thomson, J. App. Phys. **21**, 89–93 (1950).
[2] H. Reissner, Helv. Phys. Acta. **11**, 140–155 (1938).
[3] J. B. Smyth and R. B. Lindsay, J. Acous. Soc. Am. **16**, 20–25 (1944).

DEVELOPMENT OF EQUATIONS

Choosing the coordinate axes as shown in Fig. 1, the equations of reference 1 apply. From Eqs. (7), (8), and (16) of Thomson's article[1] we can write the following equations corresponding to the six boundary conditions.

The shear stress at the plate boundaries is zero:

$$\tfrac{1}{2}(\Delta'-\Delta'')\sin 2\theta_\Delta+(\omega'+\omega'')\cos 2\theta_\omega=0, \tag{1}$$

$$(i/2)(\Delta'+\Delta'')\sin 2\theta_\Delta \sin P+\tfrac{1}{2}(\Delta'-\Delta'')\sin 2\theta_\Delta\cos P +i(\omega'-\omega'')\cos 2\theta_\omega \sin Q +(\omega'+\omega'')\cos 2\theta_\omega\cos Q=0. \tag{2}$$

The particle velocity is continuous at plate boundaries:

$$c_\Delta n_\Delta(\Delta'-\Delta'')-2c_\omega l_\omega(\omega'+\omega'')=c_0 n_0(\varphi'-\varphi''), \tag{3}$$

$$ic_\Delta n_\Delta(\Delta'+\Delta'')\sin P+c_\Delta n_\Delta(\Delta'-\Delta'')\cos P -2ic_\omega l_\omega(\omega'-\omega'')\sin Q -2c_\omega l_\omega(\omega'+\omega'')\cos Q=c_2 n_2\varphi'''. \tag{4}$$

The normal stress is continuous at plate boundaries:

$$\rho c_\Delta^2(\Delta'+\Delta'')\cos 2\theta_\omega-2\rho c_\omega^2(\omega'-\omega'')\sin 2\theta_\omega =-c_0^2\rho_0(\varphi'+\varphi''), \tag{5}$$

$$\rho c_\Delta^2(\Delta'+\Delta'')\cos 2\theta_\omega\cos P+i\rho c_\Delta^2(\Delta'-\Delta'')\cos 2\theta_\omega\sin P -2\rho c_\omega^2(\omega'-\omega'')\sin 2\theta_\omega\cos Q -2i\rho c_\omega^2(\omega'+\omega'')\sin 2\theta_\omega\sin Q=-c_2^2\rho_2\varphi'''. \tag{6}$$

From Eqs. (1), (2), (3), and (4) we obtain the following:

$$\omega'+\omega''=-\tfrac{1}{2}(\varphi'-\varphi'')\sin 2\theta_0, \tag{7}$$

$$\omega'-\omega''=-\frac{i}{2}(\varphi'-\varphi'')\sin 2\theta_0\frac{\cos Q}{\sin Q}+\frac{i}{2}\varphi'''\frac{c_2 n_2}{c_0 n_0}\frac{\sin 2\theta_0}{\sin Q}, \tag{8}$$

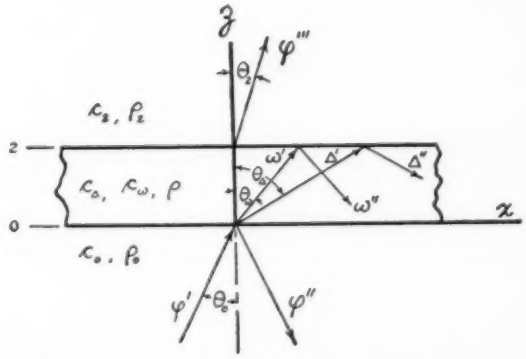

FIG. 1. Dilatational and shear waves in solid plate.

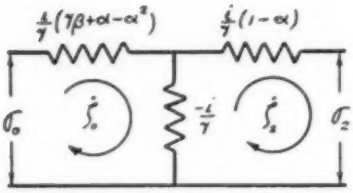

FIG. 2. Equivalent circuit for a plate transmitting dilatational and shear waves.

$$\Delta'-\Delta''=(\varphi'-\varphi'')\sin 2\theta_0\frac{\cos 2\theta_\omega}{\sin 2\theta_\Delta}, \tag{9}$$

$$\Delta'+\Delta''=i(\varphi'-\varphi'')\frac{\sin 2\theta_0\cos 2\theta_\omega\cos P}{\sin 2\theta_\Delta\sin P}-i\varphi'''\frac{c_2n_2}{c_0n_0}\frac{\sin 2\theta_0\cos 2\theta_\omega}{\sin 2\theta_\Delta\sin P}. \tag{10}$$

Substituting these into Eqs. (5) and (6) we obtain

$$\varphi'-\varphi''=\frac{\varphi'''}{N}\frac{c_2}{c_0}\left[M\frac{n_2}{n_0}+i\frac{c_2\rho_2}{c_0\rho_0}\right], \tag{11}$$

$$\varphi'+\varphi''=\frac{\varphi'''}{N}\frac{c_2}{c_0}\left[M\frac{c_2\rho_2}{c_0\rho_0}+i(N^2-M^2)\frac{n_2}{n_0}\right], \tag{12}$$

$$\frac{\varphi'''}{\varphi'}=\frac{2N(c_0/c_2)}{M\left(\frac{c_2\rho_2}{c_0\rho_0}+\frac{n_2}{n_0}\right)+i\left[(N^2-M^2)\frac{n_2}{n_0}+\frac{c_2\rho_2}{c_0\rho_0}\right]}. \tag{13}$$

$$T=\frac{c_2\rho_2|\varphi'''|^2}{c_0\rho_0|\varphi'|^2}=\frac{4N^2(c_0/c_2)(\rho_2/\rho_0)}{M^2\left(\frac{n_2}{n_0}+\frac{c_2\rho_2}{c_0\rho_0}\right)^2+\left[\frac{c_2\rho_2}{c_0\rho_0}+(N^2-M^2)\frac{n_2}{n_0}\right]^2}, \tag{14}$$

$$\frac{\varphi''}{\varphi'}=\frac{M\left(\frac{c_2\rho_2}{c_0\rho_0}-\frac{n_2}{n_0}\right)+i\left[(N^2-M^2)\frac{n_2}{n_0}-\frac{c_2\rho_2}{c_0\rho_0}\right]}{M\left(\frac{c_2\rho_2}{c_0\rho_0}+\frac{n_2}{n_0}\right)+i\left[(N^2-M^2)\frac{n_2}{n_0}+\frac{c_2\rho_2}{c_0\rho_0}\right]}, \tag{15}$$

$$R=\frac{c_2\rho_2|\varphi''|^2}{c_0\rho_0|\varphi'|^2}=\left\{\frac{M^2\left(\frac{c_2\rho_2}{c_0\rho_0}-\frac{n_2}{n_0}\right)^2+\left[(N^2-M^2)\frac{n_2}{n_0}-\frac{c_2\rho_2}{c_0\rho_0}\right]^2}{M^2\left(\frac{c_2\rho_2}{c_0\rho_0}+\frac{n_2}{n_0}\right)^2+\left[(N^2-M^2)\frac{n_2}{n_0}+\frac{c_2\rho_2}{c_0\rho_0}\right]^2}\right\}\frac{c_2\rho_2}{c_0\rho_0}. \tag{16}$$

Equations (14) and (16) are the transmission and reflection coefficients of the plate. When the two fluid mediums are the same, these equations reduce to

$$T=\frac{|\varphi'''|^2}{|\varphi'|^2}=\frac{4N^2}{4M^2+(N^2-M^2+1)^2}, \tag{17}$$

$$R=\frac{|\varphi''|^2}{|\varphi'|^2}=\frac{(N^2-M^2-1)^2}{4M^2+(N^2-M^2+1)^2}, \tag{18}$$

which agree with those of Reissner.

DEVELOPMENT OF THE EQUIVALENT CIRCUIT

In the impedance theory of tubes and horns[4] it is common practice to write the pressure and volume current at one point in terms of corresponding quantities at another point. This idea was utilized in the paper of reference 3 to consolidate the transmission equations. With this same general scheme, it is possible to go further and develop the equivalent circuit for the plate transmitting the dilatation and shear waves.

We first write the equations for σ and $\dot{\zeta}$ at the plate boundaries in terms of φ', φ'', and φ''' by substituting Eqs. (7), (8), (9), and (10) in the left side of Eqs. (3), (4), (5), and (6).

$$\sigma_0=i(\varphi'-\varphi'')\rho_0c_0^2M-i\varphi'''\rho_0c_0^2N(c_2n_2/c_0n_0), \tag{19}$$

$$\dot{\zeta}_0=(\varphi'-\varphi'')c_0\cos\theta_0, \tag{20}$$

$$\sigma_2=i(\varphi'-\varphi'')\rho_0c_0^2N-i\varphi'''\rho_0c_0^2M(c_2n_2/c_0n_0), \tag{21}$$

$$\dot{\zeta}_2=\varphi'''(c_2n_2/n_0)\cos\theta_0. \tag{22}$$

[4] Stewart and Lindsay, *Acoustics* (D. Van Nostrand Company, Inc., New York, 1930), 4th edition, Appendix III and IV.

We next seek a solution in the form

$$\sigma_2=\alpha\sigma_0-i\beta\dot{\zeta}_0, \tag{23}$$

$$\dot{\zeta}_2=\alpha\dot{\zeta}_0-i\gamma\sigma_0. \tag{24}$$

Substituting Eqs. (19) to (22) in Eqs. (23) and (24) and equating coefficients of like terms of $(\varphi'-\varphi'')$ and φ''' we obtain the following

$$\alpha=M/N, \tag{25}$$

$$\beta=(\rho_0c_0/\cos\theta_0)(M^2-N^2)/N, \tag{26}$$

$$\gamma=-(\cos\theta_0/\rho_0c_0)1/N, \tag{27}$$

$$\alpha^2+\beta\gamma=1. \tag{28}$$

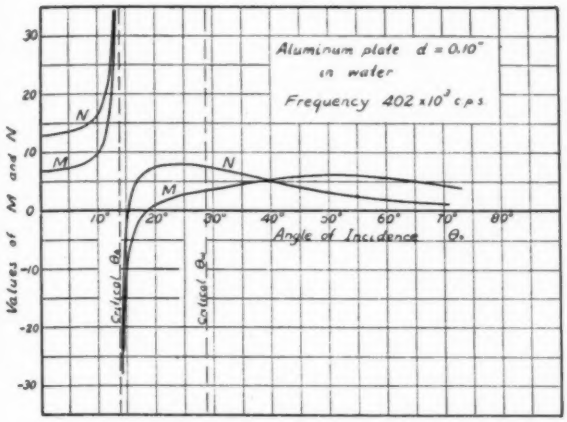

FIG. 3. Values of M and N for aluminum plate in water.

It is thus possible to write the circuit equations

$$\sigma_0-\sigma_2=(i/\gamma)(1-\alpha)\dot{\zeta}_2+(i/\gamma)(\gamma\beta+\alpha-\alpha^2)\dot{\zeta}_0, \tag{29}$$

$$\sigma_2=(-i/\gamma)(1-\alpha)\dot{\zeta}_2+(-i/\gamma)(\dot{\zeta}_0-\dot{\zeta}_2), \tag{30}$$

from which the equivalent circuit of Fig. 2 is obtained.

For this problem, the impedance of the fluid medium 2 is $\sigma_2/\dot{\zeta}_2=-(\rho_2c_2)/\cos\theta_2$ while that of medium 0 is $\sigma_0/\dot{\zeta}_0=-(\rho_0c_0/\cos\theta_0)(\varphi'+\varphi''/\varphi'-\varphi'')$. The circuit impedances are only functions of N, M, and the quantity $(\rho_0c_0)/\cos\theta_0$.

Computation

The equations show that M and N contain only one singularity at the critical angle of the dilatational wave. The transmission at this angle is, however, not zero.

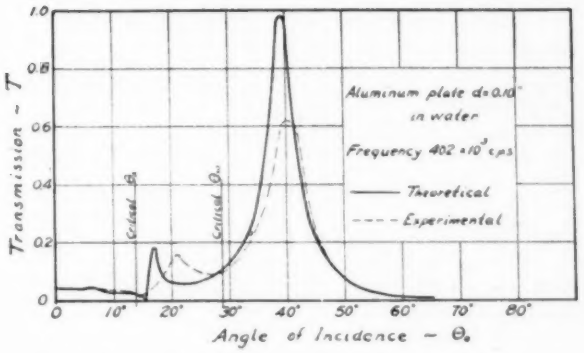

FIG. 4. Transmission curves for aluminum plate in water.

Also, for small ratios of the plate thickness to the wavelength, M and N are nearly equal for all values of θ_0, and further simplification of the transmission equations and the equivalent circuit is possible. The transmission becomes equal to zero only when $N=0$.

Due to the rather lengthy computations involved, theoretical calculations are shown only for a single case of an aluminum plate 0.10-inch thick immersed in water with an ultrasonic beam of 402 kilocycles/sec. The thickness ratio for the plate at this frequency is $d/\lambda_\Delta=0.1628$, which cannot be classified in the thin plate region where $N=M$. For an aluminum plate $d=0.015$ inch at the same frequency, the curves for N and M practically coincide.

The curves for N and M shown in Fig. 3 are typical in that the singularity is evident at the critical angle of the dilatation wave and the point $N=0$ corresponding to zero transmission occurs at a slightly larger angle. The corresponding transmission curve is shown in Fig. 4 with a comparison with experimental values taken from the dissertation* of Mr. Gerald Cohen. The transmission peak occurs near 40°, which is well beyond the critical angles for dilatation and shear. The disagreement in the peak values is evidently due to dissipation which is not accounted for in the theoretical equations.

The author is indebted to the staff of the Computing Service of the University of Wisconsin for the calculations and to the Navy Research Laboratory of the University for sponsoring the investigation carried out by Mr. Cohen.

* Gerald H. Cohen, "Ultrasonic Transmission through Thin Plates," Ph.D. thesis, University of Wisconsin Engineering College, 1950.

Gas Evolution in Liquids and Cavitation

P. H. SCHWEITZER*
The Pennsylvania State College, State College, Pennsylvania
AND
V. G. SZEBEHELY†
Virginia Polytechnic Institute, Blacksburg, Virginia
(Received February 8, 1950)

Nine heavy lubricating oils, four light lubricating oils, three aircraft engine fuels, one diesel fuel, and distilled water were tested for their air solubility and for the rate of solution and evolution of air when equilibrium is disturbed. The technique consisted of shaking of a container partly filled with liquid and taking accurate pressure measurements of the air above the liquid. Since air in solution exerts no pressure, the variation of pressure during and after the agitation furnished information on the amount of air that went into or came out of solution and their time rates. The solution was considered to have reached equilibrium when further shaking no longer changed the air content of the liquid.

A wide variation exists in the solubility constants and rates, but the rate of evolution was always found to be proportional to the supersaturation, and the rate of solution to the undersaturation, under otherwise similar conditions. At room temperature the air solubility constant for distilled water is 1.84 percent, for a gasoline approximately 20 percent, and for (light and heavy) lubricating oils approximately 10 percent. The "half-life" for evolution on the other hand was 3.86 sec. for distilled water, 0.13–0.24 sec. for gasoline, 3.6–7.6 sec. for light, and 11.6–51.4 sec. for heavy lubricating oils.

The investigation gave some insight into the phenomenon of cavitation which is still largely shrouded in mystery.

SYMBOLS

t = Time (sec.)
p_0 = Atmospheric pressure (p.s.i.)
p = Gas pressure above the liquid generally (at time t) (p.s.i.)
p_g = Gas pressure above the liquid at the beginning of the evolution or solution process (p.s.i.)
p_e, p_e' = Equilibrium or saturation pressure (gas pressure above the liquid in case of equilibrium) (p.s.i.)
Δp = Pressure difference: $p_e - p_g$ (p.s.i.)
V_l = Volume of used liquid (cu. ft.)
V = Volume of free gas dissolved in the liquid generally (at time t) (cu. ft.)
V_g = Volume of the gas section of the container (cu. ft.)
V_e, V_e' = Volume of free gas dissolved in the liquid at equilibrium (cu. ft.)
ΔV = Volume of free gas evolved from the liquid in time t (cu. ft.)
S = Solubility constant —
r = Gas-liquid volume ratio —
R_E = Rate of evolution (1/sec.)
R_S = Rate of solution (1/sec.)
T_E = Half-life of evolution (sec.)
$(T_E)_0$ = Limiting value of half-life, if $r \to \infty$ (sec.)
T_S = Half-life of solution (sec.)
s, $(-s)$ = Supersaturation (undersaturation) —.

THREE possible relations can exist between the saturation pressure and the gas pressure above the liquid:

(a) $p_e = p_g$. Case of equilibrium. The liquid can neither release nor absorb more gas.

(b) $p_e > p_g$. Case of supersaturation. The amount of gas dissolved in the liquid is greater than the amount which would correspond to the existing gas pressure. Therefore, evolution process *can* take place.

(c) $p_e > p_g$. Case of undersaturation. The amount of gas dissolved in the liquid is less than the amount which would correspond to the existing gas pressure. Therefore, solution process *can* take place. (It will be discussed later that evolution or solution process does not necessarily take place and the existence of that depends upon several other factors.)

The case of equilibrium obeys the well-known Henry's (Henry-Dalton's) law which says that if no change in molecular structure occurs during the solution or evolution process, then the free volume of dissolved gas in the liquid is directly proportional to the absolute pressure

$$V_e = S \frac{p_e}{p_0} V_l. \tag{1}$$

Next the case of supersaturation is considered. A container is partly filled with saturated liquid and gas, the gas pressure being equal to the saturation pressure. If the gas pressure is slightly reduced, diffusion and surface evasion will take place, which will be called "quiescent evolution." No bubble formation will accompany this evolution process. Our experiments have shown that the ratio between the rates of evolution obtained under agitated and quiescent conditions is always in the thousands, therefore in the following discussion, the "quiescent evolution" will be neglected.

Considering the slowly obtained small pressure drop and neglecting the quiescent evolution, a slightly supersaturated liquid is obtained. If the container is kept at rest and the pressure is further reduced very slowly to atmospheric pressure, then a supersaturated liquid is obtained. We wish to point out that considerable (up to 100 percent) supersaturation was often produced without any bubble formation.

If the pressure drop is produced suddenly, rapid evolution does take place. The liquid surface suffers a break which is equivalent to agitation and immediate bubble formation can be observed. If the liquid is well stirred or agitated, supersaturated liquid cannot be produced. If we consider breaks in the liquid surface, caused by a sudden pressure drop, as a special sort of

* Professor of Engineering Research.
† Associate Professor of Applied Mechanics.

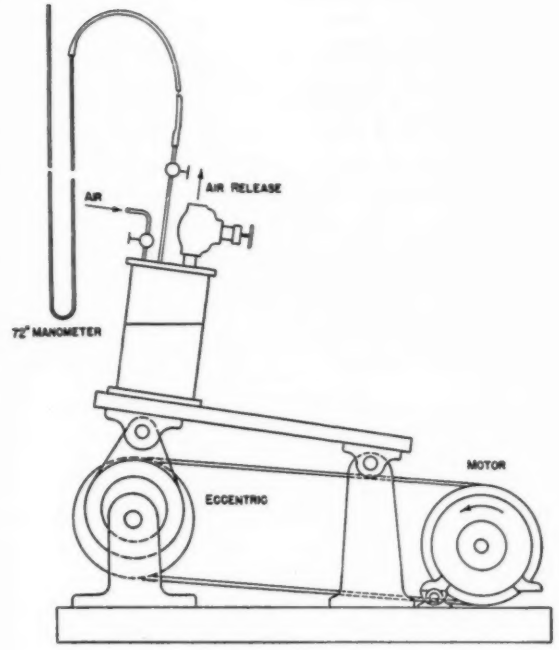

FIG. 1. Shaker.

agitation, it may be stated that bubble formation in a moderately supersaturated liquid can only set in if the liquid is agitated.

RATE OF EVOLUTION

The rate of evolution is defined as the time rate of change of the volume of free gas in solution per unit volume of the liquid

$$R_E=\frac{d}{dt}\left(\frac{V}{V_l}\right). \tag{2}$$

In order to obtain the $V(t)$ function, the following experiment was done:

First the p_e equilibrium or saturation pressure was slowly reduced to p_g, keeping the container in rest and so avoiding any bubble formation. Then agitation was started, such as shaking of the container as shown in Fig. 1. A cylindrical container of 3400 cc was shaken with a frequency of 400 cycles per minute and with a stroke of one inch. With the agitation, the evolution process starts and gas leaves the liquid. To measure the volume of the evolved gas, two methods have been used.

In the direct method, the gas pressure before the evolution process would start, must be brought to atmospheric: $p_g=p_0$. The container then is closed and connected with a volume measuring instrument. The amount of evolved air is recorded as a function of the time, keeping the pressure above the liquid always atmospheric. The original volume of dissolved air (before agitation) can be computed from formula (1). If the instantaneously recorded volume of evolved free gas is V_m, then

$$V=V_e-V_m.$$

Because accurate instantaneous recording of V_m involved experimental difficulties, we used an indirect method based on pressure measurement. The gas pressure above the liquid pressure was reduced from p_e equilibrium pressure to p_g gas pressure, which in this method need not be atmospheric. Then the container was closed and connected to a manometer. The effect of agitation was that the pressure (p) increased from p_g to a new equilibrium pressure p_e'. Obviously $p_g<p_e'<p_e$, i.e., the new equilibrium pressure is greater than the reduced gas pressure, but less than the original equilibrium pressure; they are related by Eq. (3):

$$V=S\frac{p_e'}{p_0}V_l-\frac{p-p_e'}{p_0}V_g. \tag{3}$$

The p_e' final equilibrium pressure can also be predicted from the equilibrium equation as:

$$p_e'=\frac{V_gp_g+V_lSp_e}{V_g+V_lS}=\frac{rp_g+Sp_e}{r+S}.$$

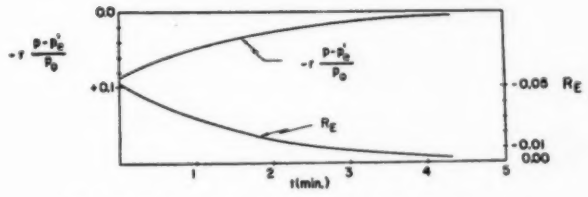

FIG. 2. Pressure *vs.* time and rate *vs.* time curves for lubricating oil.

Substituting Eq. (3) in Eq. (2), the rate of evolution is

$$R_E=-r\frac{d}{dt}\frac{p-p_e'}{p_0}.$$

Knowing r, p_e', p_0 and measuring p, the rate of evolution, R_E, can be obtained as a function of the time by graphical differentiation.

Such a plot, for a lubricating oil, is shown in Fig. 2. As the pressure appears to approach the saturation pressure p_e', the rate of evolution R_E is approaching zero.

It did not seem unreasonable to assume that the rate of evolution is always proportional to the supersaturation (and the rate of solution to undersaturation):

$$R_E=ks=k\frac{V_e'-V}{V_l}. \tag{4}$$

If this were the case Eq. (2) could be integrated with the result:

$$\frac{d}{dt}\left(\frac{V}{V_l}\right)=k\frac{V_e'-V}{V_l}$$

$$V=(V_e-V_e')e^{-kt}+V_e'. \tag{5}$$

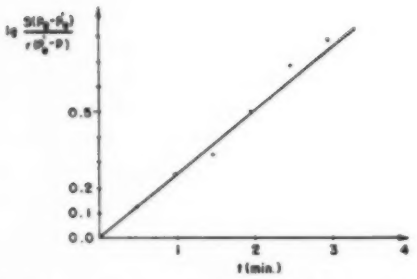

FIG. 3. Pressure *vs.* time curve plotted on semilog base.

If assumption (4) is correct then plotting $\lg(V-V_e')$ against time t should give a straight line. After a simple transformation we get in place of Eq. (5)

$$-\frac{p-p_e'}{p_0}=\frac{S}{r}\frac{p_e-p_e'}{p_0}e^{-kt}, \tag{6}$$

therefore plotting $\lg[S(p_e-p_e')/r(p_e'-p)]$ against t should also give a straight line which should go through the origin.

Figure 3 shows a plot for the above mentioned lubricating oil which was selected at random. In the course of the tests performed on 18 liquids some 150 of such plots were made for both solution and evolution runs. Except for slight inaccuracies, attributable to experimental errors, all turned out to be straight lines going through the origin. The conclusion was clear: the rate of evolution *is* proportional to the supersaturation (the rate of solution to the undersaturation) and represents, therefore, an exponential function of time.

Inspecting Eq. (5) it is seen that at zero time $V=V_e$ and if $t\to\infty$, $V\to V_e'$. Finally the total evolved gas is V_e-V_e' but infinite time is required for its evolution. Consider the time required for the evolution of one-half of the total evolved gas $(V_e-V_e')/2$ and designate it by the symbol T_E. When $t=T_E$, $V_e-V=(V_e-V_e')/2$, therefore from Eq. (5)

$$k=\frac{ln2}{T_E}=\frac{0.693}{T_E}. \tag{7}$$

T_E is designated "half-life" of evolution and is equal to the time required to half complete the gas evolution. With this new designation the gas content of the supersaturated liquid is:

$$V=(V_e-V_e')\exp\left(-0.693\frac{t}{T_E}\right)+V_e'. \tag{8}$$

In an actual case the V_e and V_e' values are not known —at least they have to be computed using the

$$V_e=S\frac{p_e}{p_0}V_l \quad \text{and} \quad V_e'=S\frac{p_e'}{p_0}V_l$$

formulas. Equation (8) can be transformed to a more useful form

$$V=\frac{S}{r+S}\frac{V_l}{p_0}\left[r(p_e-p_0)\exp\left(-0.693\frac{t}{T_E}\right)+rp_0+Sp_e\right]. \tag{9}$$

With formula (9), V, the value of free gas still dissolved in the liquid at time t can be evaluated. In many engineering applications, however, it is more important to know the amount of the evolved gas from $t=0$ to $t=t$; $\Delta V=V_e-V$. This is given by:

$$\Delta V=\frac{Sr}{S+r}\frac{p_e-p_0}{p_0}V_l\left[1-\exp\left(-0.693\frac{t}{T_E}\right)\right]. \tag{10}$$

Formula (10) furnishes two as yet unmentioned results. The $Sr/(S+r)$ factor can be represented by hyperbolas going through the origin, whether S or r is considered as the variable.

Due to the fact that the asymptotes are parallel with the horizontal axis, the effect of change in r (keeping S constant) is appreciable if r is small, but it can be neglected if r is great, (Figure 4.). For thin liquid layers ($r\to\infty$) the $Sr/(S+r)$ value is represented by S. The last factor, $1-\exp(-0.693\,t/T_E)$ is the well-known exponential function starting with zero value at time zero and approaching to 1 if $t\to\infty$.

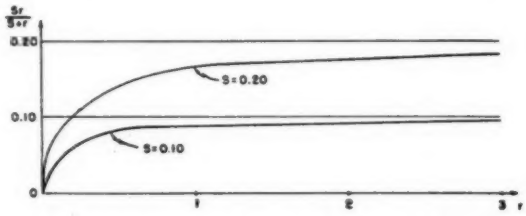

FIG. 4. The $Sr/(S+r)=f(r)$ hyperbolas for different S values.

The initial tangent (at $t=0$) to the curve is $0.693/T_E$ which together with Fig. 5 show that if the half-life time is great the evolution is slow.

An example with actually obtained values explains better the $V=f(t)$ function.

For the heavy lubricating oil referred to, the solubility constant S was 0.0815 with respect to air. The used air-oil volume ratio was $r=2$. The measured half-life was $T_E=1.205$ min. The volume of used liquid was $V_l=63.5$ cu. in. The initial saturation pressure was $p_e=38.45$ p.s.i.g. and the air pressure above the oil $p_0=21.86$ p.s.i.g.

With the above figures from formula (10):

$$\Delta V=5.6[1-\exp(-0.575t)]$$

if ΔV is in cu. in. and t in minutes. Formula (9) gives the free volume of air in solution. Substituting the numerical values: $V=5.6\exp(-0.575t)+13.1$.

Figure 6 shows the volume of evolved air and Fig. 7 the volume of air in solution in function of time.

Going back to the definition of the rate of evolution and substituting in formula (2) for V the value obtained in formula (9), it is found that the rate is a function of the half-life (T_E), of the solubility constant (S), of the gas-liquid ratio (r), of the pressure difference ($p_e - p_g$), of the atmospheric pressure (p_0) and of the time (t). It was investigated experimentally whether these variables are related to each other or are independent. It was found that the half-life is related to the gas-liquid ratio and the solubility constant but none of the other variables involved are related to each other.

For a given liquid and gas combination S is the only constant with which the evolution process can be described inasmuch as S is not a function of the other variables. Even the solubility constant varies with temperature, but in this investigation the temperature was kept constant. For the same gas-liquid combination, the half-life varies with the gas-liquid volume ratio. Therefore half-lives can be compared only at a certain r

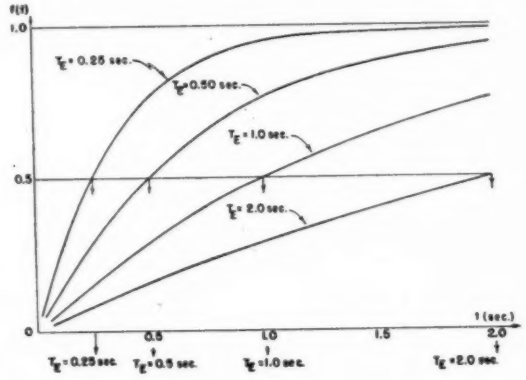

FIG. 5. The $1-\varepsilon^{-0.693(t/T_E)}=f(t)$ exponential curves for different T_E values.

value. Obviously the half-life depends also upon the method of agitation, therefore a standardized agitation is required in order to compare data. It was found that the relation between T_E and r can be described with an exponential function. Increasing the gas-liquid volume ratio by varying r from very small values up to 4.5 the following relation was indicated:

$$T_E=(T_E)_0/(1-\varepsilon^{-cr}),$$

where $(T_E)_0$ is limiting value of half-life if $r\to\infty$, i.e., if we deal with a very thin liquid film, and c is a constant. On the other hand, keeping r constant, a relation is expected between the half-life, solubility constant, viscosity, density, surface tension, etc. These investigations are extended to other details too and at the present time are conducted at the Virginia Polytechnic Institute, Department of Applied Mechanics.

SOLUTION

After the foregoing detailed discussion of the evolution process, the solution process can be settled very shortly. In the solution process a disturbed undersaturated liquid is approaching to an equilibrium condition. The analogy between evolution and solution processes is complete, therefore the same letters and steps can be used in deriving the same formula.

The gas pressure above the liquid p_g is now greater than the saturation pressure p_e. Closing this p_g pressure in the container and connecting it with a manometer or pressure gauge, after an agitation, the p_g pressure will drop to a p_e' new equilibrium pressure and some of the gas originally above the liquid will be dissolved. The definition of the rate of solution is $R_S=d/dt(V/V_l)$. The rate of solution will always be positive, due to the fact that the free volume of dissolved gas is increasing if the time is increasing. During the solution process, the pressure drops from p_g to p_e' and $p_g>p_e'>p_e$.

The $T_E(r, S)$ function was discussed already and the same can be said about the $T_S(r, S)$ function. It should not be a surprise however that using the same liquid and gas (S) as well as the same gas-liquid volume ratio (r) for an evolution and a solution process, the half-lives will not be the same. The experiments performed showed that with no exception the half-life for evolution was always shorter than that for solution, which means that the evolution process is quicker than the solution process. This difference between T_S and T_E can be explained by considering the mechanism of evolution and solution. The mechanism actually changes the effective value of r during the evolution process by exposing more surface through bubble formation, but it results in only negligible changes in r during solution. A detailed analysis of this question will be published in another paper.

RESULTS

The experimental investigation included 18 liquids and one gas, air. The liquids tested were heavy and light lubricating oils, a diesel fuel, distilled water and aircraft engine fuels. The smallest value of the solubility constant (1.84 percent) was obtained for water. For heavy lubricating oils it varied between 7.75 percent and 9.18 percent, for light oils between 9.70 percent and 11.30 percent. For the tested diesel fuel S was roughly 12 percent and the maximum obtained

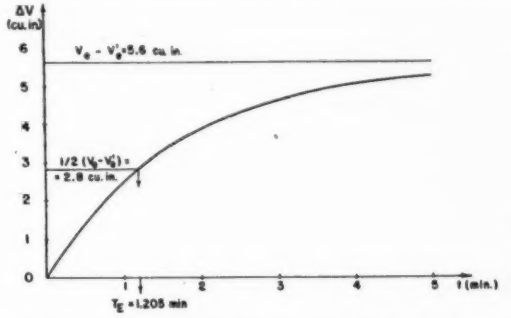

FIG. 6. Volume of evolved air for heavy lubricating oil *vs.* time. Half-life, $T_E=1.205$ min.; $S=0.0815$; $r=2$; $V_l=63.5$ cu. in.; $p_e=38.45$ p.s.i.g.; $p_g=21.86$ p.s.i.g.

value of S was 25.14 percent in case of an aircraft engine fuel.

Discussing results obtained regarding half-lives, first a standard agitation has to be established, then a certain gas-liquid ratio has to be decided at which the values can be compared. The following values of half-lives correspond to a gas-liquid ratio, $r=4$. The frequency used was 400 cycles per minute and the stroke one inch. Without any special temperature controlling equipment the results were reproducible; the usual room temperature variations did not seem to effect the results.

For heavy oils, the solution and evolution process is slow, therefore the half-lives are long. As it was explained, the evolution process is quicker than the solution. The shortest half-lives were obtained for evolution of fuels (0.128 sec.) and the longest for solution of heavy oils (414.0 sec.). In Table I the solubility constants and the half-lives for solution as well as for evolution are shown for the tested liquids.

From the tabulated data, the behavior of the liquids can be predicted after a brief and simple computation.

RELATION BETWEEN CAVITATION AND GAS EVOLUTION

In ordinary practice liquids display no tensile strength and when the absolute pressure in a liquid drops below zero, the liquid tears apart. In fact, discontinuity in the form of vapor-filled bubbles, usually occurs as soon as the pressure in the liquid is reduced to its vapor pressure. Hence, cavitation is generally associated with the vapor pressure of the liquid and is expected to take place whenever and wherever the hydraulic pressure reaches vapor pressure.

Our observations with bubble formation have convinced us that this widely held view generally is incorrect, though it appears to be valid under certain specific circumstances.

Cavitation is failure (of continuity) of the liquid in tension. Like failure in solids, it is largely controlled by contamination and surface conditions. The true tensile strength of liquids (no contamination and no surface flaw) is extraordinarily high. Our information on the

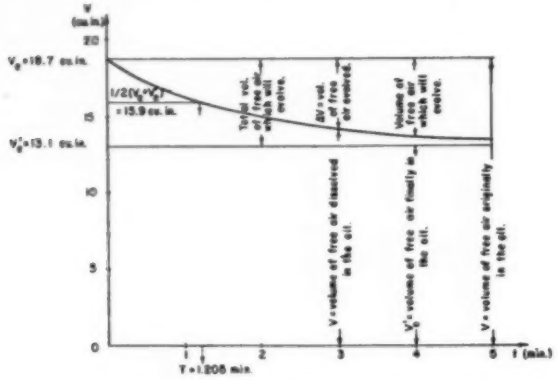

FIG. 7. Free volume of air in solution for heavy lubricating oil *vs.* time. (Specifications same as on Fig. 6.)

tensile strength of liquids is very limited because of the practical difficulty of subjecting a column of pure liquid to tension. The great difference between solids and liquids is not so much in their tensile strengths, but in their shearing strength. To test a solid rod in tension we clamp its two ends and pull them apart. The absence of shearing strength prevents us from clamping a liquid column. A liquid cannot be handled without a container. The adhesion between the liquid and the container is frequently less than the cohesion between the liquid particles themselves. Under such circumstances, the true negative pressure which is necessary to tear liquid particles apart cannot be determined. Such tests can yield only a minimum value because in measuring the tensile strength of a chain one learns something about its weakest link, nothing more.[1]

The weak link may be somewhere else. If the liquid is not completely degassed, it will usually contain some entrained air in the form of microscopic or submicroscopic bubbles either in the bulk of the liquid or near a solid contaminant or near the container wall. Such a bubble, whatever its size, represents on the one hand a flaw within the liquid and on the other hand, an adjacent gas phase into which dissolved gas can diffuse or liquid vapor can evaporate. Under such a condition, visible cavitation (macrocavitation) will take place easily and promptly. However, this represents a "false cavitation in which the cavities were derived from pre-existing gas nuclei rather than de novo."[2]

In spite of all these experimental handicaps it has been shown[2,3] that liquid water can stand a negative pressure of 50 atmospheres and more without visible failure.

Weyl and Marboe[1] tested the gas release from water saturated with carbon dioxide at atmospheric pressure. They subjected the CO_2 saturated water to a partial vacuum. When the liquid was held in an ordinary "clean" glass container, a pressure drop from 760 to 50 mm Hg abs. readily produced gas bubbles. However, if the glass container was thoroughly cleaned with dichromate-sulphuric acid solution, bubbles failed to appear upon evacuation. Clean glass powder in the liquid did not cause the release of gas bubbles either, but glass powder which had been exposed to laboratory air for a short time did. Also when the surface of the container was not thoroughly cleaned, release of gas supersaturation promptly accompanied the drop in pressure. This directed attention to the chemical structure of the contacting phases.

In our tests the container used was made of steel and Lucite. No precaution was made to have them chemically clean. With water we were unable to produce any appreciable supersaturation without observing bubble formation. However, with petroleum hydrocarbons,

[1] Weyl and Marboe, Research **2**, 19 (1949).
[2] Pease and Blinks, J. Phys. Colloid Chem. **51**, 556, No. 2 (1947).
[3] E. N. Harvey, J. App. Phys. **18**, 161 (1947).

which wet both steel and Lucite, we observed considerable supersaturations (100 percent) without bubble release, provided the liquid was kept in a quiescent state. However, when the liquid was agitated, gas supersaturation was released rapidly.

Gas may be present in a liquid in two forms, dissolved gas and entrained gas. The dissolved gas is actually no gas at all. It is invisible (the liquid is clear), and does not increase its volume and compressibility by any appreciable amount. Entrained gas is dispersed in the liquid in the form of bubbles which may give the liquid a turbid appearance. The equilibrium amount of entrained air (or ambient gas) in a quiescent liquid is zero. Churning tests showed that it reaches a maximum at certain degree of agitation and decreases again when that degree of agitation is exceeded.

From these observations the following picture emerges. No vapor-cavitation can take place without entrained air (or other gas) in the liquid. As soon as there is an air bubble, that bubble promptly fills up with vapor, provided the hydraulic pressure in the liquid is lower than its vapor pressure. As long as there is no air bubble, no vapor can form (except on the surface if the liquid has one). Evaporation takes place when liquid in the vapor phase leaves the liquid in the liquid phase. This requires an interface. Vapor cannot leave the liquid unless it goes some place. If there are air bubbles, it goes into the air bubbles through the liquid-air interface. Without air nuclei there is no evaporation (except on top surface if there is one) and no cavitation. With air nuclei present, bubble growth through gas release will set in as soon as the hydraulic pressure drops below the saturation pressure which corresponds to the air actually held in solution.

It has generally been observed that in flowing water cavitation bubbles appear whenever and wherever the hydraulic pressure drops below the vapor pressure of the water, approximately 0.36 p.s.i.a. at 70°F. This observation is the consequence of two extraneous circumstances. The first is that flowing water always contains some entrained air in the form of small bubbles either in the bulk of the liquid or adjacent to solids in contact with the water. The second is that in water, having a low air solubility, the release of dissolved air (rate of evolution) is very slow if the pressure is reduced a small amount from the saturation pressure. Therefore, the bubble growth is very slow. If the bubbles were submicroscopic at the start of the experiment (at saturation pressure), they will remain submicroscopic when the pressure is reduced a small fraction of an atmosphere. However, when the pressure reaches the vapor pressure, there is a relatively fast vapor release into the air bubbles and then their growths become visible to ordinary observation. The term "cavitation" is frequently applied to this phase of bubble growth. Then cavitation appears to set in at a locality where the pressure of the flowing water drops below its vapor pressure.

TABLE I. Summary of experimental results.

		Solubility constant (%)	Half-life at $r=4$ for evolution solution (seconds)		Kin. viscosity at 70°F (centistokes)
1	Heavy lubricating oil	7.75	51.4	414	823–974
2	Heavy lubricating oil	8.14	43.0	292	823–974
3	Heavy lubricating oil	8.15	45.0	386	762–974
4	Heavy lubricating oil	8.24	48.2	396	762–974
5	Heavy lubricating oil	8.61	37.2	244	762–974
6	Heavy lubricating oil	8.62	34.8	252	562–670
7	Heavy lubricating oil	9.05	31.0	125.4	325–411
8	Heavy lubricating oil	9.11	17.9	50.2	249–346
9	Heavy lubricating oil	9.18	11.6	32.7	88.7
10	Light lubricating oil	9.70	4.74	10.22	17.5
11	Light lubricating oil	9.95	4.18	9.77	17.5
12	Light lubricating oil	10.72	3.56	6.14	13.5
13	Light lubricating oil	11.30	7.63	9.46	17.5
14	Diesel fuel	11.98	0.301	3.08	4.4
15	Aircraft engine fuel	17.20	0.236	2.595	1.67
16	Aircraft engine fuel	22.80	0.128	1.214	0.6350
17	Aircraft engine fuel	25.14	0.137	1.344	0.6350
18	Distilled water	1.84	3.86	7.930	1.0

In order to accurately describe what takes place it is necessary to define our terms. A liquid is considered to be in *equilibrium* when its content of dissolved gas is constant with respect to time. *Cavitation* is any discontinuity in the bulk of the liquid, irrespective of the size of the cavity and whether it is filled with void, gas, or vapor. *Microcavitation* refers to bubbles of microscopic or submicroscopic size. *Macrocavitation* refers to visible bubbles. The liquid is *quiescent* when all of its parts are at rest relative to the container, except for their thermal motion. The liquid is in *agitation* when some or all of it is not quiescent.

With these definitions:

1. A liquid is in equilibrium if it has been either quiescent or under an invariable type of agitation for a sufficient length of time to assume saturation in all parts. The equilibrium is upset if either the pressure or the temperature changes locally or in the whole.
2. A quiescent liquid in equilibrium with air has a zero amount of entrained air and a saturation amount of dissolved air.
3. An agitated liquid in equilibrium has a certain amount of entrained air and a saturation amount of dissolved air.
4. A quiescent liquid, originally in equilibrium, will not cavitate until it is subjected to a negative pressure which is equal to the tensile strength of the liquid (not less than -750 p.s.i. for water).
5. A liquid in agitation and exposed to air for any length of time cavitates continuously inasmuch as it contains entrained air in the form of nuclei (microcavitation).
6. In the bulk of the liquid (a place other than the surface) neither gas evolution nor vapor evolution can take place in the absence of gas nuclei (microcavitation).
7. In an originally gas free liquid, microcavitation may set in (1) if air is introduced into it under the surface, (2) if the liquid is supersaturated *and* has chemically weak bonds with the container wall or solid contaminants, (3) if it is subjected to agitation.
8. Microcavitation will turn into macrocavitation as a result of either gas evolution, or vapor evolution, or both. Gas evolution begins at any pressure lower than saturation pressure; vapor evolution begins only below the vapor pressure of the liquid.

This explains the behavior of flowing water under ordinary conditions. Under some agitation the water contains a certain amount of entrained air in the form of microscopic or submicroscopic bubbles which are invisible. Ordinarily it also contains some air nuclei in the microscopic crevices of the container, submerged

solids, and solid contaminants. If the hydraulic pressure drops slightly, in the whole or at certain localities, slow evolution of dissolved air will follow which may be undetectable by ordinary observation. If the pressure drops suddenly, air evolution is accelerated and bubble growth may become observable before the rising bubbles reach the top surface of the water. Such bubbles will appear first near solid surfaces, not only because the hydraulic pressure usually is the lowest at such spots, but also because the chemical bonds there are weaker than the cohesion between the water molecules. If the pressure drops below the vapor pressure of the liquid, evolution of vapor into the nuclei will begin at a relatively high rate, thus resulting in fast bubble growth. Frequently this is regarded as the beginning of incipient cavitation.

With liquids other than water, or quiescent water, or with pure denucleated water flowing in a chemically clean container, the walls of which are well wetted by the water (hydrophilic material), cavitation will not, as a rule, begin at vapor pressure. A much lower pressure is required to start microcavitation and a higher than vapor pressure is sufficient to turn microcavitation into macrocavitation, both depending on exterior circumstances.

This investigation was done in 1948 and 1949 at the sponsorship of the Air Materiel Command U. S. Air Force.

Electrical Conductivity Method for Measuring Self-Diffusion of Metals

J. H. DEDRICK*
Sylvania Electric Products, Inc., Bayside, New York

AND

G. C. KUCZYNSKI
Bogotą, Colombia

(Received May 29, 1950)

A method has been proposed to measure self-diffusion in metals by measurement of the contact conductance of an interface between two metallic spheres or hemispheres. By combining Kuczynski's equation for self-diffusion with Bowden and Tabor's equation for the contact conductance between two metallic spheres a relationship has been obtained between contact conductance and the time of heating of the spheres. Thus by measurement of junction conductance as a function of time of heating, for different temperatures, diffusion coefficients and the heat of self-diffusion can be evaluated in the normal manner. A similar relationship has been obtained for two spheres or hemispheres initially pressed together to give a known contact conductance before heating.

ONE of the authors[1] developed a theory of sintering, verified by extensive experimental work, showing that the initial bonding of like metallic particles upon heating is a volume diffusion process. The relationship developed was

$$X^5/a^2 = 40\sigma\delta^3/kT \cdot Dt, \qquad (1)$$

where X is the radius of the interface between the particles (assumed to be circular) a the original radius of the particles, σ the surface tension of the material, δ the interatomic jump distance, k the Boltzman constant, T the absolute temperature, t the time, and D the coefficient of self-diffusion. This relationship shows that the fifth power of the interface radius between the particles is proportional to the time of sintering. Values of D, D_0 (frequency factor) and Q (heat of self-diffusion) obtained in this manner on copper and silver agree well with those obtained by radioactive tracer methods.

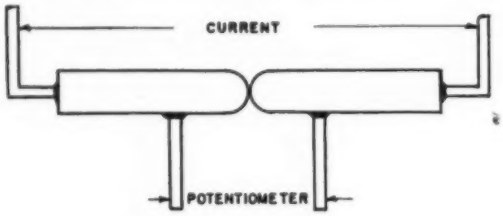

FIG. 1. Method of measuring junction conductance.

The technique used to measure the interface radius as a function of time for a given temperature was to sinter spherical metallic particles to a base plate and to measure the radius by metallographic means. This method was later changed by using wire wound around a mandrel of the same material. The use of blown-up low magnification photographs has also been resorted to for measuring contact radii of particles.[2] In this case a single close packed layer of particles was used.

This article relates to another method which might be used to measure heats of self-diffusion and self-diffusion coefficients based upon a relationship between Eq. (1) and the contact conductance of an interface between two metallic spheres or hemispheres.

* Now at Reynolds Metals Company, Louisville, Kentucky.

[1] G. C. Kuczynski, "Self-Diffusion in sintering of metallic particles," Metals Trans. 169–178 (February, 1949).

[2] J. H. Dedrick and A. Gerds, J. App. Phys. **20**, 1042–1044 (1949).

Bowden and Tabor[3] in their work on measurement of the area of contact between stationary surfaces, have shown that the junction conductance (C_j) between two metallic spheres of radius a, or crossed cylinders, joined at the contact by a circle of radius X, where X is small compared to a, is given by

$$C_j = 2\lambda X, \tag{2}$$

where λ is the specific conductance of the bulk material. Using crossed cylinders of silver (0.90-cm radius) and increasing the contact area by varying the load, they found a direct proportionality between conductance and contact radius up to a value of the latter of 0.08 cm which is approximately 18 percent of the cylinder radii.

By combining (1) and (2) the following relationship is obtained between junction conductance and time of heating of two spheres or two hemispheres in contact with each other:

$$\frac{(C_j/2\lambda)^5}{a^2} = 40\sigma\delta^3/kT \cdot Dt. \tag{3}$$

Thus from measurements of junction conductance as a function of time of heating, for different heating temperatures, D values could be obtained and D_0 and Q evaluated in the normal manner. This method makes it unnecessary to resort to metallographic work, and one set of specimens could be used for different times of sintering at a given temperature. The possibility of continuous recording of junction conductance as a function of time of heating also presents itself. A schematic sketch for the measurement of the junction conductance between two hemispherically ended specimens is shown in Fig. 1.

The discussion up to this point has been based upon the assumption that the initial point junction conductance will be very low and thus neglected. However, if this is not so, a different mode of attack would have to be resorted to and it appears that the simplest approach would be to initially press the spheres or hemispheres together with a certain force and thus produce an initial junction radius X_0, as shown in Fig. 2, from which the initial junction conductance C_j^0, prior to heating, could be measured.

In this case, it would be necessary to use the following

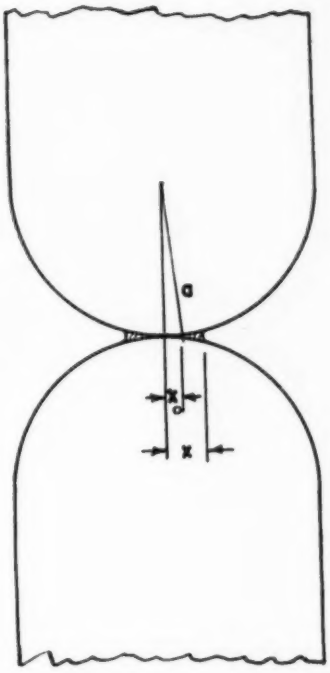

FIG. 2. Sketch of contact junction between two pressed hemispherical ended rods.

relationship based upon the geometry of the figure:

$$\frac{X^5 - X_0^5}{5} - 2X_0^2\frac{X^3 - X_0^3}{3} + X_0^4(X - X_0) = At, \tag{4}$$

where $A = (40\sigma\delta^3)/kT(a - X_0)^2D$, and which reduces to (1) when X_0 equals zero. If X is not very much larger than X_0 (4) can be written as $(4/3)X_0^2(X - X_0)^3 = At$, or

$$X = X_0\left\{1 + \left(\frac{3A}{4X_0^5}\right)^{\frac{1}{3}} t^{\frac{1}{3}}\right\}, \tag{5}$$

and by combining (2) and (5), one obtains

$$C_j = C_j^0\left\{1 + \left(\frac{24A^5}{(C_j^0)^5}\right)^{\frac{1}{3}} t^{\frac{1}{3}}\right\},$$

or

$$C_j = C_j^0\{1 + Kt^{\frac{1}{3}}\}, \tag{6}$$

where K is a constant for a given material, for a given temperature of heating and a known initial junction conductance. Thus as in the case of initially unpressed spheres or hemispheres, measurements of junction conductance as a function of time, for different heating temperatures will allow for determination of D values and evaluation of D_0 and Q.

[3] F. P. Bowden and D. Tabor, "The area of contact between stationary and moving surfaces," Proc. Roy. Soc. London **169A**, 391 (1939).

A Simple Interferometric Test for Conical Flow

J. H. Giese, F. D. Bennett, and V. E. Bergdolt
Ballistic Research Laboratories, Aberdeen Proving Ground, Maryland
(Received May 3, 1950)

In conical flows the velocity, pressure, and density do not vary on lines through the vertex of the cone. In this paper it is shown that for interferograms of general conical flows $\delta(y, z)/z = f(y/z)$, where y and z are any set of Cartesian coordinates with origin at the image of the vertex of the cone, and δ is the fringe shift at y, z. Thus, for strictly conical flow, a graph of $\delta(y, z)/z$ *versus* y/z should be a single curve. This suggests a test for approximate conicity that requires very little computation. This test is applied to interferograms obtained from a number of approximately axisymmetric flows at various Mach numbers about cone-cylinders in free flight. Plotted fringe shift data from the region near the nose fall into a narrow band, an indication of approximate conicity. They also closely check the corresponding theoretical fringe shift curve calculated for Taylor-Maccoll flow.

I. INTRODUCTION

INTERFEROMETRY offers an extremely attractive technique for investigation of gas flows. When it can be employed, an extensive region of the flow field can be surveyed almost instantaneously without disturbing the flow. Accordingly, it is well suited for examining supersonic flows about objects in free flight, as well as those about stationary models in wind tunnels. If the flow is plane or axisymmetric, the density distribution can be computed from fringe shifts observed on an interferogram, though the latter case involves formidable amounts of calculation. At present the quantitative interpretation of interferograms in less symmetrical flows, such as those about yawing bodies of revolution or about more general shapes, seems to be limited to the comparison of measured and theoretical values of fringe shifts. The calculation of theoretical fringe shifts for general flows with little or no symmetry is difficult and tedious at best, and the results depend so strongly on the shape of the body and its orientations relative to the incident stream and the interferometer beam that it seems impossible to reach interesting general conclusions without actually performing the computations. In the important special case of conical flow, however, one can easily make a useful deduction about the functional form of the theoretical fringe shift. Before this is derived, a brief digression on conical flow seems apropos.

A steady flow of a fluid with no viscosity or heat conduction is said to be *conical* if the velocity components, pressure, and density do not vary along lines emanating from some fixed point, which will be called the *vertex*.[1–3] The use of these terms is justified intuitively by applying similarity considerations to flows about one infinite nappe of a general cone placed in a uniform supersonic incident stream. If the vertex of the flow is placed at infinity, plane and swept-back plane flows result.[1] Owing to the remarkable geometrical structure of conical flow, its theory is considerably simpler than that of more general three-dimensional flows and has been developed to a much greater extent. The best known examples of non-linearized conical flows with vertices at finite locations are Taylor-Maccoll flow about a non-yawing right circular cone;[2–4] Prandtl-Meyer expansion around an edge;[3] and the flow over a wedge with attached plane shock wave.[3] The linearized theory has been applied by numerous authors to determine flows over objects ranging from elliptic cones to delta-wings.

The great theoretical interest and value of conical flows make it essential to determine how closely they correspond to flows that can actually be produced in real fluids. The commonest type of test is a measurement of the pressure distribution on the surface of a conical model in a supersonic wind tunnel.[4] Under good test conditions, the pressure is found to be reasonably constant on lines through the vertex of the model, and the observed pressures check the available linearized or non-linearized theoretical values to within a few percent. For flows about cones of revolution and wedges, measured and theoretical shock wave angles have also been compared.[4] As far as interferometry is concerned, Ladenburg[5] has found contours of constant density in the flow about a cone of revolution in an approximately axisymmetric jet. At large enough distances from the vertex of the cone, his measured densities are very nearly constant on radial lines through the vertex and check the theoretical Taylor-Maccoll values to well within two percent.

In this paper a test for conicity, based directly on interferogram fringe shifts, will be developed and applied to data obtained from conical regions in flows about bodies in free flight.

II. THEORETICAL CONSIDERATIONS

A. Functional Form of Fringe Shift

The following reasoning leads to a simple method for interpreting interferograms of general conical flows. Let

[1] A. Busemann, Luftfahrtforschung **12**, 210–220 (1935).
[2] A. Busemann, Zeits. f. angew. Math. Mech. **9**, 496–498 (1929).
[3] A. Ferri, *Elements of Aerodynamics of Supersonic Flows* (New York, 1949), Chapters 2, 3, 12.
[4] G. I. Taylor and J. W. Maccoll, Proc. Roy. Soc. **A139**, 278–311 (1933).
[5] Ladenburg, Winckler, and Van Voorhis, Phys. Rev. **73**, 1359–1377 (1948).

the vertex of the flow be at the origin of a system of rectangular coordinates. Assume that the interferometer beam that traverses the flow is parallel to the x-axis, while the photographic plate is normal thereto, so the projections of the y- and z-axes onto the plate define rectangular coordinates with origin at the image of the vertex. At (y, z) on the plate, in the absence of magnification, the fringe shift $\delta(y, z)$ is defined by

$$\delta(y, z) = (K/\lambda) \int_{a(y,z)}^{b(y,z)} [\rho(x, y, z) - \rho_u] dx, \qquad (1)$$

where ρ_u is the density of the undisturbed fluid, assumed constant; $\rho(x, y, z)$ is the actual density at (x, y, z); K is the Gladstone-Dale constant for the fluid, i.e., the ratio of small increments of index of refraction to the corresponding small increments of density; λ the vacuum wave-length of the light used to form fringes; and the limits of integration $a(y, z)$ and $b(y, z)$ are the x coordinates of the points where the light ray through (y, z) crosses the conical shock wave, outside of which $\rho(x, y, z) = \rho_u$. For any $t > 0$

$$\delta(ty, tz) = (K/\lambda) \int_{a(ty,tz)}^{b(ty,tz)} [\rho(x, ty, tz) - \rho_u] dx.$$

Since the flow is conical, $\rho(x, ty, tz) = \rho(x/t, y, z)$, and since (ty, tz), (y, z), and $(0, 0)$ are collinear, $a(ty, tz) = ta(y, z)$, and $b(ty, tz) = tb(y, z)$. Hence

$$\delta(ty, tz) = (K/\lambda) \int_{ta(y,z)}^{tb(y,z)} [\rho(x/t, y, z) - \rho_u] dx.$$

Let $\xi = x/t$ to obtain

$$\delta(ty, tz) = t(K/\lambda) \times \int_{a(y,z)}^{b(y,z)} [\rho(\xi, y, z) - \rho_u] d\xi = t\delta(y, z), \qquad (2)$$

i.e., $\delta(y, z)$ is homogeneous of degree one. Now let $t = 1/z$, to find $\delta(y, z)/z = \delta(y/z, 1) = f(y/z)$ for some function f. Hence, *for conical flow a plot of* $\delta(y, z)/z$ *versus* y/z *should be a curve,** a conclusion that can also be obtained from similarity considerations. To test a flow qualitatively for conicity by means of an interferogram, it suffices to measure $\delta(y, z)$ as a function of y on a series of traces $z =$ constant, and to observe how closely the points y/z, $\delta(y, z)/z$ come to falling on a curve. Since this procedure involves very little computation with the measured data, it can be used advantageously in either the axisymmetrical or non-axisymmetrical conical case.

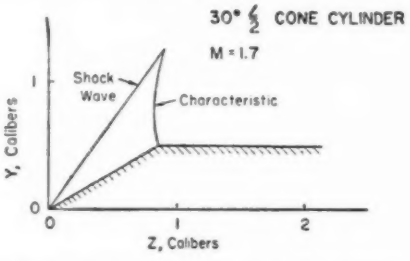

FIG. 1. Theoretical conical flow region.

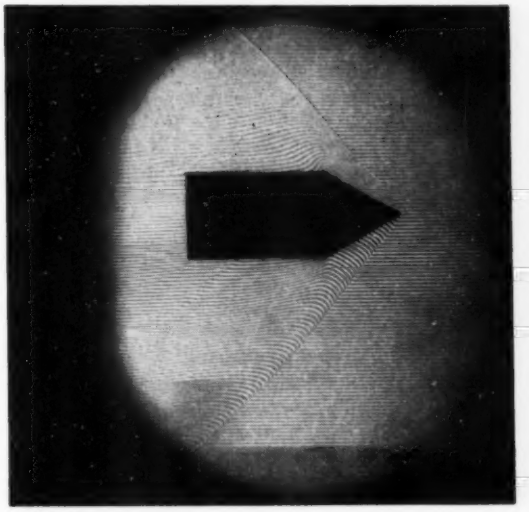

FIG. 2. Interferogram of cal. 30, 30° half-angle cone cylinder, $M = 1.7$, $p = 1$ atmos., room temperature.

B. Flows Containing Conical Regions

Let us turn, now, to the problem of producing an approximately conical flow to which to apply this test. Earlier remarks suggest the use of a conical model. If the flow is supersonic, the effects of the disturbance produced by ending the cone at some finite distance from its vertex will merely be propagated downstream without influencing conditions near the vertex. Thus at supersonic speeds high enough to assure the presence of an attached conical shock wave, the flow about a conical model in a wind tunnel or about a projectile with a conical nose should contain a finite region of conical flow bounded by the following surfaces as indicated in Fig. 1: a conical segment of the shock wave; the conical part of the model's surface; and a characteristic surface through the curve at which the physical cone ends. In particular, if the model is axisymmetric and does not yaw, then near its vertex there will be a region of Taylor-Maccoll flow.

C. Taylor-Maccoll Fringe Shifts

In order to provide a quantitative comparison for the measurements of flows about cone-cylinders that will be presented later, theoretical fringe shift curves will be required. These can be computed as follows: In conical flow that is axisymmetric about the z-axis,

$$\rho = \rho(\theta), \quad \tan^2\theta = (x^2 + y^2)/z^2,$$

$$\lambda\delta(y, z)/2K\rho_u z = \int_0^b (\rho(\theta)/\rho_u - 1) dx/z$$

* Since the pressure $p(x, y, z)$ and density $\rho(x, y, z)$ are homogeneous of degree zero, plots of $(p - p_u)/\frac{1}{2}\rho_u q_u^2$ or of ρ/ρ_u (where ρ_u and q_u are the density and speed of the undisturbed flow) *versus* y/z on a surface $x/z = f(y/z)$ should also be curves. Of course, such plotting is equivalent to testing for constancy of p and ρ on lines through the vertex.

where $b^2=z^2\tan^2\theta_w-y^2$; $\tan\theta_s\leqq y/z\leqq\tan\theta_w$; and θ_s and θ_w are the semi-vertex angles of the cone and shock wave, respectively. Integrate the constant term in the integrand, and transform the variable from z to θ to obtain

$$\lambda\delta(y,z)/2K\rho_u z=\int_{\tan^{-1}y/z}^{\theta_w}[\rho(\theta)/\rho_u]\tan\theta\sec^2\theta \times(\tan^2\theta-y^2/z^2)^{-\frac{1}{2}}d\theta-(\tan^2\theta_w-y^2/z^2)^{\frac{1}{2}}. \quad (3)$$

Behind the shock wave, $p/p_0=(\rho/\rho_0)^\gamma$, where p is the local static pressure; p_0 and ρ_0 are the stagnation pressure and density, respectively; and γ is the ratio of the specific heat at constant pressure to that at constant volume. The local speed of sound, a, is defined by $a^2=dp/d\rho=\gamma p/\rho$. Then $\rho/\rho_0=(a/a_0)^{2/(\gamma-1)}$, where a_0 is the stagnation speed of sound. Similarly, $\rho_u/\rho_{01}=(a_u/a_{01})^{2/(\gamma-1)}$, where ρ_{01} and $a_{01}=a_0$ are the stagnation density and speed of sound, respectively, ahead of the shock wave. By Bernoulli's equation, $\frac{1}{2}q_u^2+a_u^2/(\gamma-1)=a_0^2/(\gamma-1)$, where q_u and a_u are the undisturbed speeds of flow and of sound, respectively. Then $(a_0/a_u)^2=1+\frac{1}{2}(\gamma-1)M^2$, where $M=q_u/a_u$ is the Mach number of the undisturbed flow. Thus

$$\rho/\rho_u=(\rho_0/\rho_{01})[1+\tfrac{1}{2}(\gamma-1)M^2]^{1/(\gamma-1)}(a(\theta)/a_0)^{2/(\gamma-1)}.$$

Since θ_w, ρ_0/ρ_{01}, and $a^2(\theta)$ (in velocity units such that $a_0=1$) have been tabulated as functions of θ_s, M, and θ by Kopal[6] by numerical integration $\lambda\delta(y,z)/2K\rho_u z$ can be determined as a function of y/z. The singularity of the integrand at $\theta=\tan^{-1}y/z$ can easily be avoided by splitting the integration into two parts: one with respect to θ from some convenient $\theta_0>\tan^{-1}y/z$ to θ_w; the other with respect to x from 0 to $(z^2\tan^2\theta_0-y^2)^{\frac{1}{2}}$. In actual use, the values of $\delta(y,z)/z$ so computed will have to be multiplied by a magnification factor appropriate to the experimental optical system. It must also be mentioned, as an aid to plotting, that one can easily show that $d[\delta(y,z)/z]/d(y/z)$ is infinite at $y/z=\tan\theta_w$.

III. EXPERIMENTAL RESULTS AND DISCUSSION

Flows to be tested for conicity were produced by firing cal. 0.30 cone-cylinders at an absolute pressure of one atmosphere in the range described Bergdolt *et al.*[7] During these firings interferograms of which Fig. 2 is typical were obtained from a Mach-Zehnder interferometer with two-inch plates, used in conjunction with a rotating mirror which approximately stopped the images of the bullets. The light employed was from the 5460A line of mercury, produced during a flash of about 2 microseconds duration from a BH6 mercury tube. Other relevant data are appended to the plots of smoothed fringe shift measurements shown in Figs. 3 to 6.

In general, the points plotted in Figs. 3 to 6 lie in

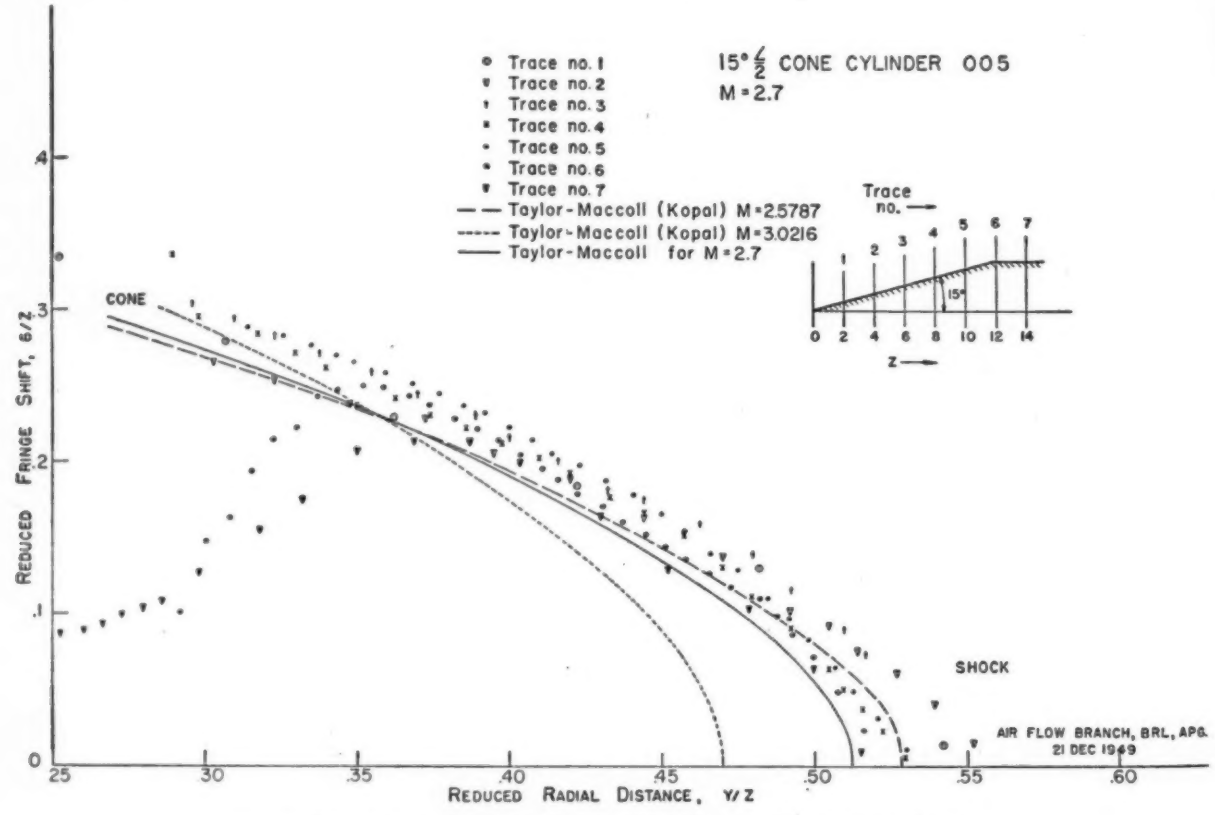

FIG. 3. Conical flow test plot showing departure from conicity in expansion region.

[6] Z. Kopal, *Tables of Supersonic Flow around Cones* (Cambridge, Mass., 1947).
[7] Bergdolt, Greenwald, and Sleator, Phys. Rev. **76**, 879 (1949).

rather narrow bands, which encourages the belief that these flows came fairly close to being conical. In Fig. 3, for traces beyond the shoulder of the cone-cylinder, the points near the shock wave lie close to the conical flow band, while those near the body fall far outside. This verifies that the region of conical flow is really qualitatively of the theoretical form shown in Fig. 1. Actually this is also clear by direct inspection of Fig. 2, where the trace of the characteristic surface that bounds the region of conical flow is plainly discernible. Since the vertex of a conical flow is a singularity of the theoretical flow field, close to which the velocity and other properties of the flow have large gradients, even for a perfectly pointed model one would expect the behavior of a real viscous fluid to differ considerably there from that of the theoretical perfect fluid. The actual body, however, must have a slightly blunted nose, so the shock wave must be detached and doubly curved rather than conical. *A fortiori*, one would expect deviations from conicity near the tip of the body; however, the present measurements do not seem to exhibit such effects. In Figs. 3 and 6, points of the first trace bear no particularly significant relation to those of others farther downstream. In Figs. 4 and 5, on the other hand, points of the first traces are systematically displaced above the rest. The magnitude of this displacement is consistent with the assumption that an error of the order of 0.2 mm was made in determining the location of the vertex on the interferogram. Such errors can arise, for example, if the vertex falls on a dark fringe. For an interferogram with well defined vertex, no such displacements are observed, and all of the plotted points fall within a narrow band, as in Fig. 6.

Estimates of the erratic experimental error $\Delta\delta$ in fringe shift indicate that $\Delta\delta \leqslant 0.05$ for all of the measurements reported here. For a given trace, percentage error in δ will vary from a large value near the shock wave to a minimum at the projectile body. Fringe shift generally increases from the tip of the projectile toward the rear; so percentage erratic error is higher for low trace number than for high.

For the data represented in Fig. 6 $\Delta\delta \leqslant 0.05$ indicates error for trace No. 1 of 18 percent or less at the projectile boundary. This upper bound falls to 10 percent for trace No. 2, 6 percent for trace No. 3, 4 percent for trace No. 5, and less than 3 percent for the remaining traces. These estimates apply to the δ/z values as well; for the erratic error in location of z is of the order of a few tenths percent even for smallest z.

IV. COMPARISON WITH TAYLOR-MACCOLL FLOW

A quantitative check of observed fringe shifts requires a corresponding theoretical flow model. In the present case the obvious choice, Taylor-Maccoll flow, must be justified by inquiring how well the fundamental assumptions of uniformity ahead of the shock wave, inviscidness, steadiness, and axisymmetry are satisfied. As far as viscosity is concerned, reasonably high

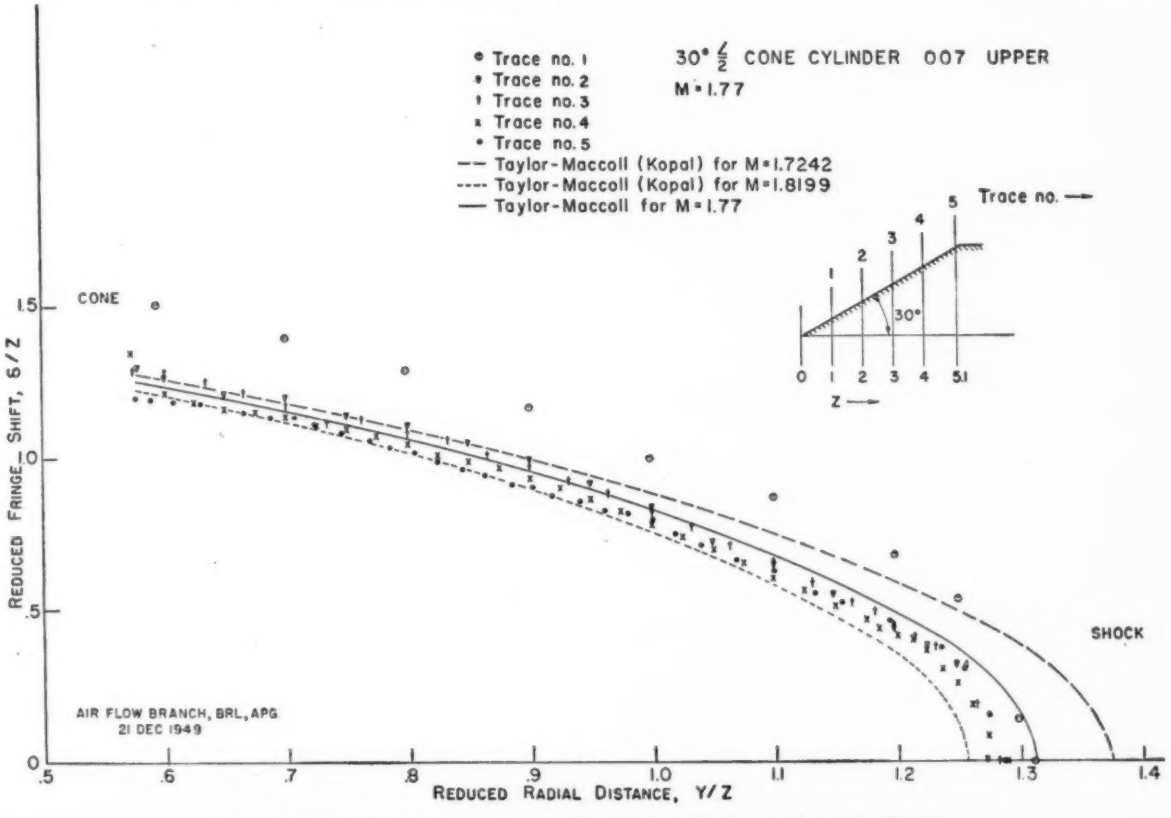

FIG. 4. Conical flow test plot of upper half of interferogram shown in Fig. 2.

Reynolds numbers, on the order of 3×10^5 based on the altitude of the cone, lead one to expect only very thin boundary layers. Actually, no boundary layer effects are readily perceptible on the interferograms, since the appearance of the fringes near the cone discloses nothing comparable to the hooks in Bershader's fringes in a well developed boundary layer.[8] Though the body is spin stabilized, on the cone the component of velocity due to spin is at most 4 percent of the forward velocity and thus will certainly not contribute significantly to viscosity effects. Unsteadiness may be produced by the deceleration and oscillation of the bodies. A rough estimate of the deceleration is 700 ft./sec.^{2}. At a velocity of 2000 ft./sec. the relative change in velocity is approximately $\Delta v/v=0.7\times10^{-5}$ during the time required for passage through the conical region, which is less than 20 microseconds outside the boundary layer. A crude upper bound on the frequency of oscillations in the flow can be derived from the fact that the fringes are steady and sharply defined during a 2 microsecond exposure. As for oscillations of the body, the precessional and nutational components of its motion have frequencies of less than 20 and 200 cycles/sec., respectively. The corresponding periods are quite long by contrast with the time of passage through the conical region. The fact that the body is in free supersonic flight in still air assures one that the flow ahead of the shock will be uniform; this is confirmed by the straightness of the undisturbed fringes. Finally, as for axisymmetry, though small yaws are inevitable, for conventional projectiles at normal pressures it is difficult to produce large yaws. Actually, measurement of the interferograms shows that the inclination of the body's axis to the trajectory is about half a degree in this projection. As a check on the influences of such small yaws and of the differences in fringe geometry, results from the upper and lower halves of the same interferogram are shown in Figs. 4 and 5.

Granting that conditions favorable for approximately Taylor-Maccoll flow occur in the present case, there will still be errors in the data. Two types will be considered here. First, in the calculation of Taylor-Maccoll fringe shifts by the method of Section II, it is assumed that the interferometer beam is normal to the axis of symmetry. Now the dynamic history along the trajectory cannot easily be predicted with great precision; moreover, it will vary from one round to the next with the geometrical and physical properties of the body. If for this reason the curvature of the trajectory and the oscillations of the body are neglected, the best approximation to the axis of symmetry is that of the gun barrel. The inclination of the interferometer beam relative to this axis was probably within two degrees of orthogonality. Calculations show that the effects of such an error in inclination are negligible. Secondly, no instrumentation

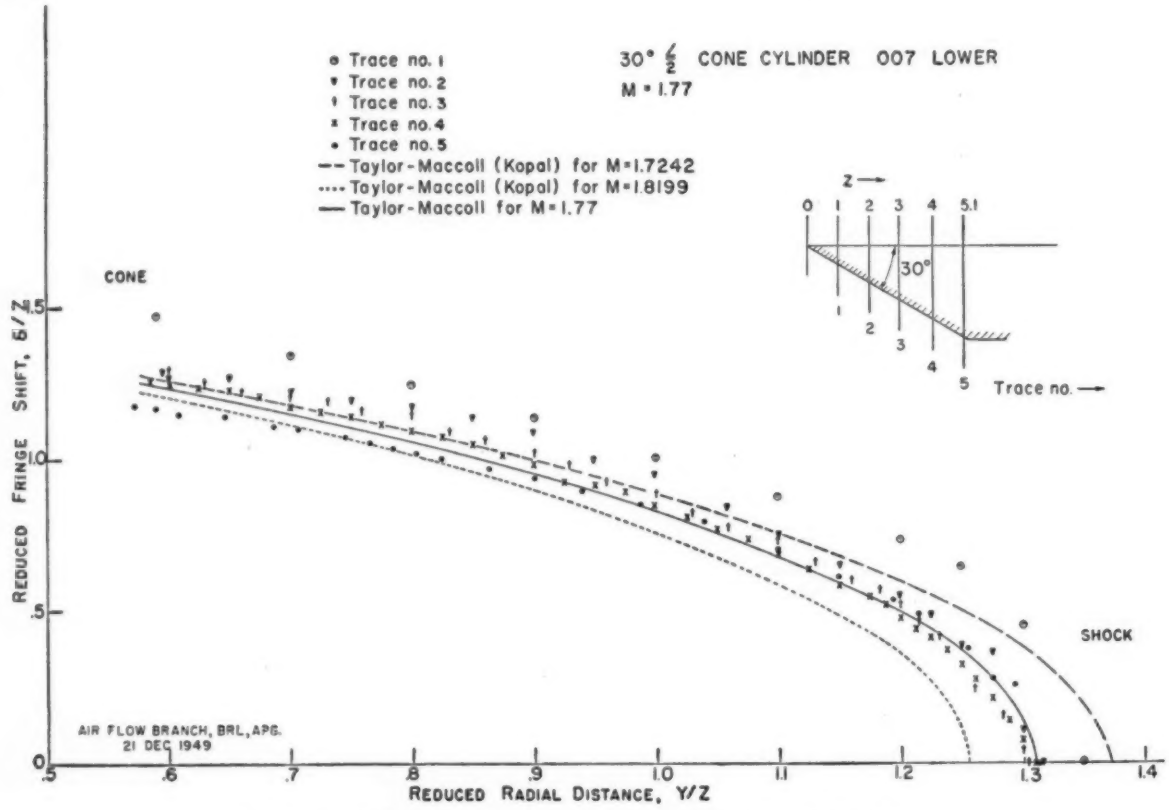

FIG. 5. Conical flow test plot of lower half of interferogram shown in Fig. 2.

[8] D. Bershader, Rev. Sci. Inst. **20**, 260–275 (1949).

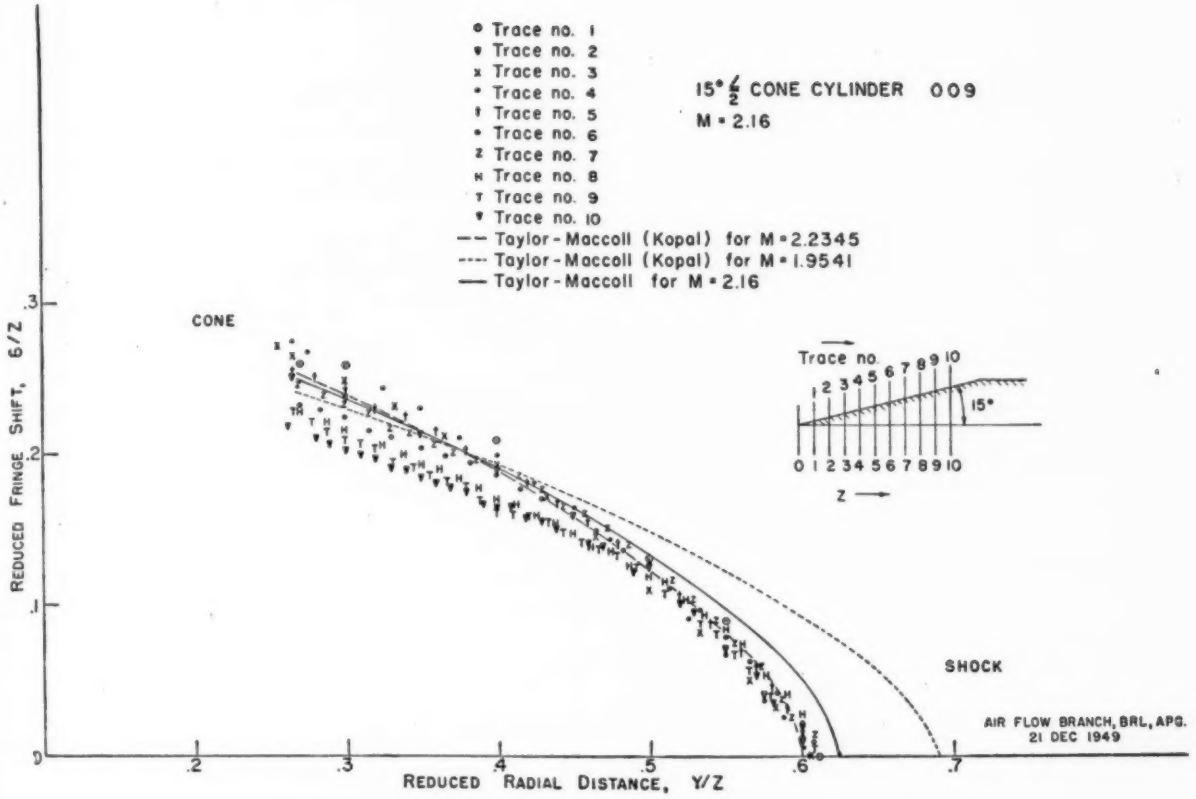

FIG. 6. Conical flow test plot for cal. 30, 15° half-angle cone cylinder—best data available.

for directly measuring velocities was available for the present firings. As a first approximation, the velocity was taken to be the average observed in firings of the same type of body with the same weight of powder in other ranges equipped with counter chronographs. A more refined estimate of the Mach number was based on the theoretical shock wave angle in Taylor-Maccoll flow, which is justified, *a posteriori*, by the agreement that will be found between the experimental data and the theoretical curves.

Figures 4 and 5 show fringe shift curves for $M=1.72$ and 1.82, calculated with $\gamma=1.4$ for Taylor-Maccoll flows tabulated in reference 6. The curve for $M=1.77$ was obtained by linear interpolation between the other two. In general, the agreement between the experimental data and theoretical curves is good, the poorer agreement in Fig. 5 being caused, possibly, by errors in the location of the axis and vertex. The scatter of the points at the shock ends of the curves may be partly due to curvature of the shock wave and partly to measurement errors, the fringe shifts being smallest there. At the cone end of the curves, the spread could conceivably originate in the boundary layer, since the traces farthest downstream, in which coordinate errors are least, seem in some instances to be displaced toward lower values.

From the quantitative estimates of error given in the last paragraph it appears that the scatter of points near the projectile body for traces posterior to No. 5 should be less than 3 percent from a mean curve. Inspection of the plotted points in Fig. 6 confirms this view. It is noteworthy that as trace number increases these latter traces fall increasingly below the Taylor-Maccoll curve for $M=2.16$ as well as below the mean curve for the first 5 traces. Translation of the data for any trace to bring the shockwave point into coincidence with that of the calculated Taylor-Maccoll curve does not improve matters much, since near the cone the latter traces still fall below the theoretical curve by several percent. We see then that the data suggests two types of deviation from conical flow (1) deviation from the Taylor-Maccoll theoretical flow of the latter traces and (2) deviation of the latter traces from the conical flow defined by the mean curve of the former traces. It is possible that these deviations can arise in the boundary layer as suggested above; however further study is required to obtain more than tentative conclusions to this effect.

Theory of Collinear Antennas

RONOLD KING
Cruft Laboratory, Harvard University, Cambridge, Massachusetts
(Received May 1, 1950)

If N collinear antennas are individually center driven, the only transmission line in the neutral plane is the one for a central unit if N is odd. Since lines that are not in a neutral plane constitute antennas, such an array is not practically useful.

For a single driven unit with symmetrical, parasitic, collinear elements, the driving transmission line is in the neutral plane and may be replaced by an equivalent generator and terminal-zone network. An array with two parasites is analyzed. Since the currents in the halves of the three units are not alike, three simultaneous integral equations occur. By making reasonable assumptions these are reduced to the single equation of the isolated antenna but with a different kernel. Approximate expressions are obtained for the currents and for the mutual and self-impedances of the elements.

The collinear antenna with outer elements driven from the central one by phase-reversing stubs is studied. For three elements components of the currents in the several possible modes are obtained with different degrees of approximation. The in-phase currents in the antennas are greatest, and are obtained with considerable accuracy. The currents in the outer units are not symmetrical, but with elements of length $\lambda/2$ the odd components of the currents are shown to be negligible.

1. INTRODUCTION AND GENERAL FORMULATION OF THE PROBLEM

THE analysis of the two individually driven collinear antennas in Fig. 1a is complicated by the fact that the axes of the transmission lines are not in neutral planes of the electromagnetic field. As a result, the forces acting on currents and charges in the two conductors of each line are not equal and opposite even at distances from the antennas that are great compared with the normal terminal zone[1] near each junction. Therefore, the transmission lines are not balanced, and the codirectional currents on each pair of conductors (or on the outside of the shield if a coaxial line is used) contribute significantly to the electromagnetic field at distant points. The actual radiating system in Fig. 1a is not limited to the two collinear antennas but includes the transmission lines. Clearly, such a system is not practically useful since its circuit and field properties depend on the length and orientation of the feeder lines.[2]

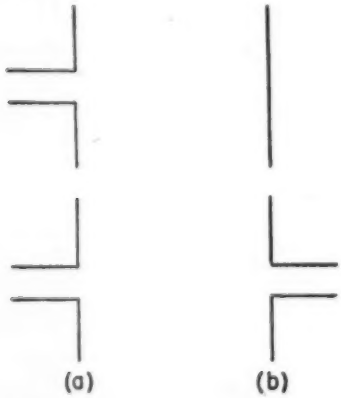

FIG. 1. Arrays of two collinear antennas.

The same difficulty exists if one of the two elements is parasitic as in Fig. 1b; or if three individually center-driven elements are used as in Fig. 2a. On the other hand, the array in Fig. 2b, in which only the central one of an odd number of collinear elements is directly driven, does not have the same serious disadvantage. The single transmission line is in the neutral plane of the array, so that unbalanced currents are not excited and radiation from the line is negligible.

The complication introduced by the two-wire line in Fig. 2b differs in no essential way from that already resolved for a single, center-driven antenna.[1] The presence of the two parasitic elements has no effect on the coupling between antenna and line since this is confined to short distances from the line-antenna junction of the order of magnitude of ten times the line spacing. It follows that the same terminal-zone network designed for a single isolated center-driven antenna may be used in conjunction with the antenna, treated as though driven by a discontinuity in scalar potential. This and following sections are concerned with the analysis of a three-element collinear array arranged and numbered as in Fig. 2b but with the central unit driven by a discontinuity in scalar potential, i.e. by a two-wire line with negligible line spacing. The analysis is carried out conveniently in the following parts:

(1) *The Symmetrical Problem:* The elements of the array are individually center-driven by discontinuities in scalar potential given by

$$V_{10}=V_1^s=V^s;\quad V_{20}=V_{30}=V_2^s=f^sV^s. \qquad (1.1a)$$

V_2^s is so chosen that the currents at the centers of the identical outer elements are equal to the current at

* The research reported in this document was supported in part by the Navy Department (ONR), the Signal Corps of the U. S. Army, and the U. S. Air Force, under contract N5-ori-76, T.O. 1/.

[1] R. King, J. App. Phys. **20**, 832–850 (1949).

[2] An approximate analysis of the two-element collinear array in which no account is taken of the practical problem of driving the array is that of C. W. Harrison, Jr., Proc. I.R.E., **33**, 398–408 (1945). Zeroth-order mutual impedances given by Harrison coincide with those derived in this paper. The general solutions differ in that Harrison did not include the effect of the coupled antenna in the kernel of the integral equation, nor did he take account of the distribution of current in deriving his expansion parameter.

the center of the middle element. That is, so that

$$I_2^s(z_2=0)=I_3^s(z_3=0)=I_1^s(z_1=0) \qquad (1.1b)$$

where z_1, z_2, and z_3 are measured from the centers of the elements indicated by the subscripts.

(2) *The Antisymmetrical Problem:* The three elements of the array are individually center-driven by

$$V_{10}=V_1^a=V^a; \quad V_{20}=V_{30}=-V_2^a=-f^aV^a \qquad (1.2a)$$

V_2^a is chosen that the currents at the centers of the outer elements are equal in magnitude but opposite in direction to the current at the center of the middle unit. That is, so that

$$I_2^a(z_2=0)=I_3^a(z_3=0)=-I_1^a(z_1=0). \qquad (1.2b)$$

(3) *The Parasitic Array:* By superimposing the solutions for the currents in problems (1) and (2) in the special case when

$$V_2^a=V_2^s \quad \text{or} \quad f^aV^a=f^sV^s, \qquad (1.3a)$$

the effective driving voltages and driving-point currents are

$$V_{10}=V^s+V^a=V^a(1+f^a/f^s)=V^a(1+k), \qquad (1.3b)$$

$$I_1(z_1)=I_1^s(z_1)+I_1^a(z_1), \qquad (1.3c)$$

and

$$V_{20}=V_2^s-V_2^a=0, \qquad (1.3d)$$

$$I_2(z_2)=I_2^s(z_2)-I_2^a(z_2)$$

$$=I_{\text{even}}^s(z_2)+I_{\text{odd}}^s(z_2)-I_{\text{even}}^a(z_2)-I_{\text{odd}}^a(z_2). \qquad (1.3e)$$

Since $V_{20}=0$, the outer units are parasitic. Moreover, since the currents in the outer units are not symmetrical with respect to the centers of the respective elements,

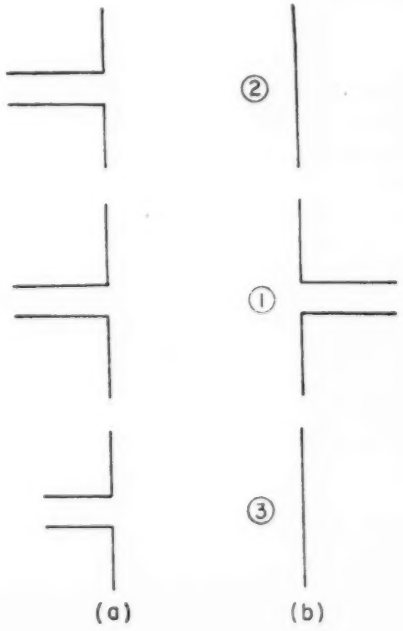

FIG. 2. Arrays of three collinear antennas.

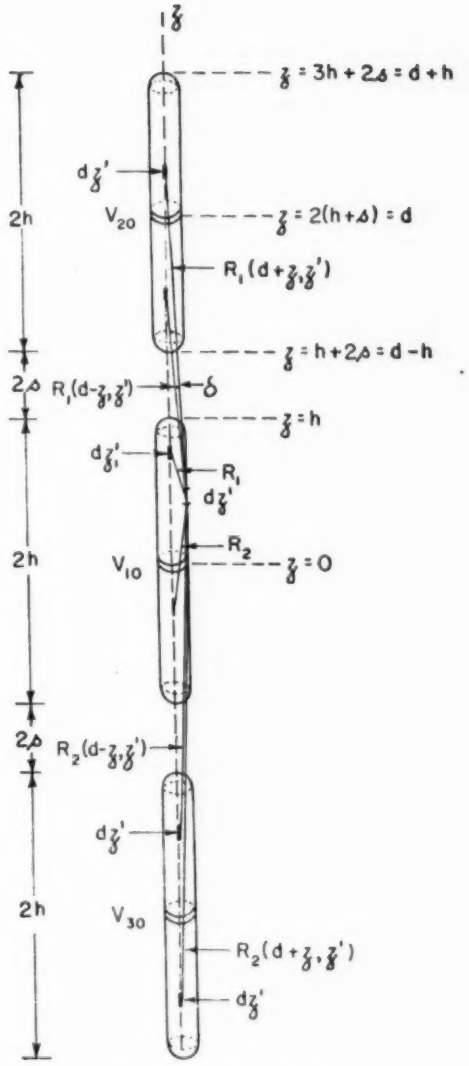

FIG. 3. Collinear array with slice generators.

the symmetrical and antisymmetrical currents are each the sum of even and odd components that must be determined separately.

(4) *The General Problem:* If the following condition is satisfied in place of (3a) or (3d):

$$V_{20}=V_2^s-V_2^a=-I_2(z_2=0)Z_L, \qquad (1.4)$$

the solution with each outer unit center-loaded with a lumped impedance Z_L is obtained. Note that $I_3(-z_3)=I_2(z_2)$.

The particular array studied in this and following sections is in Fig. 3. The three antennas are identical, each of half-length h and radius a. The conditions

$$a \ll h; \quad 2\pi a/\lambda_0=\beta_0 a \ll 1 \qquad (1.5)$$

are postulated. The distance between centers of the antennas is d, the distance between adjacent ends is $2s$ so that $d=2(h+s)$. The origin of a cylindrical system of coordinates r, θ, z, is at the center; the z-axis coin-

cides with the axes of the cylinders. The centers of the three units are at $z=0, \pm d$. Each unit is center-driven by discontinuities in scalar potential. Referring to Fig. 3 the conditions for the symmetrical drive are as in (1.1a), i.e.,

$$V_{10}=\lim_{\delta\to 0}[\phi(\delta)-\phi(-\delta)]=V_1^s=V^s \tag{1.6a}$$

$$V_{20}=\lim_{\delta\to 0}[\phi(d+\delta)-\phi(d-\delta)]=V_2^s=f^sV^s \tag{1.6b}$$

$$V_{30}=\lim_{\delta\to 0}[\phi(-d+\delta)-\phi(-d-\delta)]=V_2^s=f^sV^s \tag{1.6c}$$

where V_2^s or f^s is so chosen that (1.1b) is satisfied, i.e.,

$$I_3^s(-d)=I_2^s(d)=I_1^s(0). \tag{1.6d}$$

Similarly, the conditions for the antisymmetrical drive are as in (1.2a) with V_2^a or f^a chosen so that (1.2b) is satisfied, i.e.,

$$I_3(-d)=I_2(d)=-I_1(0). \tag{1.7}$$

Since the array is symmetrical with respect to its center, for both sets of driving conditions,

$$I(-z)=I(z); \quad q(-z)=-q(z), \tag{1.8a}$$

$$A(-z)=A(z); \quad \phi(-z)=-\phi(z). \tag{1.8b}$$

The subscript z is omitted on current and vector potential, since only z-components are involved. The vector and scalar potentials, evaluated at $r=a$ on the surfaces of the conductors, are

$$A(z)=\frac{1}{4\pi\nu_0}\left(\int_{-d-h}^{-d+h}+\int_{-h}^{h}+\int_{d-h}^{d+h}\right)I(z')K_1(z,z')dz'$$

$$=\frac{1}{4\pi\nu_0}\left(\int_{0}^{h}+\int_{d-h}^{d+h}\right)I(z')K(z,z')dz' \tag{1.9a}$$

$$\phi(z)=\frac{1}{4\pi\epsilon_0}\left(\int_{0}^{h}+\int_{d-h}^{d+h}\right)q(z')K(z,z')dz', \tag{1.9b}$$

where

$$K(z,z')=K_1(z,z')+K_2(z,z')=\frac{e^{-j\beta_0R_1}}{R_1}+\frac{e^{-j\beta_0R_2}}{R_2} \tag{1.9c}$$

and where

$$R_1=((z-z')^2+a^2)^{\frac{1}{2}}; \quad R_2=((z+z')^2+a^2)^{\frac{1}{2}}. \tag{1.9d}$$

The differential equation for the vector potential is the same as for a single antenna, viz.,

$$\frac{\partial^2A(z)}{\partial z^2}+\beta_0^2A(z)=j\frac{\beta_0^2}{\omega}z^iI(z); \quad (r=a). \tag{1.10a}$$

The solution consists of three equations of the form

$$A(z)=\frac{-j}{v_0}[C_1\cos\beta_0z+C_2\sin\beta_0z]; \quad (r=a) \tag{1.10b}$$

with different constants C_1 and C_2 in the equations applying, respectively, to the three sections of conductor extending from 0 to h, $d-h$ to d, d to $d+h$. A particular integral involving z^i as a factor has been omitted from (1.10b); it usually contributes negligibly.

Since the currents in the upper half of the central unit and the lower and upper halves of the upper unit are all different, the rigorous solution for these currents is complicated. Fortunately, an approximate solution may be obtained by making assumptions that are reasonable and that lead to integral equations like that for a single antenna.

2. THREE-ELEMENT COLLINEAR ARRAY; GENERAL ANALYSIS OF CENTRAL ANTENNA

The current $I_1(z)$ in the upper half of the central unit depends primarily upon the following integral equation valid at $r=a$ with $0\leqq z\leqq h$.

$$J_a+(J_b+J_c)=\frac{-j4\pi}{\zeta_0}[C_1\cos\beta_0z+\tfrac{1}{2}V_{10}\sin\beta_0z]. \tag{2.1}$$

For the upper sign, $V_{10}=V^s$; for the lower sign $V_{10}=V^a$. In (1),

$$J_a\equiv\int_0^h I_1(z')K(z,z')dz', \tag{2.2a}$$

$$J_b\equiv\int_{d-h}^{d}I_2(z')K(z,z')dz'$$

$$=\int_0^h I_2(d-z')K(z,d-z')dz', \tag{2.2b}$$

$$J_c\equiv\int_{d}^{d+h}I_2(z')K(z,z')dz'$$

$$=\int_0^h I_2(d+z')K(z,d+z')dz'. \tag{2.2c}$$

The current $I_1(z)$ in the central unit occurs also in two equations similar to (1) with integrals evaluated, respectively, over the halves of antenna 2. With (1) these constitute three simultaneous integral equations in the currents.

Equation (1) was obtained by substituting (1.9a) in (1.10b), evaluating $C_2=\frac{1}{2}V_{10}$, and replacing v_0/ν_0 by its equivalent, $\zeta_0=376.7$ ohms. The last integrals in (2.2b) and (2.2c) are derived from the first integrals by changing the variable of integration to u, by setting $z'=d-u$ in (2.2b) and $z'=d+u$ in (2.2c), and then substituting z' for u. Note that each integral in (2.2a) to (2.2c) may be expanded into two integrals in the form $J_{i1}+J_{i2}$, $i=a, b, c$, by setting

$$K(z,v)=K_1(z,v)+K_2(z,v)$$

$$=\frac{e^{-j\beta_0R_1(z,v)}}{R_1(z,v)}+\frac{e^{-j\beta_0R_2(z,v)}}{R_2(z,v)}, \tag{2.3a}$$

where

$$R_1(z, v)=((z-v)^2+a^2)^{\frac{1}{2}};\quad R_2(z, v)=((z+v)^2+a^2)^{\frac{1}{2}} \quad (2.3b)$$

and

$$v=z',\quad d-z',\quad d+z'. \quad (2.3c)$$

Since the point z, where the vector potential is evaluated, is on the surface of the upper half of antenna 1 between $z=0$ and $z=h$, the contributions to the total vector potential by the integrals in (2.2a) to (2.2b) differ widely. Although the distributions of the currents in the six halves of the three antennas are not all the same, they are sufficiently alike to have the same average order of magnitude *if made equal at the centers of the antennas*. Consequently, in determining the current in the *central unit*, the currents in all units may be assumed the same. Since the currents for $z<0$ are obtained from the currents for $z>0$ using (1.8a), the following expressions relate *all* currents:

$$I_2^s(d-z')\doteq I_1^s(z')\doteq I_2^s(z'+d);\quad (0\leqq z'\leqq h) \quad (2.4a)$$

$$-I_2^a(d-z')\doteq I_1^a(z')\doteq -I_2^a(z'+d);\quad (0\leqq z'\leqq h). \quad (2.4b)$$

With (2.4a, b), (2.1) becomes

$$\int_0^h I(z')K_c(z, z')dz'$$

$$=\frac{-j4\pi}{\zeta_0}[C_1\cos\beta_0 z+\tfrac{1}{2}V_{10}\sin\beta_0 z]:$$

$$(r=a;\quad 0\leqq z\leqq h). \quad (2.5)$$

When $V_{10}=V^s$, $I=I^s$, $C_1=C_1^s$, $K_c=K_c^s$; when $V_{10}=V^a$, $I=I^a$, $C_1=C_1^a$, $K_c=K_c^a$. The new kernel, $K_c(z, z')=K_{c1}(z, z')+K_{c2}(z, z')$, is defined as follows:

$$K_c(z, z')\equiv\left\{\begin{matrix}K_c^s(z, z')\\ K_c^a(z, z')\end{matrix}\right\}\equiv K(z, z')$$

$$\pm[K(z, d-z')+K(z, d+z')] \quad (2.6)$$

with $K(z, v)$ defined as in (2.3a). Note that with (2.3b)

$$R_1(z, d-z')=((z-d+z')^2+a^2)^{\frac{1}{2}}=R_1(d-z, z'), \quad (2.7a)$$

$$R_1(z, d+z')=((z-d-z')^2+a^2)^{\frac{1}{2}}=R_2(d-z, z'), \quad (2.7b)$$

$$R_2(z, d-z')=((z+d-z')^2+a^2)^{\frac{1}{2}}=R_1(d+z, z'), \quad (2.7c)$$

$$R_2(z, d+z')=((z+d+z')^2+a^2)^{\frac{1}{2}}=R_2(d+z, z'). \quad (2.7d)$$

It follows that

$$K(z, d-z')+K(z, d+z')=K(d-z, z')+K(d+z, z') \quad (2.8)$$

so that

$$K_c(z, z')=K(z, z')\pm[K(d-z, z')+K(d+z, z')]. \quad (2.9)$$

This form of the kernel is convenient in the evaluation of the expansion parameter.

Since (2.5) is an integral equation like that for the single antenna,[3a,3b] the same formal solution is obtained with a new kernel. The current in the upper half of the central unit of the collinear array is given by (3) in reference 3b with $K_c(z, z')$ substituted for $K(z, z')$. Thus,

$$I_1(z)=\frac{j2\pi V}{\zeta_0\Psi_{Kc}}\left\{\frac{\sin\beta_0(h-z)+M_{c1}(z)/\Psi_{Kc}+\cdots}{\cos\beta_0 h+A_{c1}/\Psi_{Kc}+\cdots}\right\}. \quad (2.10)$$

Similarly, the impedance of the central unit is

$$Z_{0c}=\frac{-j\zeta_0\Psi_{Kc}}{2\pi}\left\{\frac{\cos\beta_0 h+A_{c1}/\Psi_{Kc}+\cdots}{\sin\beta_0 h+B_{c1}/\Psi_{Kc}+\cdots}\right\}. \quad (2.11)$$

Each of these formulas applies to the symmetrically

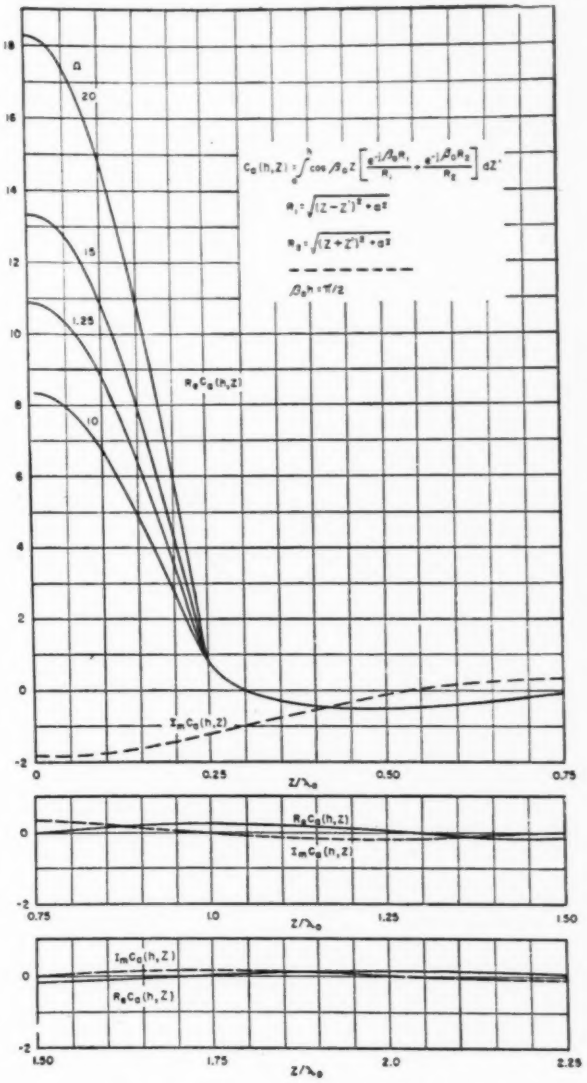

FIG. 4. The function $C_0(h, z)$ for $\beta_0 h=\pi/2$.

[3a] R. King and D. Middleton, Quart. App. Math. **3**, 302–335 (January, 1946) and **4**, 199–200 (July, 1946).
[3b] D. Middleton and R. King, J. App. Phys. **17**, 273–284 (1946).

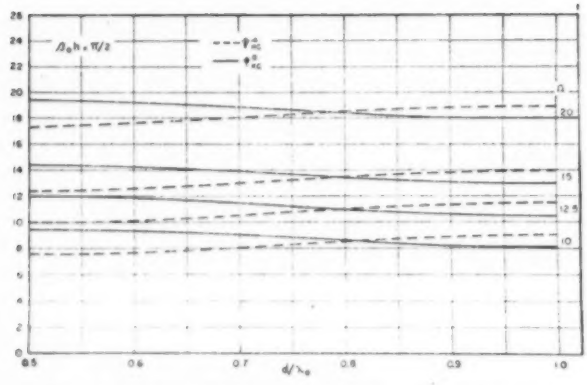

FIG. 5. The expansion parameters for the central unit in a three-element array.

driven array when a superscript s is affixed to V, I, M, B, A, Ψ and Z and the upper sign is used, and to the antisymmetrically driven array when the superscript a is affixed to these symbols and the lower sign is used. The quantities $M_{c1}(z)$, $B_{c1}=M_{1c}(0)$, and A_{c1} are the same as in reference 3 with $K_c(z, z')$ in (2.9) substituted for $K(z, z')$, and with Ψ_{Kc} replacing $\Psi=\Psi_{K1}$.

The expansion parameter Ψ_{Kc} is defined as is Ψ in reference 3. The steps include

$$\Psi_{Kc}(z)=\psi_{Kc}(z)/\sin\beta_0(h-z), \tag{2.12}$$

$$\psi_{Kc}(z)=\sin\beta_0 h\int_0^h \cos\beta_0 z' K_c(z, z')dz' - \cos\beta_0 h\int_0^h \sin\beta_0 z' K_c(z, z')dz'. \tag{2.13}$$

The integrals in (13) involve only the functions[4] $C_a(h, v)$ and $S_a(h, v)$ defined in references 3 and 4. Their introduction yields:

$$\psi_{Kc}(z)=\psi_1(z)\pm[\psi_1(d-z)+\psi_1(d+z)], \tag{2.14}$$

where

$$\psi_1(v)=C_a(h, v)\sin\beta_0 h-S_a(h, v)\cos\beta_0 h. \tag{2.15}$$

By far the most important case in practice is with $\beta_0 h=\pi/2$ for which

$$\psi_{Kc}(z)=C_a(h, z)\pm[C_a(h, d-z)+C_a(h, d+z)]; \quad h=\lambda_0/4. \tag{2.16}$$

The function of $C_a(h, z)$ for $\beta_0 h=\pi/2$ is given in Fig. 4. The function in (12) is:

$$\Psi_{Kc}(z)=\Psi_{K1}(z)\pm[\Psi_{K1}(d-z)+\Psi_{K1}(d+z)] \tag{2.17}$$

where $\Psi_{K1}(z)$ applies to the central unit when isolated.

Since the general behavior of $\Psi_{Kc}(z)$ as a function of z is like that of $\Psi_{K1}(z)$ for all possible values of d, the expansion parameter for the central unit may be defined as for the isolated antenna. Specifically,

$$\Psi_{Kc}=\begin{cases} |\Psi_{Kc}(0)|=|\Psi_{K1}(0)\pm 2\Psi_{K1}(d)| \\ \qquad\qquad \text{for} \quad \beta_0 h\leqq\pi/2 \\ |\Psi_{Kc}(h-\lambda_0/4)|=|\Psi_{K1}(h-\lambda_0/4) \\ \qquad \pm[\Psi_{K1}(d-h+\lambda_0/4) \\ \qquad +\Psi_{K1}(d+h-\lambda_0/4)]| \\ \qquad\qquad \text{for} \quad \beta_0 h\geqq\pi/2. \end{cases} \tag{2.18}$$

A superscript s is added to Ψ_{Kc} for $V=V^s$, and the upper signs are used; a superscript a is added for $V=-V^a$, and the lower signs are used. $\Psi_{Kc}{}^s$ and $\Psi_{Kc}{}^a$ are shown in Fig. 5.

It is clear from (2.18) that when the elements of the collinear array are driven in phase, current and impedance of the central unit are like those of an isolated antenna with a larger Ψ_{K1} and hence smaller radius. Alternatively, when the two outer units are driven 180 degrees out of phase with the central unit, this behaves like an isolated antenna with a smaller Ψ_{K1} and greater radius. This is true for $d/\lambda_0<0.8$.

The impedances Z^s and Z^a determined from (2.11) with appropriate superscripts s and a, and the corresponding currents $I_1{}^s(z)$ and $I_1{}^a(z)$ as given by (2.10) in terms of the driving voltage $V=V^s$ or $V=V^a$, are valid *only if the outer units are driven* so that the currents at their centers are equal to $I_1{}^s(0)$ in the symmetrical case, or to $-I_1{}^a(0)$ in the antisymmetrical case. Evidently, the problem of the central unit is not solved until $V_2{}^s=f^sV^s$ and $V_2{}^a=f^aV^a$ are known. They are determined in Sec. 3. Once f^s and f^a are known, a superposition of the solutions for which $V_2{}^s=V_2{}^a$ yields the solution of the array with parasitic outer elements. Since in this case

$$V^s/V^a=f^s/f^s=k, \tag{2.19a}$$

it follows that

$$\frac{1}{Z_{\text{lin}}}=Y_{\text{lin}} =\frac{I_1(0)}{V_{10}}=\frac{I_1{}^s(0)+I_1{}^a(0)}{V^s+V^a}=\frac{I_1{}^s(0)}{V^s(1+k^{-1})} +\frac{I_1{}^a(0)}{V^a(1+k)}=\frac{1}{Z_{0c}{}^s(1+k^{-1})}+\frac{1}{Z_{0c}{}^a(1+k)}. \tag{2.19b}$$

Solving for Z_{lin} gives the input impedance of the three-element collinear array with the outer units parasitic.

$$Z_{\text{lin}}=\frac{2Z_{0c}{}^sZ_{0c}{}^a}{Z_{0c}{}^s+Z_{0c}{}^a}F_1=Z_{\text{lin}}{}'F_1, \tag{2.19c}$$

[4] The functions are:

$$C_a(h, z)\equiv\int_0^h \cos\beta_0 z'\left[\frac{\exp(-j\beta_0 R_1)}{R_1}+\frac{\exp(-j\beta_0 R_2)}{R_2}\right]dz'$$

$$S_a(h, z)\equiv\int_0^h \sin\beta_0 z'\left[\frac{\exp(-j\beta_0 R_1)}{R_1}+\frac{\exp(-j\beta_0 R_2)}{R_2}\right]dz'$$

$$R_1\equiv((z-z')^2+a^2)^{\frac{1}{2}}; \quad R_2\equiv((z+z')^2+a^2)^{\frac{1}{2}}.$$

where

$$F_1=1+\frac{(Z_{0c}{}^s-Z_{0c}{}^a)(k-k^{-1})}{2Z_{0c}{}^s(1+k^{-1})+Z_{0c}{}^a(1+k)}. \quad (2.19d)$$

The determination of k is in Section 3. The numerical evaluation of Z_{1in} for $\beta_0 h=\pi/2$ is in Section 4.

The current in the central unit is given by

$$I(z)=I_1{}^s(z)+I_1{}^a(z) \quad (2.20)$$

where $I_1{}^s(z)$ is given by (2.10) with superscripts s and with $V=V^s=V_{10}/(1+k^{-1})$, and where $I_1{}^a(z)$ is given by (2.10) with superscripts a and with $V=V^a=V_{10}/(1+k)$. Once k is determined $I_1(z)$ may be calculated in terms of V_{10}, the actual driving voltage when the outer units are parasitic.

3. THREE-ELEMENT COLLINEAR ARRAY; GENERAL ANALYSIS OF OUTER ANTENNAS

The currents in the outer antennas cannot be determined so accurately as the currents in the central unit since they are not symmetrical with respect to the centers of these antennas. However, since it is not possible to center drive these units without the addition of unbalanced transmission lines, the only practically significant application of the theory as developed up to this point is with the outer units parasitic. Since in this case the currents in the parasites are not involved directly in the driving-point impedance, but only in f^s and f^a, and in obtaining the electromagnetic field of the array, it is adequate to determine approximate currents. For this purpose the principal assumption is that the current in each outer unit is composed of even and odd parts of which the odd is *not* large compared with the even. In general, this means that $\beta_0 h$ must not be near enough to π, 2π, $3\pi\cdots$ to make the odd part of the current the resonant part. When $\beta_0 h$ is near $\pi/2$ the even part of the current is resonant and the assumption is an excellent one.

The integral equation for the current in the halves of antenna 2 (Fig. 3) are

$$4\pi\nu_0 A(z_2)=\frac{-j4\pi}{\zeta_0}[C_1\cos\beta_0 z_2+C_2\sin\beta_0 z_2];$$

$$(0\leqq z_2\leqq h), \quad (3.1a)$$

$$4\pi\nu_0 A(z_2)=\frac{-j4\pi}{\zeta_0}[C_1\cos\beta_0 z_2+C_4\sin\beta_0 z_2];$$

$$(-h\leqq z_2\leqq 0), \quad (3.1b)$$

where

$$4\pi\nu_0 A(z_2)=\left(\int_{-h}^{h}+\int_{-d-h}^{-d+h}+\int_{-2d-h}^{-2d+h}\right)\times I(z_2')K_1(z_2, z_2')dz_2' \quad (3.2a)$$

with

$$K_1(z_2, z_2')=\frac{e^{-j\beta_0 R_1(z_2, z_2')}}{R_1(z_2, z_2')};$$

$$R_1(z_2, z_2')=((z_2-z_2')+a^2)^{\frac{1}{2}}. \quad (3.2b)$$

By setting $z'=d+z_2'$ in the second integral, $z_3'=2d+z_2'$ in the third integral and noting that

$$R_1(z_2, z'-d)=((d+z_2-z')^2+a^2)^{\frac{1}{2}}=R_1(d+z_2, z') \quad (3.3a)$$

$$R_1(z_2, z_3'-2d)=((2d+z_2-z_3')^2+a^2)^{\frac{1}{2}}=R_1(2d+z_2, z_3'). \quad (3.3b)$$

(3.2a) may be expressed as follows:

$$4\pi\nu_0 A(z_2)=\int_{-h}^{h}I_2(z_2')K_1(z_2, z_2')dz_2'+\int_{-h}^{h}I_1(z')K_1(d+z_2, z')dz'+\int_{-h}^{h}I_3(z_3')K_1(2d+z_2', z_3')dz_3'. \quad (3.4)$$

As a consequence of symmetry,

$$I_3(z_3')=I_2(-z_2'). \quad (3.5)$$

Since $I_1(z')$ is an even function of z' and symmetrical or antisymmetrical driving voltages are provided so that $I_1(z'=0)=\pm I_2(z_2'=0)$, a satisfactory approximation is

$$I_1(z')=\pm\tfrac{1}{2}[I_2(z_2')+I_2(-z_2')] \quad (3.6)$$

where the upper sign applies to the symmetrical, the lower sign to the antisymmetrical case. Substitution of (3.5) and (3.6) in (3.4) gives

$$4\pi\nu_0 A(z_2)=\int_0^h\{I_2(z_2')K_{1d}(z_2, z_2')+I_2(-z_2')K_{2d}(z_2, z_2')\}dz_2' \quad (3.7)$$

where

$$K_{1d}(z_2, z_2')\equiv K_1(z_2, z_2')\pm\tfrac{1}{2}[K_1(d+z_2, z_2')+K_2(d+z_2, z_2')]+K_2(2d+z_2, z_2') \quad (3.8a)$$

$$K_{2d}(z_2, z_2')\equiv K_2(z_2, z_2')\pm\tfrac{1}{2}[K_2(d+z_2, z_2')+K_1(d+z_2, z_2')]+K_1(2d+z_2, z_2'). \quad (3.8b)$$

The following notation is used:

$$K_1(u, z_2') \equiv \frac{e^{-j\beta_0 R_1(u, z_2')}}{R_1(u, z_2')};$$

$$K_2(u, z_2') \equiv \frac{e^{-j\beta_0 R_2(u, z_2')}}{R_2(u, z_2')}, \quad (3.9a)$$

$$R_1(u, z_2') \equiv ((u-z_2')^2+a^2)^{\frac{1}{2}};$$

$$R_2(u, z_2') = ((u+z_2')^2+a^2)^{\frac{1}{2}}. \quad (3.9b)$$

These formulas apply in the following two cases:

Symmetrical Case:

$$\left.\begin{aligned} &V_{10}=V^s; \quad V_{30}=V_{20}=V_2{}^s=f^sV^s; \\ &I_2(z_2')=I_2{}^s(z_2') \\ &K_{1d}(z_2, z_2') \text{ with upper sign} = K_{1d}{}^s(z_2, z_2'). \end{aligned}\right\}, \quad (3.10a)$$

Antisymmetrical Case:

$$\left.\begin{aligned} &V_{10}=V^a; \quad V_{30}=V_{20}=-V_2{}^a=-f^aV^a; \\ &I_2(z_2')=I_2{}^a(z_2') \\ &K_{1d}(z_2, z_2') \text{ with lower sign} = K_{1d}{}^a(z_2, z_2') \end{aligned}\right\}. \quad (3.10b)$$

The first step in the solution of (3.1a) with (3.7) is to resolve both sides into even and odd functions of z_2 and in this way obtain two equations, the one for the even part of $I_2(z_2)$, the other for the odd part. The conditions for the even parts of the vector potential and current are

$$A_{\text{even}}(z_2)=\tfrac{1}{2}[A(z_2)+A(-z_2)];$$

$$I_{\text{even}}(z_2)=\tfrac{1}{2}[I_2(z_2)+I_2(-z_2)] \quad (3.11a)$$

so that with (3.1a)

$$4\pi\nu_0 A_{\text{even}}(z_2) = \frac{-j4\pi}{\zeta_0}[C_{\text{even}}\cos\beta_0 z_2+\tfrac{1}{2}V_{20}\sin\beta_0 z_2]; \quad -h\leqq z_2\leqq h) \quad (3.11b)$$

where $C_{\text{even}}=\frac{1}{2}(C_1+C_3)$ and $\frac{1}{2}V_{20}=\frac{1}{2}(C_2-C_4)$. The even part of the vector potential in the range $(-h\leqq z_2\leqq 0)$ is obtained from $A_{\text{even}}(-z_2)=A_{\text{even}}(z_2)$.

The conditions for the odd part of the vector potential and current are

$$A_{\text{odd}}(z_2)=\tfrac{1}{2}[A(z_2)-A(-z_2)];$$

$$I_{\text{odd}}(z_2)=\tfrac{1}{2}[I_2(z_2)-I_2(-z_2)] \quad (3.12a)$$

so that with (1a)

$$4\pi\nu_0 A_{\text{odd}}(z_2)=\frac{-j4\pi}{\zeta_0}C_{\text{odd}}\sin\beta_0 z_2; \quad (-h\leqq z_2\leqq h) \quad (3.12b)$$

where $C_{\text{odd}}=\frac{1}{2}(C_2+C_4)$ and $\frac{1}{2}(C_1-C_3)=0$ since $A_{\text{odd}}(-z_2)=A_{\text{odd}}(z_2)=0$ at $z_2=0$. The odd vector potential in the range $(-h\leqq z_2\leqq 0)$ is obtained from $A_{\text{odd}}(-z_2)=-A_{\text{odd}}(z_2)$.

The integrals and equations for the even and odd parts of the vector potential are obtained using (3.11a, b) and (3.12a, b). They are

$$4\pi\nu_0 A_{\text{even}}(z_2)=\int_0^h \{I_2(z_2')K_{1\text{even}}(z_2, z_2') + I_2(-z_2')K_{2\text{even}}(z_2, z_2')\}dz_2' = \frac{-j4\pi}{\zeta_0}[C_{\text{even}}\cos\beta_0 z_2+\tfrac{1}{2}V_{20}\sin\beta_0|z_2|]; \quad (-h\leqq z_2\leqq h) \quad (3.13a')$$

$$4\pi\nu_0 A_{\text{odd}}(z_2)=\int_0^h \{I_2(z_2')K_{1\text{odd}}(z_2, z_2') + I_2(-z_2')K_{2\text{odd}}(z_2, z_2')\}dz_2 = \frac{-j4\pi}{\zeta_0}C_{\text{odd}}\sin\beta_0 z_2; \quad (-h\leqq z_2\leqq h) \quad (3.13b)$$

where

$$K_{1\text{even}}(z_2, z_2')\equiv\tfrac{1}{2}[K_{1d}(z_2, z_2')+K_{1d}(-z_2, z_2')], \quad (3.14a)$$

$$K_{2\text{even}}(z_2, z_2')\equiv\tfrac{1}{2}[K_{2d}(z_2, z_2')+K_{2d}(-z_2, z_2')], \quad (3.14b)$$

$$K_{1\text{odd}}(z_2, z_2')\equiv\tfrac{1}{2}[K_{1d}(z_2, z_2')-K_{1d}(-z_2, z_2')], \quad (3.14c)$$

$$K_{2\text{odd}}(z_2, z_2')=\tfrac{1}{2}[K_{2d}(z_2, z_2')-K_{2d}(-z_2, z_2')]. \quad (3.14d)$$

In an asymmetrical geometrical arrangement like that of the outer elements in a collinear array, contributions to the even as well as the odd parts of the vector potential come from *both* even and odd parts of the currents in the three units. Consequently (3.13a) and (3.13b) cannot be solved directly for $I_{\text{even}}(z_2)$ and $I_{\text{odd}}(z_2)$. However, an approximate procedure is available. The current may be expanded into its even and odd parts by setting

$$I_2(z_2')=I_{\text{even}}(z_2')+I_{\text{odd}}(z_2');$$

$$I_2(-z_2')=I_{\text{even}}(z_2')-I_{\text{odd}}(z_2') \quad (3.15a)$$

where by definition

$$I_{\text{even}}(z_2')=\tfrac{1}{2}[I(z_2')+I_2(-z_2')]=I_{\text{even}}(-z_2'), \quad (3.15b)$$

$$I_{\text{odd}}(z_2')=\tfrac{1}{2}[I(z_2')-I_2(-z_2')]=-I_{\text{odd}}(-z_2'). \quad (3.15c)$$

If (3.15a) is substituted in (3.13a) and (3.13b), the

results are:

$$4\pi\nu_0 A_{\text{even}}(z_2)=\int_0^h \{I_{\text{even}}(z_2')[K_{1\text{even}}(z_2, z_2') + K_{2\text{even}}(z_2, z_2')]+I_{\text{odd}}(z_2')[K_{1\text{even}}(z_2, z_2') - K_{2\text{even}}(z_2, z_2')]\}dz_2' \quad (3.16a)$$

$$4\pi\nu_0 A_{\text{odd}}(z_2)=\int_0^h \{I_{\text{even}}(z_2')[K_{1\text{odd}}(z_2, z_2') + K_{2\text{odd}}(z_2, z_2')]+I_{\text{odd}}(z_2')[K_{1\text{odd}}(z_2, z_2') - K_{2\text{odd}}(z_2, z_2')]\}dz_2'. \quad (3.16b)$$

Let the following kernels be defined:

$$K_{\text{even}}(z_2, z_2')\equiv K_{1\text{even}}(z_2, z_2')+K_{2\text{even}}(z_2, z_2')=\tfrac{1}{2}[K_{1d}(z_2, z_2')+K_{2d}(z_2, z_2')+K_{1d}(-z_2, z_2')+K_{2d}(-z_2, z_2')]$$
$$=K_1(z_2, z_2')+K_2(z_2, z_2')\pm\tfrac{1}{2}[K_1(d+z_2, z_2')+K_2(d+z_2, z_2')+K_1(d-z_2, z_2')+K_2(d-z_2, z_2')]$$
$$+\tfrac{1}{2}[K_1(2d+z_2, z_2')+K_2(2d+z_2, z_2')+K_1(2d-z_2, z_2')+K_2(2d-z_2, z_2')] \quad (3.17a)$$

$$K_{e0}(z_2, z_2')\equiv K_{1\text{even}}(z_2, z_2')-K_{2\text{even}}(z_2, z_2')=\tfrac{1}{2}[K_{1d}(z_2, z_2')-K_{2d}(z_2, z_2')+K_{1d}(-z_2, z_2')-K_{2d}(-z_2, z_2')]$$
$$=-\tfrac{1}{2}[K_1(2d+z_2, z_2')-K_2(2d+z_2, z_2')+K_1(2d-z_2, z_2')-K_2(2d-z_2, z_2')] \quad (3.17b)$$

$$K_{0e}(z_2, z_2')\equiv K_{1\text{odd}}(z_2, z_2')+K_{2\text{odd}}(z_2, z_2')=\tfrac{1}{2}[K_{1d}(z_2, z_2')+K_{2d}(z_2, z_2')-K_{1d}(-z_2, z_2')-K_{2d}(z_2, z_2')]$$
$$=\pm\tfrac{1}{2}[K_1(d+z_2, z_2')+K_2(d+z_2, z_2')-K_1(d-z_2, z_2')-K_2(d-z_2, z_2')]$$
$$+\tfrac{1}{2}[K_1(2d+z_2, z_2')+K_2(2d+z_2, z_2')-K_1(2d-z_2, z_2')-K_2(2d-z_2, z_2')] \quad (3.17c)$$

$$K_{\text{odd}}(z_2, z_2')\equiv K_{1\text{odd}}(z_2, z_2')-K_{2\text{odd}}(z_2, z_2')=\tfrac{1}{2}[K_{1d}(z_2, z_2')-K_{2d}(z_2, z_2')-K_{1d}(-z_2, z_2')+K_{2d}(-z_2, z_2')]$$
$$=K_1(z_2, z_2')-K_2(z_2, z_2')-\tfrac{1}{2}[K_1(2d+z_2, z_2')-K_2(2d+z_2, z_2')]$$
$$+\tfrac{1}{2}[K_1(2d-z_2, z_2')-K_2(2d-z_2, z_2')]. \quad (3.17d)$$

Examination of (3.17b) as it appears in (3.16a) shows that it represents the contribution to the even part of the vector potential on antenna 2 by the odd parts of the currents in antenna 3. Since the odd currents involved are assumed to be relatively small, and in any case the distances are large, this term is negligible compared with the very much greater contribution from the large even currents in all three antennas. Since $R_1(2d\pm z_2, z_2')$ differs very much less from $R_2(2d\pm z_2, z_2')$ than does $R_1(z_2, z_2')$ from $R_2(z_2, z_2')$ it follows that the principal contributions to $K_{\text{odd}}(z_2, z_2')$ in (3.17d) are from the first two terms. That is,

$$K_{\text{odd}}(z_2, z_2')\doteq K_1(z_2, z_2')-K_2(z_2, z_2'). \quad (3.17e)$$

Neglecting the term in $K_{e0}(z_2, z_2')$, the two integral equations are:

$$4\pi\nu_0 A_{\text{even}}(z_2)=\int_0^h I_{\text{even}}(z_2')K_{\text{even}}(z_2, z_2')dz_2'$$
$$=\frac{-j4\pi}{\zeta_0}[C_{\text{even}}\cos\beta_0 z_2+\tfrac{1}{2}V_{20}\sin\beta_0 z_2]; \quad (-h\leqq z_2\leqq h) \quad (3.18a)$$

$$4\pi\nu_0 A_{\text{odd}}(z_2)=\int_0^h I_{\text{even}}(z_2')K_{0e}(z_2, z_2')dz_2' + \int_0^h I_{\text{odd}}(z_2')K_{\text{odd}}(z_2, z_2')dz_2'$$
$$=\frac{-j4\pi}{\zeta_0}C_{\text{odd}}\sin\beta_0 z_2; \quad (-h\leqq z_2\leqq h). \quad (3.18b)$$

Of these the first may be solved directly for $I_{\text{even}}(z_2)$; using this known value, the second equation may be solved for $I_{\text{odd}}(z_2)$. Note that the equations apply only in the symmetrical and antisymmetrical cases defined in (3.10a, b) but that the general case may be constructed by superposition.

The Eq. (3.18a) for the even part of the current is in exactly the same form as the equation for a single antenna. The solution may be written down directly in the form

$$I_{\text{even}}(z_2)=\frac{j2\pi V_{20}}{\zeta_0\Psi_{\text{even}}}\times\left\{\frac{\sin\beta_0(h-z_2)+M_{\text{even}1}(z_2)/\Psi_{\text{even}}+\cdots}{\cos\beta_0 h+A_{\text{even}1}/\Psi_{\text{even}}+\cdots}\right\}. \quad (3.19a)$$

The impedance is

$$Z_{\text{even}}=\frac{-j\zeta_0\Psi_{\text{even}}}{2\pi}\left\{\frac{\cos\beta_0 h+A_{\text{even}1}/\Psi_{\text{even}}+\cdots}{\sin\beta_0 h+B_{\text{even}1}/\Psi_{\text{even}}+\cdots}\right\}. \quad (3.19b)$$

For the symmetrical case a superscript s is added to I, Ψ, M, B, A, and Z, and V_{20} is replaced by $V_2{}^s$; for the antisymmetrical case a superscript a replaces the superscript s. The functions M, B, A, and Ψ are defined as for a single antenna but using a different kernel.

An important object in evaluating $I_{\text{even}}{}^s(z_2)$ and $I_{\text{odd}}{}^a(z_2)$ is to determine the factor f^s and f^a. They may be evaluated directly from (3.19a, b) as follows. Since the odd part of $I_2(z_2)$ necessarily is zero at $z_2=0$, the

entire current at this point is even. Hence, using (1.6) and (1.7),

Symmetrical case:

$$V_{20}=V_2{}^s=I_2{}^s(z_2=0)Z_{\text{even}}{}^s$$

$$=I_1{}^s(0)Z_{\text{even}}{}^s=\frac{V^s}{Z_{0c}{}^s}\cdot Z_{\text{even}}{}^s=f^sV^s. \quad (3.20a)$$

Therefore,

$$f^s=Z_{\text{even}}{}^s/Z_{0c}{}^s. \quad (3.20b)$$

Antisymmetrical case:

$$V_{20}=-V_2{}^a=I_2{}^a(z_2=0)Z_{\text{even}}{}^a$$

$$=-I_1{}^a(0)Z_{\text{even}}{}^a=\frac{-V^a}{Z_{0c}{}^a}Z_{\text{even}}{}^a=-f^aV^a. \quad (3.21a)$$

Therefore,

$$f^a=Z_{\text{even}}{}^a/Z_{0c}{}^a. \quad (3.21b)$$

$Z_{0c}{}^s$ and $Z_{0c}{}^a$ are given by (2.11) with appropriate superscripts. The complex factor k defined in (2.19a) is given by

$$k=f^a/f^s=\frac{Z_{\text{even}}{}^a}{Z_{\text{even}}{}^s}\cdot\frac{Z_{0c}{}^s}{Z_{0c}{}^a}. \quad (3.22)$$

It is this factor that is required in order to calculate the input impedance of the three-element array with the outer units parasitic using (2.19c).

The even part of the current in the outer antennas when these are parasitic is given by

$$I_{2\text{even}}(z_2)=I_{\text{even}}{}^s(z_2)-I_{\text{even}}{}^a(z_2) \quad (3.23a)$$

where $I_{\text{even}}{}^s(z_2)$ is obtained from (3.19a) with appropriate superscripts s and with $V_{20}=V_2{}^s$, and where $I_{\text{even}}{}^a(z_2)$ is given by (3.19a) with superscripts a and with $V_{20}=V_2{}^a$. Note that

$$V_2{}^a=V_2{}^s=f^sV^s=f^aV^a=V_{10}/2F_2 \quad (3.23b)$$

where

$$F_2\equiv(f^a+f^s)/2f^af^s. \quad (3.23c)$$

Thus,

$$I_{2\text{even}}(z_2)=\frac{j\pi V_{10}}{\zeta_0F_2}\left\{\frac{1}{\Psi_{\text{even}}{}^s}\left[\frac{\sin\beta_0(h-z_2)+M_{\text{even}1}{}^s(z_2)/\Psi_{\text{even}}{}^s+\cdots}{\cos\beta_0h+A_{\text{even}1}{}^s/\Psi_{\text{even}}{}^s+\cdots}\right]\right.$$

$$\left.-\frac{1}{\Psi_{\text{even}}{}^a}\left[\frac{\sin\beta_0(h-z_2)+M_{\text{even}1}{}^a(z_2)/\Psi_{\text{even}}{}^a+\cdots}{\cos\beta_0h+A_{\text{even}1}{}^a/\Psi_{\text{even}}{}^a+\cdots}\right]\right\}. \quad (3.23d)$$

$I_{2\text{even}}(z_2)$ does not differ greatly from $I_1(z)$ since both are even functions that are equal at the centers of all three antennas.

The odd part of the current in antenna 2 must be determined from (3.18b) using the known value of $I_{\text{even}}(z_2)$ obtained from the solution (3.19a) of (3.18a). Thus,

$$\int_0^h I_{\text{odd}}(z_2')K_{\text{odd}}(z_2,z_2')dz_2'$$

$$=\frac{-j4\pi}{\zeta_0}[C_{\text{odd}}\sin\beta_0z_2+U(z_2)];\quad(0\leqq z_2\leqq h) \quad (3.24a)$$

where

$$U(z_2)\equiv\frac{-j\zeta_0}{4\pi}\int_0^h I_{\text{even}}(z_2')K_{0e}(z_2,z_2')dz_2'. \quad (3.24b)$$

$K_{\text{odd}}(z_2,z_2')$ is given by (3.17e) and $K_{0e}(z_2,z_2')$ by (3.17c). The upper sign in (3.17c) applies to the symmetrical, the lower sign to the antisymmetrical case. Note that $K_{\text{odd}}(z_2,z_2')$ is the same for both. The evaluation of $I_{\text{odd}}(z_2)$ from (3.24a) is involved particularly when β_0h is near π since it then is a resonant-mode current whereas the even current is not. On the other hand, when β_0h is near $\pi/2$ the even distribution is resonant, the odd is not and, therefore, relatively small. Since the only practically important case, and at the same time the one for which an approximate evaluation of (3.24a) is readily carried out, is with $\beta_0h=\pi/2$, only this is considered.

The first step in the solution of (3.24a) is the simplification of the function $U(z_2)$. Since z_2 cannot exceed h, and $d\geqq 2h$ occurs in all distances R in $K_{0e}(z_2,z_2')$, the term a^2 in these distances is negligible. It follows that in the range $0\leqq z_2\leqq h$, $0\leqq z_2'\leqq h$, (3.17c) may be simplified into

$$K_{0e}(z_2,z_2')\doteq\pm\tfrac{1}{2}e^{-j\beta_0(d+z_2)}\left[\frac{e^{j\beta_0z_2'}}{d+z_2-z_2'}+\frac{e^{-j\beta_0z_2'}}{d+z_2+z_2'}\right]$$

$$\mp\tfrac{1}{2}e^{-j\beta_0(d-z_2)}\left[\frac{e^{j\beta_0z_2'}}{d-z_2-z_2'}+\frac{e^{-j\beta_0z_2'}}{d-z_2+z_2'}\right]$$

$$+\tfrac{1}{2}e^{-j\beta_0(2d+z_2)}\left[\frac{e^{j\beta_0z_2'}}{2d+z_2-z_2'}+\frac{e^{-j\beta_0z_2'}}{2d+z_2+z_2'}\right]$$

$$+\tfrac{1}{2}e^{-j\beta_0(2d-z_2)}\left[\frac{e^{j\beta_0z_2'}}{2d-z_2-z_2'}+\frac{e^{-j\beta_0z_2'}}{2d-z_2+z_2'}\right]. \quad (3.25)$$

As a next step in the simplification let z_2' be neglected in the denominators throughout. This is a good approximation for all values of z_2' in most of the terms, a poor approximation only in one term and then only when

$z_2=h$ and when z_2' approaches h. Since the current vanishes at h, an error here is of no great importance. Hence, setting $z_2'=0$ in the denominators, (3.25) reduces to

$$K_{0e}(z_2, z_2')=\left[\pm\frac{e^{-j\beta_0(d+z_2)}}{d+z_2}\mp\frac{e^{-j\beta_0(d-z_2)}}{d-z_2}+\frac{e^{-j\beta_0(2d+z_2)}}{2d+z_2}+\frac{e^{-j\beta_0(2d-z_2)}}{2d-z_2}\right]\cos\beta_0 z_2'. \quad (3.26)$$

Since with $\beta_0 h=\pi/2$, the even current is well approximated by

$$I_{\text{even}}(z_2)\equiv\frac{V}{Z_{0e}}\cos\beta_0 z_2' \quad (3.27)$$

the integral in (3.24b) may be evaluated directly using (3.26). It involves

$$\int_0^h \cos^2\beta_0 z_2' dz_2'=\pi/4\beta_0. \quad (3.28)$$

Accordingly,

$$U(z_2)\doteq\frac{j\zeta_0 V}{8Z_{0e}}\left\{\frac{\pm e^{-j\beta_0 d}}{\beta_0(d^2-z_2^2)}[z_2\cos\beta_0 z_2+jd\sin\beta_0 z_2]+\frac{e^{-j2\beta_0 d}}{\beta_0(4d^2-z^2)}[z_2\cos\beta_0 z_2+j2d\sin\beta_0 z_2]\right\}. \quad (3.29)$$

In the range $0\leqq\beta_0 z_2\leqq\pi/2$, the approximation $\beta_0 z_2\doteq\sin\beta_0 z_2$ is satisfactory except near $\beta_0 z_2=\pi/2$ where, however, the current vanishes and an error in $U(z_2)$ is immaterial. With this approximation,

$$U(z_2)\doteq\frac{\zeta_0 V}{8Z_{0e}\beta_0 d}F(z_2)\sin\beta_0 z_2\equiv\bar{U}(z_2)\sin\beta_0 z_2 \quad (3.30a)$$

where $\bar{U}(z_2)$ is defined by (3.30a) and where

$$F(z_2)=-\left\{\frac{\pm e^{-j\beta_0 d}}{(1-z_2^2/d^2)}\left[1-j\frac{\cos\beta_0 z_2}{\beta_0 d}\right]+\frac{e^{-j2\beta_0 d}}{(1-z_2^2/4d^2)}\left[1-j\frac{\cos\beta_0 z_2}{2\beta_0 d}\right]\right\}. \quad (3.30b)$$

Since $z_2/d\leqq\frac{1}{4}$, and $\beta_0 d\geqq\pi$, $F(z_2)$ does not vary rapidly. It follows that $U(z_2)$ varies approximately as $\sin\beta_0 z_2$. With (3.30a, b) the integral equation (3.24a) reduces to

$$\int_0^h I_{\text{odd}}(z_2')K_{\text{odd}}(z_2, z_2')dz_2'=\frac{-j4\pi}{\zeta_0}[C_{\text{odd}}+\bar{U}(z_2)]\sin\beta_0 z_2. \quad (3.31)$$

This integral equation can be solved for the current by the usual method of iteration. Let

$$I_{\text{odd}}(z_2')=I_{\text{odd}}(z_2)g(z_2, z_2') \quad (3.32)$$

where $g(z_2, z_2')$ is a distribution function that is chosen to make $I_{\text{odd}}(z_2)\Psi_{\text{odd}}(z_2)$ approximate closely the integral on the left in (3.31) with

$$\Psi_{\text{odd}}(z_2)=\int_0^h g(z_2, z_2')K_{\text{odd}}(z_2, z_2')dz_2'=\Psi_{\text{odd}}+\gamma_{\text{odd}}(z_2). \quad (3.33)$$

Ψ_{odd} is a mean constant value of the integral defined at a suitable reference point. With (3.32) and (3.33)

$$I_{\text{odd}}(z_2)=\frac{-j4\pi}{\zeta_0\Psi_{\text{odd}}}[C_{\text{odd}}+\bar{U}(z_2)]\sin\beta_0 z_2-\frac{1}{\Psi_{\text{odd}}}\left[I_{\text{odd}}(z_2)\gamma_{\text{odd}}(z_2)+\int_0^h[I_{\text{odd}}(z_2')-I_{\text{odd}}(z_2)g(z_2, z_2')]K_{\text{odd}}(z_2, z_2')dz_2'\right]. \quad (3.34)$$

By using the term in $\sin\beta_0 z_2$ as the zeroth-order current, and substituting this in the integrals, these may be evaluated assuming $\bar{U}(z_2)$ to be constant, and added to the zeroth-order current. This process of iteration can be repeated. The current then appears in the form

$$I_{\text{odd}}(z_2)=\frac{-j4\pi}{\zeta_0\Psi_{\text{odd}}}[C_{\text{odd}}+\bar{U}(z_2)]\times\left[\sin\beta_0 z_2+\frac{S_1(z_2)}{\Psi_{\text{odd}}}+\frac{S_2(z_2)}{\Psi_{\text{odd}}^2}+\cdots\right]. \quad (3.35)$$

The constant C_{odd} may be evaluated by requiring the current to vanish at $z_2=h$. Then

$$C_{\text{odd}}=-U(h) \quad (3.36)$$

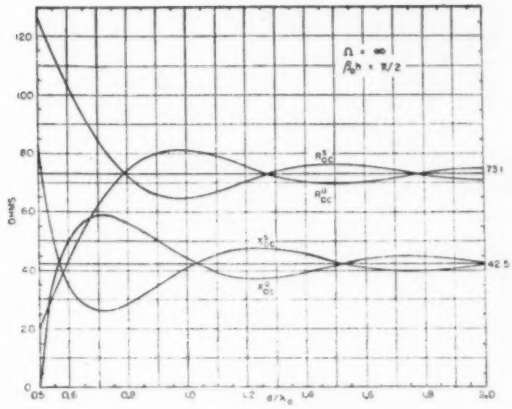

FIG. 6. Symmetrical and antisymmetrical impedances of the central unit in a three-antenna array.

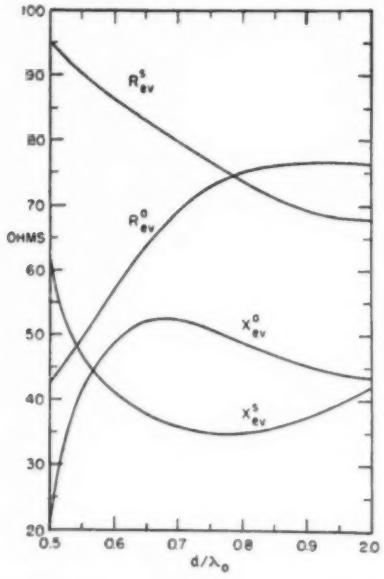

FIG. 7. Symmetrical and antisymmetrical impedances of the outer units in a three-element array.

so that

$$I_{odd}(z_2)=\frac{-j4\pi}{\zeta_0\Psi_{odd}}[U(z_2)-U(h)]\times\left[\sin\beta_0 z_2+\frac{S_1(z_2)}{\Psi_{odd}}+\frac{S_2(z_2)}{\Psi_{odd}^2}+\cdots\right]. \quad (3.37)$$

It follows from (3.30b) that with $\beta_0 h=\pi/2$, an approximate result is:

$$U(z_2)-U(h)\doteq\frac{j\zeta_0 VD(d)}{8Z_{0c}}\cos\beta_0 z_2, \quad (3.38a)$$

where

$$D(d)\equiv\frac{1}{\beta_0^2 d^2}\left[\pm\frac{e^{-j\beta_0 d}}{(1-h^2/d^2)}+\frac{e^{-j2\beta_0 d}}{2(1-h^2/4d^2)}\right]. \quad (3.38b)$$

Substitution of (3.38a) in (3.37) gives the following simple expressions for the zeroth-order odd currents in the outer units when $\beta_0 h=\pi/2$:

$$I_{odd}{}^s(z_2)=\frac{V^s}{Z_{0c}{}^s}\frac{\pi D^s(d)}{4\Psi_{odd}}\sin 2\beta_0 z_2 \quad (3.39a)$$

$$I_{odd}{}^a(z_2)=\frac{V^a}{Z_{0c}{}^a}\frac{\pi D^a(d)}{4\Psi_{odd}}\sin 2\beta_0 z_2 \quad (3.39b)$$

where $D^s(d)$ is (3.38b) with the upper sign and $D^a(d)$ is (3.38b) with the lower sign. Note that $V^s/Z_{0c}{}^s=I_1{}^s(0)$; $V^a/Z_{0c}{}^a=I_1{}^a(0)$. The odd part of the current in the outer units when these are parasitic is given by the sum of (3.39a) and (3.39b). Noting that as in (2.19b), $V^s=V_{10}/(1+k^{-1})$, $V^a=V_{10}/(1+k)$, it follows that

$$I_{2odd}(z_2)=I_{odd}{}^s(z_2)+I_{odd}{}^a(z_2)=\frac{V_{10}\pi}{4\Psi_{odd}}\left[\frac{D^s(d)}{Z_{0c}{}^s(1+k^{-1})}+\frac{D^a(d)}{Z_{0c}{}^a(1+k)}\right]\sin 2\beta_0 z_2; \quad (\beta_0 h=\pi/2). \quad (3.40)$$

The total current in the outer antennas is the sum of (3.40) and (3.23d) with $\beta_0 h=\pi/2$. Note that as the antenna is made thinner, i.e. $\Omega=2\ln(2h/a)$ increased, the odd current does not approach a value independent of Ω when $\beta_0 h=\pi/2$ as does the even current.

The final step in the complete evaluation of $I_{odd}(z_2)$ is the determination of Ψ_{odd} from (3.33). Since the zeroth-order distribution leads to a distribution function $g(z_2, z_2')=\sin 2\beta_0 z'/\sin 2\beta_0 z$ that does not permit the ready evaluation of Ψ_{odd}, the simpler procedure of assuming a sensibly uniform current and neglecting retardation is more convenient and adequate. This is equivalent to setting

$$\Psi_{odd}(z_2)=\int_0^h\left[\frac{1}{[(z_2'-z_2)^2+a^2]^{\frac{1}{2}}}-\frac{1}{[(z_2'+z_2)^2+a^2]^{\frac{1}{2}}}\right]dz_2'. \quad (3.41)$$

Since the odd current is most nearly constant near $z_2=h/2$ and this is its greatest value, it is a good approximation to choose the reference point for Ψ_{odd} at $z_2=h/2$. Thus

$$\Psi_{odd}=\int_{-h/2}^{h/2}\frac{du}{(u^2+a^2)^{\frac{1}{2}}}-\int_{h/2}^{3h/2}\frac{du}{(u^2+a^2)^{\frac{1}{2}}}=\ln\left(\frac{h^2}{3a^2}\right)=\Omega-2.5, \quad (3.42)$$

where $\Omega=2\ln(2h/a)$.

In this section general expressions have been obtained for the symmetrical and antisymmetrical components of the even current in the outer units of the three-element array. An approximate formula for the odd currents has been derived in the important special case, $\beta_0 h=\pi/2$. As a part of the determination of the even currents, relations between the three driving voltages were established which assure that the currents at the centers of all three units are equal in magnitude and either in-phase or 180 degrees out-of-phase as required by the conditions for the symmetrical and antisymmetrical cases. Thus, in Section 2 and this section the general formulas for the currents in collinear arrays are derived in the special case of the three-element array.

4. COLLINEAR ARRAY OF THREE HALF-WAVE DIPOLES

The most useful collinear array of three antennas consists of identical units each of electrical half-length $\beta_0 h = \pi/2$. The middle antenna No. 1 is center-driven from a balanced two-wire transmission line. As with the single antenna[1] this line may be replaced by an appropriate terminal-zone network with a slice generator. The two outer antennas, No. 2 and No. 3, are parasitic as shown in Fig. 2b.

The driving voltages for the three units are

$$V_{10} = V^s + V^a = V^s(1+k^{-1}) = V^a(1+k);$$

$$V_{20} = V_{30} = V_2{}^s - V_2{}^a = f^s V^s - f^a V^a = 0 \quad (4.1a)$$

where

$$k = \frac{f^a}{f^s}; \quad f^a = \frac{Z_{\text{even}}{}^a}{Z_{0e}{}^a}; \quad f^s = \frac{Z_{\text{even}}{}^s}{Z_{0e}{}^s}, \quad (4.1b)$$

and where Z_{even} is the impedance of each outer unit, Z_{0e} of the central unit. V^s is the driving voltage of the central unit when the other two are center-driven by voltages $V_3{}^s = V_2{}^s = f^s V^s$ such that the *currents* at the *centers* of all three units are equal and in phase. V^a is the driving voltage of the central unit when the two outer antennas are center-driven by voltages $V_3{}^a = V_2{}^a = f^a V^a$ such that the currents at the centers of the two outer units are equal to and in-phase with each other, but both equal to and 180 degrees out-of-phase with the current at $z=0$ in the central unit.

The first-order symmetrical and antisymmetrical currents in the central unit are given by (2.10) with $\beta_0 h = \pi/2$ and appropriate superscripts. Thus,

$$I_1{}^s(z) = \frac{j2\pi V^s}{\zeta_0 A_{e1}{}^s}[\cos\beta_0 z + M_{e1}{}^s(z)/\Psi_{Ke}{}^s];$$

$$(0 \leqq z \leqq h) \quad (4.2a)$$

$$I_1{}^a(z) = \frac{j2\pi V^a}{\zeta_0 A_{e1}{}^a}[\cos\beta_0 z + M_{e1}{}^a(z)/\Psi_{Ke}{}^a];$$

$$(0 \leqq z \leqq h). \quad (4.2b)$$

The total first-order current in the central unit when the outer units are parasitic is the sum of (4.2a) and (4.2b). With (4.1a, b) it is,

$$I_1(z) = I_1{}^s(z) + I_1{}^a(z) = \frac{j2\pi V_{10}}{\zeta_0}$$

$$\times\left\{\left[\frac{1}{A_{e1}{}^s(1+k^{-1})} + \frac{1}{A_{e1}{}^a(1+k)}\right]\cos\beta_0 z\right.$$

$$\left.+\left[\frac{M_{e1}{}^s(z)}{A_{e1}{}^s(1+k^{-1})\Psi_{K1}{}^s} + \frac{M_{e1}{}^a(z)}{A_{e1}{}^a(1+k)\Psi_{K1}{}^a}\right]\right\}. \quad (4.3)$$

The first-order symmetrical and antisymmetrical impedances of the central unit are

$$Z_{0e}{}^s = \frac{-j\zeta_0 A_{e1}{}^s}{2\pi}[1 + B_{e1}{}^s/\Psi_{Ke}{}^s]^{-1};$$

$$Z_{0e}{}^a = \frac{-j\zeta_0 A_{e1}{}^a}{2\pi}[1 + B_{e1}{}^a/\Psi_{Ke}{}^a]^{-1}. \quad (4.4a)$$

The first-order input impedance of the array when the outer units are parasitic is

$$Z_{1\text{in}} = \frac{-j\zeta_0}{2\pi}\left\{\left[\frac{1}{A_{e1}{}^s(1+k^{-1})} + \frac{1}{A_{e1}{}^a(1+k)}\right]\right.$$

$$\left.+\left[\frac{B_{e1}{}^s}{A_{e1}{}^s(1+k^{-1})\Psi_{K1}{}^s} + \frac{B_{e1}{}^a}{A_{e1}{}^a(1+k)\Psi_{K1}{}^a}\right]\right\}^{-1}. \quad (4.4b)$$

where

$$B_{e1}{}^s \equiv M_{e1}{}^s(0); \quad B_{e1}{}^a \equiv M_{e1}{}^a(0). \quad (4.4c)$$

For antennas that have a reasonably large value of h/a, $\Psi_{K1}{}^s$ and $\Psi_{K1}{}^a$ are sufficiently great to make the contributions by the $1/\Psi_{K1}$ terms in (2.2a, b), (2.3) and (2.4a, b) relatively small. When this is true the following expressions are satisfactory approximations:

$$I_1{}^s(z) \doteq \frac{V^s}{Z_{0e}{}^s}\cos\beta_0 z; \quad I_1{}^a(z) \doteq \frac{V^a}{Z_{0e}{}^a}\cos\beta_0 z;$$

$$I_1(z) = \frac{V_{10}}{Z_{1\text{in}}}\cos\beta_0 z \quad (4.5a)$$

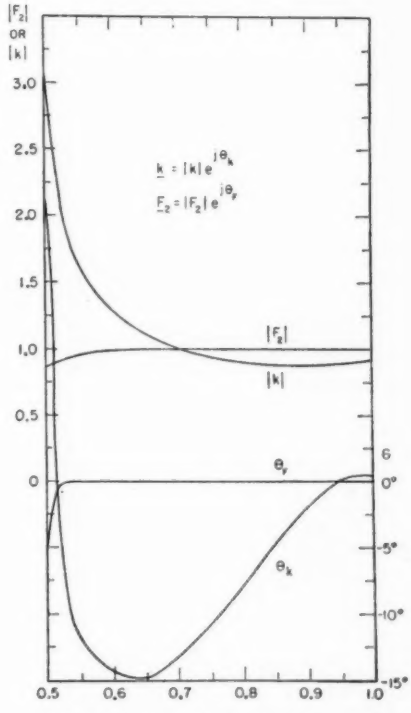

FIG. 8. The complex factors k and F_2.

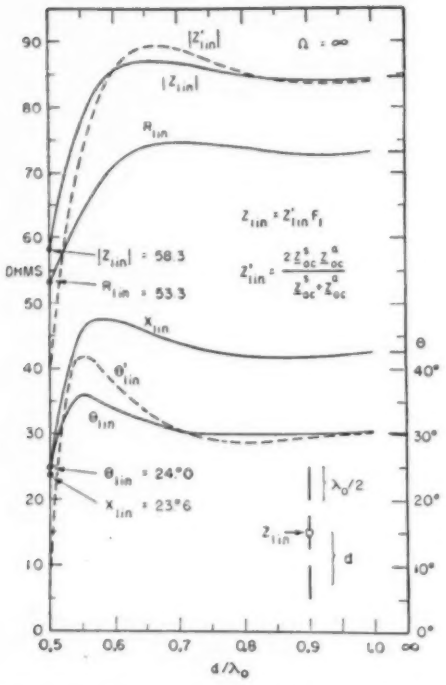

FIG. 9. Input impedance of antenna with two collinear parasites.

where

$$Z_{0c}{}^s \doteq \frac{-j\zeta_0 A_{c1}{}^s}{2\pi}; \quad Z_{0c}{}^a \doteq \frac{-j\zeta_0 A_{c1}{}^a}{2\pi} \tag{4.5b}$$

and where, using (2.19c, d),

$$Z_{1in} = \left[\frac{1}{Z_{0c}{}^s(1+k^{-1})} + \frac{1}{Z_{0c}{}^a(1+k)}\right]^{-1} = Z_{1in}{}' F_1 \tag{4.5c}$$

where

$$Z_{1in}{}' = \frac{2Z_{0c}{}^s Z_{0c}{}^a}{Z_{0c}{}^s + Z_{0c}{}^a};$$

$$F_1 = 1 + \frac{[Z_{0c}{}^s - Z_{0c}{}^a][k-k^{-1}]}{2[Z_{0c}{}^s(1+k^{-1}) + Z_{0c}{}^a(1+k)]}. \tag{4.5d}$$

It is seen from (4.5) that $I_1(z)$ and Z_{1in} involve only $A_{c1}{}^s$, $A_{c1}{}^a$, and k. As with the isolated antenna, the former are defined as follows when $\beta_0 h = \pi/2$:

$$A_{c1} \equiv F_{c1}(h) = -\int_{-h}^{h} \cos\beta_0 z' K_{c1}(h, z') dz'; \quad h = \lambda_0/4 \tag{4.6}$$

where

$$K_{c1}(h, z') = K_1(h, z') \pm [K_1(d-h, z') + K_1(d+h, z')]; \quad h = \lambda_0/4. \tag{4.7}$$

Using the integrals given in reference 4, (4.6) may be expressed as follows:

$$A_{c1} = -\{C_a(h, h) \pm [C_a(d-h, h) + C_a(d+h, h)]\}; \quad h = \lambda_0/4. \tag{4.8}$$

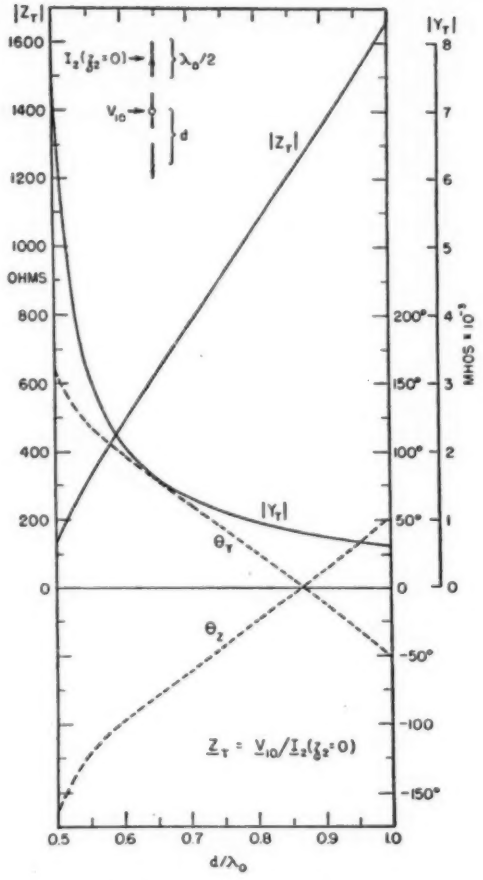

FIG. 10. Transfer impedance and admittance for antenna with two collinear parasites.

The upper sign requires a superscript s, the lower sign a superscript a on A_{c1}. It follows that

$$Z_{0c} = \frac{j\zeta_0}{2\pi}[C_a(h, h) \pm C_a(d-h, h) \pm C_a(d+h, h)];$$

$$h = \lambda_0/4 \tag{4.9}$$

where the upper sign is for $Z_{0c}{}^s$, the lower sign for $Z_{0c}{}^a$. The symmetrical and antisymmetrical impedances of the three element array as given in (4.9) are in Fig. 6. The impedance $Z_{1in}{}'$ defined in (4.5c), which is the principal part of Z_{1in}, is shown in Fig. 9 together with Z_{1in}. Note that Z_{1in} reduces to $Z_{1in}{}'$ when d is sufficiently great so that $k \doteq 1$. It is not possible to determine Z_{1in} until k is available. This requires the evaluation of $Z_{even}{}^s$ and $Z_{even}{}^a$ in addition to $Z_{0c}{}^s$ and $Z_{0c}{}^a$.

The first-order symmetrical and antisymmetrical even currents in the outer units are given by (3.19a) with $\beta_0 h = \pi/2$. They are

$$I_{even}{}^s(z_2) = \frac{j2\pi V_2{}^s}{\zeta_0 A_{even1}{}^s} \times [\cos\beta_0 z_2 + M_{even1}{}^s(z_2)/\Psi_{even}{}^s] \tag{4.10a}$$

$$I_{\text{even}}{}^{a}(z_2)=\frac{j2\pi V_2{}^{a}}{\zeta_0 A_{\text{even1}}{}^{a}}$$

$$\times[\cos\beta_0 z_2+M_{\text{even1}}{}^{a}(z_2)/\Psi_{\text{even}}{}^{a}]. \quad (4.10b)$$

When the outer units are parasitic

$$V_2{}^{s}=V_2{}^{a}=f^{s}V^{s}=f^{a}V^{a}=V_{10}/2F_2;$$

$$F_2\equiv\frac{f^{a}+f^{s}}{2f^{a}f^{s}}=\frac{1}{2}\left[\frac{Z_{0c}{}^{s}}{Z_{\text{even}}{}^{s}}+\frac{Z_{0c}{}^{a}}{Z_{\text{even}}{}^{a}}\right] \quad (4.10c)$$

as in (3.23a) and the total current is given by,

$$I_{2\text{even}}(z_2)=I_{\text{even}}{}^{s}(z_2)-I_{\text{even}}{}^{a}(z_2)$$

$$=\frac{j\pi V_{10}}{\zeta_0 F_2}\left\{\left[\frac{1}{A_{\text{even1}}{}^{s}}-\frac{1}{A_{\text{even1}}{}^{a}}\right]\cos\beta_0 z_2\right.$$

$$\left.+\left[\frac{M_{\text{even1}}{}^{s}(z_2)}{A_{\text{even1}}{}^{s}\Psi_{\text{even}}{}^{s}}-\frac{M_{\text{even1}}{}^{a}(z_2)}{A_{\text{even1}}{}^{a}\Psi_{\text{even}}{}^{s}}\right]\right\};$$

$$\beta_0 h=\pi/2. \quad (4.11)$$

The first-order symmetrical and antisymmetrical impedances of the outer units are

$$Z_{\text{even}}{}^{s}=\frac{-j\zeta_0 A_{\text{even1}}{}^{s}}{2\pi}[1+B_{\text{even1}}{}^{s}/\Psi_{\text{even}}{}^{s}]^{-1};$$

$$Z_{\text{even}}{}^{a}=\frac{-j\zeta_0 A_{\text{even1}}{}^{a}}{2\pi}[1+B_{\text{even1}}{}^{a}/\Psi_{\text{even}}{}^{a}]^{-1}. \quad (4.12a)$$

The transfer impedance when the outer units are parasitic is

$$Z_T=\frac{-j\zeta_0 F_2}{\pi}\left\{\left[\frac{1}{A_{\text{even1}}{}^{s}}-\frac{1}{A_{\text{even1}}{}^{a}}\right]\right.$$

$$\left.+\left[\frac{B_{\text{even1}}{}^{s}}{A_{\text{even1}}{}^{s}\Psi_{\text{even}}{}^{s}}-\frac{B_{\text{even1}}{}^{a}}{A_{\text{even1}}{}^{a}\Psi_{\text{even}}{}^{a}}\right]\right\}^{-1} \quad (4.12b)$$

where

$$B_{\text{even1}}{}^{s}\equiv M_{\text{even1}}{}^{s}(0); \quad B_{\text{even1}}{}^{a}\equiv M_{\text{even1}}{}^{a}(0). \quad (4.12c)$$

For sufficiently great values of $\Psi_{\text{even}}{}^{s}$ and $\Psi_{\text{even}}{}^{a}$ the leading terms are good approximations. They are

$$I_{\text{even}}{}^{s}(z_2)\doteq\frac{V_2{}^{s}}{Z_{\text{even}}{}^{s}}\cos\beta_0 z_2;$$

$$I_{\text{even}}{}^{a}(z_2)\doteq\frac{V_2{}^{a}}{Z_{\text{even}}{}^{a}}\cos\beta_0 z_2;$$

$$I_{2\text{even}}(z_2)=\frac{V_{10}}{Z_T}\cos\beta_0 z_2 \quad (4.13a)$$

where

$$Z_{\text{even}}{}^{s}=\frac{-j\zeta_0 A_{\text{even1}}{}^{s}}{2\pi}; \quad Z_{\text{even}}{}^{a}=\frac{-j\zeta_0 A_{\text{even1}}{}^{a}}{2\pi}, \quad (4.13b)$$

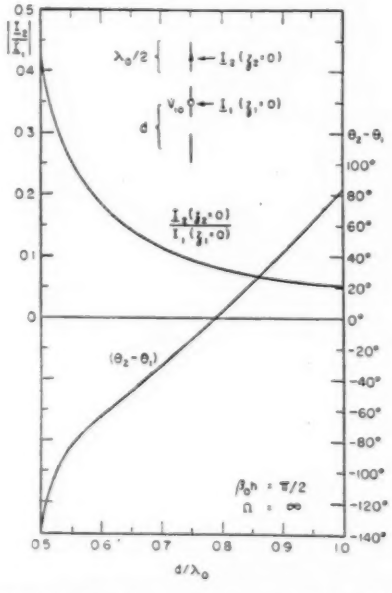

FIG. 11. Ratio of current in parasite to current in driven element.

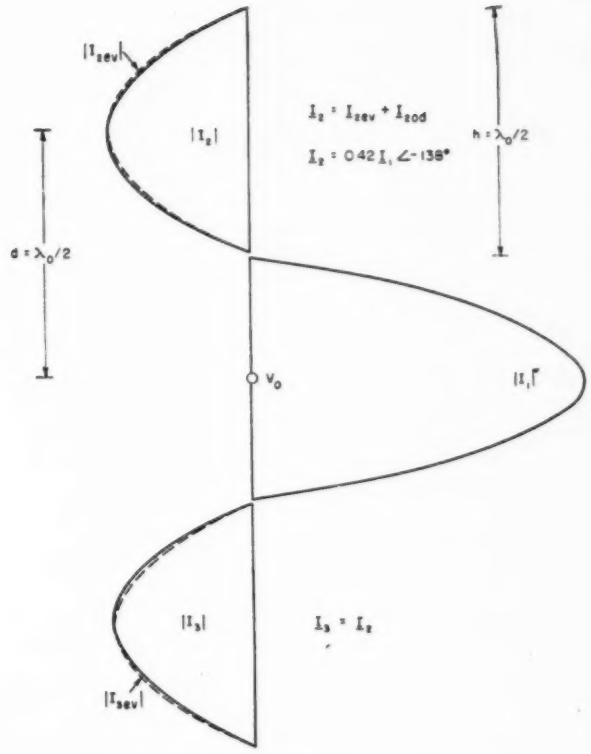

FIG. 12. Distributions of current on collinear array with outer elements parasitic.

$$Z_T = Z_T' F_2; \quad Z_T' \equiv \frac{2Z_{\text{even}}{}^s Z_{\text{even}}{}^a}{Z_{\text{even}}{}^a - Z_{\text{even}}{}^s};$$

$$F_2 = \frac{1}{2}\left[\frac{Z_{0e}{}^s}{Z_{\text{even}}{}^s} + \frac{Z_{0e}{}^a}{Z_{\text{even}}{}^a}\right] \doteq 1. \quad (4.13c)$$

The ratio of currents at the centers of the outer parasitic units to the current at the center of the driven unit is given by

$$I_2(z_2=0)/I_1(0) = Z_{1\text{in}}/Z_T = \left|\frac{I_2(0)}{I_1(0)}\right| e^{j(\theta_2-\theta_1)}, \quad (4.14)$$

where $Z_{1\text{in}}$ is given by (4.5c) and Z_T by (4.13b). It is shown later (Fig. 8) that the factor F_2 differs negligibly from unity as indicated in (4.13c) except when d/λ_0 is at or very near 0.5. As in (4.6), but with a different kernel,

$$A_{\text{even}1} = F_{\text{even}1}(h) = -\int_{-h}^{h} \cos\beta_0 z_2' K_{1\text{even}}(h, z_2')dz_2' = -\int_0^h \cos\beta_0 z_2' K_{\text{even}}(h, z_2')dz_2' \quad (4.15)$$

where $K_{\text{even}}(h, z_2')$ is given by (2.17a) with $z_2 = h = \lambda_0/4$. Thus,

$$K_{\text{even}}(h, z_2) = K(h, z_2') \pm \tfrac{1}{2}[K(d-h, z_2') + K(d+h, z_2')] + \tfrac{1}{2}[K(2d-h, z_2') + K(2d+h, z_2')] \quad (4.16)$$

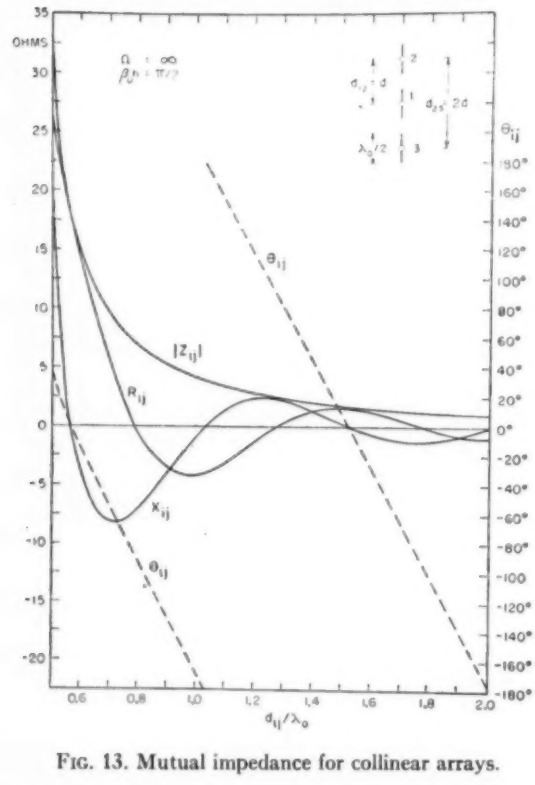

FIG. 13. Mutual impedance for collinear arrays.

where, as usual, $K \equiv K_1 + K_2$. With reference 4 the integrals in (4.13a) with (14.4) may be expressed as follows:

$$A_{\text{even}1} = -\{C_a(h, h) \pm \tfrac{1}{2}[C_a(d-h, h) + C_a(d+h, h)] + \tfrac{1}{2}[C_a(2d-h, h) + C_a(2d+h, h)]\}; \quad (h = \lambda_0/4). \quad (4.17)$$

The upper sign in (4.17) goes with a superscript s on $A_{\text{even}1}$, the lower sign with a superscript a. The corresponding impedances are

$$Z_{\text{even}} = \frac{j\zeta_0}{2\pi}\{C_a(h, h) \pm \tfrac{1}{2}[C_a(d-h, h) + C_a(d+h, h)] + \tfrac{1}{2}[C_a(2d-h, h) + C_a(2d+h, h)]\}; \quad h = \lambda_0/4, \quad (4.18)$$

where the upper sign is for $Z_{\text{even}}{}^s$, the lower sign for $Z_{\text{even}}{}^a$. They are in Fig. 7.

With $Z_{\text{even}}{}^s$ and $Z_{\text{even}}{}^a$ determined, the functions k, f^a and f^s defined in (4.1b) and the function F_2 defined in (4.5d) may be evaluated k and F_2 are in Fig. 8 in polar form. With k available and $Z_{1\text{in}}'$ known, the approximate input impedance $Z_{1\text{in}}$ (as defined in (4.5c)) may be evaluated. It is shown in Fig. 9 along with $Z_{1\text{in}}'$ which it approaches as k approaches unity with increased d. With F_2 available the transfer impedance Z_T may be determined using its principal factor Z_T'. Z_T and Z_T' are in Fig. 10. Note that $Z_T \doteq Z_T'$ except when $d/\lambda_0 \doteq 0.5$, and even here the departure is small. The ratio of currents (4.14) is shown in Fig. 11 as a function of d/λ_0 and the distribution in Fig. 12 for $d = \lambda_0/2$. Note that when $d = \lambda_0/2$ the currents in the parasites are nearly opposite in phase to the current in the central unit.

The general equations for the three-element array in which the outer units are always identical are

$$V_{10} = I_{10}Z_{s1} + I_{20}Z_{12} + I_{30}Z_{13} = I_{10}Z_{s1} + 2I_{20}Z_{12} \quad (4.19a)$$

$$V_{20} = I_{10}Z_{21} + I_{20}Z_{s2} + I_{30}Z_{23} = I_{10}Z_{12} + I_{20}(Z_{s2} + Z_{23}). \quad (4.19b)$$

When the units are symmetrically driven,

$$V^s = I_{10}(Z_{s1} + 2Z_{12}), \quad (4.20a)$$

$$V_2{}^s = I_{10}(Z_{s2} + Z_{12} + Z_{23}). \quad (4.20b)$$

When the units are antisymmetrically driven,

$$V^a = I_{10}(Z_{s1} - 2Z_{12}), \quad (4.21a)$$

$$V_2{}^a = -I_{10}(Z_{s2} - Z_{12} + Z_{23}). \quad (4.21b)$$

Comparison with (9) and (18) shows that when $\beta_0 h=\pi/2$ these approximate expressions for the symmetrical and antisymmetrical impedances are consistent with the following definitions:

$$Z_{s1}\doteq Z_{s2}\doteq(j\zeta_0/2\pi)C_a(h,h), \tag{4.22a}$$

$$Z_{12}=Z_{13}\doteq\frac{j\zeta_0}{2\pi}\frac{1}{2}[C_a(d-h,h)+C_a(d+h,h)], \tag{4.22b}$$

$$Z_{23}\doteq\frac{j\zeta_0}{2\pi}\frac{1}{2}[C_a(2d-h,h)+C_a(2d+h,h)]. \tag{4.22c}$$

The functions Z_{12} and Z_{23} may be obtained from Fig. 13. It may be concluded that in general, when $\beta_0 h=\pi/2$, the zeroth-order self-impedance of each of N collinear antennas is

$$Z_{s1}=\cdots Z_{sN}\doteq\frac{j\zeta_0}{2\pi}C_a(h,h)=73.13+j42.5 \text{ ohms}. \tag{4.23a}$$

Similarly the zeroth-order mutual impedances between two collinear antennas numbered m and n and separated a distance $(n-m)d$ between centers, is

$$Z_{mn}\doteq\frac{j\zeta_0}{2\pi}\frac{1}{2}\{C_a[(n-m)d-h,h]+C_a[(n-m)d+h,h]\}. \tag{4.23b}$$

For collinear elements that are *not* near $\beta_0 h=\pi/2$ in electrical half-length the self- and mutual impedances cannot be expressed in this simple form. Only when $\beta_0 h=\pi/2$ and the identical antennas are sufficiently thin so that Ψ_{even^s} and Ψ_{even^a} are large compared with unity are the simple relations (4.22a, b, c) and (4.23a, b) moderately good approximations. In general, if the antennas are sufficiently thin so that (4.23a) is a good approximaion, it may be assumed that (4.23b) is an even better approximation. Tables of the several zeroth-order impedances involved in the three-element collinear array are in Table I.

The odd currents in the parasitic elements are evaluated in Section 3 when $\beta_0 h=\pi/2$. The approximate expression given in (3.40) is

$$I_{2odd}(z_2)=\frac{V_{10}}{\Psi_{odd}}K\sin 2\beta_0 z_2 \tag{4.24a}$$

where

$$K\equiv\frac{\pi}{4}\left[\frac{D^s(d)}{Z_{0c^s}(1+k^{-1})}+\frac{D^a(d)}{Z_{0c^a}(1+k)}\right] \tag{4.24b}$$

where $D^s(d)$ and $D^a(d)$ are given by (3.38b) respectively with the upper and lower sign, and where k is defined in (4.22). It is now readily verified that with $\beta_0 h=\pi/2$ the odd part of the current in the parasites

TABLE I. Zeroth-order impedances for three-element collinear array.

$\beta_0 d/\pi$	Z_{0c^s}	Z_{0c^a}	Z_{even^s}	Z_{even^a}
1.0	126 +j82.8	20.3 +j 2.22	95.3 +j62.0	42.6 +j21.6
1.1	114 +j47.2	32.6 +j37.8	90.3 +j46.4	49.5 +j41.7
1.2	102 +j34.5	43.8 +j50.5	86.4 +j41.0	56.7 +j49.0
1.3	92.4 +j28.4	53.8 +j56.6	83.2 +j38.0	63.9 +j52.0
1.4	84.0 +j26.2	62.2 +j58.8	80.0 +j35.8	69.2 +j52.0
1.5	77.1 +j26.5	69.1 +j58.6	76.8 +j34.8	72.8 +j50.8
1.6	72.0 +j28.8	74.3 +j56.2	73.8 +j35.0	75.0 +j48.6
1.7	68.2 +j31.4	78.0 +j53.6	71.2 +j35.7	76.1 +j46.8
1.8	65.9 +j34.7	80.3 +j50.4	69.3 +j37.4	76.5 +j45.2
1.9	64.9 +j38.0	81.4 +j47.0	68.2 +j39.6	76.4 +j44.0
2.0	64.8 +j41.0	81.4 +j44.0	68.0 +j41.8	76.3 +j43.2

$\beta_0 d/\pi$	Z_{12}	Z_{23}	Z_{lin}	Z_T
1.0	26.4 +j20.2	−4.16 −j .725	53.2 +j23.6	−131 −j 41.8
1.1	20.2 +j 2.35	−3.00 +j1.56	63.6 +j46.0	−157 −j 278
1.2	14.6 −j 4.00	−1.27 +j2.50	71.2 +j47.4	− 72.0 −j 462
1.3	9.66 −j 7.05	0.437 +j2.46	74.0 +j45.6	103.4 −j 618
1.4	5.44 −j 8.14	1.48 +j1.36	74.8 +j44.1	356 −j 688
1.5	2.00 −j 8.01	1.73 +j .289	74.6 +j42.4	638 −j 632
1.6	−0.588 −j 6.84	1.32 −j .747	74.0 +j42.0	947 −j 474
1.7	−2.45 −j 5.56	0.538 −j1.24	73.2 +j41.6	1190 −j 164
1.8	−3.60 −j 3.92	− .184 −j1.16	72.5 +j42.2	1310 +j 266
1.9	−4.12 −j 2.24	− .805 −j .704	72.7 +j42.1	1280 +j 782
2.0	−4.16 −j .725	− .958 +j .017	73.2 +j42.8	1020 +j1290

$$Z_{s1}=Z_{s2}=Z_{23}=73.1+j42.5$$

is quite small compared with the even parts. Thus, when $\beta_0 d=\pi$, $h/d=\frac{1}{2}$,

$$D^s(d)=\frac{1}{\pi^2}\left(-\frac{4}{3}+\frac{8}{15}\right)=-0.08, \tag{4.25a}$$

$$D^a(d)=\frac{1}{\pi^2}\left(\frac{4}{3}+\frac{8}{15}\right)0.19. \tag{4.25b}$$

Also,

$$Z_{0c^s}(1+k^{-1})=196.9\underline{/28°.3};$$

$$Z_{0c^a}(1+k)=82.7\underline{/22.2°}. \tag{4.26}$$

With these values,

$$K\doteq 1.56\times10^{-3}\underline{/-21°} \tag{4.27}$$

so that with $\Omega=12.5$, $\Psi_{odd}=10$,

$$I_{odd}(z_2)=1.56\times10^{-4}V_{10}e^{-j21°}\sin 2\beta_0 z_2. \tag{4.28}$$

The corresponding value for the even current with $\beta_0 d=\pi$ is obtained from (4.13a) with $Z_T=137.7\underline{/-162°}$.

$$I_{even}(z_2)=\frac{V_{10}}{Z_T}\cos\beta_0 z_2$$

$$=72.8\times10^{-4}V_{10}e^{j162°}\cos\beta_0 z_2. \tag{4.29}$$

Combining (4.28) with (4.29) gives

$$I_2(z_2)=72.8\times10^{-4}V_{10}e^{j162°}\times[\cos\beta_0 z_2-e^{-j3°}0.022\sin 2\beta_0 z_2]. \tag{4.30}$$

It is seen from (4.30) that the amplitude of the odd current is only 2 percent of the amplitude of the even current for $\Omega=12.5$. For thicker antennas the odd currents are relatively greater. The current in (4.30) is shown in Fig. 12 together with the current in the central unit.

5. THE CENTER-DRIVEN COLLINEAR ARRAY WITH THE PHASE-REVERSING STUBS

It is shown in Section 4 that the currents in the two outer units of a three-element collinear array are nearly *opposite* in direction and equal in magnitude to the current in the central unit if the distance between adjacent ends of the elements is very small. The electromagnetic field of such a distribution of current is characterized by large maxima both along the plane bisecting the antenna and along symmetrical cones in the hemispheres. Between these maxima are deep minima. Whereas such a pattern is useful for certain applications, it is undesirable when a field is required that has a large amplitude only in the central plane. It is known that such a field is maintained by a collinear array if the currents are all about equal and in phase. Such a distribution can be maintained in the antennas if each unit is center-driven but, in practice, this involves long transmission lines in non-neutral planes. A better way is to drive only the central unit and to excite the outer units by coupling networks that connect the adjacent ends of the several units. The function of such networks is to *reverse the phase* of the currents in the outer antennas.

A simple phase-reversing network is a high-impedance, transmission-line stub. In Fig. 14a a three-element array is shown with two *phase-reversing stubs* constructed of low loss two-wire line. *If properly adjusted* in length, the transmission-line impedance of each stub to *equal and opposite currents* is very great.

The approximate determination of the current and impedance of the array in Fig. 14a may be carried out as for the array with parasitic elements. The analysis is resolved into two parts the superposition of which yields the desired result. These are (1) the symmetrical part with all three units individually center-driven by slice generators with voltages that maintain equal currents in phase at the centers of the antennas, and (2), the antisymmetrical part in which the driving voltages are so chosen that the currents at the centers of the outer antennas are reversed. These two parts are considered in turn and combined later.

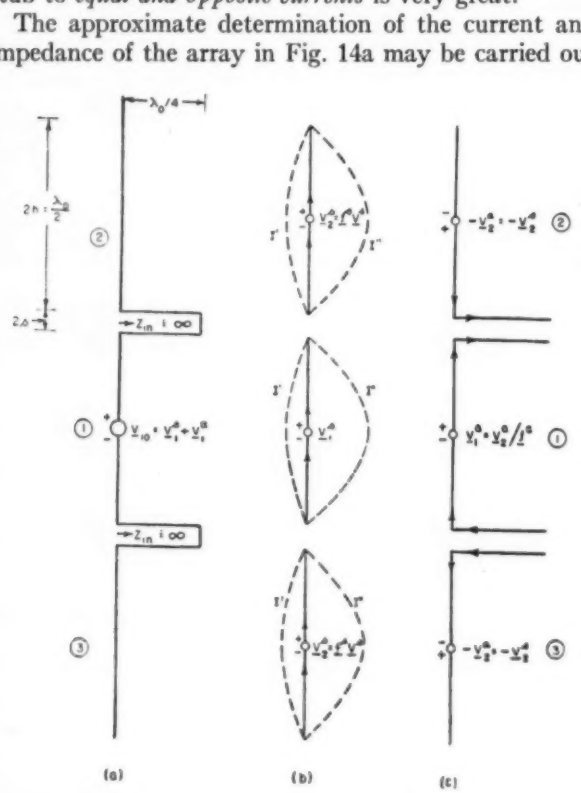

FIG. 14. Collinear array with transmission-line coupling.

The Symmetrical Problem

Let the voltages required to maintain equal currents at the centers of all three units, $I_1^s(0)=I_2^s(z_2=0)=I_3^s(z_3=0)$, be represented as in (3.20a)

$$V_{10}=V_1^s=V^s; \quad V_{30}=V_{20}=V_2^s=f^sV^s. \tag{5.1}$$

It is shown readily that f^s in (5.1) is effectively the same function as in (3.20b) even though the array differs from that involved in Section 3 by the presence of the stubs. Since the currents that enter the stubs from the attached antennas are essentially equal and opposite, and since the stubs are adjusted to offer an extremely high impedance to equal and opposite currents, the currents actually existing at the ends of the antennas where they are connected to the stubs are very small. This does not mean that transmission-line currents all along the stubs are as small as the input currents. Actually, the distribution of transmission-line currents on the high-impedance stubs is approximately sinusoidal with a small amplitude at the input end and a large amplitube in the terminating bridge. However, with closely spaced good conductors the ohmic losses in the stubs and the radiation losses from them are insignificant compared with radiation from the array as a whole, and they contribute nothing to the far-zone field. Indeed, there can be no significant change in either the input impedance of the array or the distribution of current in the three antennas if the stubs are removed as in Fig. 14b, leaving the circuit already analyzed in Section 4 where it constitutes the symmetrical part of the collinear array with parasitic outer units. The symmetrical current $I_1^s(z)$ in the central unit is given by (4.2a) or (4.5a); the symmetrical impedance Z_{0c}^s of the central unit is given by (4.9a) and graphically in Fig. 6. The currents in the outer units are well approximated by (4.10a) or (4.13a) since the odd components of current are negligible in determining the far-zone field of the array. The approximate currents are

$$I_1^s(z)=(V^s/Z_{0c}^s)\cos\beta_0 z \tag{5.2a}$$

$$I_3^s(z_3)=I_2^s(z_2)=(V_2^s/Z_{\text{even}}^s)\cos\beta_0 z_2$$
$$=(V^sf^s/Z_{\text{even}}^s)\cos\beta_0 z_2=I_1^s(z) \tag{5.2b}$$

where Z_{0c}^s is in (4.9a), Z_{even}^s is in (4.18a), and $f^s=Z_{\text{even}}^s/Z_{0c}^s$.

The Antisymmetrical Problem

Let the driving voltages required to maintain the currents $I_3^a(z_3=0)=I_2^a(z_2=0)=-I_1^a(0)$ in the array in Fig. 14a be represented as in (3.21a):

$$V_{10}=V_1^a=V^a;\quad V_{30}=V_{20}=-V_2^a=-f^aV^a. \tag{5.3}$$

The function f^a in (3) is *not* the same as in (3.21b). Since the currents in the two parallel conductors of the phase-reversing stubs are nearly equal and codirectional, these two conductors are always at the same potential at opposite points. Therefore, the terminating bridge may be removed (or replaced by an equivalent open end) without significant effect. Thus, the solution of the antisymmetrical problem of Fig. 14a reduces to the analysis of Fig. 14c. Unfortunately, this presents an intricate problem in a quantitative sense except for conductors of very small radius. Nevertheless, much valuable information on the general nature of the distribution of current and the operation of the array, and even a fair estimate of the impedance can be acquired from a rough quantitative investigation.

It has been shown[5] for parallel antennas that the current in an antenna that is coupled to another is determined in *major outline* by the dimensions of the antenna itself even if the coupling is quite close. Therefore, the first step in the study of Fig. 14c is directed toward the behavior *when isolated* of each of the three antennas with its attached half of the now open stub. It is reasonable to assume that the effects of the right-angled bends in the conductors can, at most, lead to a small quantitative modification, but not to essential changes in the distributions of current and charge. This is indicated from the study of the V-antenna.[6] Accordingly, the distributions of current in antennas 1 and 2 of Fig. 14c must be approximately the distributions in the same conductors when these are straightened as in Fig. 15. This makes the central unit equivalent to a center-driven antenna of electrical half-length $\beta_0 h=\pi$. The distribution of current on such an antenna is reproduced in Fig. 15f, and transferred to the bent antenna in Fig. 15e as an approximation. The impedance is simply

$$Z_{0c}{}^a=Z_0(\beta_0 h=\pi)\equiv Z_\pi \tag{5.4}$$

The bent antenna 2 in Fig. 15a may be approximated by the asymmetrically driven straight antenna in Fig. 15b. The analysis of this[7] has shown that in solving for the current in either half, this half may be assumed to be erected on an infinite, perfectly conducting plane and driven by a slice generator with appropriate voltage. For the upper half with an electrical length $\beta_0 h=\pi/2$ and an impedance $\frac{1}{2}Z_0(\beta_0 h=\pi/2)\equiv(Z_{\pi/2})/2$ the driving voltage is

$$V_{\pi/2}\equiv -V_2{}^aZ_{\pi/2}/(Z_\pi+Z_{\pi/2}); \tag{5.5a}$$

for the lower half (which has an electrical length $\beta_0 h=\pi$ and an impedance $\frac{1}{2}Z_0(\beta_0 h=\pi)\equiv(Z_\pi)/2$) the driving voltage is

$$V_\pi=-V_2{}^aZ_\pi/(Z_{\pi/2}+Z_\pi). \tag{5.5b}$$

Since the two antennas are in series, the resultant driving voltage is $-V^a$ as assumed in (5.3). The impedance is

$$Z_2{}^a=\tfrac{1}{2}(Z_\pi+Z_{\pi/2}). \tag{5.6}$$

The distributions of current on the two dissimilar parts of the outer antennas are shown in Fig. 15c, d with phases referred to $-V_2{}^a$. It is assumed that these distributions for isolated straight asymmetrical antennas approximate the distributions on the bent antenna in Fig. 15a.

With approximate distributions of current in the three antennas of Fig. 14c determined under the assumption that they are isolated, it remains to evaluate the effect of their interaction. An estimate of this may be obtained as follows. The most closely coupled parts of antennas 1 and 2 are the parallel ends at right angles to the axis of the array. These parts carry co-directional currents. It is known that the effect upon a given isolated antenna of a closely spaced parallel antenna with equal co-directional current is to increase the expansion parameter somewhat. That is, Ψ_{s1} for two symmetrically driven, parallel antennas is greater than Ψ_{K1} for the isolated antenna if b/λ_0 is small. For close

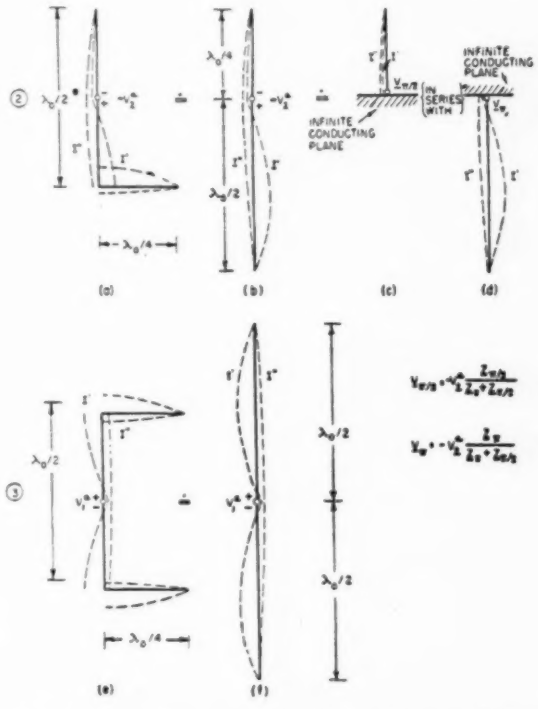

FIG. 15. Approximate equivalents of antisymmetrically driven antennas in three-element collinear array.

[5] C. T. Tai, Proc. I.R.E. **36**, 487–500 (1948).
[6] R. King, "Theory of V-Antennas," Cruft Laboratory Technical Report No. 96 (February, 1950).
[7] R. King, "Asymmetrically driven antennas and the sleeve dipole," Cruft Laboratory Technical Report No. 93, (December, 1949). Proc. I.R.E. **38**, 1154–1164 (1950).

spacing this increase is of the order of magnitude of 3 to 6. For thick antennas with $\Omega=2\ln(2h/a)$ not very large, the percentage change in Ψ_{K1} is great; for very thin wires it is quite small. The collinear parts of antennas 1 and 2 carry currents that are practically equal and opposite. It has been shown in Section 2 that a coupled antenna carrying an equal and opposite currents reduces the expansion parameter approximately in the same proportion as it is increased when the currents are co-directional. Thus, antenna 1 in the proximity of antennas 2 and 3 in Fig. 14c behaves roughly like a straight isolated antenna of the same length of conductor which has outer halves that are effectively of smaller radius, inner halves that are effectively of greater radius than when isolated. The same reasoning applies to the outer antennas.

To summarize, it is evident that a good estimate of the distribution of current and of the driving-point impedance of the three-element collinear array in Fig. 14a may be obtained by superimposing the solution of the symmetrically driven array in Fig. 14b upon the solution of the antisymmetrically driven array in Fig. 14c. In this latter, the currents in the central unit are like that in Fig. 15f. The resultant current is the algebraic sum of these symmetrical and antisymmetrical currents. In addition, there is the transmission-line distribution of equal and opposite currents on the stubs with large amplitude in the connecting bridges. Evidently, the method applied to the three-element array may be extended to any number of units. Note that the approximations involved improve as the value of $\Omega=2\ln(2h/a)$ increases.

Since the amplitude of the current in an antenna of electrical half-length $\beta_0 h=\pi$ is very much smaller than in an antenna for which $\beta_0 h=\pi/2$ when both are driven by the same voltage (for $\Omega=20$ the ratio of maximum currents is roughly 1 to 12), and since the antisymmetrically driven array in Fig. 15c corresponds roughly to elements with $\beta_0 h=\pi$, whereas the symmetrically driven array in Fig. 15b corresponds roughly to elements with $\beta_0 h=\pi/2$, it follows that even for moderately large ratios h/a, the predominating currents are the symmetrical currents of Fig. 14b as given in (5.1). *It is primarily these currents that determine the far-zone electromagnetic field.* Note that they are co-directional in the several units. That is, the phase-reversing stubs have, indeed, effectively reversed the *significantly radiating currents* in the outer units. Note that additional currents are maintained both on the stubs and on the antennas, but their principal role is to maintain the desired co-directional currents on the antennas while contributing negligibly to the radiation field either because they are small (viz., additional currents on antennas and co-directional currents on stubs) or, if large, because they are equal, opposite, and close together (as with the transmission-line currents on the stubs).

The driving-point admittance of the central unit and, hence, of the entire array is formally like (2.19b), viz.,

$$Y_{in}=\frac{I_1(0)}{V_{10}}=\frac{I_1^s(0)+I_1^a(0)}{V^s+V^a}$$

$$=\frac{1}{Z_{0c}^s(1+k^{-1})}+\frac{1}{Z_{0c}^a(1+k)}, \quad (5.7)$$

where Z_{0c}^s is given by (4.9a) and is plotted in Fig. 6, $Z_{0c}^a=Z_\pi$, and k is defined by

$$k\equiv\frac{f^a}{f^s};\quad f^a=\frac{Z_2^a}{Z_{0c}^a}=\frac{Z_\pi+Z_{\pi/2}}{2Z_\pi};\quad f^s=\frac{Z_2^s}{Z_{0c}^s}=\frac{Z_{\text{even}}^s}{Z_{0c}^s} \quad (5.8)$$

where Z_{even}^s is given by (4.18a) and is plotted in Fig. 7. If the separation b of the conductors of the transmission-line stubs is very small, $d/\lambda_0\doteq 0.5$. For this value $Z_{0c}^s\doteq 126+j83$, $Z_{\text{even}}^s\doteq 95+j62$; $f^s\doteq 0.75$. For sufficiently thin antennas, $|Z_\pi|\gg|Z_{\pi/2}|$ so that $f^a\doteq 0.5$. Hence $k\doteq\frac{2}{3}$. With this value,

$$Z_{in}=\frac{1}{Y_{in}}=\frac{Z_{0c}^s Z_\pi(1+\frac{2}{3})(1+\frac{3}{2})}{Z_{0c}^s(1+\frac{3}{2})+Z_\pi(1+\frac{2}{3})}. \quad (5.9)$$

Since for thin antennas, $|Z_\pi|\gg|Z_{0c}^s|$, it follows that

$$Z_{in}\doteq Z_{0c}^s(1+\tfrac{3}{2})=2.5Z_{0c}^s=2.5(126+j83)$$

$$=315+j207. \quad (5.10)$$

This value corresponds to $73.1+j42.5$ for a single unit. More accurate numerical results may be obtained for specific values of Z_π and $Z_{\pi/2}$ if desired. Other values of d/λ_0 may be used provided the spacing b of the stub wires satisfies $\beta_0 b\ll 1$.

Although the investigation of the three-element center-driven collinear array with phase-reversing stubs is not rigorous, it does provide an excellent picture of the several components of current and their distributions. Moreover, it justifies the conventional practice of assuming currents in the elements of the array co-directional, and sinusoidally distributed with equal amplitude in determining radiation-field patterns with $\beta_0 h=\pi/2$. That is, the dominant, symmetrical distribution in Fig. 14b approximates the distribution

$$I_z\doteq I_0\cos\beta_0 z_i;\quad i=1,2,3 \quad (5.11)$$

where z_i is measured from the center of antenna i.

The advantages of the collinear array with phase-reversing stubs over the same antennas with each element center-driven from a transmission line are clear. In the first place, it is much simpler from the constructional point of view. In the second place, it provides a far-zone field that is determined entirely by currents in the antennas and not by currents in the feeding lines. While it is true that the stub sections of line have unbalanced currents, it has been shown that these are

small compared with the principal currents on the antennas. Moreover, the stubs are of fixed and relatively short length so that contributions from small unbalanced currents in them are both negligible and determinate. Since individual transmission lines usually are long, and unbalanced currents in them may be large if the over-all electrical length of the line and attached metal at the generator-end happen to be self-resonant, their contribution to the far-zone field is neither determinate nor is it usually small.

Beam Oscillations in an F-M Cyclotron*

T. TEICHMANN
Princeton University, Princeton, New Jersey
(Received May 8, 1950)

This paper considers the radial and vertical oscillations of a synchro-cyclotron beam. It is found that various oscillations of substantially constant or increasing amplitude may occur in certain regions of the field, in which there are angular or other asymmetries, though only one possible oscillation (that at $n\simeq\frac{1}{3}$) can occur in a field that is cylindrically and vertically symmetric. The conditions for the various oscillations, and their behavior, are discussed.

I. INTRODUCTION

THE aim of this paper is to give a general discussion of various oscillations of a cyclotron beam which are induced (or permitted) by the particular shape or angular inhomogeneity of the magnetic field.[1]

The calculation is given only for small oscillations (i.e., oscillations of amplitude small compared to the radius of the beam) and depends on the adiabatic approximation, i.e., on the smallness of the fractional gain of energy of the beam over the period of several oscillations. The discussion is substantially non-relativistic, but can easily be extended to small relativistic energies.

II. NOTATION

One thus considers the motion of a particle of charge e, mass m, and energy $E=mv^2/2$, in a temporally constant magnetic field with cylindrical components (H_r, H_θ, H_z). Because of the particular design of cyclotrons, it is possible to find a median plane (usually parallel to and midway between the pole faces of the magnet) and a perpendicular axis, such that the field may be represented in good approximation by the cylindrical-components $(0, 0, H_n)(H_n=\text{constant})$. This plane and axis are then taken as the basis for a cylindrical coordinate system to describe the position of the particles (r, θ, z) and the spatial variation of the field. If the field were exactly $(0, 0, H_n)$ and the particle were set moving in the median plane, the subsequent motion would be of constant angular frequency

$$w_n=eH_n/mc \tag{2.1}$$

in a circle of radius

$$r_n=v/w_n. \tag{2.2}$$

In practice, because of the field variation, and possible angular inhomogeneities, the motion will be almost periodic (instead of strictly periodic) and may be regarded as uniform circular motion with superposed vertical and radial oscillations about the instantaneous equilibrium orbit (to be denoted by "i.o." in the following). The accelerating field of the dees will, of course, gradually increase the velocity v, and hence the i.o., but over a large portion of the particles path in the synchro-cyclotron this increment is relatively small over several periods of the oscillations considered, and the i.o. radius r_n may be regarded as constant in the region of any particular oscillation. If the oscillations about the equilibrium have a very large period, this (adiabatic) approximation loses its validity (see below).

It is convenient to refer all quantities to the i.o. and to introduce the new (non-dimensional) coordinates,

$$x=(r-r_n)/r_n \tag{2.3}$$

$$y=z/r_n, \tag{2.4}$$

and the velocity v_n of motion in the i.o. with angular velocity w_n,

$$v_n=-r_nw_n. \tag{2.5}$$

The magnetic field $\mathbf{H}=(H_r, H_\theta, H_z)$ is then most conveniently written in the form

$$\mathbf{H}=H_n(R, Q, Z) \tag{2.6}$$

(where $R\simeq0, Q\simeq0, Z\simeq1$). The (non-dimensional) components R, Q, Z, may be expanded in double Taylor series in x, y about any equilibrium radius r_n, and in Fourier series in θ. Carrying the Taylor series up to second-degree terms (i.e., using a parabolic approximation)

$$R=R_0+R_xx+R_yy+\tfrac{1}{2}R_{xx}x^2+R_{xy}xy+\tfrac{1}{2}R_{yy}y^2 \tag{2.7}$$

---

* This work was assisted in part by the joint program of the ONR and AEC.

[1] The discussion is thus an extension to other regions of the field of considerations given by Hamilton and Lipkin (unpublished) for $n\simeq\frac{1}{3}$.

and Q, Z may be expressed in the same way. Further,

$$R_y=\sum_{-\infty}^{+\infty} R_y{}^k e^{ik\theta}, \text{ etc.} \tag{2.8}$$

Note that H_n is a parameter which is regarded as constant over the domain of any oscillation, but which varies from i.o. to i.o. (as r_n increases). The normalization is so chosen that

$$Z_0=1+\sum_{k\neq 0} Z_0{}^k e^{ik\theta}. \tag{2.9}$$

Because of the electromagnetic equations curl$\mathbf{H}=0$, and div$\mathbf{H}=0$, and possible symmetries, the coefficients defined above satisfy certain linear equations which are listed in the Appendix, and used in the remainder of this paper. The most important of these relations are the following:

$$\int_{-\pi}^{\pi} Q d\theta=0, \text{ implying } Q_\alpha{}^0=0, \text{ for all } \alpha=x, y \text{ etc.} \tag{2.10}$$

$$R_y=Z_x \tag{2.11}$$

$$R_{xy}=Z_{xx} \tag{2.12}$$

$$R_{yy}=Z_{xy}. \tag{2.13}$$

If the vertical component of the field is symmetric about the median plane, one has the additional relations

$$Z_y=Z_{xy}=R_{yy}=0. \tag{2.14}$$

The usual definition

$$n=-d\log H_z/d\log r \tag{2.15}$$

is also slightly modified here to apply only to the angularly symmetric part of H_z, i.e.,

$$Z_x{}^0=-nZ_0{}^0=-n \tag{2.16}$$

and hence,

$$Z_{xx}{}^0=(n^2+n-n'), \quad n'=dn/dx. \tag{2.17}$$

III. SUMMARY OF RESULTS

It is found that approximately periodic oscillations about the i.o. can occur only in the neighborhood of certain particular values of n, and that the possibility of developing an appreciable amplitude then depends not only on the shape of the field, but also on the initial phase u which is in general determined both by the field shape and by the initial displacement of the particle from the i.o., and its velocity. When they do occur, these oscillations have the form†

$$A(\theta)\cos(c\theta+\phi) \tag{3.1}$$

where $\theta\simeq w_n t$ is the path length, and $A(\theta)$ is a slowly varying function of θ. Only the cases in which $A(\theta)$ can remain substantially constant, or increase, are of practical interest.

(i) There are only two oscillations which can occur if the field is cylindrically symmetric, the most important of these being a coupled radial-vertical oscillation which occurs near $n\simeq\frac{1}{3}$, and is fully discussed in reference 1. If X and Y are the amplitudes of the oscillations of x and y (i.e., the ratios of the amplitudes of the radial and vertical oscillations to the i.o. radius r_n), then

$$4X^2+Y^2=\text{constant}, \tag{3.2}$$

so that the oscillations are substantially limited by their initial values, though a radial deviation will turn into a vertical one in the course of time and conversely.

(ii) The other possible oscillations (except at $n\simeq\frac{1}{2}, \frac{4}{5}$) depend on the presence of fundamental or second harmonic terms in the Fourier expansions of R, Q and Z. Proceeding systematically in the direction of increasing n, there is first a purely vertical oscillation at $n\simeq\frac{1}{3}$. For small θ the amplitude has the form

$$Y=Y_0/(1-Y_0|C|\cos u\cdot\theta), \tag{3.3}$$

Y_0 being the initial amplitude (deviation from i.o.), and C a certain linear combination of first Fourier coefficients [see Eq. (5.4)]. Since Y_0, $|C|$ are positive by definition, unpleasant oscillations are only likely if $\cos u>0$.

(iii) At $n\simeq\frac{1}{4}$ a purely vertical oscillation may again occur, though of rather different form, to wit,

$$Y=Y_0\exp(|D|\cos u\cdot\theta) \tag{3.4}$$

for small θ. D is substantially the fundamental Fourier coefficient of Z_x, i.e., of dH_z/dr. Here again nasty oscillations may occur if $\cos u>0$.

(iv) At $n\simeq 9/25$ coupled radial-vertical oscillations may occur both if certain fundamental Fourier coefficients and/or if certain second harmonics are present in the field, though if both types of terms are present together the equations are rather too complicated to be solved in an informative manner. In each separate case the amplitudes satisfy relations of the type

$$|M|X^2\pm|L|Y^2=\text{constant}, \tag{3.5}$$

the quantities L and M being linear combinations of the Fourier coefficients involved. If the plus sign obtains, the oscillations are unlikely to become obtrusive, since they are substantially limited by their initial values, though coupling from radial to vertical oscillation, or the converse, may give rise to trouble, especially if L and M differ widely in magnitude. If the minus sign obtains, on the other hand, the oscillations may grow very large, since it then turns out that X and Y may be represented approximately by hyperbolic functions of θ [see Eq. (5.24)ff].

(v) When $n\simeq 4/9$ there is again the possibility of a purely vertical oscillation, of similar form to that at $n\simeq\frac{1}{3}$, the only difference being that the coefficient C

† The frequencies of the oscillations discussed below are respectively, $w_n(1-n)^{\frac{1}{2}}$ and $w_n(n)^{\frac{1}{2}}$ for the radial and vertical oscillations.

now depends on the second harmonics in the field components.

(vi) At $n\simeq\frac{1}{2}$ there is the possibility of a coupled oscillation if the field is not vertically symmetric about the median plane, quite apart from any angular inhomogeneity. The amplitudes satisfy the relation

$$X^2+Y^2=\text{constant}, \tag{3.6}$$

so that the oscillations are not likely to be troublesome. For small θ, X and Y are themselves approximately periodic in θ with period

$$2\pi/B\cos u. \tag{3.7}$$

Proceeding to larger values of n, one finds that oscillations may occur for those values of $1-n$ for which oscillations occur at n (as above), with the difference that the roles of radial and vertical oscillations are interchanged. It is not of interest to discuss these further, except to remark that the oscillation at $n\simeq\frac{4}{3}$, which is the analog of that at $n\simeq\frac{1}{3}$, here depends on the existence of an asymmetry about the median plane [by virtue of (2.13)], and hence may be avoided in practice.

The upshot of these considerations is that by careful design of the vertical and cylindrical symmetry of the field it is possible to get rid of all the oscillations of the beam, except that at $n\simeq\frac{1}{3}$, which is by its nature generally of limited amplitude.

IV. EQUATION OF MOTION OF THE BEAM (PARTICLES)‡

The motion of a particle of charge e and mass m, in a magnetic field (H_r, H_θ, H_z) is determined by the equations

$$\dot{v}_r=\ddot{r}-r\dot{\theta}^2=(e/mc)(v_\theta H_z-v_z H_\theta) \tag{4.1}$$

$$\dot{v}_\theta=r\ddot{\theta}+2\dot{r}\dot{\theta}=(e/mc)(v_z H_r-v_r H_z)+\text{accelerating force} \tag{4.2}$$

$$\dot{v}_z=\ddot{z}=(e/mc)(v_r H_\theta-v_\theta H_r). \tag{4.3}$$

Instead of Eq. (4.2) it is more convenient to use

$$v^2=v_r^2+v_\theta^2+v_z^2 \tag{4.4}$$

which is essentially the energy integral. The effect of the accelerating force is to change v as the motion progresses, and the adiabatic approximation is permissible provided that this change is relatively small during the time of one radial or vertical oscillation, whichever is the larger; a small relative change per revolution of the particle is not enough. Consequently the method below should not be taken too seriously for n near 0 or 1, unless the fractional increase in energy is exceedingly small at these values.

In terms of the quantities w_n, r_n, and the new variables x, y, the equations of motion become

$$\ddot{x}=w_n(v_\theta Z/r-\dot{y}Q)+v_\theta^2/rr_n \tag{4.5}$$

$$\ddot{y}=w_n(\dot{x}Q-v_\theta R/r) \tag{4.6}$$

and (4.4) (since $v_r=r_n\dot{x}$, $v_\theta=r\dot{\theta}$, $v_z=r_n\dot{y}$). It is now convenient to introduce the new variable $\vartheta=w_n t$. In view of the smallness of the oscillations and the adiabatic principle, $\vartheta\simeq\theta$. Actually they are related by $\vartheta/\theta=w_n/\dot{\theta}$, and $w_n/\dot{\theta}\simeq 1$. In the following it will be assumed that $\vartheta=\theta$. x' then denotes $dx/d\theta$, etc. It is also convenient to write

$$v^2=v_n^2(1+\epsilon) \tag{4.7}$$

(i.e., the total energy $mv^2/2$ = energy of rotation in an idealized i.o. $mv_n^2/2$ + additional energy $\epsilon mv_n^2/2$ due to the fact that oscillations occur and that the i.o. is idealized). Due to the assumed smallness of the oscillations ϵ is a small quantity; thus

$$v_\theta\simeq v_n(1+\tfrac{1}{2}\epsilon-\tfrac{1}{2}x'^2-\tfrac{1}{2}y'^2) \tag{4.8}$$

up to terms of the second degree. Equations (4.5) and (4.6) then become, respectively,

$$x''+(1-n)x=F=-(1+\tfrac{1}{2}\epsilon-\tfrac{1}{2}x'^2-\tfrac{1}{2}y'^2)(Z_0+(Z_x-n)x+Z_y y+\tfrac{1}{2}Z_{xx}x^2+\cdots)-y'(Q_0+Q_x x+Q_y y+\cdots)+1+\epsilon+x^2-x'^2-y'^2 \tag{4.9}$$

$$y''+ny=G=x'(Q_0+Q_x x+Q_y y+\cdots)+(1+\tfrac{1}{2}\epsilon-\tfrac{1}{2}x'^2-\tfrac{1}{2}y'^2)(R_0+R_x x+(R_y-n)y+\tfrac{1}{2}R_{xx}x^2+\cdots) \tag{4.10}$$

using some of the results of Section II. It is possible to eliminate the constant terms on the right of Eqs. (4.9) and (4.10) by a slight definition of the i.o. [*viz.*, replacing r_n by $r_n+\epsilon/2(1-n)$ eliminates the constant term in (3.9) to first order, while raising the equilibrium plane by an amount $\sim r_n R_0^0/n$ gets rid of the constant term in (4.10)]. It will be assumed that this has been done, and that only the non-constant terms in F and G need be considered. For the sake of simplicity let

$$a=(1-n)^{\frac{1}{2}},\quad b=(n)^{\frac{1}{2}}. \tag{4.11}$$

If $F\equiv 0$, $G\equiv 0$, equations (4.9) and (4.10) have the solutions[2]

$$x=X\sin(a\theta+\phi) \tag{4.12}$$

$$y=Y\sin(b\theta+\psi), \tag{4.13}$$

X, Y, ϕ, and ψ being suitable constants. Since F and G are not constant, but involve x, y, and θ in a complicated way, the solutions may still be written in the same form, but with X, Y, ϕ, and ψ taken as functions of θ. Imposing the additional conditions

$$x'=aX\cos(a\theta+\phi) \tag{4.14}$$

$$y'=bY\cos(b\theta+\psi), \tag{4.15}$$

‡ The first part of this section is a summary of portions of reference 1 in which a more detailed discussion is given.

[2] See A. Kryloff and N. Bogoliuboff, *Non-Linear Mechanics*, Princeton University Press, 1943 for further details of this method.

one finds that $X(\theta)$, $Y(\theta)$ satisfy the first-order differential equations

$$X' = F\cdot\cos(a\theta+\phi)/a \tag{4.16}$$

$$Y' = G\cdot\cos(b\theta+\psi)/b. \tag{4.17}$$

The right-hand sides of these equations are small, and almost periodic in θ, so that in general, the average of X', Y' over several periods of the motion will be zero or negligible. This will not be the case if there are secular (θ-independent) or almost secular (very long period) terms in the right-hand sides. In this case X' or Y' or both will be of constant sign over many periods of the oscillations, and X, Y may become appreciable despite insignificant initial values. In this approximation, therefore, appreciable oscillations may arise for those values of a and b for which secular terms appear in the right-hand sides of Eqs. (4.16) and (4.17).

In terms of the original equations (4.9) and (4.10) the interpretation of these oscillations is somewhat as follows. The beam has in first approximation two modes of oscillation, a radial mode with frequency $w_r = w_n(1-n)^{\frac{1}{2}}$, and a vertical mode with frequency $w_z = w_n(n)^{\frac{1}{2}}$. The equations of motion are linear in this approximation, and thus the amplitude of the oscillations will be constant and determined by their initial values. In higher approximation, the equations of motion contain complicated non-linear terms (F, G) which may cause suppression of the oscillations due to interference, and will generally prevent any increase in the amplitudes, if not actively decreasing them. For certain particular values of n, however, these non-linear terms give rise to a species of subharmonic resonance, so that the initial oscillations of the beam may increase in amplitude.

It is to be noted that ϕ and ψ also satisfy first-order differential equations, similar in form to (4.16) and (4.17). If one is interested mainly in the amplitudes of individual oscillations, these phase variations will not play a significant role. On the other hand, if the motion is to be traced through from one region of oscillation to another, phase changes will be important, because of their effect on the initial values, and the equations for ϕ' and ψ' may have to be discussed in a similar way to that in which (4.16) and (4.17) are dealt with below. This is, however, not required in the sequel.

V. POSSIBLE OSCILLATIONS

This section is devoted to the task of finding for what values of a and b (i.e., of n) secular terms may arise in $F\cos(a\theta+\phi)$ and $G\cos(b\theta+\psi)$, and to discussing briefly the corresponding oscillations. The calculation is, of course, only carried out up to second-degree terms, and since it is straightforward, though tedious, no details of the first part of the computation are given here.

Since a and b are symmetric about $n=\frac{1}{2}$, and F, G both contain terms of substantially the same type, it is easy to see that any oscillation which occurs for $n=\frac{1}{2}-j$ will also occur for $n=\frac{1}{2}+j$, with the roles of x and y interchanged. Because of this, and also because the beam is usually extracted well before $n=\frac{1}{2}$, only the oscillations in the range $0<n\leqslant\frac{1}{2}$ are discussed here.

Inspection of F and G shows that in this range secular terms may arise from sines or cosines with the following arguments: (i) $(a-2b)\theta$, $n\simeq\frac{1}{5}$; (ii) $(1-3b)\theta$, $n\simeq\frac{1}{9}$; (iii) $(1-2b)\theta$, $n\simeq\frac{1}{4}$; (iv) $(1-2a-b)\theta$, $(2-a-2b)\theta$, $n\simeq 9/25$; (v) $(2-3b)\theta$, $n\simeq 4/9$; (vi) $(a-b)\theta$, $n\simeq\frac{1}{2}$. The corresponding amplitudes X and Y then satisfy equations as follows.

(i) $n\simeq\frac{1}{5}$, $a\simeq 2b$

In this case one finds the coupled oscillations

$$\left.\begin{aligned} X' &= -KY^2\cos p \\ Y' &= 4KXY\cos p \end{aligned}\right\}. \tag{5.1}$$

Here

$$16K = (5)^{\frac{1}{2}}Z_{xx}{}^0 = (5)^{\frac{1}{2}}(6/25-n') \tag{5.2}$$

$p=(a-2b)\theta+u$, and u, the initial phase, depends only on the initial phases of the two individual oscillations, ϕ_0 and ψ_0, $u=\phi_0-2\psi_0$. It follows from (5.1) that $4X^2+Y^2=$constant. These oscillations are dealt with *in extenso* in reference 1, and therefore will not be discussed further here, though similar oscillations are considered in more detail in (iv) below.

(ii) $n\simeq\frac{1}{9}$, $1\simeq 3b$

Here there is only a vertical oscillation, satisfying the equation

$$Y' = |C|\,Y^2\cos p \tag{5.3}$$

$$C = \int_{-\pi}^{\pi}(9Z_{xy}-R_0)e^{i\theta}d\theta/48\pi \tag{5.4}$$

$$p=(1-3b)\theta+u,\ u=-3\psi_0+\text{phase } C.$$

Thus,

$$Y = Y_0/(1-Y_0|C|\cdot\int_0^{\theta}\cos p\cdot d\theta). \tag{5.5}$$

Noting that $(1-3b)\theta\simeq 0$, and choosing the origin of θ at the point where $1=3b$, p may be approximated by

$$p = u-3\theta^2 db/d\theta = u-9g^2\theta^2\pi/2 \tag{5.6}$$

$$\pi g^2 = (dn/dr)(dr/d\theta) = n'\cdot\Delta E/4(1-n)E\cdot\pi,$$

i.e.,

$$g^2 = \frac{1}{\pi}\cdot\frac{dn}{dr}\cdot\frac{dr}{d\theta} = \frac{n'}{4\pi^2(1-n)}\cdot\frac{\Delta E}{E}. \tag{5.7}$$

ΔE = energy per revolution of the beam, E = total energy. (See Appendix I.)

Thus,

$$\int_0^{\theta}\cos p\cdot d\theta = (\cos u\cdot\mathfrak{C}(3g\theta)+\sin u\cdot\mathfrak{S}(3g\theta))/3g, \tag{5.8}$$

where

$$\mathcal{C}(\theta)=\int_0^\theta \cos\frac{\pi}{2}\theta^2 d\theta, \quad \mathcal{S}(\theta)=\int_0^\theta \sin\frac{\pi}{2}\theta^2\cdot d\theta \quad (5.9)$$

are the usual Fresnel functions.

The behavior of the oscillations thus depends both on the magnitude of C and on the initial phase u. In order to examine the behavior more closely, one assumes that $g^2\theta^2$ is small enough not only for (5.6) to be valid, but also to permit the right-hand side of (5.8) to be replaced by $|C|\cos u\cdot\theta$, so that

$$Y=Y_0/(1-Y_0|C|\cos u\cdot\theta). \quad (5.10)$$

Since Y and $|C|$ are positive, increasing oscillations can only occur for

$$\cos u>0. \quad (5.11)$$

This approximation also defines a limiting value of the path length θ

$$\theta_1=1/Y_0|C|\cos u \quad (5.12)$$

beyond which the method is not valid, despite the smallness of $g^2\theta^2$. A similar, though rather more complicated effect may also take place in the approximation (5.8).

(iii) $n\simeq\frac{1}{4}$, $1\simeq 2b$

Here again there is only a vertical oscillation, the amplitude of which satisfies the equation

$$Y'=|D|Y\cos p \quad (5.13)$$

$$D=\int_{-\pi}^{\pi} Z_z e^{i\theta}d\theta/2\pi \quad (5.14)$$

$$p=(1-2b)\theta+u,\ u=-2\psi_0+\text{phase}(1/D).$$

Thus

$$Y=Y_0\exp(|D|\int_0^\theta \cos p d\theta). \quad (5.15)$$

Proceeding as in (ii)

$$p=u-2\pi g^2\theta^2 \quad (5.16)$$

and hence

$$Y=Y_0\exp(|D|(\cos u\cdot\mathcal{C}(2g\theta)+\sin u\cdot\mathcal{S}(2g\theta))/2g). \quad (5.17)$$

For small enough $g^2\theta^2$, one has

$$Y\simeq Y_0\exp(|D|\cos u\cdot\theta). \quad (5.18)$$

If $\cos u>0$, Y will increase approximately exponentially, with "time constant" $1/w_n|D|\cos u$, and thus, if conditions are favorable, very disturbing oscillations may arise in this region. It is interesting to remark, parenthetically, that there was strong evidence of this type of oscillation in the Princeton cyclotron: the edges of the dees were found to be strongly radioactive in the region $n\simeq\frac{1}{4}$, indicating that the beam was vertically splayed out in this region.

(iv) $n\simeq 9/25$, $2a-b\simeq 1$ and/or $a+2b\simeq 2$

In this case there are coupled oscillations satisfying the equations

$$X'=|L|XY\cos p+|N|Y^2\cos q$$
$$Y'=|M|X^2\cos p^*+|P|XY\cos q^* \quad (5.19)$$

$$L=\int_{-\pi}^{\pi}(5Z_{xy}+3iQ_z)e^{i\theta}d\theta/32\pi \quad (5.20)$$

$$M=\int_{-\pi}^{\pi}(25R_{zz}+16R_0)e^{i\theta}d\theta/240\pi$$

$$N=\int_{-\pi}^{\pi}(25Z_{yy}+30iQ_y+9Z_0)e^{2i\theta}d\theta/320\pi \quad (5.21)$$

$$P=\int_{-\pi}^{\pi}(5Z_{zz}+4iQ_y)e^{2i\theta}d\theta/24\pi$$

$$p=(1-2a+b)\theta+u, \qquad p^*=(1-2a+b)\theta+u^*$$
$$q=(2-a-2b)\theta+s, \qquad q^*=(2-a-2b)\theta+s^*$$
$$u=-2\phi_0+\psi_0+\text{phase}L,\ u^*=-2\phi_0+\psi_0+\text{phase}M$$
$$s=-\phi_0-2\psi_0+\text{phase}N\ \ s^*=-\phi_0-2\psi_0+\text{phase}P$$

The first terms on the right arise from the fundamental Fourier coefficients, and correspond to the near vanishing of $1-2a+b$, while the second terms come from the second harmonics, and correspond to the smallness of $2-a-2b$.

Equations (5.19) are pretty complicated even when the approximation $p=p^*=q=q^*=0$ is made. However, an indication of the sort of thing that happens is given by taking $N=P=0$ (absence of higher harmonics in the field), and placing $u=u^*$. This latter assumption may make it necessary to replace $|M|$ by $-|M|$, to obtain a reasonable representation of what happens if u and u^* differ widely. The equations then become [see (i)]

$$X'=|L|XY\cos p$$
$$Y'=\pm|M|X^2\cos p. \quad (5.22)$$

If the plus sign obtains,

$$(X^2/|L|)-(Y^2/|M|)=k^2, \quad (5.23)$$

and one may put

$$X=k(|L|)^{\frac{1}{2}}\sec(W-W_0),$$
$$Y=k(|M|)^{\frac{1}{2}}\tan(W-W_0) \quad (5.24)$$

whence W satisfies the differential equation

$$W'=-k|L|(|M|)^{\frac{1}{2}}\cos p. \quad (5.25)$$

For small enough θ,

$$W-W_0\simeq -k|L|(|M|)^{\frac{1}{2}}\cos u\cdot\theta. \quad (5.26)$$

Because of (5.24) one again obtains a limiting value for

the angular path length θ

$$\theta_1=\pi/2k|L|(|M|)^{\frac{1}{2}}\cos u. \tag{5.27}$$

It is clear that in this case both the radial and vertical oscillations may reach uncomfortably large amplitudes, unless their initial values are both zero. This is not so however if the minus sign applies in Eqs. (5.22); the equations then obtained are the analog of (5.1), with the roles of X and Y interchanged. (5.23) is replaced by

$$(X^2/|L|)+(Y^2/|M|)=k^2 \tag{5.28}$$

and one writes

$$X=k(|L|)^{\frac{1}{2}}\sin(W-W_0),$$
$$Y=k(|M|)^{\frac{1}{2}}\cos(W-W_0). \tag{5.29}$$

W satisfies the equation

$$W'=k|L|(|M|)^{\frac{1}{2}}\cdot\sin(W-W_0)\cdot\cos p \tag{5.30}$$

so that

$$W-W_0=\arctan\exp\int_0^\theta k|L|(|M|)^{\frac{1}{2}}\cos p\,d\theta \tag{5.31}$$

or, for small θ,

$$W-W_0\simeq\arctan\exp k|L|(|M|)^{\frac{1}{2}}\cos u\cdot\theta. \tag{5.32}$$

Here the combined amplitudes are limited by their initial values, though disturbing oscillations may still occur, due to coupling between the radial and vertical modes, if L and M differ widely in magnitude. Similar results are obtained if there are only second harmonics in the field, *viz.*, $L=M=0$, N, $P\neq 0$.

(v) $n\simeq 4/9$, $2\simeq 3b$

The vertical oscillation has the same form as that occurring at $n\simeq\frac{1}{9}$, except that the coefficient C now depends on the corresponding second harmonics in the field components. [See (ii).]

(vi) $n\simeq\frac{1}{2}$, $a\simeq b$

Using the normalization described following (4.10), the coupled oscillations satisfy the equations

$$\begin{aligned} X'&=BY\cos p\\ Y'&=-BX\cos p\\ B&=Z_y^0/\sqrt{2}\\ p&=(a-b)\theta+u,\quad u=\phi_0-\psi_0. \end{aligned} \tag{5.33}$$

In general $B=0$, since the vertical component of the field is usually symmetric about the plane in which $R_0^0=\int_0^{2\pi}R_0 d\theta/2\pi=0$. The redefinition of coordinates involved in attaining this state of affairs may however distort the median "plane" into slightly conical form (deviation$\sim r_n R_0^0/n$) so that then B is not zero. Equation (5.33) yields the relation

$$X^2+Y^2=k^2B. \tag{5.34}$$

Writing

$$X=k(B)^{\frac{1}{2}}\sin(W-W_0),\quad Y=k(B)^{\frac{1}{2}}\cos(W-W_0) \tag{5.35}$$

one finds

$$W'=B\cos p \tag{5.36}$$

so that, proceeding in the usual way,

$$W-W_0=2^{\frac{1}{2}}B[\cos u\cdot\mathcal{C}(g\theta/2^{\frac{1}{2}})+\sin u\cdot\mathcal{S}(g\theta/2^{\frac{1}{2}})]/g. \tag{5.37}$$

For sufficiently small θ,

$$W-W_0\simeq B\cos u\cdot\theta. \tag{5.38}$$

Thus X and Y are themselves approximately periodic with period

$$2\pi/B\cos u. \tag{5.39}$$

The amplitudes are here again limited by their initial values.

VI. GENERAL REMARKS

The discussion of the previous section was concerned chiefly with the possibility and behavior of self-maintaining or increasing oscillations. It is also fitting to make some brief comments about the oscillations in general, i.e., when the particular cases of Section V do not obtain.

Since in this case the oscillations are small, and (by hypothesis) not self-maintaining, it is sufficient to consider the differential equations (4.9) and (4.10) only up to first-degree terms, *viz.*,

$$x''+a^2x=-(Z_x-n)x-Z_y y-(Z_0-1)-Q_0y' \tag{6.1}$$

$$y''+b^2y=(R_y-n)y+R_x x+(R_0-R_0^0)+Q_0x'. \tag{6.2}$$

The coefficients on the right are in general Fourier series in θ with period 2π. Because of this, these equations are closely related to the Mathieu equations: alternatively, attempting to solve these equations by Laplace transforms leads to a set of difference equations. Unless something fairly specific is known about the magnitudes of the Fourier coefficients, there is not much to be gained by pursuing such a mathematically detailed treatment further, all the more in view of the many preceding approximations. Brief consideration will thus only be given to the approximate solution of the system (6.1) and (6.2).

Because of the form of the differential operator on the left, terms containing (say) $\cos k\theta$ on the right will yield similar terms with a multiplicative factor $1/(a^2-k^2)$, $1/(b^2-k^2)$, respectively. Hence only the first few terms need be considered in the Fourier series on the right, at least in an approximate treatment. Incidentally, the values of n for which alarming oscillations may occur may be found in this way (successive substitutions), by placing $x=X\sin a\theta$, $y=Y\sin b\theta$ on the right, and looking for those values of a, b for which some of the a^2-k^2, b^2-k^2 reduce to zero. Second-order terms should also be considered in this case.

It is not difficult to see that even in the absence of an initial deviation there will be a forced oscillation due to

the cylindrical asymmetry of the field, of the form

$$x = -Z_0^1 \cos\theta/n \tag{6.3}$$

$$y = R_0^1 \cos\theta/(1-n^*) \tag{6.4}$$

(if only fundamentals are present in the field). The "oscillations" (6.3), (6.4) denote, respectively, a displacement of the center of the i.o. by an amount $Z_0^1 r_n/n$, and a tilting of its plane by an angle $\sim R_0^1/(1-n)$. If higher harmonics are present the interpretation is no longer so simple: the i.o. is no longer a circle, nor even a plane curve, though it will generally be fairly close to the more idealized i.o. as initially defined. In higher approximation, not only will higher Fourier components appear in x and y but also small constant terms which may be removed by further renormalization of the original i.o. radius r_n, and the i.o. plane [see (4.10)f]; these latter correspond to the fact that any "excess" energy of the beam is shared between the various modes (*viz.*, the rotational, as well as the two vibrational modes).

Inspection of (6.1) and (6.2) shows that if the beam contains some components of its normal modes to start with, it will also contain terms of the type $\sin(k+a)\theta$, etc. In general, if the more exact equations of motion are considered, the deviations from equilibrium have the form

$$\sum_k \sum_l \sum_m A_{klm} \sin[(k+la+mb)\theta+\phi_{klm}] \tag{6.5}$$

so that the motion is generally not even approximately periodic. In special cases when $la+mb$ is an integer, the deviation becomes approximately periodic and much larger; these cases correspond to the oscillations considered in Section V.

APPENDIX I. CHANGE OF RADIUS WITH PATH LENGTH

The radius of the equilibrium orbit given by

$$r = (mc/e)(v/H),$$

H being the vertical component of the field, so that the relation between the increments is

$$(\Delta r/r) = (\Delta v/v) - (\Delta H/H).$$

Since the energy

$$E = mv^2/2$$
$$(\Delta v/v) = (\Delta E/2E),$$

while by definition of n

$$(\Delta H/H) = -n(\Delta r/r).$$

Thus

$$(\Delta r/r) = (\Delta E/2(1-n)E).$$

Taking E to be the increment in energy per revolution (i.e., the energy gained from the r-f field of the dees per revolution) one finds for the average rate of increase of radius per angular path length

$$dr/d\theta = (r \cdot \Delta E/4\pi(1-n)E).$$

APPENDIX II. DESCRIPTION OF THE FIELD

Using the definition (2.6) of the field, and the electromagnetic equations $\mathrm{curl}\mathbf{H}=0$, $\mathrm{div}\mathbf{H}=0$, one has

$$\frac{\partial Z}{\partial\theta} - (1+x)\frac{\partial Q}{\partial y} = 0 \qquad Q + (1+x)\frac{\partial Q}{\partial x} - \frac{\partial R}{\partial\theta} = 0$$

$$\frac{\partial Z}{\partial x} - \frac{\partial R}{\partial y} = 0 \qquad R + (1+x)\frac{\partial R}{\partial x} + \frac{\partial Q}{\partial\theta} + (1+x)\frac{\partial Z}{\partial y} = 0.$$

Inserting the Eqs. (2.7) and (2.8), i.e., the expansions of R, Q, Z, in Taylor series in x, y and Fourier series in θ, and equating coefficients, one finds the following relations, which prove useful in specific calculations:

$$\begin{aligned}
Z_x^k &= R_y^k & ikZ_0^k &= Q_y^k \\
Z_{xy}^k &= R_{yy}^k & ikZ_x^k &= Q_y^k + Q_{xy}^k \\
Z_{xx}^k &= R_{xy}^k & ikZ_y^k &= Q_{yy}^k \\
ikR_0^k &= Q_0^k + Q_x^k & -ikQ_0^k &= R_0^k + R_x^k + Z_y^k \\
ikR_x^k &= Q_{xx}^k + 2Q_x^k & -ikQ_x^k &= R_{xx}^k + 2R_x^k + Z_y^k \\
& & -ikQ_y^k &= R_y^k + R_{xy}^k + Z_{yy}^k.
\end{aligned}$$

Taking $k=0$ these equations show that

$$\int_{-\tau}^{\tau} Q d\theta = 0,$$

which must of course be the case in the absence of a vertical component of the magnetizing current.

The author is indebted to Drs. P. C. Gugelot and H. J. Lipkin for helpful discussions and suggestions.

On the Theory of Dislocations*

JOHN LEE BOGDANOFF
Department of Civil Engineering, Columbia University, New York, New York
(Received May 12, 1950)

If, in a multiply-connected elastic solid, discontinuities are permitted across a stationary barrier in either the strain or its first derivatives or both, dislocations of a more general type than encountered in classical theory are possible. A number of these more general dislocations have been obtained for states of plane and anti-plane strain in a hollow right circular cylinder when the surface of discontinuity is a single stationary plane barrier. Some of the dislocations found possess the characteristic that although the strain is continuous across the barrier the displacement discontinuity is *not* one which would be possible in a rigid body. Examination of the conditions for the uniqueness of solution of the boundary value problems of elasticity reveals that when dislocations of the more general type are admitted appropriate data must be given at each point on the specified barrier in addition to the usual information.

Notation

r, θ, z: Cylindrical coordinates.
$\sigma_\theta, \tau_{r\theta}, \tau_{rz}, \sigma_r, \tau_{\theta z}, \sigma_z$: Components of stress tensor.
$e_{rr}, e_{r\theta}, e_{rz}, e_{\theta\theta}, e_{\theta z}, e_{zz}$: Components of strain tensor.
u_r, u_θ, u_z: Displacement components.
ω_z: z component of rotation.
E: Young's modulus.
σ: Poisson's ratio.

I. INTRODUCTION

IN the classical theory of dislocations in a multiply-connected body, Weingarten's theorem[1] plays a fundamental role. According to it, the displacement of the matter immediately on one side of a barrier with respect to the matter on the other side is one which would be possible in a rigid body. Inherent in the proof of this theorem is the assumption that the strain is continuous of class $C^{(2)}$ throughout. We now ask the following question: If discontinuities in the strain or its first derivatives or both are permitted across a stationary barrier, what new displacement discontinuities are allowed? It must be expected in this case that the displacement discontinuity cannot be represented by a displacement possible in a rigid body. The existence of dislocations of a more general type than those of classical theory has been suggested by Goodier.[2]

The six dislocations of classical theory possible in a hollow right circular cylinder are known and have been described in detail by Volterra.[3] In particular there are three in plane strain and one in anti-plane strain. We shall seek dislocations of the less restricted type in the same body for states of plane and anti-plane strain when there is a single plane barrier Ω.

If the strain is discontinuous across Ω, it follows that discontinuities also exist across the same surface in the stress components. It is known[4] however, that in the absence of body forces equilibrium requires the traction on a stationary surface of discontinuity to be continuous across it. Hence, we are restricted to have discontinuities only in those components of the stress which do not enter the expression for the traction on Ω. Because of this condition, it is convenient in what follows to work directly with the stresses.

II. STATEMENT OF PROBLEM

We consider the equilibrium of a hollow right circular cylinder of isotropic elastic material in which there are no body forces. Let the z axis of a cylindrical coordinate system (r, θ, z) coincide with the axis of the cylinder, and let the surface of discontinuity Ω be the intersection of the half-plane $\theta=0$ with the cylinder. The angular coordinate is restricted by

$$0 \leq \theta \leq 2\pi. \tag{2.01}$$

In order to obtain dislocations of the more general type we must seek stress systems in which the stresses or their derivatives or both are discontinuous across Ω. Further, these stresses must satisfy both the differential equations of equilibrium and the compatibility equations; and the traction on Ω must be continuous across this surface.

The procedure followed in obtaining appropriate stress systems is the same for both the anti-plane strain and plane strain problems. First, we assume that at least one of the components of traction on the barrier is expressed by means of functions that are continuous of class $C^{(2)}$ in the simply-connected region formed by introducing Ω and continuous across this surface. Next,

* As used in the present paper, the term dislocation means a state of strain in a multiply-connected elastic solid in which the displacement is discontinuous across one or more barriers. However, this term has a different meaning in theories concerning the plasticity of matter. For a definition of this second meaning and for a discussion of the uses of the dislocations defined above in plastic theories, the reader should consult the references given at the end of Chapter 2 in the book, *The Inelastic Behavior of Engineering Materials and Structures*, A. M. Freudenthal (John Wiley and Sons, Inc., New York, 1950).

[1] A. E. H. Love, *Mathematical Theory of Elasticity* (Cambridge University Press, London 1927), 4th Edition, pp. 221–224.

[2] J. N. Goodier, "On the theory of dislocations and on application to the plane stress problem of a system of forces acting at a hole," 5th International Congress for Applied Mechanics (John Wiley & Sons, Inc., New York, 1938), pp. 129–133.

[3] V. Volterra, "Sur l'equilibre des corps elastiques multiplement connexes," Paris, Ann. Ec. norm. (Ser. 3), t 24, 1907, pp. 401–517.

[4] J. W. Gibbs, "On the equilibrium of hetrogeneous substances," *Collected Works of J. W. Gibbs* (Yale University Press, New Haven, 1948), Vol. 1, pp. 183–194.

using this assumption, stresses are derived (in which discontinuities may exist) that satisfy the differential equations of equilibrium and compatibility relations. Finally, after rejecting those systems that either are continuous of class $C^{(2)}$ throughout the cylinder or have discontinuities which do not meet the requirements of continuous traction on crossing Ω, the displacements are determined. Any remaining stress systems that have discontinuities in displacement across the barrier, constitute dislocations of the desired type.

The barrier is at $\theta=0$ in what follows. To secure complete freedom in choosing the angular position, corresponding dislocations are needed also for Ω at $\theta=\pi/2$. Since the procedures are identical for both positions, we shall indicate only the initial step when the barrier is in the second position. It will be recalled that, in the case of dislocations in classical theory, the position of the barrier is immaterial.

3. ANTI-PLANE STRAIN

In a state of plane strain, the stress components, σ_r, σ_θ, σ_z and $\tau_{r\theta}$ are functions of r and θ while τ_{rz} and $\tau_{\theta z}$ vanish. In a state of anti-plane strain, the converse is true. Then, the differential equations of equilibrium require the existence of a function $\varphi(r,\theta)$ such that

$$\tau_{rz}=r^{-1}\partial\varphi/\partial\theta, \quad \tau_{\theta z}=-\partial\varphi/\partial r; \tag{3.01}$$

and the compatibility relations require

$$(\partial^2/\partial r^2+r^{-1}\partial/\partial r+r^{-2}\partial^2/\partial\theta^2)\varphi\equiv\nabla^2\varphi=d_0\,(\text{const.}), \tag{3.02}$$

where φ is a continuous function of class $C^{(2)}$ in the simply-connected cylinder. For continuity of traction on Ω, we must have

$$\Delta\tau_{\theta z}\equiv\tau_{\theta z}\,|_{\theta=2\pi}-\tau_{\theta z}\,|_{\theta=0}=0. \tag{3.03}$$

Let us now assume that $\tau_{\theta z}$ is expressed by

$$-(\tau_{\theta z})_n=\xi_n(r)\theta\,\sin n\theta+\eta_n(r)\,\cos n\theta+\eta_0(r) \tag{3.04}$$

where n is an integer, $\xi_n(r)$, $\eta_n(r)$, and $\eta_0(r)$ are continuous functions of class $C^{(2)}$, and

$$0\leq\theta\leq 2\pi.$$

Equation (3.03) is satisfied by this assumption.

The stress function φ_n we seek must satisfy (3.02) and

$$\partial\varphi_n/\partial r=\xi_n(r)\theta\,\sin n\theta+\eta_n(r)\,\cos n\theta+\eta_0(r). \tag{3.05}$$

The function φ which satisfies these equations is

$$\varphi\equiv\sum_{n=1}^{\infty}\varphi_n=\sum_{n=1}^{\infty}a_nr^n(\theta\,\sin n\theta-\log r\,\cos n\theta)+\sum_{n=1}^{\infty}b_nr^{-n}(\theta\,\sin n\theta+\log r\,\cos n\theta)$$

$$+L(\theta^2-\log^2 r)+\sum_{n=1}^{\infty}(c_nr^n+d_nr^{-n})\,\cos n\theta+a_0+b_0\,\log r+c_0\theta+\frac{d_0r^2}{4}. \tag{3.06}$$

The terms on the last line of this equation give stresses that are continuous of class $C^{(2)}$ throughout the cylinder. Hence, they are of no interest to us, except for noting that the term $b_0\log r$ represents a dislocation of classical theory of order 3.[3] The stresses for the remaining terms are

$$\left.\begin{aligned}\tau_{rz}&=\sum_{n=1}^{\infty}a_nr^{n-1}[n\theta\,\cos n\theta+(n\,\log r+1)\,\sin n\theta]\\&\quad+\sum_{n=1}^{\infty}b_nr^{-n-1}[n\theta\,\cos n\theta\\&\quad-(n\,\log r-1)\,\sin n\theta]+L\theta r^{-1},\\\tau_{\theta z}&=-\sum_{n=1}^{\infty}a_nr^{n-1}[n\theta\,\sin n\theta-(n\,\log r+1)\,\cos n\theta]\\&\quad+\sum_{n=1}^{\infty}b_nr^{-n-1}[n\theta\,\sin n\theta\\&\quad+(n\,\log r-1)\,\cos n\theta]+Lr^{-1}\,\log r.\end{aligned}\right\} \tag{3.07}$$

The components of displacement u_r, u_θ, u_z are related to the strains e_{rz}, $e_{\theta z}$ and the stresses τ_{rz}, $\tau_{\theta z}$ by the following expressions

$$\left.\begin{aligned}2\tau_{rz}(1+\sigma)/E&=e_{rz}=\partial u_r/\partial z+\partial u_z/\partial r,\\2\tau_{\theta z}(1+\sigma)/E&=e_{\theta z}=r^{-1}\partial u_z/\partial\theta+\partial u_\theta/\partial z,\end{aligned}\right\} \tag{3.08}$$

where σ is Poisson's ratio and E is Young's modulus. The displacements corresponding to (3.07) are

$$\left.\begin{aligned}u_r&=0,\\u_\theta&=0,\\u_z&=2(1+\sigma)E^{-1}\{\sum_{n=1}^{\infty}a_nr^n(\theta\,\cos n\theta+\log r\,\sin n\theta)\\&\quad-\sum_{n=1}^{\infty}b_nr^{-n}(\theta\,\cos n\theta-\log r\,\sin n\theta)+L\theta\,\log r\},\end{aligned}\right\} \tag{3.09}$$

the terms which represent the displacement of the cylinder as a rigid body being omitted.

Inspection of (3.07) and (3.09) shows that τ_{rz} and u_z are discontinuous across Ω, and $\tau_{\theta z}$, u_r, and u_θ are not. Therefore, (3.07) represent dislocations of the desired

type. The discontinuities have the forms

$$\left.\begin{aligned}\Delta\tau_{rz}&\equiv\tau_{rz}\big|_{\theta=2\pi}-\tau_{rz}\big|_{\theta=0}\\&=2\pi\Big[\sum_{n=1}^{\infty}n(a_nr^{n-1}+b_nr^{-n-1})+Lr^{-1}\Big],\\\Delta u_z&\equiv u_z\big|_{\theta=2\pi}-u_z\big|_{\theta=0}=4\pi(1+\sigma)E^{-1}\\&\quad\times\Big[\sum_{n=1}^{\infty}(a_nr^n-b_nr^{-n})+L\log r\Big].\end{aligned}\right\}\tag{3.10}$$

We also note that the stress system given by $L(\theta^2-\log^2 r)$ has a resultant force acting on a cylindrical surface which encloses the z axis.

Equation (3.04) may be altered to place Ω at $\theta=\pi/2$ by assuming

$$-(\tau_{\theta z})_n=\xi_n(r)\theta\cos n\theta+\eta_n(r)\sin n\theta+\eta_0(r).\tag{3.11}$$

4. PLANE STRAIN

We assume that the displacements u_r and u_θ are functions of r and θ only while u_z is zero. The strain components e_{rz}, $e_{\theta z}$, e_{zz} vanish throughout the cylinder; and the formulas connecting the strains, displacements and stresses are

$$\left.\begin{aligned}e_{rr}&=\partial u_r/\partial r=(\sigma_r-\sigma'\sigma_\theta)/E',\\e_{r\theta}&=\partial u_\theta/\partial r-r^{-1}u_\theta+r^{-1}\partial u_r/\partial\theta\\&=2(1+\sigma')\tau_{r\theta}/E',\\e_{\theta\theta}&=r^{-1}\partial u_\theta/\partial\theta+r^{-1}u_r=(\sigma_\theta-\sigma'\sigma_r)/E',\end{aligned}\right\}\tag{4.01}$$

and

$$\sigma_z=\sigma'(\sigma_r+\sigma_\theta)\tag{4.02}$$

where $\sigma'=\sigma/1-\sigma$, $E'=E/1-\sigma^2$. Then the differential equations of equilibrium are the conditions for the existence of a function $\chi(r,\theta)$ such that

$$\sigma_r=\frac{\partial\chi}{r\partial r}+\frac{\partial^2\chi}{r^2\partial\theta^2},\quad\tau_{r\theta}=-\frac{\partial}{\partial r}\left(\frac{\partial\chi}{r\partial\theta}\right),\quad\sigma_\theta=\frac{\partial^2\chi}{\partial r^2},\tag{4.03}$$

where Airy's stress function χ is a continuous function of class $C^{(2)}$ in the simply-connected region. The compatibility relations require that χ be biharmonic:

$$\nabla^4\chi=0.\tag{4.04}$$

The requirement of continuity of traction on crossing Ω is expressed by

$$\left.\begin{aligned}\Delta\tau_{r\theta}&\equiv\tau_{r\theta}\big|_{\theta=2\pi}-\tau_{r\theta}\big|_{\theta=0}=0,\\\Delta\sigma_\theta&\equiv\sigma_\theta\big|_{\theta=2\pi}-\sigma_\theta\big|_{\theta=0}=0.\end{aligned}\right\}\tag{4.05}$$

We assume first that $\tau_{r\theta}$ and σ_θ are given by the real and imaginary parts of expressions of the type

$$(\tau_{r\theta})_n=f_n(r)e^{in\theta},\quad(\sigma_\theta)_n=g_n(r)e^{in\theta},\tag{4.06}$$

where $f_n(r)$ and $g_n(r)$ are continuous functions of class $C^{(2)}$ and n is an integer including zero. Clearly, these expressions satisfy (4.05).

We must now determine stresses $(\sigma_r)_n$, $(\tau_{r\theta})_n$, and $(\sigma_\theta)_n$ that satisfy the differential equations of equilibrium, the compatibility equations, and (4.06); in the process, we must not exclude those stress systems for which $(\sigma_r)_n$ is discontinuous. These requirements are fulfilled provided the stresses are derived from an Airy stress function χ_n which satisfies

$$-\frac{\partial}{\partial r}\left(\frac{\partial\chi_n}{r\partial\theta}\right)=f_n(r)e^{in\theta},\quad\frac{\partial^2\chi_n}{\partial r^2}=g_n(r)e^{in\theta},$$

$$\nabla^4\chi_n=0.\tag{4.07}$$

Upon integrating these equations, we obtain

$$\begin{aligned}\chi=\sum_{n=1}^{\infty}\chi_n&=A_0r^2+B_0r^2(\log r-1)+C_0\log r+D_0\theta\\&\quad+(A_1r+B_1r^{-1}+B\theta r+C_1r^3+D_1r\log r)e^{i\theta}\\&\quad+\sum_{n=2}^{\infty}(A_nr^n+B_nr^{-n}+C_nr^{n+2}+D_nr^{-n+2})e^{in\theta}\\&\quad+L(\theta^2-\log^2 r)re^{i\theta}.\end{aligned}\tag{4.08}$$

The stresses corresponding to the terms of the first three lines of (4.08) are continuous of class $C^{(2)}$ throughout the cylinder.[5] Therefore, the only function of immediate interest is

$$L(\theta^2-\log^2 r)re^{i\theta}.\tag{4.09}$$

We note in passing that the classical dislocations of orders 1, 2 and 6[3] are given by $Dr\log r\sin\theta$, $D'r\log r\cos\theta$, $B_0r^2\log r$.

The stresses for the real and imaginary parts of (4.09) are respectively

$$\left.\begin{aligned}\sigma_r&=2L_2r^{-1}[(1-\log r)\cos\theta-2\theta\sin\theta],\\\tau_{r\theta}&=-2L_2r^{-1}\log r\sin\theta,\\\sigma_\theta&=-2L_2r^{-1}(1+\log r)\cos\theta,\end{aligned}\right\}\tag{4.10}$$

and

$$\left.\begin{aligned}\sigma_r&=2L_1r^{-1}[(1-\log r)\sin\theta+2\theta\cos\theta],\\\tau_{r\theta}&=2L_1r^{-1}\log r\cos\theta,\\\sigma_\theta&=-2L_1r^{-1}(1+\log r)\sin\theta.\end{aligned}\right\}\tag{4.11}$$

Examination of these formulas reveals that in (4.10) all the stresses (and hence the strains) are continuous across Ω, but $\partial\sigma_r/\partial\theta$ is discontinuous; while in (4.11), σ_r and $\partial\sigma_r/\partial r$ are discontinuous across the same surface, the discontinuity in σ_r being

$$\Delta\sigma_r\equiv\sigma_r\big|_{\theta=2\pi}-\sigma_r\big|_{\theta=0}=8\pi L_1r^{-1}.\tag{4.12}$$

Both stress systems have a resultant force acting on a cylindrical surface enclosing the z axis.

The displacements corresponding to (4.10) and (4.11)

[5] These three lines constitute the stress function given by J. H. Michell in "On the direct determination of stress in an elastic solid," Proc. London Math. Soc. 31, 100–124 (1900).

are given by

$$\left.\begin{aligned} E'u_r &= L_2\{[2(1+\sigma')\log r-(1-\sigma')\log^2 r]\cos\theta \\ &\quad +[(1-\sigma')\theta^2-4\theta\log r]\sin\theta\}, \\ E'u_\theta &= L_2\{[(1-\sigma')\theta^2-4\sigma'\theta-2(1-\sigma') \\ &\quad -4\theta\log r]\cos\theta+(1-\sigma') \\ &\quad \times[\log^2 r-2(1+\theta)]\sin\theta\}, \end{aligned}\right\} \quad (4.13)$$

and

$$\left.\begin{aligned} E'u_r &= L_1\{[4\theta\log r-(1-\sigma')\theta^2]\cos\theta \\ &\quad +[2(1+\sigma')\log r-(1-\sigma')\log^2 r]\sin\theta\}, \\ E'u_\theta &= L_1\{(1-\sigma')[2(1+\theta)-\log^2 r]\cos\theta \\ &\quad +[(1-\sigma')\theta^2-4\sigma'\theta-2(1-\sigma') \\ &\quad -4\theta\log r]\sin\theta\}, \end{aligned}\right\} \quad (4.14)$$

where the rigid body terms have been omitted. The discontinuities in displacement across Ω are

$$\Delta u_r=\text{const.},\quad \Delta u_\theta=\text{const.}-8\pi L_2\log r/E', \quad (4.15)$$

$$\Delta u_r=\text{const.}+8\pi L_1\log r/E',\quad \Delta u_\theta=\text{const.}, \quad (4.16)$$

respectively, where $\Delta u_r\equiv u_r\big|_{\theta=2\pi}-u_r\big|_{\theta=0}$ and $\Delta u_\theta\equiv u_\theta\big|_{\theta=2\pi}-u_\theta\big|_{\theta=0}$. Since the displacements have discontinuities on crossing Ω involving $\log r$ the stress systems (4.10) and (4.11) represent dislocations of the general type.

When Ω is at $\theta=\pi/2$, the roles of the real and imaginary parts of (4.09) are interchanged.

The stress function (4.09) was obtained on the assumption that $\tau_{r\theta}$ and σ_θ have the forms given by (4.06); obviously this is not the only starting point. However, rather than assume other forms for these stress components and proceed as before, it is convenient at this point to make use of information already obtained. We recall that both $\chi_1=r\varphi_1\sin\theta+\varphi_2$ and $\chi_2=r\varphi_1\cos\theta+\varphi_2$, where φ_1 and φ_2 are harmonic functions, are solutions of $\nabla^4\chi=0$. For φ_1 and φ_2 we choose the function given by the first two lines of (3.06). Thus,

$$\begin{aligned} \chi_1 &= \sum_{n=1}^{\infty}[A_n r^{n+1}(\theta\sin n\theta-\log r\cos n\theta) \\ &\quad +B_n r^{-n+1}(\theta\sin n\theta+\log r\cos n\theta)]\sin\theta \\ &\quad +\sum_{n=1}^{\infty}[C_n r^n(\theta\sin n\theta-\log r\cos n\theta) \\ &\quad +D_n r^{-n}(\theta\sin n\theta+\log r\cos n\theta)] \\ &\quad +L_1(\theta^2-\log^2 r)r\sin\theta+G_1(\theta^2-\log^2 r) \end{aligned} \quad (4.17)$$

and

$$\begin{aligned} \chi_2 &= \sum_{n=1}^{\infty}[A_n' r^{n+1}(\theta\sin n\theta-\log r\cos n\theta) \\ &\quad +B_n' r^{-n+1}(\theta\sin n\theta+\log r\cos n\theta)]\cos\theta \\ &\quad +\sum_{n=1}^{\infty}[C_n' r^n(\theta\sin n\theta-\log r\cos n\theta) \\ &\quad +D_n' r^{-n}(\theta\sin n\theta+\log r\cos n\theta)] \\ &\quad +L_2(\theta^2-\log^2 r)r\cos\theta+G_2(\theta^2-\log^2 r). \end{aligned} \quad (4.18)$$

The requirement that the traction on Ω be continuous across this surface can be met by setting

$$C_n=D_n=G_1=0,\quad (n=1, 2, \cdots); \quad (4.19)$$

and

$$\left.\begin{aligned} C_n' &= -A_{n-1}'\frac{n-1}{n}, \quad (n=2, 3, \cdots), \\ D_n' &= -B_{n+1}\frac{n+1}{n}, \quad (n=1, 2, \cdots), \\ G_2 &= -B_1. \end{aligned}\right\} \quad (4.20)$$

With these equations, we find that the stresses corresponding to (4.17) and (4.18) are

$$\left.\begin{aligned} 2\sigma_r &= \sum_{n=1}^{\infty}A_n r^{n-1}\{-(2n-3)\sin(n-1)\theta+(2n+1)\sin(n+1)\theta-n(n-3)\theta\cos(n-1)\theta+n(n+1)\theta\cos(n+1)\theta \\ &\quad -\log r[-n(n-3)\sin(n-1)\theta+n(n+1)\sin(n+1)\theta]\}+\sum_{n=1}^{\infty}B_n r^{-n-1}\{-(2n-1)\sin(n-1)\theta \\ &\quad +(2n+3)\sin(n+1)\theta-n(n-1)\theta\cos(n-1)\theta+n(n+3)\theta\cos(n+1)\theta+\log r[n(n-1)\sin(n-1)\theta \\ &\quad -n(n+3)\sin(n+1)\theta]\}+4L_1 r^{-1}[(1-\log r)\sin\theta+2\theta\cos\theta], \\ 2\tau_{r\theta} &= \sum_{n=1}^{\infty}A_n r^{n-1}\{(2n-1)\cos(n-1)\theta-(2n+1)\cos(n+1)\theta-n(n-1)\theta\sin(n-1)\theta+n(n+1)\theta\sin(n+1)\theta \\ &\quad +\log r[n(n-1)\cos(n-1)\theta-n(n+1)\cos(n+1)\theta]\}+\sum_{n=1}^{\infty}B_n r^{-n-1}\{(2n-1)\cos(n-1)\theta \\ &\quad +(2n+1)\cos(n+1)\theta-n(n-1)\theta\sin(n-1)\theta+n(n+1)\theta\sin(n+1)\theta \\ &\quad +\log r[-n(n-1)\cos(n-1)\theta+n(n+1)\cos(n+1)\theta]\}+4L_1 r^{-1}(1+\log r)\sin\theta, \\ 2\sigma_\theta &= \sum_{n=1}^{\infty}A_n r^{n-1}\{(2n+1)[\sin(n-1)\theta-\sin(n+1)\theta]+n(n+1)\theta[\cos(n-1)\theta \\ &\quad -\cos(n+1)\theta]+n(n+1)\log r[\cos(n-1)\theta-\cos(n+1)\theta]\} \\ &\quad +\sum_{n=1}^{\infty}B_n r^{-n-1}\{(2n-1)[\sin(n-1)\theta-\sin(n+1)\theta]+n(n-1)\theta[\cos(n-1)\theta-\cos(n+1)\theta] \\ &\quad -n(n-1)\log r[\sin(n-1)\theta-\sin(n+1)\theta]\}-4L_1 r^{-1}(1+\log r)\sin\theta; \end{aligned}\right\} \quad (4.21)$$

and

$$
\left.\begin{aligned}
2\sigma_r=&\sum_{n=1}^{\infty}A_n'r^{n-1}\Big\{(2n-3)\cos(n-1)\theta-\frac{(n-1)(2n+1)}{n+1}\cos(n+1)\theta-n(n-3)\theta\sin(n-1)\theta\\
&+n(n-1)\theta\sin(n+1)\theta-\log r[n(n-3)\cos(n-1)\theta-n(n-1)\cos(n+1)\theta]\Big\}\\
&+\sum_{n=2}^{\infty}B_n'r^{-n-1}\Big\{-\frac{(n+1)(2n-1)}{n-1}\cos(n-1)\theta+(2n+3)\cos(n+1)\theta+n(n+1)\theta\sin(n-1)\theta\\
&-n(n+3)\theta\sin(n+1)\theta+\log r[n(n+1)\cos(n-1)\theta-n(n+3)\cos(n+1)\theta]\Big\}\\
&+B_1'r^{-2}[5\cos2\theta-1-4\theta\sin\theta+2\log r(1-2\cos2\theta)]+4L_2r^{-1}[\cos\theta-2\theta\sin\theta-\log r\cos\theta],\\
2\tau_{r\theta}=&-\sum_{n=1}^{\infty}A_n'r^{n-1}\Big\{(2n-1)\sin(n-1)\theta-\frac{(n-1)(2n+1)}{n+1}\sin(n+1)\theta+n(n-1)\theta[\cos(n-1)\theta-\cos(n+1)\theta]\\
&+n(n-1)\log r[\sin(n-1)\theta-\sin(n+1)\theta]\Big\}-\sum_{n=1}^{\infty}B_n'r^{-n-1}\Big\{\frac{(n+1)(2n-1)}{n-1}\sin(n-1)\theta\\
&-(2n+1)\sin(n+1)\theta+n(n+1)\theta[\cos(n-1)\theta-\cos(n+1)\theta]-n(n+1)\log r[\sin(n-1)\theta\\
&-\sin(n+1)\theta]\Big\}+B_1'r^{-2}[\sin2\theta-2\theta(1-\cos2\theta)+2(1-\log r)\sin2\theta]-4L_2r^{-1}\sin\theta,\\
2\sigma_\theta=&\sum_{n=1}^{\infty}A_n'r^{n-1}\Big\{-(2n+1)\cos(n-1)\theta-\frac{(n-1)(2n+1)}{n+1}\cos(n+1)\theta+n(n+1)\theta\sin(n-1)\theta\\
&-n(n-1)\theta\sin(n+1)\theta-\log r[n(n+1)\cos(n-1)\theta-n(n-1)\cos(n+1)\theta]\Big\}\\
&+\sum_{n=2}^{\infty}B_n'r^{-n-1}\Big\{\frac{(n+1)(2n-1)}{n-1}\cos(n-1)\theta-(2n-1)\cos(n+1)\theta-n(n+1)\theta\sin(n-1)\theta\\
&+n(n-1)\theta\sin(n+1)\theta-\log r[n(n+1)\cos(n-1)\theta-n(n-1)\cos(n+1)\theta]\Big\}\\
&+B_1'r^{-2}[1-\cos2\theta-2\log r]-4L_2r^{-1}(1+\log r)\cos\theta,
\end{aligned}\right\}\qquad(4.22)
$$

respectively. By means of (4.01), the displacements can be found for these stress systems. The discontinuities in the stresses and the displacements across Ω are

$$
\left.\begin{aligned}
\Delta\sigma_r&=4\pi[\sum_{n=1}^{\infty}n(A_nr^{n-1}+B_nr^{-n-1})+2L_1r^{-1}],\\
E'\Delta u_r&=4\pi[\sum_{n=1}^{\infty}(A_nr^n-B_nr^{-n})+2L_1\log r],\\
\Delta\sigma_\theta&=\Delta\tau_{r\theta}=\Delta u_\theta=0;
\end{aligned}\right\}\qquad(4.23)
$$

and

$$
\left.\begin{aligned}
E'\Delta u_\theta&=4\pi[-\sum_{n=1}^{\infty}A_n'r^n+\sum_{n=2}^{\infty}B_n'r^{-n}\\
&\qquad+B_1'r^{-1}+2L_2\log r],\\
\Delta u_r&=\Delta\sigma_r=\Delta\tau_{r\theta}=\Delta\sigma_\theta=0.
\end{aligned}\right\}\qquad(4.24)
$$

Equations (4.21) and (4.22) thus represent general dislocations.

As before, χ_1 and χ_2 may be suitably altered to place the barrier at $\theta=\pi/2$.

5. DISCUSSION

After the first draft of this paper was prepared, Mann[6] published an article in which many of the stress functions obtained above were given. In addition, she also solved several boundary value problems (of interest in connection with slip theories of plasticity) for states of plane and anti-plane strain in a hollow cylinder, and she indicated a general procedure for dealing with such problems. There is no need then for additional discussion of these aspects of the solutions.

It was not noticed in reference 6, however, that it is possible to divide the dislocation in the plane strain problem into two distinct classes, and those stress functions involving $(\theta^2-\log^2 r)$, i.e.

$$L_2(\theta^2-\log^2 r)r\cos\theta,\quad L_1(\theta^2-\log^2 r)r\sin\theta,\qquad(4.09a)$$

$$L(\theta^2-\log^2 r)\qquad(3.06a)$$

were not found. As these two points are of some importance, we shall comment on them and then conclude with a remark on the requirements for uniqueness of solution of boundary value problems involving a sta-

[6] E. H. Mann, "An elastic theory of dislocations," Proc. Royal Soc. **A199**, No. 1058, 376-394 (1949).

tionary barrier across which the strains or their derivatives are discontinuous.

In a course of the proof of Weingarten's theorem, we find by means of Cesaro's theorem[7] that for the plane strain problem

$$\left.\begin{aligned}\Delta u_r^{(1)} &= \Delta u_r^{(0)} + \int_{r_0}^{r_1} \Delta e_{rr}\,dr,\\ \Delta u_\theta^{(1)} &= \Delta u_\theta^{(0)} + (r_1 - r_0)\Delta\omega_z^{(0)} + \int_{r_0}^{r_1} \{\Delta e_{r\theta}/2\\ &\quad - (r_1 - r)[\Delta\partial e_{r\theta}/2\partial r - \Delta(\partial e_{rr}/r\partial\theta)]\}\,dr\end{aligned}\right\} \tag{5.01}$$

where it has been assumed that the strains are continuous of class $C^{(2)}$ and satisfy the compatibility relations in the simply-connected cylinder, r_0 and r_1 are any two points on Ω, and ω_z is the z component of the rotation. As the traction on Ω must be continuous across this surface,

$$\Delta e_{r\theta} = \Delta(\partial e_{r\theta}/\partial r) = 0, \tag{5.02}$$

for an isotropic solid. Hence, (5.01) becomes

$$\left.\begin{aligned}\Delta u_r^{(1)} &= \Delta u_r^{(0)} + \int_{r_0}^{r_1} \Delta e_{rr}\,dr,\\ \Delta u_\theta^{(1)} &= \Delta u_\theta^{(0)} + (r_1 - r_0)\Delta\omega_z^{(0)}\\ &\quad + \int_{r_0}^{r_1} (r_1 - r)\Delta(\partial e_{rr}/r\partial\theta)\,dr.\end{aligned}\right\} \tag{5.03}$$

In the classical dislocation theory, the strains are continuous of class $C^{(2)}$ throughout the body. The integrals on the right-hand side of (5.03) therefore vanish, and the displacement discontinuity has the form predicted by Weingarten's theorem.

Two possibilities arise in the case of dislocations of the general type. First, if we assume that the strains (and hence the stresses) are continuous across Ω, $\Delta e_{rr} = 0$, but discontinuities in displacement can still exist provided that $\Delta(\partial e_{rr}/\partial\theta) = 0$; in this case

$$\begin{aligned}\Delta u_r^{(1)} &= \Delta u_r^{(0)},\\ \Delta u_\theta^{(1)} &= \Delta u_\theta^{(0)} + (r_1 - r_0)\Delta\omega_z^{(0)}\\ &\quad + \int_{r_0}^{r_1} (r_1 - r)\Delta(\partial e_{rr}/r\partial\theta)\,dr.\end{aligned} \tag{5.04}$$

Second, if we assume that $\Delta e_{rr} \neq 0$ and $\Delta(\partial e_{rr}/\partial\theta) = 0$, the displacement discontinuity across Ω is

$$\begin{aligned}\Delta u_r^{(1)} &= \Delta u_r^{(0)} + \int_{r_0}^{r_1} \Delta e_{rr}\,dr,\\ \Delta u_\theta^{(1)} &= \Delta u_\theta^{(0)} + (r_1 - r_0)\Delta\omega_z^{(0)}.\end{aligned} \tag{5.05}$$

Thus, there is a division of the general dislocations belonging to the plane strain problem considered in this paper into two classes. In the class given by (5.04), the strains and u_r are continuous across Ω and u_θ is discontinuous; and Δe_{rr}, $\Delta e_{\theta\theta}$, and Δu_r are not zero while $\Delta e_{r\theta}$ and Δu_θ are zero in the class expressed by (5.05), assuming $\Delta u_r^{(0)} = \Delta u_\theta^{(0)} = \Delta\omega_z^{(0)} = 0$, of course.

The dislocations belonging to the class represented by (5.05), i.e. (4.22), reveal an omission in a proof of Weingarten's theorem given in reference 2. In the course of this proof, it is stated that if the strains are continuous across a barrier, which is a surface of discontinuity in displacement, the only possible displacement discontinuity is one that might take place in a rigid body. The stresses, and hence the strains, are continuous across Ω in the dislocations of (4.22), but the displacement discontinuity cannot be represented by the displacement of a rigid body. Hence, we must assume that the strains, together with at least their first derivatives, are continuous across a barrier in order to establish the theorem.

Equations (4.21) represent all the dislocations of the two classes needed to represent specified discontinuities in u_θ and u_r, respectively. For, by assigning appropriate values to the coefficients in these equations, it is seen, from (4.23) and (4.24), that we can express any given discontinuity in u_θ and u_r which is an analytic function of r every where except for possible singularities at $r = 0$ and $r = \infty$. The importance of having the terms of the form (4.09a) is that they are required in order to provide the logrithmic singularity in displacement discontinuity at the axis of the cylinder.

When the solid is not isotropic, the division into two classes of the dislocations in this plane strain problem is not usually possible.

In the anti-plane strain problem considered, there is only one class of general dislocations. The second of equations (3.10) shows that (3.07) provides all dislocations required to represent any specified discontinuity in u_z. The term (3.06a) provides the logrithmic singularity in Δu_z at $r = 0$.

When general dislocations are admitted, the theorems on uniqueness of solution require modification. In addition to the usual quantities, we must now specify at each point on Ω either the traction or the displacement discontinuity or an appropriate combination of the components of each. With the dislocations of classical theory, we recall that we only need specify either the resultant force and couple acting on the barrier or the six constants of the displacement discontinuity or a suitable combination of these quantities. The location and shape of the barrier must also be given when dealing with general dislocations, whereas this information does not have to be supplied in classical theory.

The author wishes to acknowledge that the stress functions given in Eqs. (3.06a) and (4.09a) were disclosed to him by R. D. Mindlin. The author also wishes to thank Prof. Mindlin for helpful discussions during the course of this study.

[7] E. Cesaro, see references 1 and 3.

A Microwave Study of the High Pressure Arc

J. D. Cobine, E. P. Cleary,* and W. C. Gray†
General Electric Research Laboratory, Schenectady, New York
(Received April 26, 1950)

The impedance of an atmospheric pressure d.c. arc was measured at 1000 mc/sec. by means of a coaxial line and standing wave detector. The reactance and resistance of the arc, an essentially lumped load at the end of the line, increase with length of arc. The resistance decreases with increasing current and is approximately the same as the d.c. "resistance." The reactance is capacitive and nearly independent of current. Air, argon, and helium were studied at currents from 1–4 amp. d.c. arc current.

INTRODUCTION

THE following research was initiated in order to determine the possibilities of using microwave techniques to investigate high pressure heavy-current arcs. Measurements made with microwaves would be expected to indicate the actual electron conditions, since only electrons can respond to such high frequencies. The d.c. arc was studied as a lumped load at the end of a coaxial line. An r-f generator and measuring equipment with a 10-cm wave-length was used to study the discharge. The use of cavities and a 3-cm wave-length equipment was found to be unsatisfactory because of the high value of electron density in the high pressure arc.

APPARATUS

The arc chamber, shown schematically in Fig. 1, was arranged so that the arc burned as a section of the inner conductor of the coaxial line. Because of the necessity for water-cooled tungsten electrodes and in order to confine the position of the arc foot-points, the arc was placed $\frac{1}{2}$ wave-length from the shorted end of the line to produce the effect of a short circuit at one electrode surface. It was believed that by keeping the arc length less than 0.1λ the condition of a pure lumped load would be rather closely approached. The shorted end assembly permits changes in the arc length. The arc chamber was mounted vertically and a stabilizing flow of gas was provided by means of three gas inlets set to give a spiral flow of gas around the arc column and exhaust through outlet ports at the top of the device. The fixed electrode assembly had a quarter-wave choke stub to permit direct connection to the d.c. and to admit cooling water. A tuned choke was used with a tapered adapter to connect by a flexible conductor to the microwave generator.

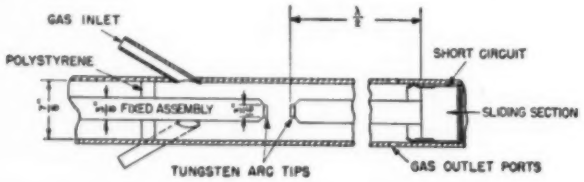

FIG. 1. Arrangement of parts in arc section.

A portion of the outer conductor below the arc chamber consisted of a slotted section for standing wave measurements.

The experimental arrangement is shown in Fig. 2. The microwave generator was an AN/APT5 Radar Set (Carpet Jamming Transmitter) set at 30 cm wave-length, unmodulated, and at minimum power output (~0.1 watt). The attenuator was a length of lossy line having an attenuation at 1000 mc/sec. of 11 db. The arc was maintained by the laboratory d.c. supply with a ballast inductance L and a current controlling resistance R in series. The standing wave measurements were made by means of a crystal detector and microammeter with the slotted line section.

EXPERIMENTAL RESULTS

The impedance, reactance, and resistance of the arc at a 30 cm wave-length were determined by calculation from standing wave data in the usual way with due regard for the reactance of the gap without the arc. It was found that each of these quantities increase with arc length and the resistance decreases with increasing d.c. current in the range 1 to 4 amperes. The arc reactance was found to be capacitive.

Figure 3 shows the resistance of arcs in air for currents from 1 to 4 amperes. A d.c. "resistance," obtained by dividing the d.c. arc voltage by the current, is included. This resistance, except for the longer lengths, is seen to be of the same order of magnitude as the r-f value and has the same trend. It is probable that the rapid decrease in R at short lengths (less than 0.25 cm) is due to the constriction that occurs in the column near electrodes and to the presence of some metal vapor in that

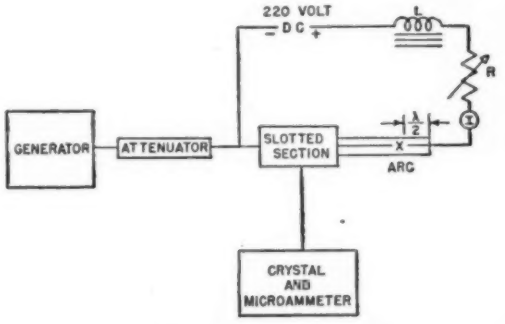

FIG. 2. Diagram of apparatus.

* Now at Electronics Laboratory, Electronics Department, General Electric Company, Syracuse, New York.

† Now at the Knolls Atomic Power Laboratory, General Electric Company, Schenectady, New York.

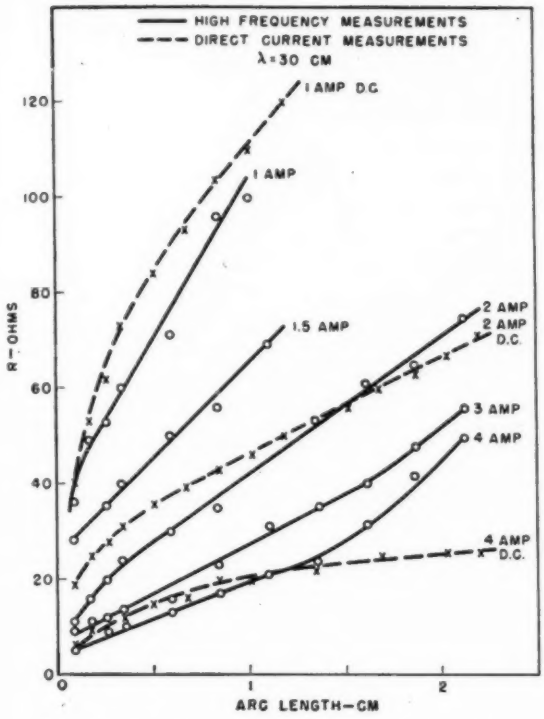

FIG. 3. Resistance characteristics of d.c. arcs in air.

legion. The upward trend of the r-f resistance of the ronger gap lengths may be due to the presence of hot ionized gas flowing along the half-wave section of the upper electrode. This would introduce losses in that section, increasing the measured value. The fact that this trend is most pronounced at the higher current is in agreement with this concept.

The arc consists of three zones of markedly different characteristics. At the cathode is a positive ion space-charge zone having a d.c. voltage drop of the order of the ionization potential of the gas. At the anode is an electron space charge zone that may have a voltage drop as high as the ionization potential of the gas. Both of these space-charge zones are of the order of a few mean free paths ($\sim 10^{-4}-10^{-5}$ cm) thick and the current density[1] at each is of the order of 50,000 amp./cm^2. Between these small zones is the column, which is of essentially uniform current density, except for constrictions near the ends where space charge zones develop. The current density for the low current arc column is approximately uniform along the column and is of the order of 10 amp./cm^2. The column gradient is uniform and relatively low. It is evident that a "resistance" obtained by dividing the total arc drop by the current might be considerably different from that measured by the r-f. The entire r-f resistance might be assumed to reside in the column. In this case, the d.c. column resistance is obtained by subtracting a reasonable maximum value of anode plus cathode voltage drops (15+15) from the total voltage and dividing by

[1] J. D. Cobine and C. J. Gallagher, Phys. Rev. **74**, 1524 (1948).

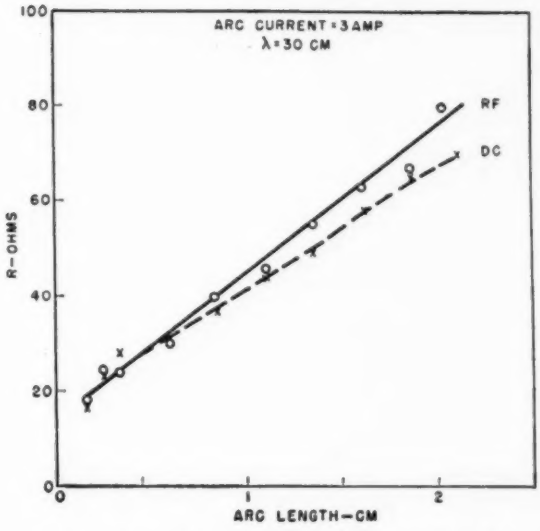

FIG. 4. Resistance characteristics of d.c. arcs in helium.

the current. The resulting resistance curves are not as good in absolute value as those shown in Fig. 3, except for 2 amperes where r-f and d.c. values are very nearly the same throughout most of the range in length studies. However, the slopes of the d.c. resistance *vs.* length curves thus obtained were nearly the same as for the high frequency curves over most of the range. The greatest error here may be in assuming the anode drop to have its maximum value; actually, it may have been only a few volts. Few really reliable values of anode drop have been measured for the high pressure arc.

The r-f resistances of arcs in helium and argon are shown in Figs. 4 and 5. The helium characteristic does not curve upwards at the longer gaps as does that for

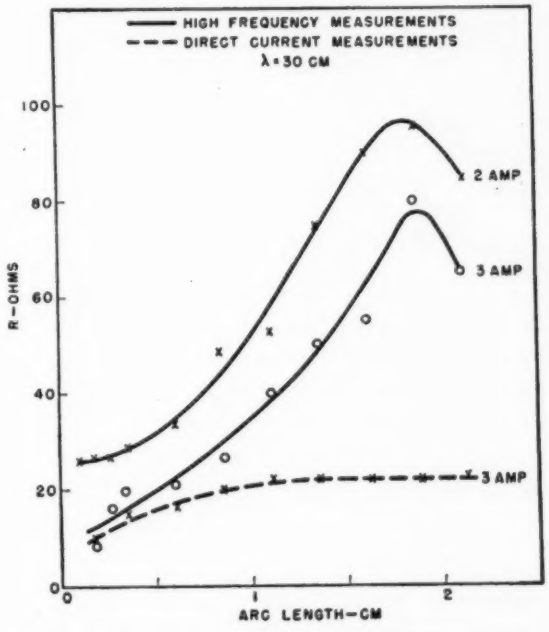

FIG. 5. Resistance characteristics of d.c. arcs in argon.

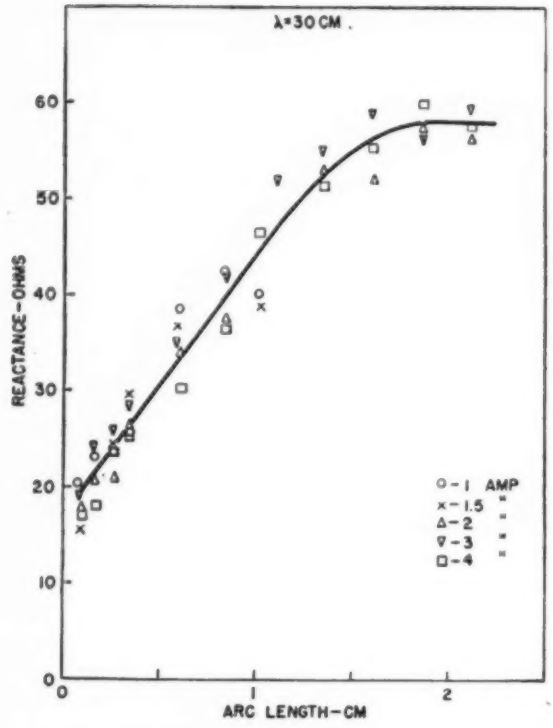

FIG. 6. High frequency reactance of d.c. arcs in air.

air. This might be the result of a lower temperature column of different size and more rapidly cooled residual gas than was true for air. The argon characteristic exhibits a definite maximum that was present in all the runs taken. There is no obvious explanation for this nor for the marked departure of the d.c. resistance from the r-f at the longer gap lengths.

The effects of arc current and gap length on the reactance of the d.c. arc in air are shown in Fig. 6. The reactance is capacitive. It is evident that arc current has very little effect on the reactance measured. Probably the principal effect in the straight line portion is due to the increase in column diameter as current is increased. There seems to be a systematic trend at the longer gap length for each current where the data indicate a departure from linearity; in fact, there may be a maximum near the end for each current. This departure occurs at increasingly greater gap lengths as the current is increased. There is no obvious explanation for this at present. The reactances for helium, air, and argon are compared in Fig. 7 for a 3-ampere arc. The general characteristics are the same for each gas. A definite maximum appears in the curves for helium and argon.

COMPARISON WITH THEORY

The fact that an atmospheric pressure arc in the low current range studied exhibits a capacitive reactance at high frequencies may be shown to be in agreement with the analysis of discharge admittance made by Everhart and Brown.[2] According to their analysis, a high conductivity discharge will have a capacitive reactance when the ratio

$$\gamma=\omega/\nu_c\leqq 0.25,$$

where ω is the angular frequency of the r-f and ν_c is the collision frequency of the electrons. The collision frequency is the ratio of the average velocity of the electrons to their mean free path. The average velocity may be taken as the average thermal velocity $\bar{c}$ of the electrons. If the arc temperature is assumed to be 6000°K, the value of $\bar{c}$ is 4.8×10^7 cm/sec. The probability of collision for electrons[3] of about this energy is 30 for N_2 and 20 for O_2. The gases in a high pressure arc column have a rather high degree of dissociation so that Brode's data are not strictly applicable. However, there seem to be no data for the probability of collision in atomic nitrogen or oxygen. Using the value for N_2 and correcting to 760 mm and 6000°K gives an electron mean free path $L_e=9.65\times10^{-4}$. Then

$$\nu_c=\bar{c}/L_e=4.8\times10^7/9.65\times10^{-4}=4.97\times10^{10}.$$

For an r-f frequency of 10^9 c.p.s. this gives

$$\gamma=2\pi10^9/4.97\times10^{10}=0.126.$$

Thus the conditions for a capacitive reactance are satisfied, provided the discharge is of high conductivity. The high frequency conductivity of the plasma can be calculated from the analysis of Margenau[4] as follows. The quantity $x_1(=m(\omega L_e)^2/2kT$, Reference 4, Eq. 20)

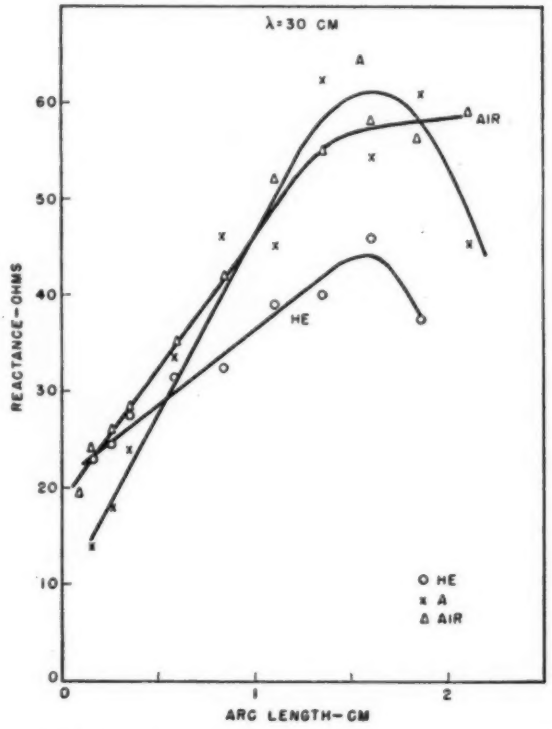

FIG. 7. High frequency reactance of 3-ampere d.c. arcs in helium, argon, and air.

[2] E. Everhart and S. C. Brown, Phys. Rev. **76**, 839 (1949).

[3] R. B. Brode, Rev. Mod. Phys. **5**, 257 (1933).

[4] H. Margenau, Phys. Rev. **69**, 508 (1946).

has the value 2.02×10^{-2} when the above value of L_e is used and the electrons are assumed in thermal equilibrium at 6000°K. Thus the limiting values of $K_2=1$ and $K_1=\frac{1}{2}\pi^{\frac{1}{2}}$ may be used. The complex conductivity then becomes

$$\sigma=(ne^2/\omega m)[(4x_1^{\frac{1}{2}}/3\pi^{\frac{1}{2}})-j(2x_1/3)].$$

This may be compared with the free space susceptance by dividing by $\omega\epsilon_0$. Substituting the numerical values gives

$$\sigma/\omega\epsilon_0=8.62\times10^{-12}n-j1.09\times10^{-12}n.$$

If n is assumed to be of the order of 10^{14} for the high pressure arc[5]

$$\sigma/\omega\epsilon_0=8.62\times10^{2}-j1.09\times10^{2}.$$

Therefore the value of the Everhart and Brown constant $\eta\ (=|\sigma_{c0}|/\omega\epsilon_0)$ is of the order of 1000 and the discharge lies in the capacitive zone of their Fig. 2. Thus, the arc appears to be an example of a discharge having a positive susceptance, although the imaginary part of the complex conductivity is negative. Similar conditions were found at lower pressures by Everhart and Brown.[2] Their theory seems to agree with the observed results even though it was derived for a sinusoidal distribution of electrons along the arc, whereas in the arc the distribution is essentially uniform. A considerable discrepancy exists between the observed and theoretical values of conductivity which is not understood.

[5] C. G. Suits, Physics **6**, 190, 315 (1935).

ACKNOWLEDGMENTS

Mr. R. H. Johnston took much of the data included in this paper. The coaxial line approach was suggested by Dr. M. D. Fiske of this Laboratory. Helpful suggestions were made by Professor Sanborn C. Brown of M.I.T. and by R. A. Dehn and Dr. C. J. Gallagher of this Laboratory.

A Relationship between Resistance and Temperature of Thermistors

G. Bosson, F. Gutmann, and L. M. Simmons
The New South Wales University of Technology, Sydney, Australia

(Received May 22, 1950)

The equation $\log R=A+B/(T+\theta)$ for the resistance R of a thermistor at T°K is proposed. Least square analyses of the most precise resistance-temperature data available for three different thermistor materials show that the equation is a considerable improvement over its predecessors; the standard relative errors of fit are 0.4 percent, 0.17 percent, and 0.91 percent.

THE $1/T$ law for thermistors

$$\log R=A+B/T \qquad (1)$$

derived from consideration of the free energy of an electron gas,[1] is known to be only approximate, since plots of $\log R$ *versus* $1/T$ yield bowed lines. By assuming that the slopes of these plots increase linearly with temperature, Becker, Green, and Pearson[2] proposed the following improved relationship, to which we shall refer as the B.G.P. law:

$$\log R=\log A-C\log T+B/2.303T. \qquad (2)$$

We have carried out a least square analysis of this law, using data kindly supplied by Bell Telephone Laboratories relating to the Western Electric Thermistor Material No. 1, the precision being: temperatures ±0.02°K, resistances ±0.02 percent. The results, shown in Table I, indicate clearly that considerable deviations occur between the resistances calculated from the B.G.P. law (R_b) and those observed (R_0).

TABLE I. Comparison between the goodness of fit of the B.G.P. and proposed laws according to data for Western Electric Thermistor No. 4756-12 (No. 1 Material).

		B.G.P. law		Proposed law	
Absolute temperature, °K	Observed resistance r_0 megohms	Residuals r_b-r_0 megohms	Percentage discrepancy $100(r_b-r_0)/r_0$	Residuals r_e-r_0 megohms	Percentage discrepancy $100(r_e-r_0)/r_0$
204.71	10.5587	+1.755	+16.6	+0.0646	+0.61
209.17	7.3683	+0.9516	+12.9	+0.0778	+1.06
216.95	4.1301	+0.2344	+ 5.68	−0.0076	−0.18
224.16	2.4654	+0.0330	+ 1.34	−0.0089	−0.36
232.54	1.3988	−0.0341	− 2.44	−0.0072	−0.51
240.05	0.86497	−0.04223	− 4.88	−0.00485	−0.56
247.74	0.54051	−0.03459	− 6.40	−0.00151	−0.28
257.18	0.31504	−0.02521	− 8.00	−0.00140	−0.44
266.48	0.19043	−0.01640	− 8.61	−0.00051	−0.27
276.34	0.11521	−0.00999	− 8.67	−0.00006	−0.05
286.27	0.071585	−0.005931	− 8.29	+0.000087	+0.12
296.35	0.045383	−0.003365	− 7.41	+0.000167	+0.37
308.54	0.027163	−0.001695	− 6.24	+0.000083	+0.31
320.24	0.017104	−0.000778	− 4.55	+0.000075	+0.44
331.57	0.011289	−0.000350	− 3.10	+0.000004	+0.04
344.07	0.0072974	−0.0000463	− 0.63	+0.0000142	+0.19
357.16	0.0047611	+0.0001019	+ 2.14	+0.0000120	+0.25
369.36	0.0032825	+0.0001552	+ 4.73	+0.0000034	+0.10
382.29	0.0022638	+0.0001750	+ 7.73	0.0000000	0.00
394.74	0.0016157	+0.0001745	+10.8	−0.0000015	−0.09
407.17	0.0011776	+0.0001662	+14.1	−0.0000044	−0.37

Standard relative error of fit:

$$\left(\frac{\sum(\overline{r_b-r_0}/r_0)^2}{21}\right)^{\frac{1}{2}}=0.0804;\quad \left(\frac{\sum(\overline{r_e-r_0}/r_0)^2}{21}\right)^{\frac{1}{2}}=0.00395.$$

r_b = resistance calculated from the B.G.P. law.
r_e = resistance calculated from the proposed law.

[1] N. F. Mott and R. W. Gurney, *Electronic Processes in Ionic Crystals* (Oxford University Press, London, 1948), second edition, p. 157.
[2] Becker, Green, and Pearson, Elec. Eng. Trans. **65**, 713 (1946).

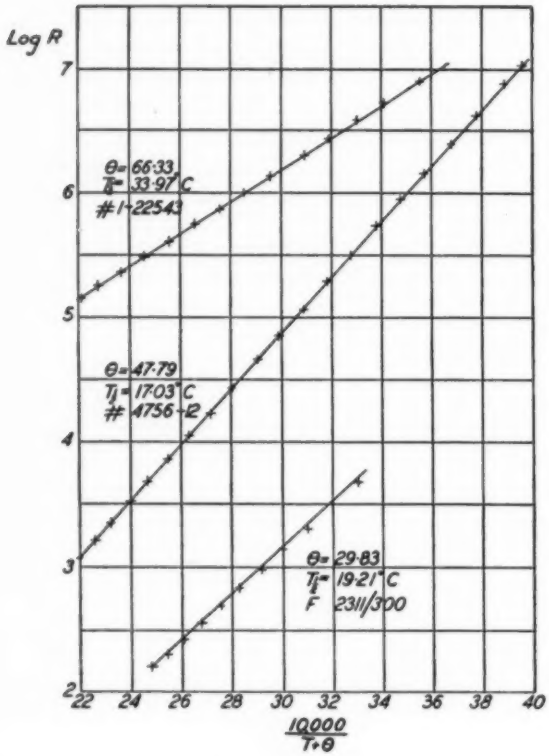

FIG. 1. Plots of log$R$ *versus* $10^4/(T+\theta)$ for three different thermistor materials.

The following empirical law is now proposed:

$$\log R = A + \frac{B}{T+\theta}. \qquad (3)$$

It indicates a linear relationship between log$R$ and $1/(T+\theta)$, and this is shown in Fig. 1 to hold for the three thermistor materials investigated, viz. Western Electric Material No. 1, Western Electric Zinc Ferrite No. 1-22543, and Standard Telephones and Cables, Ltd. Thermistor Type F2311/300. The values for θ were obtained by least square analyses of data supplied by Bell Telephone Laboratories, N. J., and Standard Telephones and Cables Ltd., London. These results are shown in Table II, which further demonstrates that Eq. (3) permits the resistance of a thermistor to be predicted from its temperature sufficiently closely for all but the most precise work.

TABLE II. The goodness of fit of the proposed law with data for three different thermistor materials.

°K	Resistance observed for thermistor No. 4756-12 megohms	No. 1-22543 megohms	*F*2311/300 ohms	Residuals in ohms	Percentage discrepancy
204.71	10.5587			+64600	+0.61
209.17	7.3683			+77800	+1.06
215.32		7.8491		+ 1700	+0.02
216.95	4.1301			− 7600	−0.18
224.16	2.4654			− 8900	−0.36
226.80		5.1994		−23000	−0.43
232.54	1.3988			− 7200	−0.51
236.29		3.7655		− 7800	−0.21
240.05	0.86497			− 4850	−0.56
247.21		2.6609		+ 1200	+0.05
247.74	0.54051			− 1510	−0.28
256.80		2.0044		+ 600	+0.03
257.18	0.31505			− 1400	+0.44
266.48	0.19043			− 510	−0.27
271.16		1.3499		+ 1700	+0.13
273.16			4733	+ 38	+0.80
276.34	0.11521			− 60	−0.05
284.04		0.97377		+ 1600	+0.17
286.27	0.071585			+ 87	+0.12
293.16			2003	− 5	−0.25
296.01		0.73361		+ 1800	+0.25
296.35	0.045383			+ 167	+0.37
303.16			1369	+ 5	+0.37
308.54	0.027163			+ 83	+0.31
309.47		0.54624		+ 740	+0.14
313.16			946	− 2	−0.21
320.24	0.017104			+ 75	+0.44
323.16			672	0	0.00
324.72		0.40050		+ 370	+0.09
331.57	0.011289			+ 4	+0.04
333.16			485.3	− 0.8	−0.16
339.85		0.30144		− 60	−0.02
343.16			354.7	− 2.9	−0.82
344.07	0.0072974			+ 14.2	+0.19
353.16			267.3	0	0.00
355.14		0.23082		− 180	−0.08
357.16	0.0047611			+ 12	+0.25
363.16			201.5	− 1.3	−0.65
369.36	0.0032825			+ 3.4	+0.10
371.98		0.17580		− 2600	−0.15
373.16			160.0	+ 4.0	+2.50
382.29	0.0022638			0	0.00
386.29		0.14156		− 120	−0.08
394.74	0.0016157			− 1.5	−0.09
407.17	0.0011776			− 4.4	−0.37
Standard relative error of fit:	0.00395	0.00170	0.00908		

TABLE III. Thermistor constants.

Thermistor	A	B°K	θ°K	$T_{\frac{1}{2}}$
S.T.C. F2311/300	−2.28697	1805.41	29.83	19.21
Zinc Ferrite 1-22543	+2.27698	1300.64	66.33	33.97
No. 1 Material 4756-12	−1.86554	2245.18	47.79	17.03

Table III shows the values of the constants A, B and θ for the three thermistors discussed, together with their half-temperatures at $T_{\frac{1}{2}}$ 300°K.

A High Intensity Short Duration Spark Light Source*,**

J. A. Fitzpatrick, J. C. Hubbard, and W. J. Thaler
Department of Physics, Catholic University of America, Washington, D. C.
(Received May 25, 1950)

The spark described here provides a high intensity light source, whose effective duration approaches 10^{-7} second. The light intensity is nine hundred times greater than that obtained using RG8U cable cut for 10^{-7} second duration discharge. The cable described here is coaxial with silver conductors fired on the dielectric, a compound of barium titanate. The gain in light intensity is apparently due to both the higher capacity of the barium titanate cable and its very low characteristic impedance.

A COAXIAL cable compounded of barium titanate provides a spark light of both high intensity and short duration. This is accomplished by applying the method employed by Beams *et al.*[1] to a cable of low characteristic impedance. Since the velocity of propagation of the discharge wave is low, a short length of cable, 16.5 cm is used. The cable is cylindrical, the outside conducting surface having a diameter of five centimeters and the inside a diameter of two and one-half centimeters, with the dielectric forming the body of the cable.

The discharge producing the light is confined to a small hole made with a number 80 drill, 0.013-inch diameter and 4-mm long drilled in a piece of unfired soapstone, Fig. 1. For some applications a triggering gap is fitted in series with the light producing gap to discharge the cable at a specific time.

The dielectric constant of the material forming the cable has been measured at frequencies up to 250 megacycles. A General Radio Impedance Bridge was used for the low frequency measurement at 1000 c.p.s. For the higher frequencies resort was had to using the cable as a shorted and open end transmission line, and observing the resonance frequencies indicated on a grid dip meter connected as a generator to the sending end of the line. For a short circuited line the impedance presented to the generator is zero for an infinitely short line, becoming an increasing inductive reactance as the line is lengthened until the impedance becomes infinitely great for a value of $2\pi l/\lambda = \pi/2$ when l, the length of the cable, equals one quarter wave-length in the dielectric. Since the length l of the cable was fixed at 16.5 cm, the frequency of the generator was varied between a range of 2 to 250 megacycles and the frequencies of resonance or maximum impedance observed as the patterns of standing waves on the line were established. Knowing the frequency and wave-length, the velocity of propagation was determined as well as the dielectric constant. The values shown in Table I were obtained for both an open and short circuited line.

The characteristic impedance of the line is a function of the dielectric constant. Since a cable will discharge in a square wave of current if terminated in its characteristic impedance, it is desirable to make such a termination. We see from Table I that it is impossible to assign a fixed value to the characteristic impedance which will satisfy all the frequencies present in the discharge. The terminal impedance corresponding to the lowest value of the dielectric constant is 1.5 ohms while the value for the highest is 1.2 ohms. The writers have inserted various resistors of between one and two ohms in series with the gap but were unable to observe any effects on shadowgraphs made of progressive ultrasonic waves such as shown in Figs. 2–4, even when terminating resistors were eliminated. It is believed that the resistance of the fittings of the spark head as well as some resistance presented by the spark gap are close enough to the characteristic impedance of the cable to allow the omission of a resistor in series with the gap.

The duration of light produced by the barium titanate cable has been compared with a section RG8U cable cut for 10^{-7} second discharge, approximately 9½-meters long. Both discharges were made in confined gaps. Figure 5 shows a cathode ray oscilloscope trace and a five megacycle time marking signal superimposed on the discharge. These traces were made with a photo-

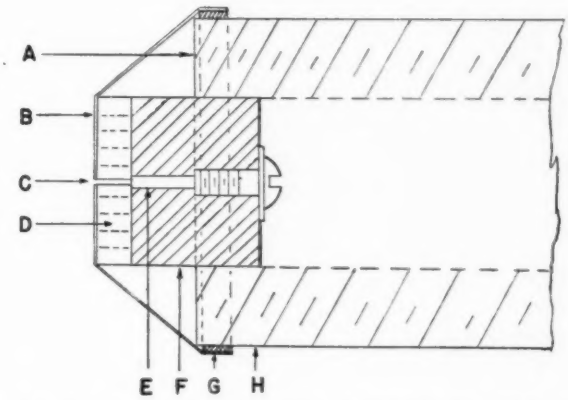

Fig. 1. Detail of light source. *A*, cylinder of barium titanate dielectric; *C*, gap space, hole of 0.013-inch diameter in unfired soapstone cylinder, *D*, between stainless steel electrode, *B*, and tungsten electrode, *E*, fitted to an adjusting screw; *F*, polystyrene support; *G*, clamp to silver outer conductor, *H*, of the cable.

* Work supported by ONR.
** Presented at A.P.S. meeting, Washington, D. C., April 28, 1950.
[1] Beams, Kuhlthau, Lapsley, McQueen, Snoddy, and Whitehead, Jr., J. Opt. Soc. Am. 37, 868 (1947).

TABLE I. Measured value of the dielectric constant of the barium titanate compound forming the coaxial cable.

Resonant frequency megacycles	λ(cm)	Velocity of propagation (cm/sec.) $\times 10^{-8}$	Dielectric constants
(a) Shorted line			
15.5	66	10.2	860
50	22	11.0	745
75	13.2	9.9	925
105	9.44	9.9	925
140	7.32	10.25	854
167	6.0	10.0	900
190	5.08	9.64	970
250	4.4	11.0	745
(b) Open line			
26.9	33	8.88	1140
76	11	8.36	1290
143	6.8	9.72	955
187	4.71	8.80	1162
240	3.67	8.80	1162
(c) 1000 c.p.s. bridge (G.R. type 650A)			1575

multiplier tube and synchronoscope combination.*** The following comparative data are obtained.

	RG8U Cable	$BaTiO_3$ Cable
Over-all light duration	7×10^{-7} sec.	12×10^{-7} sec.
Decay time, peak to $1/e$ peak	1.9×10^{-7} sec.	2×10^{-7} sec.
Rise time, zero to peak	1×10^{-7} sec.	1×10^{-7} sec.
Fifty percent of peak limits	1.5×10^{-7} sec.	1.8×10^{-7} sec.

The series of spark shadowgraphs shown in Figs. 2, 3, and 4 show the approach to a resolution limit as the frequency of the progressive ultrasonic waves is increased from three to nine megacycles. A quartz crystal having a fundamental frequency of one megacycle was driven at 3, 7, and 9 times its fundamental frequency to obtain these shadowgraphs. The method used was that devised by Hubbard, Zartman, and Larkin.[2]

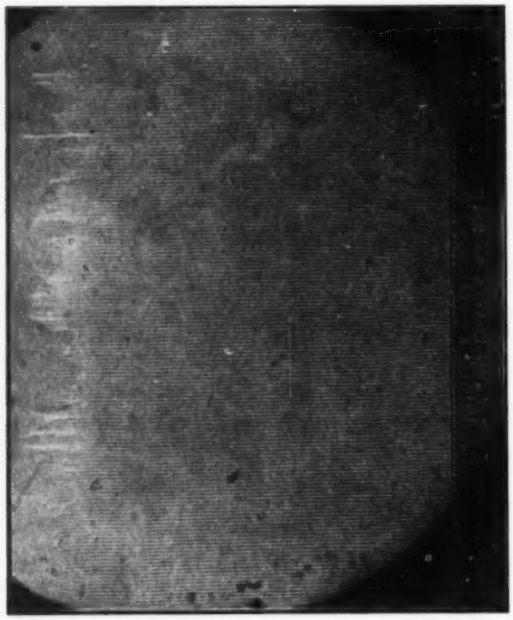

FIG. 2. Shadowgraph of 3.0 Mc progressive ultrasonic wave in water. The scale shown is in cm. Water temperature—25°C.

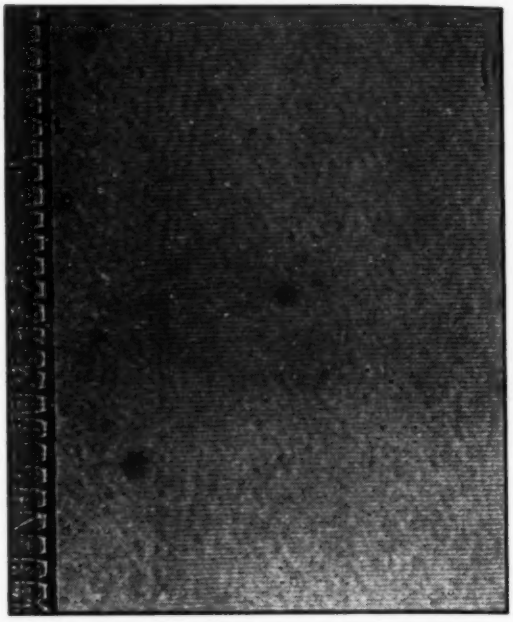

FIG. 3. Shadowgraph of 7.0 Mc progressive waves in water. Note that definition is not as good as that shown in Fig. 1. See also caption in Fig. 4.

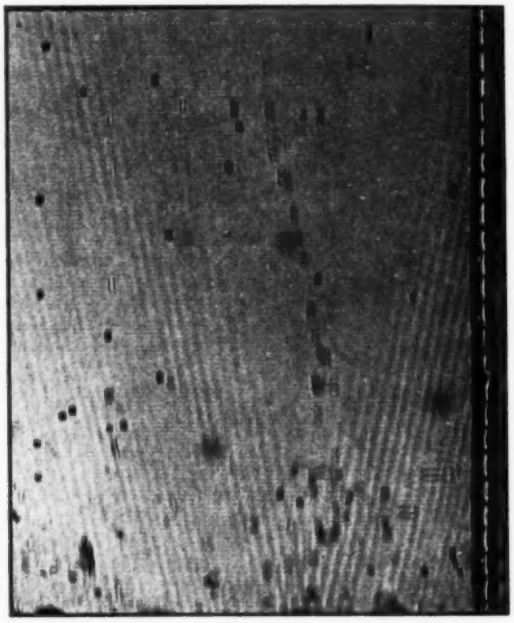

FIG. 4. Shadowgraph of 9 Mc progressive wave in water. The wave pattern here is not very distinct indicating that the acoustic wave has moved an appreciable part of a wave-length during the period of illumination. A diminution of the sound intensity is seen in the short distance covered by this picture. The marginal spacing is in mm.

*** These traces were made through the courtesy of Mr. Wm. T. Whelan of the Naval Ordnance Laboratory.

[2] Hubbard, Zartman, and Larkin, J. Opt. Soc. Am. **37**, 832 (1947).

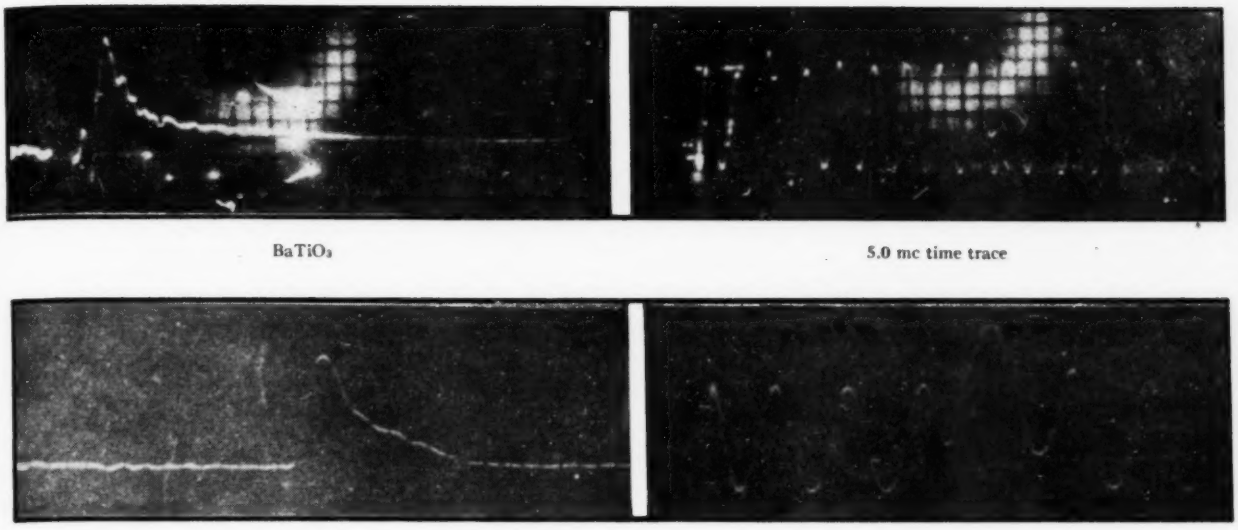

FIG. 5. Photograph of cathode-ray oscilloscope traces of light from spark sources as a function of time. The time scale is given by the sinusoidal traces on the right of frequency 5 Mc/sec.

Comparative light intensities have been made by discharging both the RG8U cable and the $BaTiO_3$ cable through the same spark electrodes and allowing the divergent light to fall on the sensitive plate of a photomultiplier tube the output of which was coupled to a ballistic galvanometer. To obtain the same deflection from the galvanometer as was obtained from discharging the RG8U cable at a fixed distance it was necessary to move the barium titanate light source to 30 times the distance from the photo-cell, thus indicating a light intensity nine hundred times as great as that produced by the RG8U cable. It is possible to obtain good spark photographs on lantern slide plates four feet away from the barium titanate divergent light source. Apparently the nine-hundred fold gain in light intensity is due to the elimination of the loss inherent in the fifty ohm terminating resistor associated with the RG8U cable since at the most, the electrical capacity of the barium titanate cable is only twenty times that of the RG8U cable used here.

The high light intensity and short time of the spark together with the convenient size of the cable make it particularly useful for studying high speed phenomena such as turbulence and ultrasonic wave-systems where photographic methods are used. We have observed while employing this device that the light intensity and spark duration are functions of many parameters principal of which are, gap spacing, current density in the gap, which depends on the initial charge on the line (the results shown here have been made, with the cable charged to 10,000 volts), and type of confining gap; a confined spark produces higher intensity but longer duration, an open gap less light intensity but shorter duration.

The authors wish to acknowledge with thanks the advice of Mr. Bert H. Marks, Product Engineer for Centralab Incorporated, which fabricated the cable.

Emissivity Changes of Thoria Cathodes*

O. A. Weinreich
Bartol Research Foundation of The Franklin Institute, Swarthmore, Pennsylvania
(Received June 1, 1950)

Spectral and total emissivity measurements of thoria-coated tungsten filaments show that irreversible and reversible changes of the emissivity occur. ϵ_λ ($\lambda=0.65\mu$) varies from 0.2 to 0.7 and ϵ_t from 0.2 to 0.5.

Certain variations of the thermal radiation can be related to changes of thermionic emission.

Passage of current through the coating affects emissivity and thermionic emission. This is shown by measuring infra-red radiation and electron current simultaneously. The existing relationship between emissivity and thermionic activation is discussed.

1. INTRODUCTION

THE numerous published values[1–7] of spectral emissivities for thoria vary over a wide range. (If thin coatings on metals are investigated, one should keep in mind that part of the radiation comes from the base metal.) The extinction coefficient at $\lambda=0.665\mu$ for thoria sleeves has been found to be 26 cm^{-1}.[8] The results of our investigations show that both reversible and irreversible changes in spectral and total emissivities can be effected by various treatments of the thoria.

Spectral and total emissivity measurements of thoria-coated tungsten cathodes are of interest in two respects:

(1) Total emissivity changes of thoria cathodes which occur during processing and life affect temperature and heater power; emissivity changes in the red affect the pyrometer corrections.

(2) Emissivity changes, insofar as they involve impurity levels, may yield information on the mechanism of thermionic emission.

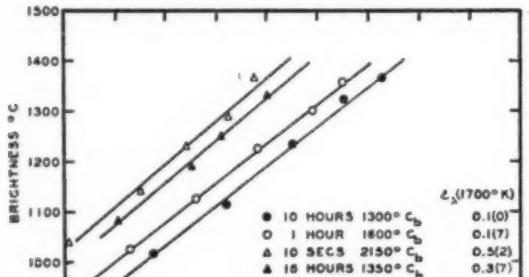

FIG. 1. Spectral emissivity ($\lambda=0.65\mu$) of a thoria-coated tungsten filament (coating thickness 50μ) after various heat treatments. True temperature is measured by filament resistance. Calibration curve not shown.

2. EMISSIVITY CHANGES OF THORIA-COATED W FILAMENTS

In an earlier paper[9] it was shown that a small spot of thoria on a tungsten filament appeared brighter than the tungsten, when previously flashed to ~2800°K. The brightness of the spot relative to the brightness of the tungsten decreased at lower temperatures with time. In the present investigation the emissivity changes of thoria-coated cathodes were investigated further by using thoria-coated tungsten filaments with potential leads. The filament resistance can be taken as a measure of the true temperature for the thoria surface if we assume that:

(1) The temperature drop in coatings $\leqq 50\mu$ is negligible, which appears to be justified on account of the relatively high thermal conductivity of thoria, 0.01 cal. per cm deg.[10]

(2) The change of the tungsten filament resistance due to chemical reaction between tungsten and thoria is negligible. This has been shown to be true by evaporating completely a 10μ thoria coating from a tungsten filament. Before coating and after evaporation the resistance was the same within the experimental errors.

Tungsten filaments of 10 and 12 mils diameter and about 25 cm length were used. The potential leads of 2 mils diameter were spot-welded about 3 cm above the

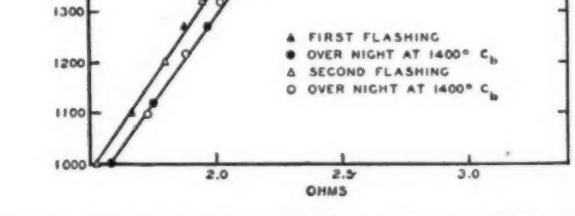

FIG. 2. Reversible spectral emissivity changes ($\lambda=0.65\mu$) of a thoria-coated tungsten cathode. Flashing to about 2300°C_b increases the emissivity to $\epsilon_\lambda=0.7$ and subsequent heating at 1400°C_b causes the emissivity to drop to $\epsilon_\lambda=0.4$.

* Part of the results described here have been presented at the New York Meeting of the Physical Society (Division of Electron Physics), January, 1950.

[1] Coblentz, Bur. Stand. Bull. **9**, 283 (1913).
[2] Burgess and Waltemberg, Bur. Stand. Bull. **11**, 591 (1915).
[3] W. E. Forsythe, Phys. Rev. **25**, 252 (1925).
[4] G. Liebmann, Zeits. f. Physik **63**, 404 (1930).
[5] D. A. Wright, Nature **160**, 129 (1947).
[6] E. T. Hanley, J. App. Phys. **19**, 583 (1948).
[7] S. Mesnard, Comptes Rendus **230**, 1582 (1950).
[8] W. E. Danforth, private communication.
[9] O. Weinreich, Rev. Gen. d'El. **54**, 243 (1945).
[10] W. E. Danforth, private communication.

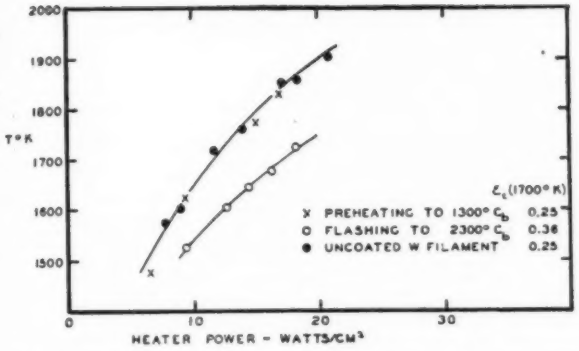

FIG. 3. Total emissivity of a thoria-coated tungsten filament. Coating thickness 10μ. Flashing to 2300°C$_b$ increases the total emissivity from $\epsilon_t=0.25$ to $\epsilon_t=0.36$ (at 1700°K).

filament terminals. The resistance was measured by the current through the filament and the voltage drop across the potential leads. The general procedure was the following: Filaments with potential leads were mounted in a tube which was pumped and baked in the usual manner, and the resistance-temperature characteristic of the uncoated tungsten filament was measured using pyrometer readings and corrections for the spectral emissivity of tungsten. The tube was then taken off the pumping system and opened, and a thoria coating was deposited on the filament. Commercial thoria powder supplied by Lindsay Light and Chemical Company was suspended in butyl alcohol, and the particles charged by addition of a small amount of thorium nitrate, as described by E. T. Hanley.[11] The tube was then sealed and put back on the pumping system. The resistance of the coated W filament was measured with the same instruments as used for the resistance-temperature plot of the pure tungsten filament.

Figure 1 shows the change of the apparent spectral emissivity of a thoria coating of 50μ thickness, when heated in steps to higher temperatures. The brightness temperature is plotted against the filament resistance. We see that heat treatment of the filament at increasing temperatures increases the spectral emissivity; i.e., for a given filament resistance the brightness temperature increases. (It should be noted that the initial emissivity increase may be partly an apparent increase due to a sintering effect, prior to which a temperature difference between filament and coating may exist.) The emissivity increase after flashing to ~2800°K is not stable but decreases with time if the filament is allowed to remain at lower temperatures, e.g., 1350°C$_b$.

The reversible change of the spectral emissivity of another filament is shown in Fig. 2. The emissivity increases, after flashing, to $\epsilon_\lambda=0.7$ and decreases with time, when held at 1400°C, to $\epsilon_\lambda=0.4$. This process can be repeated until finally the coating thickness decreases by evaporation during the flashing.

Changes of the total emissivity which occur with the same heat treatments are shown in Fig. 3. The heater

[11] E. T. Hanley, J. App. Phys. **19**, 583 (1948).

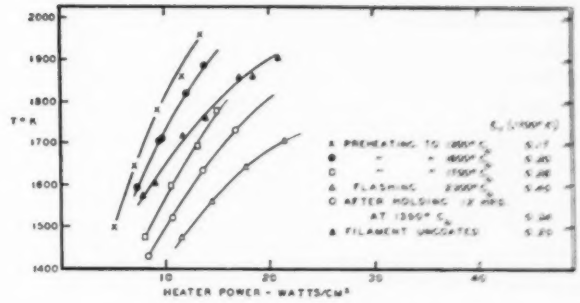

FIG. 4. Total emissivity of a thoria-coated tungsten filament (coating thickness 50μ) after various heat treatments.

power in watts/cm² is plotted against the temperature as measured by the filament resistance. The coating thickness is 10μ. The initial total emissivity at 1300°C$_b$ is very near to that of the pure tungsten, $\epsilon_t=0.25$. Again, as seen for the emissivity in the red, the total emissivity also increases, $\epsilon_t=0.36$, as a result of the flashing.

Figure 4 shows the same measurements for a 50μ coating. An initial heat treatment not exceeding 1300°C$_b$ gives $\epsilon_t=0.17$, which value increases after flashing to $\epsilon_t=0.45$. As the temperature is allowed to remain at 1350°C$_b$ the emissivity drops to $\epsilon_t=0.34$.

3. EMISSIVITY CHANGES AND ACTIVATION CHANGES OBSERVED WITH DIODES

As was shown in an earlier paper,[9] flashing to 2800°K increases electron emission and emissivity. Subsequent current drawing accelerates the deactivation, which normally occurs slowly with time after flashing if the cathode is maintained at a lower temperature. Here we

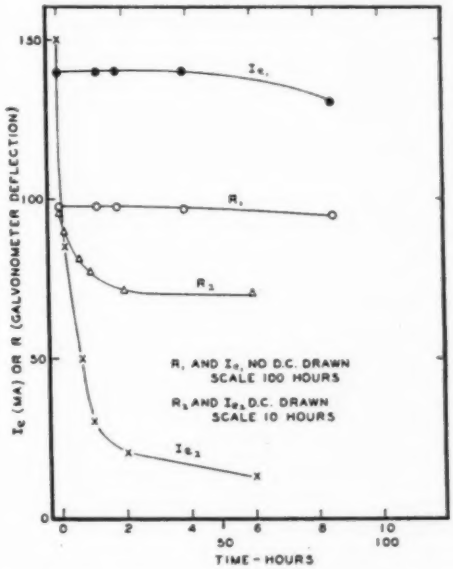

FIG. 5. Electron emission Ie and radiation $R(\lambda=1\mu)$ at $T=1175$°C of a thoria-coated tungsten filament as a function of time after flashing to 2300°C$_b$. Curves Ie_2 and R_2 show that the rates of decrease of Ie and R are highly increased if electron emission is drawn.

observe further the emissivity changes of a thoria cathode by measuring the intensity of radiation at an arbitrary wave-length in the infra-red with a thermopile, if the true temperature is kept constant by keeping the filament resistance at a constant value. Several diodes, the cathodes of which had potential leads, were made. The cylindrical anodes were made of tungsten mesh. In this way the decrease of the spectral emissivity with time, together with the thermionic deactivation after the flashing could be measured. The following

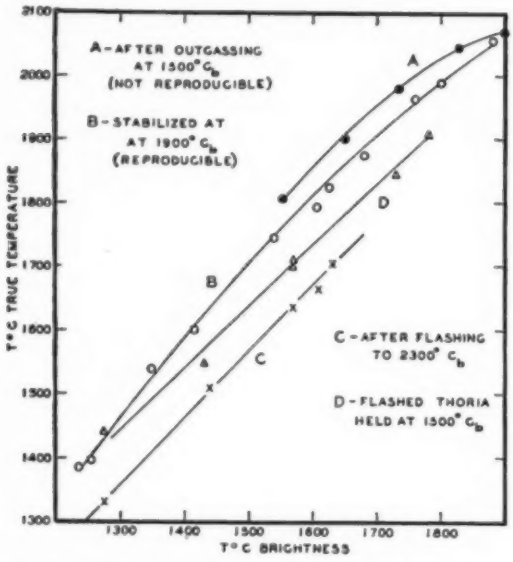

FIG. 6. Irreversible (curves A and B) and reversible (curves C and D) changes of the spectral emissivity ($\lambda=0.65\mu$) of a thoria-coated tungsten cathode after various heat treatments. The true temperature is measured by a Mo–W thermocouple.

observations were made at lower temperatures after flashing the cathode to ~2800°K:

(a) If no electron emission is drawn, both intensity of radiation and thermionic activity decrease slowly with time. The rate of this decrease depends on the temperature. For example, at 1400°C radiation and emission decreased about 10 percent after 100 minutes, while at 1150°C, no appreciable decrease was seen after 85 hours.

(b) The drawing of electron currents accelerates drastically the rate of deactivation and of emissivity decrease. For example, at 1400°C the electron emission decreased 50 percent and the radiation by 33 percent after ten minutes.

(c) The accelerated decrease of thermionic emission and emissivity due to the drawing of current could still be seen if, after flashing, the cathode was first held "quiescent" at 1400°C for 16 hours and then the anode voltage applied. The described phenomena were qualitatively reproducible and observed with several diodes and at different wave-lengths. Figure 5 shows the results for 1175°C at $\lambda=1\mu$.

4. EMISSIVITY CHANGES AS OBSERVED WITH A THERMOCOUPLE

Further verification of the emissivity changes of thoria was made using a W–Mo thermocouple,[12] spot-welded to a 20 mil tungsten filament to measure the true temperature. The known spectral emissivity of the uncoated tungsten filament was used to calibrate the e.m.f. of the thermocouple against true temperatures. A plot of the true temperature against the e.m.f. was made over a range from 1200° to 2100°C. The tube was then opened, the tungsten filament coated with thoria by cataphoresis (about 20μ thick), sealed, and put again on the pumping system. In Fig. 6 the brightness temperatures of the thoria coating are plotted against the true temperatures as measured by the thermocouple. After outgassing at 1500°C$_b$ the temperature of the filament was raised in steps to 1900°C$_b$ (curve A). Curve B, obtained by decreasing the temperature from 1900°C to 1200°C does not coincide with curve A and is the reproducible curve. In contrast, curve A is not reproducible. This behavior is believed to be the result of a certain sintering action, which occurs along curve A and is completed at 1900°C. (The very low initial value of the spectral emissivity of thoria coatings ($\epsilon_\lambda=0.09$) found recently by S. Mesnard[7] may be an apparent one for the same reason.) Following flashing to 2300°C$_b$ temperature measurements gave curve C. After several hours at 1500°C$_b$, curve D is obtained. The spectral emissivity values ($\lambda=0.65\mu$) for the different states, taken from Fig. 6 for $T=1700$°C are:

Before flashing: $\epsilon_\lambda=0.3$ (curve B).
After flashing: $\epsilon_\lambda=0.7$ (curve C).
After flashing and 10 hours at 1500°C$_b$: $\epsilon_\lambda=0.4$ (Curve D).

The tube was now sealed off, and after a new flashing to 2300°C$_b$ the radiation of the thoria-coated filament at $\lambda=1\mu$, as obtained from the galvanometer deflections of the thermopile of the spectrograph, was plotted against time for a temperature of 1520°C, this temperature being maintained constant by holding the e.m.f. of the thermocouple on the filament at a constant value. Again, the emissivity decreased with time as was expected from the previous measurements when the true temperature was measured by the resistivity.

5. CONCLUSION

It is premature to attempt to draw theoretical conclusions from the results presented here. However, apart from the bearing on practical problems of heater power and pyrometer corrections, it seems that the results show the existence of a relationship between intensity of thermal radiation and thermionic activation.

Undoubtedly chemical reactions occur between tungsten and thoria when flashed to 2800°K. Reaction products may be metallic thorium and/or some thorium

[12] F. H. Morgan and W. E. Danforth, J. App. Phys. **21**, 112 (1950).

suboxide. W. L. B. Burgers and T. M. Liempt[13] have made x-ray analyses of thoriated tungsten filaments. They found that when these tungsten filaments are heated to 2500°K, thoria is partly reduced to metallic thorium. Besides this, their results show some evidence for incomplete reduction and formation of an oxide with an oxygen content between Th and ThO_2. The authors found a similar reaction product when heating superficially oxidized thorium rods. The only impurity considered so far for thoria cathodes is free thorium, and many activation phenomena fit into this picture.[14] On account of Burgers and Liempt's work, one should also consider the possibility of suboxide impurities.

Some doubt may be held as to whether or not a density of impurity centers, sufficient to account for conduction and thermionic emission, is also sufficient to provide observable changes of optical emission. It is possible that our reversible emissivity changes might be linked to thermionic activation in an indirect way only, i.e., impurity material produced in such quantity that colloidal agglomeration occurs. Present views concerning thoria[15,16] indicate a density of impurity centers of the order of 10^{18} cm^{-3}. This figure, although its value is subject to further investigation, is of the same order as the density of color centers of the alkali halides in which measurable optical effects are found. It therefore seems possible that knowledge regarding impurity levels in thoria might be gained from infra-red emission studies, and further work is in progress in this connection.

ACKNOWLEDGMENT

The writer wants to thank Mr. F. H. Morgan for his aid in assembling and calibrating the W—Mo thermocouples and for his assistance in carrying out the experiments described in Sec. 4.

[13] W. L. B. Burgers and T. M. Liempt, Zeits. f. anorg allge. Chemie **193**, 144 (1930).
[14] H. Y. Fan, J. App. Physics **20**, 682 (1949).
[15] D. A. Wright, Proc. Phys. Soc. **B62**, 188 (1949).
[16] W. E. Danforth and F. H. Morgan, Phys. Rev. **79**, 142 (1950).

Techniques for Measuring the Dynamic Characteristics of a Low Pressure Discharge

BENTLEY T. BARNES AND STEPHEN EROS
General Electric Company, Lamp Development Laboratory, Nela Park, Cleveland, Ohio

(Received June 13, 1950)

The dynamic characteristics of a discharge can be determined by making square-wave changes of arc current. This is done by putting the discharge tube in the plate circuit of a group of pentodes connected in parallel and supplied with a square-wave signal superimposed on a d.c. bias.

Probes operated at constant current are very useful in recording the characteristics of a modulated discharge. For measuring electron temperature (T_e), two identical probes are centered about points having the same space potential. If the probes are operated at different fixed currents on the straight line part of the probe characteristic, the voltage between them is proportional to T_e. Longitudinal voltage gradient or radial potential differences may be recorded by use of identical probes operated at the same current.

A probe operated at a suitable current will follow roughly the variations in space potential of the adjacent region of the discharge. Another probe made sufficiently negative with respect to such a probe will collect only positive ions. A probe made 0–10 volts positive with respect to the constant-current one gives records from which electron concentrations can be computed. In this case, a bias connection without current flow is obtained by use of a cathode-follower with two stages of direct-coupled amplification.

The oscillograph amplifier used for dynamic probe records must be either a differential one or one with ungrounded power supply. In the latter case, the stray capacitance is many times larger; but fairly reliable records can be obtained if the arc current is 0.1 ampere or more, and if the time constant for the decay of the transient effects being measured is at least 10 microseconds. The oscilloscope amplifier and any preamplifier used for recording spectral intensities should be direct-coupled.

IF a discharge is operated on a.c. at a frequency of 1000 c.p.s., or more, the volt-ampere curve obtained on an oscilloscope screen is quite different from the curve obtained by plotting voltage readings taken on a d.c. discharge operated at various currents. This difference in behavior shows that the dynamic characteristics of a discharge are not the same as those indicated by a series of static tests. Since this is of considerable interest from both practical and theoretical viewpoints, we have developed methods for getting fairly complete data on the dynamics of a discharge. The latter is subjected to square-wave changes of arc current. The time between successive square-wave changes should, of course, be long enough to permit the discharge to approach steady-state conditions. This permits one to observe both the instantaneous effect of a change in current and the rate of adjustment toward the steady state. To make measurements under these conditions, one needs to modify the techniques developed by Langmuir[1,2] for measurements on discharges operated at a constant current. In this article we describe equipment and procedures for obtaining square-wave changes of arc current and for recording the instantaneous values of various properties of the discharge.

SQUARE-WAVE MODULATION

The circuit used for controlling arc current is shown in Fig. 1. We have used twelve 6L6 tubes, connected in

[1] I. Langmuir, G. E. Rev. **26**, 731 (1923).
[2] I. Langmuir and H. Mott-Smith, Jr., G. E. Rev. **27**, 449 (1924).

parallel except for a non-inductive resistor in series with each grid. These resistors prevent parasitic oscillations. They are connected to the cathode-follower output stage of a square-wave generator. To provide the proper bias for the 6L6's, the negative terminal of the voltage supply for the square-wave generator is put at -60 volts with respect to the negative lead of the voltage supply for the circuit shown in Fig. 1. Figure 2 shows how provision is made for controlling both the d.c. bias and the amplitude of the square-wave signal. This permits one to adjust the modulation and the average arc current independently.

With the circuit shown in Fig. 1, inductance in the leads of the voltage supply tends to round the corners of the square wave. Although the plate current of a pentode is insensitive to changes in plate voltage, it is affected to a much greater extent by changes in screen voltage. A better wave-shape would be obtained if a separate low-impedance supply were used for the screens of the 6L6's. This improvement may not be needed in a study of the dynamics of the flow of ions to the tube wall, but it is essential if one wishes to record the increase in ion concentration when the current is suddenly increased. In the latter case, a square wave with a rise time which does not exceed a few microseconds is required for even a rough separation of instantaneous effects from subsequent adjustments toward steady state conditions.

We have not tested the circuit change suggested in the preceding paragraph, partly because it did not occur to us until after a fairly complete set of data had been taken, and partly because our oscilloscope equipment could not resolve the details of changes which take place within a few microseconds. With a common plate-screen supply, 90 percent of a square-wave change in lamp current was made in about 80 microseconds. With the lamp current zero, the corresponding change in the grid voltage of the 6L6 tubes took less than one-third of this time.

PROBE TECHNIQUES

Sudden large changes in arc current are accompanied by proportionately larger instantaneous changes* in the

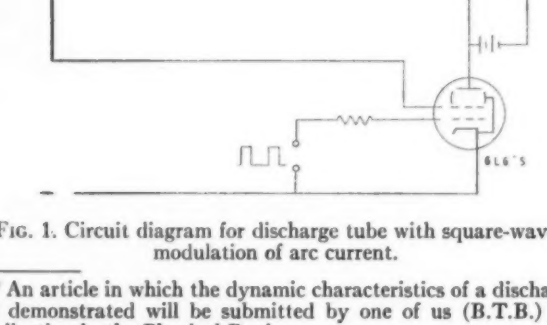

FIG. 1. Circuit diagram for discharge tube with square-wave modulation of arc current.

* An article in which the dynamic characteristics of a discharge are demonstrated will be submitted by one of us (B.T.B.) for publication in the Physical Review.

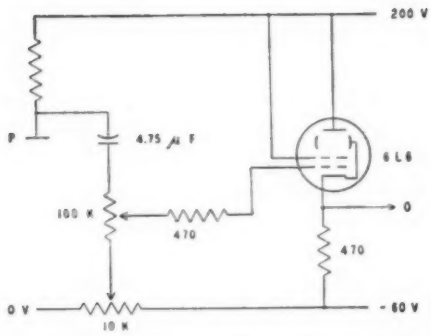

FIG. 2. Output stage of square-wave generator. *P*. Plate of clipper stage. *O*. Output to pentode current-control tubes.

longitudinal voltage gradient. These variations make it inconvenient to use a constant-voltage probe for recording arc characteristics throughout a cycle of modulation. It is much simpler to obtain these records with the aid of a probe operated at constant current, or a pair of these probes. Probe current can be held constant by use of the floating-pentode circuit shown in Fig. 3.

If the electrons in a discharge have a Maxwellian distribution of velocities, the usual plot of the logarithm of the electron current to a probe against the probe voltage has a straight-line portion[1] whose slope is proportional to the reciprocal of the electron temperature T_e. If the probe current i_P is at least 10 percent of the current i_s drawn when the probe is at space potential,† then the electron current to the probe is many times larger than the positive-ion current. In this case, the probe voltage V_P with respect to space potential is approximately equal to $(T_e/5040)\log(i_P/i_s)$. If two probes of the same area are located in regions of the discharge having the same average potential, but are operated at different currents which are on the straight-line portion of the characteristic, then the voltage between the probes is proportional to T_e. Thus two constant-current probes can be used to get a continuous record of T_e during the cycle of modulation described above, or during any transient for which the variations in i_s and T_e are small enough to permit both values of probe current to remain on the straight-line portion of the characteristic. When i_s does not vary by more than a factor of ten, the constant-current technique is more convenient than the floating-double-probe technique described by Johnson and Malter,[3] since the former gives T_e directly on a single oscillogram. (Ordinarily, two oscillograms are taken, with the probes interchanged to eliminate errors due to contact differences of potential.) One could cover a larger range of i_s by using two or more sets of probe currents, provided that one used only the portion of each record corresponding to the straight-line part of the probe characteristic. However, even this part of each oscillogram might not be a true record of T_e if the oscillograph amplifier were overloaded at any

† The average potential of adjacent regions of the discharge.

[3] E. O. Johnson and L. Malter, Phys. Rev. **76**, 1411 (1949).

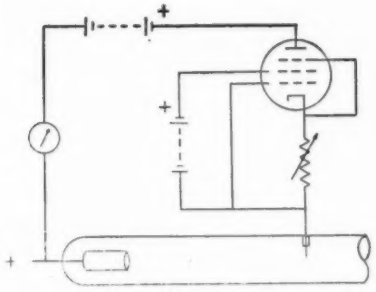

FIG. 3. Circuit used for holding probe current constant.

time during the cycle. Recovery from an overload may not be complete until several milliseconds after the input signal returns to the normal range.

If the distribution of electron velocities is non-Maxwellian, the probe characteristics may have no straight-line portion. In this case, the voltage between two constant-current probes measures the slope of a chord drawn between two points on the characteristic. The apparent T_e indicated by this slope would depend on the values chosen for the two probe currents. To find how the velocity distribution varied during a transient one would have to take a series of oscillograms—using several pairs of values for the probe currents, distributed over the probe characteristic.

Constant-current probes also are useful for measuring the difference of potential between two points in a discharge. If T_e is the same at the two points, one operates the probes at currents which are the same fraction of the respective values of i_s. This procedure allows one to obtain a continuous record of longitudinal voltage gradient, or of the radial fall in potential between the axis of the tube and the inner edge of the wall sheath.

A constant-current probe is useful as an auxiliary in two other types of probe measurement. If the current is made a little less than the minimum value of i_s, the probe will follow roughly the variations in space potential in the adjacent region of the discharge. (When i_e is at its maximum value, the probe may be 2–3 volts negative with respect to space potential.) A nearby probe made sufficiently negative with respect to the auxiliary one will collect only positive ions. By inserting a suitable resistance between the bias battery and the second probe, one can obtain a continuous record of positive ion current during a cycle of modulation.

Figure 4 shows an elaboration of this procedure which is useful for obtaining records of probe current near space potential. The cathode follower shown in this circuit allows one to bias the measuring probe with respect to the auxiliary one, and to draw whatever probe current is appropriate with this bias. In case a single 6L6 output tube does not furnish sufficient current, two or three of them are used in parallel. Two stages of direct-coupled amplification make it possible to cover a wide range of probe current with only a small change in the voltage between the input grid and the common cathode lead of the amplifier-cathode-follower circuit. Thus the voltage of the second probe follows quite closely the voltage variations of the auxiliary probe.

Using this cathode-follower, oscillograms of probe current can be taken with various bias voltages. If the latter are so chosen that probe potentials above and below space potential are obtained, then one can find i_s by making the usual semilogarithmic plot.[1] From the measured values of i_s and T_e, one can compute the electron concentration in the adjacent region of the discharge. (See reference 2, Eq. (44).)

AMPLIFIERS FOR PROBE MEASUREMENTS

In the probe measurements described above, both leads to the oscillograph amplifier have varying potentials during a cycle of modulation. One must use either a differential amplifier or an amplifier whose power supply is ungrounded. In the latter case, one must make sure that the capacitance associated with the negative lead of the supply does not cause serious errors. With a rectifier type of supply, the principal source of unwanted capacitance may be that between the primary and the secondary windings of the power transformer. In a small amplifier, this capacitance is likely to be of the order of 1×10^{-9} farads. Its effect would be most marked if the space potential at the probe suddenly shifted in the positive direction, because this would reduce the probe current. The current charging the stray capacitance in the amplifier-probe circuit could not exceed the current for which the floating pentode (Fig. 3) connected to the probe was set. If this were 10 milliamperes and if space potential shifted 10 volts, a capacitance of 1×10^{-9} farads would require only one microsecond to charge completely, if the full current were available for this time. Actually, the required time would be longer because the probe would start drawing current as its voltage approached its equilibrium value; in a typical case the adjustment would be 98 percent complete in 1.25 microseconds. Thus an amplifier with single-ended input may be entirely satisfactory for instantaneous probe measurements such as we have described, provided that the negative return lead of the

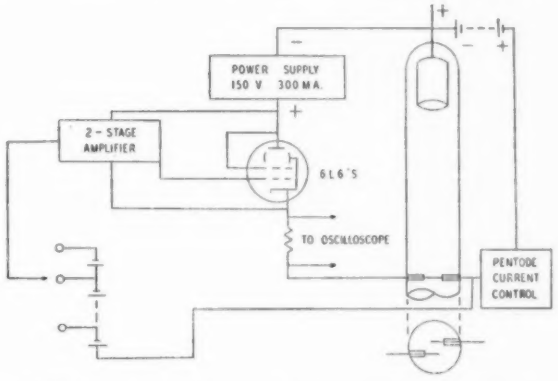

FIG. 4. Circuit for recording probe current at voltages near space potential, in order to determine electron concentration.

power supply is connected to a probe from which a current of several milliamperes is drawn.

It is advantageous to use a direct-coupled amplifier for probe measurements, since the d.c. components of voltage are needed. The frequency response should be essentially constant from 0 to at least 100,000 cycles per second. An input resistance of about 0.2 megohms and a maximum sensitivity such that two volts gives full-scale deflection have been satisfactory for our conditions of measurement (arc current >0.2 amp.). If the arc current were less than 0.1 amp., a more sensitive amplifier might be needed in order to get a reliable record of positive ion current.

RECORDING SPECTRAL INTENSITIES

To record the intensity of a spectral line or band during a cycle of modulation, one may need to use a photo-multiplier tube. An output current of the order of 10 μamp from the multiplier tube would deflect the oscilloscope spot the full height of the screen, if an amplifier similar to the one described in the preceding paragraph were used.

If the line or band to be measured is fairly strong and can be isolated with a filter, an ordinary photo-tube may suffice. In this case, it probably will be necessary to add a direct-coupled preamplifier to the amplifier used for probe measurements. To maintain adequate speed of response, the input resistance of the preamplifier ordinarily should be made no larger than 0.2 megohms. To insure sufficient stability of the zero-input trace, a d.c. heater supply should be provided for the preamplifier.

DISCUSSION

The circuits described in this article were developed for use with a mercury-vapor discharge operated in the presence of rare gas at a pressure of a few millimeters. In this case, the transient effects accompanying a sudden change in current may last several milliseconds. If the rare gas had not been present, the transients obtained with a mercury-vapor pressure of a few microns would have lasted only a few microseconds.[4] Then a 100-fold increase in both the frequency of modulation and in the speed of response of the measuring circuits would have been needed in order to get satisfactory oscillograms. This would not be possible unless the stray capacitance were kept to a minimum by use of a suitable differential amplifier and by other precautions.

Even with a gas pressure of a few millimeters, stray capacitance will be troublesome if the arc current is quite low (50 milliamperes, or less). In this case, probe currents and photo-currents will be so small that the resistors used for measuring them will have relatively high values. Then the spurious effects introduced by stray capacitance will have time constants of the same order of magnitude as those of the transients one wishes to record.

When a differential amplifier is used for probe measurements during a cycle of modulation, care must be taken to keep the amplifier operating within its linear range. Because of variations in space potential, the voltage difference between the constant-current probe and the anode or the cathode may vary over a wide range—perhaps several times as much as the voltage one wishes to measure. To offset this, one must either (1) connect the amplifier ground to a probe near to the one, or pair, with which measurements are being made, or (2) make the linear range of plate voltage for the output tubes several times the maximum voltage to be applied between the deflection plates of the oscilloscope.

SUMMARY

In studying the dynamic characteristics of a low-pressure discharge, we have found the following procedures and equipment particularly useful.

1. Pentodes in series with the discharge tube provide a convenient means of making square-wave changes in arc current.

2. A floating, self-biased pentode in series with a probe permits one to hold probe-current constant in spite of changes in the voltage gradient in the discharge. Pairs of constant-current probes can be used to get instantaneous records of electron temperature or of the voltage difference between two points in the discharge.

3. A constant-current probe is a useful auxiliary in making records of positive-ion current during a transient.

4. For measuring variations in ion concentration when the arc current is modulated, one can use a probe biased positive by various amounts with respect to a constant-current probe. The bias voltage is applied by use of a cathode-follower with two stages of direct-coupled amplification.

5. The oscilloscope amplifier used for recording probe characteristics must have both input terminals floating. An amplifier with single-ended input and ungrounded power supply may be satisfactory, but a differential amplifier is required if the arc current is relatively low or if the transients to be recorded are of very short duration.

6. Amplifiers for recording discharge characteristics should be direct-coupled.

[4] Z. P. Galkena and V. L. Granovsky, J. Tech. Phys. U.S.S.R. 18, 585 (1948).

On the Radiation Patterns of Dielectric Rods of Circular Cross Section—the $TM_{0,1}$ Mode*†

C. W. Horton, F. C. Karal, Jr., and C. M. McKinney
Defense Research Laboratory, The University of Texas, Austin, Texas
(Received July 12, 1950)

The radiation patterns have been measured for five dielectric rods of circular cross section which were excited in the $TM_{0,1}$ mode. These rods were each $0.870\lambda_0$ in diameter, and the lengths were $2\lambda_0$, $4\lambda_0$, $6\lambda_0$, $8\lambda_0$, and $10\lambda_0$. The theoretical radiation patterns have been computed by means of equivalent surface electric and magnetic currents. Excellent agreement is obtained when it is assumed that the diameter of the surface on which these currents are distributed is 0.65 of the diameter of the dielectric rod. Representative experimental and theoretical patterns are shown for the full 360°.

INTRODUCTION

ONE of the authors (C.W.H.) has developed a theory[1,2] of the radiation patterns of dielectric rods based on the radiation theorems of Schelkunoff. This theory was expanded and supplemented by experimental measurements in two later papers[3,4] of which this is a continuation. This early work was applied to dielectric rods of rectangular cross section and, consequently, suffered from a lack of knowledge of the electromagnetic field components in and on the surface of the rod. In order to minimize this difficulty, the theory has been applied to rods of circular cross section which are excited in the transverse magnetic mode with radial symmetry.

The theory developed in Part I can be applied directly to this problem. It is assumed that the contributions to the surface integral over Σ arise only from the cylindrical surface $S(r=a, 0\leqslant z\leqslant l)$ shown in Fig. 1 and, to a negligible amount, from the end cap $C(0\leqslant r\leqslant a, z=l)$. One would expect that the radius a of the surface S should be equal to the radius b of the dielectric rod. it is found, on the contrary, that the agreement with experimental data is significantly improved if the radius of S is smaller than that of the rod.

In lieu of a rigorous solution to the radiation problem, it is assumed that the fields interior to and on the surface of the dielectric rod are the same as those on an infinitely long dielectric rod of the same material and diameter. In order to test the validity of this assumption, the electric field components over the surface of the radiating rod were measured with a probe.

Since the field in a radiating rod of finite length cannot be the same as that in an infinitely long rod, two factors are introduced whose variation can be used to achieve agreement between theory and experiment. One of these factors is the radius of the surface S over which the equivalent electric and magnetic currents are distributed. The other factor arises from the assumption that the amplitude of the field components is a function of the distance along the rod.

THEORETICAL DEVELOPMENT

The nature of the waves propagated along a dielectric rod of circular cross section is discussed by Stratton.[5] He shows that a dielectric rod will propagate a transverse magnetic wave of radial symmetry, provided the frequency is greater than some minimum value. It can be shown from Stratton's discussion that in the case of a nonmagnetic and lossless dielectric rod surrounded by free space, the field components inside and on the surface of the dielectric rod are given by

$$\left.\begin{aligned} E_r &= -iE_0[n_a/(n^2-n_a^2)^{\frac{1}{2}}]J_1(\lambda_1 r)\,\exp(ikn_a z-i\omega t)\\ E_\xi &= 0\\ E_z &= E_0 J_0(\lambda r)\,\exp(ikn_a z-i\omega t)\end{aligned}\right\}, \quad (1)$$

$$\left.\begin{aligned} H_r &= 0\\ H_\xi &= -i(E_0/Z_0)[n^2/(n^2-n_a^2)^{\frac{1}{2}}]J_1(\lambda_1 r)\\ &\qquad \times\exp(ikn_a z-i\omega t)\\ H_z &= 0\end{aligned}\right\}. \quad (2)$$

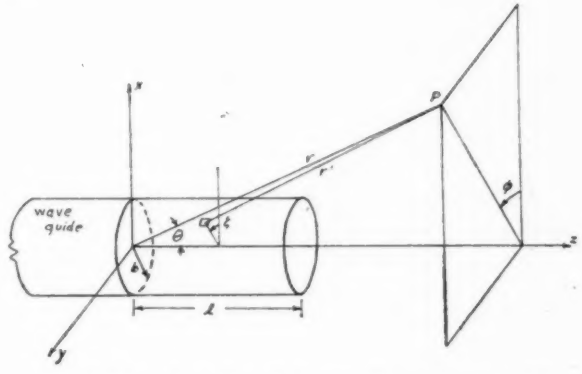

FIG. 1. The orientation of the coordinate systems with respect to the dielectric rod.

* The work described in this paper was done at the Defense Research Laboratory under the sponsorship of the Bureau of Ordnance, Navy Department.
† This paper was read at the 1950 Annual Meeting of the American Physical Society, Columbia University, New York.
[1] C. W. Horton, "On the dielectric rod as an antenna," Report No. CM-272, Defense Research Laboratory, The University of Texas, July 9, 1946.
[2] C. W. Horton, "On the dielectric rod as an antenna, II," Report No. CF-481, Defense Research Laboratory, The University of Texas, November 8, 1946.
[3] R. B. Watson and C. W. Horton, J. App. Phys. **19**, 661 (1948). This will be referred to as Paper A.
[4] R. B. Watson and C. W. Horton, J. App. Phys. **19**, 836 (1948). This will be referred to as Paper B.
[5] J. A. Stratton, *Electromagnetic Theory* (McGraw-Hill Book Company, Inc., New York, 1945), pp. 524–27.

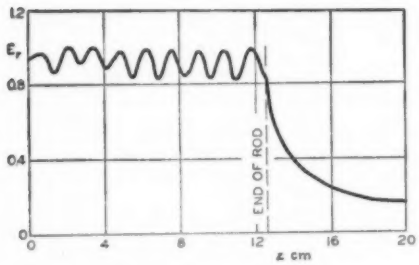

FIG. 2. The variation of the electric field component E_r with the distance along a radiating dielectric rod $4\lambda_0$ long. The mouth of the wave guide is at $l=0$.

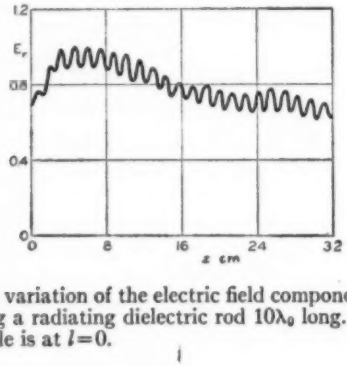

FIG. 3. The variation of the electric field component E_r with the distance along a radiating dielectric rod $10\lambda_0$ long. The mouth of the wave guide is at $l=0$.

Here, n=index of refraction of the rod material, n_a=apparent index of refraction, $k=2\pi/\lambda_0=2\pi/$free space wave-length, Z_0=impedance of free space, E_0=amplitude factor, ω=angular frequency, b=radius of the rod, and $\lambda_1=k(n^2-n_a^2)^{\frac{1}{2}}$. The apparent index of refraction, which is the ratio of the free space wave-length and the guided wave-length, is a function of the index of refraction n, the radius of the rod b, and the order of the radial mode. The value of n_a for any rod may be measured experimentally, or it may be computed from the characteristic equation.[6]

The radiation through the end C has been computed by the same method used earlier in a study of horn patterns.[7] If the dielectric rod is longer than one guided wave-length, the error introduced by neglecting the end C is not greater than 1 db at $\theta=10°$ and 1.5 db at $\theta=90°$. As the length of the rod is increased, the error caused by neglecting the end fluctuates but does not decrease because of the periodicity of the field along the rod.

When the radiation through the end C of the dielectric rod is neglected, the radiation pattern can be computed by a straightforward evaluation of a surface integral over S. The analysis is so similar to that given in Papers A and B that only the final radiation formulas are given. The integral over S reduces to the product of an integral I_1 around the circumference of S and an integral I_2 along the length of S.

In Papers A and B the possibility of radiation from standing waves as well as traveling waves was considered. The measurements of the surface fields shown in Figs. 2 and 3 show that most of the energy is found in the traveling wave. Thus the analysis of Paper B is relevant and one has for I_2

$$I_2=\frac{1}{2}\int_0^l \omega(z)\exp(iqkz)dz, \tag{3}$$

where $\omega(z)$=a shading function arbitrarily introduced to allow for the termination of the rod, $q=n_a-\cos\theta$, and θ=angle between the axis of the rod and a line to the field point (see Fig. 1).

For the transverse magnetic wave whose components are given by (1) and (2), the components of the radiation field at a point P in the far zone are given by

$$E_r=0,$$

$$E_\theta=-(ika/2\pi r)(\exp ikr)I_2$$

$$\times\int_0^{2\pi}[Z_0\bar{H}_\zeta\sin\theta-\bar{E}_z\cos(\phi-\zeta)] \tag{4}$$

$$\times\exp[-ika\sin\theta\cos(\phi-\zeta)]d\zeta,$$

$$E_\phi=0.$$

Here the barred quantities $\bar{H}_\zeta$ and $\bar{E}_z$ are the same as the corresponding unbarred quantities except that the factor $\exp(ikn_az)$ has been split off. The components of **H** are easily found, since this is a transverse wave.

Since it has been found necessary to introduce a distinction between the physical radius of the rod and the radius of the equivalent surface S, one would expect

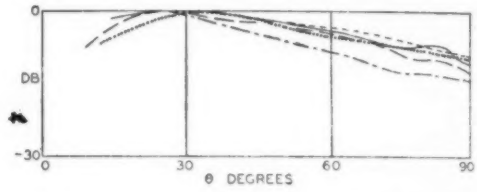

FIG. 4. The envelopes of the experimental patterns *versus* angle. — — — — $l=10\lambda_0$. ——— $l=8\lambda_0$. — — — — — $l=6\lambda_0$. — — — — — — — $l=4\lambda_0$. . . . . $l=2\lambda_0$.

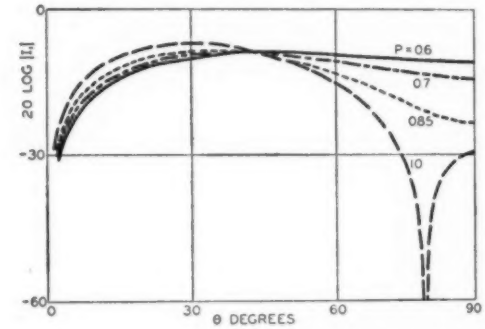

FIG. 5. The angular variation of $20\log|I_1|$ for various values of the ratio P of the radius of the surface S to the radius of the dielectric rod. The field components E_z and H_ζ are evaluated on the surface S.

[6] See reference 5, Eq. (9), p. 526.
[7] C. W. Horton, Proc. I.R.E. **37**, 744 (1949).

that field components H_ξ and E_z should be evaluated on the surface S. This has been done and good agreement was obtained. However, it was necessary in this case to make the radius of the surface S smaller as the length of the rod was increased. On the other hand, if the field components were evaluated on the surface of the physical rod, a constant diameter for S is obtained for rod lengths from $2\lambda_0$ to $10\lambda_0$. Furthermore, the agreement between experimental and theoretical patterns is even better than in the first case.

When one examines (4), it is clear that the choice of the surface S on which H_ξ and E_z are evaluated is significant only in that it determines the ratio E_z/H_ξ, or, in other words, it changes the relative contribution of the magnetic currents and the electric currents to the radiation field.

When the integration is performed, one finds

$$E_\theta \propto \psi I_1 I_2, \tag{5}$$

where the constant of proportionality is immaterial for relative patterns. In Eq. (5)

$$\psi=(1/r)\exp(ikr-i\omega t),$$
$$I_1=J_0(ka\sin\theta)\sin\theta-CJ_1(ka\sin\theta), \tag{6}$$

$$C=\left.\frac{E_z}{H_\xi}\right|_r=\frac{(n^2-n_a^2)^{\frac{1}{2}}}{n^2}\frac{J_0(\lambda_1 r)}{J_1(\lambda_1 r)}, \tag{7}$$

r=surface at which E_z and H_ξ are evaluated.

The integral I_2, which is defined in (3), will be discussed later. The envelope of the radiation pattern is determined primarily by I_1, while the lobe structure arises from I_2.

EXPERIMENTAL OBSERVATIONS

In order to test the equations derived in the preceding section, a series of rods of constant radius were constructed of Lucite. The diameter of each of these rods was $0.870\lambda_0$, but the lengths of the rods were $2\lambda_0$, $4\lambda_0$, $6\lambda_0$, $8\lambda_0$, and $10\lambda_0$. The rods fitted snugly in the wave guide, and the ends of the rods were terminated by a tapered section to avoid a sudden discontinuity. The index of refraction of the Lucite was measured[8] by a transmission method and a reflection method and found to be 1.60 ± 0.01.

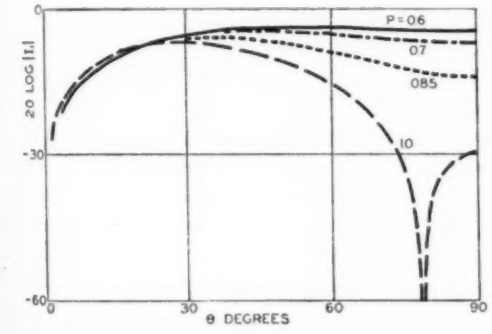

FIG. 6. The angular variation of $20\log|I_1|$ for various values of the ratio P of the radius of the surface S to the radius of the dielectric rod. The field components E_z and H_ξ are evaluated on the surface of the dielectric rod.

TABLE I. The value of the parameters d and D that yield best agreement with the experimental patterns. $b=0.435\lambda_0$; $P=0.65$.

Length l/λ_0	d	D
2	2.0	−0.5
4	1.11	−0.1
6	1.0	0
8	0.5	1.0
10	0.3	2.33

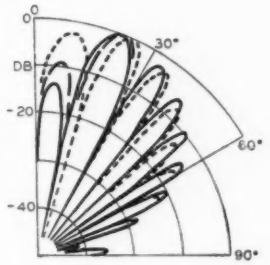

FIG. 7. An illustration of the effect of the shading factor d on the theoretical pattern. —— $d=1.0$; — — — $d=0.5$; - - - - $d=0.2$. Length of rod $=6\lambda_0$. $P=1.0$.

In the experimental pattern measurements, the dielectric rods were used as transmitters. The power source consisted of a type 723 a/b velocity modulated tube operated at a frequency of 9375 m c.p.s. or a wavelength of 3.20 cm. The $TM_{0,1}$ mode was obtained with a mode transducer. A motor-driven turntable was used to rotate the transmitting antenna through 360° in azimuth. The receiving antenna was 40 feet from the transmitting antenna, and both antennas were mounted approximately 12 feet above the roof of a three-story building. The output of the receiver was recorded on an Esterline-Angus recording milliammeter.

Figures 2 and 3 show the dependence of E_r at the surface of the rod on the distance along the rod for the rods of length $4\lambda_0$ and $10\lambda_0$, respectively. These measurements were made with a small probe while the antenna was radiating. These measurements and similar ones on the other rods of the series show low standing wave ratios. They also show that the apparent index of refraction for the series of rods is 1.163 ± 0.008. The value obtained from long rods used as wave guides is 1.175 ± 0.008. It is interesting to note that the transition from the field in the metallic guide to the field in the dielectric guide appears to be complete in a distance of approximately one or two guide wave-lengths.

THE CONTRIBUTION OF THE INTEGRAL I_1

The envelopes of the experimental patterns throughout the first 90° of the five rods are shown in Fig. 4. It appears that the envelope oscillates about a mean value that is independent of the length. Figure 5 shows a series

[8] C. G. Montgomery, *Technique of Microwave Measurements* (McGraw-Hill Book Company, Inc., New York, 1947), Chapter 10.

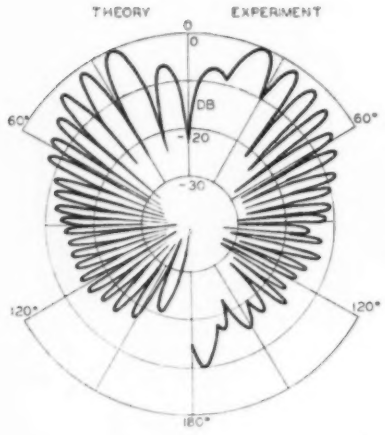

FIG. 8. The experimental and theoretical patterns of a Lucite rod $10\lambda_0$ long and $0.87\lambda_0$ in diameter.

of curves of $20 \log|I_1|$ for various values of P, the ratio of the radius of the surface S to the radius of the dielectric rod; i.e., $P=a/b$. In calculating these curves, the field components E_z and H_ξ are evaluated on the surface S. The curves are plotted to 90° only, because the theoretical curve for I_1 is symmetric about 90°. Also, beyond 90° the influence of I_2 is so great that the behavior of I_1 alone is not significant.

Figure 5 shows that the pattern depends on the radius of the surface S qualitatively in the same way that any radiation pattern depends on a physical dimension of the source. Further, it is evident that agreement with the experimental curves shown in Fig. 4 will not be obtained unless P is less than one. In particular, it was found that if the field components were evaluated on S, the optimum values of P depended on the length as follows: $P=0.85$, 0.70, 0.65, 0.625, 0.60 for $l/\lambda_0=2$, 4, 6, 8, 10, respectively.

Figure 6 shows a plot of $20 \log|I_1|$ for various values of P when the field components E_z and H_ξ are evaluated on the surface of the physical rod. A comparison of Figs. 5 and 6 shows that the variation of $|I_1|$ with the angle θ is less when the ratio E_z/H_ξ is evaluated on the surface of the physical rod than when it is evaluated on the surface S.

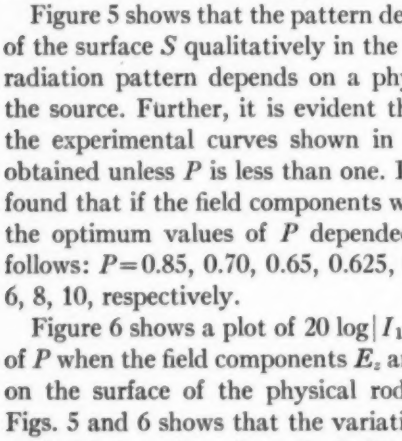

FIG. 9. The experimental and theoretical patterns of a Lucite rod $6\lambda_0$ long and $0.87\lambda_0$ in diameter.

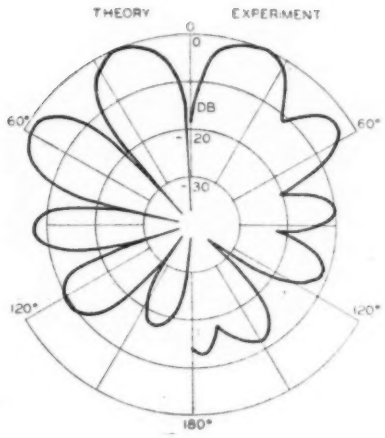

FIG. 10. The experimental and theoretical patterns of a Lucite rod $2\lambda_0$ long and $0.87\lambda_0$ in diameter.

THE VARIATION OF AMPLITUDE ALONG THE LENGTH OF THE ROD

Before one can compute theoretical patterns for comparison with theory, it is necessary to evaluate the integral I_2 defined in (3). Undoubtedly, the best method of procedure would be to determine the shading function $\omega(z)$ for each individual rod from surface measurements such as those shown in Figs. 2 and 3. However, since a very large number of patterns have been measured and computed, it is more convenient to choose a standard form for the function $\omega(z)$ and to obtain agreement with the theoretical patterns by a variation of the parameters in this function.

Mueller and Tyrell[9] have found that a function $\omega(z)$ of the form

$$\omega(z)=d+(1-d)\sin(\pi z/l), \tag{8}$$

is useful in discussions of dielectric rods. This function includes as a special case, $d=1$, the case treated in Paper B. When (8) is substituted into (3), one obtains

$$I_2=\frac{ld}{2}\left|\frac{(\pi/2)D\cos\phi}{(\pi/2)^2-\phi^2}+\frac{\sin\phi}{\phi}\right|\exp(i\phi), \tag{9}$$

where

$$\phi=(kl/2)(n_a-\cos\theta),$$
$$D=(1-d)/d.$$

The constant factor $(ld/2)$ may be ignored in a study of relative patterns.

In order to illustrate the effect of d (or D) on the pattern, three theoretical patterns are shown in Fig. 7 in which only d is changed. These patterns are computed for the rod F-4 when the radius of the surface S is equal to the radius of the dielectric rod. It is seen that the first lobe is very sensitive to the choice of d, while the third and higher lobes are not very sensitive. This conclusion is borne out by a study of the extrema of (9).

The first major lobes of the patterns result from the interaction of I_1 and I_2 and not from a maximum in either one separately. The remaining lobes are caused

[9] G. E. Mueller and W. A. Tyrell, *Bell Syst. Tech. J.* **26**, 837 (1947).

by extrema in I_2, although their exact positions are influenced by the behavior of I_1. This interaction is significant in the rods $2\lambda_0$ and $4\lambda_0$ long, but when the rod is $6\lambda_0$ or more in length, the angular positions of the lobes agree with the extrema of $(\sin\phi)/\phi$ within the limits of experimental error.

THE THEORETICAL PATTERNS

When the values of d (or D) are adjusted to give best agreement with the experimental data, one finds the values listed in Table I. The values are based on the assumption that the electromagnetic field components are evaluated on the surface of the rod but that the radius of the surface S is only 0.65 of the radius of the rod.

Theoretical patterns for all the rods were computed by means of (5) on the basis of the assumptions just mentioned and for the values of d shown in Table I. The excellence of the agreement is illustrated in Fig. 8 which shows on the right the experimental pattern of a rod $10\lambda_0$ long and on the left the theoretical pattern computed by means of (5). Figures 9 and 10 show similar patterns for rods $6\lambda_0$ and $2\lambda_0$ long, respectively.

SUMMARY

In view of the accurate knowledge that one has of the distribution of the field components in a dielectric rod of circular cross section, the formulas developed in this paper apply to any length of rod unless the rod is so short that the effect of the end cannot be neglected. This is in pleasing contrast to the work in Paper A in which the theory failed for rods longer than $6\lambda_0$. The difficulty with the height of the minor lobe encountered in Fig. 6 of Paper A has vanished also.

Precision Determination of the Lattice Constants of Zinc Oxide

R. B. Heller, J. McGannon,† and A. H. Weber
Physics Department, Saint Louis University, St. Louis, Missouri
(Received June 12, 1950)

A total of 350 back-reflection ZnO powder x-ray diffraction lines on 25 photographic films have been measured and analysed by the Cohen analytical least squares extrapolation method to yield $a=(3.2495\pm0.0000_2)$A, $c=(5.2069\pm0.0001_1)$A; where the stated errors are the probable errors. The statistical reliability of the results is emphasized.

In the measurement of the Debye-Scherrer ring radii the accuracy obtained with a metric scale and indicator (employing no optical lens system) and with a dividing engine equipped with a microscope are compared and the former simpler method is found more reliable. It is concluded that the use of precision measuring instruments for observing diffraction ring radii are unnecessary and even undesirable apparently because the magnifying power of the optical system of precision micrometers leads to uncertainties in settings on photographic lines.

THE Cohen analytical extrapolation method[1] has been applied to twenty-five powder photographs of ZnO in the back-reflection region using Cu $K\alpha$ x-radiation employing the Straumanis technique.

The specimen was granulated ZnO powder* of purity better than 99.85 percent. The powder was ground and sifted through a 200-mesh screen to insure some uniformity of fragment size. It was packed into an enamel tube (0.025-in. diameter, 0.5-in. length). This cylindrical specimen holder is the coating of magnet wire,** sleeved off by stretching the wire. The specimen was then carefully centered in a Debye camera (57.296-mm radius) and exposed to x-rays. The Debye-Scherrer rings were measured to 0.005 in. with a metric scale.

From each of the twenty-five photographs data were recorded for a total of fourteen lines, using reflections of the $K\alpha_2$ and $K\alpha_1$ radiations. The procedure was to convert all $K\alpha_2$ reflections to the equivalent $K\alpha_1$ reflection by multiplying $\sin^2\theta$ by $(\lambda K\alpha_1/\lambda K\alpha_2)^2$. The values[2] of Cu wave-lengths ($\lambda K\alpha_1=1.54050$A, $\lambda K\alpha_2=1.54434$A) recommended by the American Society for X-ray and Electron Diffraction were used.

Data taken from one of the films are shown in Table I. $\Phi'=(\pi-2\theta/2)$ is one-half the back-reflection angle and θ is the Bragg angle. The results for the twenty-five films are shown in Table II. The stated error is the probable error of all the determinations.

To determine the effect of measuring a greater number of significant figures in the Debye-Scherrer radii, a dividing engine reading to 0.00025 cm was employed for remeasuring of the same twenty-five films. Because of the limited length of the dividing engine scale, the Straumanis method could not be employed. Instead, a constant R, obtained by calibrating the camera with NaCl, was used. The application of the Cohen method yields: $a=(3.24892\pm0.00008)$A and $c=(5.20489\pm0.00037)$A. The spread for a is 0.00244A and that for c is 0.01245A. Note that the spread here is greater than that of the results shown in Table II.

† Now at Creighton University, Omaha, Nebraska.
[1] M. U. Cohen, Rev. Sci. Inst. 6, 68 (1935).
* Obtained from Mallinkrodt Chemical Works, St. Louis, Mo.
** Obtained from Westinghouse Electric Corporation, East Pittsburgh, Pa.
[2] E. A. Wood, Phys. Rev. 72, 436 (1947).

TABLE I. Detailed data for film 5 using the first method (Straumanis method, employing simple measuring scale).

s* (cm)	Φ' (radian)	θ (radian)	hkl	α	γ	$(\sin^2\theta_{\text{assumed}}-\sin^2\theta_{\text{exp}})$** $=\gamma\times10^{-7}$	δ
1.061	0.0926	1.4782	222	12	4	0.99117948−0.98652603=0.465345	0.033738
1.330	0.1161	1.4547	222	12	4	0.99117948−0.98658209=0.459739	0.052951
1.672	0.1460	1.4248	310	13	0	0.97840682−0.97397438=0.443244	0.082452
1.868	0.1631	1.4077	310	13	0	0.97840682−0.97363461=0.477221	0.102681
3.619	0.3159	1.2549	220	12	0	0.90314476−0.89899759=0.414717	0.347067
3.710	0.3239	1.2469	220	12	0	0.90314476−0.89870885=0.443591	0.364125
4.091	0.3572	1.2136	214	7	16	0.87897334−0.87338604=0.558730	0.427101
4.148	0.3621	1.2087	214	7	16	0.87897334−0.87451729=0.445605	0.438947
4.279	0.3734	1.1974	106	1	36	0.86757458−0.86262977=0.494481	0.459141
4.356	0.3803	1.1905	106	1	36	0.86757458−0.86221381=0.536077	0.475205
4.534	0.3959	1.1749	205	4	25	0.85126527−0.84705720=0.420807	0.503879
4.607	0.4022	1.1686	205	4	25	0.85126527−0.84590896=0.535631	0.518990
5.797	0.5062	1.0646	302	9	4	0.76539329−0.76111732=0.427597	0.715704
5.844	0.5103	1.0605	302	9	4	0.76539329−0.76143044=0.396285	0.726616

$$\alpha=(h^2-k^2-hk),\quad \gamma=l^2,\quad \delta=\sin^2 2\theta_{\text{exp}}.$$

Employing the Cohen‡ analysis:

$$\begin{aligned}
1208\,\Delta A_1+\ \ 664\,\Delta C+36.05034\,D&=0.5266834,\\
664\,\Delta A_1+\ 4418\,\Delta C+79.1810\ D&=0.840763,\\
36.05034\,\Delta A_1+79.1810\,\Delta C+2.649494\,D&=0.02431065.
\end{aligned}$$

$$\Delta A_1=0.000345186,\quad A_1'=0.075262063,\quad A_1=A_1'-\Delta A_1';$$
$$\Delta C=0.00012523,\quad C'=0.02200868,\quad C=C'-\Delta C.$$

Finally,

$$a=\frac{\lambda}{(3A_1)^{\frac{1}{2}}}=3.2495\text{A},\quad c=\frac{\lambda}{(4C)^{\frac{1}{2}}}=5.2068\text{A}.$$

* Each s value is the mean of five readings.
** Numerical values from: Federal Works Agency, Work Projects Administration for the City of New York, *Tables of Sines and Cosines*, 1940, which permit accurate interpolation for eight figures in sine value for five figures in θ.
‡ See reference 1.

TABLE II. Lattice constants of ZnO. Results from twenty-five films using the first method (Straumanis method, employing simple measuring scale). $\lambda K\alpha_1=1.54050$A; $\lambda K\alpha_2=1.54434$A.

a	c
3.2495A	5.2070A
3.2497	5.2072
3.2496	5.2076
3.2497	5.2088
3.2495	5.2068
3.2495	5.2063
3.2494	5.2077
3.2494	5.2066
3.2494	5.2060
3.2494	5.2075
3.2492	5.2064
3.2493	5.2065
3.2493	5.2058
3.2493	5.2052
3.2495	5.2071
3.2495	5.2060
3.2494	5.2063
3.2493	5.2069
3.2496	5.2066
3.2496	5.2082
3.2495	5.2067
3.2498	5.2083
3.2496	5.2074
3.2496	5.2065
3.2494	5.2063
(mean) $\overline{3.2495\text{A}}$	(mean) $\overline{5.2069\text{A}}$

$$a=(3.2495\pm0.00002)\text{A},$$
$$c=(5.2069\pm0.00011)\text{A}.$$

To determine whether this larger spread is due to employing a constant R (not using the individual calibration of the Straumanis method) or to greater uncertainties in the dividing engine readings, five of the twenty-five films were analyzed in the following manner. The Debye-Scherrer radii measurements of the second method (employing dividing engine) were combined with the Straumanis calibration for camera radius data available from the first method. The results of this procedure are $a=3.24877$A with a spread of 0.00127A and $c=5.20549$A with a spread of 0.00414A. The values of a and c determined from the same five films using the second method (dividing engine and constant R) show a spread in a of 0.00125A and a spread in c of 0.00415A. These almost identical results show definitely that the uncertainties in setting the dividing engine, not the small variation in R, are responsible for the original larger spread of the second method. Therefore, a practical conclusion is that the use of a precision measuring instrument, such as the dividing engine, for measuring Debye-Scherrer ring radii is not necessary and is even undesirable apparently because the magnifying power of the optical system of precision micrometers leads to uncertainties in settings on the photographic lines.

Bunn's values[3] for a and c (obtained by the Bradley-Jay graphical extrapolation method, not the Cohen analytical method) corrected for the wave-lengths here employed are: $a=(3.2492\pm0.0001)$A and $c=(5.2054\pm0.0003)$A. It is seen that the present Table II results are somewhat larger than those of Bunn. As originally observed and explained by Bunn,[3] in the present work the error in c is larger than the error in a. It is pointed out that in the present work a total of 350 back-reflection lines were measured and therefore the statistical reliability should be good.

[3] C. W. Bunn, Proc. Roy. Soc. **47**, 835 (1935).

The Virtual Mass of a Sphere Entering Water Vertically*

ALBERT MAY AND JEAN C. WOODHULL
Naval Ordnance Laboratory, White Oak, Silver Spring, Maryland
(Received June 23, 1950)

The manner in which a sphere behaves when it enters the water from air depends on the rate at which energy is taken from it, and most of this energy is utilized in setting water into motion. The virtual mass is a partial measure of this motion. An investigation of virtual mass for spheres shortly after vertical water entry is described. The spheres used had specific gravities between 1.06 and 16.77 and impact velocities ranged from 21 to 103 ft./sec. The value of the virtual-mass coefficient was found to be much smaller than had previously been estimated, an average value of 0.08 being obtained. The method used recognizes the dependence of C_D on sphere speed and depth, and makes comparisons only where these parameters have the same value.

INTRODUCTION

THE concept of virtual mass is well known[1] in its application to the motion of a body completely immersed in a fluid. It arises from the fact that when a body moves through a fluid a quantity of fluid shares in the motion of the body. When the body is accelerated, this virtual mass (or "apparent additional," "induced," or "dragged" mass) must be accelerated also, and the body accordingly behaves approximately as though its mass were increased by an amount equal to the virtual mass.

The virtual-mass concept is useful, but not necessary, in the mathematical treatment of such problems as the accelerated motion of a completely immersed body. When this concept is used the assumption is made that the drag force, dependent on the speed but not on the acceleration, acts on both the moving body and on the entrained mass of water. In other words, the entrained water is treated as if it were a part of the moving body and the effective forces are those which act on their combined masses. This viewpoint has been used in the present report. Alternatively, attention could be focused on the actual forces (e.g., drag) acting on the sphere alone. For accelerated motion the magnitude of such forces would depend on the amount of water entrained by the body. Hence from this second viewpoint the drag coefficient is a function of the acceleration of the body, but the drag forces act totally on the sphere itself.

If potential flow is assumed, computation for a completely immersed sphere moving through a fluid shows the increase of mass to be one-half the mass of the displaced fluid.[2] This result is reasonably verified by experiment.[3]

The drag which a body experiences when it moves in a fluid is not measured directly but is deduced from the acceleration. Generally it is expressed in terms of the drag coefficient C_D which is defined by the relation,

$$\text{drag}=\tfrac{1}{2}\rho v^2 A C_D, \tag{1}$$

where ρ is the density of the fluid, and v and A are the speed and cross-sectional area of the missile.

The equation of motion of a body moving through a fluid may be written

$$-(1/v^2)dv/dt=d(1/v)/dt=\alpha, \tag{2}$$

where the retardation coefficient α is constant or variable, depending upon the conditions under which the body is moving. Obviously from Eq. (2), if $1/v$ is plotted against t, the slope of the graph will be α. To study the drag at water entry[4] high-speed motion pictures are taken of the entry, time and position data are read from the film, and instantaneous values of speed are obtained from increments of distance and time. Next a graph is drawn of reciprocal speed against time and from its slope α is obtained.

So far the analysis has been entirely kinematic. Since α is a measure of the acceleration, its value, of course, depends on the mass of the sphere, but it is uniquely determined by position-time data and does not depend on the viewpoint that is chosen in regard to the mass of the moving body, that is, whether it is taken as the mass of the body alone or this increased by the virtual mass.

The mass of a homogeneous body may be written as $V\sigma\rho$, where V is the volume of the body, σ its specific gravity relative to water, and ρ the absolute density of water. When the body is moving in water the mass of entrained water may be written $kV\rho$, where k is a proportionality constant which will be called the virtual-mass coefficient. This coefficient has also been known as the "induced mass factor" and the "relative apparent mass." The total mass accelerated is therefore $(\sigma+k)V\rho$.

From Eq. (2) the acceleration is αv^2. Hence,

$$\text{drag}=(\sigma+k)V\rho\alpha v^2. \tag{3}$$

Suppose that two spheres differing only in specific gravity are moving vertically downward at the same speed. If it is assumed that the drag force is the same

* Sponsored by the ONR.

[1] Cf. H. Bateman, "Report of the Committee on Hydrodynamics," Part IV; National Research Council Bulletin No. 84 (National Research Council, Washington, D. C., 1932).

[2] H. Lamb, *Hydrodynamics* (Dover Publications, Inc., New York, 1945), 6th Edition, p. 124.

[3] G. Cook, Phil. Mag. **39**, 350 (1920).

[4] A. May and J. C. Woodhull, J. App. Phys. **19**, 1109 (1948).

TABLE I. Measured specific gravities of ½-inch spheres used.

Material	Specific gravity
Polystyrene	1.06
Magnesium	1.79
Steel	7.76
Tungsten	16.77

for the two spheres, and that it acts both on the sphere itself and on the added mass of the entrained water, then

$$\text{drag}=(\sigma_1+k)V\rho\alpha_1 v^2=(\sigma_2+k)V\rho\alpha_2 v^2, \qquad (4)$$

where the subscripts 1 and 2 refer to the lighter and heavier spheres, respectively. From Eq. (4) we may write

$$k=\frac{\sigma_2\alpha_2-\sigma_1\alpha_1}{\alpha_1-\alpha_2}. \qquad (5)$$

The experiment just outlined furnishes one of the principal means of investigating virtual mass.

DETAILS OF THE METHOD

In the present paper, calculations of virtual mass will be given only for the vertical water entry of spheres and in particular for that phase which immediately follows the actual entry, during which an air-filled cavity is still attached to the sphere. Previous determinations of virtual mass for this case have been made in an attempt to systematize the empirical data of water entry but have apparently been described only in literature which was restricted in distribution for reasons of national security. A value of 0.40 or 0.45 was generally reported for k. The values of α (or C_D) from which these determinations were made were not comparable in precision with values obtainable today.

Numerous improvements in method were found desirable or necessary in the course of the present work. In the determinations of α that we reported previously,[4] values of $1/v$ were plotted against t and the slope of a least-square straight line through these points was taken as the value desired. The accuracy has now been improved sufficiently to justify replacing this straight line by a curve which yields instantaneous values of α.

When Eq. (5) is used for determining the virtual-mass coefficient it is assumed that the same drag acts on the two spheres used. Forces which are not hydrodynamic in nature should preferably be eliminated but it is sufficient that they be the same for the two spheres. In obtaining values of k from Eq. (5), we have always compared two spheres when the speed and depth of the spheres were the same and their cavities had the same pressure. Further, as will be discussed later, the contribution of weight to the total force on the sphere was removed mathematically.

Each determination of k was made from the water entry of a pair of half-inch spheres: one of steel or tungsten and the other of polystyrene or magnesium. The measured specific gravities of these spheres are given in Table I. The choice of such a pair depends on the fact that if two shots are so chosen that the entry speed of the lighter is slightly greater than that of the heavier, corresponding points can always be found in the two trajectories where the depths and speeds are the same. The choice of such conditions prevents the drags differing because of different speeds and should result in reasonably equal hydrostatic buoyant forces on the two spheres.

The effect of cavity pressure was removed by reducing the air pressure above the water, thus preventing surface closure of the cavity.[5] The cavities obtained and the considerable difference in cavity formation for light and heavy spheres can be seen in the photographs of Fig. 1. These were taken 26 milliseconds after the ½-inch tungsten and polystyrene spheres had entered the water at 63 ft./sec. The tungsten sphere had reached about three times the depth of the polystyrene sphere and was traveling about three times as fast. At shallower and equal depths the cavities are much more alike than those of Fig. 1. This is important since different

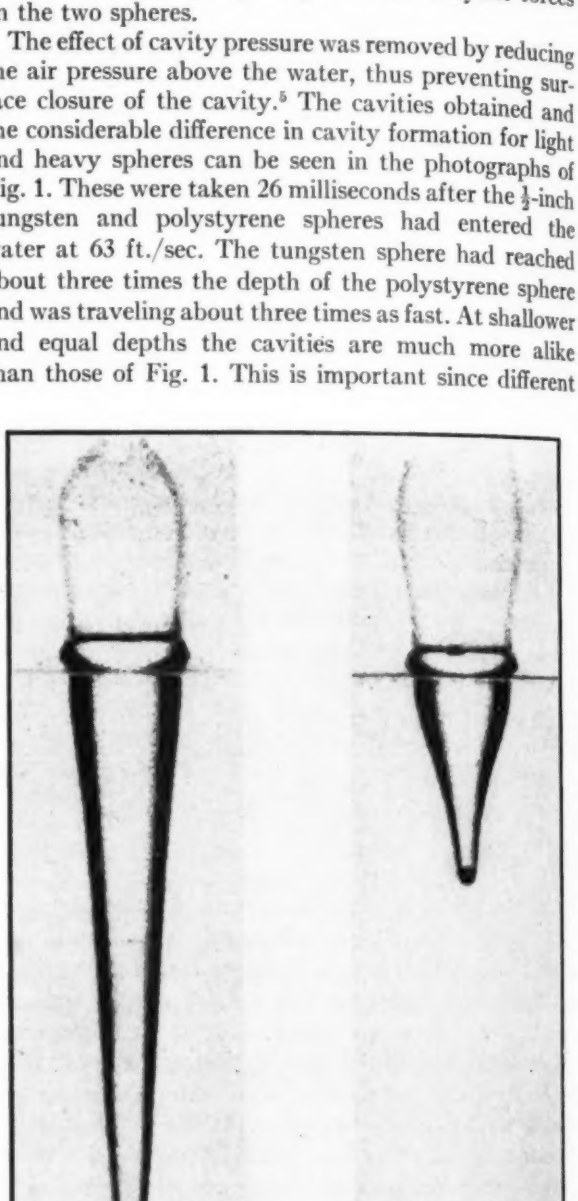

a b

FIG. 1. a. Tungsten; b. Polystyrene. Photographs of ½-inch spheres 26 milliseconds after they entered water at 63 ft./sec., showing dependence of cavity shape on sphere density.

[5] D. Gilbarg and R. A. Anderson, J. App. Phys. **19**, 127 (1948).

TABLE II. Determinations of virtual-mass coefficient.

Low density sphere				High density sphere				Compared at		
Mat'l	Entry speed (ft./sec.)	α_2(in.$^{-1}$)	C_D	Mat'l	Entry speed (ft./sec.)	α_1(in.$^{-1}$)	C_D	Speed (ft./sec.)	Depth in diameters	k
Poly.	59	0.356	0.251	Steel	21	0.0527	0.273	18.1	6.4	0.11
Poly.	59	0.350	0.247	Steel	32	0.0514	0.266	29.0	3.7	0.10
Poly.	59	0.350	0.247	Steel	38	0.0487	0.252	34.2	2.6	0.03
Poly.	62	0.358	0.253	Steel	32	0.0514	0.266	29.0	3.6	0.06
Poly.	64	0.347	0.245	Steel	21	0.0527	0.273	17.9	6.6	0.14
Poly.	64	0.341	0.241	Steel	32	0.0516	0.267	28.9	3.8	0.14
Poly.	64	0.341	0.241	Steel	38	0.0506	0.262	34.2	2.8	0.11
Poly.	64	0.341	0.241	Steel	38	0.0487	0.252	34.2	2.8	0.04
Poly.	103	0.344	0.243	Steel	32	0.0520	0.269	26.6	7.1	0.13
Poly.	103	0.343	0.242	Steel	65	0.0522	0.270	59.9	2.3	0.14
Poly.	103	0.343	0.242	Steel	78	0.0524	0.271	76.6	0.9	0.15
Poly.	103	0.344	0.243	Tungsten	40	0.0231	0.258	39.1	4.7	0.07
Poly.	103	0.343	0.242	Tungsten	62	0.0245	0.274	59.5	2.3	0.15
Poly.	103	0.343	0.242	Tungsten	62	0.0248	0.277	58.7	2.4	0.16
Mg.	62	0.228	0.273	Steel	21	0.0551	0.285	15.9	12.1	0.10
Mg.	62	0.218	0.261	Steel	32	0.0522	0.270	26.3	7.7	0.09
Mg.	62	0.218	0.261	Steel	38	0.0510	0.264	31.7	6.0	0.03
Mg.	62	0.218	0.261	Steel	38	0.0495	0.256	31.7	6.0	−0.04
Mg.	95	0.247	0.296	Steel	21	0.0572	0.296	14.5	16.3	0.00
Mg.	95	0.200	0.263	Steel	32	0.0529	0.274	23.6	11.9	0.10
Mg.	95	0.221	0.264	Steel	38	0.0516	0.267	28.9	10.0	0.03
Mg.	95	0.223	0.267	Steel	38	0.0502	0.260	28.9	10.0	−0.04
Mg.	95	0.218	0.261	Steel	58	0.0522	0.270	53.4	4.5	0.08
Mg.	95	0.218	0.261	Steel	65	0.0522	0.270	58.0	3.6	0.08
Mg.	95	0.217	0.260	Steel	78	0.0524	0.271	77.0	0.8	0.11
Mg.	95	0.219	0.262	Tungsten	40	0.0232	0.259	37.9	7.8	−0.02
Mg.	95	0.218	0.261	Tungsten	62	0.0246	0.275	58.5	3.7	0.11
Mg.	95	0.218	0.261	Tungsten	62	0.0248	0.277	57.5	3.8	0.12

cavity shape means a different flow pattern and probably different drag.

In writing Eq. (2) the effect of gravity was omitted. Instead, it may be written

$$d(1/v)/dt = -g/v^2 + \alpha. \tag{6}$$

It is seen from Eq. (6) that the slope of the $1/v$ against t graph is $-g/v^2+\alpha$. The effect of gravity can be eliminated and α determined, by adding g/v^2 to the slope of the graph at any desired point. This correction of α effectively eliminates the weight which otherwise would make large and considerably different contributions to the drag of the light and heavy spheres.

RESULTS

High-speed motion pictures were taken of numerous shots of each of the spheres listed in Table I at various entry speeds from 21 to 103 ft./sec. Position-time data were read from each film, values of $1/v$ were plotted against t, and a smooth curve was drawn. By comparing each shot of a dense sphere with each suitable shot of a light one, the corresponding positions were found where the speed and depth of the spheres were the same. The slopes of the $1/v$ against t graphs were read at these points and values of α were obtained by adding g/v^2 to the slopes. Finally k was found by means of Eq. (5).

The values found for k and related information are given in Table II. These values for k range from -0.04 to 0.16. Negative values are surely meaningless but may give some indication of the accuracy attainable. It should be noted especially that the values here reported for k are considerably smaller than the values of about 0.45 previously obtained by others. A small part of this difference may be due to the low ambient pressure used in the present work. This changes the cavity shape and hence the flow pattern, and may change the virtual mass slightly.

An attempt was made to determine whether the variations of k shown in Table II were due to variations of depth or of instantaneous velocity, by plotting the k values against these quantities as coordinates in Fig. 2. Nothing significant appears in this presentation.

In studying the self-consistency of the data, the scatter of the data will appear worst if all variation of k is regarded as due to experimental error, rather than to dependence of k on experimental parameters. On this basis the data yield a mean value of 0.08 for k and a standard deviation of 0.06.

It should be noted that the average value of k obtained by use of polystyrene spheres was twice that for the magnesium spheres: 0.109 for polystyrene, 0.054 for magnesium. The reason for this is not known.

An interesting view of the virtual-mass coefficient may be obtained by a method which requires that random errors in determining the values of α be more important than actual variations in the value of α. Suppose that $1/v^2$ times the drag, in Eq. (4), is negligibly dependent on sphere density, depth and speed. Then, since the expression in Eq. (4) has the same value for either subscript 1 or 2, this subscript can be written as i,

and Eq. (4) becomes:

$$\alpha_i\sigma_i + k\alpha_i = \text{constant}. \tag{7}$$

If $\alpha_i\sigma_i$ is plotted against α_i, Eq. (7) shows that a straight line should be obtained, of slope $-k$. The data of Table II are plotted in Fig. 3, but no attempt has been made to draw in this line for the determination of k, because of the large spread in the data. Instead groups of straight lines are seen drawn transverse to the principal extension of the data. Each of these lines represents the spread of data obtained from one water entry and the individual values of α from Table II are shown as dots on these lines. To determine k it would be possible to draw straight lines which lie within the range of values plotted for all materials. They would give k values between 0.07 and 0.13.

DISCUSSION

The reasons why the value of virtual mass obtained for the cavity phase of vertical water entry is so small can best be understood by considering the significance of virtual mass as it occurs in various idealized hydrodynamic problems.

For potential flow about a completely immersed body, with no attached cavity, energy is conserved and the drag is zero. The fluid surrounding the body has at each point a speed which is proportional to that of the body, and the body is in "immediate" communication with all of the water affected by the body's motion. When the speed of the body changes, the speed of each particle of the water changes proportionately. The virtual mass is that mass of the fluid which would have a kinetic energy equal to the actual kinetic energy of the fluid if this mass had the same speed as the body, or $(\int v^2 dm)/v_s^2$, where v is the speed of the fluid at any point and v_s is the speed of the body at the same instant. For this situation all the water which is in motion contributes in some degree to the virtual mass.

Let us now determine the virtual mass by subjecting the completely immersed body to an imaginary acceleration. The speeds of all water particles will be changed proportionately and the total work done by the accelerating force will be that done in changing the speed of the combined mass; mass of the sphere plus virtual mass.

Next let the proposed experiment be repeated with two bodies that differ only in specific gravity, and arrange that the total forces are the same on the two bodies (disregarding gravity, whose influence can be removed mathematically). The accelerations will be different for the two bodies. From the accelerations the virtual mass can be calculated. The experimental tests described in this report were of this type except that cavities were attached to the bodies.

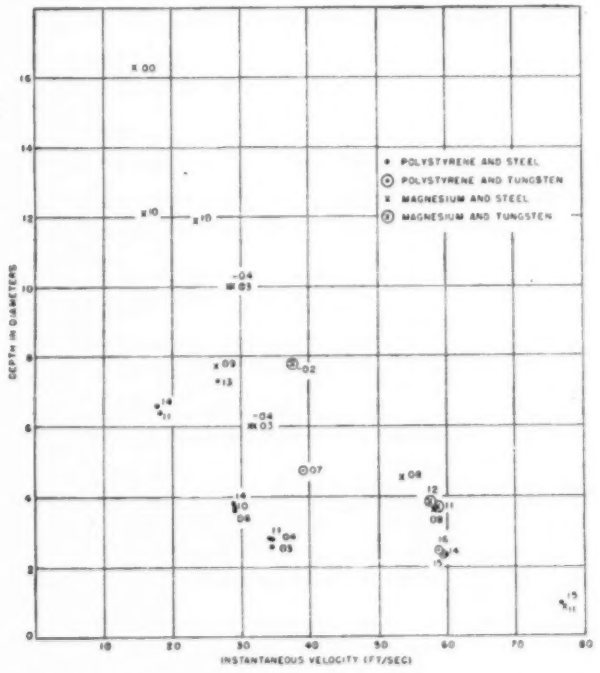

FIG. 2. Virtual-mass coefficient for vertical water-entry of spheres. Values (in percent) are plotted against the depth of the sphere and its velocity, at the instants for which the values were determined.

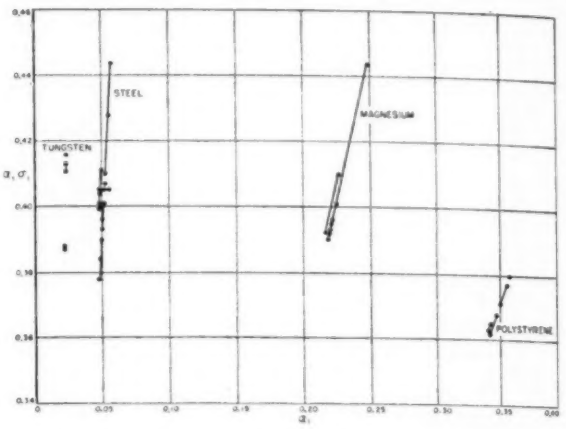

FIG. 3. Plot for the determination of virtual-mass coefficient on assumption that it has a single fixed value. The value required would be the negative of the slope of a straight line (not shown) passing through the center of several groups of points.

Before discussing the case of the water-entry cavity it is instructive to consider the steady-state cavity behind an obstacle in a water tunnel. One important difference between this case and the case of potential flow without a cavity is the absence of liquid immediately behind the body. There are still forces on the rear of the body due to water vapor and perhaps air in the cavity, but the "immediate" connection between the body and much of the water which it affects has disappeared. If the water throughout the tunnel were given a sudden increment of speed, water surrounding after-portions of the cavity would not be informed of the change of relative velocity between the water and the body for an appreciable time. The transverse diameter of any section of the cavity, therefore, depends not

so much on the present relative speed between body and water, as on the relative speed when that cross section of water was traversing the body's nose. (This effect is evident in the water-entry case shown in Fig. 1 where the diameters of the two cavities are nearly the same at the water surface because the speeds of entry were the same, and in spite of the greatly different speeds that existed later.) Because of this effect the virtual mass associated with steady-state cavity flow will be small.

Water which is set into motion by the body and is then without hydrodynamic contact with it, contributes to the drag but not to the virtual mass. It is evident from the geometry of the cavity that only a small amount of the water pushed out of the way by a body followed by a cavity, remains in hydrodynamic communication with the body, and this means simply that the virtual mass is small. While the cavity phase of water-entry is more difficult of treatment it is reasonable that it should have a virtual mass similar to that of the water-tunnel cavity.

CONCLUSION

The values reported here for virtual mass in the cavity phase of water-entry are small and show large percentage fluctuations. No systematic trends in the data and no reasons for the fluctuations have been found. However, it is not surprising that the small value of virtual mass should vary considerably because of the transient and variable character of the motion.

Because its magnitude is small and variable it appears improbable that virtual mass can help greatly in systematizing the data from water-entry experiments.

ACKNOWLEDGMENTS

The authors wish to express their indebtedness to members of the Hydroballistics Division, especially to Dr. J. Howard McMillen for stimulating discussions during the progress of this work, and to Mr. D. J. Milano who carried out the experimentation; also to Mr. Noel R. Corngold for his assistance in analyzing the data and to Professor Garrett Birkhoff for his many helpful discussions.

Plastic Flow of Platinum Wires

R. P. Carreker, Jr.

Research Laboratory, General Electric Company, Schenectady, New York

(Received June 16, 1950)

The strain-time behavior of annealed platinum wires at constant stress and temperature is reported for a wide range of experimental conditions, namely: 1550 to 78°K, 900 to 40,000 p.s.i., 0.001 to 0.1 strain, 10^{-1} to 10^{-6} min.$^{-1}$ strain rate.

The following relations were found to describe the results satisfactorily:

$$\sigma = A\dot{\epsilon}^{n}|_{\epsilon,T}; \quad \sigma = Be^{pT}|_{\epsilon,\dot{\epsilon}},$$
$$\epsilon = Ct^{a}|_{\sigma,T}; \quad \frac{\partial n}{\partial T} = \frac{\partial p}{\partial \log\dot{\epsilon}}|_{\epsilon},$$
$$Q \sim \log\sigma|_{\epsilon,t};$$

where σ=stress, ϵ=strain, $\dot{\epsilon}$=strain rate, T=absolute temperature, Q=activation energy for rate of deformation, t=time, and A, B, C, a, n, and p are constants.

INTRODUCTION

THERE is a paucity of good experimental data on the resistance to plastic deformation as a function of the amount, temperature, and rate of the deformation. Many experiments pertaining to deformation are reported in the literature, but surprisingly few data exist for which tests were performed on a single material with a definite prior history, under definitely stated and controlled conditions, over a sufficiently wide range of rate and temperature to be useful in formulating and testing theories of deformation.

This paper reports the results of a study of the strain-time behavior of a pure metal as a function of stress and temperature. The tests were of the short-time variety, lasting from a few seconds to several days.

MATERIAL

In view of the large number of identical specimens required, small wire specimens seemed appropriate. All specimens were taken from the same length of 99.98+ percent platinum[1] wire, which was cold-drawn through diamond dies from 0.020 to 0.015 in. diameter. After mounting in the testing equipment each specimen was annealed *in situ* for 10 min. at 1670°K by passing a predetermined electric current through the wire. This treatment produced a grain size of two to four grains per cross section.

TESTING EQUIPMENT

The testing apparatus was obtained from S. Dushman, of this Laboratory. A description of its original form has been published.[2] Extension of the wire specimen permits the movement of a grating parallel to a similar stationary grating, modulating a light beam

[1] Spectrographic analysis indicated traces (<0.01 percent) of Fe and Pd.

[2] Dushman, Dunbar, and Huthsteiner, J. App. Phys. **15**, 108 (1944).

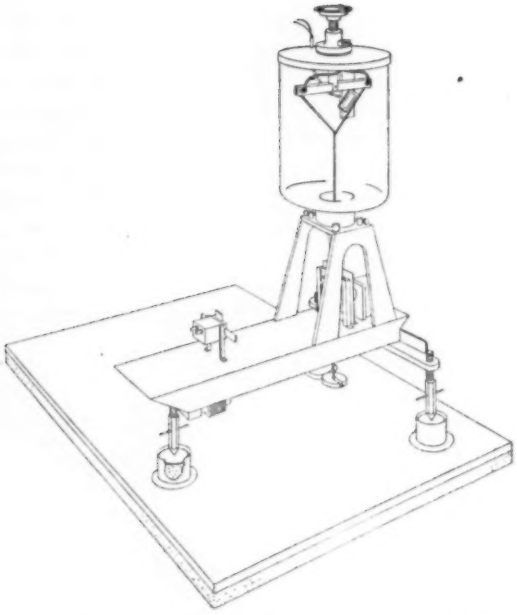

FIG. 1. Creep test equipment used above 1200°K.

striking a photo-cell. A change in light intensity from a minimum to a maximum corresponds to a grating displacement of 0.004 in. This system necessarily records only time-dependent strain.

Figure 1 shows the apparatus, as modified for use at temperatures above approximately 1200°K. In this arrangement the specimen is in the shape of a "V," supported at each end and loaded at the vertex. The specimen is heated internally by an electric current. Temperature of the specimen was indicated by a galvanometer which was activated by a photo-cell. The galvanometer was calibrated using an optical pyrometer as a secondary standard, correcting for emissivity and transmission effects. A black screen, not shown in Fig. 1, surrounded the glass test chamber, eliminating light from sources other than the specimen. Temperature control was achieved by bringing the specimen to the desired temperature, noting the reading of the indicating galvanometer, and manually adjusting the input voltage to correct any temperature change. Control within ± 10°K was attained.

Figure 2 shows the equipment as modified for use in the range 300 to 1200°K. A straight wire specimen was used, heated by a surrounding electric furnace that was controlled within ± 5°K by a Bristol potentiometer controller.

A liquid nitrogen bath was used to obtain the testing temperature of 78°K. In this case an insulated tank replaced the furnace of Fig. 2. Care was taken to maintain a constant bath level during each test. Temperatures were maintained within five degrees of the boiling point of liquid nitrogen, 78°K.

The choice of platinum as the specimen material eliminated the problem of oxidation at high temperatures. Pure dry nitrogen was passed through the furnace to increase the useful life of the stainless steel grips used with the straight wire specimens. The "V"-type specimens were tested in air.

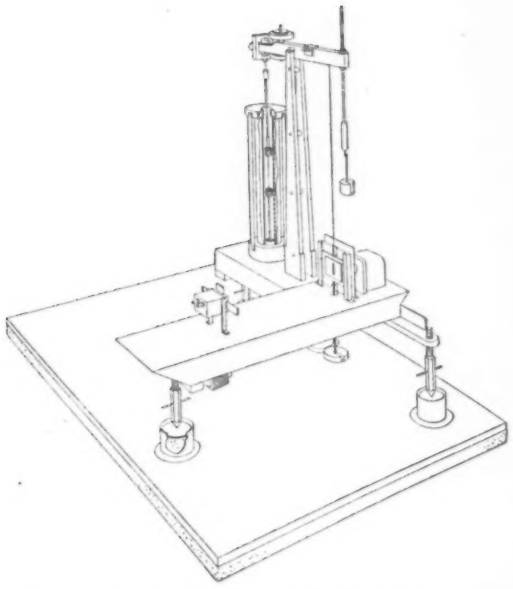

FIG. 2. Creep test equipment used between 300 and 1200°K.

CONSTANT STRESS

Two devices were used to maintain constant stress. The initial vertex angle of the "V" specimen was chosen to be 93°, so that constant stress was automatically maintained within 0.5 percent as the specimen elongated and the vertex angle became more acute.[3] The straight wire specimens were loaded through the bent lever shown in Fig. 2, whose dimensions were chosen to maintain constant stress within 0.2 percent as the specimen elongated.[4] Neither of these methods maintains constant stress after necking begins.

TESTING PROCEDURE

A. High Temperature "V"-Type Specimen

The specimen was mounted in the grips so that the distance between leg extremities was 20 cm. After annealing, the temperature was adjusted to the proper testing temperature by regulating the current flowing in the specimen. The load was placed on a weight pan hanging beneath the movable grating; a long, hooked wire (stainless steel 0.100 in. diameter) was then attached to the top of the movable grating and the hook lowered into the vertex of the "V." The displacement of the vertex was recorded as a function of time.

B. Straight Wire Specimens

The specimen was mounted between appropriate grips to give a gauge length of 3.0 in. The specimen and

[3] J. C. Fisher and R. P. Carreker, J. Metals **6**, 178 (1949).
[4] Fullman, Carreker, and Fisher (to be published).

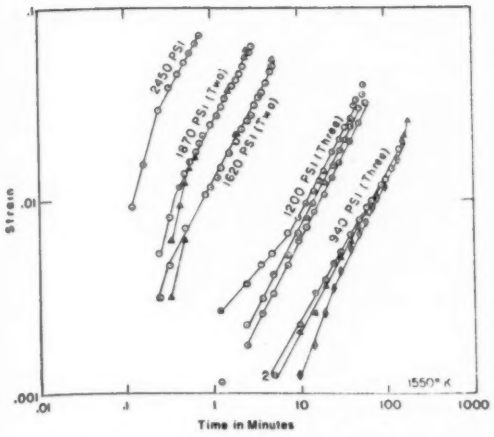

FIG. 3. Plastic strain of platinum as a function of time.

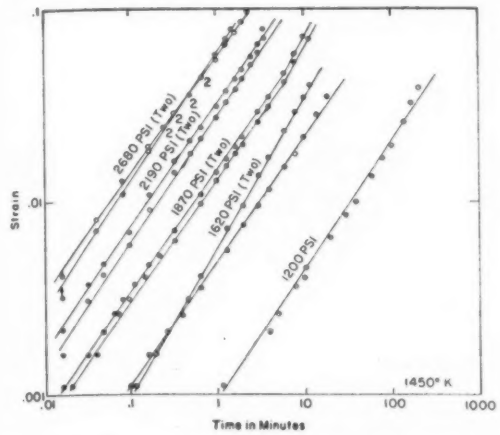

FIG. 4. Plastic strain of platinum as a function of time.

grips were lowered into the uniform temperature zone of the furnace, the lower grip securely fastened, and the upper grip attached to the constant stress lever. The position of the lever was such that no force was exerted on the specimen at this time. Electrical leads were fastened temporarily to the upper and lower grips for the annealing treatment. After removing the electrical leads from the specimen grips, the furnace (or tank) was brought from room temperature to the testing temperature. The selected load was then applied to the lever arm. Elongation of the specimen was recorded automatically as a function of time.

EXPERIMENTAL RESULTS

Several tests at different stresses were made at each of the following temperatures: 1550, 1450, 1350, 1250, 1100, 950, 850, 750, 650, 550, 450, 300, and 78°K. The experimental data are presented as plots of log time-dependent strain *vs.* log time in Figs. 3 to 15, each figure presenting the data obtained at a particular temperature.

Short-time points are absent in the data taken at 1550°K. In this series the specimens were first loaded at room temperature and the heating current then applied. The recorded movement was corrected for total thermal expansion. A short time elapsed before temperature equilibration was attained. Thus, this technique did not give satisfactory results during the first few seconds of the test. The 1550°K data have been included for their value at large strains. At all other temperatures the specimens were at temperature prior to loading.

In general, the log strain *vs.* log time plots are straight lines or approach straight lines at times in excess of one minute. The departures from linearity at short times are probably due to the difficulty in establishing the zero of time-dependent strain. This error is particularly noticeable at small strains and at times comparable with that required to apply the load to the specimen, approximately 1 to 2 sec. The error is negligible at strains greater than 0.01 and times greater than 1 min.

ANALYSIS OF EXPERIMENTAL RESULTS

The slopes of the log strain *vs.* log time plots, at strains not appreciably influenced by the zero error, depend strongly on temperature but are insensitive to

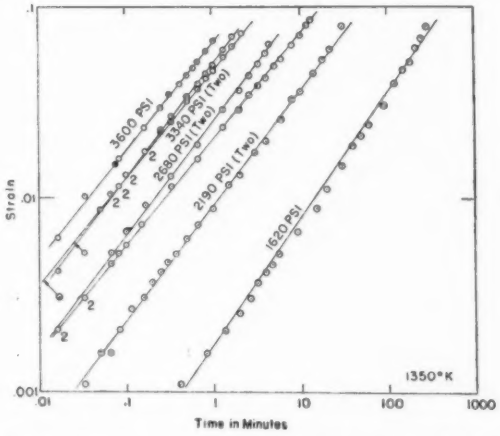

FIG. 5. Plastic strain of platinum as a function of time.

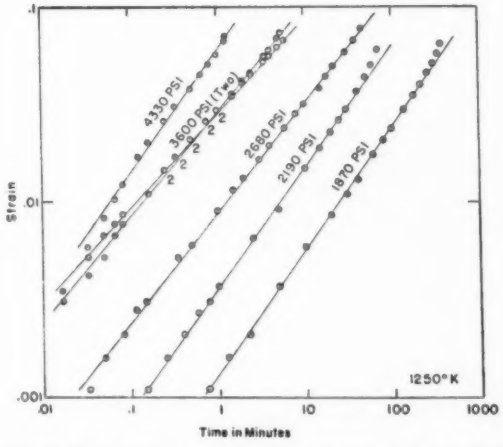

FIG. 6. Plastic strain of platinum as a function of time.

stress. These slopes have been plotted *vs.* temperature in Fig. 16. Figures 3 to 16 suggest the equation[5]

$$\epsilon = Ct^a,$$

where a is a number which apparently approaches 1.0 at the melting point and is small but positive at 0°K.

Consider the strain rates $\dot{\epsilon}$ of the various strain-time curves, at a particular value of the strain ϵ, as a function of the stress σ. At a strain of 0.01, the data from Figs. 3 to 15, when plotted as log stress *vs.* log strain rate, give the family of straight lines shown in Fig. 17, each line representing the results obtained at a particular temperature. Straight-line plots obtained in this manner imply that the relationship between stress and strain rate is of the form $\sigma = A\dot{\epsilon}^n|_{\epsilon,T}$. There is some scatter, but the trends are well established. Similar families were obtained by considering the results for strains equal to 0.005, 0.01, 0.02, and 0.03.

Consider the relationship between temperature and the stress necessary to produce a given strain rate at a given strain. The necessary data were obtained from Fig. 17 and plotted in Fig. 18. Log stress is linear in temperature, with some uncertainty below 450°K. Similar plots were obtained at strains of 0.005, 0.01, 0.02, and 0.03.

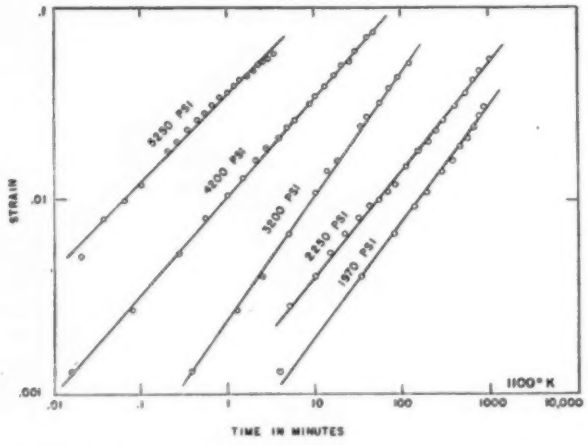

FIG. 7. Plastic strain of platinum as a function of time.

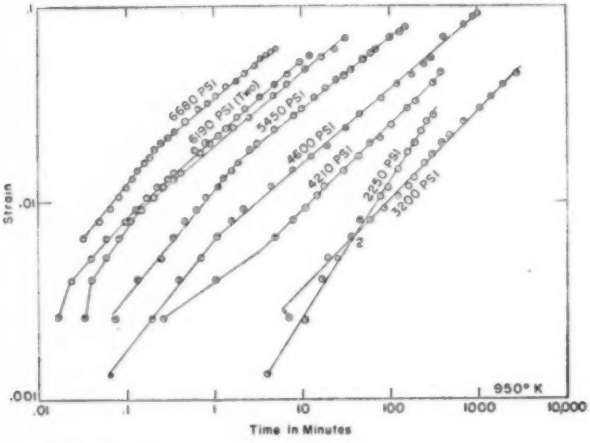

FIG. 8. Plastic strain of platinum as a function of time.

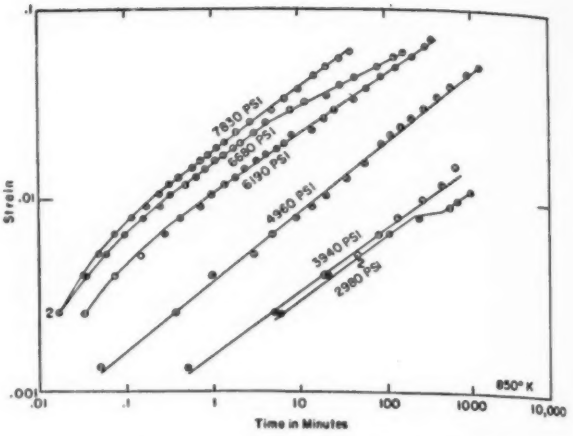

FIG. 9. Plastic strain of platinum as a function of time.

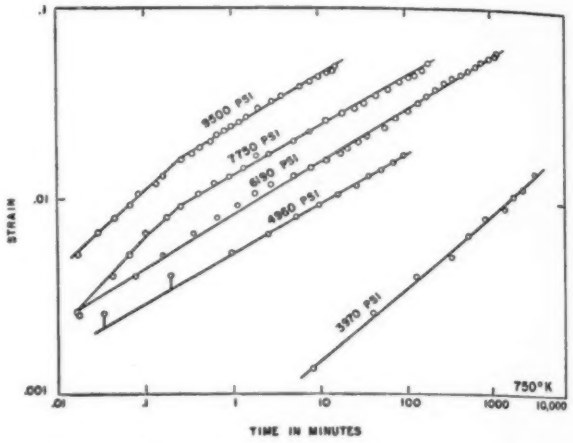

FIG. 10. Plastic strain of platinum as a function of time.

From consideration of Figs. 17 and 18, the following equations may be written:

$$\log\sigma = \log A + n\log\dot{\epsilon}|_{\epsilon,T} \tag{1}$$

and

$$\log\sigma = \log B + pT|_{\epsilon,\dot{\epsilon}}. \tag{2}$$

Previous research[6] has established the relation

$$\log\sigma = \log K + m\log\epsilon|_{\dot{\epsilon},T}. \tag{3}$$

If it is assumed that stress is a point function of strain, strain rate, and temperature, one may write

$$d\log\sigma = \frac{\partial\log\sigma}{\partial\log\epsilon}d\log\epsilon + \frac{\partial\log\sigma}{\partial\log\dot{\epsilon}}d\log\dot{\epsilon} + \frac{\partial\log\sigma}{\partial T}dT, \tag{4}$$

or

$$d\log\sigma = md\log\epsilon + nd\log\dot{\epsilon} + pdT. \tag{5}$$

[5] The following notations are used throughout this analysis: t = time. σ = stress = applied force ÷ instantaneous area. ϵ = natural strain = $\ln(l/l_0)$. $\dot{\epsilon}$ = strain rate. T = absolute temperature. $e = 2.718\cdots$. A, B, C, a, n, and p = constants.

[6] J. H. Hollomon, Metals Tech. 162, 268 (1945).

It is then possible to obtain analytically the general solution of Eq. (4).[7] Lubahn[8] has geometrically derived a general equation $\sigma=f(\dot{\epsilon}, \epsilon, T)$ using the relationships expressed in (1) and (3) and an expression for the activation energy for the deformation process. His equation may be written in the form

$$\sigma=CG^{T}(\dot{\epsilon}/\dot{\epsilon}_0)^{DT}e^{(E+E'T-FT\ \ln\dot{\epsilon}/\dot{\epsilon}_0)}, \qquad (6)$$

where C, G, $\dot{\epsilon}_0$, D, E, E', and F are constants. It should be noted that Eq. (6) includes the term $E'T$ which was omitted through a typographical error in the last equation of reference 8.[9] This equation is identical with that Leschen obtained analytically by the method of the exact differential and Eqs. (1) to (3).

The following relationships are obtained by differentiating the general equation (6). These relations offer alternative methods of determining the material constants from experimental data.

$$\frac{\partial^2 \log\sigma}{(\partial \log\dot{\epsilon})(\partial \log\epsilon)}=\frac{\partial m}{\partial \log\dot{\epsilon}}=\frac{\partial n}{\partial \log\epsilon}=-FT, \qquad (7)$$

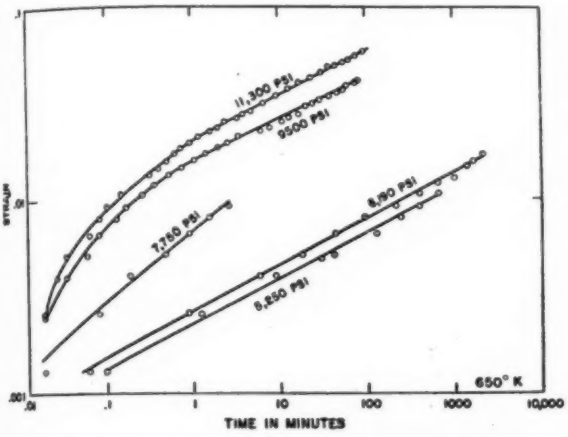

FIG. 11. Plastic strain of platinum as a function of time.

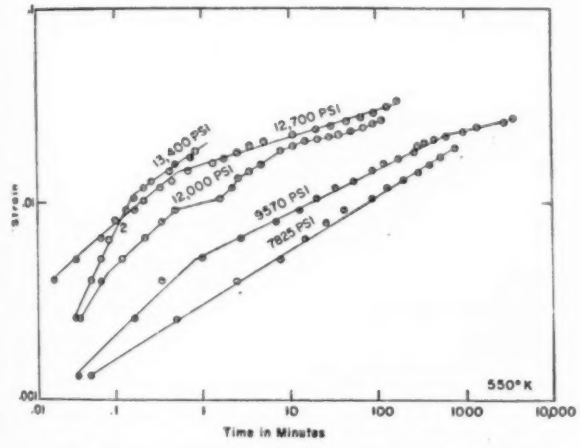

FIG. 12. Plastic strain of platinum as a function of time.

[7] J. G. Leschen (unpublished research).
[8] J. D. Lubahn, J. App. Mech. A-229 (September, 1947).
[9] C. Zener (private communication).

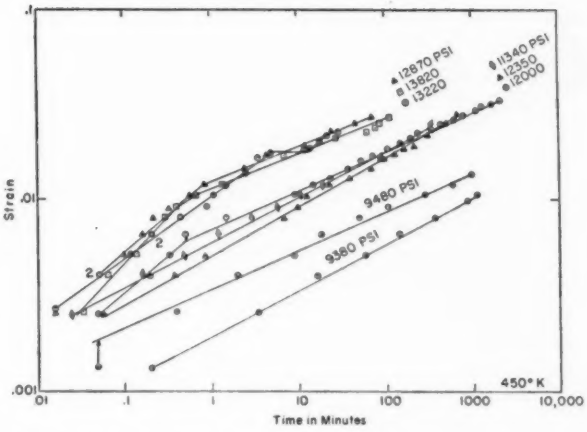

FIG. 13. Plastic strain of platinum as a function of time.

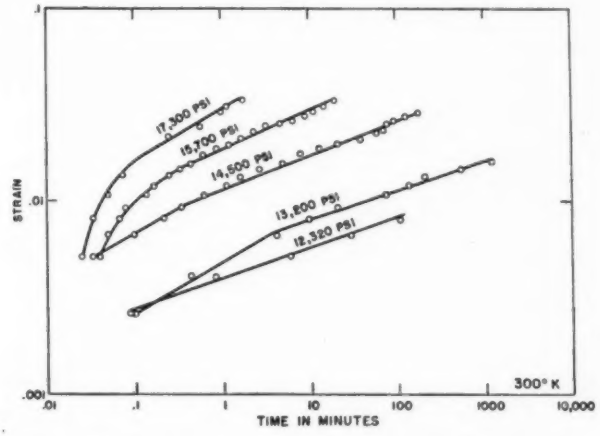

FIG. 14. Plastic strain of platinum as a function of time.

$$\frac{\partial^2 \log\sigma}{(\partial T)(\partial \log\dot{\epsilon})}=\frac{\partial n}{\partial T}=\frac{\partial p}{\partial \log\dot{\epsilon}}=D-F\log\epsilon, \qquad (8)$$

$$\frac{\partial^2 \log\sigma}{(\partial T)(\partial \log\epsilon)}=\frac{\partial m}{\partial T}=\frac{\partial p}{\partial \log\epsilon}$$

$$=E'-F\log\left(\frac{\dot{\epsilon}}{\dot{\epsilon}_0}\right), \qquad (9)$$

$$\frac{\partial^3 \log\sigma}{(\partial \log\epsilon)(\partial \log\dot{\epsilon})(\partial T)}=-F. \qquad (10)$$

Values of $\partial n/\partial T$ and $\partial p/\partial \log\epsilon$ may be obtained at constant values of strain. Values of n may be obtained from the slopes of the lines relating log stress to log strain rate at constant strain and temperature in Fig. 17. A plot of n *vs.* temperature is presented in Fig. 19. The points at 78°K are poorly defined due to the limited number of tests and small slopes at this temperature. Limits of 0.005 to 0.025 may be set with reasonable assurance. Values of p may be obtained from the slopes of the lines relating log stress to temperature at constant strain and strain rate in Fig. 18.

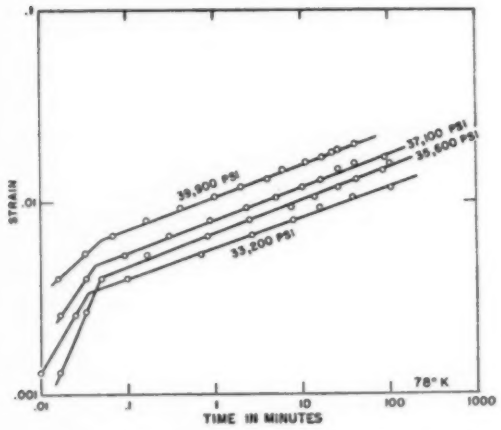

FIG. 15. Plastic strain of platinum as a function of time.

A plot of p *vs.* log strain rate is presented in Fig. 20. Equation (8) predicts that $\partial n/\partial T = \partial p/\partial \log\dot{\epsilon}|_{\epsilon}$. The following values for these quantities were obtained from Figs. 19 and 20:

$$\partial n/\partial T = 1.04\times10^{-4}\ \text{deg.}^{-1}$$

and

$$\partial p/\partial \log\dot{\epsilon} = 1.06\times10^{-4}\ \text{deg.}^{-1}.$$

Equations (7) to (9), together with Figs. 19 and 20, permit the quantity F to be taken as zero. Equation (6) then simplifies to the form

$$\sigma/\sigma_0 = (\dot{\epsilon}/\dot{\epsilon}_0)^{DT}\epsilon^{(E+E'T)}. \qquad (11)$$

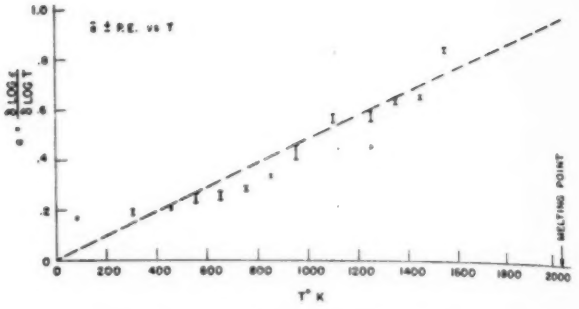

FIG. 16. Slopes of log strain-log time curves as a function of temperature (mean slope plus and minus probable error of mean).

In a creep test σ and T are constant and (11) can be reduced to $\epsilon = Ct^{n}$, the form observed in the present experiments.

Many rate processes are dependent on temperature through a relationship of the form

$$\text{rate} \sim e^{-Q/RT},$$

where Q is the "activation energy" of the process per gram atom, $R = 1.968$ cal. deg.$^{-1}$ mole^{-1} is the gas constant, and T is the absolute temperature. It may be instructive to consider deformation to be such a rate process. Then

$$d\epsilon/dt = \dot{\epsilon} = Ke^{-Q/RT}|_{\sigma,\epsilon}. \qquad (12)$$

Thus, a value of Q may be obtained from the slope of a

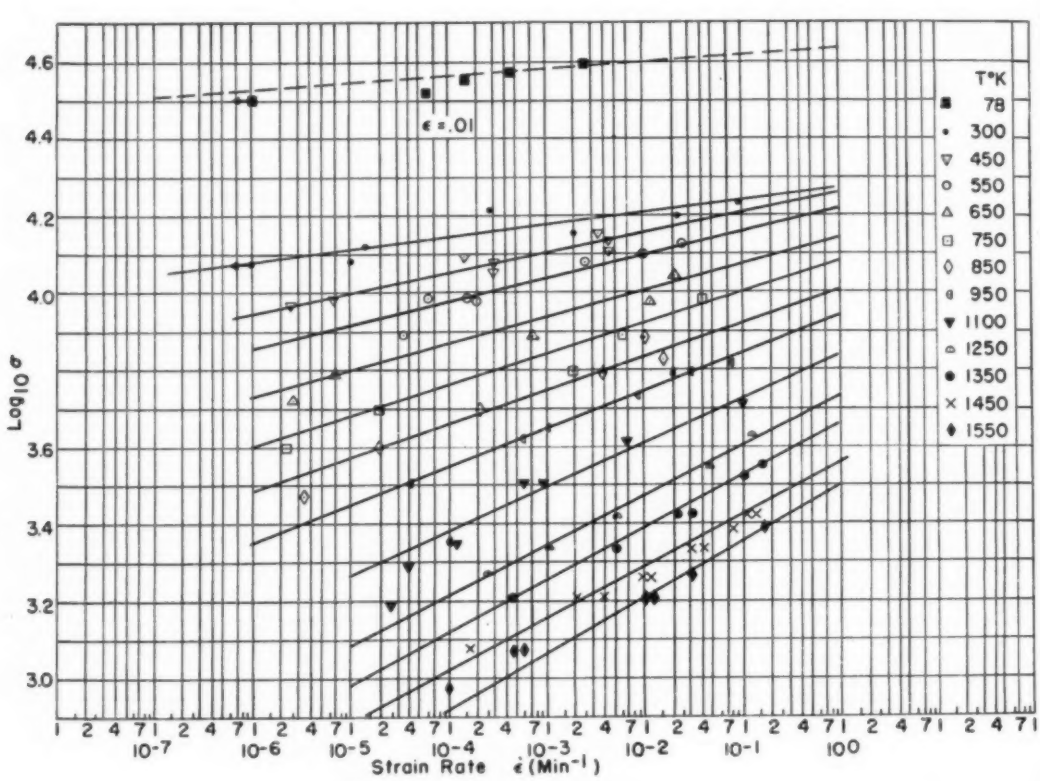

FIG. 17. Strain rate at a strain of 0.01 as a function of stress at several temperatures.

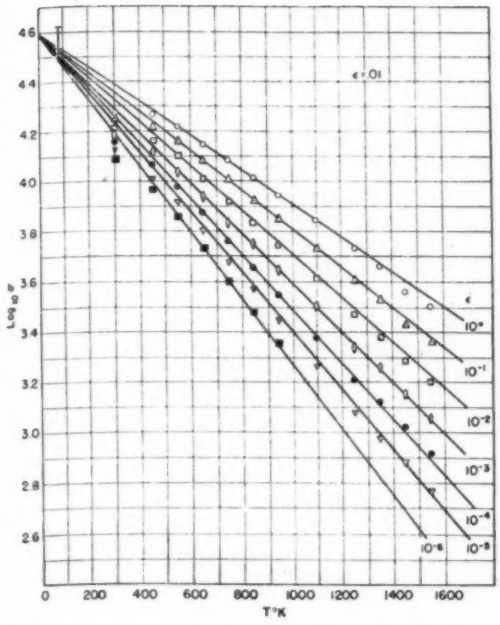

FIG. 18. Stress to produce several strain rates at a strain of 0.01 as a function of temperature.

plot of log$\dot{\epsilon}$ *vs.* $1/T$ at a particular value of stress and strain. The procedure may be repeated at other values of stress and strain to give the dependence of the activation energy on those variables. The data of Fig. 17 were cross plotted according to this procedure, resulting in Figs. 21 and 22. A similar procedure was followed considering strains of 0.005, 0.01, 0.02, and 0.03.

The form of the $Q=f(\sigma)$ relationship is of particular theoretical interest. Figure 22 shows that the decrease in Q with stress is not linear. The Becker[10]-Orowan[11] theory, in which attention is focused on the shear stress

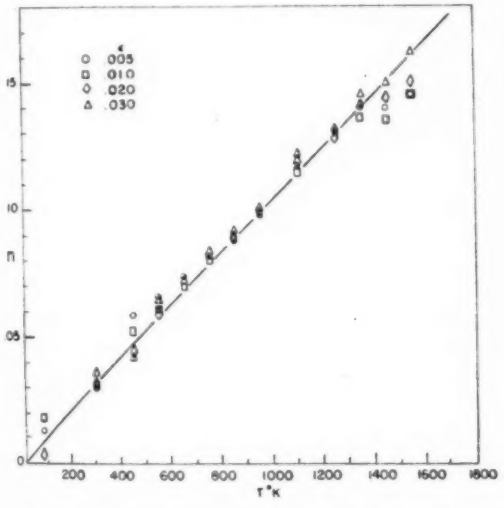

FIG. 19. Slopes of log stress-log strain rate curves as a function of temperature.

[10] R. Becker, Zeits. f. tech. Physik **7**, 547 (1926).
[11] E. Orowan, Zeits. f. Physik **89**, 605 (1934); **98**, 382 (1936).

required to plastically deform an elementary region, predicts a linear relationship between $Q^{\frac{1}{2}}$ and σ. The data do not conform to this relationship. Nucleation theory, as applied to the formation of slip bands by Leschen, Carreker, and Hollomon,[12] predicts linearity between $Q^{\frac{1}{2}}$ and σ. The data do not confirm this prediction. The (empirical) equation (6) predicts Q to be linear in logσ, at constant strain.[13] Figure 23 shows the data plotted in this manner. The relationship is more nearly linear than the other functions of stress considered.

A CRITICAL APPRAISAL

There are definite undesirable features in the experimental techniques employed in this investigation. The most important of these is the narrow range of strain available for analysis. The upper limit of strain, 0.03, was dictated by the practical consideration of time per test at low strain rates and a desire to avoid strains near fracture, which occurred at 0.05 to 0.10. The lower value, a strain of 0.005, was limited by the accuracy with which the zero of time-dependent strain

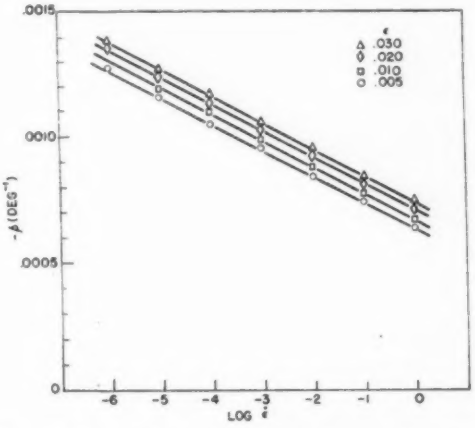

FIG. 20. Slopes of log stress-temperature curves as a function of strain rate.

could be established. The zero of strain was established within 0.001.

The effective initial gauge lengths of the specimens were taken as 3.0 in. for the straight specimens and 5.57 in. for the "V" specimens, but these values are subject to some error. The wires were inserted in the grips and the lengths measured within 0.1 in. The grips would not be expected to influence the stress pattern in more than ten diameters (0.15 in.) of the specimen length. The "V" wires were heated by electric current and had cold ends where they contacted more massive pieces of metal. The distance affected by such end losses was estimated at less than 0.5 in. from each point of contact. Thus, the gauge lengths of the high tem-

[12] Leschen, Carreker, and Hollomon, Metals Tech. **15**, T.P. 2476 (1948).
[13] J. H. Hollomon and J. D. Lubahn, Gen. Elec. Rev. (February and April, 1947).

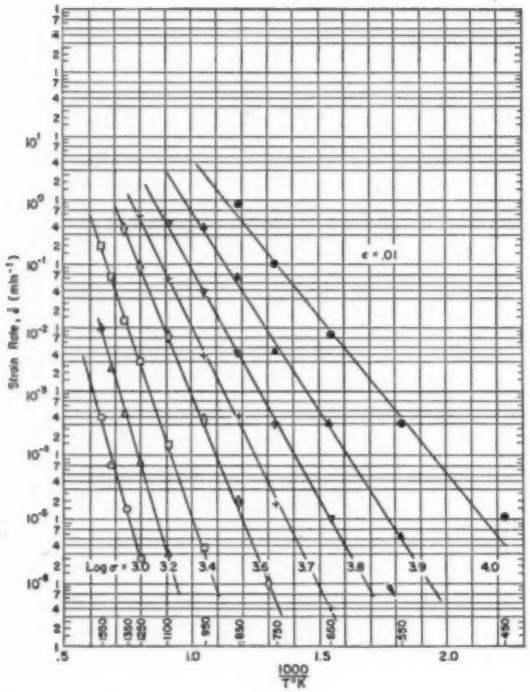

FIG. 21. Log strain rate at a strain of 0.01 *vs.* $1/T$ for several stresses.

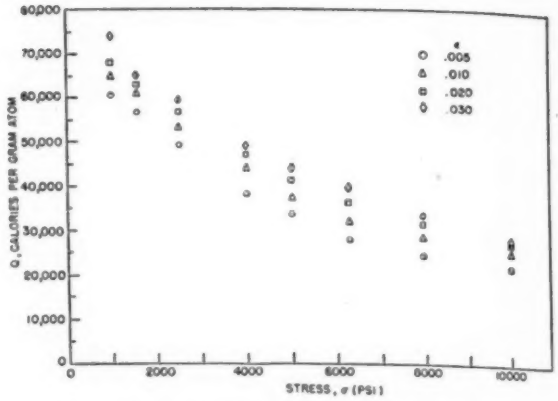

FIG. 22. Activation energy for plastic flow as a function of stress at several strains.

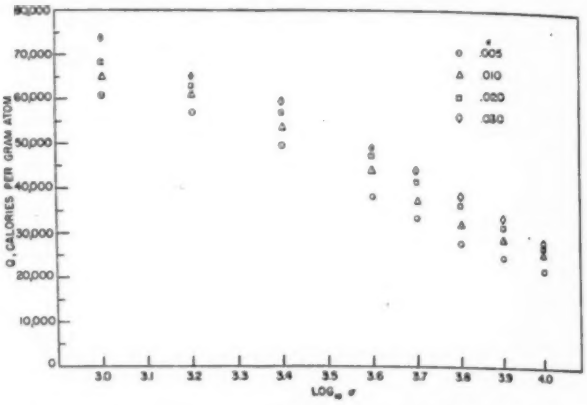

FIG. 23. Activation energy for plastic flow *vs.* logarithm of the stress at several strains.

perature "V"-type specimens were subject to a maximum error of 18 percent while the gauge lengths of the straight wire specimens were subject to a maximum error of eight percent. These errors might possibly lead to a maximum error of a factor of 1.2 in the strain rates. This error is negligible, considering the wide range of rates covered, and is certainly much less than the experimental scatter.

Although it is possible to measure and control temperature more accurately than was done in these experiments, it is felt that any errors in temperature are negligible with respect to the range of temperature explored.

It is believed that the experimental errors are insignificant with respect to the magnitude of the measured effects and that they do not obscure the basic description of the creep of platinum. The consistency and regularity of the data substantiate this belief.

The relations obtained from the present experiments were determined under a particular stress history, namely, constant stress. Tensile tests on the same material would be desirable as they would incorporate a different stress history and establish its effect, if any, upon these relations.

The assumption that σ is a point function of ϵ, $\dot{\epsilon}$, and T, which forms the basis of the foregoing empirical analysis, is not strictly correct. Dorn[14] has shown that the $\sigma-\epsilon$ relationship is influenced by temperature history when $\dot{\epsilon}$ is constant. In the present experiments σ and T were constant, during any one test, while ϵ and $\dot{\epsilon}$ were changing. The assumption appears to be valid under these conditions.

It is interesting and important that the strain-time behavior of a metal subjected to such a wide range of experimental conditions can be described by simple relationships, even though these relationships are empirical. The present results indicate that useful information might be obtained by conducting similar experiments on other materials. Such experiments are in progress in this laboratory.

[14] J. E. Dorn *et al.*, Trans. A.I.M.E. **180**, 205 (1949).

ACKNOWLEDGMENT

The writer wishes to acknowledge the assistance of Mrs. M. Wells in the experimental portion of this work; J. G. Leschen's contribution in developing the general equation relating stress, strain, strain rate, and temperature; and S. Dushman's contribution of equipment. The continued interest and helpful criticism of members of the Metallurgy Division of this Laboratory is sincerely appreciated.

The Effect of Magnetic Field on the Breakdown of Gases at Microwave Frequencies*

BENJAMIN LAX,† W. P. ALLIS, AND SANBORN C. BROWN
Research Laboratory of Electronics, Massachusetts Institute of Technology
(Received July 3, 1950)

The effect of magnetic field on the high frequency breakdown of gases has been studied. The presence of energy resonance and the modification of diffusion are shown experimentally and explained theoretically. An application is made of both the average electron theory and the Boltzmann theory, and the correspondence between these two theories is discussed.

THE breakdown of gases by high frequency electric fields in the presence of a constant magnetic field has been studied by Townsend and Gill[1] and by A. E. Brown.[2] It is the purpose of this paper to carry the analysis further, including the effect of the magnetic field on both the random diffusion of the electrons and their directed mobility.

Two approaches are available to such kinetic problems, and as there are advantages to each, both will be used. In Part I, the average electron theory will be given. In this method the orbit of a free electron in the assumed fields is computed first, and from this one computes the displacement and the energy gain in the time $\tau=t-t_0$ elapsed since a collision. These quantities are then averaged over the phase of the a.c. field at the time t_0 of the last collision, over the direction in space of the velocity after the collision, and over the free time up to the next collision. The result is the mean square displacement and energy gain of the average electron between collisions. One can then discuss an average electron from its initial low energy until it ionizes a gas atom or diffuses out of the tube. The condition for breakdown is that these two final achievements be equally probable. This method has the advantage that each step in the analysis has a direct physical meaning.

In Part II the Boltzmann transport equation is expanded in spherical harmonics in space, and in Fourier series in time. There results a differential equation for the distribution function which is integrated. Most of the properties of a discharge follow directly from a knowledge of the distribution function.

I. AVERAGE ELECTRON THEORY

Velocity between Collisions

Consider the motion of an electron between collisions under the influence of an electric field along the x-axis, $E=E_p\exp(j\omega t)$, and a constant magnetic field B along the z-axis. The equation of motion is then

$$\mathbf{F}=-e\mathbf{E}-e\mathbf{v}\times\mathbf{B}=m\dot{\mathbf{v}}. \tag{1}$$

The solution of this equation is the sum of a general and a particular integral, which correspond to the superposition of a circular helical motion and a plane elliptical motion. For the helical motion whose axis is along the magnetic field, the velocity is

$$\left.\begin{aligned} v_{1x}&=(a+jb)\exp(j\omega_b\tau)\\ v_{1y}&=(b-ja)\exp(j\omega_b\tau)\\ v_{1z}&=c \end{aligned}\right\} \tag{2}$$

and oscillates at the cyclotron frequency $\omega_b=eB/m$. Because the helical motion contains the three arbitrary constants, the energy of this motion is constant and is given in electron-volts by:

$$u_1=\frac{mv_1^2}{2e}=\frac{m}{e}\frac{a^2+b^2+c^2}{2}. \tag{3}$$

For the elliptical motion, the velocity is

$$\left.\begin{aligned} v_{2x}&=\frac{eE_p}{m}\frac{j\omega}{\omega^2-\omega_b^2}\exp(j\omega t)\\ v_{2y}&=\frac{eE_p}{m}\frac{\omega_b}{\omega^2-\omega_b^2}\exp(j\omega t) \end{aligned}\right\} \tag{4}$$

and oscillates at the frequency of the applied field. The kinetic energy of this motion is uniquely determined by the magnitude and frequency of the applied field and is given by:

$$u_2=\frac{eE_p^2}{8m}\left[\frac{1}{(\omega-\omega_b)^2}+\frac{1}{(\omega+\omega_b)^2}+\frac{2\cos 2\omega t}{\omega_b^2-\omega^2}\right]. \tag{5}$$

The total energy $u=(m/2e)|(\mathbf{v}_1+\mathbf{v}_2)|^2$ will contain cross product terms u_{12} which are important but rather lengthy to write down. Their average value will be given later. The three constants, a, b, c, of the helical motion are determined by the velocity $\mathbf{v}_0=\mathbf{v}_1(\tau=0)+\mathbf{v}_2(t=t_0)$ immediately after a collision. As the time τ has been used in Eqs. (2) one has simply

$$\left.\begin{aligned} a&=v_{0x}-\frac{eE_p}{m}\frac{j\omega}{\omega^2-\omega_b^2}\exp(j\omega t_0)\\ b&=v_{0y}-\frac{eE_p}{m}\frac{\omega_b}{\omega^2-\omega_b^2}\exp(j\omega t_0)\\ c&=v_{0z}. \end{aligned}\right\} \tag{6}$$

*This work has been supported in part by the Signal Corps, the Air Materiel Command, and ONR.
†Now at Geophysical Directorate, USAF Cambridge Research Laboratories.
[1] J. S. Townsend and E. W. B. Gill, Phil. Mag. **26**, 290 (1938).
[2] A. E. Brown, Phil. Mag. **29**, 302 (1940).

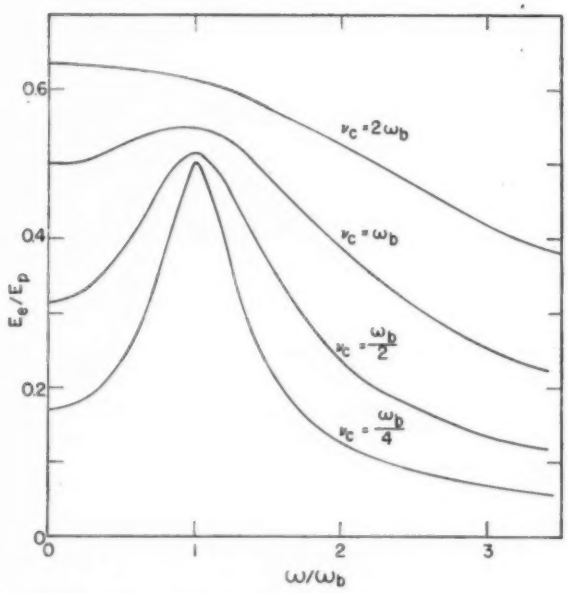

FIG. 1. The effective field E_e as a function of the frequency showing the resonance in the presence of a magnetic field.

It is noted that the elliptical motion exhibits a resonance at frequencies near the cyclotron frequency. Exactly at this frequency Eqs. (4) no longer hold and the solution corresponds to a spiral, but as collisions interrupt the motion it will not be necessary to use this singular solution.

Diffusion

From the velocities one obtains the displacements x_1, y_1, z_1, x_2, y_2 by integration. From these one can calculate the mean displacements $\langle x_1\rangle$, etc. but these all vanish on averaging over orientations of v_0, which is assumed isotropic, and over collision times t_0. In the average, an electron stays where it is in a high frequency discharge.

We are interested, however, in the mean square displacements $\langle x_1^2\rangle$, $\langle y_1^2\rangle$, $\langle z_1^2\rangle$ because these lead[3] to the diffusion coefficient. One finds the cross product terms such as $\langle x_1 y_1\rangle$ all vanish when averaged.

$$x_1^2+y_1^2=2\frac{a^2+b^2}{\omega_b^2}(1-\cos\omega_b\tau)$$

$$z_1^2=c^2\tau^2. \tag{7}$$

Averaging over orientations and times t_0, one finds that

$$\langle a^2\rangle=\langle b^2\rangle=\langle c^2\rangle=\frac{v_1^2}{3};\quad \langle ab\rangle=0. \tag{8}$$

The cross terms between the helical and elliptical motions also vanish but terms $\langle x_2^2\rangle$ and $\langle y_2^2\rangle$ do not vanish. However, these latter terms represent the mean square displacements due to mobility in the applied a.c. field and are not wanted in calculating the diffusion.

The average of a quantity X over the free times $\tau_c=1/\nu_c$ between collisions is, by definition,

$$\bar{X}=\int_0^\infty X\exp(-\nu_c\tau)\nu_c d\tau. \tag{9}$$

Applying this to the quantities in Eqs. (7) and defining the diffusion coefficients in terms of the mean square displacements, we obtain

$$D_{yy}=D_{xx}=\frac{\langle x_1^2\rangle}{2\tau_c}=\frac{v_1^2\nu_c}{3(\omega_b^2+\nu_c^2)}$$

$$D_{zz}=v_1^2/3\nu_c. \tag{10}$$

This definition of the diffusion tensor is of necessity symmetric. We shall see later that there are skew-symmetric terms which the random-walk definition cannot give. Diffusion along the z-axis is not altered by the magnetic field, but in the plane at right angles to the field it is reduced in the ratio $\nu_c^2/(\omega_b^2+\nu_c^2)$. For a given collision frequency, the diffusion coefficient is proportional to the energy of the electrons in their helical motion.

Energy Gain

The mean energy gain between collisions is best obtained by considering the power input to an electron $P=-e\mathbf{E}\cdot\mathbf{v}$. As the velocity v_{2x} is out of phase with the field, the corresponding power P_2 into this motion is zero in the average and only the power P_1 need be considered where

$$P_1=-eE_p\cos\omega t(a\cos\omega_b\tau-b\sin\omega_b\tau) \tag{11}$$

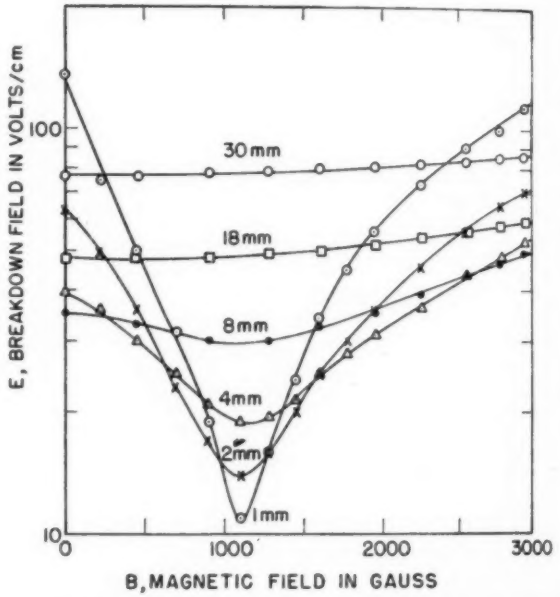

FIG. 2. Breakdown of helium in transverse electric and magnetic fields. (Diameter=7.32 cm and height=4.60 cm.)

[3] E. H. Kennard, *Kinetic Theory of Gases* (McGraw-Hill Book Company, New York, 1942), p. 286.

and the constants a and b are given by Eqs. (6). Averaging over orientations of the initial velocity the terms in v_0 drop out. Averaging over l_0 also we obtain

$$\bar{P}=\frac{e^2E_p^2}{4m}\left[\frac{\sin(\omega+\omega_b)\tau}{\omega+\omega_b}+\frac{\sin(\omega-\omega_b)\tau}{\omega-\omega_b}\right] \quad (12)$$

from which the average energy is obtained by integrating with respect to τ from 0 to τ.

$$\langle u_{12}\rangle=\frac{eE_p^2}{4m}\left[\frac{1-\cos(\omega+\omega_b)\tau}{(\omega+\omega_b)^2}+\frac{1-\cos(\omega-\omega_b)\tau}{(\omega-\omega_b)^2}\right]. \quad (13)$$

Averaging this quantity over collision times gives the mean energy gain between collisions

$$u_e=\frac{eE_p^2}{4m}\left[\frac{1}{(\omega+\omega_b)^2+\nu_c^2}+\frac{1}{(\omega-\omega_b)^2+\nu_c^2}\right]\equiv\frac{eE_e^2}{m\nu_c^2}. \quad (14)$$

This is a fundamental quantity in this theory. At low pressures ($\nu_c\to 0$) we see that it approaches twice the mean energy $\bar{u}_2$ of the elliptical motion of an electron, and in no case does it exceed this. At higher pressures, such that there are many collisions per oscillation, the energy $\bar{u}_2$ loses its meaning and the collision energy becomes $eE_p^2/2m\nu_c^2$. One can use Eq. (14) to define an effective field E_e which is the root-mean-square-field at high pressure. This concept is useful when the collision frequency ν_e is independent of velocity as this single function takes into account the effects of frequency and magnetic field on the energy.

At low pressures the effective field has a maximum at resonance with the cyclotron frequency as shown in Fig. 1.

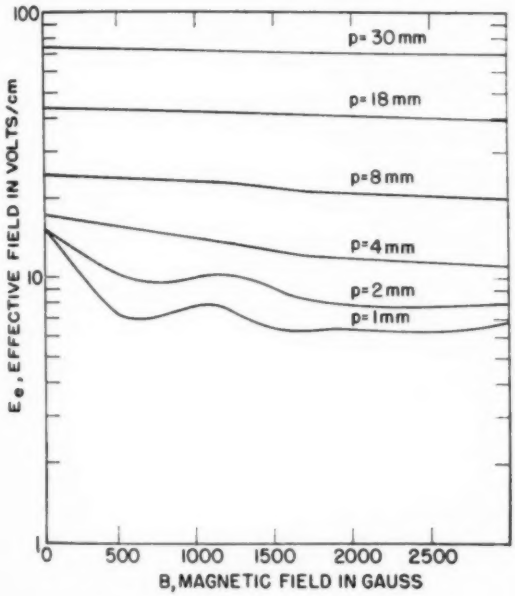

FIG. 3. Representation of experimental data of Fig. 2 in terms of the effective field.

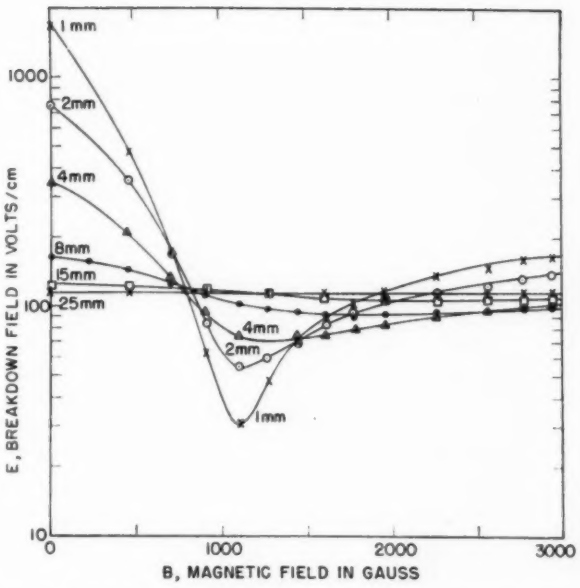

FIG. 4. Breakdown of helium in transverse electric and magnetic fields. (Diameter = 7.32 cm and height = 0.318 cm.)

Breakdown

The electrons produced by ionization have initially very little energy, but this increases by steps of u_e until the energy reaches a value u_i, at which ionization occurs. This is above the ionization potential V_i by an amount which we shall neglect. Excitations are disregarded in the following simple theory. The number N of free times to ionize is $N=u_i/u_e$ when ν_e is constant.

The electrons thus double their number by ionization every N collisions and unless some equally effective process exists which removes electrons their number will increase exponentially. In most cases diffusion to the walls of the discharge tube is the balancing process. In absence of the magnetic field, the random walk theory[4] gives the mean square distance $\Lambda^2=Nl^2/3$ reached in N free paths of mean square length l^2, so that if the average electron reaches the wall in a distance Λ the diffusion process will just balance ionization. This is the condition for breakdown and we can write it

$$\frac{u_e}{u_i}=\frac{\langle l^2\rangle}{3\Lambda^2}=\frac{\langle v^2\rangle}{3\Lambda^2\nu_c^2} \quad (15)$$

where Λ is now a length characteristic of the discharge tube and known as the diffusion length.[5]

If there is a magnetic field u_e will be altered according to Eq. (14). At the same time the random walk theory must be altered to take into account the curved paths between collisions. This may be done by appropriately decreasing l or increasing Λ. We shall adopt the latter and denote the new length by Λ_e. Its value will be given later.

[4] See reference 3, p. 271.
[5] M. A. Herlin and S. C. Brown, Phys. Rev. 74, 291 (1948).

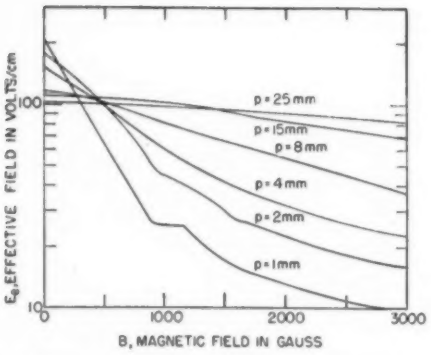

FIG. 5. Representation of experimental data of Fig. 4 in terms of the effective field.

When the mean free path is much smaller than Λ_e, the intercollision energy gain u_c is correspondingly smaller than the ionization potential. From Eq. (15) we see that breakdown should occur at the same effective field if the ratio of the mean free path to the effective diffusion length is the same, that is, the effective field for breakdown is a function of $p\Lambda_e$ only.

Combining Eqs. (14) and (15) we get

$$E_e^2=\frac{2\,\bar{u}u_i}{3\,\Lambda_e^2}. \tag{16}$$

Experimental data for breakdown in helium containing small admixtures of mercury vapor are shown in Fig. 2. The result of using the effective field with $\nu_c=2.37\times10^9 p$ as given by Brode's[6] collision probability measurements in place of the actual field but without taking the variation of Λ_e into account is shown in Fig. 3 for the same data. This shows that the resonance effect of the magnetic field and the high frequency are removed by using the effective field.

In order to test formula (10) for the diffusion coefficient, breakdown was studied in a flat cylindrical cavity whose length was very short compared to the radius. With the magnetic field placed transverse to the axis most of the diffusion has to take place perpendicular to the magnetic field and hence will show the full reduction. By Eq. (10) the mean square of the distance travelled by an electron is proportional to the diffusion coefficient D, and therefore the effective diffusion length Λ_e appropriate to infinite parallel plates is

$$\Lambda_e^2=\frac{\omega_b^2+\nu_c^2}{\nu_c^2}\Lambda^2. \tag{17}$$

The effect of a magnetic field is to make the dimensions of the cavity at right angles to the field appear larger to an electron. By Eq. (16) this should reduce the effective field for breakdown in the same proportion. Figure 4 shows a set of breakdown curves for helium in a cavity $2\frac{7}{8}$ in. in diameter and $\frac{1}{8}$ in. high. In Fig. 5 the effective field for the same data is plotted. In this figure the resonance peak has been removed as in Fig. 3, but now the curves are not horizontal because the magnetic field is increasing the effective cavity size.

However, Eq. (16) does not correspond with experiment except when used for comparative purposes. Equation (14) and the random walk theory give the number of free times for the average electron to ionize and reach the wall, respectively. But in a discharge it is the "faster-than-average" electron which ionizes and the "more-mobile-than-average" electron which leaves the tube and these are not the same electron. The mean free path method must therefore fail in predicting quantitative breakdown, and the failure should be worst when there are many collisions and therefore the greatest deviations from the mean.

II. BOLTZMANN THEORY

Spherical and Fourier Expansions

The Boltzmann transport equation is given by

$$C=\frac{\partial F}{\partial t}+\nabla\cdot(\mathbf{v}F)-\nabla_v\cdot\frac{e\mathbf{E}F}{m}-\nabla_v\cdot\frac{e}{m}\mathbf{v}\times\mathbf{B}F \tag{18}$$

where C is the production rate due to collisions per unit volume in phase space, ∇ and ∇_v are gradients in configuration and velocity space, respectively, and F is the distribution function. If F and C are expanded in spherical harmonics and substituted into the transport equation, we obtain two equations by equating the zero and first order terms

$$\begin{aligned}C_0&=\frac{\partial F_0}{\partial t}+\frac{v}{3}\nabla\cdot\mathbf{F}_1-\frac{e\mathbf{E}}{3mv^2}\cdot\frac{\partial(v^2\mathbf{F}_1)}{\partial v}\\ \mathbf{C}_1&=\frac{\partial\mathbf{F}_1}{\partial t}+v\nabla F_0-\frac{e}{m}\mathbf{E}\frac{\partial F_0}{\partial v}-\frac{e}{m}\mathbf{B}\times\mathbf{F}_1.\end{aligned} \tag{19}$$

We consider separately the elastic and inelastic collisions. Let C_{el} represent the elastic collision term. Morse, Allis and Lamar[7] have computed the zero- and first-order components of this term:

$$\begin{aligned}C_{0,el}&=\frac{m}{M}\frac{1}{v^2}\frac{\partial}{\partial v}\left(\frac{v^4F_0}{l}\right)\\ \mathbf{C}_{1,el}&=-\frac{v}{l}\mathbf{F}_1,\end{aligned} \tag{20}$$

where M is the mass of the gas molecule and l the mean free path of the electron.

The inelastic term C_{in} shows no angular dependence and hence, $C_{1,in}=0$ and only $C_{0,in}$ is retained. Equation

[6] R. B. Brode, Rev. Mod. Phys. 5, 243 (1933).

[7] Morse, Allis, and Lamar, Phys. Rev. 48, 412 (1935).

(19) then becomes

$$[0]\quad C_{0,in}+\frac{m}{M}\frac{1}{v^2}\frac{\partial}{\partial v}(\nu_c v^3 F_0)=\frac{\partial F_0}{\partial t}$$
$$+\frac{v}{3}\nabla\cdot\mathbf{F}_1-\frac{e}{3mv^2}\frac{\partial(v^2\mathbf{E}\cdot\mathbf{F}_1)}{\partial v} \quad (21)$$

$$[1]\quad 0=\nu_c\mathbf{F}_1+\frac{\partial\mathbf{F}_1}{\partial t}+v\nabla F_0-\frac{e}{m}\mathbf{E}\frac{\partial F_0}{\partial v}-\frac{e}{m}\mathbf{B}\times\mathbf{F}_1.$$

If the electric field is given by $\mathbf{E}=\mathbf{E}_p\exp(j\omega t)$, the Fourier expansions become

$$\mathbf{F}_1=\mathbf{F}_1^0+\mathbf{F}_1^1\exp(j\omega t)$$

and, with due caution in multiplying complex quantities,

$$\mathbf{E}\cdot\mathbf{F}_1=\tfrac{1}{2}\mathbf{E}_p\cdot(\mathbf{F}_1^1)_r+\mathbf{E}_p\cdot\mathbf{F}_1^0\exp(j\omega t),$$

where $(\mathbf{F}_1^1)_r$ is the real part of $\mathbf{F}_1^1$. These are now substituted into (21) and the Fourier components equated term by term. Only the constant term of the first equation is needed but the d.c. and a.c. terms of the second must be kept. In the steady state $\partial F_0/\partial t=0$.

$$[0,0]\quad C_{0,in}+\frac{m}{M}\frac{1}{v^2}\frac{\partial}{\partial v}(\nu_c v^3 F_0)-\frac{v}{3}\nabla\cdot\mathbf{F}_1^0$$
$$+\frac{e}{m}\frac{1}{3v^2}\frac{\partial}{\partial v}\left[\frac{v^2}{2}\mathbf{E}_p\cdot(\mathbf{F}_1^1)_r\right]=0 \quad (22)$$

$$[1,0]\quad \nu_c\mathbf{F}_1^0+v\nabla F_0-\frac{e}{m}\mathbf{B}\times\mathbf{F}_1^0=0$$

$$[1,1]\quad (\nu_c+j\omega)\mathbf{F}_1^1-\frac{e}{m}\mathbf{E}_p\frac{\partial F_0}{\partial v}-\frac{e}{m}\mathbf{B}\times\mathbf{F}_1^1=0.$$

These are the necessary equations for handling breakdown problems, which represent steady state conditions for the electrons. The above equations are applicable for any orientation of **E** and **B**. We shall only consider the cases when they are perpendicular or parallel to each other.

Diffusion Tensor

Integrating the [0,0] equations over velocity space in spherical coordinates, the second and fourth terms vanish at the limits. The first term gives the total production rate of electrons, $\nu_i n$, due to ionization. This is because excitations merely withdraw fast electrons to replace them by slow ones, whereas ionizations add an extra electron. The third term gives the divergence of a flow vector $\mathbf{\Gamma}$

$$\mathbf{\Gamma}=\int_0^\infty\frac{4\pi}{3}\mathbf{F}_1^0 v^3 dv \quad (23)$$

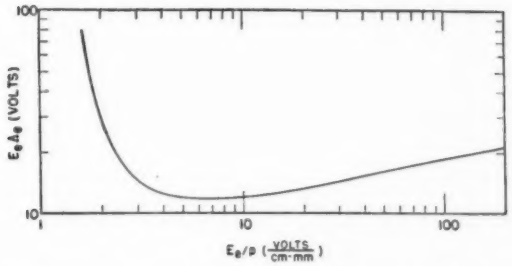

FIG. 6. Theoretical curve for the effective breakdown in helium.

so that

$$n\nu_i=\nabla\cdot\mathbf{\Gamma}. \quad (24)$$

Solving Eq. [1,0] for $\mathbf{F}_1^0$ we find

$$\mathbf{F}_1^0=-\frac{v}{\nu_c}\frac{\nu_c^2+\omega_b\omega_b\cdot+\nu_c\omega_b\times}{\nu_c^2+\omega_b^2}\nabla F_0 \quad (25)$$

and this must be substituted in (23) and, assuming that F_0 can be written as a product $n(x,y,z)f_0(v)$ we find that $\mathbf{\Gamma}$ is proportional to ∇n but not necessarily in the same direction. Accordingly it is possible to define a diffusion coefficient but it must be a tensor

$$(D_{ij})=\int_0^\infty\frac{lv}{3(1+b^2)}$$
$$\times\begin{pmatrix}(1+b_x^2) & (b_xb_y-b_z) & (b_xb_z+b_y)\\ (b_xb_y+b_z) & (1+b_y^2) & (b_yb_z-b_x)\\ (b_xb_z-b_y) & (b_yb_z+b_z) & (1+b_z^2)\end{pmatrix}4\pi v^2 f_0 dv \quad (26)$$

$$\Gamma_i=-\textstyle\sum_j D_{ij}\dfrac{\partial n}{\partial j};\quad i,j=x,y,z$$

where $b_z=(\omega_b)_z/\nu_c$ and $b^2=b_x^2+b_y^2+b_z^2$. This expression reduces to the ordinary coefficient $D=\langle v^2\rangle/3\nu_c$ with no magnetic field when $b=0$. If the magnetic field is taken along the z-axis, it reduces to

$$D_{ij}=\int_0^\infty\frac{lv}{3(1+b^2)}\begin{pmatrix}1 & -b & 0\\ b & 1 & 0\\ 0 & 0 & 1+b^2\end{pmatrix}4\pi v^2 f_0 dv, \quad (27)$$

which is equivalent to Eq. (10) except that the present tensor has skew-symmetric terms which were not obtained by the random walk definition.

Substituting in (24) we obtain the diffusion equation

$$D_{xx}\frac{\partial^2 n}{\partial x^2}+D_{yy}\frac{\partial^2 n}{\partial y^2}+D_{zz}\frac{\partial^2 n}{\partial z^2}+\nu_i n=0 \quad (28)$$

which determines the spatial distribution of the electrons. One can use the normal diffusion coefficient D provided lengths are expanded at right angles to the magnetic field in the ratio $(1+b^2)^{\frac{1}{2}}$.

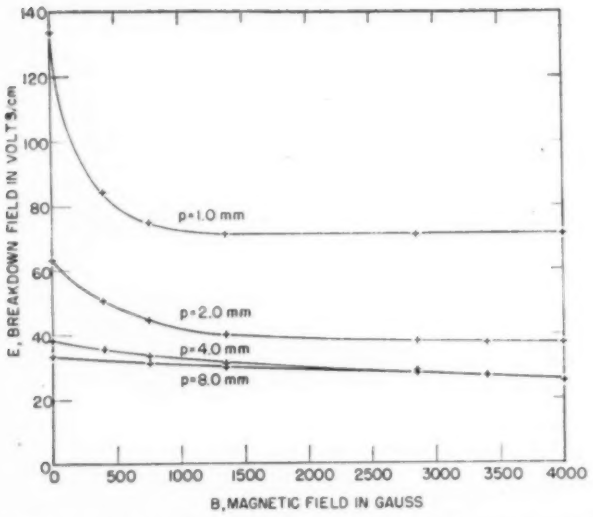

FIG. 7. Breakdown of helium in parallel electric and magnetic fields in a cylindrical cavity (diameter = 7.32 cm, height = 4.60 cm). The solid curves are theoretical and the points are experimental.

The solution of this equation depends on the boundary conditions. One must define an effective diffusion length Λ_e for the whole cavity which takes into account these expansions

$$\frac{1}{\Lambda_e^2}=\left(\frac{1}{\Lambda_x^2}+\frac{1}{\Lambda_y^2}\right)\frac{\nu_c^2}{\nu_c^2+\omega_b^2}+\frac{1}{\Lambda_z^2}. \tag{29}$$

The condition for the existence of a solution of (28) satisfying the boundary conditions is

$$D=\Lambda_e^2\nu_i \tag{30}$$

where D is the ordinary diffusion coefficient. The effect of the magnetic field is equivalent to expanding the cavity in the ratio $(\nu_c^2+\omega_b^2)^{\frac{1}{2}}\nu_c$ in all directions perpendicular to the magnetic field.

Differential Equation for F_0

The distribution function F_0 is obtained by eliminating $\mathbf{F}_1^0$ and $\mathbf{F}_1^1$ from Eqs. (22). One obtains in this way

$$C_{0,in}=\frac{v^2F_0}{3\nu_c\Lambda_e^2}-\frac{1}{v^2}\frac{\partial}{\partial v}\left[\frac{m}{M}\nu_c v^3F_0+\frac{e^2E_e^2}{3m^2\nu_c}v^2\frac{\partial F_0}{\partial v}\right] \tag{31}$$

where the effective field E_e is defined by (14) when E is at right angles to B. Should E make any other angle with B, the component at right angles is reduced by Eq. (14), and the square of this added to the mean square along B. Introducing the energy variable $u=mv^2/2e$ and the inelastic ratio $h=-C_{0,in}/\nu_cF_0$, Eq. (31) becomes

$$\frac{1}{(u)^{\frac{1}{2}}\nu_e}\frac{\partial}{\partial u}\left[\frac{2m}{M}\nu_c u^{\frac{1}{2}}F_0+\frac{2eE_e^2}{3m\nu_c}u^{\frac{1}{2}}\frac{\partial F_0}{\partial u}\right]=\left(h+\frac{2eu}{3m\nu_c^2\Lambda_e^2}\right)F_0. \tag{32}$$

The four terms of this equation are readily interpreted: the first, with $2m/M$, represents energy lost to recoil of the atoms, the second, with E_e^2, is the energy gain due to the field, h gives the loss of electrons through inelastic collisions, and the last term, in $1/\Lambda_e^2$, the loss through diffusion to the walls. It is noted that the magnetic field and the frequency are entirely contained in the effective quantities E_e and Λ_e. The pressure enters only in ν_e and indirectly through ν_c into E_e and Λ_e. The pressure cancels out of the first and third terms, and the only experimental parameters are thus E_e/p in the second term and $p\Lambda_e$ in the fourth. The other quantities are universal constants such as e/m and m/M and atomic constants such as the excitation and ionization cross sections included in h. It follows that all the breakdown data should plot on a single curve when $E_e\Lambda_e$ is plotted against E_e/p. This exact law is, however, of very limited applicability. The effective quantities E_e and Λ_e depend on ν_c, which is a function of the electron's energy. It is therefore in general impossible to make the effective values the same at all energies as the law requires. For helium and hydrogen the collision frequency ν_c is very nearly constant so the effective values are significant as shown in Fig. 6.

Because inelastic impacts set in discontinuously at the excitation potential u_x, it is necessary to solve Eq. (32) in two parts: Below u_x, $h=0$ and above u_x recoil and diffusion may generally be neglected. The solution of this equation in the completely analogous non-magnetic case has been carried out by MacDonald and Brown.[8]

The Boltzmann theory can be compared with the simple average electron theory in the case of helium

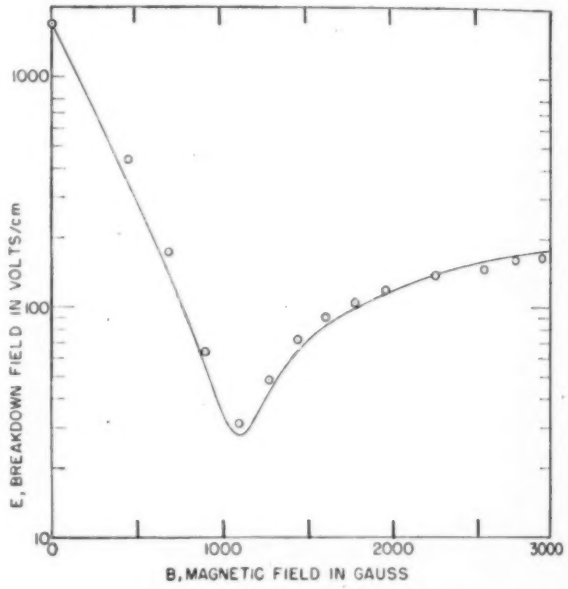

FIG. 8. Breakdown of helium at 1 mm pressure in a cylindrical cavity (diameter = 7.60 cm, height = 0.318 cm). Solid line is obtained from the Boltzmann theory and points are experimental.

[8] A. D. MacDonald and S. C. Brown, Phys. Rev. **75**, 411 (1949).

containing traces of mercury so that all excitations result in ionizations. We must then neglect the recoil and excitation terms. The solution of the Eq. (32) is then expressible in terms of Bessel functions of order $\pm 1/4$. Setting the coefficients so that the function vanishes at u_i

$$F_0 = w^{-1/4}[J_{1/4}(w_i)J_{-1/4}(w) - J_{-1/4}(w_i)J_{1/4}(w)]$$

where

$$w = ju/\Lambda_e E_e.$$

The breakdown condition then reduces to

$$(1/4)!J_{1/4}(w_i) = 2w_i^{1/4}$$

or

$$u_i = 2.273\Lambda_e E_e.$$

This corresponds to using for the mean energy in (16)

$$\bar{u} = u_i/3.44.$$

III. NON-UNIFORM FIELDS

To study the effect of the magnetic field on diffusion alone the electric and magnetic fields are oriented in the same direction, and in order to reduce diffusion along the magnetic field it is necessary to perform the experiment in a cavity whose height is greater than the radius. In such a cavity the electric field may no longer be considered uniform and a correction to the computations must be made in a manner which has been shown by Herlin and Brown.[9] In the presence of the longitudinal magnetic field the equivalent diffusion length of the cylinder, from Eq. (29), is

$$\frac{1}{\Lambda_e^2} = \frac{\nu_c^2}{\nu_c^2 + \omega_b^2}\left(\frac{2.405}{R}\right)^2 + \left(\frac{\pi}{L}\right)^2.$$

Using this and the non-uniform field correction to the Boltzmann theory one obtains the agreement with experiment shown in Fig. 7. This result confirms the predicted effect of the magnetic field upon diffusion.

The breakdown measurements shown in Fig. 4 were made in a flat cavity with the magnetic field transverse to the axis. The effect of the latter is to require the solution of the diffusion equation in an elliptical cylinder whose diffusion length is then given by

$$\frac{1}{\Lambda_e^2} = \frac{\nu_e^2}{\nu_e^2 + \omega_b^2}\left[\left(\frac{\pi}{L}\right)^2 + \frac{1}{2}\left(\frac{2.405}{R}\right)^2\right] + \frac{1}{2}\left(\frac{2.405}{R}\right)^2.$$

Using this and the non-uniform field correction gives the theoretical curves shown in Fig. 8.

IV. EXPERIMENTAL APPARATUS AND PROCEDURE

The block diagram of the experimental equipment is shown in Fig. 9. The source of microwave energy is a

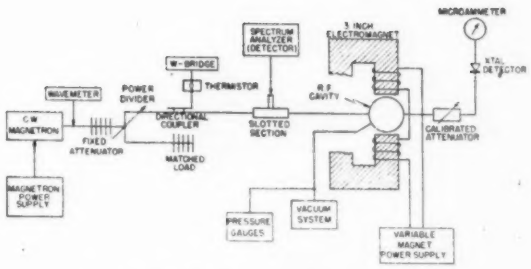

FIG. 9. Block diagram of the apparatus.

10-cm tunable c-w magnetron whose frequency is monitored by a calibrated wavemeter. The power fed into the cavity is varied by a balanced power divider and measured through a directional coupler by a bolometer, consisting of a thermistor and a balanced power bridge. The slotted section and detector are used to determine the electrical constants of the cavity.[10] The cavity, which is vacuum-tight, is loop coupled to the transmission line on either side. The output loop feeds into a variable calibrated attenuator, a crystal detector and a sensitive microammeter, which are adjusted to measure the power fed into the cavity at resonance. The magnetic field across the cavity is applied by an adjustable electromagnet. The magnetic field for a given gap size is calibrated as a function of the current through the coils by the use of a snatch coil and a ballistic galvanometer or by a compensated torque type fluxmeter. The pressure in the cavity during the experiment is measured by a McLeod gauge.

The breakdown experiment was performed at fixed values of pressure while the current through the coils and hence the magnetic field was set at different values. The power fed into the cavity was increased from nearly zero until the needle on the microammeter rose to a maximum and then suddenly dropped. This occurred at breakdown since the sudden increase in electron density detuned the cavity and produced a mismatch in the line. The setting of the calibrated attenuator and the maximum reading of the microammeter measured the power fed into the cavity. The breakdown field was then calculated from the measured constants and geometrical dimensions of the cavity.

V. CONCLUSIONS

The two principal effects of a magnetic field on high frequency breakdown of gases, the energy resonance with transverse fields and the reduction of diffusion, have been demonstrated experimentally and explained theoretically. The diffusion effect was shown to exist by itself when the electric and magnetic fields were parallel. The resonance phenomenon could not be separated because of the presence of diffusion at all times. Nevertheless this effect was brought into major

[9] M. A. Herlin and S. C. Brown, Phys. Rev. **74**, 1650 (1948).

[10] S. C. Brown *et al.*, "Methods of measuring the properties of ionized gases at microwave frequencies," Technical Report No. 66, Research Laboratory of Electronics, M.I.T., Cambridge, Massachusetts.

prominence in breakdown by reducing the diffusion loss in a large cavity.

The development of the diffusion tensor in the presence of a magnetic field resulted in a more general diffusion equation. This led to the concept of the effective diffusion length, which together with the effective field, extended here to include the magnetic field, served to generalize the theory. The correspondence of the Boltzmann theory and the average electron theory was shown.

Quantum Limits of the Electrostatic Image Force Theory

R. G. Sachs and D. L. Dexter*
Department of Physics, University of Wisconsin, Madison, Wisconsin
(Received July 17, 1950)

The quantum mechanical problem of the interaction of a charged macroscopic body with a metal surface is treated by means of the variation method. The resulting expression for the interaction energy is the same as that obtained by the classical image force method except for three correction terms. These corrections are caused by the change in kinetic energy associated with the concentration of the electrons on the surface of the metal, the reduction in the electron-electron interaction energy in the metal resulting from the antisymmetrization of the wave function and the effect of the finite thickness of the surface charge. It is found that these terms are negligible except for distances between the charged body and metal surface such that surface structure effects are important.

I. INTRODUCTION

THE calculation of the interaction between a charged body and a much larger metal body is usually carried out by means of the classical image force theory. This treatment is certainly justified when the ratio of the distance between the bodies to atomic dimensions is sufficiently great. However, the method may be questioned when this ratio is of the same order of magnitude as the square root of the ratio of the total charge on the body to the electronic charge.[1] Such a condition may occur in experiments on the Schottky effect[2] and in the Van der Waals adsorption of molecules on a metal surface. The latter effect has been discussed by Lennard-Jones[3] from the point of view of the image force theory. A discussion of the limitations of this treatment due to the fact that the molecule must be treated quantum mechanically has been given by Bardeen.[4]

Bardeen has in addition treated the image force problem for an electron from the quantum mechanical point of view and has demonstrated that the classical formula for the force on an electron can be expected to hold asymptotically when the electron is at great distances from the metal. It is the purpose of this paper to determine the order of magnitude of the distance at which the classical formulas break down. In determining this distance, account will not be taken of the detailed surface structure of the metal, but the order of magnitude of the deviation from the classical formula due to purely quantum effects in the metal will be obtained.

This deviation is due to three effects. The first is the change in kinetic energy of the electrons that is associated with the increased charge density on the surface of the metal. The second effect is that due to the antisymmetrization of the wave function. This increases the average distance between electrons and therefore causes the electron-electron interaction to be smaller than that expected from classical considerations. Finally, in the determination of the self-interaction of the induced charge density account must be taken of the fact that one cannot assume an infinitely thin surface layer of charge in the quantum treatment since such an assumption would lead to an infinite kinetic energy of the electrons on the surface.

II. CLASSICAL TREATMENT

The classical theory of image forces will be briefly reviewed in this section from a point of view that may be easily compared with the quantum treatment. It will be assumed throughout the paper that a charged body (taken positive for the sake of definiteness), which gives rise to a potential $v(\mathbf{r})$ in the absence of other matter, interacts with the plane surface of a half-infinite metal body at distance R away. The origin of the coordinate system used is at the foot of the normal from the charged body to the metal surface. The positive z axis is taken as the normal into the metal and $\mathbf{s}$ is the two dimensional position vector on the surface of the metal.

In electrostatic theory it is shown that the potential $v(\mathbf{r})$ gives rise to a charge density, $\sigma_0(\mathbf{s})$, on the surface of the metal. The interaction energy, $W(R)$, is the sum of two terms. The first is the direct interaction between

* Research supported in part by ONR.

[1] Classical image force theory would not be expected to hold when the induced charge density, ρ', becomes equal to ρ_0, the charge density of free electrons in the metal. Since $\rho' \approx \sigma/a \approx Q/R^2 a$, where Q is the magnitude of the external charge, R its distance from the metal, and a is an atomic dimension, and since $\rho_0 \approx e/a^3$, ρ' becomes equal to ρ_0 when $Q/e \approx (R/a)^2$.

[2] E. Guth and C. J. Mullin, Phys. Rev. **59**, 575 (1941).

[3] Lennard-Jones, Trans. Faraday Soc. **28**, 334 (1932).

[4] J. Bardeen, Phys. Rev. **58**, 727 (1940).

the charge density $\sigma_0(\mathbf{s})$ and the potential $v(\mathbf{r})$, and is given by

$$W_1(R)=\int \sigma_0(\mathbf{s})v(\mathbf{s})dS, \tag{1}$$

where the integration is carried out over the surface of the metal. The second term is due to the interaction of the charge density on the surface with itself:

$$W_2(R)=\frac{1}{2}\int\int \frac{\sigma_0(\mathbf{s})\sigma_0(\mathbf{s}')dSdS'}{|\mathbf{s}-\mathbf{s}'|}. \tag{2}$$

We can now make use of the fact that the total potential due to the charged body and the surface charge must vanish everywhere within the metal:

$$v(\mathbf{r})+\int \frac{\sigma_0(\mathbf{s}')dS'}{|\mathbf{r}-\mathbf{s}'|}=0, \tag{3}$$

for $Z>0$, from which it follows that

$$2\pi\sigma_0(\mathbf{s})=\left.\frac{\partial v(\mathbf{r})}{\partial z}\right|_{z=0}.$$

Since the integral in Eq. (3) is a continuous function of z (although its derivative is not), we can set

$$v(\mathbf{s})=-\int \frac{\sigma_0(\mathbf{s}')dS'}{|\mathbf{s}-\mathbf{s}'|}.$$

Therefore

$$\int\int \frac{\sigma_0(\mathbf{s})\sigma_0(\mathbf{s}')dSdS'}{|\mathbf{s}-\mathbf{s}'|}=-\int v(\mathbf{s})\sigma_0(\mathbf{s})dS, \tag{3'}$$

and the total interaction energy is given by

$$W(R)=W_1(R)+W_2(R)=\frac{1}{2}\int \sigma_0(\mathbf{s})v(\mathbf{s})dS. \tag{4}$$

For future reference we wish to show that the energy $W(R)$ is a minimum with respect to variations in the charge density $\sigma(\mathbf{s})$. The variation of

$$W(R)=\int v(\mathbf{s})\sigma(\mathbf{s})dS+\frac{1}{2}\int\int \frac{\sigma(\mathbf{s})\sigma(\mathbf{s}')dSdS'}{|\mathbf{s}-\mathbf{s}'|}, \tag{5}$$

associated with the variation $\delta\sigma$ of σ is

$$\delta W(R)=\int v(\mathbf{s})\delta\sigma(\mathbf{s})dS+\frac{1}{2}\int\int \frac{\delta\sigma(\mathbf{s})\sigma(\mathbf{s}')dSdS'}{|\mathbf{s}-\mathbf{s}'|}+\frac{1}{2}\int\int \frac{\sigma(\mathbf{s})\delta\sigma(\mathbf{s}')dSdS'}{|\mathbf{s}-\mathbf{s}'|}.$$

Since the latter two integrals are equal, the condition that $\delta W(R)=0$ becomes

$$\int\left[v(\mathbf{s})+\int \frac{\sigma(\mathbf{s}')dS'}{|\mathbf{s}-\mathbf{s}'|}\right]\delta\sigma(\mathbf{s})dS=0,$$

and, taking into account the fact that the variations $\delta\sigma$ are arbitrary, this is equivalent to

$$v(\mathbf{s})+\int \frac{\sigma(\mathbf{s}')dS'}{|\mathbf{s}-\mathbf{s}'|}=0.$$

According to Eq. (3), this condition is satisfied by our choice of $\sigma_0(\mathbf{s})$. It follows that the energy given by Eq. (4) is a stationary value of Eq. (5); it also seems reasonable on physical grounds to assert that this stationary value is a minimum.

III. THE VARIATION METHOD

The wave equation for the metal electrons can be set up formally but, of course, it cannot be solved directly. The problem can, however, be treated by the variation method. In choosing a trial function, it will be assumed that the function leads to the classical surface charge density in very good approximation. All other details of the function will remain arbitrary. When this function is inserted into the variation integral, terms of the type (1) and (2) will occur. In addition there will be terms due to the change in kinetic energy, to the reduced interaction between electrons associated with the antisymmetric wave function, and to the non-zero thickness of the surface charge density. These latter terms turn out to be small compared to those given by Eqs. (1) and (2) as long as the distance between the charged body and metal surface is sufficiently great. Therefore, for such distances, the variation energy is essentially equal to (5). Since it has been shown in Section II that (4) is the minimum of Eq. (5) for variations in σ, it follows that, except for the small terms, this will also be the minimum of the energy with respect to variations in the wave function. It is, therefore, the proper energy associated with the wave equation as long as the correction terms may be neglected. Thus the quantum treatment leads directly to the same interaction as the classical image force theory.

In order to estimate the order of magnitude of the distance at which the image force theory may be expected to break down, it is necessary to seek that region in which the terms that have been neglected become of the same order of magnitude as the image force energy.

We consider as a variation function the normalized function $\Psi(\mathbf{r}_1, \mathbf{r}_2, \cdots \mathbf{r}_N)$ of the positions of the N electrons in the metal. The electronic charge density associated with this function is

$$\rho(\mathbf{r})=-e\sum_{j=1}^{N}\int\int\cdots\times\int|\Psi(\mathbf{r}_1, \mathbf{r}_2, \cdots \mathbf{r}_{j-1}, \mathbf{r}, \mathbf{r}_{j+1}, \cdots \mathbf{r}_N)|^2 d\tau^{N-1}, \tag{6}$$

where the $d\tau^{N-1}$ indicates that the integration is to be carried out over all the electrons except the j'th. e is the absolute value of the electronic charge. It is assumed that Ψ is chosen in such a way that $\rho=\rho_0+\rho'(\mathbf{r})$, where ρ_0, a constant, is the electronic charge density in the metal when the charged body is absent and $\rho'(\mathbf{r})$ is a small added volume density that arises in the presence of the charged body. It is also assumed that the charge distribution of the positive ions may be represented by a charge density $-\rho_0$, which is unchanged in the presence of the charged body. This assumption is certainly valid if $\rho'(\mathbf{r})$ varies slowly over the lattice spacing.

The general form of ΔE, the change in the energy of the system external charge plus metal, can be easily determined. There must be a term [see Eq. (1)]

$$\Delta E_V=\int \rho'(\mathbf{r})v(\mathbf{r})d\tau, \tag{1'}$$

corresponding to the interaction between the additional charge density $\rho'(\mathbf{r})$ and the potential $v(\mathbf{r})$. Also there is a term [see Eq. (2)]

$$\Delta E_R=\frac{1}{2}\int\int \frac{\rho'(\mathbf{r})\rho'(\mathbf{r}')d\tau d\tau'}{|\mathbf{r}-\mathbf{r}'|}, \tag{2'}$$

for the self-interaction of the additional charge density. The change ΔT in the kinetic energy of the electrons associated with a change in the wave function will have the form of a volume integral of some function of ρ over the metal, minus a volume integral of the same function of ρ_0 over the metal as long as changes in ρ are small within an electron wave-length. Expanding these functions in power series in ρ' and integrating, it is clear that the leading term will be of the form $\int\rho'^2d\tau$ since the terms involving only ρ_0 will cancel and the volume integral of ρ' is zero. Finally there must be a correction term ΔE_A to Eq. (2'), taking account of the reduced interaction between the metal electrons due to correlations of pairs of electrons. By the same argument used in connection with ΔT, ΔE_A will have a leading term $\int\rho'^2d\tau$. Thus

$$\Delta E=\int \rho'(\mathbf{r})v(\mathbf{r})d\tau + \frac{1}{2}\int\int \frac{\rho'(\mathbf{r})\rho'(\mathbf{r}')d\tau d\tau'}{|\mathbf{r}-\mathbf{r}'|}+\kappa\int\rho'(\mathbf{r})^2d\tau, \tag{7}$$

where κ is a constant depending on the detailed quantum properties of the metal electrons.

To estimate the order of magnitude of κ, we apply the Fermi-Thomas-Dirac statistical model to the metal electrons. According to this model, if the electron density is $n=-\rho/e$, the total kinetic energy of the electrons in the metal is

$$T=\left(\frac{3}{8\pi}\right)^{\frac{2}{3}}\left(\frac{3h^2}{10m}\right)\int n^{5/3}d\tau,$$

where the integration is carried out over the volume of the metal. Therefore, for a small change, $n'=-\rho'/e$, in n the change in T is

$$\Delta T=\frac{h^2}{2m}\left(\frac{3n_0}{8\pi}\right)^{\frac{2}{3}}\int n'd\tau+\frac{h^2}{6mn_0}\left(\frac{3n_0}{8\pi}\right)^{\frac{2}{3}}\int n'^2d\tau.$$

The first term vanishes because of the condition for the conservation of charge and we are left with

$$\Delta T=\frac{(2\pi)^2}{6}\left(\frac{3}{8\pi}\right)^{\frac{2}{3}}\frac{h^2}{me^2}n_0^{-\frac{1}{3}}\int\rho'(\mathbf{r})^2d\tau. \tag{8}$$

ΔE_A can be estimated in a similar way. The change in the electron-electron interaction due to the antisymmetrization of plane electron waves is

$$-\frac{3}{2}\left(\frac{3}{8\pi}\right)^{\frac{1}{3}}e^2\int n^{4/3}d\tau,$$

and the change in this quantity associated with a change, n', in n can be obtained just as before. The result is

$$\Delta E_A=-\frac{1}{3}\left(\frac{3}{8\pi}\right)^{\frac{1}{3}}n_0^{-\frac{1}{3}}\int\rho'(\mathbf{r})^2d\tau; \tag{9}$$

so

$$\kappa\approx-\frac{1}{3}\left(\frac{3}{8\pi}\right)^{\frac{1}{3}}n_0^{-\frac{1}{3}}+\frac{(2\pi)^2}{6}\left(\frac{3}{8\pi}\right)^{\frac{2}{3}}\frac{h^2}{me^2}n_0^{-\frac{1}{3}}. \tag{10}$$

κ is of the order of the square of the inter-electronic distance for the free electrons and is a positive quantity; letting β denote the distance into the metal within which ρ' differs appreciably from zero, it is clear that in order to use the Fermi-Thomas approximation β must be larger than the free electron wave-length, or $\beta\gtrsim\kappa^{\frac{1}{2}}$. If β is the distance over which ρ' is not ≈0, ρ' in this region is of the order $\sigma(\mathbf{s})/\beta$; then the third term in Eq. (7) is of the order βR^{-1} times the first or second term, and for R large enough it is a small correction. Thus for large R, ρ' will be closely equal to the classical value $\sigma_0(\mathbf{s})\delta(z)$ where $\delta(z)$ is the Dirac delta function. But because of the third term in Eq. (7) we expect ρ' to have a small but non-zero extension in the z direction. The thickness of this region will be estimated below.

In order to evaluate ΔE, let us approximate $\rho'(\mathbf{r})$ by

$$\begin{aligned}\rho'(\mathbf{r})&=\beta^{-1}\sigma(\mathbf{s}) \quad \text{for} \quad z<\beta,\\ &\approx0 \quad\quad\quad\ \text{for} \quad z>\beta,\end{aligned}$$

where $\sigma(\mathbf{s})$ is a surface charge density. Then the variation $\delta\Delta E$ in the energy ΔE associated with the variation

$\delta\beta$ in β and $\delta\sigma(\mathbf{s})$ in $\sigma(\mathbf{s})$ is

$$\delta\Delta E=\Big\{-\frac{1}{\beta^2}\int\int_0^\beta v(\mathbf{r})\sigma(\mathbf{s})d\tau+\frac{1}{\beta}\int v(\mathbf{s},\beta)\sigma(\mathbf{s})dS$$
$$-\frac{1}{\beta^3}\int_0^\beta\int_0^\beta\int\int\frac{\sigma(\mathbf{s})\sigma(\mathbf{s}')dSdS'dzdz'}{|\mathbf{r}-\mathbf{r}'|}$$
$$+\frac{1}{\beta^2}\int_0^\beta\int\int\frac{\sigma(\mathbf{s})\sigma(\mathbf{s}')dz'dSdS'}{((\mathbf{s}-\mathbf{s}')^2+(\beta-z')^2)^{\frac{1}{2}}}$$
$$-\frac{\kappa}{\beta^2}\int\sigma^2(\mathbf{s})dS\Big\}\delta\beta+\int\Big\{\frac{1}{\beta}\int_0^\beta v(\mathbf{r})dz$$
$$+\frac{1}{\beta^2}\int_0^\beta\int_0^\beta\int\frac{\sigma(\mathbf{s})dzdz'dS'}{|\mathbf{r}-\mathbf{r}'|}+\frac{2\kappa}{\beta}\sigma(\mathbf{s})\Big\}\delta\sigma(\mathbf{s})dS.$$

This leads to the following two conditions to be satisfied for minimum energy:

$$\int\int_0^\beta v(\mathbf{r})\sigma(\mathbf{s})d\tau-\beta\int v(\mathbf{s},\beta)\sigma(\mathbf{s})dS$$
$$+\frac{1}{\beta}\int_0^\beta\int_0^\beta\int\int\frac{\sigma(\mathbf{s})\sigma(\mathbf{s}')d\tau d\tau'}{|\mathbf{r}-\mathbf{r}'|}$$
$$-\int\int\int_0^\beta\frac{\sigma(\mathbf{s})\sigma(\mathbf{s}')dSdS'dz'}{((\mathbf{s}-\mathbf{s}')^2+(\beta-z')^2)^{\frac{1}{2}}}$$
$$+\kappa\int\sigma^2(\mathbf{s})dS=0, \quad (11A)$$

$$\int_0^\beta v(\mathbf{r})dz+\frac{1}{\beta}\int_0^\beta\int_0^\beta\int\frac{\sigma(\mathbf{s}')dzdz'dS'}{|\mathbf{r}-\mathbf{r}'|}$$
$$+2\kappa\sigma(\mathbf{s})=0. \quad (11B)$$

To zero order in β Eq. (11B) reads

$$v(\mathbf{s})+\int\frac{\sigma(\mathbf{s}')dS'}{|\mathbf{s}-\mathbf{s}'|}=0,$$

and since this is the condition satisfied by the classical surface charge density, $\sigma(\mathbf{s})$ may be written as $\sigma(\mathbf{s})=\sigma_0(\mathbf{s})+\sigma_1(\mathbf{s})$ where $\sigma_0(\mathbf{s})$ is the classical density and $\sigma_1(\mathbf{s})$ is a first order correction term.

For convenience let us define the quantity

$$\theta(\mathbf{r})\equiv v(\mathbf{r})+\frac{1}{\beta}\int_0^\beta dz'\int\frac{\sigma(\mathbf{s}')dS'}{|\mathbf{r}-\mathbf{r}'|}, \quad z\gtrless 0.$$

This is the total potential within the metal, and to a zero order approximation $\theta(\mathbf{r})$ is clearly zero. Using this definition (11A) and (11B) become

$$\int\sigma(\mathbf{s})\theta(\mathbf{s},\beta)dS=-\kappa/\beta\int\sigma^2(\mathbf{s})dS, \quad (12A)$$

$$\int_0^\beta\theta(\mathbf{r})dz=-2\kappa\sigma(\mathbf{s}). \quad (12B)$$

Now according to Eq. (3) θ may be written

$$\theta(\mathbf{r})=v(\mathbf{r})-\frac{1}{\beta}\int_0^z dz'v(\mathbf{s},z-z')$$
$$-\frac{1}{\beta}\int_z^\beta dz'v(\mathbf{s},z'-z)+\frac{1}{\beta}\int_0^\beta\int\frac{dz'\sigma_1(\mathbf{s}')dS'}{|\mathbf{r}-\mathbf{r}'|}.$$

Since $v(\mathbf{r})$ is a well-behaved function of z, we may expand in a Taylor's series about $z=z'$ and obtain

$$\theta(\mathbf{r})=-2\pi\frac{\sigma_0(\mathbf{s})}{\beta}\Big\{z^2-2z\beta+\frac{\beta^2}{2}\Big\}$$
$$+\frac{1}{\beta}\int_0^\beta dz'\int\frac{\sigma_1(\mathbf{s}')dS'}{|\mathbf{r}-\mathbf{r}'|}. \quad (13)$$

Introducing this expression into (12B) results in

$$\int\frac{\sigma_1(\mathbf{s}')dS'}{|\mathbf{s}-\mathbf{s}'|}=-\frac{2\kappa}{\beta}\sigma_0(\mathbf{s})-\frac{\pi\beta}{3}\sigma_0(\mathbf{s}). \quad (14)$$

Putting (13) and (14) in (12A) and integrating, we obtain the thickness of the surface layer

$$\beta=(3/2\pi)^{\frac{1}{3}}\kappa^{\frac{1}{3}}.$$

Now the expression for ΔE (Eq. 7) can be readily evaluated. Substituting (11) in (7) we obtain

$$\Delta E=\frac{1}{2\beta}\int_0^\beta dz\int\sigma(\mathbf{s})v(\mathbf{r})dS$$
$$+\frac{1}{2\beta}\int_0^\beta dz\int\sigma(\mathbf{s})\theta(\mathbf{r})dS+\frac{\kappa}{\beta}\int\sigma^2(\mathbf{s})dS$$
$$=W(R)+\frac{1}{2}\int\sigma_1(\mathbf{s})v(\mathbf{s})dS+\frac{\pi\beta}{2}\int\sigma^2(\mathbf{s})dS,$$

and using (14), there results

$$\Delta_1E\equiv\Delta E-W(R)=(8\pi/3)^{\frac{1}{3}}\kappa^{\frac{1}{3}}\int\sigma^2(\mathbf{s})dS. \quad (15)$$

Since $\int\sigma^2(\mathbf{s})dS$ is of the order $R^{-1}|W(R)|$, this equation shows that for R large compared with the spacing between the free metal electrons the quantum mechanical correction Δ_1E to the classical image energy $W(R)$ is small.

In the case of copper, n_0 is about one free electron per 100 $(\hbar^2/me^2)^3$, and the plane wave estimate of κ is 3.7 $(\hbar^2/me^2)^2$. Thus β becomes 1.3 $\hbar^2/me^2$ or $\beta \approx a$ where a is the lattice spacing. It is apparent that this is not consistent with the assumption we made when we replaced the positive ion charge density by $-\rho_0$, i.e., $\beta \gg a$. But since the region of high electron density coincides with a surface layer in which the positive ion density is larger than $-\rho_0/e$, it appears that we have underestimated the absolute magnitude of the (negative) interaction energy between the electrons and the positive ions. That is, the energy $\Delta_1 E$ which we have calculated appears to be too large. Thus it would seem that by taking into account the discrete character of the positive ions, energy could be gained by further compressing the charge density near the surface. However, it must be recognized that the electrons with which we form the surface density are taken from the top of the Fermi lake, or, since we are dealing with a metal, from the middle of an energy band. The electrons in the lower part of the band concentrate around the positive ions and provide enough shielding so that the discrete character of the ions is pretty well washed out in its influence on the wave function of a mid-band electron. Thus our estimate of β and $\Delta_1 E$ should be reasonable as long as just a few electrons near the top of the Fermi lake are influenced by the presence of the external field.

Since our calculated $\Delta_1 E$ becomes negligible for $R \gg a$, it is assured that the purely quantal properties of the metal are unimportant unless the charge is so close to the metal that surface structure effects are already important.

In the case of a potential due to a point charge $\Delta_1 E$ becomes

$$\Delta_1 E = 0.46 \kappa^{\frac{1}{2}} R^{-1} |W(R)|,$$

and for copper this is

$$\Delta_1 E = 0.89 (\hbar^2/me^2) R^{-1} |W(R)|.$$

It would perhaps be expected that better approximations to $\rho'(\mathbf{r})$, and hence lower values for $\Delta_1 E$, could be made by using smoother functions of z than the step function. A similar calculation using a triangular function in z

$$\rho'(\mathbf{r}) = \frac{2}{\beta^2}(\beta - z)\sigma(\mathbf{s}) \quad \text{for} \quad z \leqslant \beta$$

$$\approx 0 \quad \text{for} \quad z \geqslant \beta,$$

results in

$$\beta = (10/3\pi)^{\frac{1}{2}} \kappa^{\frac{1}{2}},$$

$$\Delta_1 E = 2.55 \kappa^{\frac{1}{2}} \int \sigma_0^2(\mathbf{s}) dS.$$

Since $(8\pi/3)^{\frac{1}{2}}$ [see Eq. (15)] is 2.89, the energy $\Delta_1 E$ is in fact lowered by this choice of $\rho'(\mathbf{r})$.

For the exponential in z

$$\rho'(\mathbf{r}) = \beta^{-1} e^{z/\beta} \sigma(\mathbf{s}),$$

we obtain

$$\beta = (\kappa/2\pi)^{\frac{1}{2}},$$

$$\Delta_1 E = 2.51 \kappa^{\frac{1}{2}} \int \sigma_0^2(\mathbf{s}) dS.$$

It should perhaps be mentioned that for some metals (e.g., Bi) the free electronic density n_0 is so small that the plane wave estimate of κ becomes negative. In this case the Fermi-Thomas-Dirac method as used here is inadequate and better wave functions are required to estimate κ.

It has been assumed throughout this discussion that $\rho' \ll \rho_0$. This condition is satisfied for an external charge of the order of e unless it is so close to the metal that surface structure effects have already become important.[1] If a macroscopic point charge, say 10^{10} e, could be brought up to the metal surface, a deviation from classical results would be expected at a distance $R \approx 10^{-3}$ cm. In general the distance R at which deviations are expected is $R \approx Q^{\frac{1}{2}} a$, where Qe is the charge on the macroscopic body assumed to be a sphere of radius r. Then r must necessarily be less than R and the potential V required to charge up the sphere is $Qe/r > Qe/R = (R/a)(e/a) = 27(R/a)$ volts. To observe a macroscopic effect, R/a must be $\gtrsim 10^5$, which requires a potential $V > 10^6$ volts. Thus it seems safe to assume that this effect has no practical importance.

Production of 2537 Radiation and the Role of Metastable Atoms in an Argon-Mercury Discharge

CARL KENTY
Lamp Development Laboratory, General Electric Company, Nela Park, Cleveland, Ohio
(Received July 17, 1950)

The average population of 6^3P_1 mercury atoms is calculated from the measured 2537 output and resonance radiation diffusion theory. Average populations of $6^3P_{2,0}$ are then found by comparing the absorptions of 5461, 4358, and 4047. Populations for a 0.42-amp. discharge in 3.5-mm argon of high purity plus Hg vapor at 42°C in a tube 1½ inches in diameter are for $6^3P_{2,1,0}$, respectively, 7.6×10^{11}, 1.9×10^{11}, and 3.5×10^{11} cm^{-3}; these are ⅓, 1/20, and ⅓ of the corresponding Boltzmann populations, for the electron temperature of 11,100°K.

Rates of collisions of the first and second kinds involving electrons (average concentration 2.1×10^{11} cm^{-3}), and the 6^1S_0 and $6^3P_{2,1,0}$ states are calculated using known excitation functions and detailed balancing. The results predict populations for $6^3P_{2,1,0}$ within 10 percent of those observed; they further predict that ⅔ of the observed 2537, ⅔ of the visible triplet, and ¾ of the 3650 group are produced stepwise via 6^3P. Quenching collisions involving argon are assumed negligible.

The results account fairly well for the maximum in the 2537 *versus* Hg pressure curve, for the decrease in the 2537 output efficiency with increasing current, and for the decrease in electron temperature which is associated with both these effects.

INTRODUCTION

THE phosphor in a fluorescent lamp is activated primarily by the resonance radiation of Hg at 2537A. It is a known fact that this radiation does not increase linearly with current as might be expected if excitation and ionization were produced only by single-stage impacts. The present study[1] indicates that two-stage processes involving the resonance and metastable levels of Hg play a far more important role than direct excitation and ionization from the normal state.

In arriving at this conclusion it has been necessary to consider quantitatively the diffusion of resonance radiation, the populations of the $6^3P_{2,1,0}$ states of Hg and the various elementary processes of excitation and de-excitation involving these states.

The discharge studied is a positive column of 420 ma in a 1½-inch tube containing 3½-mm argon plus Hg vapor at $\sim7\mu$ pressure. This is approximately the discharge met with in the standard 40 w fluorescent lamp.

On account of the retarding effect of the argon, few metastable Hg atoms will be able to diffuse to the wall before they are destroyed by collisions with electrons. These collisions will be of a number of types; (1) collisions of the second kind which return the metastable state to the normal state, or in the case of 6^3P_2 to a lower 6^3P state, (2) collisions of the first kind raising a metastable state to a higher excited state, and (3) collisions resulting in ionization of the metastable state. The resonance state 6^3P_1 will suffer similar collisions, but to a smaller extent, owing to its smaller population (as limited by its radiation of 2537). In the attempt to estimate the rates of all these processes it was first necessary to determine the populations of the $6^3P_{2,1,0}$ states with the help of measurements of the relative absorption of the visible triplet lines. These lines, 5461, 4358, and 4047, have 7^3S_1 as a common initial level and end on $6^3P_{2,1,0}$ respectively.

[1] The principal results as stated here were reported at the Columbus Meeting of the Ohio Section of the American Physical Society, March 13, 1948 [Phys. Rev. 74, 114 (1948)] and at the April 1948 M.I.T. Electronics Conference.

ABSORPTION MEASUREMENTS

Absorption measurements were carried out by placing an emission lamp (1) behind an absorption lamp (2) and arranging a slit system requiring that a beam of light originating in (1) pass through (2) before reaching a photo-cell. The slits were 3½-mm wide and 2-cm long, cut in sheets of aluminum foil wrapped around the lamps. Corning monochromatic filters, placed before the cells, were used to isolate the lines. The lamps were placed 1 cm apart. The photo-cell had an opening 1-cm wide and was placed 10 cm in front of lamp (2).

The fractional absorption A of the beam will be given by

$$A=(I_1+I_2-I_{1+2})/I_1, \qquad (1)$$

where I_1 is the intensity of 2537 received when only lamp (1) is on, I_2 the intensity when only lamp (2) is on and I_{1+2} the intensity when both lamps are on. Measurements were made over a current range of 0.1 to 420 ma in the absorption lamp and of 50 to 500 ma in the emission lamp. Results for equal currents in emission and absorption lamps are shown in Fig. 1. Absorptions were read when the wall temperature of the absorption tube was 42°C, as measured by a fine thermocouple on the tube wall. With a current of 420 ma in the emission lamp, its temperature was also 42°C. The lamps were heated solely by their own currents, and in the case of the absorption lamp, the current was dropped from 420 ma only long enough to obtain an absorption reading. In this time the lamp temperature dropped by only a small amount and the absorption, a slowly varying quantity, did not change appreciably.

In Fig. 1, 5461 is seen to be more strongly absorbed than 4047, indicating a higher population for 6^3P_2 than for 6^3P_0. Substantial saturation is seen to set in at

$\sim$100 ma. Since saturation means constancy of population, it is concluded that at $\sim$100 ma the loss of metastables by diffusion to the walls is no longer important as compared with losses by quenching collisions with electrons. Thus beyond $\sim$100 ma the processes of excitation and destruction of metastables, both being proportional to the electron concentration, will increase with current at about the same rate so no great change in population will result.

The absorption of 4358 in Fig. 1 is seen to be the smallest and to show distinctly less saturation than the others. This is due to the fact the loss of 6^3P_1 by radiation is still high compared with loss by collisions of the second kind with electrons.

Regarding the saturation of the metastable populations at low current, it is instructive to consider the time taken for a metastable to reach the walls. Thus with a mean free path of $\sim$0.006 cm, and a speed of $\sim 1.8\times10^4$ cm sec.$^{-1}$, a metastable will require a time of the order of

$$(1.8/0.006)^2\times0.006/(1.8\times10^4)\cong0.03 \text{ sec.},$$

to reach the wall of a tube 1.8 cm in radius. Calculations show that this is ample time for dissipative collisions with electrons to occur, even with small currents. This means that the distribution of metastables over the cross section of the lamp will be much flatter than that of the resonance atoms as Fabrikant[2] has shown.

The gas in the lamps contained <2 parts per million of impurities and quenching of the 6^3P Hg states by them was negligible. Complete evidence for this, and further evidence concerning the saturation of the metastable populations, resulting from an extended study of these discharges at low currents will be given in a later paper. Quenching of metastables by argon is negligible in comparison to quenching by electrons (cf. the work of Panevkin, to be discussed further below).

While the absorption data were obtained with a d.c. discharge, and the 2537 and visible triplet data were obtained with the usual a.c. discharge, this is probably not of great importance here since within the present accuracy the a.c. and d.c. spectral characteristics are similar.[3]

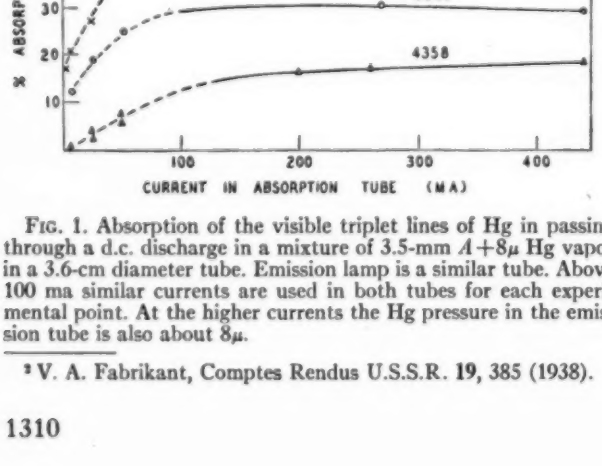

FIG. 1. Absorption of the visible triplet lines of Hg in passing through a d.c. discharge in a mixture of 3.5-mm $A+8\mu$ Hg vapor in a 3.6-cm diameter tube. Emission lamp is a similar tube. Above 100 ma similar currents are used in both tubes for each experimental point. At the higher currents the Hg pressure in the emission tube is also about 8μ.

[2] V. A. Fabrikant, Comptes Rendus U.S.S.R. **19**, 385 (1938).

CALCULATION OF THE RELATIVE POPULATIONS OF THE $6^3P_{2,1,0}$ STATES FROM THE ABSORPTIONS

If in the above absorption study the line radiation passed through the absorbing gas unchanged in nature, the number of absorbing atoms would be proportional to A, for small absorptions, and in general to $\log(1/1-A)$. The values of $\log(1/1-A)$ for 0.42 amp have been evaluated, and their ratios are given in Table I. But the core of the line is relatively the most absorbed and so the line is broadened as it passes through the discharge. Also the breadths of the lines from the emission tube will in general be different. There is one case however solved by Ladenburg and Reiche,[4] where k_0, the absorption coefficient of the core of the line can be deduced from the measured A; this is the case where conditions in the emission and absorption tubes are the same. It was for this reason that care was taken to have currents and temperatures the same at 420 ma in Fig. 1. The value of k_0 for the different lines has been evaluated, using the relation of Ladenburg and Reiche, from the A values of Fig. 1 and are given in Table I. The procedure has followed that of Fabrikant, Butaeva, and Zirg.[5] It has been stated by these authors that the atomic absorption coefficients for the lines of the visible triplet are all equal; this can be proved by application of the sum rules and the Einstein theory of radiation. Consequently the average concentrations of the absorbing atoms will be proportional to the k_0's in Table I, where the ratios are given in the last column.

It will be seen that the k_0's give somewhat smaller relative populations to 6^3P_1 and 6^3P_0 than do the values of $\log(1/1-A)$. This is to be expected since 4358, for example, is relatively sharper coming from the emission lamp than 5461 and, therefore, is more highly absorbed, per absorbing atom.

CALCULATION OF THE POPULATION OF 6^3P_1 ATOMS FROM THE 2537 OUTPUT

Thayer and Barnes[6] determined that in the present lamp operating on a.c. at 420 ma in 3.5-mm A plus Hg at 7.6μ (43°C), about 60 percent of the 40w input, or 24 watts, is converted into radiation able to excite the phosphor. According to further unreported work by the same authors in this laboratory, probably 2 watts of this is 1849 radiation; 22 watts is therefore taken as the 2537 output. Division of this by the length of the dis-

[3] W. E. Forsythe and E. Q. Adams, *Fluorescent and Other Gaseous Discharge Lamps* (Murray Hill Book Company, New York, 1948), p. 152.

[4] See A. C. G. Mitchell and M. W. Zemansky, *Resonance Radiation and Excited Atoms* (Cambridge University Press, London, 1934), p. 118 ff. and Table p. 323.

[5] Fabrikant, Butaeva, and Zirg, Physik. Zeits. Sowjetunion **11**, 576 (1937); **13**, 23 (1938).

[6] R. N. Thayer, Trans. Electrochem. Soc. **87**, 413 (1945).

charge, about 110 cm, between electrodes, and by the energy equivalent of the 2537 quantum (7.78×10^{-19} joule) gives the rate of escape R of 2537 quanta to be 2.5×10^{17} per cm length per second. Assuming that net quenching losses of the 6^3P_1 state are small, and for simplicity that the radial distribution of 6^3P_1 atom concentration n_1 will be roughly the parabolic one

$$n_1=(n_1)_0[1-(r^2/a^2)], \tag{2}$$

where $(n_1)_0$ is the concentration at the center and a is the tube radius, the concentration gradient at the wall will be $-2(n_1)_0/a$ and this multiplied by the diffusion coefficient of the radiation D and the circumference of the tube $2\pi a$ should give the rate of escape. Thus

$$R=4\pi(n_1)_0D. \tag{3}$$

The diffusion coefficient used is the approximate one arrived at by the author[7] and put into more convenient form by Zemansky.[8] Namely,

$$D=1/(4\bar{k}^2\tau). \tag{4}$$

Here τ is the mean life of the 6^3P_1 state (1.08×10^{-7} sec.) and $\bar{k}^2$ is the effective average square absorption coefficient. Tables for $\bar{k}$ the r.m.s. or "equivalent" absorption coefficient are given by Zemansky[9] in the form of $\bar{k}l$ as a function of k_0 where l is the thickness of the absorption cell and k_0 is the absorption coefficient of the core of the line. For the present case $k_0=n_ak_0'$ where k_0' is the atomic absorption coefficient for the core of the line and n_a is the concentration of Hg atoms. Substitution[10] of $k_0'=1.21\times10^{13}$, $n_a=2.13\times10^{14}$ cm^{-3} and $l\cong4/3a$ or 2.4 cm, gives $k_0=27$, $\bar{k}=6.7$ and $D=5.2\times10^4$.

Substitution for D and R in Eq. (3) then yields for $(n_1)_0$ the value 3.8×10^{11} cm^{-3}, an average value of n_1 over the cross section of 1.9×10^{11} cm^{-3}, and a total number N in a 1-cm length of tube (cross section ~10 cm^2) of 1.9×10^{12}. To account for the observed output, $R=2.5\times10^{17}$ per sec. per cm, the effective life T of the 2537 quantum within the tube would need to be $N/R=0.76\times10^{-5}$ sec.

The reciprocal of $\bar{k}$ is the effective mean free path or 0.15 cm. According to the principle of the random walk, the number of absorptions and re-emissions suffered by a quantum generated at the center before escape will be of the order of $(a/\lambda)^2$, i.e., $(1.8/0.15)^2\cong140$. The average for all quanta will be less than this; half the above number or 70 would be closely in accord with value of effective life of 0.76×10^{-5} sec. arrived at above.[11]

[7] C. Kenty, Phys. Rev. **42**, 823 (1932).
[8] M. W. Zemansky, Phys. Rev. **42**, 843 (1932).
[9] See also reference 4, Table XII, p. 331.
[10] k_0' has been calculated from Garrett's value of τ of 1.08×10^{-7} sec., following Zemansky, Phys. Rev. **36**, 229 (1930). n_a has been calculated for 7.6μ Hg pressure on an average gas temperature in the lamp of 73°C (346°K) as found in work in this laboratory to be reported elsewhere.
[11] V. A. Fabrikant, Comptes Rendus U.S.S.R. **19**, 389 (1938) gives the approximate expression $3k_0a\tau$ for this effective life. With $k_0=26$, $a=1.8$ cm and $\tau=1.08$ sec. This expression gives $T=1.5\times10^{-5}$ sec. which is twice the value obtained here.

TABLE I. Absorption of the visible triplet. A, absorption taken from Fig. 1; k_0, absorption coefficient for core of line as obtained from Ladenburg and Reiche's relation between k_0l and A (reference 3 l has been taken as 3.6 cm).

Line	A	Relative $\log(1/1-A)$	k_0	Relative k_0
5461	0.51	100	0.32	100
4358	0.18	28	0.083	25
4047	0.30	49	0.15	46

The problem may be attacked alternatively using the more recent and exact radiation diffusion theory of Holstein.[12] According to this theory, the distribution of 6^3P_1 atoms across a tube quickly assumes a characteristic form after the excitation, in whatever manner, is cut off, and the 2537 emitted thereafter decays with a characteristic time T given by[13]

$$T=\tfrac{5}{8}k_0a\tau(\pi\log k_0a)^{\frac{1}{2}}, \tag{5}$$

where a is the tube radius. Substitution of the values of the constants already used yields $T=0.72\times10^{-5}$ sec. This value of the decay time, or average life, is seen to be only slightly smaller than the average life obtained by the first method (0.76×10^{-5} sec.); which attests to the essential equivalence of the two methods for a case like the present. The first method suffers from the arbitrariness of the choices of the parabolic distribution and of the value of $l=(4/3)a$ as the thickness of the equivalent absorption cell. In the second method, the formula used applies to the characteristic distribution of 6^3P_1 atoms and not necessarily to the distribution existing in the actual discharge. In any case, since the practical difference in the two methods appears to be so small, the results will be left in their original form as based on $T=0.76\times10^{-5}$ sec.

THE POPULATIONS OF THE $6^3P_{2,1,0}$ STATES

If there were thermal equilibrium between the 6^3P states and the electrons at their temperature T_e, their populations would be given by

$$n=n_a(g/g_a)e^{-(eV_e)/(kT_e)}, \tag{6}$$

where $n_a=2.13\times10^{14}$ is the concentration of normal atoms, g_a is the statistical weight of the normal atom, g is the weight of the 6^3P atom in question, and V_e is its excitation potential. For T_e the value of 11,100°K is used, based on probe measurements made in this laboratory by M. A. Easley.[14] The populations as thus calculated are given in Table II. The last column of the table gives the ratios of the populations calculated from absorption to the Boltzmann populations.

[12] T. Holstein, Phys. Rev. **72**, 1212 (1947); see also L. M. Bieberman, J. Exp. Theor. Phys. **17**, 416 (1947).
[13] Alpert, McCoubrey, and Holstein, Phys. Rev. **76**, 1257 (1949). The formula as quoted in their article inadvertently omits the factor τ.
[14] The author is indebted to Miss Easley for permission to use her unpublished values for both T_e and n_e.

TABLE II. Comparison of populations with Boltzmann populations. V_e, excitation potential; g, statistical weight; k_0, absorption coefficient of core of line (from Table I); n, calculated from the ratio of the k_0's and $n=1.9\times10^{11}$ cm^{-3} for 6^3P_1, obtained from output and diffusion of 2537; n_B, Boltzmann population for $T_e=11{,}100°$K.

State	V_e	g	Ratio k_0	$n\times10^{11}$	$n_B\times10^{11}$	n/n_B
6^3P_2	5.43	5	100	7.6	36.4	0.21
6^3P_1	4.86	3	25	1.9	40.2	0.047
6^3P_0	4.66	1	46	3.5	16.3	0.21

The use of a temperature here for the electrons is taken to be justified even though the distribution may differ from Maxwellian in being deficient in the very high speed members; for the experiments of Miss Easley indicate that such deficiency occurs only for electrons of considerably higher energy than is here involved.

Fabrikant, Butaeva, and Zirg[15] calculated absolute values for the populations of $6^3P_{2,1,0}$ directly from their absorption measurements. They deduced k_0 in each case from the measured absorption by use of the Ladenburg-Reiche formula, as was done above, and used known relations[16] connecting the k_0's with τ, the mean life of the 7^3S_1 state. For τ they used Mitchell and Murphy's value[17] of $0.8\pm0.1\times10^{-8}$ sec. They assumed Doppler broadening and that therefore (with gas atoms at substantially room temperature) the five hyperfine structure components did not overlap, so that the number of absorbing atoms was $\frac{1}{5}$th the number in the state concerned. If the same procedure is followed here, populations are obtained which are about a third those found above. Panevkin[18] following the same procedure as Fabrikant, Butaeva, and Zirg, and studying a discharge rather similar to the present one, has obtained $6^3P_{2,1,0}$ populations one-third to one-fourth as large as those found here. It is believed that the optical densities involved are too great for such application (in the absolute) of the Ladenburg-Reiche formula, the values of k_0 derived with it being too small. Such an error becomes very pronounced[19] if an attempt is made to apply this method to the case of the 1-At. Hg arc where the densities of the 6^3P atoms are about 100-fold higher. Since the populations in Fabrikant, Butaeva, and Zirg's discharge were of the same order as those found here, it is believed their estimates are too low, perhaps by a factor of 2 or 3. In accord with this is the fact that they need populations several-fold higher than they calculate, in order to explain their observed 2537 output.[20]

QUASI EQUILIBRIUM FOR THE METASTABLE STATES

It was at first thought that the flatness of the absorption curves for these states in Fig. 1 indicated a true state of thermal equilibrium with the electrons. However, Table I does not indicate this. Further, following Panevkin,[21] true thermal equilibrium in a case like this would require, not constant populations with regard to current increase, but decreasing ones due to the fact that T_e decreases with current. It is concluded therefore that the absorption curves represent a state of quasi equilibrium with the electrons in which detailed balancing is not yet complete. Thus the populations of the metastable states are determined solely by electron collisions and the balance (not yet a Boltzmann one) changes only slowly with the current. All 6^3P states are closely tied together through collisions of the first and second kinds as Yavorsky[22] has shown; as will appear below, 6^3P_2 and 6^3P_0 are held below Boltzmann populations because of the important "leakage" of 2537.

The flatness of the absorption curves, considering the falling T_e, really means a gradual approach toward true thermal equilibrium conditions in which $^3P_2$ for example would be quenched to normal by electrons as fast as

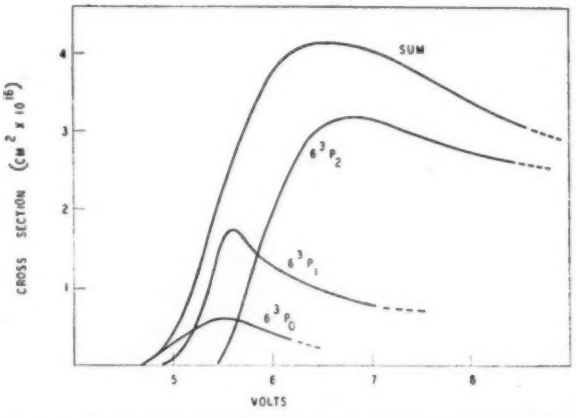

FIG. 2. Excitation function for the 6^3P states of Hg. That for 6^3P_1 is Nottingham's photoelectrically determined curve. The relative heights of the maxima of the three curves and also as far as possible their relative shapes are in accord with the quantum mechanical calculations of Penney and of Yavorsky. The scale of the three curves and some details of their shapes are chosen so that their sum reproduces the curve of Arnot and Baines, obtained from purely electrical measurements.

[15] Fabrikant, Butaeva, and Zirg, Physik. Zeits. Sowjetunion **11**, 576 (1937) and other papers in this series.

[16] See reference 4, p. 101 ff., where $1/\tau$ of Eq. (35) is to be replaced by the Einstein transition probability A, for the line in question and the measured τ of the 7^3S_1 state is the reciprocal of the sum of the A's for the green blue and violet lines. The relation between the A's being given by the sum rules which state that $A\propto g\nu^3$, g being the statistical weight of the lower state concerned, and ν being the frequency of the line.

[17] A. C. G. Mitchell and J. M. Murphy, Phys. Rev. **46**, 53 (1934).

[18] K. Panevkin, Papers of Acad. of Sci. U.S.S.R. **59**, 683 (1948).

[19] Using Barnes and Adams' [Phys. Rev. **53**, 545 (1937)] measurements of the absorption of 5461, 4358, and 4047 for a ½-atmosphere pressure Hg arc, the same method has yielded populations for the 6^3P states which are at least 25-fold smaller than those calculated from Boltzmann's theorem and the temperature as determined by x-rays [C. Kenty and W. J. Karash, Phys. Rev. **78**, 625 (1950)].

[20] While the authors seem to obtain an agreement, they base it on a speed of escape of 2537 through the Hg vapor which is much faster than that allowed by the present treatment of radiation diffusion or by Fabrikant's own (presumably) later treatment (reference 11).

[21] K. Panevkin, J. Phys. U.S.S.R. **2**, 39 (1940). See also V. Fabrikant and K. Panevkin, Comptes Rendus U.S.S.R. **20**, 441 (1938).

[22] B. Yavorsky, J. Phys. U.S.S.R. **10**, 476 (1946).

excited from normal and all other processes would be balanced by their opposites.

COMPUTATION OF THE RATES OF EXCITATION OF THE $6^3P_{2,1,0}$ STATES

While existing knowledge of the excitation functions for the 6^3P states of Hg leaves much to be desired, the following calculations, based on what are judged to be the best of the evidence, yield results which are in remarkably good agreement with the observed 2537 output. This agreement is believed to lend substantial support to the essential validity of the functions chosen. For 6^3P_1 Nottingham's photoelectric relative excitation function[23] has been used. For 6^3P_0 and 6^3P_2, approximate relative shapes for the functions have been taken from Penney's[24] and Yavorsky's quantum mechanical calculations.[25] The functions chosen are shown in Fig. 2. The relative heights of the three maxima are approximately also in shape with that found by Arnot and Baines[26] from purely electrical measurements of inelastic cross sections.

This procedure gives a maximum for 6^3P_1 substantially in agreement with Bricout's optically determined value of 6 cm^2 cm^{-3} or 1.7×10^{-16} cm^2 as quoted by Brode.[27,28] (The latter number is obtained from 6 cm^2 cm^{-3} by dividing by 3.56×10^{16}, the number of molecules in 1 cm^3 of gas at 1 mm pressure and 0°C.) All cross section maxima used or deduced in the present study are assembled in Table III.

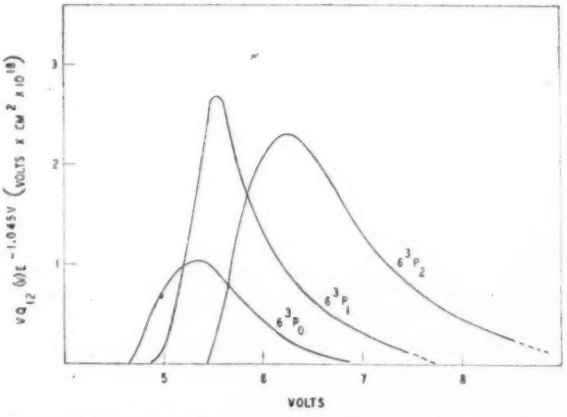

FIG. 3. Plots of the function $VQ_{12}(V)\epsilon^{-1.045V}$ for the 6^3P levels of Hg. $Q_{12}(V)$ is the cross section in cm^2 for the excitation of the level by electrons of energy V volts. The areas under the curves are proportional to the rates of excitation of the levels.

[23] W. B. Nottingham, Phys. Rev. **55**, 203 (1939).
[24] W. G. Penney, Phys. Rev. **39**, 467 (1932).
[25] B. Yavorsky, Bull. Acad. Sci. U.S.S.R. **9**, 233 (1945). While Penney has given only relative values, Yavorsky has calculated absolute ones which are stated to be in accord with the results of Arnot and Baines. Both authors agree fairly well as to the relative heights of the maxima, but Yavorsky's maxima occur at considerably higher voltages, and the shapes are otherwise somewhat different from Penney's.
[26] F. Arnot and O. Baines, Proc. Roy. Soc. **A151**, 256 (1935).
[27] R. B. Brode, Rev. Mod. Phys. **5**, 257 (1933).
[28] The cross section per atom is obtained from the total cross section per cm^3 at 1 mm pressure by dividing by 3.56×10^{16}, i.e., the concentration of molecules at 1 mm and 0°C.

TABLE III. Cross section maxima per atom used or implied in the present study; $Q_{12}(V)$ for electron collisions of the first kind, $Q_{21}(V)$ for electronic collisions of the second kind.

Transition	Threshold (volts)	$Q_{12}(V)$ max. cm^2 $\times10^{16}$	$Q_{21}(V)$ max. cm^2 $\times10^{16}$	Reference
$6^1S_0\rightleftarrows6^3P_2$	5.43	3.2	4.1	Nottingham,* Penney,** Yavorsky***
$6^1S_0\rightleftarrows6^3P_1$	4.86	1.74	4.6	Arnot and Baines†
$6^1S_0\rightleftarrows6^3P_0$	4.66	0.58	4.5	Bricout†† (see text)
$6^1S_0\rightarrow7^3S_1$	7.69	0.45		Yavorsky†††
$6^3P_2\rightarrow7^3S_1$	2.26	~4.0		Fabrikant, Butaeva and Zirg‡ (see text)
$6^3P_1\rightarrow7^3S_1$	2.83	~4.00		
$6^3P_0\rightarrow7^3S_1$	3.04	3.9		Yavorsky***
$6^3P_1\rightleftarrows6^3P_2$	0.57	19.3	44.0	Yavorsky‡‡
$6^3P_0\rightleftarrows6^3P_1$	0.20	(~15.0)	(~58.0)	(See text)

* See reference 23.
** See reference 24.
*** See reference 25.
† See reference 26.
†† See reference 27.
††† See reference 30.
‡ See reference 5.
‡‡ See reference 22.

Assuming a Maxwellian distribution for the electrons, the rate of excitation Y per cm of length will be given by

$$Y=2.66\times10^{14}\frac{a^2n_en_a}{T_e}\int_{V_e}^{\infty}VQ_{12}(V)\epsilon^{-(eV/kT_e)}dV, \quad (7)$$

where $Q_{12}(V)$ is the excitation cross section in cm^2 as a function of the electron energy V in volts and n_e is the electron concentration averaged across the tube (2.1×10^{11} cm^2 according to Easley's[14] probe measurements). With $a=1.8$ cm and $T_e=11{,}100$°K, Eq. (7) becomes

$$Y=1.64\times10^{20}n_a\int_{V_e}^{\infty}VQ_{12}(V)\epsilon^{-1.045V}dV. \quad (8)$$

Plots of the quantity $VQ_{12}(V)\epsilon^{-1.045V}$ are given in Fig. 3. The areas under these curves were found graphically and taking $n_a=2.13\times10^{14}$ cm^{-3}, the rates of excitation were found to be 1.35×10^{17}, 0.90×10^{17} and 0.40×10^{17} for the $6^3P_{2,1,0}$ states respectively.

An attempt has been made in Fig. 4 to portray the various transitions. Here the thickness of the 6^3P levels have been drawn pictorially in the ratios of the populations, i.e., calculated n values in Table II. Transitions by collisions of the first kind (excitation by electrons) are represented by straight arrows pointed upward, and collisions of the second kind (de-excitation by electrons) by straight arrows pointed downward. Radiations are represented by wavy arrows. A strength of 3×10^{16} transitions per sec. per cm length has been given to full arrows (either straight or wavy). Dotted arrows have the strengths indicated in decimals of the same unit. The relative total rate of any transition may then be visualized by adding the number of full arrows involved and the decimal part of an arrow. Thus the rates of excitation from normal of the $6^3P_{2,1,0}$ states calculated above are represented by 4.5, 3.0, and 1.33 arrows respectively, and the absolute rates may be found by multiplying these numbers by 3×10^{16}. Wavy arrows represent *measured* outputs in all cases.

QUENCHING TO THE NORMAL STATE

In complete thermal equilibrium with the electrons at their temperature T_e, quenching of any level to the normal state by electrons would, by the principle of detailed balancing, take place at the same rate as excitations to that level from the normal state. Since the rate of quenching will be proportional to the population of the upper state in question, and since the populations of the metastable states have each been estimated as 0.21 times the Boltzmann populations, their rates of quenching to normal by electrons will be 0.21 times their rates of excitation from normal, which rates have been calculated above. Likewise the rate of quenching of 6^3P_1 to normal will be 0.047 times the rate of excitation from normal. These quenching rates are shown by downward arrows in Fig. 4; 0.95 arrow for 6^3P_2, 0.14 arrow for 6^3P_1, and 0.28 arrow for 6^3P_0. The sum of these, 1.37, is 16 percent of the total excitations from normal.

Calculation of the actual quenching cross section curves[29] brings out the interesting circumstance that the maxima of these curves are all about equal (see Table III), while the Q_{12} maxima are approximately in the ratio of the g's.

The escaping 2537 has been represented in Fig. 4 as 8.3 wavy arrows to represent the measured 2537 output. The heavy wavy arrows represent the absorptions and re-emissions of 2537 before they escape; they have a strength each of the order of $\sim 70 \times 8.3$ or ~ 580 of the other full arrows. Their effect is merely to increase about 70-fold the effective lifetime of the 6^3P_1 state, a circumstance which has already been taken account of in calculating the population of this state.

TRANSFERS AMONG THE $6^3P_{2,1,0}$ STATES

The electronic excitation function for the $6^3P_1 \rightarrow 6^3P_2$ transition has been calculated from quantum mechanics by Yavorsky.[22] This is shown in Fig. 5. Again using Eq. (8) and n (in place of n_a) as 1.9×10^{11} cm^{-3} for the 6^3P_1 state, the rate of such excitations has been calculated to be 3.27×10^{16} cm^{-1} sec.$^{-1}$. This is represented by 1.09 upward arrows in Fig. 4. Figure 5 also shows the cross section $Q_{21}(V)$ for collisions of the second kind[29] quenching 6^3P_2 to 6^3P_1.

To calculate the rate of quenching transfers 6^3P_2

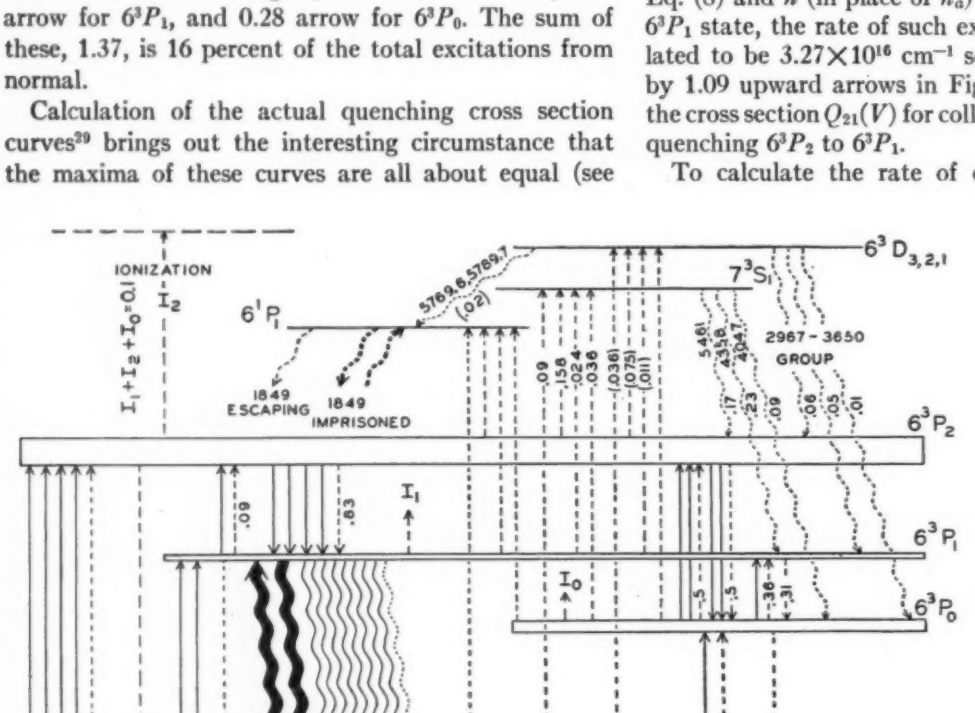

FIG. 4. Principal processes occurring in the fluorescent lamp. Straight arrows are calculated collisions of the first and second kinds. Wavy arrows are measured radiation outputs (except the heavy arrows). One full arrow, either straight or wavy represents 3×10^{16} transitions per sec. per cm of length. Decimals are fractions of full arrows. (*Correction added in proof:* There should be three full upward arrows from $6'S_0$ to 6^3P_1 instead of two as shown.)

[29] Quenching curves, $Q_{21}(V)$, have been calculated from the corresponding $Q_{12}(V)$ curves using the Klein-Rosseland relationship

$$Q_{21}(V) = \frac{g_1}{g_2} \frac{V}{V - V_e} Q_{12}(V),$$

where it is to be understood that V in $Q_{21}(V)$ on the left hand side is equal to $V - V_e$ on the right-hand side, and g_2 and g_1 are the statistical weights of the upper and lower states respectively. However, as seen above, it is not necessary to use these curves explicitly, a fact which seems not to be generally recognized.

$\rightarrow 6^3P_1$, it is first noted that if 6^3P_1 had a full Boltzmann population, the upward transition rate ($6^3P_1 \rightarrow 6^3P_2$) would be $(1/0.047) \cong 21$ times as great as it is, other things being equal, since 0.047 is the fractional Boltzmann population of 6^3P_1 (Table II). This rate of transitions (69×10^{16} sec.$^{-1}$ cm^{-1}) would also be the rate of downward ($6^3P_2 \rightarrow 6^3P_1$) transitions if 6^3P_2 had its full Boltzmann population. But since its population is actually 0.21 times this, the downward rate will be $0.21 \times 69 \times 10^{16} = 14.5 \times 10^{16}$ sec.$^{-1}$ cm^{-1}. This is shown as 4.83 downward arrows in Fig. 4. To calculate the rate of transitions in one direction from the known rate in the other direction, it is therefore only necessary to multiply by the ratio of the fractional Boltzmann populations.

Unfortunately no information exists regarding cross sections for transfers between 6^3P_0 and $6^3P_{2,1}$ states. But certain inferences may be drawn on the basis of the scheme of Fig. 4. Thus both 6^3P_2 and 6^3P_0 have, in this scheme, one quarter the Boltzmann population concerned. Transfers between the two states up and down must therefore take place at the same rate, just as they would in complete thermal equilibrium (when they would be ~five times as fast). Whatever the rate of the transfers, they will therefore not significantly change the scheme of Fig. 4 as drawn. The allotment of $2\frac{1}{2}$ arrows up and $2\frac{1}{2}$ down is arbitrary, but is compatible with a cross section for $6^3P_0 \rightarrow 6^3P_2$ of the same order as that for the $6^3P_1 \rightarrow 6^3P_2$ transfer and is in accord with evidence drawn from low current studies to be reported elsewhere. Here as elsewhere it is assumed that the number of transfers brought about by impacts of atoms or ions is negligible.[29a]

It is possible to draw more definite information regarding the transitions $6^3P_0 \rightarrow 6^3P_1$ and their reverse. Thus, in order to maintain 6^3P_0 at the constant population shown, there must be in total as many arrows leaving as ending on it. Now since a net gain of 1.05 arrows, as above defined, has already been calculated for it involving 6^1S_0, and since transfers to and from 6^3P_2 are equal and no other important losses or gains are involved, as will be seen, transfers involving $6^3P_0 \rightleftarrows 6^3P_1$ must be chosen so as to give a net gain of 1.05 arrows to 6^3P_1 from 6^3P_0. Let x be the upward rate and y the downward rate. Then $x-y=1.05$ and $x/y=0.21/0.047$ (the ratio of the fractional Boltzmann populations of Table II). Solution of these equations gives $x=1.36$, $y=0.31$. This selection of x and y would result if the cross section for $6^3P_0 \rightarrow 6^3P_1$ were 75 percent of that for 6^3P_1 and 6^3P_2. It thus appears that the cross sections for excitation from one 6^3P state to another are not greatly different from one another.

TRANSFERS INVOLVING 7^3S_1

Fabrikant, Butaeva, and Zirg[5] have concluded from their experiments that the cross sections for excitation

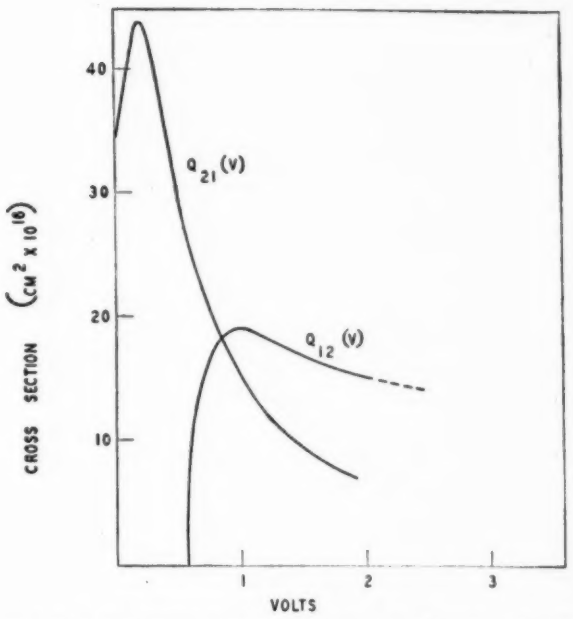

FIG. 5. $Q_{12}(V)$: Cross section for electron collisions exciting 6^3P_2 from 6^3P_1 (Yavorsky, reference 22). $Q_{21}(V)$: Cross section for collisions of the second kind with electrons returning 6^3P_2 to 6^3P_1. Yavorsky expresses his cross sections in the atomic units $10^{16}\pi a_0^2$ ($=0.87$ cm^2) per cm^3 at one mm pressure of the atoms concerned, where a_0 is the radius of the first Bohr orbit of the H atom (0.528×10^{-8} cm). The conversion factor is therefore $0.87/3.56 \times 10^{16} = 2.45 \times 10^{-17}$, so that his maximum of 78 in his units equals 19.4×10^{-16} cm^2.

of 7^3S_1 from $6^3P_{2,1,0}$ are an order of magnitude higher than that for excitation of 7^3S_1 from 6^1S_0. Their estimate was based on the observed faster-than-linear increase of the visible triplet lines with current in a pure Hg discharge at constant pressure. They had estimates of the concentrations of $6^3P_{2,1,0}$ from absorption measurements and knew n_e and T_e (the latter being assumed constant as the current varied). Having estimated the fraction of the visible triplet output due to cumulative excitation at any current, they then calculated excitation cross sections assuming that the shapes of the functions were similar to that for 6^1P_1 excitation from the normal state (broad maxima since no change in multiplicity is involved), and that the functions for all the 6^3P states were the same in magnitude at any given voltage above threshold. The resulting cross sections were 12.5 cm^2 per cm^3 (3.5×10^{-16} cm^2) at the maxima.

Yavorsky[30] has more recently calculated quantum mechanically $Q_{12(V)}$ for $6^3P_0 \rightarrow 7^3S_1$ and $6'S_0 \rightarrow 7^3S_1$. His curves are shown in Fig. 6. The maximum for $6^3P_0 \rightarrow 7^3S_1$ is seen to be 3.9×10^{-16} cm^2 (in rather good accord with Fabrikant, Butaeva, and Zirg's results) and that for $6^1S_0 \rightarrow 7^3S_1$ to be 0.45×10^{-16} cm^2. The latter is also in quite good accord with the value 0.64×10^{-16} cm^2 (1.2 cm^2 per cm^3) obtained earlier by Hanle and Schaffernicht.[31] The maximum in the case of $6^3P_0 \rightarrow 7^3S_1$ is seen to be relatively very broad.

[29a] Some of the evidence for this is summarized by C. Kenty, Phys. Rev. **42**, 823 (1932). See especially pp. 838, 839.

[30] B. Yavorsky, Comptes Rendus U.S.S.R. **48**, 175 (1945).

[31] W. Hanle and W. Schaffernicht, Ann. d. Physik **6**, 905 (1930).

The upward arrows in Fig. 4 have been calculated using the curves of Fig. 6 and the concentrations of $6^3P_{2,1,0}$ given in Table II, and assuming that the cross sections for all three 6^3P states are the same. These add up to a total of 0.31 arrow or 0.93×10^{16} transitions sec.$^{-1}$ cm^{-1}. This indicates that about two thirds of the excitation of 7^3S_1 comes via the $6^3P_{2,1,0}$ states.

THE OUTPUT OF 5461, 4358 AND 4047

The 7^3S_1 state will radiate these lines in the ratio 100:117:49, i.e., in the ratio $g\nu^3$. However, these ratios will be modified somewhat by absorption. Thus 5461, being more strongly absorbed will be weakened relatively to the others and particularly with respect to 4358 which is least absorbed. It is to be noted however that the number of quanta emitted is not changed by absorption since the population of 7^3S_1 is too small for detectable quenching. The calculated excitation rate of 7^3S_1 may thus be compared with the measured rate of emission of the visible triplet.

According to Forsythe and Adams,[32] the outputs of 5461, 4358, and 4047 from the lamp under consideration (40 watt) amount to 0.6 percent, 1.05 percent, and 0.45 percent respectively, of the positive column input (about 33 watts). Converting these to quanta per sec. per cm length one obtains 0.50×10^{16}, 0.70×10^{16}, and 0.28×10^{16}, respectively (corresponding wavy arrows shown in Fig. 4). The sum of these is 1.48×10^{16} sec.$^{-1}$ cm^{-1} and it is seen that the calculated excitation rate of 7^3S_1 (0.93×10^{16} sec.$^{-1}$ cm^{-1}) falls short of this by 37 percent.

The degree of accord is considered good in view of the assumptions made. The disagreement might be accounted for if (a) Yavorsky's excitation function for $6^3P_0\rightarrow7^3S_1$ does not rise sharply enough from onset, or (b) the assumption of the equality of the excitation cross sections for all three transitions $6^3P_{2,1,0}\rightarrow7^3S_1$ is incorrect, or if (a) and (b) are both partly true. (a) seems to be a possibility since in the case of the excitation functions for the 6^3P states from normal, Yavorsky's theoretical curves[25] do not rise nearly as sharply from the onset as the experiments of Nottingham or Arnot and Baines would indicate. In regard to (b) it might be noted that if the cross section for $6^3P_2\rightarrow7^3S_1$ were increased by a factor of two, the discrepancy would be removed.

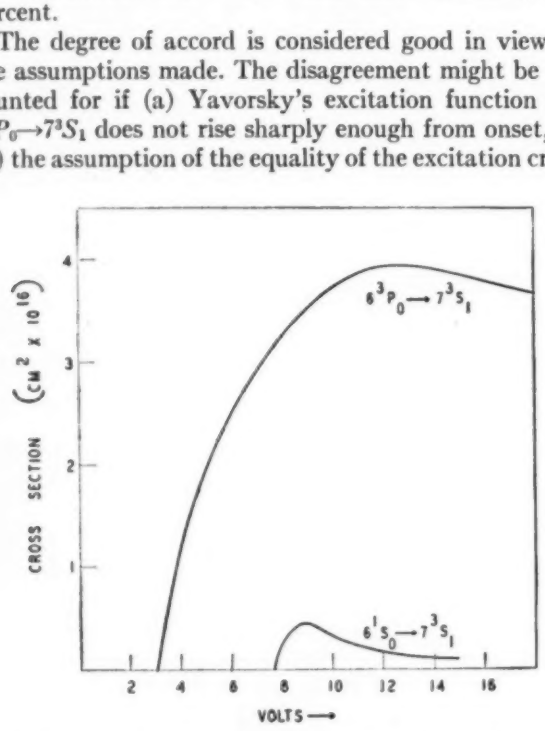

FIG. 6. Yavorsky's calculated cross sections for excitation of 7^3S_1 from 6^1S_0. Reproduced from reference 30, p. 177.

As to the experimental cross sections of Fabrikant, Butaeva, and Zirg,[5] which agree quite well with Yavorsky's[30] results, at least as to the heights of the maxima, it may be that they have, in their calculations, used a function which rises more steeply from onset than does Yavorsky's in order to account for the output. While their estimate seems to be quite good, it is believed that it involves two rather large errors which substantially neutralize each other: (1) Their estimates of 6^3P populations, based on absorption, are, according to the views mentioned above, two- or threefold too low; while (2) the fraction of the visible triplet taken by them to be due to cumulative acts is probably too small by a factor of two or more because of their assumption of the constancy of T_e as the current in their discharge in 1μ pure Hg vapor is raised. Thus their measured 2537 output per electron is markedly decreasing with rising current, showing a falling T_e, and since the direct excitation of 7^3S_1 per electron should decrease faster than that of $6^3P_{2,1,0}$ (i.e., than the 2537 output), it follows that the remainder of the 7^3S_1 excitation, namely that due to cumulative acts, must be greater than they have assumed. Their curves indicate that an error of a factor of two could thus easily have been made. In any case it seems likely that at least 67 percent of the excitation of 7^3S_1 in the fluorescent lamp under consideration comes stepwise via the 6^3P states.

TRANSFERS INVOLVING $6^3D_{3,2,1}$

Cross sections for the excitation of the $6^3D_{3,2,1}$ states (treated as one) have been roughly estimated from the data given by Forsythe and Adams.[32] These authors give as the output of the 40 watt fluorescent lamp the following: for the three lines ending on 6^3P_2 (called 3654), 0.32 percent; for the two lines ending on 6^3P_1 (called 3121), 0.37 percent; and for the yellow lines together, 0.12 percent of the positive column wattage (33 watts). A little over half of the energy of the yellow lines may be taken as coming from 6^3D, i.e., about 0.07 percent. Also the energy of the single line ending on 6^3P_0 (2967) may be taken[33] as 25 percent of that of the 3654 group or 0.08 percent. These percentages have been converted into quanta per sec. per cm length of lamp and are represented by the arrow strengths shown in Fig. 4. The total of the transitions amounts to 4.3×10^{15} sec.$^{-1}$ cm^{-1} or 0.14 arrow. It has been found

[32] W. E. Forsythe and E. Q. Adams, reference 3, Table 11, p. 86.

[33] Private information of Dr. B. T. Barnes.

that this total rate of excitation of 6^3D can be accounted for on the basis of excitation cross section curves, the same as were used for calculating 7^3S_1 transitions but increased 10 percent in magnitude. According to these curves the excitation of 6^3D is distributed as indicated by the arrows in Fig. 4, 75 percent of it coming from the 6^3P states.

TRANSFERS FROM $6^3P_{2,1,0}$ TO 6^1P_1

No data exist for estimating the transfers from the 6^3P states to 6^1P_1. If the cross sections were the same as for the transfers 6^3P to 7^3S_1, a rough calculation shows that transfers would take place about twice as fast to 6^1P_1 as to 7^3S_1. This would give such transfers an importance too small to upset the balance of Fig. 4 appreciably. That such transfers are relatively few is also indicated by the work of Butaeva and Fabrikant[34] which shows that the excitation of 1849, unlike that of 2537, is mainly directly from the normal state.

IONIZATION OF THE 6^3P STATES

The work of Klarfeld[35] has indicated that the cross sections for the ionization of the 6^3P states are an order of magnitude higher than that for ionization of 6^1S_0. Unpublished calculations made on this basis, and observations in this laboratory to be reported later, have indicated that practically all the ionization in the present lamp comes from 6^3P. The importance of such transfers for the present picture can be estimated from observed positive ion current to the wall, $\sim 50\mu$a cm^{-2}, or $\sim 500\mu$a per cm of length. This amounts to 3×10^{15} ions sec.$^{-1}$ cm^{-1}, a relatively negligible effect. It is to be noted that on account of the relative nearness of 6^3P_2 to ionization and of its relatively high population, most of the ionization will come from this state. Direct experimental evidence of this has been found in this laboratory and will be published elsewhere.

DISCUSSION

The various transitions shown in Fig. 4 have been summarized in Table IV, with a view to showing the degree of balance attained for each state. As for 6^3P_0 it is to be remembered that transitions to and from 6^3P_1 were chosen partly with a balance in view. In the other cases, no such arbitrary adjustments were made, the balances depending on 6^3P populations based on measured 2537 output; 2537 diffusion theory and relative absorption measurements; measured electron temperature and concentration and published experimental and theoretical excitation cross section curves. The degree of balance attained among all the processes is considered to be better than the accuracy of some of the data warrant. But the self-consistency shown is believed to be good evidence that the over-all picture cannot be far wrong. Possibly it can be used as evidence for the essential correctness of some of the data used, e.g., the more important cross sections.

TABLE IV. Summary of the transition rates represented in Fig. 4, showing the degree of balance attained for each of the 6^3P states and 7^3S_1 states.

State 1	State 2	Transitions* arriving at state 1 from state 2	Transitions* leaving state 1 for state 2	Net gain %
6^3P_2	6^1S_0	4.5	0.95	
	6^3P_1	1.09	4.83	
	6^3P_0	3.0	3.0	
	7^3S_1	$0.17L$**	0.16	
	6^3D	$0.06L$	0.8	
	Total	8.82	9.02	−1.1
6^3P_1	6^1S_0	3.01	0.14 $8.30L$	
	6^3P_2	4.83	1.09	
	6^3P_0	1.36	0.31	
	7^3S_1	$0.23L$	0.024	
	6^3D	$0.05L$	0.011	
	Total	9.48	8.90	6.5
6^3P_0	6^1S_0	1.33	0.28	
	6^3P_2	3.0	3.0	
	6^3P_1	0.31	1.36	
	7^3S_1	$0.09L$	0.036	
	6^3D	$0.01L$	0.017	
	Total	4.73	4.69	1.0
7^3S_1	6^1S_0	0.09	—	
	6^3P_2	0.158	$0.17L$	
	6^3P_1	0.024	$0.23L$	
	6^3P_0	0.036	$0.09L$	
	Total	0.31	0.49	−37.0

* In units of 3×10^{16} sec.$^{-1}$ cm^{-1} (arrows in Fig. 4).
** L refers to measured radiation.

Panevkin,[18] studying a decaying plasma, initially essentially like the present discharge, observed, by absorption measurements, decay times for $6^3P_{2,1,0}$ of 4×10^{-5}, 1×10^{-5}, and 6×10^{-5} sec. respectively. The value for 6^3P_1 namely 1×10^{-5} sec. agrees fairly well with that predicted here (0.76×10^{-5} sec.), considering that in Panevkin's case this state is being replenished from $6^3P_{2,0}$ by electronic collisions (the electrons disappearing by diffusion and recombination relatively slowly on this time scale). Indeed on the present picture it would have been expected that after an initial short period of adjustment this replenishment would have caused 6^3P_1 to decay along with the metastables. It is believed that this may have been the case, but was not shown up in Panevkin's experiments because of the difficulty of making the absorption measurements on 6^3P_1, at appreciable times after cut-off, with the necessary accuracy.

The present scheme accounts rather well for the initial rates of decay of the 6^3P states, especially $6^3P_{2,1}$, found by Panevkin.

According to Fig. 4 about one third of the excitation of 2537 comes directly from 6^1S_0 and two thirds stepwise via the metastables. The same conclusion was arrived at by Panevkin[18] and earlier by Butaeva and

[34] F. Butaeva and V. Fabrikant, J. Tech. Phys. U.S.S.R. **18**, 1127 (1948).
[35] B. Klarfeld, Tech. Phys. U.S.S.R. **5**, 913 (1939); Comptes Rendus U.S.S.R. **24**, 251 (1939).

Fabrikant.[36] These authors do not give the details of their calculations. Since as noted above Panevkin has used 6^3P populations which are one fourth to one third as great as those found here, it is to be inferred that he has used quite different values of T_e and n_e or else that his cross sections for transfers among the 6^3P states were several-fold larger than those used here. However, he quotes the same authority for these as that used here.[22]

Evidence for the essential correctness of the present scheme is found in the fact that it can be used along with the observed change in voltage to estimate with some accuracy the effect of changing Hg density and changing current on the 2537 output, and on the electron temperature and concentration.

The method consists in finding a new balance, corresponding to Fig. 4 which will satisfy the new conditions; it may be illustrated as follows. Suppose it is desired to find the effect of increasing by a certain factor the concentration n_a of Hg atoms, the current being kept constant. A consideration of the 2537 diffusion problem shows that the time of imprisonment T will increase roughly as $n_a^{1.17}$. The average concentration n_1 of 6^3P_1 atoms will as before be related to the 2537 output R quanta per cm length of the tube per sec. by the relation

$$\pi a^2 n_1 = RT.$$

The concentration n_1 will increase with T (although R may or may not, depending on the initial n_a) and this will allow the populations n_2 and n_0 of $6^3P_{2,0}$ to increase. Larger populations of the 6^3P states will, other things being equal, give a larger excitation of the visible and near ultraviolet lines and, more importantly for the discharge, a larger rate of ion production. The last result causes the observed drop in voltage and an increase in n_e (obtained with the use of the mobility equation), and a decrease in T_e.

It is now possible to find, largely by trial and error, a new T_e and a new corresponding set of 6^3P populations which will balance the excitation and de-excitation processes, and at the same time yield the needed rate of ion production (assumed proportional to n_e). It has been possible in this way, without too much labor, to predict a maximum in the 2537 output at around 40°C (6.1μ Hg pressure) as is observed.[37,38]

When the current (alone) is increased, T will not change but all processes depending on n_2 will increase. Most important is the resultant increase in n_1, which allows n_2 and n_0 to increase slightly, other things being equal. This increase in the 6^3P populations allows more efficient ion production, but it also gives a greater relative excitation of the visible and near ultraviolet lines at the expense of 2537. It has been found possible by the above method to find a new T_e, and n_e (corresponding with the observed drop in voltage) which will yield a new set of 6^3P populations, balancing all excitation and de-excitation processes and at the same time yield the needed ionization. The result predicts a decrease in the production efficiency of 2537 in good accord with the observed.

Butaeva and Fabrikant[34] have given an interesting discussion of the variation of 2537 output with Hg pressure and current but this method cannot suffice for the present case because it does not take into account the variation in T_e.

In the scheme of Fig. 4 the populations of the 6^3P states are held down to the observed small fraction of the Boltzmann populations by the "leakage" of 2537. It was seen above that about 84 percent of the total excitation of $6^3P_{2,1,0}$ is radiated as 2537, the remainder or 16 percent being returned to normal by collisions of the second kind. As the current (alone) increases, the latter percentage will increase, and when it has become all important and the 2537 leakage (and efficiency of production) negligible, the true Boltzmann populations will have been reached. In this process 6^3P_1 will increase relatively faster than 6^3P_2 and 6^3P_0, but due to falling T_e it may be that the absolute populations of $6^3P_{2,0}$ will decrease slightly as Panevkin[21] has shown (see also Fig. 1).

The writer is indebted to many of his colleagues for helpful discussions and particularly to Dr. C. G. Found, Dr. N. L. Oleson (now of the Postgraduate School, U. S. Naval Academy, Annapolis, Md.), Dr. B. T. Barnes, and Miss M. A. Easley.

[36] F. Butaeva and V. Fabrikant, Bull. Acad. Sci. U.S.S.R. Ser. Phys. 9, 230 (1945).

[37] W. E. Forsythe and E. Q. Adams, reference 3, p. 154ff and references therein.

[38] General Electric Lamp Bulletin LD-1, 59 (1946).

Vibrational Relaxation Times in Gases*

WAYLAND GRIFFITH†
Department of Engineering Sciences and Applied Physics, Harvard University, Cambridge, Massachusetts
(Received July 17, 1950)

Relaxation times for seventeen gases have been measured using a steady flow method, the velocity field being found numerically by Southwell's Relaxation Method. Where a comparison is possible the results are found to be in good agreement with sound dispersion data. The present state of knowledge about relaxation effects is discussed and a few instances of their possible appearance are cited.

INTRODUCTION

RECENT advances in the study of high speed flows have aroused new interest in the kinetic processes of fluid mechanics. In very strong shock waves, for example, conditions required by the Rankine-Hugoniot relations may be attained only outside a region considerably thicker than that usually estimated assuming internal energy equilibrium. Historically, the fact that internal energy states of molecules fail to keep up with sufficiently fast changes in their environment was first observed experimentally in 1925. Pierce[1] was able to measure dispersion of sound which could be explained only by ascribing a relaxation time to the adjustment of vibrational energy in addition to the effects of heat conduction and viscosity. Since then measurements have been made on dispersion and absorption of sound in several pure gases and many mixtures, and suitable theories advanced for interpreting the results.[2]

In 1942 Kantrowitz[3] proposed a very clever method for finding relaxation times using a steady flow of a gas. When the total pressure in a jet is measured with a pitot tube the value will be equal to the pressure in the reservoir from which the jet issues, provided the effects of viscosity and heat conduction are negligible, and provided all changes in the flow are slow compared to the rates of energy exchange between molecules. The former are usually limited to the boundary of the flow next to the walls, outside this region their effect is small. If the gas is now imagined to stop at the nose of a pitot tube quickly compared to the time for adjustment of vibrational energy, say, the compression will take place as though the gas had no vibrational energy, the specific heat ratio γ will be altered, and the resulting pressure will be different. The relaxation time enters the calculation through the time dimension involved in the stream velocity and pitot tube diameter. Kantrowitz verified the reliability of this method with measurements on carbon dioxide.

The purpose of the present investigation is threefold; (a), to measure vibrational relaxation times for several gases, (b), to extend confidence in the results of this method by using careful techniques and an exact solution of the flow pattern, and (c), to find as nearly as possible the limits of the method, for example in detecting very fast adjustments.

In the following section a very brief presentation of the thermodynamics appropriate to these experiments will be given, along with a physical explanation which it is hoped will aid in understanding the kinetic processes involved. Also, "relaxation time" will be defined.

THERMODYNAMICS FOR A GAS WITH LAGGING INTERNAL ENERGY

In addition to the usual thermodynamic variables for a gas it is appropriate to define a new one which describes the energy of vibration in the molecules. There are fairly good reasons to suppose that the various modes are in equilibrium among themselves even though they exchange energy slowly with the external motions of translation and rotation. In the first place there is always a certain amount of anharmonic coupling. Secondly, the lifetime is found experimentally to extend over hundreds or thousands of collisions. Although no direct evidence is available for it, a mechanism by which vibrational energy is redistributed within a molecule during a collision would have ample chance to operate. Accordingly T_{vib} will be defined as the temperature in the Boltzmann formula corresponding to the population distribution among vibrational states.

Three variables are therefore needed to specify a thermodynamic state for the gas, pressure and temperature say, and T_{vib}. The specific heat will be regarded as arising from two sources, vibrational motion, and all the rest. Following the nomenclature of Kantrowitz $c_{\text{vib}} \equiv dE_{\text{vib}}/dT_{\text{vib}}$, where E_{vib} is the energy in vibrational motion. C_p' will refer to the specific heat at constant pressure not counting vibration. Thus the usual specific heat $C_p = C_p' + C_{\text{vib}}$ when $T = T_{\text{vib}}$. Similarly C_v and C_v' will be used for constant volume specific heats. The Ideal Gas equation of state is assumed throughout.

The entropy change in going from one state to another is $\Delta S = \int dQ/T$, where any reversible path may be used to evaluate ΔS. By considering such a reversible change between two states which are allowed to approach one another indefinitely, one easily arrives at a

* Doctoral Thesis, Harvard University, 1949.
† Now at Palmer Physical Laboratory, Princeton, New Jersey.
[1] G. W. Pierce, Proc. Am. Acad. Sci. **60**, 271 (1925).
[2] An excellent review on sound dispersion and a bibliography is given by W. T. Richards, Rev. Mod. Phys. **11**, 36 (1939).
[3] A. Kantrowitz, J. Chem. Phys. **10**, 145 (1942).

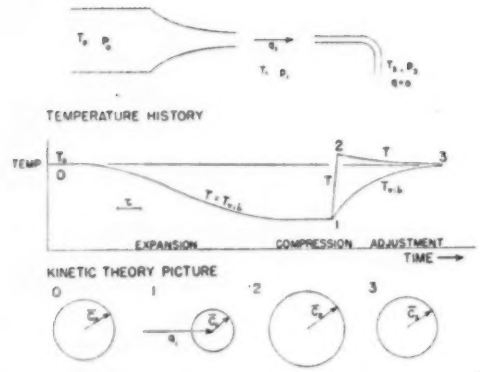

FIG. 1. Schematic drawing of the experiment, temperature history of the gas, and the variation in velocities according to kinetic theory.

formula for the entropy change as

$$dS=C_p'dT/T+C_{\text{vib}}dT_{\text{vib}}/T_{\text{vib}}-Rdp/p. \quad (1)$$

A familiar form of the Second Law results when T becomes equal to T_{vib}. We see that this is strictly applicable only when changes in temperature are slow compared to internal adjustments.

In many flow problems involving gases it is possible to neglect the viscosity, heat conductivity, and external forces in comparison to the other terms, and to assume constant specific heats without introducing serious errors. The equations for a compressible fluid with possible separate translational and vibrational temperatures are then

$$\text{Continuity} \qquad \partial\rho/\partial t+\partial\rho q_i/\partial x_i=0 \quad (2)$$

$$\text{Momentum} \qquad \rho\frac{dq_i}{dt}=-\partial p/\partial x_i \quad (3\text{–}5)$$

$$\text{Energy} \quad \frac{\partial}{\partial x_i}\rho q_i\left(C_{\text{vib}}T_{\text{vib}}+C_v'T+\frac{p}{\rho}+\frac{q_j^2}{2}\right)$$

$$=-\frac{\partial}{\partial t}\rho\left(C_{\text{vib}}T_{\text{vib}}+C_v'T+\frac{q_j^2}{2}\right). \quad (6)$$

Eliminating the velocity from the energy and momentum equations gives

$$d/dt(C_{\text{vib}}T_{\text{vib}}+C_p'T)-(RT/p)dp/dt=0. \quad (7)$$

Combining this with (1) gives the entropy as a function of T and T_{vib};

$$dS=(1/T_{\text{vib}}-1/T)dC_{\text{vib}}T_{\text{vib}}. \quad (8)$$

This is what one might write down intuitively by considering the transfer of energy $dC_{\text{vib}}T_{\text{vib}}$ from the temperature T to T_{vib}.

A consideration of the actual collisions is required in order to find an expression for the rate at which the above exchange will take place. Using simplified models Bethe and Teller derived formulas predicting the decay function for adjustment and its dependence on pressure, vibration frequency, and temperature. Details in the steps are not included here but may be found in the papers by Bethe and Teller,[4] Landau,[5] and Landau and Teller.[6]

The variation of T_{vib} is found to be

$$dC_{\text{vib}}T_{\text{vib}}/dt=C_{\text{vib}}(T-T_{\text{vib}})/\tau, \quad (9)$$

where the relaxation time has the following functional dependence;

$$\tau\approx p^{-1}(\nu s)^{-\frac{1}{3}}\left(\frac{m}{T}\right)^{-\frac{1}{2}}\exp\left\{(\nu s)^{\frac{1}{3}}\left(\frac{m}{T}\right)^{\frac{1}{2}}\right\}. \quad (10)$$

The new quantities are ν-vibration frequency, s-molecular radius, and m-molecular mass. When changes in the temperature are small τ may be considered constant and after a time τ the temperature difference diminishes to $1/e$, or 0.368, of its original value.

With this information let us study the case mentioned earlier of a slow expansion through a nozzle to a velocity q_1 and a fast compression in front of a pitot tube. From the equations of momentum and energy

$$d/dt(C_{\text{vib}}T_{\text{vib}}+C_p'T+q^2/2)=0. \quad (11)$$

By this and Eq. (1) the ratio of reservoir pressure to pitot tube pressure will be

$$p_0/p_3=\exp\{\Delta S/R\}. \quad (12)$$

The entropy change is found from (8) and (9), the increase occurring while T and T_{vib} converge upon the stagnation value T_0. (See Fig. 1.)

$$\Delta S=\int_{T_1}^{T_0}\left(\frac{1}{T_{\text{vib}}}-\frac{1}{T}\right)dC_{\text{vib}}T_{\text{vib}}$$

$$=\int_{T_1}^{T_0}\left(\frac{1}{T_{\text{vib}}}-\frac{C_p'}{C_pT_0-C_{\text{vib}}T_{\text{vib}}}\right)dC_{\text{vib}}T_{\text{vib}}.$$

This finally gives,

$$\frac{p_0}{p_3}=\left(\frac{T_0}{T_1}\right)^{C_p/R}\left(\frac{C_p'T_0}{C_pT_0-C_{\text{vib}}T_1}\right)^{C_p'/R}. \quad (13)$$

The pressure at state 2 may also be found quite easily. Equations (9) and (1) give,

$$\frac{C_p'}{R}\frac{dT}{T}-\frac{dp}{p}+\frac{C_{\text{vib}}dt}{\tau RT}(T_{\text{vib}}-T)=0. \quad (14)$$

If τ is very long compared to other times in which changes take place in isentropic flow the last term

[4] H. A. Bethe and E. Teller, Report X-117, Ball. Res. Lab., Aberdeen Proving Ground.
[5] L. Landau, Physik. Zeits. Sowjetunion **1**, 89 (1934).
[6] L. Landau and E. Teller, Physik. Zeits. Sowjetunion **10**, 34 (1936).

vanishes and

$$p/p_0=(T/T_0)^{C_p'/R} \tag{15}$$

that is, the gas acts as though it had only the specific heat C_p'. For τ very short on the other hand, $T=T_{\text{vib}}$ and

$$\frac{p}{p_0}=\left(\frac{T}{T_0}\right)^{C_p/R} \tag{16}$$

in the usual fashion. From (11)

$$C_p(T_0-T_1)=\frac{q_1^2}{2}=C_p'(T_2-T_1). \tag{17}$$

Solving we find

$$\frac{p_0}{p_2}=\left(\frac{T_0}{T_1}\right)^{C_p/R}\left(\frac{C_p'T_0}{C_pT_0-C_{\text{vib}}T_1}\right)^{C_p'/R}. \tag{18}$$

The surprising result is that p_2 and p_3 are equal so that the adjustment of internal energy takes place at constant pressure. In his thesis* the author shows that $p_0>p_2$, which is consistent with the increased entropy.

Figure 1 shows a schematic drawing of the experiment, the time-history of the process, and a sort of kinetic theory picture of the situation at various stages of the flow. The acceleration from 0 to 1 is a conversion of random molecular motion with average velocity $\bar{c}_0$ into streaming motion of flow velocity q_1 and smaller average velocity $\bar{c}_1$. The compression from 1 to 2 returns all the stream energy into random motion without reexciting the vibrations immediately. The average velocity is higher than in the reservoir. The pressure is less, however, as the density is sufficiently lower to compensate for the higher temperature. The adjustment of internal energy takes place at constant pressure, decreasing temperature, and increasing density. The average molecular velocity returns to its original value but the gas is less dense.

With this qualitative idea of the effect in mind we can now develop the methods used for determining relaxation times from pressure measurements. Again we shall use a symbol introduced by Kantrowitz as a measure of the disequilibrium between vibration and translation,

$$\epsilon\equiv c_{\text{vib}}(T_{\text{vib}}-T). \tag{19}$$

In flows where changes in T are small compared to T itself (8) may be written

$$ds=-\frac{\epsilon dt}{\tau}\frac{T-T_{\text{vib}}}{TT_{\text{vib}}}\cong\frac{\epsilon^2 dt}{\tau C_{\text{vib}}\bar{T}^2}. \tag{20}$$

$\bar{T}^2$ is taken as the average of TT_{vib} over the whole process. From Fig. 1 a good value is seen to be $\bar{T}=\frac{1}{2}(T_0+T_1)$. The specific heats and relaxation time will be taken at this temperature as well.

When the difference $p_0-p_2=\Delta h$ is small compared to p_0,

$$\Delta S/R\cong\Delta h/p_0 \tag{21}$$

and

$$\Delta h/p_0=\int\frac{\epsilon^2 dt}{\tau C_{\text{vib}}\bar{T}^2} \tag{22}$$

where ϵ depends on the relaxation time and the history of the flow. The integral is to be taken over that part of the flow for which Δh is desired. An equation for ϵ is found by eliminating the temperature from (9), (11), and (19),

$$d\epsilon/dt+C_p\epsilon/C_p'\tau=C_{\text{vib}}/C_p'd(q^2/2)/dt \tag{23}$$

the integral being

$$\epsilon(t_1)=\exp\left(-\int^{t_1}\frac{C_p dt}{\tau C_p'}\right)\int^{t_1}\times\exp\left(\int^{t_1}\frac{C_p dt}{\tau C_p'}\right)\frac{C_{\text{vib}}}{C_p'}\frac{d(q^2/2)}{dt}dt \tag{24}.$$

This completes the thermodynamics, for a knowledge of the velocity history of the flow and the specific heats now enable one to relate pressure differences to relaxation times.

DESIGN OF THE EQUIPMENT

A review of the literature on sound dispersion indicates that relaxation times are of the order of five microseconds. Generally diatomic molecules have longer times, polyatomic gases shorter times. Accordingly a steady flow is desired in which a gas expands slowly compared to this time and stops in about five microseconds.

Because the analytical flow solutions known are limited in number and sometimes difficult to reproduce experimentally, it was decided to use a fairly simple arrangement with axial symmetry and solve the problem numerically using R. V. Southwell's Relaxation

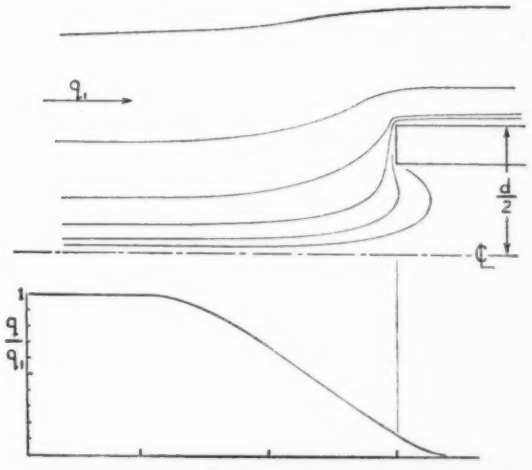

FIG. 2. Streamlines for flow past an open-ended cylinder computed numerically and the velocity along the central streamline.

Method.[7] It rests upon the accuracy with which a difference equation can be made to approximate a differential equation. An excellent discussion of the method may be found in a paper by Emmons.[8] Incompressible flow was assumed, the effect of compressibility can be found from the velocity dependence of the observations.

The solution for a plane parallel jet impinging on a flat plate was obtained first since the simplicity of this arrangement was quite attractive. The required nozzle diameter was only 0.024 in., though, so this scheme was abandoned in favor of a pitot tube to obtain sufficiently fast stopping times.

A square-ended cylinder was chosen for the shape of the tubes and the Relaxation Method used to locate streamlines. First the streamline at 2.25 d was assumed to be undisturbed; when this was moved out to 2.50 d values of the stream function were changed by less than one percent. A hollow center of diameter 0.620 d was

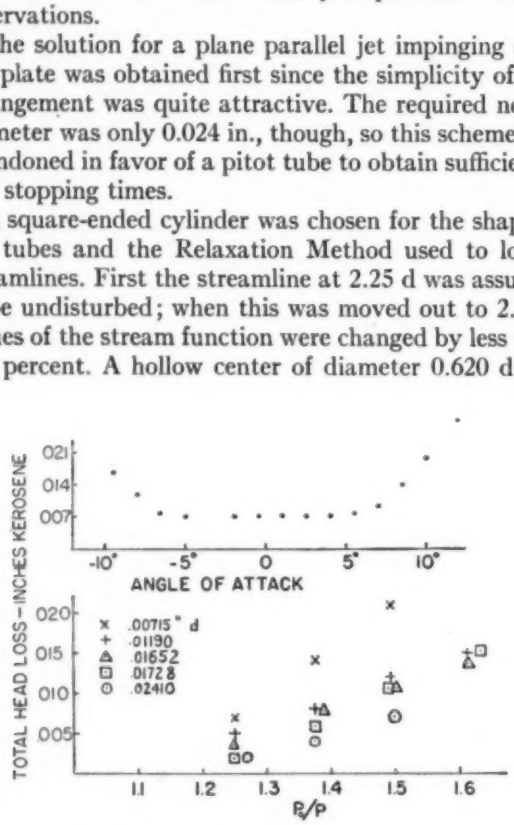

FIG. 3. The effect of angle of attack on total head loss and minimum losses for five tubes at various ratios of reservoir to stream pressure.

then included in the calculation. This made the deceleration of the flow considerably less abrupt. The streamlines and a velocity-time plot are shown in Fig. 2. For a jet velocity of 400′/sec. the diameter should then be about $400\times12\times5\times10^{-6}\times2/3=0.016$ in. It is interesting that the disturbance extends only one diameter upstream.

Glass tubes were found to be most satisfactory, being both easy to clean and relatively easy to make. With sufficient practice and patience square ends on tubes down to 0.005 in. could be ground with a fine Water of Ayr stone. Diameters of the tubes actually used in various phases of the investigation were as follows: 0.0241 in., 0.01728 in., 0.01652 in., 0.01190 in., and 0.00715 in. The respective i.d./o.d. ratios were: 0.610, 0.622, 0.590, 0.604, and 0.622.

A good design for the nozzle is important since we should like to measure only the effect due to fast stopping. Equation (23) shows that the best possible type of acceleration is one in which dq^2/dt is constant. This is the same as dT/dt constant, chosen by Kantrowitz for another reason. Two nozzles one-half inch long were made. The exit diameters were 0.070 in. and 0.040 in. The flow at 400′/sec. is 1.1 cfm through the larger nozzle and 0.36 cfm through the smaller one. A correction for the wall boundary layer was made, similar to that described in Kantrowitz's paper.

The reservoir was made from a two-foot section of three inch iron pipe. The nozzle was mounted in one end, the other having a connection for the gas supply line and a blowout diaphragm. Inside the chamber a 100-mesh screen and straightening vanes were placed twelve inches from the nozzle. The reservoir was mounted horizontally and had a thermocouple and pressure tap for measuring the stagnation conditions. Arrangements for a few experiments at elevated temperatures were made by placing a coil gas heater in the supply line and winding the reservoir with Nichrome wire and pipe insulation.

A micromanometer was devised to measure small pressure differences very accurately and quickly. A short length of glass tubing with a fine cross-hair was mounted at an angle on a frame which travelled vertically. Also mounted on the frame was an Ames dial which read distances above an arbitrary level to an accuracy of 0.0005 in. With a mirror fixed behind the cross-hair one could move the frame to align the meniscus and hairline within 0.003 in. For a slope of 1:4 in the tube, the height of the meniscus could be measured to 0.001 in. Since the meniscus is always in the same part of the tube the usual difficulties of varying wall diameter and incomplete wetting were greatly reduced. With kerosene in the manometer a change in pressure of 2×10^{-6} atmos. was detectable.

A special holder was made for the tubes which allowed independent adjustments to be made in axial and transverse positions and in direction. Once the tip of the tube was properly located in the stream the angle of attack could be changed to align it correctly. The tubing used was Seran, a transparent plastic. Reservoir pressure was measured with a mercury U-tube. All of the pressure lines were kept at one level as nearly as possible to reduce errors due to buoyancy when gases with densities quite different from air were tested. A small blower and stovepipe were used to draw off the more toxic gases.

EXPERIMENTAL METHODS AND DETERMINATION OF RESULTS

The gases used were obtained in steel cylinders from commercial supply houses. The purest form available was chosen in each case since work on sound dispersion indicated that certain impurities, especially water vapor, could cause large variations in the measured results. Preliminary runs with compressed air showed

[7] R. V. Southwell, *Relaxation Methods in Engineering Science* (Clarendon Press, Oxford, 1940).
[8] H. W. Emmons, Q. App. Math. **2**, 3, 173 (1944).

that readings could be taken once a minute. Nitrogen was chosen as the best available gas for taking minimum readings because of its very small vibrational heat capacity. The effect of the angle of attack is shown in Fig. 3. The range of minimum loss extends $\pm 5°$, thus making proper alignment fairly easy. Consistent readings were found for axial positions between one and two nozzle diameters and over three-fourths of the stream. Also shown in Fig. 3 are the minimum pressure losses at various pressure ratios using the 0.040 in. nozzle. The readings were very nearly the same for the 0.070 in. nozzle. The dependence on tube size cannot necessarily be interpreted as a relaxation effect, for the smaller tubes may be less perfect, and some loss due to viscosity might also be expected. Important to the main work is the conclusion that the losses due to other than relaxation effects can be reduced to such a small value. Before each experimental run readings with nitrogen were taken and subtracted from the observed data. A qualitative idea of relative relaxation times may be formed from Fig. 4 which shows the measured pressure loss for several of the gases tested.

The method for calculating relaxation times from these data will now be developed. Equation (23) gives

$$(d\epsilon/dt)dt+(C_p\epsilon/C_p')dt/\tau = (C_{vib}/C_p')\left(d\frac{q^2}{2}\Big/dt\right)dt. \quad (25)$$

As the time required for stopping becomes shorter the second term will become small compared to the other terms, and in the limit, when $\int \epsilon dt/\tau$ becomes negligible in comparison to the other two terms, the change in ϵ is

$$\Delta\epsilon=(C_{vib}/C_p')\Delta q^2/2.$$

In the case being considered ϵ was originally zero and the velocity was q_1. A sudden stopping then produces a value of

$$\epsilon_0=(C_{vib}/C_p')q_1^2/2.$$

With $q=0$, (25) gives for the approach to equilibrium $d\epsilon/dt=-C_p\epsilon/C_p'\tau$. The pressure change for an instantaneous compression is accordingly,

$$\Delta h_{ic}/p_0=\int_{\epsilon_0}^{0}\frac{\epsilon^2 dt}{\tau RC_{vib}\bar{T}^2}=\int_{\epsilon_0}^{0}\frac{C_p'\tau\epsilon d\epsilon}{C_p\tau RC_{vib}\bar{T}^2} =\frac{C_p'}{2C_pC_{vib}R\bar{T}^2}\left(\frac{C_{vib}q_1^2}{2C_p'}\right)^2. \quad (26)$$

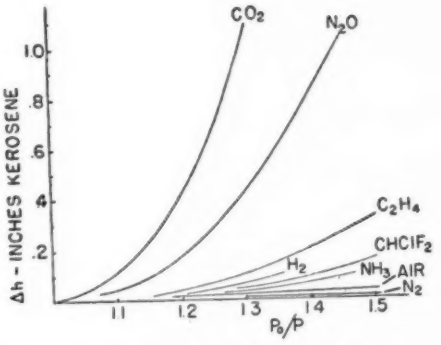

FIG. 4. Observed pressure losses for several of the gases tested.

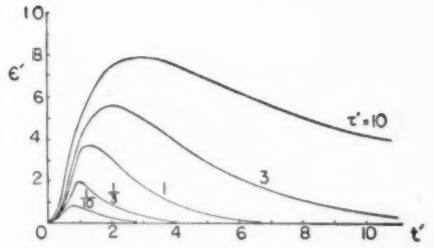

FIG. 5. The parameter ϵ' measures the disequilibrium of vibrational energy. For instantaneous stopping it would initially have the value 1; plotted are the variations in ϵ' for five values of the dimensionless relaxation time τ'.

It is more convenient at this point to substitute a set of dimensionless variables than to continue with the physical variables. Using Kantrowitz' notation again define the following dimensionless variables,

$$\tau'=\frac{C_p'}{C_p}\frac{q_1\tau}{d} \qquad t'=\frac{q_1 t}{d}$$
$$\epsilon'=\frac{\epsilon}{(C_{vib}/C_p')(q_1^2/2)} \qquad q'=q/q_1. \quad (27)$$

Using (27) and (26) in Eqs. (24) and (22) we find

$$\epsilon'=\exp\left(-\frac{1}{\tau'}\int dt'\right)\int\exp\left(\frac{1}{\tau'}\int dt'\right)\frac{dq'^2}{dt'}dt' \quad (28)$$

and

$$\frac{\Delta h}{\Delta h_{ic}}=\frac{2}{\tau'}\int\epsilon'^2 dt' \quad (29)$$

Thus we see that $\Delta h/\Delta h_{ic}$ depends only on τ' for a given flow pattern. This is the great simplification obtained by running an experiment in which only small temperature changes occur.

The integration of (28) to find ϵ' was done numerically for several values of τ'. Curves of ϵ' corresponding to these are given in Fig. 5. The mathematical difficulty of infinite stopping time on the central streamline was avoided by abandoning the integration when further contributions from the integrand became negligible. Physically the discrete nature of the gas explains the paradox.

The integration for $\Delta h/\Delta h_{ic}$ was found by counting squares in a graph of ϵ'^2 *vs.* t'. The resulting values are

τ'	1/10	1/3	1	3	10
$\Delta h/\Delta h_{ic}$	0.0828	0.226	0.480	0.723	0.908

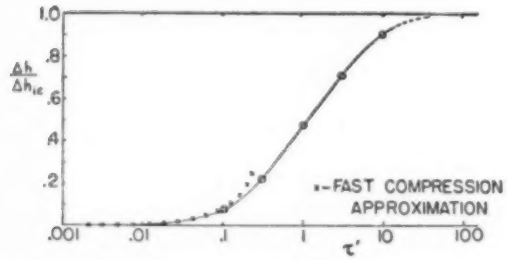

FIG. 6. Graph used to find dimensionless relaxation time τ' from observed pressure loss Δh.

For very short relaxation times an approximation method used by Kantrowitz was also applied here, the result being $\Delta h/\Delta h_{ic}=0.867\tau'$. Figure 6 shows that this is valid for $\tau'<0.08$.

The temperature T_1 was found from the pressure ratio p_1/p_0 and Eq. (16), the velocity q_1 from (17). Thus Δh_{ic} could be computed and τ' read from the graph.

EXPERIMENTAL RESULTS

The results for N_2O shown in Fig. 7 give an idea of the consistency of the method and show that no velocity dependence up to $M=0.8$ is observable. A similar test on CO_2 confirmed this result. Apparently the faster deceleration in the compression is just compensated for by the gain in collision rate. Relaxation times for the seventeen gases tested are given in Table I. The temperature dependence of τ shown in Fig. 8 was found from a few measurements; the accuracy was somewhat reduced due to difficulties in keeping the reservoir temperature equal to the gas temperature.

Hydrogen has no appreciable vibrational energy at room temperature so the observed pressure loss was ascribed to rotational lag and the same formulation assumed applicable. An upper limit for rotation of N_2 was also computed in this way. Only an upper limit could be found for four gases which showed no pressure loss greater than N_2. Two brands of CO_2 were tested, commercial CO_2 with a few percent water vapor, and a special purified lot containing 0.044 percent water vapor. This produced a large change in the result and it is felt that the time for the pure gas is somewhat longer still. This conclusion is borne out by a comparison with sound dispersion data, the most recent value for carefully purified CO_2 being about a third larger. Other impurities in other gases are not nearly as effective as this combination so the results may be considered fairly reliable. As a possible check for future work the suppliers' data on impurities are included in Table I. Also included are values from the literature on all the pure gases tested. Of the six in common beside CO_2 agreement is seen to be very good for H_2, N_2O, and C_2H_4, while agreement for SO_2, CH_4, and NH_3 extends only to the order of magnitude.

FIG. 7. Data on N_2O indicating accuracy of readings and absence of compressibility effect on results.

DISCUSSION

With the information on pure gases available from these experiments and the data already reported in the literature several conclusions may be drawn about the collisions. Relaxation times decrease for increasing temperature, supporting the theory that the fast collisions are most important. The higher the vibration frequency the longer the relaxation time; $CH_4>CH_3Cl>CHF_2Cl$; $CH_4>C_2H_6$; $C_2H_4>C_3H_6$. This indicates that the idea of resonant coupling used in deriving (10) is fairly reasonable. Since progression along the methane and ethylene series seems to give shorter relaxation times it is likely that all complicated molecules reach equilibrium quickly. Few fruitful measurements have been made on diatomic molecules, presumably because their small vibrational energy produces an exceedingly small effect. A further difficulty arises from the long times indicated; an impurity that is more effective than the molecule itself in collisions will control the adjustment.

This brings up the next important consideration, the effect of mixtures. Early experimenters were not aware of the great influence which foreign molecules with chemical affinity have. This accounts in large part for the dismaying array of values in the literature, and for the remarkable difference in the two brands of CO_2 tested here. The shift in the absorption maximum has been found linear for small amounts of impurities,[9] indicating that bimolecular collisions are responsible for energy exchange. A single exception is the case of O_2, where a quadratic dependence on water vapor content

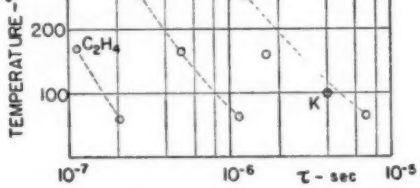

FIG. 8. Dependence of relaxation time on temperature. The point marked K is from Kantrowitz' work.

[9] V. O. Knudsen and E. F. Fricke, J. Acous. Soc. Am. **12**, 255 (1940).

points to triple collisions as the mechanism.[10] In general unlike molecules exchange energy more readily than like molecules. Since the monatomic gases and N_2 are exceptions[11] one may conclude that chemical affinity is important. The small mass and high velocity of H_2 is significant since it is more effective than D_2. To explain the orders of magnitude the moments of inertia and dipole strength must also be considered.[11,12] Eucken[13] discusses the problem from the point of view that vibrational excitation is preliminary to chemical reaction; if colliding molecules are known to react exchange of vibrational energy is likely.

Limitations of the flow method of measurement can now be outlined fairly well. The size of nozzles and pitot tubes used here represent the lower practical limit of utility and construction. A sharp-nosed tube might produce half the stopping time, but would be harder to make. Operating the entire experiment at a lower pressure lengthens the adjustment period, but reduces the sensitivity even more. For testing compounds with small vapor pressures this is necessary anyway. For diatomic molecules higher pressures would give greater sensitivity, the disadvantage being the larger gas flow. The inherent inability of this method to detect more than one rate of adjustment does not seem to be serious, since no bona fide cases of this sort have been discovered in sound dispersion.

CONCLUSIONS

The results of this investigation extend considerably the available data on pure gases. Molecular energy exchange is such a complicated process that it is unfortunately still impossible to predict a relaxation time for an untested gas or mixture. Certain limits, however, may now be set on conditions where relaxation effects will appear. Calculations show that the thickness of a shock wave in CO_2 is about a tenth of an inch; at $M=2$ the initial value of $T-T_{vib}$ is 350°F so quite a strong effect in this narrow region might be expected. Experiments to look for this using a shock tube are being planned. In the usual aerodynamic problems relaxation effects are completely negligible as has always been assumed. For extreme cases of heat and velocity as are met in rocket and meteor flight studies relaxation effects are doubtless significant, but until the large-scale effects are better understood this will not be considered.

The flow method is seen to be a very satisfactory technique for measuring vibrational relaxation times, and may be used to study many other rate processes, for example dissociation and recombination.

The author would like thank Professor Howard Emmons for many valuable discussions and continued interest during the course of this research.

TABLE I.

Gas	Temp. °F	Relaxation time μsec.	Gas purity and foreign gas Present investigation	
Hydrogen	58	0.021 (rot.)	99.8%, 0.2% H_2O	
Nitrogen	60	<0.002 (rot.)		
Nitrous oxide	65	1.12	98–99%, 1–2% N_2	
Carbon dioxide	65	6.95	99.956%, 0.044% H_2O	
Carbon dioxide (comm.)	65	2.02	x% H_2O	
Sulfur dioxide	68	0.37	99.988%, 0.002% H_2O	
Ammonia	63	0.12	99.5%, 0.005% H_2O	
Methane	60	0.48	99%, 1% C_2H_6, N_2, CO_2	
Methyl chloride	72	0.202	99.5%, <0.008% H_2O	
Freon 22	70	0.10	97%, <0.005% H_2O	
Freon 12	67	0.090	95%, <0.001% H_2O	
Ethane	57	0.003	95%, 5% C_2H_4, C_3H_8, C_3H_6	
Ethylene	60	0.207	99.5%, 0.5% air	
Propylene	70	<0.006	99%	
Propane	70	<0.007	99%	
Ethylene oxide	86	1.23	99.8%	
Butane	70	<0.018	99%	
Butadiene	70	<0.013	99.77%, 0.23% C_4H_{10}	
Results reported in the literature:				
Oxygen	70	1000		Reference [a]
Carbon monoxide	1800	10		[b]
Chlorine	70	18		[c]
Nitric oxide	60	0.8 (el. excit.)		[d]
Hydrogen	77	0.018 (rot.)		[e]
	60	0.02 (rot.)		[f]
Deuterium	60	0.015 (rot.)		[f]
Carbon dioxide	70	10.8		[f]
	70	10.26		[g]
Nitrous oxide	67	0.92		[e]
	70	1.44		[g]
Carbonyl sulfide	70	0.86		[g]
	70	1.67		[c]
Carbon disulfide	70	0.70		[g]
Sulfur dioxide	70	0.181		[g]
Water vapor	415	0.037		[h]
Ammonia	70	0.4		[i]
Ethylene	70	0.238		[j]
Methane	230	0.84		[e]

[a] See reference 12.
[b] G. G. Sherratt and E. Griffiths, Proc. Roy. Soc. London **147A**, 292 (1934).
[c] See reference 13.
[d] See reference 10.
[e] E. S. Stewart, Phys. Rev. **69**, 632 (1946).
[f] A. van Itterbeek and R. Vermaelen, Physica **9**, 345 (1942).
[g] E. F. Fricke, J. Acous. Soc. Am. **12**, 245 (1940).
[h] A. Kantrowitz and P. Huber, J. Chem. Phys. **15**, 275 (1947).
[i] O. Steil, Zeits. f. physik. Chemie **B31**, 343 (1936).
[j] See reference 11.

[10] H. O. Kneser, Ann. d. Physik. **39**, 261 (1941); J. Acous. Soc. Am. **5**, 122 (1933).
[11] W. T. Richards and J. A. Reid, J. Chem. Phys. **2**, 193 (1934); W. T. Richards **4**, 561 (1936).
[12] H. O. Kneser and V. O. Knudsen, Ann. der Phys. **21**, 682 (1935).
[13] A. Eucken and S. Aybar, Zeits. f. physik. Chemie **B46**, 195 (1940); A. Eucken and R. Becker, *ibid.* **27**, 219 (1934).

Numerical Determination of Fundamental Modes

DONALD A. FLANDERS AND GEORGE SHORTLEY*
Argonne National Laboratory, Chicago, Illinois
(Received July 12, 1950)

A convenient and practical method of numerical determination of the fundamental eigenfunction and eigenvalue in a class of linear eigenvalue problems has been developed and applied in two and three dimensions. The method is based on use of a network and of difference equations, but departs from previous methods in that it is not iterative. Rather, a polynomial operator is applied to a trial function just once, to accomplish a determinable degree of reduction in all eigenfunctions other than the fundamental that are contained in the trial function. In the case of the diffusion equation, the polynomial operator is a Tschebyscheff polynomial of a simple averaging operator. It is shown that this operator, when of degree m, is "better" than any other polynomial operator of this degree and much "better" than m iterations of a simple averaging operator—"better" in the sense of accomplishing to a greater degree the elimination of *all* unwanted eigenfunctions. Techniques for the use of computing equipment for application of the polynomial operator are discussed. By orthogonalization, the method can be applied to modes other than the fundamental.

INTRODUCTION

IN connection with work on complex problems occurring in certain applications of diffusion theory, a convenient and practical method of numerical determination of the fundamental eigenfunction and eigenvalue in linear eigenvalue problems has been developed and applied in two and three dimensions.[1]

While the methods we have developed are applicable to a wide class of systems of linear partial differential equations and a wide variety of linear boundary conditions, we feel that the new ideas and techniques will be most useful if they are first presented in the simplest possible setting. Hence, in this paper we shall first consider in detail the numerical determination of the lowest eigenvalue and corresponding fundamental eigenfunction of the equation

$$\Delta u+\alpha u=0, \tag{1}$$

which occurs in the theories of heat conduction, diffusion, vibration, and elsewhere. For simplicity we shall fix attention on a connected two-dimensional region bounded by straight-line segments parallel to the x- and y-coordinate axes, and shall consider the simplest boundary condition

$$u=0 \qquad \text{on the boundary.} \tag{2}$$

The methods discussed can be generalized so as to apply to more general linear differential equations of elliptic type, to systems of such equations, to more complex geometrical configurations, to more general linear boundary and interface conditions and to more dimensions. Systems of equations will be discussed briefly in the last section.

We replace the continuum by a square lattice of mesh h, and equation (1) by a difference equation, in the usual way. Again for simplicity we assume that the dimensions are such that the boundaries fall along rows of lattice points, and that a lattice point falls at the origin of coordinates. We further assume that the mesh is so small that every pair of interior points can be joined by a polygonal path consisting of segments of the network lying wholly in the interior of the region; we shall say that the *interior* points are *connected* by the net. We denote the lattice points by P_{ij} and the corresponding values of u by u_{ij}, where $i=x/h$, $j=y/h$.

If we use the notation ωu_{ij} to represent the average of the values of u at the four nearest neighbors of the point P_{ij}, i.e.,

$$\omega u_{ij}=\tfrac{1}{4}(u_{i+1,j}+u_{i-1,j}+u_{i,j+1}+u_{i,j-1}),$$

the second-difference approximation[2] to Δu at the point P_{ij} is

$$\Delta u_{ij}\approx\frac{\omega u_{ij}-u_{ij}}{\tfrac{1}{4}h^2}.$$

The difference equation that approximates (1) is then

$$\omega u_{ij}-u_{ij}+\tfrac{1}{4}h^2\alpha u_{ij}=0,$$

or

$$\omega u_{ij}=\lambda u_{ij}, \tag{3}$$

where

$$\lambda=1-\tfrac{1}{4}h^2\alpha. \tag{4}$$

* Operations Research Office, The Johns Hopkins University, on leave of absence from The Ohio State University; consultant at the Argonne National Laboratory.

[1] For a review of previous work on numerical methods in two and three dimensions (mostly work on boundary-value rather than eigenvalue problems) see Thomas J. Higgins, *Numerical Methods of Analysis in Engineering* (The Macmillan Company, New York, 1949), Chapter 10. This chapter contains an extensive bibliography.

[2] Nothing we say in this paper will be changed except in minor details if one chooses to use the higher-order approximation to Δu that is obtained if we define the averaging operator ω as

$$\omega u_{ij}=\tfrac{1}{5}(u_{i+1,j}+u_{i-1,j}+u_{i,j+1}+u_{i,j-1})+\tfrac{1}{20}(u_{i+1,j+1}+u_{i-1,j+1}+u_{i+1,j-1}+u_{i-1,j-1}),$$

in which case

$$\Delta u_{ij}\approx(\omega u_{ij}-u_{ij})/\tfrac{3}{10}h^2$$

and (4) becomes

$$\lambda=1-\tfrac{3}{10}h^2\alpha.$$

This expression for Δu_{ij} is valid for any seventh-order polynomial passing through the nine points, whereas the expression in the text is valid for a cubic polynomial passing through the five points. For a detailed discussion of approximations to the Laplacian, see Shortley and Weller, J. App. Phys. 9, 345 (1938).

The highest eigenvalue λ_1 of (3) will give an approximation to the lowest eigenvalue α_1 of (1) according to the relation (4), and the corresponding eigenvector of (3) will approximate to the fundamental eigenfunction of (1). We shall not discuss in this paper the accuracy of these approximations; it is well known that the solutions of the difference equation converge to solutions of the differential equation as $h \to 0$.

We shall consider the function u_{ij} to be defined only at interior points of the region. At a point adjacent to the boundary ωu_{ij} then will be taken to represent $\frac{1}{4}$ the sum of the values at the three, two, or one neighboring interior points, since one or more zero boundary values occur in the averaging process. We assume that there are N interior points, and for convenience number them from 1 to N, replacing the double index i,j by a single index k. The set of values u_k will then be denoted by a column vector $\mathbf{u}=(u_k)$. For the sake of brevity two components of $\mathbf{u}$ will be called neighboring if they represent values of u at neighboring points of the lattice.

Let $\omega_{kl}=\frac{1}{4}$ or 0 according as u_k and u_l are neighbors or not, and let ω denote the square matrix with elements ω_{kl}. The matrix equation

$$\omega\mathbf{u}=\lambda\mathbf{u} \tag{5}$$

then represents the result of incorporating the boundary conditions into the system of Eqs. (3). Thus Eq. (5) is the complete finite-difference analog of the analytic system (1), (2). It is the algebraic eigenvalue problem set by (5) with which we shall be concerned henceforth.

BASIC PROPERTIES OF THE SOLUTIONS OF THE MATRIX EQUATION

The general theory of equations such as (5) is well known. We set down here such general facts as we shall need, and we derive certain further useful properties specific to the particular equation.

The matrix ω is real and symmetric. Hence, it has N real eigenvalues and a complete orthonormal system of eigenvectors.[3] We denote the eigenvalues by

$$\lambda_1 \geq \lambda_2 \geq \cdots \geq \lambda_N,$$

and the corresponding eigenvectors of an arbitrary (but fixed) complete orthonormal system by

$$\mathbf{u}^1, \mathbf{u}^2, \cdots, \mathbf{u}^N. \tag{6}$$

(Since $-\mathbf{u}$ is an eigenvector belonging to the eigenvalue λ if $\mathbf{u}$ is, and is normalized if $\mathbf{u}$ is, we shall assume throughout that whenever $\mathbf{u}$ denotes an eigenvector, the maximum of the absolute values of the components of $\mathbf{u}$ is equal to the value of some component u_k of $\mathbf{u}$.)

The averaging operation performed by ω cannot increase the maximum of the absolute values of the components of any eigenvector $\mathbf{u}$, so that every $|\lambda_n| \leq 1$. In fact one can readily see that only the inequality can hold because of the zero boundary condition. (It is clear that the $\leq$ sign will hold for more general operators than ω provided the corresponding matrix contains no negative elements and the sum of the elements in every row is ≤ 1, while the inequality may be asserted if in addition the sum of the elements of some row is <1.)

The highest eigenvalue, λ_1, is non-degenerate (i.e., $\lambda_1 > \lambda_2$ or, equivalently, there are not two linearly independent eigenvectors with eigenvalue λ_1), *and $\mathbf{u}^1$ is everywhere positive.* These facts may be proved by using the variational analog of the eigenvalue problem, which may be stated thus: If $\mathbf{u}^0$ is a normalized eigenvector of (5) with eigenvalue λ_0, then $\mathbf{u}^0$ is a vector that gives the quadratic form

$$(\mathbf{u}, \omega\mathbf{u}) \equiv \sum_{k,l} \omega_{kl} u_k u_l$$

the stationary value λ_0, subject to the normalization condition

$$(\mathbf{u}, \mathbf{u}) \equiv \sum_{k} u_k^2 = 1;$$

and conversely.

Let $\mathbf{v}$ be any normalized eigenvector belonging to λ_1 (i.e., with eigenvalue λ_1), and let $\mathbf{w}=(|v_k|)$. Then $\mathbf{w}$ is normalized, and we shall show that it is also an eigenvector belonging to λ_1. For since no $\omega_{kl}<0$ it follows that $\omega_{kl}w_k w_l \geq \omega_{kl}v_k v_l$ in every case, and hence that $(\mathbf{w}, \omega\mathbf{w}) \geq \lambda_1$. Since λ_1 is the maximum value that $(\mathbf{u}, \omega\mathbf{u})$ can assume for any normalized vector $\mathbf{u}$, we

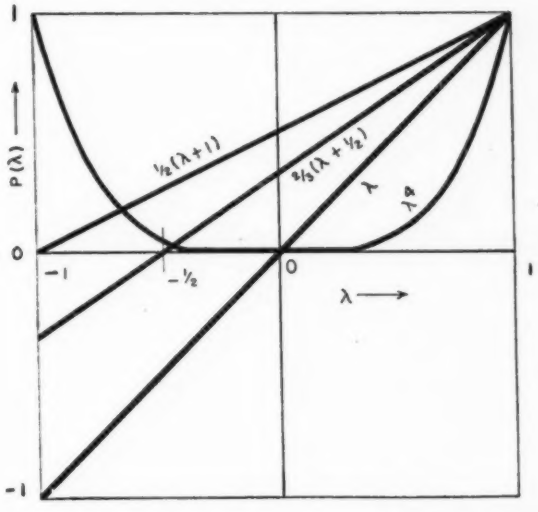

FIG. 1. The factors $P(\lambda)$ corresponding to certain polynomial operators $P(\omega)$.

[3] If ω is a real but unsymmetric matrix, and weight factors γ_i exist such that $\gamma_i\omega_{ij}=\gamma_j\omega_{ji}$, ω will have N real eigenvalues and a complete system of eigenvectors orthonormal with respect to the weight factors γ_i, the direct product being defined by

$$(\mathbf{u}, \mathbf{v}) = \Sigma_i \gamma_i u_i v_i.$$

In this case $(\mathbf{u}, \omega\mathbf{u})$ is a symmetric quadratic form that is an extremum for an eigenvector. This case is of importance when different choices of net spacing are made in different regions, the weight factor representing essentially the area of continuum associated with each net point. The weight factors for change of net spacing are given by Kimball and Shortley, Phys. Rev. **45**, 815 (1934). The techniques of the present paper are readily applicable to matrix operators of this type, and in particular to the Schrödinger problem discussed by Kimball and Shortley.

TABLE I. Reduction factor $1/T_m(d)$, where $d=(2/r)-1$.

	$r=0.9$ $d=1.22222$	0.925 1.16216	0.95 1.10526	0.96 1.08333	0.97 1.06186
$m=$ 1	0.81818	0.86047	0.90476	0.92308	0.94175
2	0.50311	0.58781	0.69290	0.74227	0.79676
3	0.27499	0.35816	0.47961	0.54477	0.62361
4	0.14490	0.20884	0.31588	0.38023	0.46502
6	0.03393	0.06890	0.12996	0.17425	0.24138
8	0.01061	0.02229	0.05251	0.07792	0.12123
12	0.00077	0.00238	0.00852	0.01542	0.03001
16	0.00006	0.00025	0.00138	0.00305	0.00740
24			0.00004	0.00012	0.00045
32					0.00003

	$r=0.98$ $d=1.04082$	0.985 1.03046	0.99 1.02020	0.9925 1.01511	0.995 1.01005
$m=$ 1	0.96078	0.97044	0.98020	0.98511	0.99005
2	0.85719	0.88993	0.92454	0.94259	0.96117
3	0.72066	0.77799	0.84264	0.87814	0.91603
4	0.58076	0.65559	0.74637	0.79932	0.85846
6	0.35076	0.43397	0.55043	0.62750	0.72281
8	0.20285	0.27373	0.38606	0.46941	0.58347
12	0.06555	0.10396	0.17853	0.24514	0.35360
16	0.02101	0.03892	0.08052	0.12382	0.20514
24	0.00215	0.00543	0.01620	0.03098	0.06686
32	0.00022	0.00076	0.00325	0.00772	0.02149
40	0.00002	0.00011	0.00065	0.00193	0.00692
48		0.00001	0.00013	0.00048	0.00223
56			0.00003	0.00012	0.00072
64			0.00001	0.00003	0.00023
72					0.00008
80					0.00002

must have $(\mathbf{w}, \omega\mathbf{w})=\lambda_1$, and hence $\mathbf{w}$ is an eigenvector belonging to λ_1. Thus $\omega w_k \equiv \sum_l \omega_{kl} w_l = \lambda_1 w_k$ for every k.

Now $\mathbf{v}$ (and hence $\mathbf{w}$) can have no zero component. For if $\mathbf{w}$ has any zero values, there must be at least one point P_r for which $w_r=0$ that has a neighboring point P_s for which $w_s>0$. This follows because $\mathbf{w}$ does not vanish identically and because the interior points are connected by the net. But we have arrived at a contradiction since on the one hand $\omega w_r=\lambda_1 w_r=0$, while on the other ωw_r is a sum of non-negative terms $\omega_{rl} w_l$ of which at least one, $\omega_{rs} w_s$, is not zero.

Further, no component of $\mathbf{v}$ is negative. As before one could find neighboring values $v_r<0, v_s>0$ ($v_k=0$ having been excluded). But now we have $(\mathbf{w}, \omega\mathbf{w})>(\mathbf{v}, \omega\mathbf{v})$ since $\omega_{rs} w_r w_s = -\omega_{rs} v_r v_s > 0 > \omega_{rs} v_r v_s$.

Finally, no two linearly independent eigenvectors can belong to λ_1. For if $\mathbf{v}^1$ and $\mathbf{v}^2$ were such eigenvectors, normalized and with only positive components, their difference would be an (unnormalized) eigenvector belonging to λ_1 that would have both positive and negative values, which is impossible. Thus $\mathbf{u}^1$ is unique and is everywhere positive. Since every eigenvector belonging to a different eigenvalue must be orthogonal to $\mathbf{u}^1$, $\mathbf{u}^1$ must be the only everywhere positive eigenvector in the set $\mathbf{u}^1, \cdots, \mathbf{u}^N$.

We have thus proved that

$$1>\lambda_1>\lambda_2\geq\lambda_3\geq\cdots\geq\lambda_N>-1. \tag{7}$$

An arbitrary vector $\mathbf{v}$ has a unique expansion in terms of the set (6):

$$\mathbf{v}=\sum_n c_n \mathbf{u}^n, \tag{8}$$

where c_n is the inner product of $\mathbf{v}$ and $\mathbf{u}^n$, that is

$$c_n=(\mathbf{v}, \mathbf{u}^n)=\sum_k v_k u^n{}_k.$$

If $\mathbf{v}$ is everywhere positive the coefficient c_1 must also be positive, and if furthermore $\mathbf{v}$ is reasonably pillow-shaped, c_1 will probably be larger than the magnitude of any other coefficient.

The effect of applying the operator ω to an arbitrary vector is to produce the vector

$$\omega\mathbf{v}=\sum_n \lambda_n c_n \mathbf{u}^n.$$

More generally, if $P(\omega)$ is any polynomial in ω,

$$P(\omega)\mathbf{v}=\sum_n P(\lambda_n) c_n \mathbf{u}^n,$$

that is to say that each coefficient c_n is multiplied by the value of the polynomial $P(\lambda)$ at $\lambda=\lambda_n$. Figure 1 shows the graphs of the factors $P(\lambda)$ corresponding to the operators ω, ω^4 and $(\omega-a)/(1-a)$ for $a=-1$ and for $a=-\frac{1}{2}$.

It is clear from Fig. 1 that the operator ω will reduce the magnitude of every coefficient c_n in proportion to the nearness of the corresponding eigenvalue to 0, but that if $|\lambda_n|$ is close to λ_1 the reduction relative to c_1 will be small, or there may even be a relative increase if $|\lambda_n|>\lambda_1$. Iteration of the operator ω, represented by the operator ω^p, is seen to have the same properties, except that the relative effect increases with increasing p. On the other hand the operator $(\omega-a)/(1-a)$ can be chosen with a negative so that every $c_n(\neq c_1)$ is reduced in magnitude, not only absolutely, but relatively to the magnitude of c_1.

TECHNIQUES FOR THE SOLUTION OF THE MATRIX EQUATION

By iterative application to a trial vector (8) of a polynomial operator $P(\omega)$ of the type shown in Fig. 1 it is possible to obtain a sequence of vectors $\mathbf{v}^0(=\mathbf{v})$, $\mathbf{v}^1, \cdots, \mathbf{v}^j, \cdots$, such that the ratios $|c_n{}^j/c_1{}^j|$ are successively reduced. Past procedures for obtaining the fundamental solution of such a matrix equation have been of this type. p iterations of a polynomial operator $P_d(\omega)$ of degree d are equivalent to the operator $[P_d(\omega)]^p$, which is of degree pd. We shall now show that for given degree m there exists a "best" polynomial operator $P_m(\omega)$. Since this polynomial is not a power of any polynomial of lower degree, it is therefore "better" than the result of p iterations of any operator of degree d such that $pd\leq m$.

The criterion for the "best" polynomial operator $P(\omega)$ of degree m may be rigorously expressed in the following form: We assume that the eigenvalues of the

problem lie in an interval $(-a, c)$ and that there is an interval $(-a, b)$, with $b<c$, within which it is desired that the maximum of $|P(\lambda)/P(c)|$ shall be a minimum. By limiting consideration to those polynomials for which $P(c)=1$ we then seek among such polynomials those for which the maximum of $|P(\lambda)|$ is a minimum throughout the interval $(-a, b)$. If such a polynomial exists for each choice of m, a, b, c, then by taking $a=-\lambda_N$, $b=\lambda_2$, $c=\lambda_1$ we can preserve the magnitude of c_1 in the expansion of an arbitrary trial vector (8), and obtain the maximum reduction in magnitude of the remaining coefficients.[4] In practice, we do not know in advance what values should be assigned to a, b, and c. In later sections we shall show how such assignments may reasonably be made.

The existence of the desired "best" polynomial is given by the following theorem, in which, for convenience, we have made the changes of variable

$$\Omega=\frac{2}{a+b}\omega+\frac{a-b}{a+b}, \qquad \mu(\lambda)=\frac{2}{a+b}\lambda+\frac{a-b}{a+b} \tag{9}$$

[so that $\mu(-a)=-1$, $\mu(b)=+1$], and have set $d=\mu(c)\equiv 2(a+c)/(a+b)-1>1$.

THEOREM: Among all polynomials of degree m in μ having the value $+1$ at $\mu=d>1$, there is just one having the minimum maximum absolute value throughout the interval $(-1, +1)$, namely the polynomial

$$S_m(\mu)=T_m(\mu)/T_m(d), \tag{10}$$

where $T_m(\mu)$ is the mth-order Tschebyscheff polynomial,[5] obtained by expanding

$$T_m(\mu)=\cos(m \arccos\mu)$$

in powers of μ.

PROOF: $T_m(\mu)$ is alternately $+1$ and -1 at the $m+1$ points $\mu_k=\cos(k\pi/m)$ $(k=0, 1, \cdots, m)$. Consequently $|S_m(\mu)|$ has $1/T_m(d)$ as its maximum at these $m+1$ values of μ. Suppose that $R(\mu)$ is a polynomial of degree m that is $=1$ at $\mu=d$ and has equal or smaller maximum absolute value in the interval $(-1, +1)$. Let $Q(\mu)=S_m(\mu)-R(\mu)$. Then $Q(\mu)$ is of degree m or less, $Q(d)=0$, and $Q(\mu_k)\geq 0$ or ≤ 0 according as k is even or odd. We proceed to show that $Q(\mu)$ has at least $m+1$ zeros in the closed interval $[-1, d]$, which is possible only if $Q\equiv 0$, i.e., if $R\equiv S_m$. Note that if $0<k<m$ and $Q(\mu_k)=0$ then μ_k is a multiple zero since both S_m and R must have natural extrema at μ_k, and hence $S_m'(\mu_k)-R'(\mu_k)=Q'(\mu_k)=0$. Now consider the interval $[\mu_k, \mu_{k+1}]$ $(k=1, \cdots, m-2)$. Either Q is positive at one end of this interval and negative at the other, in which case there is a zero in the interior of the interval; or Q is zero at one or both ends of the interval. In the latter case Q has at least two zeros in the closed interval—let us assign *one* of these zeros to the interval $[\mu_k, \mu_{k+1}]$ and one to the adjoining interval that has the double zero at its end point. In this way we see that Q has at least one zero assignable to each of the $m-2$ intervals mentioned above. The intervals $[\mu_0, \mu_1]$ and $[\mu_{m-1}, \mu_m]$ have (at least) either an interior zero, a double zero at μ_1 or μ_{m-1}, or a single zero at μ_0 or μ_m. Hence at least one zero is assignable to each of the m intervals $[\mu_k, \mu_{k+1}]$ $(k=0, \cdots, m-1)$. Q also has a zero at d. Hence it has at least $m+1$ zeros, which proves that $Q\equiv 0$ and $R\equiv S_m$.

The quantity $1/T_m(d)$ is the maximum of $|S_m(\mu)|$ in the interval $[-1, +1]$, and is therefore the measure of the reduction of the coefficients of all eigenfunctions with eigenvalue in the range $-a<\lambda<b$, relative to an eigenfunction with eigenvalue c, when $S_m(\Omega)$ is applied to a trial vector (8). Table I gives this reduction factor, and can be used to determine the degree of the polynomial required to remove unwanted eigenfunctions to any given degree of accuracy. The parameter d has been replaced by the quantity $r=(a+b)/(a+c)$, which is more directly related to the spacing of the eigenvalues.

Figure 2 illustrates the effect of the operator $S_6(\Omega)$ for the case $a=1$, $b=0.9$, $c=1$ $(r=0.95)$. All eigenfunctions with eigenvalues in the range from -1 to $+0.9$ are multiplied by a factor of 0.13 or less, as shown by the curve $S_6[(20\lambda+1)/19]$. For comparison the sixth order curve λ^6 is shown, and the range over which this is less than 0.13 is indicated. In an actual computation

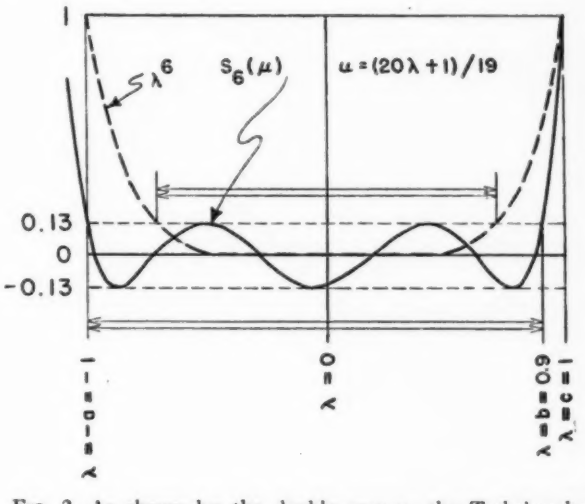

FIG. 2. As shown by the double arrows, the Tschebyscheff operator $S_6(\Omega)$ will accomplish a given reduction over a much wider range than will the operator ω^6. (In the upper right-hand corner, u should be μ.)

[4] In one sense the "best" polynomial would be $(\omega-\lambda_2)(\omega-\lambda_3)\cdots(\omega-\lambda_N)$, since this would eliminate every eigenvector except $\mathbf{u}^1$. But in any practical case such as we envisage, where the number of eigenvectors is large (in the hundreds or thousands), this would not actually be as useful (even assuming the eigenvalues known) as the polynomial we describe, since it would be of much higher degree.

[5] We are indebted to Drs. Tukey and Grosch for suggesting the possible usefulness of Tschebyscheff polynomials, in the course of a discussion of this work at the IBM Seminar on Scientific Computation held in Endicott, New York in November, 1949. We had previously used polynomials with zeros equally spaced. These were fairly efficient, but appreciably less so than the Tschebyscheff polynomials.

a polynomial of order higher than six would always be used.

In the practical application of an operator $S_m(\Omega)$ to a trial vector it is often convenient to use the following factor formula for Tschebyscheff polynomials:

$$T_{pq}(x)=\prod_{k=1}^{p}\left[T_q(x)-\cos\frac{2k-1}{p}\frac{\pi}{2}\right]. \tag{11}$$

This follows from the identity

$$\cos(pq\arccos x)\equiv\cos\{p\arccos[\cos(q\arccos x)]\},$$

which may be written

$$T_{pq}(x)=T_p[T_q(x)].$$

Since $T_p(y)$ has p zeros located at $y=\cos[(2k-1)/p](\pi/2)$ $(k=1,\cdots,p)$, (11) results from setting $y=T_q(x)$ in the factored form of $T_p(y)$.

If we have a vector $\mathbf{v}$ that is known to be a linear combination of just the first two eigenvectors, i.e.,

$$\mathbf{v}=c_1\mathbf{u}^1+c_2\mathbf{u}^2, \tag{12a}$$

one can determine λ_1, λ_2, $\mathbf{u}^1$, $\mathbf{u}^2$ by the following "harmonic analysis": First compute $\omega\mathbf{v}$ and $\omega^2\mathbf{v}$,

$$\omega\mathbf{v}=\lambda_1c_1\mathbf{u}^1+\lambda_2c_2\mathbf{u}^2, \tag{12b}$$

$$\omega^2\mathbf{v}=\lambda_1^2c_1\mathbf{u}^1+\lambda_2^2c_2\mathbf{u}^2. \tag{12c}$$

Next form the inner products

$$\left.\begin{aligned}(\mathbf{v},\mathbf{v})&\equiv A=c_1^2+c_2^2,\\(\mathbf{v},\omega\mathbf{v})&\equiv B=\lambda_1c_1^2+\lambda_2c_2^2,\\(\omega\mathbf{v},\omega\mathbf{v})\equiv(\mathbf{v},\omega^2\mathbf{v})&\equiv C=\lambda_1^2c_1^2+\lambda_2^2c_2^2,\\(\omega\mathbf{v},\omega^2\mathbf{v})&\equiv D=\lambda_1^3c_1^2+\lambda_2^3c_2^2.\end{aligned}\right\} \tag{13}$$

When c_1^2 and c_2^2 are eliminated from the equations (13) there result two independent equations for λ_1 and λ_2, which may be written in the form

$$\begin{vmatrix}A&1&1\\B&\lambda_1&\lambda_2\\C&\lambda_1^2&\lambda_2^2\end{vmatrix}=\begin{vmatrix}B&\lambda_1&\lambda_2\\C&\lambda_1^2&\lambda_2^2\\D&\lambda_1^3&\lambda_2^3\end{vmatrix}=0. \tag{14}$$

If these be solved for λ_1 and λ_2, and the possibilities $\lambda_1=0$, $\lambda_2=0$, $\lambda_1=\lambda_2$ (which do not concern us here) be discarded, the two λ's will be found to be the roots of the equation

$$\begin{vmatrix}A&B&1\\B&C&\lambda\\C&D&\lambda^2\end{vmatrix}=0. \tag{15}$$

$c_1\mathbf{u}^1$ and $c_2\mathbf{u}^2$ can then be determined from (12a, b) by

$$\left.\begin{aligned}c_1\mathbf{u}^1&=\frac{1}{\lambda_1-\lambda_2}\omega\mathbf{v}-\frac{\lambda_2}{\lambda_1-\lambda_2}\mathbf{v},\\c_2\mathbf{u}^2&=\frac{-1}{\lambda_1-\lambda_2}\omega\mathbf{v}+\frac{\lambda_1}{\lambda_1-\lambda_2}\mathbf{v}.\end{aligned}\right\} \tag{16}$$

If $\mathbf{v}$ is only approximately represented by the linear combination (12a), so that relations (13) are only approximately true, the solutions of (15) will give approximate values, λ_1' and λ_2', of λ_1 and λ_2. Since λ_1' and λ_2' $(\lambda_1'>\lambda_2')$ satisfy (13) exactly, $\lambda_1'A\equiv\lambda_1'(c_1^2+c_2^2)>\lambda_1'c_1^2+\lambda_2'c_2^2\equiv B$, $\lambda_1'>B/A\equiv(\mathbf{v},\omega\mathbf{v})/(\mathbf{v},\mathbf{v})$, i.e., λ_1' is greater than the estimate of λ_1 that would be obtained directly from the variational principle. In the examples we have tried we have always found $\lambda_1'<\lambda_1$, but we have not been able to prove that this will be true in general.

APPLICATION OF THE TECHNIQUES

In this section we shall discuss in some detail the application of the techniques developed in the preceding section. The general idea is first to do enough preliminary work to determine the rough shape of the eigenvector and approximate values of λ_1 and λ_2; then to make reasonable choices of a, b, and c, compute $r=(a+b)/(a+c)$, and choose an order m from Table I that will give adequate elimination of unwanted eigenfunctions. Then the operator $S_m(\Omega)$ given by (9) and (10) is applied to the rough eigenfunction to accomplish this elimination.

The problems for which these techniques were developed were based on relatively complicated regions that necessitated the use of hundreds or thousands of points to get even a moderately acceptable representation of the region and its boundary by the network. This has meant that the computations were possible only with the assistance of fairly high-speed computing machinery with a large memory, such as IBM punched-card equipment, particularly the 604 electronic computer. The following remarks are assumed to be concerned with such large-scale problems computed with comparable equipment.

In starting it is generally worth while to use a rather coarse net, even at the expense of considerably oversimplifying the geometry; e.g., if the region contains holes on whose boundaries the function is 0, it may be worth while to select a mesh so large that such a hole is represented by a single point at which the function is 0. The particular advantages of such a rough first approximation are that (a) the eigenvalues are much less densely spaced, so that approximate values of λ_1 and λ_2 are much more easily determined; (b) relation (4) shows that if λ' and λ'' are the eigenparameters for networks of mesh h' and h'', respectively, then λ_1'' and λ_2'' may be approximated from λ_1' and λ_2' by using $\lambda''=1-(h''/h')^2(1-\lambda')$; (c) the simplest possible interpolation in the vector derived from the coarse net will generally yield a vector that differs from the fundamental for the fine net principally by eigenvectors with eigenvalues near -1 (i.e., high-frequency oscillations), which are easy to eliminate. Thus, one may get a good starting vector for the fine network by treating the solution for the coarse network as a stepfunction in the fine network and smoothing it by a few preliminary operations with $(\omega+1)/2$, about equal in number to the ratio of h' to h''. A better starting func-

tion would be obtained by using an interpolation based on the difference equation (3) itself. Thus if 1, 2, 3, 4 are four points at the corners of a square of diagonal $2h'$, the difference equation determines the value u_0 at the center of the square as

$$u_0=(1/\lambda_1')\,\tfrac{1}{4}(u_1+u_2+u_3+u_4),$$

where λ_1' is the eigenvalue appropriate to a net of mesh h'. If we start with a net of mesh h, we can first use $h'=h/\sqrt{2}$ to fill in the center points of the meshes, then $h'=h/2$ to fill in the remaining points in a net of mesh $\frac{1}{2}h$.

The form of the starting function for the coarse network is not too important, provided the generally convex character of the function is observed. Advantage should be taken of any symmetries in the figure to reduce the number of points, which not only reduces the number of eigenfunctions but also decreases the density of the eigenvalues. It should be noted that the matrix resulting from using only a portion of a symmetrical figure is no longer symmetrical. For example, if the full figure is symmetrical along a diagonal and half the figure is used, the neighbors of a diagonal point are the neighbors on one side counted twice. The eigenvectors of the resulting matrix will not then be orthogonal in general. Their orthogonality will be restored if they are treated as eigenvectors of the matrix associated with the complete figure, which is done simply by giving to each point in the subregion actually used a weight equal to the number of points in the full region for which it stands.

In problems of the type considered here one may assume $a=1$ throughout, since $\lambda_N\approx-1$; and $c=1$ initially, since $\lambda_1\approx+1$. The first step is to pick an operator Ω and a polynomial $S_m(\Omega)$ of low degree that will enable one to compute λ_1 and λ_2 by the crude harmonic analysis of the previous section with fair accuracy. Thus, with $a=c=1$ the choice of $r=0.9$ and $m=8$ corresponds to $b=0.8$, $d=1.222$, $\Omega=(10\omega+1)/9$, $1/T_m(d)=0.0106$. This $S_m(\Omega)$ will reduce the coefficients of all eigenvectors in the expansion of $\mathbf{v}$ with eigenvalues lying in the range $-1\leq\lambda\leq0.8$ by at least the factor 0.01, and those with eigenvalues in the range $0.8\leq\lambda\leq1$ at least in proportion to the ratio $(\lambda-0.8)/0.2$. Ordinarily this will permit a harmonic analysis that will determine λ_1 and λ_2 with sufficient accuracy to choose a final operator for this network. However, if the number of points in the coarse network is rather large, it may be worth while to take r and m larger.

In the actual performance of an operation $S_m(\Omega)$ one is faced with a choice of methods. On the one hand $S_m(\Omega)\mathbf{v}$ may be computed by iterating with the operator Ω and then forming the polynomial as a linear combination of the results. This has the practical disadvantage that with large m the sizes of the terms are so disparate that a great deal of accuracy is lost in taking differences of large multiples of the results of the iterations. At the other extreme, $S_m(\Omega)$ may be factored into its linear factors,

$$S_m(\Omega)=\prod_{k=1}^{m}\frac{\Omega-\mu_k}{d-\mu_k},\quad\left(\mu_k=\cos\frac{2k-1}{m}\frac{\pi}{2}\right)\qquad(17)$$

and these linear operators applied successively. This method suffers from the disadvantage that the coefficients of the operator must be changed at each step, which is a dangerous source of error in machine operation. A reasonable practical compromise combines the two methods by use of the factor formula (11). Thus if we set

$$S_m(\Omega)=\prod_{k=1}^{p}\frac{T_q(\Omega)-\cos[(2k-1)/p]\pi/2}{T_q(d)-\cos[(2k-1)/p]\pi/2},\qquad(18)$$

where q is about 6 or 8[6] and $p=m/q$, we may iterate q times with Ω, follow this with the computation of the first of the p polynomials, iterate on the result q times with Ω, compute the second polynomial factor, and so on. Since the cosine term in the denominator is small compared to $T_q(d)$, it may be omitted. This has the effect of changing the scale of the vector slightly, which is of no theoretical importance. If this omission is made, then the operator used in the iterations is always the same, while the coefficients used in the successive polynomials differ only in the constant term. Loss of significant figures is avoided by keeping q relatively small. When q is at least as large as 6 or 8, the change of scale produced by neglecting the cosine term in the denominator is not bothersome. (If the function does grow out of bounds, cutting it in half once will generally be sufficient. Note that this should be done *after* a polynomial factor is computed, not in the course of a set of iterations preparatory to the computation of such a polynomial.)

When a satisfactory solution for the coarse network has been obtained, a starting vector for the fine network may be constructed along the lines suggested above. At this point procedure will depend to some extent on whether the interest in the problem centers in the determination of the fundamental eigenvalue or of the fundamental eigenfunction. If the former, then b may safely be chosen somewhat less than λ_2 and we may determine λ_1 by harmonic analysis. If λ_1 and λ_2 are widely separated this method may also be used for determining the vector $c_1\mathbf{u}^1$. However, the determination of $c_1\mathbf{u}^1$ from (16) generally involves great loss of accuracy because of the nearness of λ_1 and λ_2, so if interest is centered in the eigenfunction, one is forced to choose b close to λ_2 with consequent increase in the size of m.

HIGHER MODES

While the method we have outlined is peculiarly adapted to obtaining the fundamental mode, it is pos-

[6] T_6 and T_8, which we have found most useful, are given by

$$2^{-5}T_6(\Omega)=\Omega^6-\tfrac{3}{2}\Omega^4+\tfrac{9}{16}\Omega^2-\tfrac{1}{32}$$
$$2^{-7}T_8(\Omega)=\Omega^8-2\Omega^6+\tfrac{5}{4}\Omega^4-\tfrac{1}{4}\Omega^2+\tfrac{1}{128}.$$

sibly useful for obtaining a limited number of the higher modes. Once the fundamental has been accurately obtained for the network, a trial vector for the next mode can be chosen that is accurately orthogonal to the fundamental. Application of $P(\omega)$ to such an orthogonal vector should not reintroduce (except as a result of rounding-off errors) any of the fundamental. Hence it should be possible to obtain a higher mode by orthogonalizing the trial vector to the predetermined lower modes, applying a suitable Tschebyscheff operator, and re-orthogonalizing as necessary. One useful application of this technique might be in the solution of Schrödinger's equation for diatomic molecules.

MORE GENERAL PROBLEMS

Several of the problems we have solved by a procedure similar to the above have been of a more general type than the one proposed in the introduction. Since the modifications introduced by this generalization may assist others in applying the procedure, we shall state briefly the most important features of the more general problems and their solution.

The single dependent variable u is replaced by two functions u and v that are to satisfy simultaneous equations

$$\left.\begin{aligned}(\Delta-E)u+Fv&=-\alpha u\\ Gu+(\Delta-H)v&=-\alpha v.\end{aligned}\right\} \tag{19}$$

The fundamental region is divided into subregions within each of which the coefficients E, F, G, H are constant functions of a parameter ρ. Certain homogeneous conditions are imposed across the interfaces. It is desired to determine ρ so that the fundamental eigenvalue $\alpha_1=0$, and to find the corresponding pair of eigenfunctions u, v.

The matrix equation analogous to (5) is then of the form

$$\begin{pmatrix}\omega-\frac{1}{4}h^2E & \frac{1}{4}h^2F\\ \frac{1}{4}h^2G & \omega-\frac{1}{4}h^2H\end{pmatrix}\begin{pmatrix}\mathbf{u}\\ \mathbf{v}\end{pmatrix}=\lambda\begin{pmatrix}\mathbf{u}\\ \mathbf{v}\end{pmatrix}, \tag{20}$$

where $\lambda=1-\frac{1}{4}h^2\alpha$, and consequently it is desired that $\lambda_1=1$. As in the first problem the introduction of the boundary conditions (and here of the interface conditions as well) results in modification of the interpretation of the operator ω at certain points, but ω still represents a linear combination of neighboring values with non-negative coefficients whose sum is ≤ 1. The two vectors $\mathbf{u}$, $\mathbf{v}$ are considered to form a single vector for the purposes of the computation.

Note that the matrix is no longer symmetric. This means that the eigenvectors may not be assumed to be orthogonal. Hence it is necessary ultimately to compute the adjoint solution in order to form correct inner products if a harmonic analysis is to be carried out. In the early stages this is not necessary since it can be shown that the λ_1 and λ_2 determined by the analog of (15) represent the result of fitting relations (12) by least squares. The λ's thus determined are, however, less accurate than those determined by true inner products.

In these problems h is chosen sufficiently small so that the coefficients h^2E, h^2F, h^2G, h^2H are small compared to 1. Hence the operator is nearly the operator $\begin{pmatrix}\omega 0\\ 0\omega\end{pmatrix}$. Aside from the asymmetry the principal effect of the more general matrix is to increase the range of the eigenvalues. Since it is possible to estimate ρ (on physical grounds) with fair accuracy in advance, λ_1 is still approximately $+1$. λ_N, however, may be considerably less than -1, say -3 or -4 if $\mathbf{u}$ and $\mathbf{v}$ are disparate in size. Our first problem is then to estimate λ_N. This may be done by choosing a sequence of operators of the type $(\omega-a)/(1-a)$ to replace ω in the matrix. If one takes $a=0$ and applies the resulting operator two or three times, the presence of eigenvectors with eigenvalue <-1 will be revealed by their coefficients being multiplied by negative factors of large absolute value, which thus produces oscillations of increasing amplitude in the successive vectors. (That such eigenvectors will appear, provided $\lambda_N<-1$, is practically guaranteed by the rounding-off errors introduced into the computation.) When the existence of such large negative eigenvalues has been established, similar operations may be carried out with $a=-1$, $-\frac{3}{2}$, -2, etc., until the phenomenon disappears. Thus a practical value of a for use in determining the operator Ω in the Tschebyscheff polynomial is achieved. The polynomial operator S_m is now not a function of Ω but of the matrix operator in (20) with Ω substituted for ω.

A final word about the treatment of the interface conditions. The particular conditions imposed are expressed in the difference equations by assertions of the form: the value of u at an interface point is a weighted average of certain neighboring values of u in the adjacent regions. It would be possible to eliminate all interface points from the vector in a manner similar to that in which the boundary points were eliminated. However, since λ_1 is very nearly $+1$ in these problems it is more convenient to retain the interface points, replacing their values at each stage by the weighted average specified in the interface conditions. This averaging then becomes part of the operator. Since we are doing the averaging and determining the interface values always one step late, this procedure is only exact for an eigenfunction of eigenvalue unity.

We are indebted to many of the members of the Theoretical Physics Division of the Argonne Laboratory, and in particular to Drs. Frank Hoyt and Elmer Eisner, for helpful discussions during the development of these techniques.

Determination of Eigenvalues Using a Generalized Laplace Transform*

MORRIS D. FRIEDMAN
N.A.C.A., Ames Aeronautical Laboratory, Moffett Field, California
(Received August 14, 1950)

The classical eigenvalue problems of mathematical physics are solved by means of a Laplace Transform extended, not over the interval $(0, \infty)$ but over the interval of interest for the differential equation. The method is applied to the Hermite, Laguerre and Bessel equations and to the equation for the hypergeometric polynomials which include the Legendre, Tschebyscheff, and Jacobi polynomials as special cases.

INTRODUCTION

IN many fields of mathematical physics, for example, quantum mechanics, electro-magnetics, acoustics, there occur second-order differential equations depending on a parameter λ which have satisfactory or well-behaved solutions only for particular values of λ. A solution is said to be well behaved if it is single-valued, continuous, and finite throughout the configuration space of the system (i.e., for all values of x which x may assume). In case the range of the variable x is infinite an extra condition about the behavior of the solution at infinity is needed. The values of the parameter λ for which the solutions are well behaved functions are called eigenvalues and the corresponding solutions eigenfunctions. This paper proposes a general method for finding the eigenvalues of a second-order differential equation.

The usual method of solving these second-order equations, called the Sommerfeld Polynomial Method, is to substitute a power series expansion (whose form is determined by an asymptotic solution of the differential equation) for the unknown function and then to determine the coefficients by equating like powers of x. This gives the general solution of the equation. Then the radius of convergence of the power series is investigated in order to find for which values of λ the solution is well behaved. This method is long, and it will be shown that by using a generalized Laplace transform,[1] the same results can be achieved in a more direct way and with less labor.

Those equations which can be put into the Sturm-Liouville[2] form will be treated. The Bessel, Hermite, Laguerre, Legendre, Jacobi, Tschebyscheff, and the Trigonometric equations will be special cases. These equations can be put into the following general form:

$$[P(x)U'(x)]'-[Q(x)-\lambda R(x)]U(x)=0. \quad (1)$$

Since the solutions of (1) have singularities at the zeros of $P(x)$ or at ∞, the problem is to find values of λ for which $U(x)$ is well behaved at these singular points. The method proposed is as follows.

Multiply each term of Eq. (1) by $e^{-sx}dx$ and integrate over a suitably chosen contour. In general, the contour will be a line joining the singularities of the differential equation, that is, either the real axis between two zeroes of $P(x)$, or the part of the real axis connecting a zero of $P(x)$ to ∞. The fact that $U(x)$ is well behaved at the singular points implies that the transformed function must be a regular, analytic function of s. Those values of λ for which the transform is analytic are the eigenvalues.

Consider

$$\int_C [P(x)U'(x)]'e^{-sx}dx - \int_C [Q(x)-\lambda R(x)]U(x)e^{-sx}dx=0. \quad (2)$$

When the first term on the left is integrated by parts twice, there results

$$\{P(x)U'(x)e^{-sx}+sP(x)U(x)e^{-sx}\}_C + s^2\int_C P(x)U(x)e^{-sx}dx - \int_C [sP'(x)+Q(x)-\lambda R(x)]U(x)e^{-sx}dx=0. \quad (3)$$

Now, if that contour is selected which will make the braces vanish, there results the integral equation:

$$\int_C [s^2P(x)-sP'(x)-Q(x)+\lambda R(x)]U(x)e^{-sx}dx=0, \quad (4)$$

or dividing by $R(x)$

$$\int_C \left[s^2\frac{P(x)}{R(x)}-s\frac{P'(x)}{R(x)}+\frac{Q(x)}{R(x)}+\lambda\right]U(x)R(x)e^{-sx}dx=0. \quad (5)$$

Suppose now that $P(x)/R(x)$, $P'(x)/R(x)$ and $Q(x)/R(x)$ are polynomials. This is actually the case in the standard eigenvalue problems. Put

$$U(x)R(x)=\bar{U}(x), \quad (6)$$

* Submitted in partial fulfillment of the requirements for the Master of Science degree.

[1] L. Pauling and E. B. Wilson, *Introduction to Quantum Mechanics* (McGraw-Hill Book Company, Inc., New York, 1935), first edition.

[2] R. Courant and D. Hilbert, *Methoden der Mathematische Physik* (J. Springer, Berlin—Photo-lithoprint, Interscience Publications, New York, 1937), Vol. I.

and let

$$\int_C \bar{U}(x)e^{-sx}dx = U(s), \tag{7}$$

where $U(s)$ is a generalized Laplace transform of $\bar{U}(x)$. Under certain conditions, multiplication of the integral in (7) by a power of x is equivalent to multiplying the derivative to that order by (-1) to that power; e.g.

$$\int x\bar{U}(x)e^{-sx}dx = -v'(s),$$

$$\int x^2\bar{U}(x)e^{-sx}dx = v''(s), \text{ etc.}^3$$

Therefore, Eq. (6) may be represented as the result of a function of s and the differential operator with respect to s acting on the integral of $\bar{U}(x)e^{-sx}dx$, or

$$g(s, D)\int_C \bar{U}(x)e^{-sx}dx = g(s, D)v(s) = 0, \tag{8}$$

where D is the differential operator with respect to s and $v(s)$ is the Laplace transform of $U(x)$. The result is, thus, a differential equation in $v(s)$ depending upon the parameter λ. The method consists in finding those values of λ for which $v(s)$ is an analytic function of s.

EIGENVALUES OF THE HYPERGEOMETRIC EQUATION

The method will first be applied to the particular case of the hypergeometric equation whose form is[4]

$$[(1+x)^r(1-x)^{p+q-r+1}U'(x)]' - \lambda(1+x)^{r-1}(1-x)^{p+q-r}U(x) = 0. \tag{9}$$

From this equation can be derived the Jacobi ($r=P+1$; $q=0$; $p=Q+P+1$), the Tschebyscheff ($r=\frac{1}{2}$; $p=q=0$), and the Legendre ($r=1$, $p+q=r$) equations. It will be shown that substitution of these values in the solution of λ for the hypergeometric equation will yield the corresponding solutions for the eigenvalues of the respective equations.

Since $P(x)$ in (9) has zeroes at $x=+1$ and $x=-1$, the terms of (9) are multiplied by e^{-sx} and the result is integrated between the limits of -1 and $+1$:

$$\int_{-1}^{1}[(1+x)^r(1-x)^{p+q-r+1}U'(x)]'e^{-sx}dx - \int_{-1}^{1}\lambda(1+x)^{r-1}(1-x)^{p+q-r}U(x)e^{-sx}dx = 0, \tag{10}$$

which can be written as

$$\int_{-1}^{1}[s^2(1+x)^r(1-x)^{p+q-r+1} - sr(1+x)^{r-1}(1-x)^{p+q-r+1} + s(p+q-r+1)(1+x)^r(1-x)^{p+q-r} + \lambda(1+x)^{r-1}(1-x)^{p+q-r}][U(x)e^{-sx}dx] = 0, \tag{11}$$

the same form as (5). Now, let

$$\int_{-1}^{1}(1+x)^{r-1}(1-x)^{p+q-r}U(x)e^{-sx}dx = v(s). \tag{12}$$

Recalling that multiplication of the transform by a power of x is equivalent to differentiation, (11) then becomes

$$s^2v - s^2v'' - srv - srv' + s(p+q-r+1)v - s(p+q-r+1)v' + \lambda v = 0, \tag{13}$$

where $v=v(s)$ and v' and v'' are derivatives of $v(s)$ with respect to x.

From (12) it is seen that if $U(x)$ is well behaved then $v(s)$ is an analytic function of s for all values of s. It is now necessary to find for which values of λ, (13) has analytic solutions. If $v(s)$ is analytic, then it can be written as

$$v(s) = \sum_0^\infty a_k s^k; \text{ and similarly,}$$

$$v'(s) = \sum_0^\infty k a_k s^{k-1}; \text{ and } v''(s) = \sum_0^\infty k(k-1)a_k s^{k-2}.$$

When these series are substituted in (13), there results

$$\sum a_{k-2}s^k - \sum (k^2-k)a_k s^k - r\sum a_{k-1}s^k + (p+q-r+1)\sum a_{k-1}s^k - (p+q-r+1)\sum k a_k s^k + \sum \lambda a_k s^k = 0, \tag{14}$$

or

$$(k^2+kp+kq-\lambda)a_k - a_{k-2} - (p+q-r+1)a_{k-1} = 0; \text{ for } k=0, 1, 2, \cdots. \tag{15}$$

(*Note:* $a_{-1}=a_{-2}=0$.)

Suppose, now, that a_n is the first non-zero coefficient. Then for $k=n$, (15) becomes

$$(n^2+np+nq-\lambda)a_n = 0, \tag{16}$$

so that λ must be

$$\lambda = n^2+np+nq, \tag{17}$$

and then the n-th eigenvalue is

$$\lambda_n = n(n+p+q). \quad n=1, 2, \cdots.$$

Notice that if a_n is the first non-zero coefficient then $v(0)=v'(0)=\cdots=v^{(n-1)}(0)=0$; or

$$(-1)^k v^k(0) = \int_{-1}^{1}(1+x)^{r-1}(1-x)^{p+q-r}U(x)x^k dx \neq 0 \qquad (k=0, 1, \cdots, n-1), \tag{18}$$

[3] R. V. Churchill, *Modern Operational Methods in Engineering* (McGraw-Hill Book Company, Inc., New York, 1944), first edition.

[4] E. T. Whittaker and G. N. Watson, *Modern Analysis* (Cambridge University Press, New York, 1947). (Note: In this paper, all equations were put in the self-adjoint form before solving. Differentiating the self-adjoint form and dividing by the common factor will bring the equation to the form listed in the reference.)

so that $U(x)$, the solution corresponding to the n-th eigenvalue is orthogonal to x^k $(k=0, 1, \cdots, n-1)$ with the weight function $(1+x)^{r-1}(1-x)^{p+q-r}$. This contains the well-known orthogonality property of the Jacobi, Tschebyscheff, and Legendre functions.[2,5]

If those values of p and q which were mentioned before are substituted in (17), the eigenvalues for the Jacobi, Tschebyscheff, and Legendre equations are a result.

The Legendre equation of higher order[2]

$$[(1-x^2)U'(x)]'-h^2(1-x^2)^{-1}U(x)+\lambda U(x)=0, \quad (19)$$

can be put in a more manageable form by the substitution of $Z(x)=(1-x^2)^{\frac{1}{2}h}U(x)$. The resulting equation

$$[(1-x^2)^{h+1}Z'(x)]'-[h(h+1)-\lambda](1-x^2)^hZ(x)=0, \quad (20)$$

transforms into the differential equation

$$s^2v''(s)+2s(h+1)v'(s)-(s^2+h(h+1)+\lambda)v(s)=0. \quad (21)$$

From (21), it is determined that

$$\lambda=n^2+n+2nh+h^2+h, \quad (h=0, 1, 2, \cdots).$$

THE CONFLUENT HYPERGEOMETRIC EQUATION

Another class of equations, the confluent hypergeometric, is allied to the hypergeometric mentioned above. The equations of this new class which will be treated are the Hermite, Laguerre, and Bessel.[2,4]

The Hermite equation, in self-adjoint form, is[2]

$$[e^{-x^2}U'(x)]'+\lambda e^{-x^2}U(x)=0. \quad (22)$$

Solutions are desired such that $e^{-x^2}U(x)$ is zero at $x=\pm\infty$.

$$\int_{-\infty}^{\infty}[e^{-x^2}U'(x)]'e^{-sx}dx+\int_{-\infty}^{\infty}\lambda e^{-x^2}U(x)e^{-sx}dx=0. \quad (23)$$

If the first integral on the left is integrated by parts; twice:

$$\left\{e^{-x^2-sx}U'(x)+se^{-x^2-sx}U(x)\right\}_{-\infty}^{\infty}$$
$$+s\int_{-\infty}^{\infty}(s+2x)e^{-x^2-sx}U(x)dx$$
$$+\int_{-\infty}^{\infty}\lambda e^{-x^2-sx}U(x)dx=0. \quad (24)$$

Now, around the chosen contour, if $U(x)$ is well behaved, the braces are zero and

$$v(s)=\int_{-\infty}^{\infty}e^{-x^2-sx}U(x)dx,$$

is substituted in (25), recalling that the product of a power of x and the integrand in the integral for which $v(s)$ is being substituted is a derivative of $v(s)$, then

$$s^2v(s)-2sv'(s)+\lambda v(s)=0. \quad (25)$$

This equation can be solved by separation of variables

$$v'(s)/v(s)=(s^2+\lambda)/2s-s/2+\lambda/2s, \quad (26)$$

or

$$\log v=s^2/4+(\lambda\log s)/2. \quad (27)$$

And, therefore

$$v(s)=s^{\frac{1}{2}\lambda}\exp(\tfrac{1}{4}s^2). \quad (28)$$

It is concluded that in order for $v(s)$, determined in (27), to be analytic λ must be $2n$, where n is a positive integer.

It will now be shown that the well behaved solutions of the Hermite equation are polynomials. Assume that $\lambda=2n$ and that the corresponding solution of $U(x)$ may be written as

$$U(x)=e^{x^2}[e^{-x^2}V(x)]',$$

then (25) becomes

$$V(s)=\int_{-\infty}^{\infty}e^{-sx}[e^{-x^2}V(x)]'dx. \quad (29)$$

After an integration by parts,

$$V(s)=e^{-sx-x^2}V(x)\Big|_{-\infty}^{\infty}+s\int_{-\infty}^{\infty}e^{-sx-x^2}V(x)dx, \quad (30)$$

so that from (28)

$$\int_{-\infty}^{\infty}e^{-sx-x^2}V(x)dx=s^{n-1}\exp(s^2/4). \quad (31)$$

By induction, it is seen that if

$$U(x)=e^{x^2}\frac{d^n}{dx^n}[e^{-x^2}W(x)]; \quad (32)$$

then

$$\int_{-\infty}^{\infty}e^{-sx-x^2}W(x)dx=\exp(s^2/4). \quad (33)$$

But

$$\int_{-\infty}^{\infty}e^{-sx-x^2}dx$$
$$=\int_{-\infty}^{\infty}\exp[-(x+\tfrac{1}{2}s)^2]\exp(s^2/4)dx$$
$$=\int_{-\infty}^{\infty}\exp(s^2/4)\exp(-y^2)dy=\pi^{\frac{1}{2}}\exp(\tfrac{1}{4}s^2), \quad (34)$$

so that

$$\int_{-\infty}^{\infty}e^{-sx-x^2}(dx/\pi^{\frac{1}{2}})=\exp(\tfrac{1}{4}s^2), \quad (35)$$

[5] P. Frank and R. Von-Mises, *Differentiale Gleichungen—Vol. I* (Mary S. Rosenberg, New York, 1943), second edition.

and $W(x)$ may be taken equal to $\pi^{-\frac{1}{2}}$ to satisfy Eq. (33). This shows that

$$U(x)=\frac{e^{x^2}}{\pi^{\frac{1}{2}}}\frac{d^n}{dx^n}(e^{-x^2}). \tag{36}$$

The confluent hypergeometric equation also contains, as a special case, the Laguerre equation.[2,4]

$$[xe^{-x}U'(x)]'+\lambda e^{-x}U(x)=0. \tag{37}$$

A well behaved solution of this equation is one which is regular at $x=0$ and such that $e^{-x}U(x)$ vanishes at $x=\infty$. Just as for the Legendre equation, so too, for the Laguerre there is an equation for functions of higher order. This equation

$$[x^{k+1}e^{-x}U'(x)]'+\lambda x^k e^{-x}U(x)=0, \tag{38}$$

can be solved in the same manner as the equation of first order.

Multiply (38) by e^{-sx} and integrate along C, the real axis from 0 to ∞. Then

$$\int_C [xe^{-x}U'(x)]'e^{-sx}dx+\int_C \lambda e^{-x}e^{-sx}U(x)dx=0. \tag{39}$$

This Eq. (39) is similar in form to Eq. (2) and since the contour selected will cancel all integrated terms, (40) can immediately be put in the form (5) as follows:

$$s^2\int_C xe^{-x-sx}U(x)dx+s\int_C xe^{-x-sx}U(x)dx$$

$$-s\int_C e^{-x-sx}U(x)dx+\int_C \lambda e^{-x-sx}U(x)dx=0. \tag{40}$$

Now let the transform be

$$v(s)=\int_0^\infty e^{-x(1+s)}U(x)dx, \tag{41}$$

then (41) becomes

$$-s^2v'(s)-sv'(s)-sv(s)+\lambda v(s)=0. \tag{42}$$

After collection of terms and separation of variables, there results

$$\frac{v'(s)}{v(s)}=\frac{-s}{s(s+1)}=\frac{\lambda}{s}-\frac{1+\lambda}{s+1}, \tag{43}$$

and

$$\log v=\lambda\log s-(1+\lambda)\log(s+1), \tag{44}$$

or

$$v(s)=s^\lambda/(s+1)^{1+\lambda}. \tag{45}$$

Since $U(x)$ behaves like $e^{x-\epsilon}$ at $x=\infty$, $v(s)$ must be regular at $x=0$. Were λ negative, $v(s)$ would have a pole; were λ a fraction there would be a branch point, and since both assumptions are contrary to the conditions, then $\lambda=n$, a positive integer.

(Note that the transform of x^n is $n!/(1+s)^{n+1}$; so if $v(s)$ be expanded in inverse powers of $(1+s)$, $U(x)$ can be found.)

From (45), for $\lambda=n$,

$$v(s)=(1+s-1)^n/(1+s)^{n+1}=\frac{1}{s+1}\left(1-\frac{1}{s+1}\right)^n, \tag{46}$$

and

$$v(s)=\sum_0^n \frac{(-1)^k\binom{n}{k}}{(1+s)^{k+1}}. \tag{47}$$

The inverse transform of $v(s)$ in (47) is[2]

$$U(x)=\sum_0^n (-1)^k\frac{x^k}{k!}\frac{n!}{k!(n-k)!}, \tag{48}$$

which is a solution of (37).

The Bessel equation[6]

$$x^2U''(x)+(2x+2)U'(x)-\lambda U(x)=0,$$

can also be put into the self-adjoint form with the weight function $\exp(-2/x)$. The result is

$$[\exp(-2/x)x^2U'(x)]'-\lambda\exp(-2/x)U(x)=0, \tag{49}$$

and the more general form

$$[\exp(-b/x)x^aU'(x)]'-\lambda\exp(-b/x)x^{a-2}U(x)=0, \tag{50}$$

which are also special cases of the confluent hypergeometric equation.

A solution single-valued on the unit circle $|x|=1$ is desired. Again, multiply the equation, in this case (49), by e^{-sx} and integrate around C, the unit circle, obtaining

$$\int_C [\exp(-2/x)x^2U'(x)]'e^{-sx}dx$$

$$-\int_C \lambda\exp(-2/x)e^{-sx}U(x)dx=0. \tag{51}$$

Integrating as before, yields the result in the form of (4)

$$\{\exp(-2/x)x^2e^{-sx}U'(x)+s\exp(-2/x)x^2e^{-sx}U(x)\}_C$$

$$+\int_C (s^2x^2-2sx+2s-\lambda)$$

$$\times\exp(-2/x)e^{-sx}U(x)dx=0. \tag{52}$$

Now, around this contour, because $U(x)$ is single-valued, the braces evaluate to zero. Then, putting

$$v(s)=\int_C \exp(-s/x)e^{-sx}U(x)dx, \tag{53}$$

[6] J. Kroll and O. Frink, "A new class of orthogonal polynomials," Abstract 249, Bull. Am. Math. Soc., July 1948.

the resulting equation is

$$s^2v''(s)+2sv'(s)+2sv(s)-\lambda v(s)=0. \tag{54}$$

Substituting a power series for $v(s)$, and equating coefficients of like powers of s, yields

$$n^2-n+2n=\lambda, \tag{55}$$

or

$$\lambda=n^2+n.^5$$

In Eq. (50), λ can be determined to be $n(n-a+1)$.[6]

The property of orthogonality demonstrated for the Jacobi equation can, similarly, be shown to apply to the other equations treated.

Finally, consider the special case of the Sturm-Liouville type equation, the Trigonometric[2]

$$U''(x)+\lambda^2U(x)=0, \tag{56}$$

with the conditions $U(0)=U(1)=0$.

Multiply (56) by e^{-sx} and integrate from 0 to 1. Thus

$$\int_0^1 U''(x)e^{-sx}dx+\int_0^1 \lambda^2U(x)e^{-sx}dx=0. \tag{57}$$

Integrate the first integral by parts twice:

$$\left\{U'(x)e^{-sx}+sU(x)e^{-sx}\right\}_0^1+s^2\int_0^1 U(x)e^{-sx}dx + \int_0^1 \lambda^2U(x)e^{-sx}dx=0. \tag{58}$$

Evaluate the brace and set

$$v(s)=\int_0^1 U(x)e^{-sx}dx, \tag{59}$$

obtaining

$$U'(1)e^{-s}-U'(0)+(s^2+\lambda^2)v(s)=0. \tag{60}$$

Solving for $v(s)$

$$v(s)=\frac{U'(0)-U'(1)e^{-s}}{s^2+\lambda^2}. \tag{61}$$

Now, for $v(s)$ to be analytic, it is necessary to get rid of the poles at $s=\pm i\lambda$. Therefore the numerator of (61) must be zero when $s=\pm i\lambda$.

Inserting $\pm i\lambda$ for s and solving simultaneously

$$\begin{aligned} U'(0)-U'(1)e^{-i\lambda}&=0,\\ U'(0)-U'(1)e^{+i\lambda}&=0, \end{aligned} \tag{62}$$

$$U'(1)(e^{i\lambda}-e^{-i\lambda})=0. \tag{63}$$

Since $U'(1)$ is not zero, the parenthesis must be, and therefore

$$\sin\lambda=0,$$

or

$$\lambda=n\pi; \quad \lambda^2=n^2\pi^2.$$

SUMMARY

A method which can be used to determine the eigenvalues of equations of mathematical physics has thus been demonstrated on the equations of the Sturm-Liouville type. The method also demonstrates that the solutions have certain orthogonality properties and in the special cases of the Hermite and Laguerre equations allows the solution to be found.

Letters to the Editor

Comment on "Relationship between Gough-Joule Coefficients and Moduli of Vulcanized Rubbers"[1]

M. Mooney
United States Rubber Company, Passaic, New Jersey
August 31, 1950

In the article of the title quoted above the authors were interested in establishing by experiment the theoretical equality between the tangent shearing modulus of a rubber and the ratio of the temperature coefficient of shearing stress to the negative temperature coefficient of shearing strain. Their published data can be used also for calculating the value of an important property, the relative temperature coefficient of relative stress, σ, at constant strain, γ, or $T/\sigma(\partial\sigma/\partial T)_\gamma$. The value of this coefficient is unity if there is entropy change but no energy change in an isothermal strain, as is postulated in the kinetic theory of elasticity.

The values of the coefficient can be calculated from the data given by Conant, Hall, and Thurman for σ/γ, $1/\gamma(\partial\sigma/\partial T)_\gamma$, and T, the reference temperature.

The calculations yield the results:

Compound	$T/\sigma(\partial\sigma/\partial T)_\gamma$
Hevea *B*	0.82
GR-S	1.33
Butaprene	0.90
Butyl	1.05
Neoprene	1.04
Hevea *A*	0.81
Hevea *C*	0.67

While the values of the coefficient are correct in order of magnitude, they depart from unity in many cases by amounts which are presumably larger than the experimental error. These results are qualitatively in agreement with those published by Copeland and Mooney,[2] who also found significant departures from the theoretical value, unity, in several cases. Quantitatively, however, the results of the two groups of experimentalists are not in good agreement.

Obviously more work in the field of thermo-elasticity is called for to determine whether the differences in results are caused by the use of different compounds, different test methods, or other factors. However, it is growing more and more evident that, contrary to the kinetic theory of elasticity, the energy of an elastomer subjected to isothermal strain sometimes contributes appreciably to the stress.

Concerning the experimental method used by Conant and associates, it may be remarked, incidentally, that the constraints on the thermal expansion imposed by a sandwich type of sample involves some corrections which may be appreciable, and certainly are not easily estimated.

[1] F. S. Conant, G. L. Hall, and G. R. Thurman, J. App. Phys. **20**, 526 (1949).
[2] L. E. Copeland and M. Mooney, J. App. Phys. **19**, 450 (1948).

An Approximation Method for the Determination of the Elastic Constants of Cubic Single Crystals

J. R. Neighbours and Charles S. Smith
Case Institute of Technology, Cleveland, Ohio
Received October 5, 1950

A recent investigator[1] has shown how the elastic constants of cubic crystals may be found from measurement of the three wave velocities in an arbitrary direction in the crystal. It is the purpose of this paper to show how this approximation method may be extended to higher orders.

Materials having cubic symmetry are characterized by three elastic constants, C_{11}, C_{12}, C_{44}. These constants relate stress and strain in a particularly simple way when the reference axes, XYZ, are also the crystallographic axes. In another set of axes, $X'Y'Z'$, the relationship is more complicated.

In general, the relationship between the sets of axes is governed by the scheme of direction cosines.

	X	Y	Z
X'	l_1	m_1	n_1
Y'	l_2	m_2	n_2
Z'	l_3	m_3	n_3

(1)

If the Y' axis is arbitarily taken to lie in the $X-Y$ plane, this scheme may be written in terms of l_1, m_1, and n_1 only.

	X	Y	Z
X'	l_1	m_1	n_1
Y'	$-m_1[l_1^2+m_1^2]^{-\frac{1}{2}}$	$l_1[l_1^2+m_1^2]^{-\frac{1}{2}}$	0
Z'	$-l_1n_1[l_1^2+m_1^2]^{-\frac{1}{2}}$	$-m_1n_1[l_1^2+m_1^2]^{-\frac{1}{2}}$	$[l_1^2+m_1^2]^{\frac{1}{2}}$

(2)

It may be shown that, for irrotational plane waves traveling in the X' direction, the equations of motion are:

$$\left.\begin{aligned}\rho\frac{\partial^2u'}{\partial t^2}&=C_{11}'\frac{\partial^2u'}{\partial x'^2}+C_{16}'\frac{\partial^2v'}{\partial x'^2}+C_{15}'\frac{\partial^2w'}{\partial x'^2},\\ \rho\frac{\partial^2v'}{\partial t^2}&=C_{16}'\frac{\partial^2u'}{\partial x'^2}+C_{66}'\frac{\partial^2v'}{\partial x'^2}+C_{56}'\frac{\partial^2w'}{\partial x'^2},\\ \rho\frac{\partial^2w'}{\partial t^2}&=C_{15}'\frac{\partial^2u'}{\partial x'^2}+C_{56}'\frac{\partial^2v'}{\partial x'^2}+C_{55}'\frac{\partial^2w'}{\partial x'^2},\end{aligned}\right\} \tag{3}$$

where

$$\left.\begin{aligned}C_{11}'&=C_{11}-2[l_1^2m_1^2+l_1^2n_1^2+m_1^2n_1^2]C,\\ C_{16}'&=l_1m_1[m_1^2-l_1^2][l_1^2+m_1^2]^{-1}C,\\ C_{66}'&=C_{44}+2l_1^2m_1^2[l_1^2+m_1^2]^{-1}C,\\ C_{15}'&=-n_1[l_1^4+m_1^4-n_1^2(l_1^2+m_1^2)][l_1^2+m_1^2]^{-\frac{1}{2}}C,\\ C_{55}'&=C_{44}+2n_1^2[l_1^4+l_1^2m_1^2+m_1^4][l_1^2+m_1^2]^{-1}C,\\ C_{56}'&=l_1m_1n_1[l_1^2-m_1^2][l_1^2+m_1^2]^{-\frac{1}{2}}C,\\ C&=[C_{11}-C_{12}-2C_{44}],\end{aligned}\right\} \tag{4}$$

and u', v', w' are the displacements in the X', Y', Z' directions, respectively.

The secular equation obtained from Eq. (3) is

$$\begin{vmatrix}C_{11}'-\rho V^2 & C_{16}' & C_{15}'\\ C_{16}' & C_{66}'-\rho V^2 & C_{56}'\\ C_{15}' & C_{56}' & C_{55}'-\rho V^2\end{vmatrix}=0. \tag{5}$$

The roots of this equation may be found by the perturbation method to be

$$\left.\begin{aligned}\rho V_1^2&=C_{11}'+\left\{\left[\frac{C_{15}'^2}{C_{11}'-C_{55}'}+\frac{C_{16}'^2}{C_{11}'-C_{66}'}\right]+\left[\frac{2C_{15}'C_{16}'C_{56}'}{(C_{11}'-C_{66}')(C_{11}'-C_{55}')}\right]+\cdots\right\},\\ \rho V_2^2&=C_{66}'+\left\{\left[\frac{C_{16}'^2}{C_{66}'-C_{11}'}+\frac{C_{56}'^2}{C_{66}'-C_{55}'}\right]+\left[\frac{2C_{15}'C_{16}'C_{56}'}{(C_{66}'-C_{11}')(C_{66}'-C_{55}')}\right]+\cdots\right\},\\ \rho V_3^2&=C_{55}'+\left\{\left[\frac{C_{15}'^2}{C_{55}'-C_{11}'}+\frac{C_{56}'^2}{C_{55}'-C_{66}'}\right]+\left[\frac{2C_{15}'C_{16}'C_{56}'}{(C_{55}'-C_{11}')(C_{55}'-C_{66}')}\right]+\cdots\right\}.\end{aligned}\right\} \tag{6}$$

Combining the perturbation roots of the secular determinant with the first three of Eqs. (4) results in the set of equations:

$$\left.\begin{aligned}
C_{11}' &= C_{11}-2[l_1^2m_1^2+l_1^2n_1^2+m_1^2n_1^2]C \\
&= \rho V_1^2-\left\{\left[\frac{C_{15}'^2}{C_{11}'-C_{55}'}+\frac{C_{16}'^2}{C_{11}'-C_{66}'}\right]\right. \\
&\quad \left.+\left[\frac{2C_{15}'C_{16}'C_{56}'}{(C_{11}'-C_{55}')(C_{11}'-C_{66}')}\right]+\cdots\right\}, \\
C_{66}' &= C_{44}+2l_1^2m_1^2[l_1^2+m_1^2]^{-1}C \\
&= \rho V_2^2-\left\{\left[\frac{C_{16}'^2}{C_{66}'-C_{11}'}+\frac{C_{56}'^2}{C_{66}'-C_{55}'}\right]\right. \\
&\quad \left.+\left[\frac{2C_{15}'C_{16}'C_{56}'}{(C_{66}'-C_{11}')(C_{66}'-C_{55}')}\right]+\cdots\right\}, \\
C_{55}' &= C_{44}+2n_1^2[l_1^4+l_1^2m_1^2+m_1^4][l_1^2+m_1^2]^{-1}C \\
&= \rho V_3^2-\left\{\left[\frac{C_{15}'^2}{C_{55}'-C_{11}'}+\frac{C_{56}'^2}{C_{55}'-C_{66}'}\right]\right. \\
&\quad \left.+\left[\frac{2C_{15}'C_{16}'C_{56}'}{(C_{55}'-C_{11}')(C_{55}'-C_{66}')}\right]+\cdots\right\}.
\end{aligned}\right\} \quad (7)$$

If the three wave velocities V_1, V_2, V_3 in the X' direction are determined, then Eqs. (7) may be solved by successive approximations to yield C_{11}, C_{12}, and C_{44}. The X' direction, specified by l_1, m_1, n_1, which also must be measured, need not be a special direction in the cubic crystal. Certain exceptional directions are noted below.

The values of the perturbation terms (within braces, Eq. 6) depend in complex ways upon the elastic constants and direction in the crystal, but roughly the absolute value of the quantity $C=[C_{11}-C_{12}-2C_{44}]$ determines the magnitude of these terms. For ionic crystals such as silver chloride where the quantity $|C|$ is small, the higher order perturbation terms are quite small.[1] Much larger values for corresponding perturbation terms are found for metallic crystals such as nickel where the quantity $|C|$ is about an order of magnitude larger. In our experience, about five trials are required in making a solution of (7) for a metallic crystal.

In general, a given set of direction cosines defines any one of six crystallographically equivalent directions in the first octant, and care must be exercised to choose an advantageous order for the direction cosines. Since n_2 has been chosen equal to zero, the perturbation approximations to the roots of the secular equation will be better approximations to the actual roots for certain choices of l_1, m_1, and n_1. In practice, the better choices are those that place the X' axis near an $[h\,h\,l]$ type direction.

It should be pointed out that the directions [100] and [111] are ambiguous in that for each of these directions the two transverse wave velocities are equal. All three elastic constants, C_{11}, C_{12}, and C_{44}, cannot be determined by wave velocity measurements in these directions. Wave velocity measurements in those general directions near to these two are suitable in principle but not in practice for a determination of all three elastic constants.

The [110] direction in the cubic crystal is, on the other hand, unique in that wave velocity measurements in this direction will determine all three elastic constants, and in this direction the perturbation terms are zero. General directions near to this special direction will yield good accuracy for the constants and only small perturbation corrections will be necessary.

The elastic constants numerically computed from (7) may be checked by using the results to make a numerical solution of the secular determinant, Eq. (5). The three values for the wave velocities thus obtained from (5) should agree with the three measured wave velocities.

It is felt that the method outlined here has several advantages over that of measuring the wave velocities in crystals cut in special, simple directions. In practice, many difficulties may be experienced in attempts to grow single crystals large enough to be cut to a desired orientation. Even if crystals of adequate size are grown, use of the above perturbation method may be quicker and simpler than cutting an oriented crystal. This perturbation method has been used by the authors for determining the elastic constants of nickel, which work will be published at an early date. This work has been supported by the ONR.

[1] D. L. Arenberg, J. App. Phys. 21, 941 (1950).

Coefficient of Self-Diffusion of Copper

G. Cohen and G. C. Kuczynski
Metallurgy Department, Polytechnic Institute of Brooklyn, Brooklyn, New York
August 31, 1950

It has been shown previously[1–3] that the coefficients of self-diffusion of metals can be determined by measuring, as a function of time and temperature, the width x of the "neck" formed during sintering of a metallic wire to a cylinder of the same metal. The method was described in detail elsewhere.[3]

The specimens were prepared from OFHC copper. The annealed copper wire of 0.005-inch diameter was wound around the rods of $\frac{1}{4}$-inch diameter and heated in dry hydrogen at temperatures and for time periods indicated in Table I. After heating, the specimens were cut longitudinally, polished, etched, and measured under the microscope. The coefficients of self-diffusion D were calculated from the equation[3]

$$D=3/80\pi\ kT/\delta^3\gamma t\ x^5/a^2,$$

where k is the Boltzmann constant, a the radius of the wire, T absolute temperature, t the time of heating, δ the interatomic

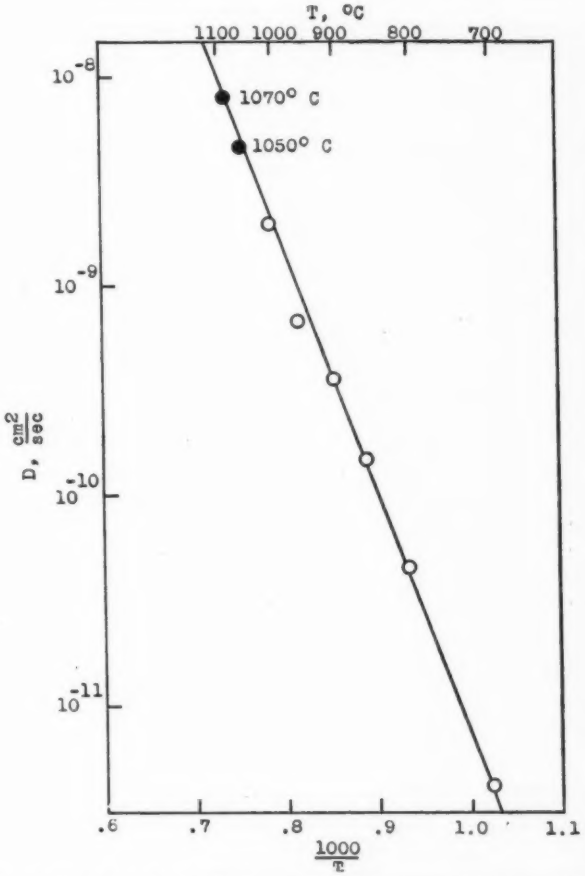

Fig. 1. Variation of self-diffusion coefficient of copper with temperature. Natural logarithm of D *versus* reciprocal of absolute temperature.

TABLE I. Self-diffusion coefficient D of copper.

Temperature, °C	Time (hrs)	$\times 10^{-4}$ cm	D cm²/sec.
700	4.0	6.1	4.06×10^{-12}
800	2.0	8.5	4.60×10^{-11}
850	1.0	9.4	1.53×10^{-10}
900	1.0	11.1	3.58×10^{-10}
950	1.0	12.2	6.80×10^{-10}
1000	0.5	13.2	1.95×10^{-9}

distance (in the present case 2.55A), and γ the surface energy of solid copper taken as 1370 ergs/cm².[4] The D-values so obtained are listed in Table I along with measured values of x. From the $\ln D/1000/T$ plot in Fig. 1, the coefficient of self-diffusion of copper was found to be expressed by the following equation: $D=4.1e^{-54,000/RT}$, which agrees fairly well with that obtained by J. Steigman, W. Shockley, and F. C. Nix,[5] which is $D=11.0e^{-57,200/RT}$. The points in Fig. 1 marked by black circles and corresponding to temperatures 1050°C and 1070°C were determined independently[6] by the same method. They fall very well on the straight line resulting from this investigation.

[1] G. C. Kuczynski, Trans. Am. Soc. Met. **55**, 169 (1949).
[2] G. C. Kuczynski, Phys. Rev. **75**, 1309 (1949).
[3] G. C. Kuczynski, J. App. Phys. **21**, 632 (1950).
[4] H. Udin, A. Shaler, and J. Wulff, Trans. Am. Soc. Met. **55**, 186 (1949).
[5] J. Steigman, W. Shockley, and F. C. Nix, Phys. Rev. **56**, 13 (1939).
[6] B. Alexander, G. C. Kuczynski, and M. Dawson, "Relations between diffusion and viscous flow in metals," Symposium of the Physics of Powder Metallurgy, Sylvania Electric Products, Inc. (August 1949) (to be published soon).

Erratum: Transonic Potential Flow of a Compressible Fluid

[J. App. Phys. **21**, 771–778 (1950)]

W. R. SEARS
Cornell University, Ithaca, New York

SINCE the publication of the above article, Professor Y. H. Kuo has changed his analysis of the stability of mixed potential flow. His conclusions are now different from those reported in my paper.

Specifically, Dr. Kuo discovered an inconsistency in the orders of magnitude of terms resulting from his boundary condition. Upon correction of this, the term k/m disappears from the definition of σ (see my Eq. (9)), and consequently the profound effect of the local slope of the body at the sonic line disappears from the results. His final conclusions, based on the revised calculation, are that accelerating transonic flow is stable with respect to the class of disturbances considered, while decelerating flow is unstable to compression disturbances, on convex surfaces regardless of the slope m. Obviously, this brings him into agreement with other authors, who have analyzed the problem from different standpoints, and seems to eliminate the interesting possibility of stable transonic potential flow sketched in my Fig. 10.

Erratum: Separation of Gases by Fractional Permeation through Membranes

[J. App. Phys. **21**, 279–283 (1950)]

SOL WELLER AND WALDO A. STEINER
Synthetic Liquid Fuels Branch, Bureau of Mines, Pittsburgh, Pennsylvania

BY an error in transcription the sign of the quantity C has been given incorrectly in some of the equations in the above paper. C should be defined by the equation

$$C=\tfrac{1}{2}[1+(\alpha-1)p/P],$$

and Eqs. (12) and (13) should read

$$x=f(i)=Ai-C+[A^2i^2+(\alpha-2AC)i+C^2]^{\frac{1}{2}}, \tag{12}$$

$$\frac{dn_B}{n_B}=\frac{di}{f(i)-i}=\frac{di}{(A-1)i-C+[A^2i^2+2Bi+C^2]^{\frac{1}{2}}}, \tag{13}$$

where $2B=\alpha-2AC$. The subsequent equations and Fig. 2 are correct.

We are grateful to Dr. T. P. Wilson for pointing out this error to us.

Deformations and Stresses in Bourdon Tubes*

R. A. CLARK** AND E. REISSNER
Department of Mathematics, Massachusetts Institute of Technology, Cambridge, Massachusetts

August 18, 1950

A BOURDON tube may be considered as a toroidal, elastic shell with thin walls, oval cross section, and with closed ends. When such a closed tube is exposed on the outside or on the inside to uniform normal wall pressure, the curvature of the center line of the tube changes proportionally with the applied wall pressure. Measurements of the resultant motion of one end of the tube with reference to the other may then be interpreted, after appropriate calibration, as pressure measurements.

The physical nature of the action of the tube may be understood by means of the following considerations. Take first a *complete* torus subject to uniform wall pressure. If the pressure is on the outside, it will produce tension in the part of the walls nearest to the axis of the torus and compression in the part of the walls furthest from the axis. This stress distribution then evidently produces an internal bending moment with axis parallel to the axis of the torus.

In the Bourdon tube *part* of the complete torus is taken and the ends are closed up. The shell is now no longer able to take the bending moment which occurred in the complete torus. Consequently one may consider the state of stress and deformation in the tube as a superposition of two states: (1) stresses and deformations in a complete torus subject to wall pressure; (2) stresses and deformations in an incomplete torus acted upon by bending moments at the ends.[1] The magnitude of the applied moment of state 2 is chosen such that it cancels the corresponding internal moment of state 1. It is the superimposed state 2 which is responsible for the change of curvature of the center line of the tube.

State 1 is treated as a problem in the theory of axi-symmetrical deformations of thin shells of revolution. State 2 is treated in the same manner after introduction into the theory of a non-axi-symmetrical component of circumferential displacement.[2]

If for the sake of discussion, the curved tube is considered as made up of two systems of curved rods, one system with circular center lines and the other system consisting of closed, oval rings, it is now understood that the action of the tube involves direct stresses and negligible bending of the circular rods and bending with negligible direct strains of the oval rings.[3–5]

There are two well-known limiting solutions both for state 1 and state 2. In the limiting solution for state 1 which concerns the complete torus under pressure the bending stresses in the oval rings are neglected and determination of the direct stresses becomes a problem of the membrane theory of thin shells.[6] In the limiting solution for state 2 the oval rings are considered rigid and the curved tube is stressed and deformed in accordance with the elementary theory of beams.

Combination of these two limiting states for a theory of the Bourdon tube has again been suggested quite recently.[7] It is, however, easy to see that joint application of the two limiting

solutions is not justified physically. The membrane solution for state 1 will be applicable only for tubes with sufficiently *thin* walls. The elementary-beam theory solution for state 2 will be applicable only for tubes with sufficiently *thick* walls. So far as is known, no results have yet been given concerning the meaning of the word "sufficiently" for the problem of state 1.

In order to gain further insight into the problem the authors have undertaken a study from the point of view of the theory of thin shells of the stresses and deformations of Bourdon tubes with elliptical cross section. In this theory the problem can be reduced to the determination of the periodic solutions of two simultaneous, linear, non-homogeneous second-order differential equations with periodic coefficients.

It is found that the solutions depend primarily on two dimensionless parameters which involve the dimensions of the tube. These parameters are of the form b/c and bc/ah, where a = radius of center line of the tube, h = wall thickness of the tube, c = major semi-axis of the elliptical cross section, and b = minor semi-axis of the elliptical cross section.

Quantitative solutions of the differential equations of the problem led to the result that the membrane solution for state 1 is adequate as soon as the parameter bc/ah is larger than about 10. On the other hand, the elementary beam-theory solution for state 2 ceases to be adequate as soon as bc/ah is larger than about 0.5.

Two different methods of solution were employed for the differential equations of the problem. For values of the parameter bc/ah up to about 5, trigonometric series were used. This led to infinite systems of simultaneous linear equations for the coefficients of the trigonometric series. These were solved approximately by retaining only a finite number of the coefficients. In this way up to ten simultaneous equations for ten unknowns were needed.

The other method of solution was an extension to *non-homogeneous* differential equations of what is often referred to as the W.K.B.J. method of asymptotic integration. This method is applicable for sufficiently large values of the parameter bc/ah. It was found that adequate results were obtained in this way as soon as bc/ah was larger than about 2. The consequent overlapping of the ranges of validity of the series solution and of the asymptotic solution permitted a check on the accuracy of either method.

Derivation of the asymptotic results proved to be very much more convenient than use of the series method. Remarkably simple explicit formulas could be obtained in the asymptotic range and these are listed below.

The sensitivity of the tube is given by the formula

$$\frac{\Delta a}{a}=\frac{p}{E}\frac{a}{b}\frac{c^2-b^2}{h^2}\left(1.63-\frac{ah}{cb}\right). \tag{1}$$

In Eq. (1) p is the applied wall pressure, E the modulus of elasticity of the tube material, and Δa the change of the radius a of the tube caused by the applied pressure. A small effect of Poisson's ratio is incorporated in the numerical coefficient 1.69 which is based on $\nu=\frac{1}{3}$. The general form of this coefficient is $[3(1-\nu^2)]^{\frac{1}{2}}$. Equation (1) is applicable as soon as cb/ah is larger than about 2. For very much larger values of cb/ah the second term inside the parenthesis becomes negligible and the result becomes still simpler.

The maximum stress in the tube is caused by bending of the elliptical rings and occurs at the ends of the major axis of the cross section. When cb/ah is larger than about 2, it is given by the formula

$$\sigma_m=1.88p(ah/cb)^{\frac{1}{2}}(c^2-b^2)/h^2. \tag{2}$$

It is further found that the stress σ_m is always smaller than the corresponding bending stress in a straight tube with the same elliptical cross section and with the same uniform wall pressure p. Denoting this stress for the straight tube by σ_{sm} it is found that, in the range of applicability of Eq. (2),

$$\frac{\sigma_m}{\sigma_{sm}}=\frac{1.87b_0}{b_0-b_1}\left(\frac{ah}{cb}\right)^{\frac{1}{2}}, \tag{3}$$

where b_0 and b_1 are expressed in terms of complete elliptic integrals in the form

$$\left.\begin{aligned} b_0&=(4/\pi)E(e), \quad e^2=1-(b/c)^2\\ b_1&=(8/3\pi e^2)[(1-e^2)K(e)-(1-\tfrac{1}{2}e^2)E(e)]\end{aligned}\right\}. \tag{4}$$

For values of bc/ah less than about 2, no simple explicit formula can be given for σ_m. An exception is the limiting relation

$$\lim_{bc/ah\to 0}\sigma_m/\sigma_{sm}=1. \tag{5}$$

Detailed derivations, together with numerical results, will be published in the near future.

* The following is based on work performed with the support of the ONR under Contract N5 ori-07834 with Massachusetts Institute of Technology.
** Now Department of Mathematics, Case Institute of Technology.

[1] In this formulation one has disregarded local effects at and near the ends of the tube which fall within the scope of St. Venant's principle.

[2] E. Reissner, *Bending of Curved Tubes*, Proc. Nat. Acad. Sci. U.S.A. **35**, 204–208 (1949).

[3] H. Lorenz, "Theorie der Röhrenfeder manometer," Physik. Zeits. **18**, 117 (1917).

[4] M. Tueda, "Mathematical theories of Bourdon pressure tubes and bending of curved pipes," Mem. Coll. Eng., Kyoto Imp. Univ. **8**, 102–115 (1934); **9**, 132–152 (1936).

[5] A. Wolf, "An elementary theory of the Bourdon gage," J. App. Mech. **13**, A207–A210 (1946).

[6] H. Lorenz, Theorie der Röhrenfeder manometer, Z. Verein Deutscher Ing. **54**, 1865 (1910).

[7] G. Schubert, *Uber Effekte zweiter Ordnung bei Biegung und Torsion dünnwandiger Rohre elliptischen Querschmitts, Ing.*—Arch **12**, 53–63 (1941).

Shadowgrams of Spherical Missiles Entering Water at Supersonic Speeds

J. H. McMillen, R. L. Kramer, and D. E. Allmand
Naval Ordnance Laboratory, White Oak, Silver Spring, Maryland
October 24, 1950

WHILE a great deal is known about the flow of water when objects are propelled through it at modest speeds, very little is known about the flow or other physical responses of the water when objects are shot into it at supersonic speeds. In order to investigate the events which accompany water entry at supersonic speeds (above 4800 ft./sec.), a shadowgraphic investigation was carried out in which spherical missiles were shot into water at speeds of 7000 ft./sec. These speeds correspond to a Mach number of 1.46 in water. Shadowgraphic records have the advantage that they indicate the simultaneous (exposure times less than a microsecond) general disposition of the transient pressure field over the entire field.

Some of the shadowgrams obtained in this investigation are reproduced in Fig. 1. The one-eighth-inch steel spheres used were not permanently deformed by the impact. These shadowgrams

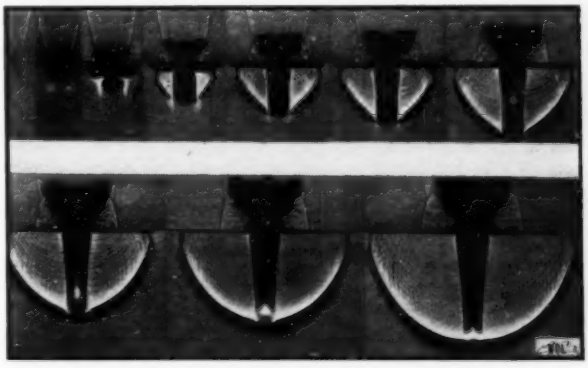

FIG. 1.

are of various shots taken at increasing depths of water penetration. The first shadowgram records the spherical missile just before impact; the last one records the entry after the shock wave has advanced eighteen sphere diameters from the surface. In the early stages of entry all the light passing through the shock wave region is strongly refracted and a complete shadow silhouette is recorded. At the later stages the light passes through with less deviation and some of the features of the interior of the region, such as cavity, can be observed. In the air above the water one finds the shadow of the splash which rises with supersonic speeds in air.

Information on the pressure field in the vicinity of the missile and shock wave can be augmented by obtaining shadowgrams using narrow $\frac{1}{8}$-inch spark beams. If the region between the shock front and the water surface is regarded as half a spherical lens, then this exploratory beam method shows that the "lens" has both a diverging and a converging action. The converging lens action occurs for rays which are nearly tangential to the shock front. These rays are refracted toward the center and produce the pattern of lines found in the shadow of the cavity. The diverging action occurs for rays striking the central portion of the shock wave region. In the early penetration stages these rays diverge so strongly that the shadow region is left completely dark and in the intermediate stages the downward refraction of these rays leaves a dark band below the water surface. A study of the refraction of individual spark beams shows that the density (or pressure) increases rapidly in going from the water surface toward the nose of the missile and also that the pressure increases abruptly in approaching the shock wave from the undisturbed region in front. These pressure gradients are quite large, since the distances are small; the peak pressure or stagnation pressure is at least 20,000 atmospheres at entry.

It is also interesting to note that the missile is set into vibration at impact and secondary waves are produced throughout the missile's water flight. In the last shadowgram one can observe these secondary waves after they have been reflected in the surface.

This investigation was partially supported by the ONR.

Author Index to Volume 21

References with (L) are to Letters to the Editor

Abbott, F. R. and C. J. Fisher. Graphical analysis of the interference patterns of an elevated ultra-high frequency antenna under conditions of atmospheric stratification—636
Affleck, John H. (see Hensley, Eugene B.)—938 (L)
Agnor, T. J. and M. E. Shank. Fracture modes in high purity metals—939 (L)
Alexander, Leroy. Geometrical factors affecting the contours of x-ray spectrometer maxima. II. Factors causing broadening—126
—— Analysis of intensities obtainable using pinhole and slit collimators in x-ray powder diffraction techniques—779
—— **and Harold P. Klug.** Determination of crystallite size with x-ray spectrometer—137
Alger, R. S. Integrating crystal detectors for high energy photons and particles—30
Allis, W. P. (see Lax, Benjamin)—1297
Allmand, D. E. (See McMillen, J. H.)—1341 (L)
Anderson, Thomas F. Use of critical point phenomena in preparing specimens for the electron microscope—724 (L)
Andrews, C. L. Diffraction pattern in a circular aperture measured in the microwave region—761
Arenberg, David L. Determination of elastic constants in single crystals with especial reference to silver chloride—941 (L)
Arthur, James S. Specific heats of MgO, TiO_2, and ZrO_2 at high temperatures—732
Averbach, B. L. and B. E. Warren. Addendum: Interpretation of x-ray patterns of cold-worked metal—185, 595

Bachman, C. H. and S. J. Silverman. X-ray tube producing a beam of x-rays convergent to a point—615 (L)
Backus, Robert C. and Robley C. Williams. Use of spraying methods and of volatile suspending media in the preparation of specimens for electron microscopy—11
Bacon, Ralph Hoyt. Pursuit course—1065 (L)
Baker, W. O. (see Hopkins, I. L.)—206
Barnes, Bentley T. and Stephen Eros. Techniques for measuring the dynamic characteristics of a low pressure discharge—1275
Bartberger, C. L. Magnetic field of a plane circular loop—1108
Barton, H. M., Jr. and R. Brill. Average electron density measurements by low angle x-ray scattering—783
Bas-Taymaz, E. Aberration-phenomenon in electrostatic lenses. "Kidney effect"—1064 (L)
Bauer, S. H. (see Harvey, R. B.)—860
Beatty, Suzanne Van Dijke. Intensity correction factors for x-ray spectrometer transmission pole figure determinations—940 (L)
Beck, Fred J. (see Schorr, Marvin G.)—795
Beck, Paul A. and Philip R. Sperry. Strain induced grain boundary migration in high purity aluminum—150
——, **Philip R. Sperry, and Hsun Hu.** Orientation dependence of the rate of grain boundary migration—420
Becker, John V. Results of recent hypersonic and unsteady flow research at the Langley Aeronautical Laboratory—619
Beeman, W. W. (see Ritland, H. N.)—838
Benitez, L. E. and S. S. Penner. Emission of radiation from nitric oxide: Approximate calculations—907
Bennett, F. D. (see Giese, J. H.)—1226
Bennett, Willard H. Radiofrequency mass spectrometer—143; Erratum—723
Bergdolt, V. E. (see Giese, J. H.)—1226
Bershader, D. and S. I. Pai. On turbulent jet mixing in two-dimensional supersonic flow—616 (L)
Birks, L. S. (see Wilkinson, P. G.)—60 (L)
Bjorklund, F. E. (see Hodgdon, F. B.)—1156
Blair, G. W. Scott (see Reiner, M.)—1195 (L)
Blankenship, E. B. (see Hughes, D. S.)—294
Bogdanoff, John L. Theory of dislocations—1258
Boonstra, B. B. S. T. Stress-strain properties of natural rubber under biaxial strain—1098
Borts, R. B. (see Woonton, G. A.)—428
Bosson, G., F. Gutmann, and L. M. Simmons. Relationship between resistance and temperature of thermistors—1267
Bourque, O. J. (see Quinn, H. F.)—995
Bower, John L. Note on the error coefficients of a servo mechanism—723 (L)
Boyer, R. F. Random noise in dielectric materials—469
Brice, T. J. (see Wilson, W. A.)—203
Briggs, Lyman J. Limiting negative pressure of water—721 (L)
Brill, R. (see Barton, H. M., Jr.)—783
Brock, John E. Some non-linear systems permitting simple harmonic motion—238
Brown, A. A., L. J. Neelands, and H. E. Farnsworth. Thermionic work function of the (100) face of a tungsten single crystal—1
Brown, Sanborn C. (see Lax, Benjamin)—1297
Browne, S. H. (see Gilvarry, J. J.)—753, 1195 (L)
Browning, George V. (see Ferry, John D.)—513
Buchdahl, Rolf (see Nielsen, Lawrence E.)—488, 607
—— **and Lawrence E. Nielsen.** Transitions in high-polymeric materials—482
Buerger, M. J. Generalized microscopy and the two-wavelength microscope—909
Burte, Harris M. Non-destructive mechanical test for animal fibers—494

Carreker, R. P., Jr. Plastic flow of platinum wires—1289
Carruthers, J. A. (see Woonton, G. A.)—428
Cech, R. E. (see Turnbull, D.)—804
Chaffee, E. L. (see Yeh, Chai)—981
Cheng, David H. (see Mindlin, Raymond D.)—926, 931
Chipman, D. and B. E. Warren. X-ray measurement of long range order in β-brass—696
Chu, E. L. Upper and lower bounds of eigenvalues for composite-type regions—454
Cini, Marcello. Response characteristics of linear systems—8
Clark, John W. and Ralph E. Neuber. End-cooling of power tube filaments—1084
Clark, Orrin H. and M. L. Deutsch. Scheme for analyzing capillary measurements on non-Newtonian liquids—713
—— **and M. L. Deutsch.** Note on scheme for analyzing capillary measurements on non-Newtonian liquids—1195 (L)
Clark, R. A. and E. Reissner. Deformations and stresses in Bourdon tubes—1340 (L)
Clarke, A. M. (see Trump, J. G.)—345
Cleary, E. P. (see Cobine, J. D.)—1264
Cobine, J. D., E. P. Cleary, and W. C. Gray. Microwave study of the high pressure arc—1264
Cohen, G. and G. C. Kuczynski. Coefficient of self-diffusion of copper—1339 (L)
Cohn, Seymour B. Electrolytic-tank measurements for microwave metallic delay-lens media—674
Conant, F. S., G. L. Hall, and W. James Lyons. Equivalent effects of time and temperature in the shear creep and recovery of elastomers—499
——, **G. L. Hall, and G. R. Thurman.** Erratum: Relationship between Gough-Joule coefficients and moduli of vulcanized rubbers—184
Cooke, S. P. (see Willenbrock, F. K.)—114

Cowley, J. M. X-ray measurement of order in single crystals of Cu_3Au—24
Criscuolo, E. L. and D. T. O'Connor. Natural crystal Greenockite (cadmium sulfide) as an x-ray detector—1196 (L)
Crossley, H. E., Jr. (see Gilmore, F. R.)—243

Danforth, W. E. (see Morgan, F. Haydn)—112
Dannis, M. L. Studies in plasticization of polyvinyl chloride. I. Physical changes and their measurement—505
—— Studies in plasticization of polyvinyl chloride. II. Plasticizer variations in PVC-plasticizer systems—510
Dedrick, J. H. and A. Gerds. Reply to "Activation energy for copper self-diffusion"—261 (L)
—— **and G. C. Kuczynski.** Electrical conductivity method for measuring self-diffusion of metals—1224
Dekker, A. J. and Helen M. A. Urquhart. Current-hysteresis of the electrolytic aluminum-oxide rectifier—708
Delano, Victor and Clark Goodman. Shielding properties of the concrete wall of the M. I. T. cyclotron—1040
Deutsch, M. L. (see Clark, Orrin H.)—713, 1195 (L)
Dexter, D. L. (see Sachs, R. G.)—1304
Dienes, G. J. Frequency factor and activation energy for the volume diffusion of metals—1189
—— (see Fleeman, J.)—1193 (L)
Dornfeld, E. G. (see Reisner, John H.)—1131
Drucker, D. C. (see White, G. N., Jr.)—1013
—— **and H. Ekstein.** Dimensional analysis of metal cutting—104
Duwez, Pol (see von Karman, Theodore)—987

Ekstein, H. (see Drucker, D. C.)—104
Ellinger, F. H. (see Singer, Joseph)—467 (L)
Emmerich, Claude L. Steady-state internal temperature rise in magnet coil windings—75
Enright, D. P. (see Sonders, L. R.)—338
Eros, Stephen. (see Barnes, Bentley T.)—1275
Espersen, G. A. Thermionic emitting properties of thoria-rhenium—261 (L)
Estrin, Gerald. Effective permeability of an array of thin conducting disks—667
Ettinger, G. M. Tracing and interpretation of asymmetrical hysteresis loops—936 (L)
Evans, Marjorie W., Milton D. Scheer, Louis J. Schoen, and Emmy L. Miller. Augmented flames in half-open tubes—44

Farnsworth, H. E. (see Brown, A. A.)—1
Farrant, J. L. Wave-lengths suitable for x-ray microscopy of biological specimens—63 (L)
Feder, Josephine Carr (see Fusfeld, Herbert I.)—261 (L)
Ferry, John D. (see Marvin, Robert S.)—197
——, **W. M. Sawyer, Geo. V. Browning, and Arthur H. Growth, Jr.** Mechanical properties of substances of high molecular weight. III. Dispersion of dynamic rigidity and viscosity in concentrated polyvinyl acetate solutions—513
Findley, William N. Comments on creep and damping properties of polystyrene—258 (L)
Fischbein, Irwin W. Electron microscopy of wet biological tissues by replica techniques—1199
Fisher, C. J. (see Abbott, F. R.)—636
Fisher, J. C. Limiting hydrostatic tension of water near O°C—1068 (L)
Fitzgerald, Edwin R. (see Marvin, Robert S.)—197
Fitzpatrick, J. A., J. C. Hubbard, and W. J. Thaler. A high intensity short duration spark light source—1269
Flanders, Donald A. and George Shortley. Numerical determination of fundamental modes—1326
Fleagle, Robert G. Air temperature modification by vertical transport—326
Fleeman, J. and G. J. Dienes. Frederickson-Eyring theory of the mechanical behavior of metals—1193 (L)
Flory, Paul J. (see Fox, Thomas G., Jr.)—581
Fox, Thomas G., Jr., and Paul J. Flory. Second-order transition temperatures and related properties of polystyrene. I. Influence of molecular weight—581
Fremont, H. A. (see Koller, L. R.)—741
Frerichs, Rudolf. Cadmium sulfide x-ray detector—312
Frevel, L. K. and P. P. North. Single wave-length x-rays for powder diffraction—1038
Friedman, Morris D. Determination of eigenvalues using a generalized Laplace transform—1333
Friedman, Raymond and W. C. Johnston. Wall-quenching of laminar propane flames as a function of pressure, temperature, and air-fuel ratio—791
Fullman, R. L. Formation of annealing twins during grain growth—1069 (L)
Fusfeld, Herbert I. and Josephine Carr Feder. Study of crack propagation using high speed motion pictures—261 (L)

Gallagher, C. J. Retrograde motion of the arc cathode spot—768
Gamble, Edward H. Current build-up in a planar diode—108
Garbuny, M. Graphical representation of particle trajectories in a moving reference system—1054
Garfitt, R. G. (see Haine, M. E.)—173
Geballe, Ronald and Fred S. Linn. Electrical breakdown in CSF_8—592
Gemant, Andrew. Thermal conductivity of soils—750
George, Waller. (see Kauffman, John)—431
Gerds, A. (see Dedrick, J. H.)—261 (L)
Gerould, Charles H. Comments on the use of latex spheres as size standards in electron microscopy—183 (L)
Gettner, Mark E. (see Hillier, James)—889
Giese, J. H., F. D. Bennett, and V. E. Bergdolt. Simple interferometric test for conical flow— 1226
Gilmore, G. D. (see Spencer, R. S.)—523, 527
——, **M. S. Plesset, and H. E. Crossley, Jr.** Analogy between hydraulic jumps in liquids and shock waves in gases—243
Gilvarry, J. J. and S. H. Browne. Application of Liouville's approximation to the blind navigation problem—1195 (L)
——, **S. H. Browne, and I. K. Williams.** Theory of blind navigation by dynamical measurements—753
Gold, Louis. Compilation of body wave velocity data for cubic and hexagonal metals—541
Goodman, Clark. (see Delano, Victor)—1040
Gossick, Ben R. Distribution in energy of Johnson noise pulses—847
Goubau, Georg. Surface waves and their application to transmission lines—1119
Gray, W. C. (see Cobine, J. D.)—1264
Greeff, Max B. Thermoelectric generation of current—943 (L)
Griffith, Wayland. Vibrational relaxation times in gases—1319
Gross, B. Frictional loss in visco-elastic substances—185 (L)
Growth, Arthur H., Jr. (see Ferry, John D.)—513
Gugelot, P. C. and M. G. White. On the shielding qualities of different concrete mixtures—369
Gutmann, F. (see Bosson, G.)—1267

Haine, M. E., R. S. Page, and R. G. Garfitt. Three-stage electron microscope with stereographic dark field, and electron diffraction capabilities—173
Hall, C. E. Low temperature replica method for electron microscopy—61 (L)
Hall, G. L. (see Conant, F. S.)—184, 499
Hamm, F. A. Lapping technique: to improve the image quality of electron microscope lenses—271
Hanley, T. E. Thorium sulfide as a thermionic emitter—1193 (L)
Haringx, J. A. Note on the frictionless bearing for small angular deflections—258 (L)
Harrington, John V. Storage of small signals on a dielectric surface—1048
Harrison, S. W. (see Hutter, R. G. E.)—84

Harvey, R. B., F. A. Keidel, and S. H. Bauer. Some effects of nozzle design on the diffraction of electrons by gases—860
Hass, G. and M. E. McFarland. Aluminum oxide replicas for electron microscopy produced by a two-step process—435
Hellar, R. A. (see Widell, E. G.)—1115
Heller, R. B., J. McGannon, and A. H. Weber. Precision determination of the lattice constants of zinc oxide—1283
Henkels, Herbert W. Conductivity of liquid selenium—200°–500°C—725
Henry, C. O. (see Sidhu, S. S.)—1036
Hensley, Eugene B. and John H. Affleck. Barium oxide on tungsten cathode interface—938 (L)
Henson, A. F. Modification of the radiofrequency mass spectrometer—1063 (L)
Hernqvist, K. G. (see Linder, E. G.)—1088
Herring, Conyers. Effect of change of scale on sintering phenomena—301
—— Diffusional viscosity of a polycrystalline solid—437
Hertzberg, A. and A. Kantrowitz. Studies with an aerodynamically instrumented shock tube—874
Hetényi, M. General solution for the bending of beams on an elastic foundation of arbitrary continuity—55
Hettrick, David. Propagation of TM_{01} mode in a metal tube containing an imperfect dielectric—561
Hibbard, Walter R., Jr. (see Nielsen, John P.)—853
Hillier, J. Removable intermediate lens for extending the magnification range of an electron microscope—785
Hillier, James and Mark E. Gettner. Improved ultra-thin sectioning of tissue for electron microscopy—889
Hodgdon, F. B. and D. A. Stuart. Application of rate-process theory to glass. II. Viscosity—1160
——, **D. A. Stuart, and F. E. Bjorklund.** Application of rate-process theory to glass. I. Breaking strength—1156
Hollmann, Hans E. Semiconductive colloidal suspensions with non-linear properties—402
Hollomon, John H. Activation energy for copper self-diffusion —261 (L)
Holmboe, L. W. (see Young, R. T., Jr.)—1066 (L)
Hopkins, E. G. Vacuum tubes with mutually bombarding oxide cathodes—841
Hopkins, I. L., W. O. Baker, and J. B. Howard. Complex stressing of polyethylene—206
Horton, C. W. and R. B. Watson. On the diffraction of radar waves by a semi-infinite conducting screen—16
——, **F. C. Karal, Jr., and C. M. McKinney.** Radiation patterns of dielectric rods of circular cross section—$TM_{0,1}$ mode—279
—— (see Watson, R. B.)—802
Howard, J. B. (see Hopkins, I. L.)—206
Hsiao, C. C. and J. A. Sauer. Crazing of linear high polymers —1071
Hu, Hsun (see Beck, Paul A.)—420
Hubbard, J. C. (see Fitzpatrick, J. A.)—1269
Huggins, Maurice L. Stress phenomena from the respective viewpoints of solid-state and high polymer—518
Hughes, D. S., E. B. Blankenship, and R. L. Mims. Variation of elastic moduli and wave velocity with pressure and temperature in plastics—294
Hung, C. S. Thermionic emission from oxide cathodes: retarding and accelerating fields—37
Hutter, R. G. E. and S. W. Harrison. Method of reducing deflection defocusing in cathode-ray tubes—84

Irwin, G. R. (see Kies, J. A.)—716
Ivey, Henry F. Use of brightness temperatures in Richardson plots—616 (L)

Jacob, L. Some crossover properties in the electron immersion objective—966
Jacobs, Harold and Jack Martin. Role of cathode temperature in the glow discharge—681
Jaffe, Leonard D. Erratum: Distribution of phases in two-phase solids—468
Jansen, C. G. J. (see Loosjes, R.)—350 (L)
Jerrard, H. G. Turbulence in apparatus for measurement of streaming double refraction—1007
Johnson, G. W. Some observations on the epitaxy of sodium chloride on silver—1057
—— Surface tension effects in oriented thin silver films—449
Johnson, John C. Measurement of the surface temperature of evaporating water drops—22
Johnson, S. J. (see Rogers, T. F.)—1067 (L)
Johnson, V. A., R. N. Smith, and H. J. Yearian. D. c. characteristics of silicon and germanium point contact crystal rectifiers. Part II. The multicontact theory—283
Johnston, W. C. (see Friedman, Raymond)—791
Jones, C. K. Thin films peeled from Teflon—64 (L)

Kaesberg, P. (see Ritland, H. N.)—838
Kahler, H. and B. J. Lloyd, Jr. Metallic evaporation and the diameter of tobacco mosaic virus with the electron microscope—699
Kantrowitz, A. (see Hertzberg, A.)—874
Karal, F. C., Jr. (see Horton, C. W.)—1279
Kauffman, John and Waller George. Load induced x-ray line broadening in Nylon filaments—431
Kê T'ing-Sui. Internal friction of metals at very high temperatures—414
Keepin, George R., Jr. On the growth of metallic crystals from the vapor phase—260 (L)
Keidel, F. A. (see Harvey, R. B.)—860
Kelleher, K. S. Relations concerning wave fronts and reflectors—573
Keller, Joseph B. Reflection and transmission of electromagnetic waves by thin curved shells—896
Kemler, E. N. Bibliography on offshore petroleum developments—185 (L)
Kenty, Carl. Production of 2537 radiation and the role of metastable atoms in an argon-mercury discharge—1309
Kern, Raymond A. (see Kern, Stanley F.)—705
Kern, Stanley F. and Raymond A. Kern. Apparent size of objects as observed in the electron microscope—705
Kies, J. A., A. M. Sullivan, and G. R. Irwin. Interpretation of fracture markings—716
King, Ronold. Theory of N coupled parallel antennas—94
—— Theory of collinear antennas—1232
Kirkham, Don. Potential flow into circumferential openings in drain tubes—655
Klug, Harold P. (see Alexander, Leroy)—137
Koch, H. W. Magnetic field calculations for large cross-section cloud-chamber coils—387
Koller, L. R. and H. A. Fremont. Negative wire corona at high temperature and pressure—741
Krakauer, Vera Osman. Use of Reiner's equation for recognition of pseudoplastics from their flow curves—850
Kramer, R. L. (See McMillen, J. H.)—1341 (L)
Kraus, Gerard and John R. Thiem. Simplified air flow method for the determination of the surface area of powders—1065 (L)
Kuczynski, G. C. Measurement of self-diffusion of silver without radioactive tracers—632
—— (see Cohen, G.)—1339 (L)
—— (see Dedrick, J. H.)—1224
Kunkel, W. B. Static electrification of dust particles on dispersion into a cloud—820
—— Charge distribution in coarse aerosols as a function of time—833

La Grone, A. H. (see Straiton, A. W.)—188, 661
Landgraf, F. K. (see Zapffe, C. A.)—1197 (L)

Lax, Benjamin, W. P. Allis, and Sanborn C. Brown. Effect of magnetic field on the breakdown of gases at microwave frequencies—1297
Leitner, A. and R. D. Spence. Effect of a circular groundplane on antenna radiation—1001
Levreault, Rita. (see Nielsen, Lawrence E.)—607
Lewin, Leonard. Effective permeability of iron dust particles —722 (L)
Linder, E. G. and K. G. Hernqvist. Space-charge effects in electron beams and their reduction by positive ion trapping —1088
Linn, Fred S. (see Geballe, Ronald)—592
Lloyd, B. J., Jr. (see Kahler, H.)—699
Longini, R. L. Evaporation and outgassing in an inert atmosphere—81
Loosjes, R., H. J. Vink, and C. G. J. Jansen. Potential distribution in pulsed oxide-coated cathodes and its consequences for the velocity distribution of the emitted electrons —350 (L)
Lyons, Harold. Microwave frequency dividers—59 (L)
Lyons, W. James. Some theoretical considerations of dynamic-property data on textile specimens—520
—— (see Conant, F. S.)—499

McFarland, M. E. (see Hass, G.)—435
McKay, W. B. (see Quinn, H. F.)—995
McKinney, C. M. (see Horton, C. W.)—1279
McGannon, J. (see Heller, R. B.)—1283
McLauchlan, T. A. (see Scott, G. D.)—843
McMillen, J. H., R. L. Kramer, and D. E. Allmand. Shadowgrams of spherical missiles, entering water at supersonic speeds—1341 (L)
Marboe, Evelyn C. and W. A. Weyl. Mechano chemistry of the dispersion of mercury liquids in an ultrasonic field—937 (L)
Markovitz, Hershel. Remark on interference of growing spherical precipitate particles—1198 (L)
Marshall, Byron O., Jr. Electronic isograph for roots of polynomials—307
Martin, Jack. (see Jacobs, Harold)—681
Martinot-Lagarde, André. Remark about standardization and "Dimensional analysis of metal cutting"—1197 (L)
Marton, L. and D. L. Reverdin. Stroboscopic mapping of time-variable fields—617 (L)
—— **and D. L. Reverdin.** Electron optical properties of space-charge clouds—842
Marvin, Robert S., Edwin R. Fitzgerald, and John D. Ferry. Measurements of mechanical properties of polyisobutylene at audiofrequencies by a twin transducer—197
May, Albert and Jean C. Woodhull. Virtual mass of a sphere entering water vertically—1285
Michaelson, Herbert B. Work functions of the elements—536
Middleton, David. Effect of a video filter on the detection of pulsed signals in noise—734
Miles, A. J. (see Wilson, L. H.)—532
Miles, J. W. Errata: On the diffraction of an electromagnetic wave through a plane screen—468
Miller, Emmy L. (see Evans, Marjorie W.)—44
Miller, Kenneth S. and Ralph J. Schwarz. Analysis of a sampling servo mechanism—290
Miller, Theodore. Magnetically controlled wave-guide attenuators—722 (L)
Mims, R. L. (see Hughes, D. S.)—294
Mindlin, Raymond D. and David H. Cheng. Nuclei of strain in the semi-infinite solid—926
—— **and David H. Cheng.** Thermoelastic stress in the semi-infinite solid—931
Mooney, M. Comment on "Relationship between Gough-Joule coefficients and moduli of vulcanized rubbers"—1338 (L)
Moore, John R. Generalized response of linear systems for arbitrary initial conditions—933
Morgan, F. Haydn and W. E. Danforth. Thermocouples of the refractory metals—112
Morgan, Samuel P., Jr. Mode conversion losses in transmission of circular electric waves through slightly non-cylindrical guides—329
Morrison, H. L. (see Rogers, F. T., Jr.)—1177
Morrison, I. F. Alternative method for the summation of Fourier series—939 (L)
Munk, M. M. Reversal theorem of linearized supersonic airfoil theory—159
Murphy, James A. and Richard C. Raymond. Dielectric constants of five gases at 9400 megacycles per second—1064 (L)

Neelands, L. J. (see Brown, A. A.)—1
Neighbours, J. R. and Charles S. Smith. Approximation method for the determination of the elastic constants of cubic single crystals—1338 (L)
Nelson, Herbert. Base-metal effects in thoria-coated filaments —1194 (L)
Nesbitt, E. A. Magnetostriction of permanent magnet alloys —879
Neuber, Ralph E. (see Clark, John W.)—1084
Nielsen, John P. and Walter R. Hibbard, Jr. X-ray study of thermally induced stresses in microconstituents of aluminum-silicon alloys—853
Nielsen, Lawrence E. and Rolf Buchdahl. Mechanical properties of oriented polystyrene film—488
——, **Rolf Buchdahl, and Rita Levreault.** Mechanical and electrical properties of plasticized vinyl chloride compositions—607
—— (see Buchdahl, Rolf)—482
Nolle, A. W. and P. J. Westervelt. Resonant bar method for determining the elastic properties of thin lamina—304
North, P. P. (see Frevel, L. K.)—1038
Nowak, R. C. (see Vigness, Irwin)—445

O'Connor, D. T. (see Criscuolo, E. L.)—1196 (L)
Ōkubo, H. Endurance limit of a round bar with longitudinal grooves—1105
Oriani, R. A. Local order in solid Cu_3Au—1068 (L)
Ostroski, A. S. and R. B. Stambaugh. Emulsion polymerization with ultrasonic vibration—478

Page, R. S. (see Haine, M. E.)—173
Pai, S. I. (see Bershader, D.)—616 (L)
Papas, Charles H. Diffraction by a cylindrical obstacle—318
Penner, S. S. Emission of radiation from diatomic gases. I. Approximate calculations—685
—— (see Benitez, L. E.)—907
Penrod, E. B. Measurement of the thermal diffusivity of a soil by the use of a heat pump—425
Pierce, J. R. Stability of electron flow in the presence of positive ions—1063 (L)
Pipes, Louis A. Summation of Fourier series by operational methods—298
Plesset, M. S. (see Gilmore, F. R.)—243
Plumlee, R. H. and L. P. Smith. Mass spectrometric study of solids. I. Preliminary study of sublimation characteristics of oxide cathode materials—811
Preston, F. W. Erratum: Mechanical properties of glass—1195
Preuss, Luther E. and John H. L. Watson. Technique for taking motion pictures of electron microscope images—902
—— (see Watson, John H. L.)—904
Prince, Edward. Resolving power of an x-ray microscope—698

Quinn, H. F., W. B. McKay, and O. J. Bourque. Kerr cell camera and flash illumination unit for ballistic photography —995

Ragazzini, John R. (see Zadeh, Lotfi A.)—645
Raymond, Richard C. (see Murphy, James A.)—1064 (L)
Read, Harold J. (see Weil, Rolf)—1068 (L)
Read, W. T. Optical method for measuring the stress in glass bulbs—250
Read, W. T., Jr. Stress analysis for compressible viscoelastic materials—671
Reiner, M. and G. W. Scott Blair. Original authorship of formulas given in Clark and Deutsch's paper—1195 (L)
Reisner, John H. and Edmund G. Dornfeld. Small electron microscope—1131
Reissner E. (see Clark, R. A.)—1340 (L)
Reverdin, D. L. (see Marton, L.)—617 (L), 842
Rhodes, D. R. Theory of axially slitted circular and elliptic cylinder antennas—1181
Rhodin, T. N., Jr. Single crystal copper surfaces —971
Richtmyer, R. D. (see Von Neumann, J.)—232
Ridenour, Louis N. High speed digital computers—263
Riehl, Herbert. Model of hurricane formation—917
Ritland, H. N., P. Kaesberg, and W. W. Beeman. Double crystal and slit methods in small angle x-ray scattering—838
Robertson, J. M. (see Ross, Donald)—557
Rogell, Paul S. Modulation conversion in a wave guide—629
Rogers, F. T., Jr. (see Rogers, Marguerite M.)—60 (L)
—— **and H. L. Morrison.** Convection currents in porous media. III. Extended theory of the critical gradient—1177
Rogers, Marguerite M. and F. T., Jr. Energy partition in isothermal fracture—60 (L)
Rogers, T. F. and S. J. Johnson. Some magnetoacoustic effects in nickel—1067 (L)
Rosenholtz, Joseph L. and Dudley T. Smith. Effect of compressive stresses on the linear thermal expansion of magnesium and steel—396
Ross, Donald and J. M. Robertson. Shear stress in a turbulent boundary layer—557
Rydbeck, Olof E. H. Magneto ionic triple splitting of ionospheric waves—1205

Sachs, R. G. and D. L. Dexter. Quantum limits of the electrostatic image force theory—1304
Saenz, A. W. Determination of residual stresses of quenching origin in solid and concentric hollow cylinders from interferometric observations—962
Sauer, J. A. (see Hsiao, C. C.)—1071
Saunders, William K. (see Silver, Samuel)—153, 745
Sawyer, W. M. (see Ferry, John D.)—513
Scheer, Milton D. (see Evans, Marjorie W.)—44
Schlitt, Helmut. Reply to J. A. Haringx—258
Schoen, Louis J. (see Evans, Marjorie W.)—44
Schorr, Marvin G. and Fred J. Beck. Electromagnetic field of the conical horn—795
Schulz, L. G. Examination of thin overgrowths by multiple scattering of electrons—942 (L)
Schwarz, Ralph J. (see Miller, Kenneth S.)—290
Schweitzer, P. H. and V. G. Szebehely. Gas evolution in liquids and cavitation—1218
Scott, G. D., T. A. McLauchlan, and R. S. Sennett. Thickness measurement of thin films by multiple beam interferometry —843
Sears, G. W. Absolute measurement of copper-copper interfacial free energy—721 (L)
Sears, W. R. Transonic potential flow of a compressible fluid—771; Erratum—1340
Sennett, R. S. (see Scott, G. D.)—843
Shank, M. E. (see Agnor, T. J.)—939 (L)
Shankland, R. S. Book review—186
Shaw, Milton C. Quantized theory of strain hardening as applied to the cutting of metals—599
Shaw, Milton C. and Charles D. Strang, Jr. Metal transfer in the cutting process—349 (L)
Shaw, T. M. and J. J. Windle. Microwave techniques for the measurement of the dielectric constant of fibers and films of high polymers—956
Shortley, George. (see Flanders, Donald A.)—1326
Sidhu, S. S. and C. O. Henry. Allotropy of beryllium—1036
Silver, Samuel and William K. Saunders. External field produced by a slot in an infinite circular cylinder—153
—— **and William K. Saunders.** Radiation from a transverse rectangular slot in a circular cylinder—745
Silverman, S. J. (see Bachman, C. H.)—615 (L)
Simmons, L. M. (see Bosson, G.)—1267
Simons, J. H. (see Wilson, W.A.)—203
Sinclair, David. Bending method for measurement of the tensile strength and Young's modulus of glass fibers—380
Singer, Joseph and F. H. Ellinger. Single crystal x-ray techniques for use with alloys requiring protective atmospheres —467 (L)
Sköldborne, Holger. Light energy and spectral distribution for some important x-ray screens—546
Smith, Charles S. (see Neighbours, J. R.)—1338 (L)
Smith, Dudley T. (see Rosenholtz, Joseph L.)—396
Smith, L. P. (see Plumlee, R. H.)—811
Smith, P. D. P. Artificial field equations for a region where μ and ϵ vary with position—1140
Smith, R. N. (see Johnson, V. A.)—283
Sonders, L. R., D. P. Enright, and W. A. Weyl. Wettability, a function of the polarizability of the surface ions—338
Spence, R. D. (see Leitner, A.)—1001
Spencer, R. S. and G. D. Gilmore. Equation of state for high polymers—523
——, **G. D. Gilmore, and R. M. Wiley.** Behavior of granulated polymers under pressure—527
Sperry, Philip R. (see Beck, Paul A.)—150, 420
Stambaugh, R. B. (see Ostroski, A. S.)—478
Steinberg, Richard K. Hot-cathode arcs in cesium vapor—1028
Steiner, Waldo A. (see Weller, Sol)—279, 1340
Sterne, Theodore E. Note on collapsing cylindrical shells—73
Stevens, Victor I. Hypersonic research facilities at the Ames Aeronautical Laboratory—1150
Stout, Thomas M. Note on control area—1129
Straiton, A. W. and A. H. LaGrone. Microwave angle separation on a two and one-half mile overwater path—188
—— **and H. LaGrone.** Determination of modified index-of-refraction over the Gulf of Mexico from radio data—661
Strang, Charles D., Jr. (see Shaw, Milton C.)—349 (L)
Straumanis, M. E. Thermal expansion coefficient and the melting point of cubic elements—936 (L)
Stuart, D. A. (see Hodgdon, F. B.)—1156, 1160
Sullivan, A. M. (see Kies, J. A.)—716
Szebehely, V. G. (see Schweitzer, P. H.)—1218

Taub, A. H. and Nelson Wax. Theory of the parallel plane diode—974
Teichmann, T. Beam oscillations in an f-m cyclotron—1251
Thaler, W. J. (see Fitzpatrick, J. A.)—1269
Thiem, John R. (see Kraus, Gerard)—1065 (L)
Thomson, William T. Equivalent circuit for the transmission of plane elastic waves through a plate at oblique incidence—1215
—— Transmission of elastic waves through a stratified solid medium—89
Thurman, G. R. (see Conant, F. S.)—184
Tomiyasu, K. Unbalanced terminations on a shielded-pair line—552
Trilling, Leon. Impact of a body on a water surface at an arbitrary angle—161

Trump, J. G., K. A. Wright, and A. M. Clarke. Distribution of ionization in materials irradiated by two and three million-volt cathode rays—345
Turnbull, D. Formation of crystal nuclei in liquid metals—1022
—— **and R. E. Cech.** Microscopic observation of the solidification of small metal droplets—804
Tyndall, E. P. T. Creep-time law for zinc crystals—939 (L)

Urquhart, Helen M. A. (see Dekker, A. J.)—708

van der Ziel, A. Thermal noise at high frequencies—399
Vigness, Irwin and R. C. Nowak. Streak photography—445
Villars, D. S. Ultra speed tensile of rubber and synthetic elastomers—565
Vink, H. J. (see Loosjes, R.)—350 (L)
von Karman, Theodore and Pol Duwez. Propagation of plastic deformation in solids—987
Von Neumann, J. and R. D. Richtmyer. Method for the numerical calculation of hydrodynamic shocks—232

Wachtman, J. B., Jr. Negligible changes produced in the stress-strain curve by immersion of a copper single crystal in mercury—943 (L)
Wang, An and Way Dong Woo. Static magnetic storage and delay line—49
Warren, B. E. (see Averbach, B. L.)—185
—— **and B. L. Averbach.** Effect of cold-work distortion on x-ray patterns—595
—— (see Chipman, D.)—696
Waters, W. E. (see Young, R. T., Jr.)—1066 (L)
Watson, John H. L. (see Preuss, Luther E.)—902
—— **and Luther E. Preuss.** Motion picture studies of electron bombardment of colloidal crystals—904
Watson, R. B. and C. W. Horton. On the diffraction of a radar wave by a conducting wedge—802
—— (see Horton, C. W.)—16
Wax, Nelson. (see Taub, A. H.)—974
Weber, A. H. (see Heller, R. B.)—1283
Wehner, Gottfried. Plasma oscillator—62 (L)
Weil, Rolf and Harold J. Read. Electron-microradiography of electrodeposited metals—1068 (L)
Weinreich, O. A. Emissivity changes of thoria cathodes—1272
Weissler, Alfred. Depolymerization by ultrasonic irradiation: the role of cavitation—171
Weller, Sol and Waldo A. Steiner. Separation of gases by fractional permeation through membranes—279; Erratum—1340
Wert, C. and C. Zener. Interference of growing spherical precipitate particles—5
Wert, C. A. Measurements on the diffusion of interstitial atoms in B. C. C. lattices—1196 (L)
Westervelt, P. J. (see Nolle, A. W.)—304
Weyl, W. A. (see Sonders, L. R.)—338
—— (see Marboe, Evelyn C.)—937 (L)
Whinnery, J. R. Effect of input configuration on antenna impedance—945
White, G. N., Jr. and D. C. Drucker. Effective stress and effective strain in relation to stress theories of plasticity—1013
White, J. E. X-ray diffraction by elastically deformed crystals—855
White, M. G. (see Gugelot, P. C.)—369
Widell, E. G. and R. A. Hellar. Effect of coating composition of oxide-coated cathodes on electron emission—1115
Wiley, R. M. (see Spencer, R. S.)—527
Wilkinson, P. G. and L. S. Birks. Particle size of evaporated gold—60 (L)
Willenbrock, F. K. and S. P. Cooke. Interaction of a spiral electron beam and a resonant microwave cavity—114
Williams, I. K. (see Gilvarry, J. J.)—753
Williams, Robley C. (see Backus, Robert C.)—11
Wilson, L. H. and A. J. Miles. Application of the membrane analogy to the solution of heat-conduction problems—532
Wilson, W. A., J. H. Simons, and T. J. Brice. Dielectric strength of gaseous fluorocarbons—203
Windle, J. J. (see Shaw, T. M.)—956
Woo, Way Dong (see Wang, An)—49
Woodhull, Jean C. (see May, Albert)—1285
Woonton, G. A. Effect of an obstacle in the fresnel field on the distant field of a linear radiator—577
——, **R. B. Borts, and J. A. Carruthers.** I. Indoor measurement of microwave antenna radiation patterns by means of a metal lens—428
Wright, K. A. (see Trump, J. G.)—345

Yamamura, Sakae. Immobility phenomena and reverse driving phenomena of the electric arc—193
Yearian, H. J. D. c. characteristics of silicon and germanium point contact crystal rectifiers. Part I. Experimental—214
—— (see Johnson, V. A.)—283
Yeh, Chai and E. L. Chaffee. High frequency impedance of low pressure gaseous diodes—981
Young, D. R. Electric breakdown in CO_2 from low pressures to the liquid state—222
Young, R. T., Jr., L. W. Holmboe, and W. E. Waters, Jr. Some observations on the back heating of magnetron cathodes—1066 (L)

Zadeh, Lotfi A. Determination of the impulsive response of variable networks—642
—— Circuit analysis of linear varying parameter networks—1171
—— **and John R. Ragazzini.** Extension of Wiener's theory of prediction—645
Zapffe, C. A. and F. K. Landgraf. Tearline patterns in ferrochromium—1197 (L)
Zener, C. (see Wert, C.)—5

Subject Index to Volume 21

References with (L) are to Letters to the Editor.

Aberration-phenomenon in electrostatic lenses. "Kidney effect," E. Bas-Taymaz—1064 (L)
Absolute measurement of copper-copper interfacial free energy, G. W. Sears—721 (L)
Aerodynamically instrumented shock tube, Studies with an, A. Hertzberg and A. Kantrowitz—874
Air temperature modification by vertical transport, Robert G. Fleagle—326
Airfoil theory, linearized supersonic, Reversal theorem of, M. M. Munk—159
Allotropy of beryllium, S. S. Sidhu and C. O. Henry—1036
Alloys, permanent magnet, Magnetostriction of, E. A. Nesbitt—879
Alloys requiring protective atmospheres, Single crystal x-ray techniques for use with, Joseph Singer and F. H. Ellinger—467 (L)
Alternative method for the summation of Fourier series, I. F. Morrison—939 (L)
Aluminum, high purity, Strain induced grain boundary migration in, Paul A. Beck and Philip R. Sperry—150
Aluminum-oxide rectifier, electrolytic, Current-hysteresis of the, A. J. Dekker and Helen M. A. Urquhart—708
Aluminum oxide replicas for electron microscopy produced by a two-step process, G. Hass and M. E. McFarland—435
Analogy between hydraulic jumps in liquids and shock waves in gases, F. R. Gilmore, M. S. Plesset, and H. E. Crossley, Jr.—243
Analysis of intensities obtainable using pinhole and slit collimators in x-ray powder diffraction techniques, Leroy Alexander—779
Analysis of a sampling servo mechanism, Kenneth S. Miller and Ralph J. Schwarz—290
Animal fibers, A non-destructive test for, Harris M. Burte—494
Annealing twins during grain growth, Formation of, R. L. Fullman—1069 (L)
Antenna impedance, Effect of input configuration on, J. R. Whinnery—945
Antenna radiation, Effect of a circular groundplane on, A. Leitner and R. D. Spence—1001
Antennas, axially slitted circular and elliptic cylinder, Theory of, D. R. Rhodes—1181
Antennas, collinear, Theory of, Ronold King—1232
Antennas, Theory of N coupled parallel, Ronold King—94
Apparent size of objects as observed in the electron microscope, Stanley F. and Raymond A. Kern—705
Application of Liouville's approximation to the blind navigation problem, J. J. Gilvarry and S. H. Browne—1195 (L)
Application of the membrane analogy to the solution of heat-conduction problems, L. H. Wilson and A. J. Miles—532
Application of rate-process theory to glass. I. Breaking strength, F. B. Hodgdon, D. A. Stuart, and F. E. Bjorklund—1156
—— II. Viscosity, F. B. Hodgdon and D. A. Stuart—1160
Approximation method for the determination of the elastic constants of cubic single crystals, J. R. Neighbours and Charles S. Smith—1338 (L)
Arc, high pressure, Microwave study of, J. D. Cobine, E. P. Cleary, and W. C. Gray—1264
Arc, Retrograde motion of cathode spot, C. J. Gallagher—768
Argon-mercury discharge, Production of 2537 radiation and the role of metastable atoms in, Carl Kenty—1309
Artificial field equations for a region where μ and ϵ vary with position, P. D. P. Smith—1140
Augmented flames in half-open tubes, Marjorie W. Evans, Milton D. Scheer, Louis J. Schoen, and Emmy L. Miller—44
Automatic control, Thomas M. Stout—1129
Average electron density measurements by low angle x-ray scattering, H. M. Barton, Jr. and R. Brill—783

Ballistic photography, Kerr cell camera and flash illumination for, H. F. Quinn, W. B. McKay, and O. J. Bourque—995
Barium oxide on tungsten cathode interface, Eugene B. Hensley and John H. Affleck—938 (L)
Base-metal effects in thoria-coated filaments, Herbert Nelson—1194 (L)
β-Brass, long range order in, X-ray measurement of, D. Chipman and B. E. Warren—696
Beam of x-rays convergent to a point, X-ray tube producing a, C. H. Bachman and S. J. Silverman—615 (L)
Beam oscillations in an f-m cyclotron, T. Teichmann—1251
Beams, General solution for the bending of, on an elastic foundation of arbitrary continuity, M. Hetényi—55
Bearing, Frictionless, for small angular deflections, J. A. Haringx—258 (L)
—— Helmut Schlitt—258 (L)
Behavior of granulated polymers under pressure, R. S. Spencer, G. D. Gilmore, and R. M. Wiley—527
Bending method for measurement of the tensile strength and Young's modulus of glass fibers, David Sinclair—380
Beryllium, Allotropy of, S. S. Sidhu and C. O. Henry—1036
Bibliography on offshore petroleum developments, E. N. Kemler—185 (L)
Breakdown of gases at microwave frequencies, Effect of magnetic field on, Benjamin Lax, W. P. Allis, and Sanborn C. Brown—1297
British Journal of Physics—187 (editorial)

Cadmium sulfide x-ray detector, Rudolf Frerichs—312
Cathode-ray tubes, Method of reducing deflection defocusing in, R. G. E. Hutter and S. W. Harrison—84
Cathode rays, two and three million-volt, Distribution of ionization in materials irradiated by, J. G. Trump, K. A. Wright, and A. M. Clarke—345
Cathode, Retrograde motion in arc, spot, C. J. Gallagher—768
Cathode temperature in the glow discharge, Role of, Harold Jacobs and Jack Martin—681
Cathodes, oxide-coated, Effect of coating composition of on electron emission, E. G. Widell and R. A. Hellar—1115
Cathodes, Potential distribution in pulsed oxide-coated, and its consequences for the velocity distribution of the emitted electrons, R. Loosjes, H. J. Vink, and C. G. J. Jansen—350 (L)
Cavitation, role of, Depolymerization by ultrasonic irradiation, Alfred Weissler—171
Cavity, resonant microwave, Interaction of a spiral electron beam and a, F. K. Willenbrock and S. P. Cooke—114
Ceramics, High strength, for high temperature use—65
Charge distribution in coarse aerosols as a function of time, W. B. Kunkel—833
Circuit analysis of linear varying parameter networks, Lotfi A. Zadeh—1171
Circular aperture, Diffraction pattern in a, measured in the microwave region, C. L. Andrews—761
Circular cylinder, Radiation from a transverse rectangular slot in a, Samuel Silver and William K. Saunders—745

Cloud-chamber coils, large cross-section, Magnetic field calculations for, H. W. Koch—387
CO_2, Electric breakdown in, from low pressures to the liquid state, D. R. Young—222
Coarse aerosols as a function of time, Charge distribution in, W. B. Kunkel—833
Coefficient of self-diffusion of copper, G. Cohen and G. C. Kuczynski—1339 (L)
Cold-work distortion on x-ray patterns, Effect of, B. E. Warren and B. L. Averbach—595
Collapsing cylindrical shells, Theodore E. Sterne—73
Collimators, pinhole and slit, Analysis of intensities obtainable using, in x-ray powder diffraction techniques, Leroy Alexander—779
Colloidal crystals, Motion picture studies of electron bombardment of, John H. L. Watson and Luther E. Preuss—904
Colloidal suspensions, Semiconductive, with non-linear properties, Hans E. Hollmann—402
Compilation of body wave velocity data for cubic and hexagonal metals, Louis Gold—541
Complex stressing of polyethylene, I. L. Hopkins, W. O. Baker, and J. B. Howard—206
Compressible fluid, Transonic potential flow of, W. R. Sears —771
—— W. R. Sears—1340 (erratum)
Computers, High speed digital, Louis N. Ridenour—263
Concrete mixtures, Shielding qualities of different, P. C. Gugelot and M. G. White—369
Conducting disks, Effective permeability of an array of, Gerald Estrin—667
Conductivity of liquid selenium—200°–500°C, Herbert W. Henkels—725
Conical horn, Electromagnetic field of the, Marvin G. Schorr and Fred J. Beck—795
Control area, Note on, Thomas M. Stout—1129
Convection currents in porous media. III. Extended theory of the critical gradient, F. T. Rogers, Jr. and H. L. Morrison —1177
Copper, Coefficient of self-diffusion of, G. Cohen and G. C. Kuczynski—1339 (L)
Copper-copper interfacial free energy, Absolute measurement of, G. W. Sears—721 (L)
Copper self-diffusion, Activation energy for, John H. Holloman —261 (L)
—— J. H. Dedrick and A. Gerds—261 (L)
Crack propagation, Study of, using high speed motion pictures, Herbert I. Fusfeld and Josephine Carr Feder—261 (L)
Crazing of linear high polymers, C. C. Hsiao and J. A. Sauer —1071
Creep and damping properties of polystyrene, William N. Findley—258 (L)
Creep-time law for zinc crystals, E. P. T. Tyndall—939 (L)
Crossover properties in the electron immersion objective, L. Jacob—966
Crystal nuclei in liquid metals, Formation of, D. Turnbull— 1022
Crystal rectifiers, D. c. characteristics of silicon and germanium point contact. Part I. Experimental, H. J. Yearian— 214
Crystallite size, Determination of, with the x-ray spectrometer, Leroy Alexander and Harold P. Klug—137
CSF_6, Electrical breakdown in, Ronald Geballe and Fred S. Linn—592
Cu_3Au, single crystals of, X-ray measurement of order in, J. M. Cowley—24
Cu_3Au, solid, Local order in, R. A. Oriani—1068 (L)
Cubic elements, Thermal expansion coefficient and the melting point of, M. E. Straumanix—936 (L)
Cubic and hexagonal metals, Compilation of body wave velocity for, Louis Gold—541
Current build-up in a planar diode, Edward H. Gamble—108
Current hysteresis of the electrolytic aluminum-oxide rectifier, A. J. Dekker and Helen M. A. Urquhart—708
Cutting of metals, Quantized theory of strain hardening as applied to, Milton C. Shaw—599
Cutting process, Metal transfer in the, Milton C. Shaw and Charles D. Strang, Jr.—349 (L)
Cyclotron, f-m, Beam oscillations in, T. Teichmann—1251
Cyclotron, M. I. T., Shielding properties of the concrete wall of the, Victor Delano and Clark Goodman—1040
Cylinder, infinite circular, External field produced by a slot in an, Samuel Silver and William K. Saunders—153
Cylindrical obstacle, Diffraction by a, Charles H. Papas—318
Cylindrical shells, Collapsing, Theodore E. Sterne—73

D. c. characteristics of silicon and germanium point contact crystal rectifiers. Part I. Experimental, H. J. Yearian—214
—— Part II. The multicontact theory, V. A. Johnson, R. N. Smith, and H. J. Yearian—283
Deformations and stresses in Bourdon tubes, R. A. Clark and E. Reissner—1340 (L)
Depolymerization by ultrasonic irradiation: the role of cavitation, Alfred Weissler—171
Detection of pulsed signals in noise, Effect of a video filter on the, David Middleton—734
Determination of crystallite size with the x-ray spectrometer, Leroy Alexander and Harold P. Klug—137
Determination of eigenvalues using a generalized Laplace transform, Morris D. Friedman—1333
Determination of elastic constants in single crystals with especial reference to silver chloride, David L. Arenberg— 941 (L)
Determination of impulsive response variable networks, Lotfi A. Zadeh—642
Determination of modified index-of-refraction over the Gulf of Mexico from radio data, A. W. Straiton and H. LaGrone —661
Determination of residual stresses of quenching origin in solid and concentric hollow cylinders from interferometric observations, A. W. Saenz—962
Diameter of tobacco mosaic virus with the electron microscope, Metallic evaporation and the, H. Kahler and B. J. Lloyd, Jr.—699
Diatomic gases, Emission of radiation from. I. Approximate calculations, S. S. Penner—685
Dielectric constant of fibers and films of high polymers, Microwave techniques for the measurement of, T. M. Shaw and J. J. Windle—956
Dielectric constants of five gases at 9400 megacycles per second, James A. Murphy and Richard C. Raymond— 1064 (L)
Dielectric materials, Random noise in, R. F. Boyer—469
Dielectric rods of circular cross section, Radiation patterns of, —$TM_{0,1}$ mode, C. W. Horton, F. C. Karal, and C. M. McKinney—1279
Dielectric strength of gaseous fluorocarbons, W. A. Wilson, J. H. Simons, and T. J. Brice—203
Dielectric surface, Storage of small signals on, John V. Harrington—1048
Diffraction by a cylindrical obstacle, Charles H. Papas—318
Diffraction of electromagnetic wave through a plane screen, J. W. Miles—468 (errata)
Diffraction of electrons by gases, Some effects of nozzle design on, R. B. Harvey, F. A. Keidel, and S. H. Bauer—860
Diffraction of a radar wave by a conducting wedge, R. B. Watson and C. W. Horton—802
Diffraction of radar waves by a semi-infinite conducting screen, C. W. Horton and R. B. Watson—16
Diffraction pattern in a circular aperture measured in the microwave region, C. L. Andrews—761
Diffusional viscosity of a polycrystalline solid, Conyers Herring—437

Dimensional analysis of metal cutting, D. C. Drucker and H. Ekstein—104
Dimensional analysis of metal cutting, standardization and, André Martinot-Lagarde—1197 (L)
Diode, planar, Current build-up in a, Edward H. Gamble—108
Dislocations, Theory of, John L. Bogdanoff—1258
Distant field of a linear radiator, Effect of an obstacle in the Fresnel field on the, G. A. Woonton—577
Distribution in energy of Johnson noise pulses, Ben R. Gossick—847
Distribution of ionization in materials irradiated by two and three million-volt cathode rays, J. G. Trump, K. A. Wright, and A. M. Clarke—345
Distribution of phases in two-phase solids, Leonard D. Jaffe—468 (erratum)
Double crystal and slit methods in small angle x-ray scattering, H. N. Ritland, P. Kaesberg, and W. W. Beeman—838
Dust particles on dispersion into a cloud, Static electrification of, W. B. Kunkel—820
Dynamic characteristics of a low pressure discharge, Techniques for measuring the, Bentley T. Barnes and Stephen Eros—1275

Effect of change of scale on sintering phenomena, Conyers Herring—301
Effect of circular groundplane on antenna radiation, A. Leitner and R. D. Spence—1001
Effect of coating composition of oxide-coated cathodes on electron emission, E. G. Widell and R. A. Hellar—1115
Effect of cold-work distortion on x-ray patterns, B. E. Warren and B. L. Averbach—595
Effect of compressive stresses on the linear thermal expansion of magnesium and steel, Joseph L. Rosenholtz and Dudley T. Smith—396
Effect of input configuration on antenna impedance, J. R. Whinnery—945
Effect of magnetic field on the breakdown of gases at microwave frequencies, Benjamin Lax, W. P. Allis, and Sanborn C. Brown—1297
Effect of obstacle in the Fresnel field on the distant field of a linear radiator, G. A. Woonton—577
Effect of a video filter on the detection of pulsed signals in noise, David Middleton—734
Effective permeability of an array of thin conducting disks, Gerald Estrin—667
Effective permeability of iron dust particles, Leonard Lewin—722 (L)
Effective stress and effective strain in relation to stress theories of plasticity, G. N. White and D. C. Drucker—1013
Effects of nozzle design on the diffraction of electrons by gases, R. B. Harvey, F. A. Keidel, and S. H. Bauer—860
Elastic constants of cubic single crystals, Approximation method for the determination of, J. R. Neighbours and Charles S. Smith—1338 (L)
Elastic waves, Transmission of, through a stratified solid medium, William T. Thomson—89
Elastic waves through a plate at oblique incidence, Equivalent circuit for the transmission of plane, William T. Thomson—1215
Elastically deformed crystals, X-ray diffraction by, J. E. White—855
Elastomers, Equivalent effects of time and temperature in the shear creep and recovery of, F. S. Conant, G. L. Hall, and W. James Lyons—499
Electric arc, Immobility phenomena and reverse driving phenomena of the, Sakae Yamamura—193
Electric breakdown in CO_2 from low pressures to the liquid state, D. R. Young—222
Electric breakdown in CSF_8, Ronald Geballe and Fred S. Linn—592
Electrical conductivity method for measuring self-diffusion of metals, J. H. Dedrick and G. C. Kuczynski—1224
Electrical properties of plasticized vinyl chloride compositions, Mechanical and, Lawrence E. Nielsen, Rolf Buchdahl, and Rita Levreault—607
Electrodeposited metals, Electron-microradiography of, Rolf Weil and Harold J. Read—1068 (L)
Electrolytic aluminum-oxide rectifier, Current-hysteresis of the, A. J. Dekker and Helen M. A. Urquhart—708
Electrolytic-tank measurements for microwave metallic delay-lens media, Seymour B. Cohn—674
Electromagnetic field of the conical horn, Marvin G. Schorr and Fred J. Beck—795
Electromagnetic theory, D. R. Rhodes—1181
Electromagnetic wave, Diffraction of an, through a plane screen, J. W. Miles—468 (errata)
Electromagnetic waves, Reflection and transmission of, by thin curved shells, Joseph B. Keller—896
Electron beam, spiral, Interaction of a, and a resonant microwave cavity, F. K. Willenbrock and S. P. Cooke—114
Electron beams and their reduction by positive ion trapping, Space-charge effects in, E. G. Linder and K. G. Hernqvist—1088
Electron emission, Effect of coating composition of oxide-coated cathodes on, E. G. Widell and R. A. Hellar—1115
Electron immersion objective, Some crossover properties in the, L. Jacob—966
Electron-microradiography of electrodeposited metals, Rolf Weil and Harold J. Read—1068 (L)
Electron microscope images, Technique for taking motion pictures of, Luther E. Preuss and John H. L. Watson—902
Electron microscope lenses, Lapping technique: to improve the image quality of, F. A. Hamm—271
Electron Microscope Society of America, Proceedings of—66
Electron microscope, Three-stage, with stereographic dark field, and electron diffraction capabilities, M. E. Haine, R. S. Page, and R. G. Garfitt—173
Electron microscope, Use of critical point phenomena in preparing specimens for, Thomas F. Anderson—724 (L)
Electron microscopy, Aluminum oxide replicas for, produced by a two-step process, G. Hass and M. E. McFarland—435
Electron microscopy, Low temperature replica method for, C. E. Hall—61 (L)
Electron microscopy of wet biological tissues by replica techniques, Irwin W. Fischbein—1199
Electron microscopy, Use of latex spheres as size standards in, Charles H. Gerould—183 (L)
Electron microscopy, Use of spraying methods and of volatile suspending media in the preparation of specimens for, Robert C. Backus and Robley C. Williams—11
Electron optical properties of space-charge clouds, L. Marton and D. L. Reverdin—842
Electronic isograph for roots of polynomials, Byron O. Marshall, Jr.—307
Electrostatic image force theory, Quantum limits of the, R. G. Sachs and D. L. Dexter—1304
Electrostatic lenses, Aberration-phenomenon in. "Kidney effect", E. Bas-Taymaz—1064 (L)
Elements, Work functions of the, Herbert B. Michaelson—536
Emission of radiation from diatomic gases. I. Approximate calculations, S. S. Penner—685
Emission of radiation from nitric oxide: approximate calculations, L. E. Benitez and S. S. Penner—907
Emissivity changes of thoria cathodes, O. A. Weinreich—1272
Emulsion polymerization with ultrasonic vibration, A. S. Ostroski and R. B. Stambaugh—478
End-cooling of power tube filaments, John W. Clark and Ralph E. Neuber—1084

Endurance limit of a round bar with longitudinal grooves, H. Ōkubo—1105
Energy partition in isothermal fracture, Marguerite M. Rogers and F. T. Rogers, Jr.—60 (L)
Epitaxy of sodium chloride on silver, Some observations on, G. W. Johnson—1057
Equation of state for high polymers, R. S. Spencer and G. D. Gilmore—523
Equivalent circuit for the transmission of plane elastic waves through a plate at oblique incidence, William T. Thomson —1215
Equivalent effects of time and temperature in the shear creep and recovery of elastomers, F. S. Conant, G. L. Hall, and W. James Lyons—499
Evaporation and outgassing in an inert atmosphere, R. L. Longini—81
Examination of thin overgrowths by multiple scattering of electrons, L. G. Schulz—942 (L)
Extension of Wiener's theory of prediction, Lotfi A. Zadeh and John R. Ragazzini—645
External field produced by a slot in an infinite circular cylinder, Samuel Silver and William K. Saunders—153

Ferrochromium, Tearline patterns in, C. A. Zapffe and F. K. Landgraf—1197 (L)
Filaments, End losses in, John W. Clark and Ralph E. Neuber —1084
Filaments, thoria-coated, Base-metal effect in, Herbert Nelson —1194 (L)
Flames, Augmented, in half-open tubes, Marjorie W. Evans, Milton D. Scheer, Louis J. Schoen, and Emmy L. Miller —44
Flow, conical, Interferometric test for, J. H. Giese, F. D. Bennett, and V. E. Bergdolt—1226
Fracture markings, Interpretation of, J. A. Kies, A. M. Sullivan, and G. R. Irwin—716
Fracture modes in high purity metals, T. J. Agnor and M. E. Shank—939 (L)
Frederickson-Eyring theory of the mechanical behavior of metals, J. Fleeman and G. J. Dienes—1193 (L)
Fluorocarbons, gaseous, Dielectric strength of, W. A. Wilson, J. H. Simons, and T. J. Brice—203
Formation of annealing twins during grain growth, R. L. Fullman—1069 (L)
Formation of crystal nuclei in liquid metals, D. Turnbull— 1022
Formulas given in Clark and Deutsch's paper, Original authorship of, M. Reiner and G. W. Scott Blair—1195 (L)
Fourier series, Summation of, by operational methods, Louis A. Pipes—298
Frequency factor and activation energy for the volume diffusion of metals, G. J. Dienes—1189
Frictional loss in visco-elastic substances, B. Gross—185 (L)
Frictionless bearing for small angular deflections, J. A. Haringx—258 (L)
—— Helmut Schlitt—258 (L)
Fundamental modes, Numerical determination of, Donald A. Flanders and George Shortley—1326

Gas discharge, microwave, Effect of magnetic field on, Benjamin Lax, W. P. Allis, and Sanborn C. Brown—1297
Gas evolution in liquids and cavitation, P. H. Schweitzer and V. G. Szebehely—1218
Gaseous diodes, low pressure, High frequency impedance of, Chai Yeh and E. L. Chaffee—981
Gasses, Separation of, by fractional permeation through membranes, Sol Weller and Waldo A. Steiner—279
—— Sol Weller and Waldo A. Steiner—1340 (erratum)
Gases, Vibrational relaxation times in, Wayland Griffith—1319
General solution for the bending of beams on an elastic foundation of arbitrary continuity, M. Hetényi—55
Generalized microscopy and the two-wave-length microscope, M. J. Buerger—909
Generalized response of linear systems for arbitrary initial conditions, John R. Moore—933
Geometrical factors affecting the contours of x-ray spectrometer maxima. II. Factors causing broadening, Leroy Alexander—126
Glass, Application of rate-process theory to. I. Breaking strength, F. B. Hodgdon, D. A. Stuart, and F. E. Bjorklund —1156
Glass bulbs, Optical method for measuring the stress in, W. T. Read—250
Glass fibers, Bending method for measurement of the tensile strength and Young's modulus of, David Sinclair—380
Glass, Mechanical properties of, F. W. Preston—1195 (erratum)
Gold, evaporated, Particle size of, P. G. Wilkinson and L. S Birks—60 (L)
Gough-Joule coefficients, Relationship between, and moduli of vulcanized rubbers, F. S. Conant, G. L. Hall, and G. R. Thurman—184 (erratum)
Grain boundary migration, Orientation dependence of the rate of, Paul A. Beck, Philip R. Sperry, and Hsun Hu—420
Grain boundary migration, Strain induced, in high purity aluminum, Paul A. Beck and Philip R. Sperry—150
Graphical analysis of the interference patterns of an elevated ultra-high frequency antenna under conditions of atmospheric stratification, F. R. Abbott and C. J. Fisher—636
Graphical representation of particle trajectories in a moving reference system, M. Garbuny—1054
Greenockite (cadmium sulfide), Natural crystal, as an x-ray detector, E. L. Criscuolo and D. T. O'Connor—1196 (L)
Growth of metallic crystals from the vapor phase, George R. Keepin, Jr.—260 (L)

Heat pump, Measurement of the thermal diffusivity of a soil by the use of a, E. B. Penrod—425
High frequency impedance of low pressure gaseous diodes, Chai Yeh and E. L. Chaffee—981
High intensity short duration spark light source, J. A. Fitzpatrick, J. C. Hubbard, and W. J. Thaler—1269
High polymers, Equation of state for, R. S. Spencer and G. D. Gilmore—523
High speed digital computers, Louis N. Ridenour—263
High strength ceramics for high temperature use—65
High temperatures, Specific heats of MgO, TiO_2, and ZrO_2 at, James S. Arthur—732
Hot-cathode arcs in cesium vapor, Richard K. Steinberg— 1028
Hurricane formation, Model of, Herbert Riehl—917
Hydraulic jumps in liquids and shock waves in gases, Analogy between, F. R. Gilmore, M. S. Plesset, and H. E. Crossley, Jr.—243
Hydrodynamic shocks, Method for the numerical calculation of, J. Von Neumann and R. D. Richtmyer—232
Hypersonic and unsteady flow research at the Langley Aeronautical Laboratory, Results of recent, John V. Becker— 619
Hypersonic research facilities at the Ames Aeronautical Laboratory, Victor I. Stevens—1150
Hysteresis loops, asymmetrical, Tracing and interpretation of, G. M. Ettinger—936 (L)

Immobility phenomena and reverse driving phenomena of the electric arc, Sakae Yamamura—193
Impact of a body on a water surface at an arbitrary angle, Leon Trilling—161
Improved ultra-thin sectioning of tissue for electron microscopy, James Hillier and Mark E. Gettner—889

Indoor measurement of microwave antenna radiation patterns by means of a metal lens, G. A. Woonton, R. B. Borts, and J. A. Carruthers—428
Integrating crystal detectors for high energy photons and particles, R. S. Alger—30
Intensity correction factors for x-ray spectrometer transmission pole figure determinations, Suzanne Van Dijke Beatty —940 (L)
Interaction of a spiral electron beam and a resonant microwave cavity, F. K. Willenbrock and S. P. Cooke—114
Interference of growing spherical precipitate particles, C. Wert and C. Zener—5
Interference of growing spherical precipitate particles, Hershel Markovitz—1198 (L)
Interference patterns of an elevated ultra-high frequency antenna under conditions of atmospheric stratification, Graphical analysis of the, F. R. Abbott and C. J. Fisher —636
Interferometric test for conical flow, J. H. Giese, F. D. Bennett, and V. E. Bergdolt—1226
Internal friction of metals at very high temperatures, T'ing-Sui Kê—414
Interpretation of fracture markings, J. A. Kies, A. M. Sullivan, and G. R. Irwin—716
Interpretation of x-ray patterns of cold-worked metal, B. L. Averbach and B. E. Warren—185 (addendum)
Interstitial atoms in B. C. C. lattices, Measurements on the diffusion of, C. A. Wert—1196 (L)
Ionized gas, Techniques for measuring the characteristics of, Bentley T. Barnes and Stephen Eros—1275
Ionospheric waves, Magneto ionic triple splitting of, Olof E. H. Rydbeck—1205
Ions, positive, Stability of electron flow in the presence of, J. R. Pierce—1063 (L)
Iron dust particles, Effective permeability of, Leonard Lewin —722 (L)
Isothermal fracture, Energy partition in, Marguerite M. Rogers and F. T. Rogers, Jr.—60 (L)

Johnson noise pulses, Distribution in energy of, Ben R. Gossick—847

Kerr cell camera and flash illumination unit for ballistic photography, H. F. Quinn, W. B. McKay, and O. J. Bourque—995

Lamina, thin, Resonant bar method for determining the elastic properties of, A. W. Nolle and P. J. Westervelt—304
Laminar propane flames as a function of pressure, temperature, and air-fuel ration, Wall-quenching of, Raymond Friedman and W. C. Johnston—791
Laplace transform, generalized, Determination of eigenvalues using a, Morris D. Friedman— 1333
Lapping technique: to improve the image quality of electron microscope lenses, F. A. Hamm—271
Latex spheres, Use of, as size standards in electron microscopy Charles H. Gerould—183 (L)
Lattice constants of zinc oxide, Precision determination of, R. B. Heller, J. McGannon, and A. H. Weber—1283
Lenses, electrostatic, Aberration-phenomenon in. "Kidney effect," E. Bas-Taymaz—1064 (L)
Light energy and spectral distribution for some important x-ray screens, Holger Sköldborne—546
Light source, A high intensity short duration spark, J. A. Fitzpatrick, J. C. Hubbard, and W. J. Thaler—1269
Limiting hydrostatic tension of water near O°C, J. C. Fisher —1068 (L)
Limiting negative pressure of water, Lyman J. Briggs—721 (L)
Linear high polymers, Crazing of, C. C. Hsiao and J. A. Sauer —1071
Linear systems for arbitrary initial conditions, Generalized response of, John R. Moore—933
Linear systems, Response characteristics of, Marcello Cini—8
Liouville's approximation to the blind navigation problem, Application of, J. J. Gilvarry and S. H. Browne—1195 (L)
Liquid selenium—200°–500°C, Conductivity of, Herbert W. Henkels—725
Liquids and cavitation, Gas evolution in, P. H. Schweitzer and V. G. Szebehely—1218
Load induced x-ray line broadening in Nylon filaments, John Kauffman and Waller George—431
Local order in solid Cu_3Au, R. A. Oriani—1068 (L)
Low pressure discharge, dynamic characteristic of, Techniques for measuring, Bentley T. Barnes and Stephen Eros —1275
Low temperature replica method for electron microscopy, C. E. Hall—61 (L)

Magnesium and steel, Effect of compressive stresses on the linear thermal expansion of, Joseph L. Rosenholtz and Dudley T. Smith—396
Magnet coil windings, Steady-state internal temperature rise in, Claude L. Emmerich—75
Magnetic field calculations for large cross-section cloud-chamber coils, H. W. Koch—387
Magnetic field of a plane circular loop, C. L. Bartberger—1108
Magnetically controlled wave-guide attenuators, Theodore Miller—722 (L)
Magneto-acoustic effects in nickel, T. F. Rogers and S. J. Johnson—1067 (L)
Magneto ionic triple splitting of ionospheric waves, Olof E. H. Rydbeck—1205
Magnetostriction of permanent magnet alloys, E. A. Nesbitt —879
Magnetron cathodes, Some observations on the back heating of, R. T. Young, Jr., L. W. Holmboe, and W. E. Walters, Jr.—1066 (L)
Magnification range of an electron microscope, Removable intermediate lens for extending the, J. Hillier—785
Mass spectrometric study of solids. I. Preliminary study of sublimation characteristics of oxide cathode materials, R. H. Plumlee and L. P. Smith—811
Measurement of self-diffusion of silver without radioactive tracers, G. C. Kuczynski—632
Measurement of surface temperature of evaporating water drops, John C. Johnson—22
Measurement of the thermal diffusivity of a soil by the use of a heat pump, E. B. Penrod—425
Measurements of mechanical properties of polyisobutylene at audiofrequencies by a twin transducer, Robert S. Marvin, Edwin R. Fitzgerald, and John D. Ferry—197
Measurements on the diffusion of interstitial atoms in B. C. C. lattices, C. A. Wert—1196 (L)
Measuring self-diffusion of metals, Electrical conductivity method for, J. H. Dedrick and G. C. Kuczynski—1224
Mechanical and electrical properties of plasticized vinyl chloride compositions, Lawrence E. Nielsen, Rolf Buchdahl, and Rita Levreault—607
Mechanical properties of glass, F. W. Preston—1195 (erratum)
Mechanical properties of oriented polystyrene film, Lawrence E. Nielsen and Rolf Buchdahl—488
Mechanical properties of substances of high molecular weight. III. Dispersion of dynamic rigidity and viscosity in concentrated polyvinyl acetate solutions, John D. Ferry, W. M. Sawyer, George V. Browning, and Arthur H. Groth, Jr.—513

Mechanical test for animal fibers, Non-destructive, Harris M. Burte—494
Mechano chemistry of the dispersion of mercury in liquids in an ultrasonic field, Evelyn C. Marboe and W. A. Weyl—937 (L)
Membrane analogy, Application of the, to the solution of heat-conduction problems, L. H. Wilson and A. J. Miles—532
Mercury in liquids in an ultrasonic field, Mechano chemistry of the dispersion of, Evelyn C. Marboe and W. A. Weyl—937 (L)
Metal, cold-worked, Interpretation of x-ray patterns of, B. L. Averbach and B. E. Warren—185 (addendum)
Metal cutting, Dimensional analysis of, D. C. Drucker and H. Ekstein—104
Metal transfer in the cutting process, Milton C. Shaw and Charles D. Strang, Jr.—349 (L)
Metallic crystals, Growth of, from the vapor phase, George R. Keepin, Jr.—260 (L)
Metallic evaporation and the diameter of tobacco mosaic virus with the electron microscope, H. Kahler and B. J. Lloyd, Jr.—699
Metals, Frederickson-Eyring theory of the mechanical behavior of, J. Fleeman and G. J. Dienes—1193 (L)
Metals, Internal friction of, at very high temperatures, T'ing-Sui Kê—414
Metals, refractory, Thermocouples of the, F. Haydn Morgan and W. E. Danforth—112
Metals, self-diffusion of, Electrical conductivity method for measuring, J. H. Dedrick and G. C. Kuczynski—1224
Metastable atoms in an argon-mercury discharge, Production of 2537 radiation and the role of, Carl Kenty—1309
Method for the numerical calculation of hydrodynamic shocks, J. Von Neumann and R. D. Richtmyer—232
Method of reducing deflection defocusing in cathode-ray tubes, R. G. E. Hutter and S. W. Harrison—84
Microscope, electron, Small, John H. Reisner and Edmund G. Dornfeld—1131
Microscopic observation of the solidification of small metal droplets, D. Turnbull and R. E. Cech—804
Microwave angle separation on a two and one-half mile over-water path, A. W. Straiton and A. H. LaGrone—188
Microwave antenna radiation patterns, Indoor measurement of, by means of a metal lens, G. A. Woonton, R. B. Borts, and J. A. Carruthers—428
Microwave frequency dividers, Harold Lyons—59 (L)
Microwave metallic delay-lens media, Electrolytic-tank measurements for, Seymour B. Cohn—674
Microwave region, Diffraction pattern in a circular aperture measured in the, C. L. Andrews—761
Microwave study of the high pressure arc, J. D. Cobine, E. P. Cleary, and W. C. Gray—1264
Microwave techniques for the measurement of the dielectric constant of fibers and films of high polymers, T. M. Shaw and J. J. Windle—956
Missiles, entering water at supersonic speeds, shadowgrams of, J. H. McMillen, R. L. Kramer, and D. E. Allmand—1341 (L)
Mode conversion losses in transmission of circular electric waves through slightly non-cylindrical guides, Samuel P. Morgan, Jr.—329
Model of hurricane formation, Herbert Riehl—917
Modern arms and free men, book by Vannevar Bush, review—186
Modification of the radiofrequency mass spectrometer, A. F. Henson—1063 (L)
Modulation conversion in a wave guide, Paul S. Rogell—629
Molecular vibrations, Wayland Griffith—1319
Motion picture studies of electron bombardment of colloidal crystals, John H. L. Watson and Luther E. Preuss—904
Motion pictures, Study of crack propagation using high speed, Herbert I. Fusfeld and Josephine Carr Feder—261 (L)
Natural crystal Greenockite (cadmium sulfide) as an x-ray detector, E. L. Criscuolo and D. T. O'Connor—1196 (L)
Navigation, blind, Liouville's approximation to the problem of, J. J. Gilvarry and S. H. Browne—1195 (L)
Navigation by dynamical measurements, blind, Theory of, J. J. Gilvarry, S. H. Browne, and I. K. Williams—753
Negative wire corona at high temperature and pressure, L. R. Koller and H. A. Fremont—741
Negligible changes produced in the stress-strain curve by immersion of a copper single crystal in mercury, J. B. Wachtman, Jr.—943 (L)
Networks, Circuit analysis of linear varying parameter, Lotfi A. Zadeh—1171
Nickel, Some magneto-acoustic effects in, T. F. Rogers and S. J. Johnson—1067 (L)
Nitric oxide, Emission of radiation from: approximate calculations, L. E. Benitez and S. S. Penner—907
Non-destructive mechanical test for animal fibers, Harris M. Burte—494
Non-linear systems permitting simple harmonic motion, John E. Brock—238
Non-Newtonian liquids, Scheme for analyzing capillary measurements on, Orrin H. Clark and M. L. Deutsch—713
Note on the error coefficients of a servo mechanism, John L. Bower—723 (L)
Nuclei of strain in the semi-infinite solid, Raymond D. Mindlin and David H. Cheng—926
Numerical determination of fundamental modes, Donald A. Flanders and George Shortley—1326
Nylon filaments, Load induced x-ray line broadening in, John Kauffman and Waller George—431

Objects as observed in the electron microscope, Apparent size of, Stanley F. and Raymond A. Kern—705
Observations on the back heating of magnetron cathodes, R. T. Young, Jr., L. W. Holmboe, and W. E. Waters, Jr.—1066 (L)
Observations on the epitaxy of sodium chloride on silver, G. W. Johnson—1057
Optical method for measuring the stress in glass bulbs, W. T. Read—250
Orientation dependence of the rate of grain boundary migration, Paul A. Beck, Philip R. Sperry, and Hsun Hu—420
Oriented polystyrene film, Mechanical properties of, Lawrence E. Nielsen and Rolf Buchdahl—488
Original authorship of formulas given in Clark and Deutsch's paper, M. Reiner and G. W. Scott Blair—1195 (L)
Oscillations, Beam, in an f-m cyclotron, T. Teichmann—1251
Outgassing, Evaporation and, in an inert atmosphere, R. L. Longini—81
Oxide cathodes, Thermionic emission from: retarding and accelerating fields, C. S. Hung—37
Oxide cathodes, with mutually bombarding, Vacuum tubes, E. G. Hopkins—841

Parallel plane diode, Theory of the, A. H. Taub and Nelson Wax—974
Particle size of evaporated gold, P. G. Wilkinson and L. S. Birks—60 (L)
Particles, growing spherical precipitate, Interference of, Hershel Markovitz—1198 (L)
Petroleum developments, offshore, Bibliography on, E. N. Kemler—185 (L)
Phases, Distribution of, in two-phase solids, Leonard D. Jaffe—468 (erratum)
Photography, Streak, Irwin Vigness and R. C. Nowak—445
Photons and particles, high energy, Integrating crystal detectors for, R. S. Alger—30
Plane circular loop, Magnetic field of, C. L. Bartberger—1108
Plasma oscillator, Gottfried Wehner—62 (L)

Plastic deformation in solids, Propagation of, Theodore von Karman and Pol Duwez—987
Plastic flow of platinum wires, R. P. Carreker, Jr.—1289
Plasticized vinyl chloride compositions, Mechanical and electrical, Lawrence E. Nielsen, Rolf Buchdahl, and Rita Levreault—607
Plastics, Variation of elastic moduli and wave velocity with pressure and temperature in, D. S. Hughes, E. B. Blankenship, and R. L. Mims—294
Platinum wires, Plastic flow of, R. P. Carreker, Jr.—1289
Polycrystalline solid, Diffusional viscosity of a, Conyers Herring—437
Polyethylene, Complex stressing of, I. L. Hopkins, W. O. Baker, and J. B. Howard—206
Polyisobutylene, Measurements of mechanical properties of, at audiofrequencies by a twin transducer, Robert S. Marvin, Edwin R. Fitzgerald, and John D. Ferry—197
Polymers under pressure, Behavior of granulated, R. S. Spencer, G. D. Gilmore, and R. M. Wiley—527
Polynomials, Electronic isograph for roots of, Byron O. Marshall, Jr.—307
Polystyrene, Creep and damping properties of, William N. Findley—258 (L)
Polyvinyl chloride, Studies in plasticization of. I. Physical changes and their measurement, M. L. Dannis—505
—— II. Plasticizer variations in PVC-plasticizer systems, M. L. Dannis—510
Porous media, Convention currents in. III. Extended theory of the critical gradient, F. T. Rogers, Jr. and H. L. Morrison—1177
Potential distribution in pulsed oxide-coated cathodes and its consequences for the velocity distribution of the emitted electrons, R. Loosjes, H. J. Vink, and C. G. J. Jansen—350 (L)
Potential flow into circumferential openings in drain tubes, Don Kirkham—655
Powder diffraction, Single wave-length x-rays for, L. K. Frevel and P. P. North—1038
Precipitate particles, growing spherical, Interference of, C. Wert and C. Zener—5
Precision determination of the lattice constants of zinc oxide, R. B. Heller, J. McGannon, and A. H. Weber—1283
Proceedings of the Electron Microscope Society of America—66
Production of 2537 radiation and the role of metastable atoms in an argon-mercury discharge, Carl Kenty—1309
Propagation of plastic deformation in solids, Theodore von Karman and Pol Duwez—987
Propagation of TM_{01} mode in a metal tube containing an imperfect dielectric, David Hettrick—561
Pursuit course, Ralph Hoyt Bacon—1065 (L)

Quantized theory of strain hardening as applied to the cutting of metals, Milton C. Shaw—599
Quantum limits of the electrostatic image force theory, R. G. Sachs and D. L. Dexter—1304

Radar wave, Diffraction of, by a conducting wedge, R. B. Watson and C. W. Horton—802
Radar waves, Diffraction of, by a semi-infinite conducting screen, C. W. Horton and R. B. Watson—16
Radiation from a transverse rectangular slot in a circular cylinder, Samuel Silver and William K. Saunders—745
Radiation patterns of dielectric rods of circular cross section—$TM_{0,1}$ mode, C. W. Horton, F. C. Karal, Jr., and C. M. McKinney—1279
Radio meteorology over the Gulf of Mexico, A. W. Straiton and H. LaGrone—661
Radiofrequency mass spectrometer, Willard H. Bennett—143
—— Willard H. Bennett—723 (erratum)
Radiofrequency mass spectrometer, Modification of, A. F. Henson—1063 (L)
Random noise in dielectric materials, R. F. Boyer—469
Rate-process theory, Application to glass. I. Breaking strength, F. B. Hodgdon, D. A. Stuart, and F. E. Bjorklund—1156
—— II. Viscosity, F. B. Hodgdon and D. A. Stuart—1160
Recognition of pseudoplastics from their flow curves, Use of Reiner's equation for, Vera Osman Krakauer—850
Reflection and transmission of electromagnetic waves by thin curved shells, Joseph B. Keller—896
Relations concerning wave fronts and reflectors, K. S. Kelleher—573
Relationship between Gough-Joule coefficients and moduli of vulcanized rubbers, F. S. Conant, G. L. Hall, and G. R. Thurman—184 (erratum)
—— M. Mooney—1338 (L)
Relationship between resistance and temperature of thermistors, G. Bosson, F. Gutman, and L. M. Simmons—1267
Removable intermediate lens for extending the magnification range of an electron microscope, J. Hillier—785
Resistance and temperature of thermistors, Relationship between, G. Bosson, F. Gutman, and L. M. Simmons—1267
Resolving power of an x-ray microscope, Edward Prince—698
Resonant bar method for determining the elastic properties of thin lamina, A. W. Nolle and P. J. Westervelt—304
Response characteristics of linear systems, Marcello Cini—8
Results of recent hypersonic and unsteady flow research at the Langley Aeronautical Laboratory, John V. Becker—619
Reversal theorem of linearized supersonic airfoil theory, M. M. Munk—159
Richardson plots, Use of brightness temperatures in, Henry F. Ivey—616 (L)
Role of cathode temperature in the glow discharge, Harold Jacobs and Jack Martin—681
Rubber and synthetic elastomers, Ultra speed tensile of, D. S. Villars—565
Rubber, natural, under biaxial strain, Stress-strain properties of, B. B. S. T. Boonstra—1098
Rubbers, vulcanized, Relationship between Gough-Joule coefficients and moduli of, F. S. Conant, G. L. Hall, and G. R. Thurman—184 (erratum)

Scheme for analyzing capillary measurements on non-Newtonian liquids, Orrin H. Clark and M. L. Deutsch—713
—— Orrin H. Clark and M. L. Deutsch—1195 (L)
Second-order transition temperatures and related properties of polystyrene. I. Influence of molecular weight, Thomas G. Fox and Paul J. Flory—581
Sectioning of tissue for electron microscopy, Improved ultrathin, James Hillier and Mark E. Gettner—889
Semiconductive colloidal supensions with non-linear properties, Hans E. Hollmann—402
Separation of gases by fractional permeation through membranes, Sol Weller and Waldo A. Steiner—279
—— Sol Weller and Waldo A. Steiner—1340 (erratum)
Servo mechanism, Note of the error coefficients of, John L. Bower—723 (L)
Servo mechanism, sampling Analysis of a, Kenneth S. Miller and Ralph J. Schwarz—290
Shadowgrams of spherical missiles entering water at supersonic speeds, J. H. McMillen, R. L. Kramer, and D. E. Allmand—1341 (L)
Shear creep and recovery of elastomers, Equivalent effects of time and temperature in the, F. S. Conant, G. L. Hall, and W. James Lyons—499
Shear stress in a turbulent boundary layer, Donald Ross and J. M. Robertson—557
Shielded-pair line, Unbalanced termination on a, K. Tomiyasu—552
Shielding properties of the concrete wall of the M. I. T. cyclotron, Victor Delano and Clark Goodman—1040

Shielding qualities of different concrete mixtures, P. C. Gugelot and M. G. White—369
Shock waves in gases, Analogy between hydraulic jumps in liquids and, F. R. Gilmore, M. S. Plesset, and H. E. Crossley, Jr.—243
Silicon and germanium point contact crystal rectifiers, D. c. characteristics of. Part II. The multicontact theory, V. A. Johnson, R. N. Smith, and H. J. Yearian—283
Silver films, oriented thin, Surface tension effects in, G. W. Johnson—449
Silver without radioactive tracers, Measurement of self-diffusion of, G. C. Kuczynski—632
Simple interferometric test for conical flow, J. H. Giese, F. D. Bennett, and V. E. Bergdolt—1224
Simplified air flow method for the determination of the surface area of powders, Gerard Kraus and John R. Thiem—1065 (L)
Single crystal copper surfaces, T. N. Rhodin, Jr.—971
Single crystal x-ray technique for use with alloys requiring protective atmospheres, Joseph Singer and F. H. Ellinger —467 (L)
Single crystals, with especial reference to silver chloride, Determination of elastic constants in, David L. Arenberg—941 (L)
Single wave-length x-rays for powder diffraction, L. K. Frevel and P. P. North—1038
Sintering phenomena, Effect of change of scale on, Conyers Herring—301
Slot antennas, Samuel Silver and William K. Saunders—745
Small angle x-ray scattering, Double crystal and slit methods in, H. N. Ritland, P. Kaesberg, and W. W. Beeman—838
Small electron microscope, John H. Reisner and Edmund G. Dornfeld—1131
Soil, Measurement of the thermal diffusivity of a, by the use of a heat pump, E. B. Penrod—425
Soils, Thermal conductivity of, Andrew Gemant—750
Solid and concentric hollow cylinders from interferometric observations, Determination of residual stresses of quenching origin in, A. W. Saenz—962
Solid-state and high polymer, Stress phenomena from the respective viewpoints of, Maurice L. Huggins—518
Solidification of small metal droplets, Microscopic observation of, D. Turnbull and R. E. Cech—804
Solids, Mass spectrometric study of. I. Preliminary study of sublimation characteristics of oxide-cathode materials, R. H. Plumlee and L. P. Smith—811
Solution of heat-conduction problems, Application of the membrane analogy to the, L. H. Wilson and A. J. Miles —532
Space-charge clouds, Electron optical properties of, L. Marton and D. L. Reverdin—842
Space-charge effects in electron beams and their reduction by positive ion trapping, E. G. Linder and K. G. Hernqvist —1088
Specific heats of MgO, TiO_2, and ZrO_2 at high temperatures, James S. Arthur—732
Spectral distribution for some important x-ray screens, Light energy and, Holger Sköldborne—546
Spectrometer, Radiofrequency mass, Willard H. Bennett—143
—— Willard H. Bennett—723 (erratum)
—— Modification of, A. F. Henson—1063 (L)
Sphere entering water vertically, Albert May and Jean C. Woodhull—1285
Stability of electron flow in the presence of positive ions, J. R. Pierce—1063 (L)
Standardization and "A Dimensional analysis of metal cutting," André Martinot-Lagarde—1197 (L)
Static electrification of dust particles on dispersion into a cloud, W. B. Kunkel—820
Static magnetic storage and delay line, An Wang and Way Dong Woo—49
Steady-state internal temperature rise in magnet coil windings, Claude L. Emmerich—75
Steel, Effect of compressive stresses on the linear thermal expansion of magnesium and, Joseph L. Rosenholtz and Dudley T. Smith—396
Storage of small signals on a dielectric surface, John V. Harrington—1048
Strain hardening as applied to the cutting of metals, Quantized theory of, Milton C. Shaw—599
Strain induced grain boundary migration in high purity aluminum, Paul A. Beck and Philip R. Sperry—150
Strain in the semi-infinite solid, Nuclei of, Raymond D. Mindlin and David H. Cheng—926
Streak photography, Irwin Vigness and R. C. Nowak—445
Streaming double refraction, Turbulence in apparatus for measurement of, H. G. Jerrard—1007
Stress analysis for compressible viscoelastic materials, W. T. Read, Jr.—671
Stress in the semi-infinite solid, Thermoelastic, Raymond D. Mindlin and David H. Cheng—931
Stress phenomena from the respective viewpoints of solid-state and high polymer, Maurice L. Huggins—518
Stress-strain curve, Negligible changes produced by immersion of a copper single crystal in mercury, J. B. Wachtman, Jr. —943 (L)
Stress-strain properties of natural rubber under biaxial strain, B. B. S. T. Boonstra—1098
Stress theories of plasticity, Effective stress and effective strain in relation to, G. N. White, Jr. and D. C. Drucker —1013
Stresses in Bourdon tubes, Deformations and, R. A. Clark and E. Reissner—1340 (L)
Stroboscopic mapping of time-variable fields, L. Marton and D. L. Reverdin—617 (L)
Studies in plasticization of polyvinyl chloride. I. Physical changes and their measurement, M. L. Dannis—505
—— II. Plasticizer variations in PVC-plasticizer systems, M. L. Dannis—510
Studies with an aerodynamically instrumented shock tube, A. Hertzberg and A. Kantrowitz—874
Study of crack propagation using high speed motion pictures, Herbert I. Fusfeld and Josephine Carr Feder—261 (L)
Summation of Fourier series, Alternative method for, I. F. Morrison—939 (L)
Summation of Fourier series by operational methods, Louis A. Pipes—298
Supersonic speeds, shadowgrams of, spherical missiles entering water at, J. H. McMillen, R. L. Kramer, and D. E. Allmand —1341 (L)
Surface area of powders, Simplified air flow method for the determination of, Gerard Kraus and John R. Thiem—1065 (L)
Surface temperature of evaporating water drops, Measurement of, John C. Johnson—22
Surface tension effects in oriented thin silver films, G. W. Johnson—449
Surface waves and their application to transmission lines, Georg Goubau—1119
Synthetic elastomers, Ultra speed tensile of rubber and, D. S. Villars—565

Tearline patterns in ferrochromium, C. A. Zapffe and F. K. Landgraf—1197 (L)
Techniques for measuring the dynamic characteristics of a low pressure discharge, Bentley T. Barnes and Stephen Eros—1275
Technique for taking motion pictures of electron microscope images, Luther E. Preuss and John H. L. Watson—902
Teflon, Thin films peeled from, C. K. Jones—64 (L)

Temperature rise, Steady-state internal, in magnet coil windings, Claude L. Emmerich—75
Textile specimens, Some theoretical considerations of dynamic-property data on, W. James Lyons—520
Theoretical considerations of dynamic-property data on textile specimens, W. James Lyons—520
Theory of axially slitted circular and elliptic cylinder antennas, D. R. Rhodes—1181
Theory of blind navigation by dynamical measurements, J. J. Gilvarry, S. H. Browne, and I. K. Williams—753
Theory of collinear antennas, Ronold King—1232
Theory of dislocations, John L. Bogdanoff—1258
Theory of N coupled parallel antennas, Ronold King—94
Theory of parallel plane diode, A. H. Taub and Nelson Wax—974
Thermal conductivity of soils, Andrew Gemant—750
Thermal expansion coefficient and the melting point of cubic elements, M. E. Straumanis—936 (L)
Thermal noise at high frequencies, A. van der Ziel—399
Thermally induced stresses in microconstituents of aluminum-silicon alloys, X-ray study of, John P. Nielsen and Walter R. Hibbard, Jr.—853
Thermionic emission from oxide cathodes: retarding and accelerating fields, C. S. Hung—37
Thermionic emitter, Thorium sulfide as a, T. E. Hanley—1193 (L)
Thermionic emitting properties of thoria-rhenium, G. A. Esperson—261 (L)
Thermionic work function of the (100) face of a tungsten single crystal, A. A. Brown, L. J. Neelands, and H. E. Farnsworth—1
Thermistors, Relationship between resistance and temperature of, G. Bosson, F. Gutman, and L. M. Simmons—1267
Thermocouples of the refractory metals, F. Haydn Morgan and W. E. Danforth—112
Thermoelastic stress in the semi-infinite solid, Raymond D. Mindlin and David H. Cheng—931
Thermoelectric generation of current, Max B. Greeff—943 (L)
Thickness measurement of thin films by multiple beam interferometry, G. D. Scott, T. A. McLauchlan, and R. S. Sennett—843
Thin films peeled from Teflon, C. K. Jones—64 (L)
Thin films, Thickness measurement of, by multiple beam interferomerty, G. D. Scott, T. A. McLauchlan, and R. S. Sennett—843
Thin overgrowths, Examination of, by multiple scattering of electrons, L. G. Schulz—942 (L)
Thoria cathodes, Emissivity changes of, O. A. Weinriech—1272
Thoria-rhenium, Thermionic emitting properties of, G. A. Esperson—261 (L)
Thorium sulfide as a thermionic emitter, T. E. Hanley—1193 (L)
Three-stage electron microscope with stereographic dark field, and electron diffraction capabilities, M. E. Haine, R. S. Page, and R. G. Garfitt—173
Time-variable fields, Stroboscopic mapping of, L. Marton and D. L. Reverdin—617 (L)
TM_{01} mode in a metal tube containing an imperfect dielectric, Propagation of, David Hettrick—561
$TM_{0,1}$ mode, Radiation patterns of dielectric rods of circular cross section, C. W. Horton, F. C. Karal, Jr., and C. M. McKinney—1279
Tobacco mosaic virus, Metallic evaporation and the diameter of, with the electron microscope, H. Kahler and B. J. Lloyd, Jr.,—699
Tracing and interpretation of asymmetrical hysteresis loops, G. M. Ettinger—936 (L)
Trajectories in a moving reference system, particle, Graphical representation of, M. Garbuny—1054
Transitions in high-polymeric materials, Rolf Buchdahl and Lawrence E. Nielsen—482
Transmission lines, Surface waves and their application to, Georg Goubau—1119
Transmission of elastic waves through a stratified solid medium, William T. Thomson—89
Transmission of plane elastic waves through a plate at oblique incidence, Equivalent circuit for, William T. Thomson—1215
Transonic potential flow of a compressible fluid, W. R. Sears—771
—— W. R. Sears—1340 (erratum)
Tubes, Bourdon, Deformations and stresses in, R. A. Clark and E. Reissner—1340 (L)
Tungsten cathode interface, Barium oxide on, Eugene B. Hensley and John H. Affleck—938 (L)
Tungsten single crystal, Thermionic work function of the (100) face of a, A. A. Brown, L. J. Neelands, and H. E. Farnsworth—1
Turbulence in apparatus for measurement of streaming double refraction, H. G. Jerrard—1007
Turbulent boundary layer, Shear stress in, Donald Ross and J. M. Robertson—557
Turbulent jet mixing in two-dimensional supersonic flow, D. Bershader and S. I. Pai—616 (L)
Two-dimensional supersonic flow, Turbulent jet mixing in, D. Bershader and S. I. Pai—616 (L)
Two-wave-length microscope, Generalized microscopy and the, M. J. Buerger—909

Ultra-high frequency antenna under conditions of atmospheric stratification, Graphical analysis of the interference patterns of an elevated, F. R. Abbott and C. J. Fisher—636
Ultra speed tensile of rubber and synthetic elastomers, D. S Villars—565
Ultrasonic irradiation, Depolymerization by: the role of cavitation, Alfred Weissler—171
Ultrasonic vibration, Emulsion polymerization with, A. S. Ostroski and R. B. Stambaugh—478
Unbalanced terminations on a shielded-pair line, K. Tomiyasu—552
Upper and lower bonds of eigenvalues for composite-type regions, E. L. Chu—454
Use of brightness temperatures in Richardson plots, Henry F. Ivey—616(L)
Use of critical point phenomena in preparing specimens for the electron microscope, Thomas F. Anderson—724 (L)
Use of latex spheres as size standards in electron microscopy, Charles H. Gerould—183 (L)
Use of Reiner's equation for recognition of pseudoplastics from their flow curves, Vera Osman Krakauer—850
Use of spraying methods and of volatile suspending media in the preparation of specimens for electron microscopy, Robert C. Backus and Robley C. Williams—11

Vacuum tubes with mutually bombarding oxide cathodes, E. G. Hopkins—841
Variable linear networks, Circuit analysis of, Lotfi A. Zadeh—1171
Variable networks, Determination of the impulsive response of, Lotfi A. Zadeh—642
Variation of elastic moduli and wave velocity with pressure and temperature in plastics, D. S. Hughes, E. B. Blankenship, and R. L. Mims—294
Vibrational relaxation times in gases, Wayland Griffith—1319
Video filter on the detection of pulsed signals in noise, Effect of a, David Middleton—734
Virtual mass of a sphere entering water vertically, Albert May and Jean C. Woodhull—1285
Viscoelastic materials, compressible, stress analysis for, W. T. Read, Jr.—671
Visco-elastic substances, Frictional loss in, B. Gross—185 (L)

Volume diffusion of metals, Frequency factor and activation energy for, G. J. Dienes—1189
Vulcanized rubbers, Relationship between Gough-Joule coefficients and moduli of, M. Mooney—1338 (L)

Wall-quenching of laminar propane flames as a function of pressure, temperature, and air-fuel ratio, Raymond Friedman and W. C. Johnston—791
Water drops, evaporating, Measurement of the surface temperature of, John C. Johnson—22
Water, Limiting negative pressure of, Lyman J. Briggs—721 (L)
Water surface, Impact of a body on a, at an arbitrary angle, Leon Trilling—161
Wave fronts and reflectors, Relations concerning, K. S. Kelleher—573
Wave-guide attenuators, Magnetically controlled, Theodore Miller—722 (L)
Wave guide, Modulation conversion in a, Paul S. Rogell—629
Wave-lengths suitable for x-ray microscopy of biological specimens, J. L. Farrant—63 (L)
Waves, ionospheric, Magneto ionic triple splitting of, Olof E. H. Rydbeck—1205
Wet-replication methods, Irwin W. Fischbein—1199
Wettability, a function of the polarizability of the surface ions, L. R. Sonders, D. P. Enright, and W. A. Weyl—338
Wiener's theory of prediction, Extension of, Lotfi A. Zadeh and John R. Ragazzini—645
Wire corona at high temperature and pressure, Negative, L. R. Koller and H. A. Fremont—741
Work functions of the elements, Herbert B. Michaelson—536

X-ray detector, Cadmium sulfide, Rudolf Frerichs—312
X-ray diffraction by elastically deformed crystals, J. E. White—855
X-ray measurement of long range order in β-brass, D. Chipman and B. E. Warren—696
X-ray measurement of order in single crystals of Cu_3Au, J. M. Cowley—24
X-ray microscope, Resolving power of an, Edward Prince—698
X-ray microscopy of biological specimens, Wave-lengths suitable for, J. L. Farrant—63 (L)
X-ray patterns of cold-worked metal, Interpretation of, B. L. Averbach and B. E. Warren—185 (addendum)
X-ray patterns, Effect of cold-work distortion on, B. E. Warren and B. L. Averbach—595
X-ray powder diffraction techniques, Analysis of intensities obtainable using pinhole and slit collimators in, Leroy Alexander—779
X-ray scattering, low angle, Average electron density measurements by, H. M. Barton, Jr. and R. Brill—783
X-ray scattering, in small angle, Double crystal and slit methods, H. N. Ritland, P. Kaesberg, and W. W. Beeman—838
X-ray screens, Light energy and spectral distribution for some important, Holger Sköldborne—546
X-ray spectrometer, Determination of crystallite size with the, Leroy Alexander and Harold P. Klug—137
X-ray spectrometer maxima, Geometrical factors affecting the contours of. II. Factors causing broadening, Leroy Alexander—126
X-ray spectrometer transmission pole figure determinations, Intensity correction factors for, Suzanne Van Dijke Beatty—940 (L)
X-ray study of thermally induced stresses in microconstituents of aluminum-silicon alloys, John P. Nielsen and Walter R. Hibbard, Jr.—853
X-ray techniques, Single crystal, for use with alloys requiring protective atmospheres, Joseph Singer and F. H. Ellinger—467 (L)
X-ray tube producing a beam of x-rays convergent to a point, C. H. Bachman and S. J. Silverman—615 (L)

Zinc crystals, Creep-time law for, E. P. T. Tyndall—939 (L)
Zinc oxide, Precision determination of the lattice constants of, R. B. Heller, J. McGannon, and A. H. Weber—1283

For all your potentiometer needs check this complete L&N line

When you're looking for the right potentiometer to do a specific job, it will pay you to check the *complete* L&N line first. Whether you need the extreme precision of an N.B.S.-certified Wenner, the convenience of a Micromax or Speedomax recorder, or an intermediate instrument, you'll find the characteristics you want in a soundly engineered L&N potentiometer.

More than a score of models comprise the line. Just glance at the table below. There's a potentiometer for practically any purpose—measurement of low voltages, temperature vs. temperature-difference, calorimetry, pH and other emf cell work . . . self-contained portables for temperature and pyrometer checking . . . and the popular, general-purpose Type K's. Models run from highest to moderate precision. They come in convenient single, double, even triple ranges . . . to suit the job at hand.

Naturally, we can't begin to tell you all you want to know in so short a table. So for complete details, let us send you catalog information. Simply write our nearest office, or 4978 Stenton Ave., Phila. 44, Pa.

MODEL	CAT. NO.	PURPOSE	LIMIT OF ERROR†					RANGE
			better than .01%	.01%	.02%	.03% to .1%	.3% of range	
Wenner (N.B.S.-certified)	7559	thermocouple; other low voltages	x					0 to 0.011111 v; 0 to 0.11111 v
	7558	maintain primary standards	x					0 to 0.19111 v; 0 to 1.9111 v
White (Single)	7620	thermocouple voltages; calorimetry			x			0 to 0.01 v
	7621	thermocouple voltages; calorimetry			x			0 to 0.1 v
White (Double)	7622	temp; temp-difference;			x			0 to 0.01 v
	7623	temp-current; etc.			x			0 to 0.1 v
Type K-1	7551	general		x				0 to 0.161 v; 0 to 1.61 v
Type K-2	7552	general		x				0 to 0.0161 v; 0 to 0.161 v; 0 to 1.61 v
Students'	7651	general				x		0 to 0.016 v; 0 to 1.6 v
Indicator *	7655	pH, emf's				x		0 to 1.110 v
*	7659	corrosion testing					x	triple; 0 to 4.1 v total
Millivolt *	8667	pyrometer check (lab.); temp.				x		0 to 111 mv
Indicator *	8656 B,D,X	pyrometer check (plant); temp.					x	0 to 16 mv; 0 to 70 mv; or as spec.
*	8657	pyrometer check (plant); temp.					x	0 to 16 mv & 16 to 64 mv; or as spec.
*	8662	pyrom. check (lab. & plant); temp.				x		0 to 16.1 mv; 0 to 80.5 mv
*	8658	pyrom. check (lab. & plant); temp.					x	single; direct-reading temp.
Temperature *	8659	pyrom. check (lab. & plant); temp.					x	double; direct-reading temp.
Indicator *	8663-CD	body temps.					x	25 to 125 F; −3.9 to +51.7 C
*	8663-X	temp. check (lab. or plant)					x	single or double, as spec.
Panel Indicator *	8671-76	temp. meas.					x	single or double, as spec.
pH Indicator *	7663-A1	pH; emf cell potentials					x	0 to 13 pH; 0 to 1.100 v
Brooks (Deflection)	7630	ammeter, voltmeter, wattmeter test.				x		0 to 153 mv } used with volt boxes and shunts
	7640	lamp efficiency test.				x		0 to 1.53 v }
Micromax *		automatic indicating, recording, controlling: voltage, temp., pH, etc.					x	as spec.
Speedomax *							x	as spec.

*Self-contained: battery, standard cell, and galvanometer inside case.

†Under normal operating conditions, except when using lowest part of ranges.

MEASURING INSTRUMENTS · TELEMETERS · AUTOMATIC CONTROLS · HEAT-TREATING FURNACES

LEEDS & NORTHRUP CO.

Jrl. Ad EN(12)

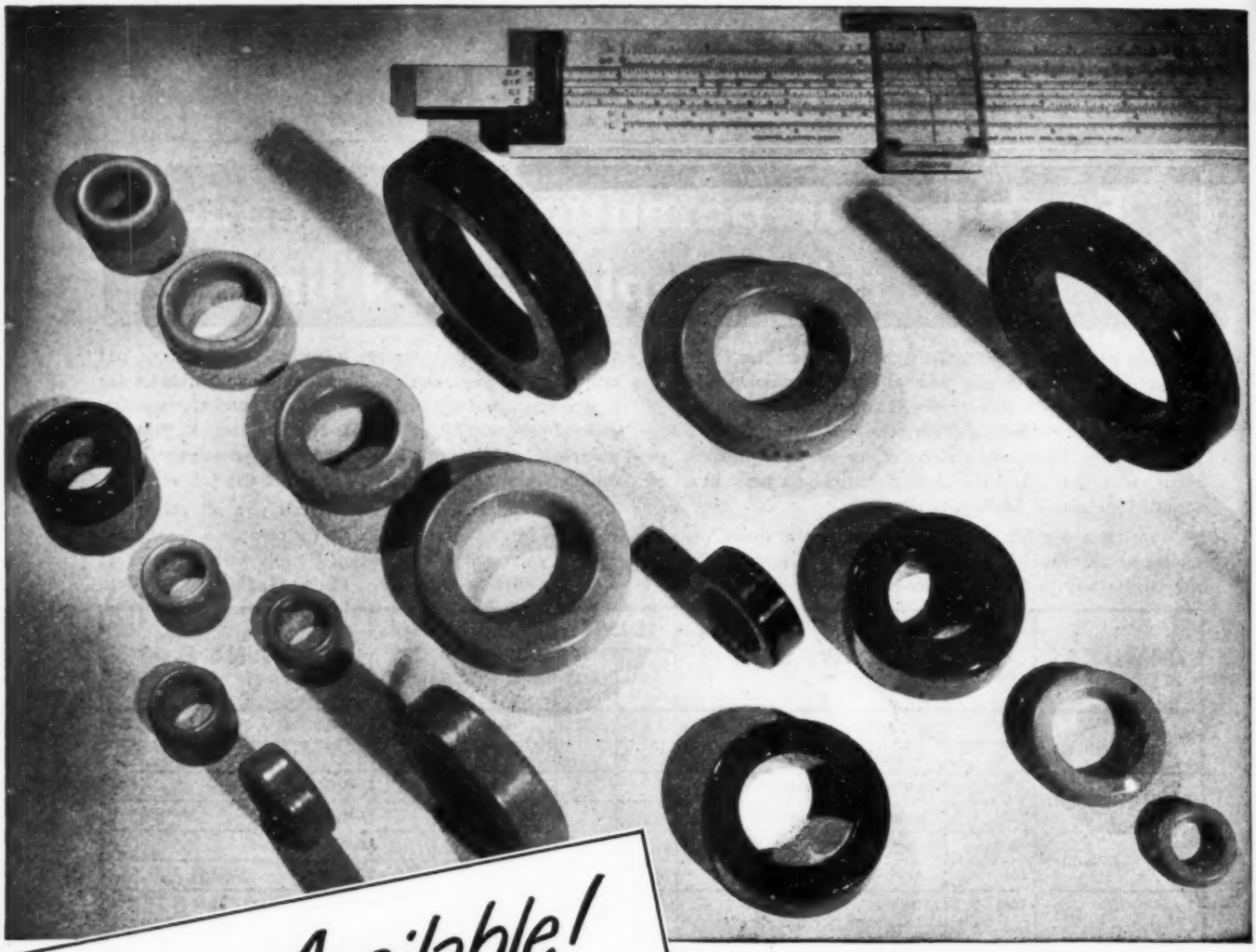

Now Available!

MOLYBDENUM PERMALLOY POWDER CORES*

HIGH Q TOROIDS for use in Loading Coils, Filters, Broadband Carrier Systems and Networks—for frequencies up to 200 KC

COMPLETE LINE OF CORES TO MEET YOUR NEEDS

- ★ **Furnished in four standard permeabilities—125, 60, 26 and 14.**
- ★ **Available in a wide range of sizes to obtain nominal inductances as high as 281 mh/1000 turns.**
- ★ **These toroidal cores are given various types of enamel and varnish finishes, some of which permit winding with heavy Formex insulated wire without supplementary insulation over the core.**

For high Q in a small volume, characterized by low eddy current and hysteresis losses, ARNOLD Moly Permalloy Powder Toroidal Cores are commercially available to meet high standards of physical and electrical requirements. They provide constant permeability over a wide range of flux density. The 125 Mu cores are recommended for use up to 15 kc, 60 Mu at 10 to 50 kc, 26 Mu at 30 to 75 kc, and 14 Mu at 50 to 200 kc. Many of these cores may be furnished stabilized to provide constant permeability (±0.1%) over a specific temperature range.

** Manufactured under licensing arrangements with Western Electric Company.*

W&D 2930

THE ARNOLD ENGINEERING COMPANY

SUBSIDIARY OF ALLEGHENY LUDLUM STEEL CORPORATION

147 EAST ONTARIO STREET, CHICAGO 11, ILLINOIS

This Divining Rod Talks to Searchers . . . prompted by DPi HIGH VACUUM

For locating and measuring leaks wherever pressure or vacuum is used

THE CONSOLIDATED MODEL 24-101A LEAK DETECTOR

TO prove absence of any leak, or to detect, locate, and measure rate of leakage in pressure or high vacuum systems, glass to metal seals in electronic equipment, valves, welded or soldered joints—these are only a few of many uses for this versatile instrument.

Employing helium gas and the mass spectrometer principle, this highly sensitive machine responds to leak rates, from atmosphere into an evacuated system, as low as 10^{-9} cubic centimeters per second.

Ruggedly built and mounted on casters for portability, the unit can be moved anywhere for testing systems by "probe" or "envelope" methods, or locating leaks in buried gas lines.

Both visual and audible indicators are standard features on the Model 24-101A.

Send for our free, 16-page bulletin describing the many features of the Consolidated Model 24-101A Leak Detector. It also explains applications and methods, and gives complete specifications. For your free copy, write: Vacuum Equipment Department, ***Distillation Products Industries,*** 769 Ridge Road West, Rochester 3, N.Y. (Division of Eastman Kodak Company).

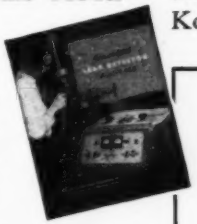

high vacuum research and engineering

DPi

Also . . . Vitamins A and E . . . distilled monoglycerides . . . more than 3300 Eastman Organic Chemicals for science and industry

Browning

INSTRUMENTS
Engineered for Engineers

SWEEP CALIBRATOR

MODEL GL-22A

A versatile source of timing markers for accurate measurement of sweep intervals with oscilloscopes and synchroscopes.

- Positive or negative markers of 0.1, 1.0, 10, 100 micro-seconds variable to 50 volts.
- Variable width and amplitude gate for blanking or timing.
- Markers from external trigger or internal generator. May be synchronized with triggers up to 100 KC. repetition rate.
- Voltage regulation to timing circuits.

Write for free bulletin.

POWER SUPPLY

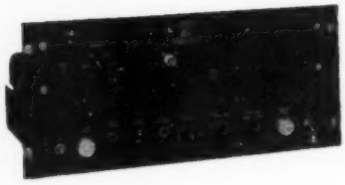

MODEL TVN-7

The basic unit of a microwave signal generator. Square-wave modulator for low-powered velocity-modulated tubes.

- Cathode voltage continuously variable 28-480 volts.
  Provision for 180-300 volt range.
- Reflector voltage range 15-50 volts.
- Provision for grid pulse modulation to 60 volts, reflector pulse modulation to 100 volts.
- Square-wave modulation variable from 600 to 2500 cycles.
- Provision for external modulation.

Write for free bulletin.

LABORATORY AMPLIFIER

MODEL TAA-16

High gain audio amplifier feeding a-c volt-meter for measurement of standing wave ratios with slotted lines.

- 500-5000 cycles with broadband selective control on front panel.
- Sensitivity: Broadband 15-microvolts; selective 10 microvolts.
- Meter scales 0-10 and standing-wave voltage ratio.
- Panel switch for bolometer voltage application.
- Master gain control switch for attenuation factors of 1, 10, and 100.
- Stable electronic power supply.

Write for free bulletin.

FM MODULATION MONITOR

MODEL MD-25

For monitoring modulation of fixed or mobile FM transmitters in bands from 30-162 mc. to comply with FCC limitations of carrier frequency swing and reduce adjacent-channel interference.

- Coverage 30-40, 40-50, 72-76, 152-162 mc.
- Flasher indicates peak modulation (peak carrier deviation).
- Meter indicates peak swings of modulation to 1 kc.
- Sensitivity: signal measurements with approximately 1 millivolt at antenna input.

Write for free bulletin.

In Canada, address
Measurement Engineering Ltd.
Arnprior, Ontario

BROWNING
Laboratories, Inc.
Winchester, Mass.
ENGINEERED FOR ENGINEERS

Testing for sound lost between telephone receiver and ear. Many subjects were used in these tests.

How to compensate for a curl . . . and add to your telephone value

Bell scientists know that the telephone is not used under ideal laboratory conditions. There is never a perfect seal between receiver and user's ear. A curl may get in the way, or the hand relax a trifle. And ears come in many shapes and sizes. So some sound escapes.

Now, sound costs money. To deliver more of it to your ear means bigger wires, more amplifiers. So Bell Laboratories engineers, intent on a thrifty telephone plant, must know how much sound reaches the ear, how much leaks away. They mounted a narrow "sampling tube" on an ordinary handset. The tube extended through the receiver cap into the ear canal. As sounds of many frequencies were sent through the receiver, the tube picked up a portion, and sent it through a condenser microphone to an amplifier. That sampling showed what the ear received.

As a result, Bell scientists can compensate in advance for sound losses—build receivers that give *enough* sound, yet with no waste. That makes telephone listening always easy and pleasant.

It's another example of the way Bell Telephone Laboratories work to keep your telephone service one of today's biggest bargains.

Automatic recorder plots sound pressures developed in the ear canal at different frequencies.

BELL TELEPHONE LABORATORIES

Working continually to keep your telephone service big in value and low in cost.

NEED FRONT SURFACE ALUMINUM MIRRORS ?

Liberty Front Surface Aluminum Mirrors are available in sizes up to 48" x 66"—and in a range of constructions to meet the most exacting requirements. The glass in these mirrors is coated with aluminum, which has a protective layer of quartz. No base metal is used because bimetallic mirrors are subject to galvanic action.

Liberty Aluminum Mirrors retain their reflectivity—and they contain a minimum of pinholes. Moreover, these few pinholes do not increase in size or number in service. Liberty's patented adhesive coatings insure exceptionally strong adhesion.

The basic design superiority and quality of Liberty Front Surface Aluminum Mirrors is evidenced by an ever-increasing list of satisfied customers. We invite your comparison test order. For a quotation, use the coupon below.

FOR COMMERCIAL AND OPTICAL FIELDS where normal cleaning is sufficient, and where exceptional exposure to salt water or salt atmosphere is not required, we recommend our Specification #1051, Finish #749.

FOR HIGH RESISTANCE TO ABRASION AND SALT AIR—and especially for high-grade optical instruments requiring maximum reflectivity and unchanging durability, we recommend our Specification #1054, Finish #752.

LIBERTY MIRROR DIVISION
LIBBEY·OWENS·FORD GLASS CO.
L2125 NICHOLAS BUILDING
TOLEDO 3, OHIO

I am interested in your Liberty Front Surface Aluminum Mirrors for

.....
(Application)

Please quote me on.....in size.....
(Quantity)

( ) Please have salesman call.

Name.....Title.....

Company.....

Address.....

City.....Zone.....State.....

LIBERTY VACUUM DEPOSITED COATINGS

Liberty Mirror Division

LIBBEY·OWENS·FORD GLASS CO. • NICHOLAS BUILDING, TOLEDO 3, OHIO

G-E PHOTOELECTRIC RECORDER CHOSEN FOR NEW "PACIFIC EVENNESS TESTER"

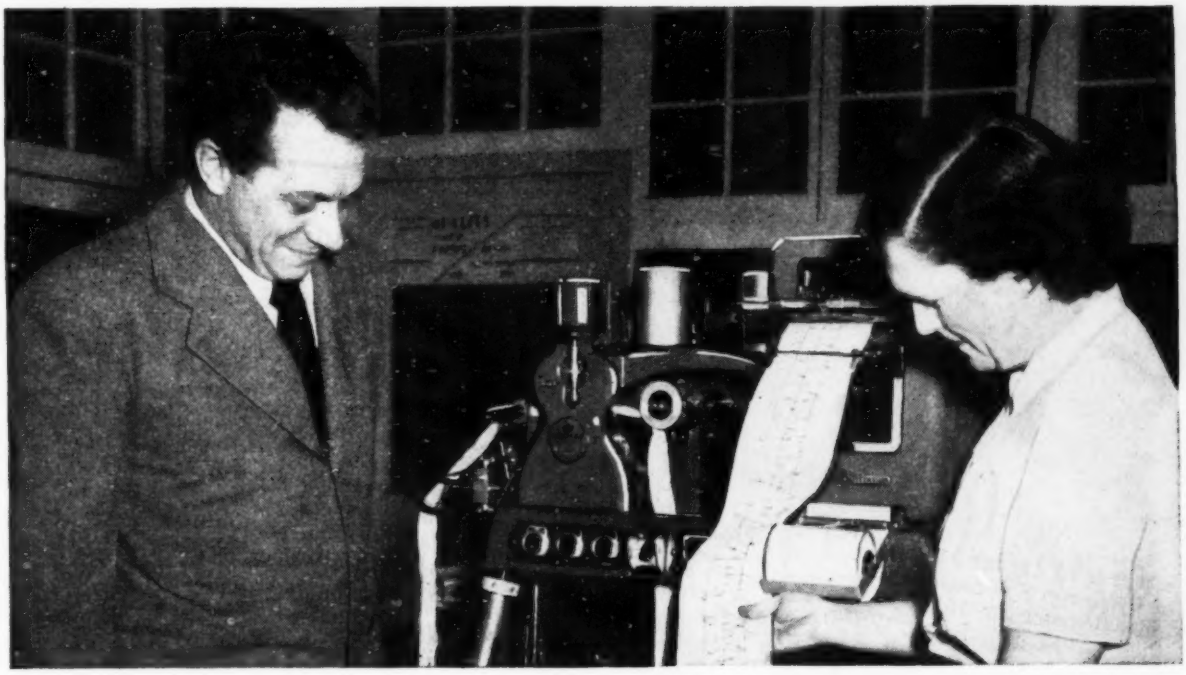

"The sustained accuracy, fast response, and high sensitivity of the G-E photoelectric recorder make it especially suitable for use with our Pacific Evenness Tester."

Mr. R. C. Wilkie (shown above), Manager
Engineering Research Department
Pacific Mills Worsted Division

The new Pacific Evenness Tester, a tremendous step forward in the field of textile quality control, measures the evenness and weight of textile strands. In keeping with the new methods of modern textile manufacture, extremely accurate control of evenness and weight is mandatory if defective cloth and twisted yarn are to be eliminated.

The G-E photoelectric recorder, an important component of the Pacific Evenness Tester, provides an accurate, easily evaluated record of the evenness of the strands under test. Designer R. C. Wilkie reports that a .002-inch deviation in strand thickness can represent full-scale deflection of the recorder. This inherent sensitivity of the recorder, plus its accuracy and high-speed response, have helped to make the Pacific Evenness Tester a real precision instrument.

This is only one of the many ways in which G-E photoelectric recorders are now being used wherever precision testing is done.

Remember: where high sensitivity (up to 1 μ full scale) and fast response ($\frac{1}{5}$ second for full-scale deflection) are required, the G-E photoelectric recorder can do the job.

Bulletin GEC-254 contains complete information. Contact your nearest G-E sales office or write directly to the Apparatus Department, General Electric Co., Schenectady 5, N. Y.

GENERAL ELECTRIC

602-194

accuracy...

at high speeds

with these world famous IMPULSE REGISTERS

Type 401-A with fully enclosed plastic desk case and non-removable-top binding posts. See the complete specifications below.

Cyclotron Specialties Impulse Registers, originally designed to meet the exacting requirements of radioactivity research workers, have become a standby in many fields of laboratory and industrial control work throughout the entire world.

The Cyclotron Specialties Registers are unique in their ability to operate at exceptionally high speeds with complete accuracy and without adjustment or maintenance. They are unexcelled for high speed impulse recording and mechanical operations requiring counting in precise quantities.

Precision Timing Measurements
By applying ordinary rectified 60 cycle power, precision measurements of time to within 1/60 second may be easily secured.

specifications
of Cyclotron Specialties Impulse Register No. 401-A

Accurately Registers Up To 60 Impulses Per Second

Main, easily-read sweep dial reads 0 to 100 directly.
Sweep dial plus auxiliaries read 0 to 9,999 impulses without extra equipment.
4000 ohm D. C. resistance.
Operates on as low as 100 milliwatt.
Small, compact, lightweight. Attractive plastic case with non-removable-top binding posts.
Durable, rugged construction.
Dimensions: 3" x 4". Weight: 2 lbs.

The operation of the Cyclotron Specialties Impulse Registers is entirely automatic. Originally designed for our Geiger-Müller Counter Sets, they have found numerous other applications . . . both industrial and research . . . including:

PRECISE CONTROL of QUANTITIES (Packaging, Sorting, etc.)

CUTTING of MATERIALS, FABRICS, etc., to EXACT LENGTHS

CONTROLLING VARIOUS MECHANICAL OPERATIONS

CONTROLLING FUNCTIONS such as TIME, DIMENSIONS, VELOCITY, etc.

FLUSH MOUNTED Type with single hole mounting and plastic case. Widely used for panel mounting.

Inquiries for special types and modifications including higher speeds, electrical reset, and higher totalization will receive prompt attention.

Immediate Delivery in Reasonable Quantities

Cyclotron Specialties Company
Moraga 3, California

HERE'S *Fast, Accurate* LAB OR PRODUCTION *Testing!*

A QUICK CHECK OF LOW RESISTANCE CONNECTIONS, BONDS, CONTACTS, etc.

Shallcross low resistance test sets greatly facilitate comparison tests between 2 and 800,000 micro-ohms. Their uses range from testing the electrical conductivity of bonds, welds and seals to contacts, filaments, armatures or for making any measurement under 1 ohm. Suitable units are available for either field, laboratory or production line use. Write for Bulletin LRT-1.

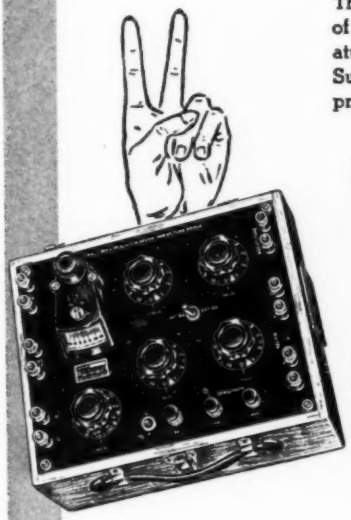

KELVIN plus WHEATSTONE RANGES IN ONE HANDY BRIDGE

Why pay for two instruments when one will do *both* jobs? Providing both Kelvin and Wheatstone ranges from 0.0001 ohm to 11.11 megohms, this Shallcross No. 638-R combined bridge is highly accurate and outstandingly convenient. Priced at only a little more than a single bridge with a limited range, it is a typical example of Shallcross instrument efficiency and economy.

DECADE RESISTANCE BOXES TO MATCH YOUR NEED... exactly

Over 40 Shallcross standard Resistance Boxes provide the widest assortment available today. Types range from 1 to 7 dials from 0.01 ohm to 111 megohms and are available in styles, sizes and prices for practically any laboratory or production testing need. Write for Bulletin.

SHALLCROSS

SHALLCROSS MANUFACTURING COMPANY

Collingdale • Penna.

Would a Monochromator

featuring

HIGH SPECTRAL PURITY
and
WIDE SPECTRAL RANGE
be useful in your research ?

CENTRAL RESEARCH LABORATORIES has now completed development of a DOUBLE MONOCHROMATOR which will interest you.

Features

- Entrance and exit slits fixed in position.
- Constant aperture ratio of f/4.5.
- Simultaneous wavelength setting and focusing with synchronous-motor drive.
- Aspheric collimator lenses.
- Pre-focused interchangeable optics cover complete range from 0.15 to 25 microns.
- Provision for evacuation and gas filling.

Your comments and inquiries are invited.

CENTRAL RESEARCH LABORATORIES, INC.
RED WING, MINNESOTA

STATHAM

DYNAMICALLY BALANCED PRESSURE TRANSDUCER
MODEL P69

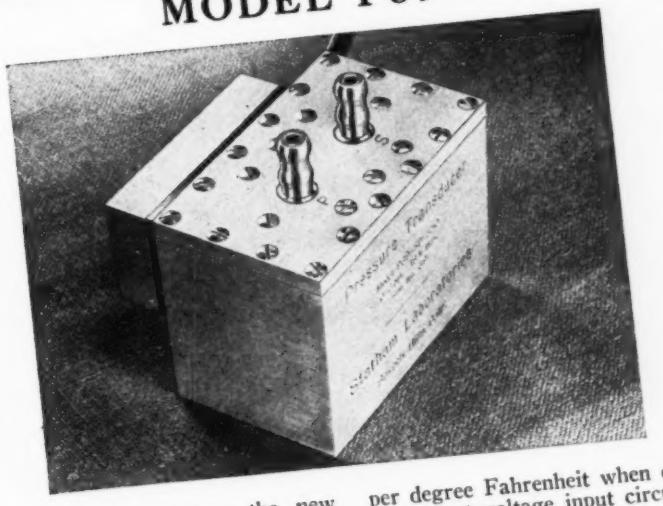

We are proud to announce the new Model P69 pressure transducer whose dynamically balanced construction assures long life and excellent performance under conditions of vibration and acceleration such as are encountered in flight test and guided missile applications. The acceleration response of the Model P69 pressure transducer is less than 0.1% of full scale per G up to 10G in any axis.

The Model P69 pressure transducer is temperature compensated over the range −65° F. to +250° F. Zero shift with temperature is not more than 0.01% of full scale per degree Fahrenheit, while the change in sensitivity is not more than 0.01% per degree Fahrenheit when operated with a constant voltage input circuit.

The Model P69 pressure transducer is available for the measurement of either gage or differential pressure in the ranges 0–1 to 0–20 p.s.i., and is offered as an absolute pressure transducer in the range 0–15 p.s.i.a. A high natural frequency, typical of all Statham transducers, has been maintained in the Model P69 transducers.

The Model P69 pressure transducer contains a full bridge transducer and will operate successfully with a wide variety of controlling, indicating, recording, and telemetering circuits.

Please request Bulletin No. 3.3

We invite correspondence with our engineering staff when you are considering instrumentation for the measurement of acceleration, pressure, force, or displacement.

STATHAM LABORATORIES SCIENTIFIC INSTRUMENTS

9328 SANTA MONICA BOULEVARD • BEVERLY HILLS, CALIFORNIA

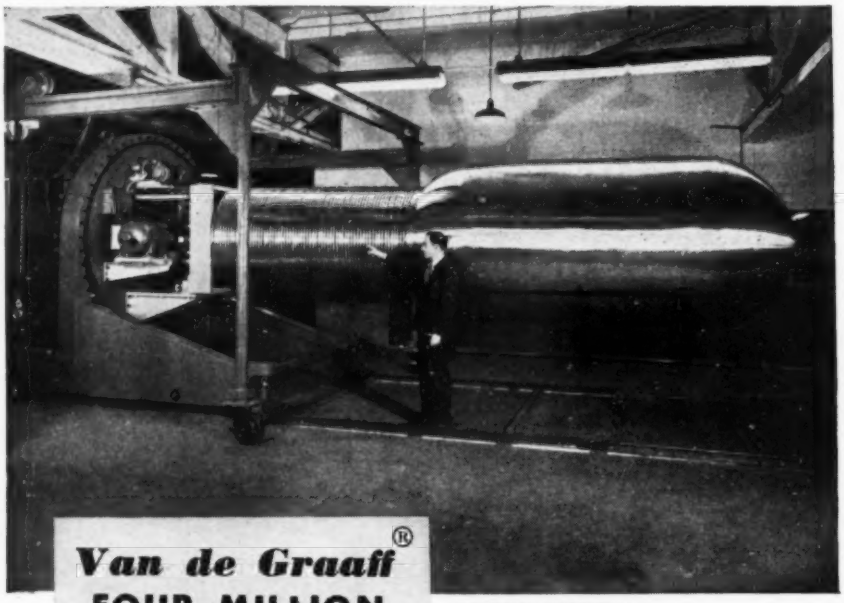

Van de Graaff®
FOUR-MILLION VOLT POSITIVE-ION ACCELERATOR

TYPE D MODEL H
Versatile Van de Graaff® Accelerator

. . . Produces a well-collimated and intense beam of charged particles, homogeneous and controllable in energy . . . with ruggedness, reliability, and the precision required for significant research.

. . . Offers the most adaptable source for constant-potential or pulsed beams of high-energy radiations . . . constructed for horizontal or vertical installations and in the energy range of two million to five million volts for specialized or general use, providing positive ions or neutrons, electrons or x-rays.

. . . Provides basic equipment for fundamental radiation research and instruction in physics, chemistry, biology, and related fields.

Your inquiries will receive prompt attention.

HIGH VOLTAGE ENGINEERING CORPORATION
7 UNIVERSITY ROAD CAMBRIDGE 38, MASSACHUSETTS

POWER AND IMPEDANCE MEASUREMENTS

DAVEN

OUTPUT POWER METERS

of unexcelled accuracy and reliability

have many applications

The DAVEN Output Power Meters are designed to measure the actual power delivered by an audio signal system to a given load. However, because of the characteristics of the circuit, they are admirably suited to other applications, namely:

1. Determination of Characteristic Impedance of an A.C. Source.
2. Effects of Load Variation on a Signal System.
3. Transmission Line Equalization Measurements.
4. Measurement of Insertion Loss in Multi-channel Mixer and other complex circuits.
5. Filter and Transformer Measurements.
6. Radio Receiver Measurements.

The equipment shown on this page is built to DAVEN'S well-known standards of precision. Please write for more detailed data. Let our engineering department help you on specific problems.

TYPE OP-182

Impedance Range: 2.5 ohms to 20,000 ohms. Remains essentially resistive over frequency range of 30 to 10,000 cps. Accuracy ±5%.

Power Range: 0.1 mw. to 5 watts in steps of 0.1 mw.

Indicating Meter: Calibrated from 0 to 50 milliwatts and from 0 to 17 db. —Zero level: 1mw.

Meter Multiplier: Will change reading of indicating meter by ratios of 0.1:1, 1:1, 10:1, 100:1, or decibel reading by —10, 0, +10, +20.

TYPE OP-962

Characteristics similar to OP-961, except that it can measure up to 100 watts.

Impedance Range: 40 selected impedances between 2.5 and 20,000 ohms. Accuracy ±2% over frequency range 30 to 10,000 cycles.

Power Range: 0.1 mw to 100 watts in 0.1 mw steps. Range may be extended below 0.1 mw by use of external amplifier.

Indicating Meter: Calibrated from .01 watt to 1 watt and from —10 to +10 db. Zero level: 1mw.

Meter Multiplier: Extends range of meter from 0.01 to 100 times scale reading.

TYPE OP-961

Impedance Range: 2.5 ohms to 20,000 ohms. Remains essentially resistive over frequency range of 30 to 10,000 cps. Accuracy ±2%.

Power Range: 0.1 milliwatts to 50 watts in steps of 0.1 milliwatts.

Indicating Meter: Calibrated from 1 to 50 milliwatts and 0 to 17 decibels. Zero level: 1mw.

Meter Multiplier: Extends the power reading of the indicating meter from 0.1x to 1,000x scale value, or the db. reading from —10 to +30 db. in steps of 2 db.

THE DAVEN CO.

193 CENTRAL AVENUE • NEWARK 4, NEW JERSEY

OUTSTANDING McGRAW-HILL BOOKS

ELASTICITY. Proceedings of Symposia in Applied Mathematics. Volume III

Edited by R. V. CHURCHILL, University of Michigan. 235 pages, $6.00

This volume consists of seventeen papers presented at the American Mathematical Society's Third Symposium on Applied Mathematics. The book represents a selection of recent developments in the mathematical theory and applications of elasticity and plasticity, and contains extensions of approximation methods and of the general theory of elastic and plastic deformation.

RADIO ENGINEERING HANDBOOK. New 4th edition

Editor-in-Chief: Keith Henney, Consulting Editor, *Electronics*. 1197 pages, $10.00

Prepared by a staff of 25 specialists in the field, this volume presents carefully selected design data—charts, tables, circuits, diagrams, and formulas. Fully enlarged and completely revised for greater usefulness, the text offers up-to-date advances and developments in every field of radio engineering.

PROCESS HEAT TRANSFER

By DONALD Q. KERN, Process Engineering Division, The Patterson Foundry & Machine Company. 855 pages, $8.00

Affords systematic instruction in the calculations, derivations and empirics of heat transfer, using the language and methods of industry. This new philosophy of the subject has entailed a radically new approach by which solutions are presented for the numerous representative problems arising in the chemical and process industries. The book develops the fundamentals of heat transfer within the actual equipment and flow patterns in which it occurs in the majority of industrial processes.

VECTOR AND TENSOR ANALYSIS

By HARRY LASS, University of Illinois. *International Series in Pure and Applied Mathematics.* 347 pages, $4.50

A basic textbook for college juniors and seniors. The purpose of the book is to acquaint the student with the methods and tools of vector and tensor analysis as applied to geometry, mechanics, electricity, hydrodynamics and the theory of relativity, and to prepare him for more advanced work in theoretical physics.

PHYSICS—Its Laws, Ideas, and Methods

By ALEXANDER KOLIN, University of Chicago. 890 pages, $6.50

A general physics text for the standard liberal arts and science course at the freshman or sophomore level. Its aim is to give a coherent presentation of physics with emphasis on an understanding of the scientific method and to provide a complete coverage of all fields and principles of physics.

Send for copies on approval

McGRAW-HILL BOOK CO., INC.

330 WEST 42ND STREET, NEW YORK 18, N. Y.

PRECISION

for stable isotopes

The precision inherent in the Model 21-201 Consolidated-Nier Isotope-Ratio Mass Spectrometer makes possible the use of stable isotopes for tracer techniques in fundamental studies. This instrument is in use in numerous medical, biological, and chemical research laboratories throughout this country and abroad, and has played an important role in recent discoveries and scientific advances.

RELIABILITY as well as PRECISION has been emphasized in this instrument. Engineering and construction of the highest quality, supplemented by the experience of Consolidated's representatives for installation and training, results in a research tool which will satisfy the most critical scientific investigator.

For further information, write for the illustrated bulletin CEC 1803-X22.

FEATURES

DUAL COLLECTION—Two separate ion collectors permit simultaneous intensity measurement of two ion beams with a direct reading of the ratio.

OPERATING CONTROLS—All controls are within easy reach of the operator.

FLEXIBILITY—Operating controls permit taking of a variety of measurements. An outlet for a pen and ink recorder is provided.

SAMPLE INTRODUCTION SYSTEM—Gas samples as small as 0.1 ml, S.T.P., can be introduced for analysis.

CONSTRUCTION—The instrument is housed in a single, well-balanced metal cabinet. All components are easily accessible.

CEC

CONSOLIDATED ENGINEERING CORPORATION

Analytical Instruments for Science and Industry

620 NORTH LAKE AVENUE • PASADENA 4, CALIFORNIA

TWO-in-ONE

D·C·P* adds or subtracts two input variables

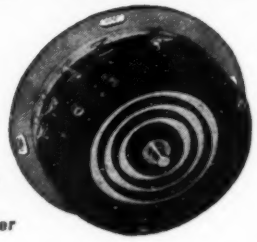

*Differential Computing Potentiometer

"Two potentiometers in one" most aptly describes the Fairchild Differential Computing Potentiometer. This versatile unit makes it possible to combine two input variables and obtain an output that is proportional to their sum or difference.

Available in quantity, the D-C-P costs less than two separate type 748 units while offering high resolution and accuracy of a single potentiometer. Linearity of ±0.10%, high resolution, long life, low noise level, and low torque—all Fairchild Linear Potentiometer features—are built into the D-C-P.

Suggested applications include servomechanisms, instrument controls, and computing and analyzing instruments. The D-C-P will directly replace two single potentiometers when one is used for compensation or correction purposes. For more data, write to Fairchild Camera and Instrument Corporation, 88-06 Van Wyck Boulevard, Jamaica 1, N. Y. Dept.140-12E.

FAIRCHILD
PRECISION POTENTIOMETERS

FOR *Stable* AMPLIFICATION OF SMALL PULSES

CHOOSE AN

ATOMIC
204-C
Linear Amplifier

When you encounter research problems requiring the amplification of small pulses for oscillographic examination, or counting with scaler or rate meter, you'll get top results with an Atomic 204C Linear Amplifier. Stability and linearity of pulse response—even at amplification of 9000 X—are exceptionally high because each of the two amplifier sections employs inverse feedback. But that's only one feature you'll like—here are others:

PULSE RESPONSE: Selector switches on front panel permit choice of input time constant from 0.16 microsec. to 16 microsec. in seven steps . . . rise time can be varied from 0.2 microsec. to 2 microsec. in five steps.

AMPLIFICATION: The voltage amplification varies between 1600 X and 9000 X depending upon the choice of input time constant and rise time. Gain control effected by attenuator having range from 0 to 30 db in 6 db steps.

INPUT VOLTAGE: Operates on pulses of either positive or negative polarity . . . minimum usable input signal varies from about 200 microvolts to 1 millivolt depending on bandwidth.

AMPLIFIER OUTPUTS: Low level output gives a maximum signal of about 5 volts . . . high level output gives a maximum signal of about 100 volts.

NOISE: Maximum noise output, including AC hum, less than 1 volt at maximum gain for all rise times.

DISCRIMINATOR: A pulse amplitude discriminator operates from the high level output of the amplifier . . . pulses above predetermined level cause the discriminator to give a 10 volt pulse of 0.4 microsec. duration . . . discrimination level is dial calibrated for output pulses from 0 to 100 volts.

Model 204B—another popular Linear Amplifier

Similar to the 204C but with choice of 3 rise time—bandwidth settings: 5 microsec., 0.1 Mc.; 0.8 microsec., 0.5 Mc.; 0.2 microsec., 2 Mc. Maximum voltage amplification 15,000, 10,000 and 3500. Gain control by two attenuators—coarse and fine.

Plate and heater voltages for pre-amplifiers are available from a power connector at the rear.

Accessories for use with Model 204C

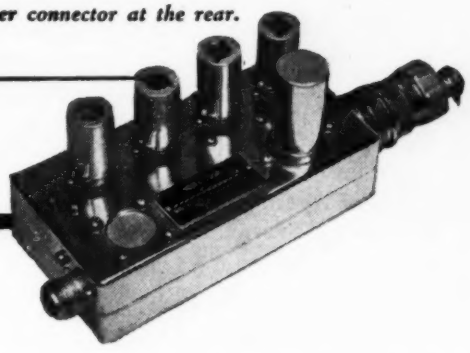

The Model 205B Linear Pre-Amplifier is used with the Model 204C for nuclear measurements with low level high impedance input. Flexible cable connection enables user to eliminate excessive input capacitance by placing first few stages of amplifier close to counting tube or ionization chamber . . . exceptionally compact . . . features a gain of 20 and a 0.2 microsecond rise time.

The Model 206A Pre-Amplifier is recommended for use in other applications where added gain is not required. The Model 206A acts as an impedance transformer having a gain of slightly less than unity.

Other Pre-Amplifiers Available: Model 206B Impedance Transformer; Model 209 Probe Type Impedance Transformer; Model 210 Quench Circuit; Model 211 Gain of Ten.

ATOMIC INSTRUMENT COMPANY

84 MASSACHUSETTS AVE. CAMBRIDGE 39, MASS.

HIGH VACUUM -- FASTER PUMPING -- QUIET OPERATION
are the outstanding characteristics of the LARGE CAPACITY TWO-STAGE DUO-SEAL VACUUM PUMP

GUARANTEED VACUUM
.0001 mm (0.1 Micron)

Patent No. 2337849

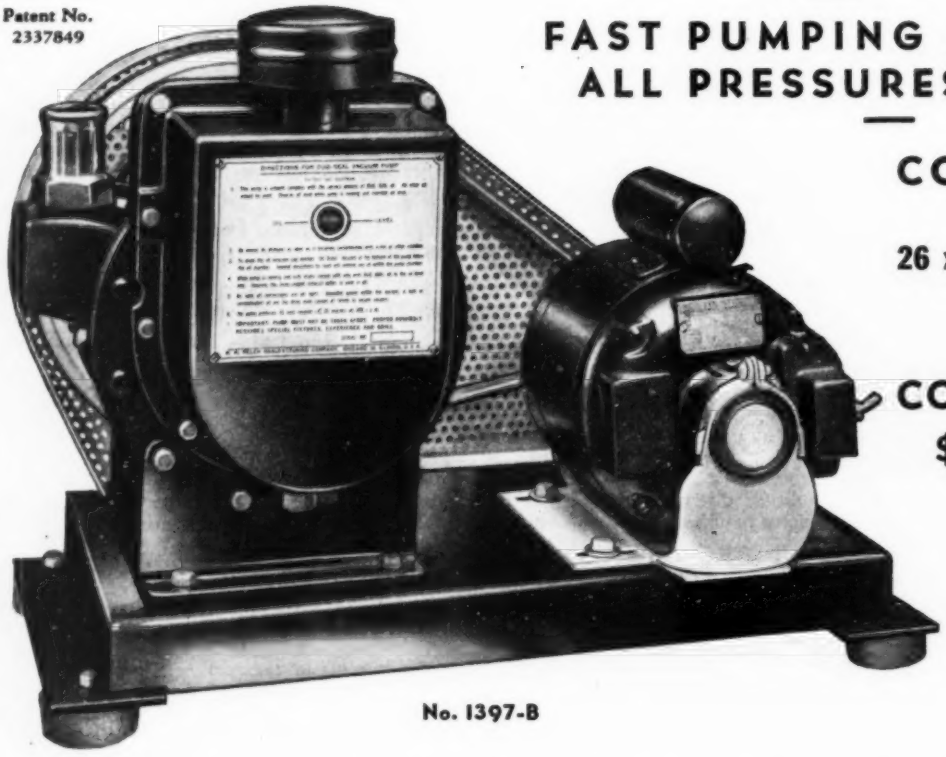

FAST PUMPING AT ALL PRESSURES

COMPACT
Size
26 x 14½ x 18½ inches

COMPLETE
$490.00

No. 1397-B

WELCH LARGE CAPACITY TWO-STAGE DUO-SEAL PUMP. Although the guaranteed vacuum is stated as 0.1 Micron, most of the tests produced a vacuum of 0.03 Micron. Free Air capacity 300 liters per minute (5 liters per second). It operates quietly with a minimum of vibration. A built-in trap prevents the oil from backing up into the system. It has been designed to prevent oil from being thrown out of discharge side of pump. Oil level shown in convenient indicator window at all times. Convenient oil drain permits oil change without dismantling system.

— WRITE FOR COMPLETE CIRCULAR GIVING RESULTS OF TEST —

W. M. WELCH SCIENTIFIC COMPANY
Established 1880
1515 SEDGWICK STREET, DEPT. C-1 CHICAGO 10, ILLINOIS, U.S.A.
Manufacturers of Scientific Instruments and Laboratory Apparatus

How the RCA *electron microscope* helps

INTERNATIONAL HARVESTER
make better equipment

IH can now forecast . . . with high accuracy . . . the behavior of metals used in building equipment for long and satisfactory service.

Here is how IH research men go about it.

With the RCA Electron Microscope, they observe the minute particles in the metals. They study the effect of carbide particle size on metal properties, make quantitive volume studies of different phases, analyze the structural changes accompanying the tempering of martensite—*and uncover new important and essential facts that help solve many manufacturing problems in the laboratories and factories!*

Consider the possibilities of this powerful instrument in your own research and production operations. You can obtain sharp images at direct magnification from 500 to 23,000 diameters, with photographic enlargements up to 100,000 diameters. You can resolve detail from 20 to 50 times finer than the best light microscope. You can bring every level of the specimen into sharp focus—regardless of the magnifying power you choose. You can also employ this versatile instrument for electron diffraction studies.

For complete data, write Dept. 51L, RCA Engineering Products, Camden, N. J.

RCA

SCIENTIFIC INSTRUMENTS

RADIO CORPORATION of AMERICA

ENGINEERING PRODUCTS DEPARTMENT, CAMDEN, N.J.

In Canada: RCA VICTOR Company Limited, Montreal

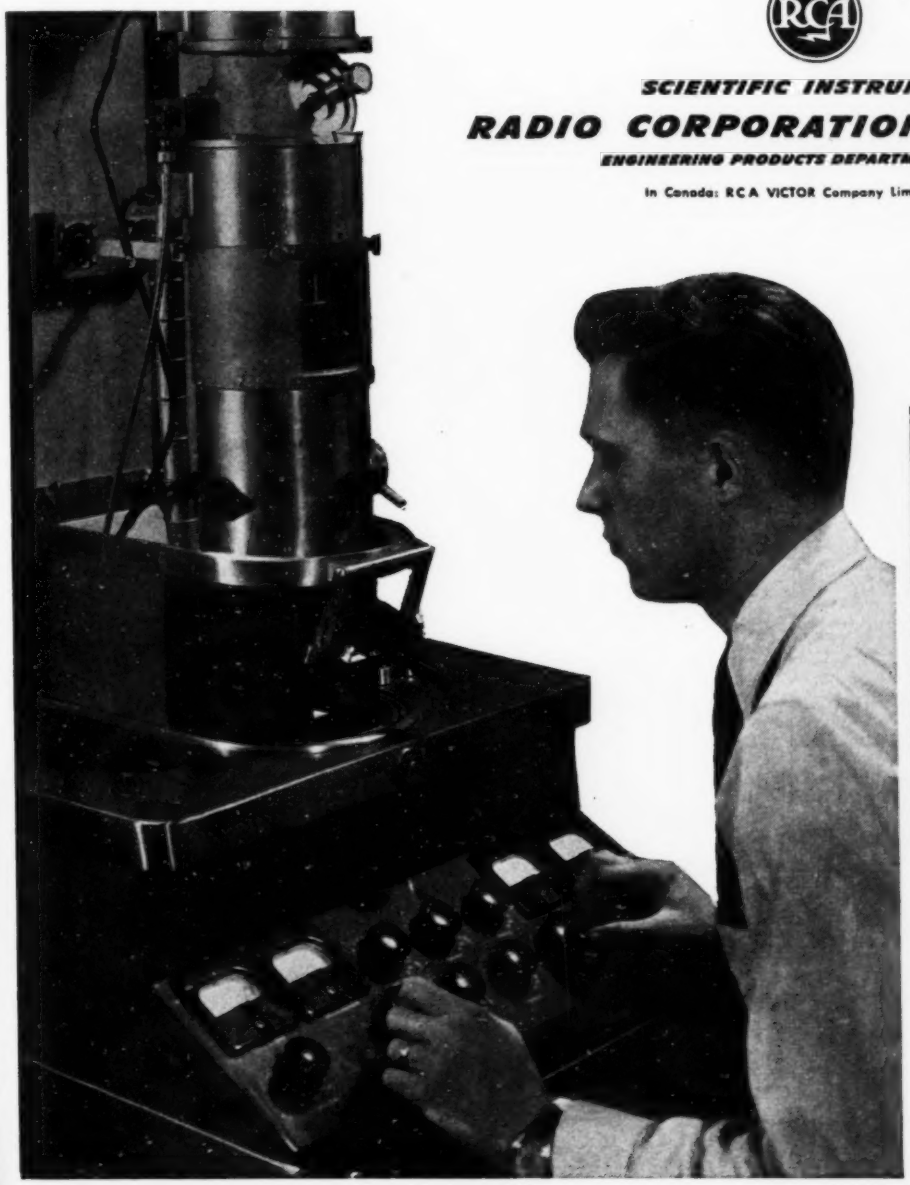

IH researcher observing a sample of steel in the RCA Electron Microscope. This instrument aids him in measuring carbide particle size and distribution—to predict the performance of the metal!

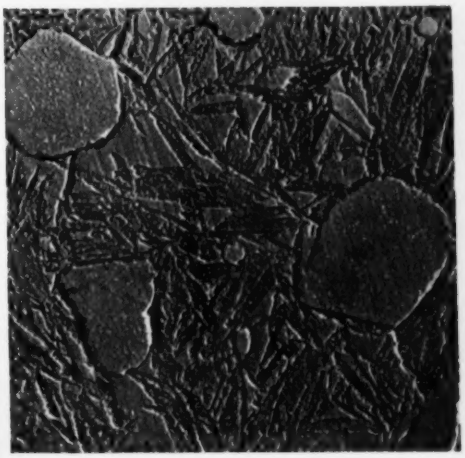

2.2% carbon, 12% chromium tool steel—magnified 7000 x by the RCA Electron Microscope. The approximately round islands are carbides; the irregular islands are austenite; the somewhat rough surface comprises martensite. The specimen was mechanically polished and etched with 4% picral. A replica was made of Formvar, then shadowed with chromium.

Phosphors for SCINTILLATION COUNTING

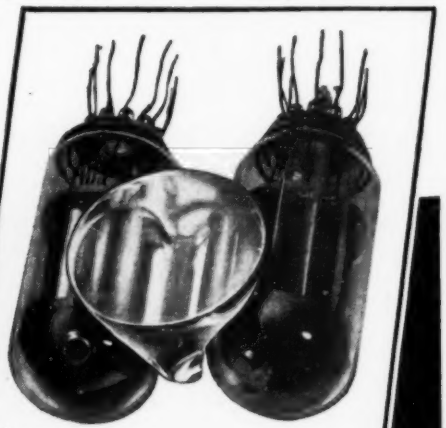

Example of the use of a solid plastic phosphor for coincidence counting with two photomultiplier tubes.

TRACERLAB now has available two versatile and highly efficient phosphorescent materials for use in scintillation detector units. One is synthetically grown stilbene crystal and the other is a new solid plastic phosphor. Single stilbene crystals up to one inch in any dimension are readily available and can be supplied in precisely machined forms.

The new solid plastic phosphor consists of a terphenyl solution in polystyrene. While plastic phosphors do not give as large pulses as stilbene, their primary advantage lies in the fact that they are available in a large variety of sizes and shapes and are considerably less expensive than crystalline phosphors. For further information write for bulletin J-30

Tracerlab

Western Division
2295 San Pablo Ave., Berkeley 2, California
New York Office
General Motors Bldg, 1775 B'way, N. Y. 19
Midwest Office
LaSalle-Wacker Bldg, 221 N LaSalle, Chicago

TRACERLAB INC., 130 HIGH STREET, BOSTON 10, MASS.

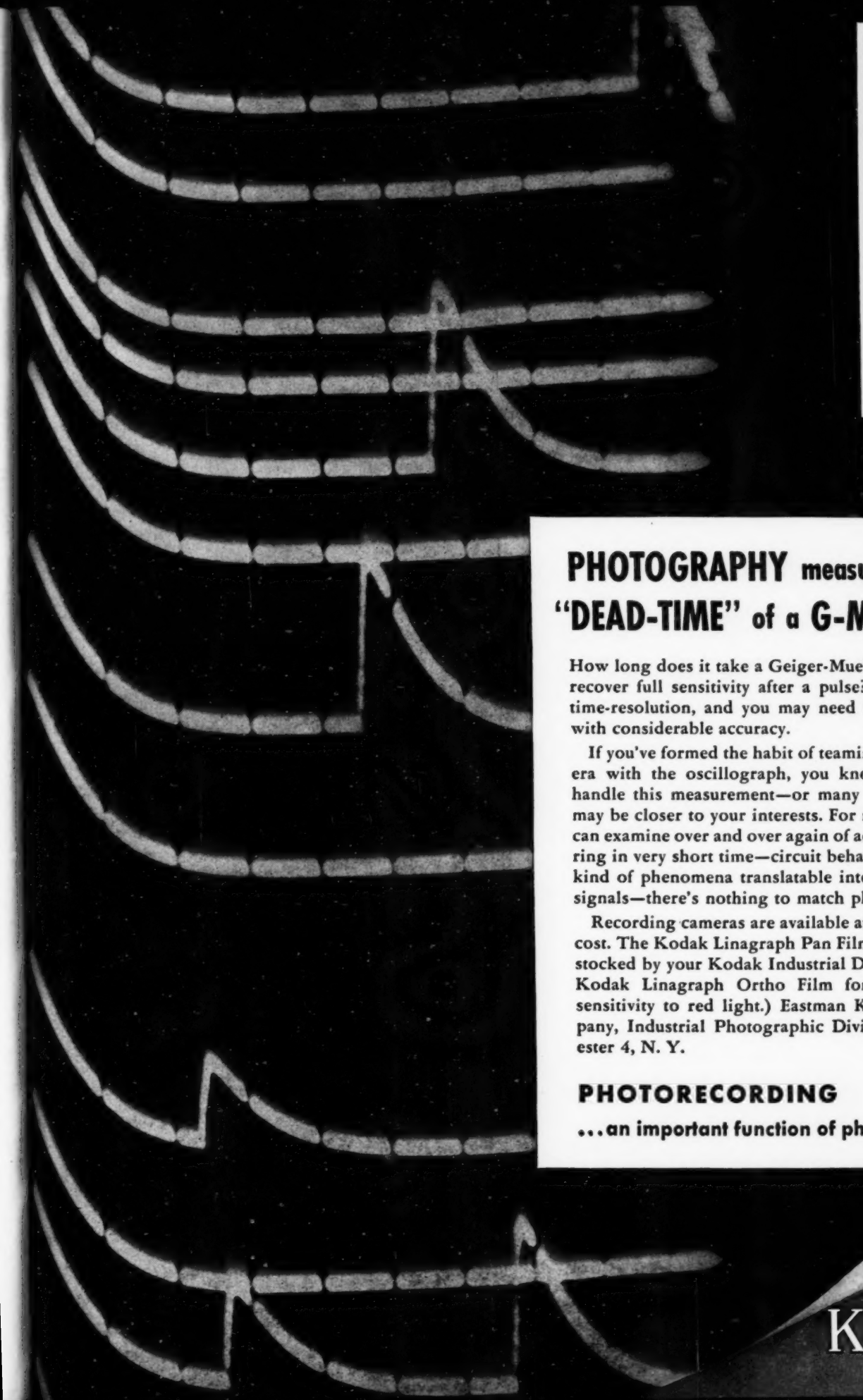

Photographed with the Du Mont Type 314A Oscillograph Recording Camera

PHOTOGRAPHY measures the "DEAD-TIME" of a G-M TUBE

How long does it take a Geiger-Mueller tube to recover full sensitivity after a pulse? That's its time-resolution, and you may need to know it with considerable accuracy.

If you've formed the habit of teaming the camera with the oscillograph, you know how to handle this measurement—or many others that may be closer to your interests. For records you can examine over and over again of action occurring in very short time—circuit behavior, or any kind of phenomena translatable into electronic signals—there's nothing to match photography.

Recording cameras are available at reasonable cost. The Kodak Linagraph Pan Film they use is stocked by your Kodak Industrial Dealer. (Also Kodak Linagraph Ortho Film for depressed sensitivity to red light.) Eastman Kodak Company, Industrial Photographic Division, Rochester 4, N. Y.

PHOTORECORDING

...an important function of photography

Kodak

TRADE-MARK

EPLAB

PYRHELIOMETER
For the Measurement of SOLAR RADIATION

Eppley Pyrheliometers are used for solar radiation measurements at twenty-eight out of twenty-nine weather stations in the continental United States, Mexico, Canada and Alaska. Ten of these stations are under the direction of the United States Weather Bureau.

The Eppley Pyrheliometer was adopted as standard equipment by the Weather Bureau after considerable experimentation. It was found to be the best instrument so far tested by the Bureau.

Used in conjunction with a suitable recorder, the Eppley Pyrheliometer will provide an accurate and reliable record of total solar and sky radiation on a horizontal surface.

Bulletin No. 2 On Request

THE EPPLEY LABORATORY, INC.

Scientific Instruments

Newport, Rhode Island, U.S.A.

THINK FIRST OF

PLUMMER AND KERSHAW

FOR PRECISION LENSES OR COMPLETE OPTICAL SYSTEMS

Ten thousand perfect, identical lenses or a single prism for a special research project, these are the day by day production of PLUMMER AND KERSHAW. Here precision workmanship is not

just a term, it is a standard, the high quality code for every detail of the working cycle. Every worker knows that, above *all else*, at P. & K. we insist on studying each job to find the best possible method of production *before* work is started. It is this constant searching for the ideal method—this fine attitude toward our work—which has brought, in a few short years, to Plummer & Kershaw, a reputation for fine, skillful workmanship.

If your needs require the manufacture of complete optical instruments to specifications, the designing of optical systems using glass, crystal or other transmission media or the production of one or many lenses, you may be sure P. & K. will make every effort to fulfill your demands. In addition we maintain a completely equipped laboratory for optical testing and are specialists in coating by the HI-VAC magnesium fluoride reflection reducing system.

We invite your inquiry.

PLUMMER AND KERSHAW

PRECISION OPTICS

2761 Frankford Ave., Phila. 34, Pa.

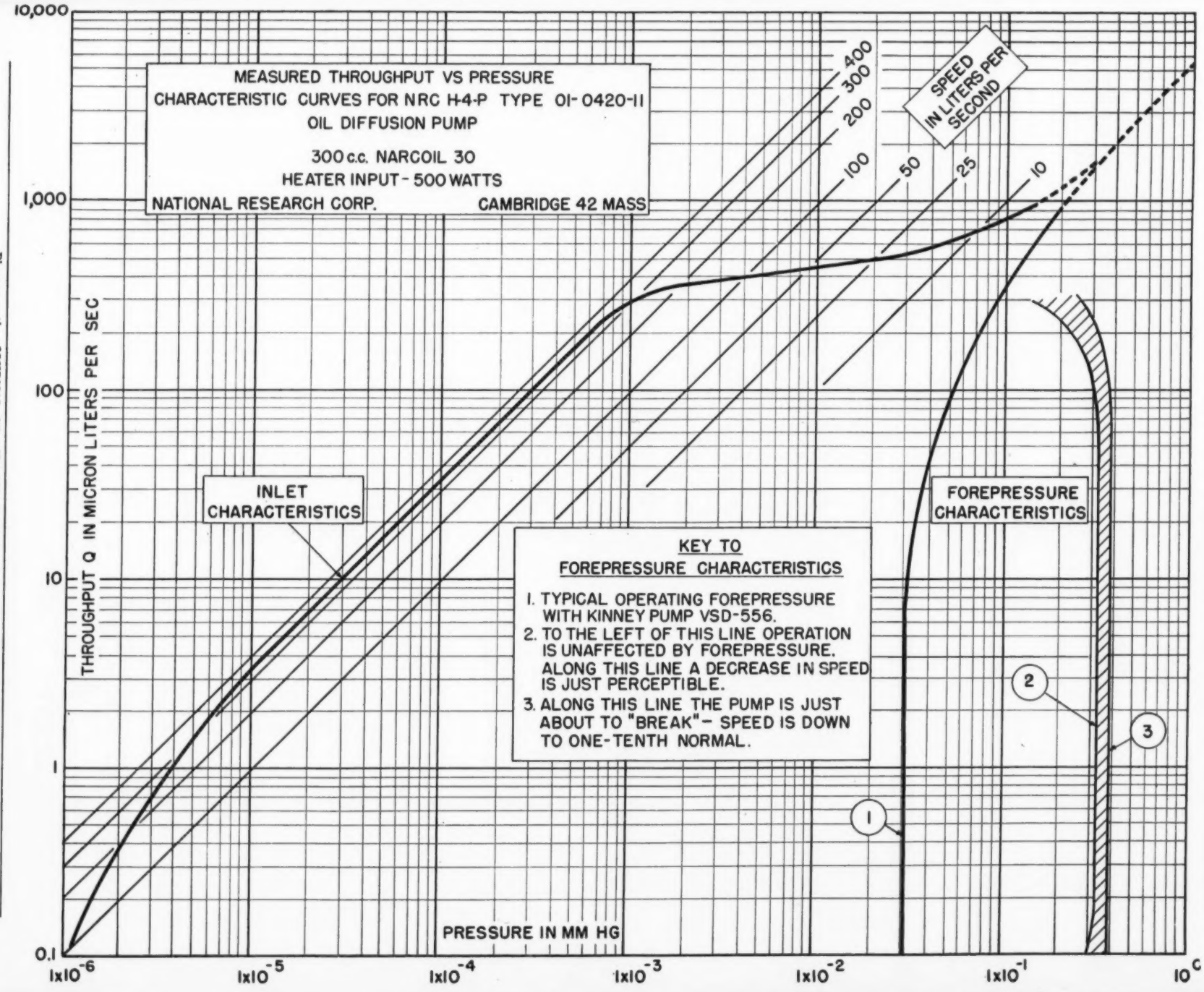

Please mention JOURNAL OF APPLIED PHYSICS when writing to advertisers

AMINCO

Light-Scattering INDICATING and RECORDING MICROPHOTOMETER

★ 100 Times the Sensitivity of Similar Instruments

★ Measures Twenty Micro-microlumens of Scattered Light

FOR THE MEASUREMENT OF:

Droplet size of aerosols . . . Purity of proteins and other colloids . . . Rate of change of molecule size in solution . . . Particle size and concentration in dispersed systems . . . Concentration and size of undissolved particles . . . Opacity of almost-opaque materials . . . Molecular aggregation in antigen-antibody reactions . . . Microfluorescence in dilute solutions . . . Depolarization, turbidity, and dissymmetry of high-molecular-weight solutions . . . Light reflectance of dark surfaces . . . Minute precipitation, flocculation, and crystallization . . . Molecular weight of high polymers in solution . . . Scintillation efficiency of nuclear-radiation-sensitive crystals and phosphors . . . Microchemical turbidity analyses.

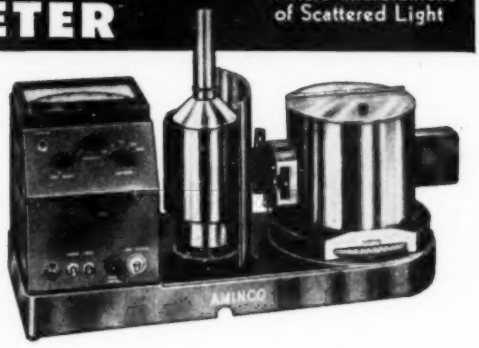

FEATURES

Excellent sensitivity.
Completely a-c. operated.
Has outlet for recorder operation.
Internal electronic stabilization.

Compact . . . accessible.
Fully accessible interior.
Comparisons of light intensities indicated as decimal percentages.

Built-in stable d-c. amplifier.
Can not be damaged by operator's carelessness.
Removable slit and optical systems.

WRITE FOR BULLETIN 2182-W

Since 1919 AMINCO

AMERICAN INSTRUMENT COMPANY, INC.

SILVER SPRING, MARYLAND — IN METROPOLITAN WASHINGTON, D. C.

Butterfly

POWER

• MICROTORQUE Variable Resistors and Potentiometers require as little as .003 in. oz. torque to operate. This unique feature makes the MICROTORQUE invaluable for applications where the position of instrument pointers, gyroscopes, and delicate instruments in general must be recorded, transmitted or indicated at a distance, and Giannini are the sole makers of MICROTORQUE Potentiometers.
A variety of resistance values and circuits available.

Write for booklet.
G. M. Giannini & Co., Inc.
Pasadena 1, California

giannini

RESEARCH POSITIONS

Physicists and Engineers with advanced experimental and theoretical experience in

- **NUCLEAR TECHNOLOGY**
- **SOLID STATE PHYSICS**
- **PHYSICAL METALLURGY**
- **POWER PLANT COMPONENTS**

are desired for research and development work on direct contract with the Reactor Division of the Atomic Energy Commission.

These positions offer unique opportunities for working with a highly trained group of scientists and for participating in theoretical and experimental studies in nuclear reactor technology. The laboratory is located in the Los Angeles area.

Please write to:

NORTH AMERICAN AVIATION, INC.
Attention: Personnel Manager
ATOMIC ENERGY RESEARCH DEPARTMENT
12214 South Lakewood Blvd.
Downey, California

Extremely High Purity PHILLIPS 66 RESEARCH GRADE Hydrocarbons

PRODUCT	PURITY, MOL. % *
PARAFFINS	
Methane	99.62
Ethane	100.00
Propane	99.99
Isobutane	99.88
Normal Butane	99.78
2,2-Dimethylpropane	99.83
Isopentane	99.80
Normal Pentane	99.88
2,2-Dimethylbutane	99.93
2,3-Dimethylbutane	99.74
2-Methylpentane	99.82
3-Methylpentane	99.80
Normal Hexane	99.85
2,4-Dimethylpentane	99.70
Normal Heptane	99.87
2,2,4-Trimethylpentane	99.87
Normal Octane	99.37
2,2,5-Trimethylhexane	99.69
Normal Nonane	99.30
CYCLOPARAFFINS	
Cyclopentane	99.95
Methylcyclopentane	99.69
Cyclohexane	99.95
Methylcyclohexane	99.77
OLEFINS	
Ethylene	99.70
Propylene	99.70
Isobutylene	99.44
Butene-1	99.88
Butene-2, Low Boiling	99.32
Butene-2, High Boiling	99.74
3-Methylbutene-1	99.70
2-Methylbutene-2	99.66
Pentene-1	99.34
Hexene-1	99.55
2,4,4-Trimethylpentene-1	99.11
CYCLOOLEFINS	
Cyclopetene	99.76
Cyclohexene	99.95
4-Vinylcyclohexene-1	99.40
DIOLEFINS	
Butadiene-1,3	99.84
2-Methylbutadiene-1,3	99.59
AROMATICS	
Benzene	99.93
Toluene	99.89
Ethylbenzene	99.82
Ortho Xylene	99.89
Isopropylbenzene	99.70
tert-Butylbenzene	99.76
sec-Butylbenzene	99.83
n-Butylbenzene	99.34

**Purity of product lots currently available*

Phillips 66 Research Grade Hydrocarbons have many valuable uses, such as the development of accurate analytical procedures and calibration of analytical instruments. They are also useful as reagents in radioactive research.

PHILLIPS PETROLEUM COMPANY

Chemical Products Division

Bartlesville, Oklahoma

Phillips 66

RCA TUBES ...

the complete line for industry...

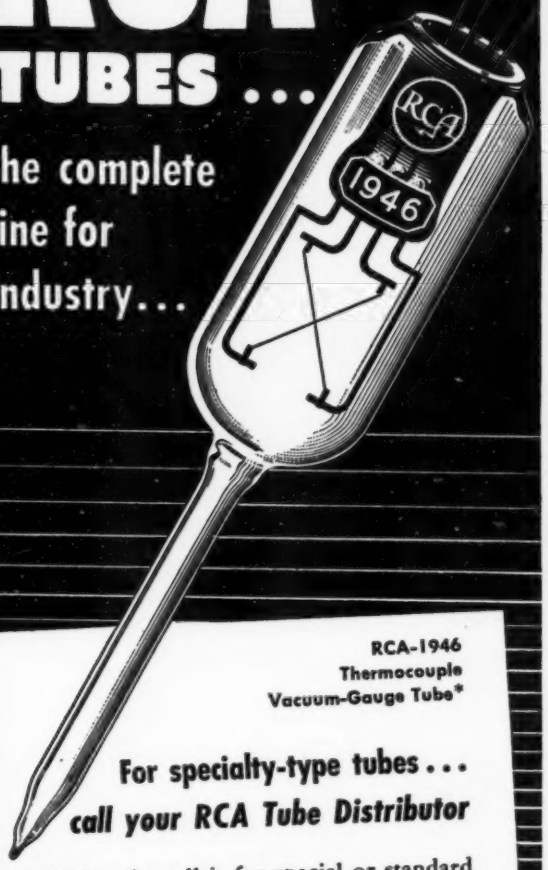

RCA-1946
Thermocouple
Vacuum-Gauge Tube*

For specialty-type tubes . . .
call your RCA Tube Distributor

Whether the call is for special or standard type electron tubes—or information on their use—your local RCA Tube Distributor is ready to serve your needs promptly and dependably.

***RCA Vacuum-Gauge Tubes** . . . include three ionization types, 1945, 1949, and 1950; a Pirani, type 1947; and a thermocouple, type 1946. Technical data sheets on these five RCA types are available without charge from your local RCA Tube Distributor.

RCA RADIO CORPORATION of AMERICA
ELECTRON TUBES HARRISON, N. J.

POSITIONS OPEN

IN RESEARCH AND ADVANCED DEVELOPMENT PROGRAMS

TO

Research Physicists
Senior Electronic Engineers
Senior Mechanical Engineers
Engineering Physicists
Circuit Engineers
Microwave Engineers
Vacuum Tube Research Engineers
Technical Report Writers
Electronic Technicians

Experienced or Holding Advanced Degrees For Research, Design, or Development In

Radar, Servomechanisms, Computers, Receivers, Photo Emission, Secondary Emission, Converters, Pulse and Timing Techniques, Special Test Equipment, Special Purpose Tubes, Circuit Design, Solid State Physics, Light and Electron Optics, etc.

We invite interested personnel with experience in the above fields to submit a complete and detailed resume of education and experience, together with salary requirements and availability date, to:

The Employment Department

CAPEHART-FARNSWORTH CORPORATION

Fort Wayne 1, Indiana

Working with Inert Gases?

Linde HELIUM · NEON
ARGON · KRYPTON · XENON

Now available in commercial-size cylinders in addition to glass bulbs. Write for information on sizes, prices, rigid purity tolerances, special rare gas mixtures . . .

THE LINDE AIR PRODUCTS COMPANY
Unit of Union Carbide and Carbon Corporation
30 East 42nd Street UCC New York 17, N. Y.
In Canada: Dominion Oxygen Company, Limited, Toronto
The term "Linde" is a registered trade-mark of The Linde Air Products Company.

PHYSICISTS AND ENGINEERS

You can find plenty of positions where you will work on minor improvements on radar, telemetering systems, and other conventional devices. However, you will find very few positions where you can break ground in new fields having tremendous significance. This you can do at the JACOBS INSTRUMENT COMPANY, whose entire effort is devoted to pioneering activities in new fields that it has opened up itself. One of these fields, for example, is that of ultra-high speed, ultra-compact digital computers and controllers. This company's JAINCOMP family of computers dominates this field. Other equally important fields are being developed. Engineers and physicists with sound backgrounds and experience in the design of advanced electronic circuits or precision mechanical instruments may qualify, also individuals with good backgrounds in applied physics. A few openings exist for outstanding junior E. E.'s and physicists, also experienced technicians; applicants for these positions must apply in person.

JACOBS
INSTRUMENT CO.
4718 Bethesda Ave., Bethesda 14, Maryland

CAMBRIDGE ROCKING MICROTOME

CUTS SECTIONS DOWN TO 1/5 MICRON

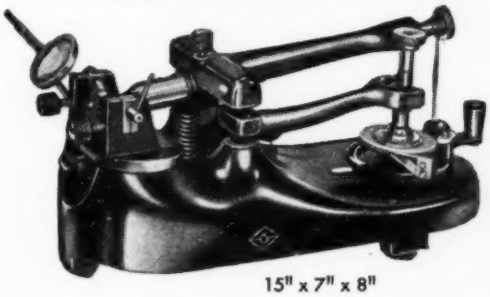

15" x 7" x 8"

This moderately priced instrument is designed specially for cutting extremely thin sections for use with the Electron Microscope. The sections cut with this Microtome are ribboned, which makes it most convenient for studies of sections serially. Will accommodate Gillette razor blade or special Microtome knife. Fitted with magnifying lens for observing work in progress.

Write for Bulletin L 293.

CAMBRIDGE INSTRUMENT CO., INC.
3773 Grand Central Terminal, New York 17, N. Y.
PIONEER MANUFACTURERS OF PRECISION INSTRUMENTS

RESEARCH OPPORTUNITIES IN THE LOS ANGELES AREA

Unusual Opportunity for Senior men with degrees and at least five years of outstanding proven accomplishment to achieve further growth by working with some of the nation's outstanding scientists on commercial and military projects in large modern electronics laboratories.

ELECTRONIC ENGINEERS
PHYSICISTS—CIRCUITRY
PHYSICISTS—ANALYSIS
PHYSICISTS—OPTICS
PHYSICISTS—ELECTRON TUBES

SERVOMECHANISMS ENGINEERS
ELECTRO MECHANICAL ENGINEERS
MECHANICAL DESIGNERS

Long term program of research and development in the fields of Radar, Guided Missiles, Computers, Electron Tubes, and related equipment.

Please do not answer unless you meet the above requirements.

RESEARCH AND DEVELOPMENT LABORATORIES
Hughes Aircraft Company
CULVER CITY, CALIFORNIA

Fast-Acting LABORATORY THERMOSWITCH* THERMOSTAT

Controls Fractional Distillation Accurately . . . Dependably

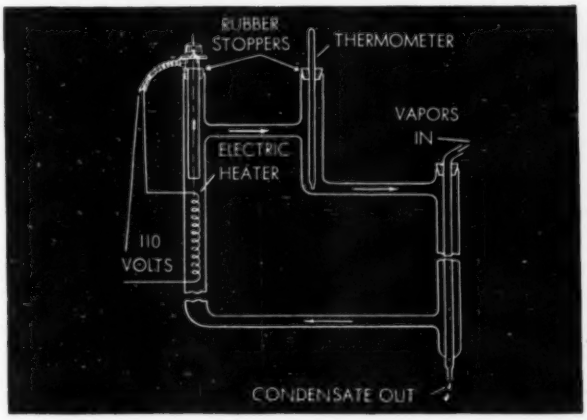

Laboratories everywhere are uncovering more and more uses for the Laboratory THERMOSWITCH Thermostat. In the diagram above, for instance, you can see how this thermostat performs a needed function for successful fractional distillation. Because of its instantaneous reaction — as well as its widely adjustable temperature range — it permits constant, effective control of the coolant thus assuring satisfactory results.

THERMOSWITCH* Thermostats owe their success to an exclusive principle of operation. Fast, accurate response is assured because the activating element is the *single-metal*, temperature-sensitive shell. This shell, in direct contact with the ambient temperature, expands *without lag*, causing the contacts inside to open.

The Laboratory THERMOSWITCH* Thermostat provides accurate heating control for solids, liquids, gases.

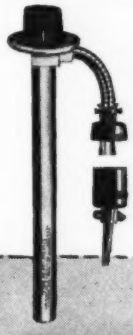

See what it will do for you! For complete information, see your Laboratory Supply house, or write for bulletin to

FENWAL INCORPORATED
1612 Pleasant Street, Ashland, Mass.
Temperature Control Engineers

Fenwal

THERMOSWITCH*

*Reg. U. S. Pat. Off.

The Precision Thermostat For Temperature Control and Detection

SENSITIVE . . . *but only to heat*

CREEP TEST INSTRUMENTS • TELESCOPES • TOOLMAKER MICROSCOPES • COMPARATORS • OPTICAL INSTRUMENTS • SPECTROMETERS **Gaertner** REFRACTOMETERS • MICROMETER SLIDES • INTERFEROMETERS • SPECTROPHOTOMETERS • LABORATORY SUPPORTS CATRETOMETERS • CHRONOGRAPHS • OPTICAL BENCHES • SPHEROMETERS • SPECTROSCOPES • DIVIDING MACHINES PHOTOELASTICITY POLARISCOPES • MICROSCOPES • SPECTROGRAPHS • POLARIMETERS • MONOCHROMATORS

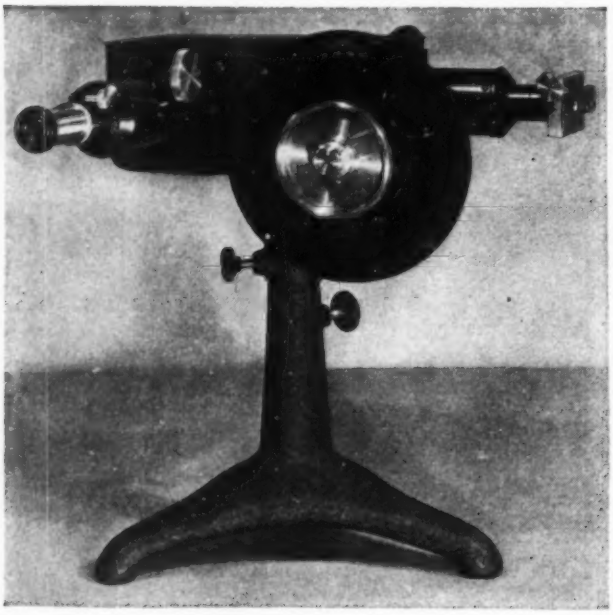

MODEL L227

WAVELENGTH SPECTROMETER AND MONOCHROMATOR

Used as a wavelength spectrometer, it provides a fast means for checking absorption properties of filters and for identifying elements having characteristic spectral lines within its range from 390 to 800 millimicrons.

Used as a monochromator by substituting an exit slit for the eyepiece, it provides a monochromatic beam of any desired visual wavelength for use in diffraction studies, microscopy, lens testing, polarimetry, irradiation studies, etc.

AVAILABLE FOR PROMPT DELIVERY

Request Bulletin 158-74
"Wavelength Spectrometers and Monochromators"

THE GAERTNER SCIENTIFIC CORPORATION
1238 WRIGHTWOOD AVE. • CHICAGO 14 • U.S.A.

PLACEMENT SERVICE REGISTER

OF THE

AMERICAN INSTITUTE OF PHYSICS

to be held in connection with the

American Physical Society Meeting, February 1, 2, and 3, 1951

Columbia University, New York, New York

LOOKING FOR PHYSICISTS?

Universities, institutions, and companies wishing to post notices of positions may send details to the Institute Office, or post them upon arrival at the meeting.

SEEKING A NEW POSITION?

Applicants may obtain registration forms and further information from the Institute office. Pre-registration is important.

INTERVIEWS.

It is to the advantage of registrants to be present. Interviews will be arranged between employers' representatives and applicants attending the meeting.

PLEASE REPORT TO THE REGISTER OFFICE UPON ARRIVAL AT THE MEETING

American Institute of Physics **57 East 55 Street, New York 22, N.Y.**

S·S·White MOLDED RESISTORS

The "All-Weather" Resistors

Of particular interest to all who need resistors with inherent low noise level and good stability in all climates

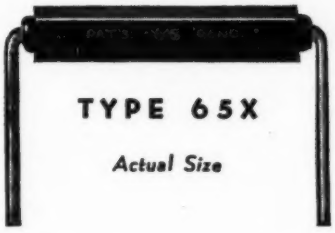

TYPE 65X

Actual Size

HIGH VALUE RANGE—10 to 10,000,000 MEGOHMS
This unusual range of high value resistors was developed to meet the needs of scientific and industrial control, measuring and laboratory equipment—and of high voltage applications.

STANDARD RANGE—1000 OHMS to 9 MEGOHMS
Used extensively in commercial equipment including radio, telephone, telegraph, sound pictures, television, etc. Also in a variety of U. S. Navy equipment.

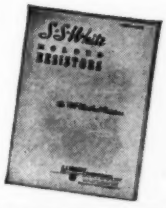

SEND FOR BULLETIN 4906

It gives details of both the Standard and High Value Resistors including construction, characteristics, dimensions, etc. Copy, with Price List mailed on request.

THE S·S·White INDUSTRIAL DIVISION
DENTAL MFG. CO.
Dept. F, 10 East 40th St.
NEW YORK 16, N. Y.

RESEARCH AND DEVELOPMENT ENGINEERS

MECHANICAL, ELECTRICAL AND ELECTRONIC ENGINEERS AND ENGINEERING PHYSICISTS

Excellent positions on experimental research and development projects related to intricate electro-mechanical and electronic devices.

Men with advanced degrees or equivalent experience may qualify for permanent positions in our laboratories in New York State.

Give full details of education and experience indicating age and marital status. Write Box 1150C, 57 East 55 Street, New York 22, New York.

PHYSICISTS AND SENIOR RESEARCH ENGINEERS

• • •

POSITIONS NOW OPEN

• • •

Senior Engineers and Physicists having outstanding academic background and experience in the fields of:

- Microwave Techniques
- Moving Target Indication
- Servomechanisms
- Applied Physics
- Gyroscopic Equipment
- Optical Equipment
- Computers
- Pulse Techniques
- Radar
- Fire Control
- Circuit Analysis
- Autopilot Design
- Applied Mathematics
- Electronic Subminiaturization
- Instrument Design
- Automatic Production Equipment
- Test Equipment
- Electronic Design
- Flight Test Instrumentation

are offered excellent working conditions and opportunities for advancement in our Aerophysics Laboratory. Salaries are commensurate with ability, experience and background. Send information as to age, education, experience and work preference to:

NORTH AMERICAN AVIATION, INC.
AEROPHYSICS LABORATORY
BOX NO. J4
12214 South Lakewood Blvd. Downey, California

GEOPHYSICS

A Journal of General and Applied Geophysics

Published Quarterly by

SOCIETY OF EXPLORATION GEOPHYSICISTS

Box 7248 Tulsa 18, Oklahoma

- The official journal of the only international group of prospecting geophysicists
- Devoted to current problems in seismograph, gravity, magnetic and other methods of geophysical prospecting for oil and other minerals
- Covers geophysical instrumentation

SUBSCRIPTION RATES

ONE YEAR (4 issues) $9.00, foreign $9.50

Price list of back issues supplied on request

PHYSICISTS, ENGINEERS APPLIED MATHEMATICIANS

Electronic and mechanical engineers physicists and applied mathematicians

POSITIONS AVAILABLE AT ALL LEVELS

for research and development in radar, microwaves, servo systems, computers, telemetering, instrumentation and nucleonics.

Permanent positions offering variety, responsibility, and challenging opportunities for advancement.

BENDIX AVIATION CORPORATION
RESEARCH LABORATORIES
4855 Fourth Ave., Detroit 1, Michigan

COCKROFT WALTON GENERATORS

FOR NUCLEAR PHYSICS STUDIES

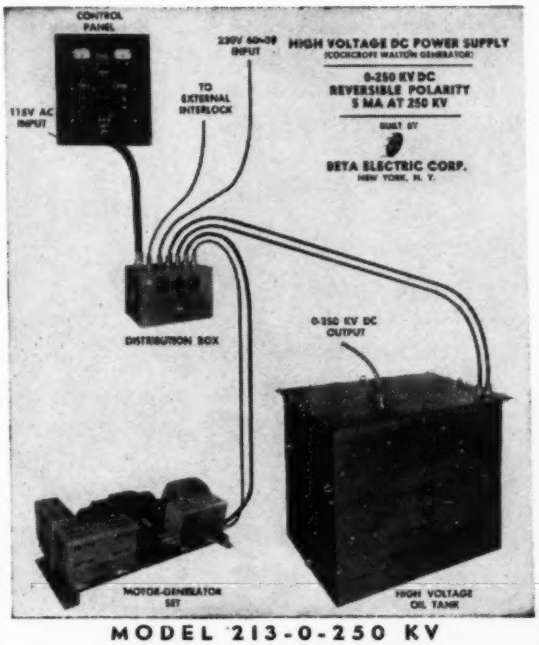

MODEL 213-0-250 KV

The Beta Electric Corporation is building Cockroft Walton generators capable of delivering up to 400 KV DC at 10 MA. A motor-generator set operating at 400 cycles permits the use of capacitors considerably smaller than 60 cycle operation would allow. However, the operating frequency is low enough to eliminate the problem of stray capacitance prevalent at RF operating frequencies. Thus an extremely compact design is achieved. The 250 KV unit illustrated has a high voltage oil filled tank only 40″ wide x 32″ deep x 36″ high.

High voltage DC power supplies, including Cockroft Walton Generators, are the specialty of the Beta Electric Corporation. Beta will build high voltage power supplies to fit any requirements for voltage, current, regulation, size, etc. Beta also makes a standard line of rugged, compact DC power supplies rated up to 30 KV. Beta products include the useful portable projection oscilloscopes and kilovoltmeters. Beta Built means excellence of design and construction—and low price!

Beta Field Engineers throughout the country are ready to discuss with you your high voltage problems and equipment needs.

BETA ELECTRIC CORP.
333 East 103 St., New York 29

The Oscillograph designed for the student

Specially designed to meet the needs of modern education, the Hathaway Type S-14 six-element Student's Oscillograph is an essential part of the modern college laboratory. The high standards of accuracy inherent in other Hathaway instruments have been maintained in the S-14 to make it a valuable tool for the critical researcher. Simplicity and ease of operation have been built into the S-14 for the undergraduate student.

The six-element S-14 is ideal in all applications requiring a simple and versatile instrument at a relatively low price.

For further information, write for Bulletin 2D1E

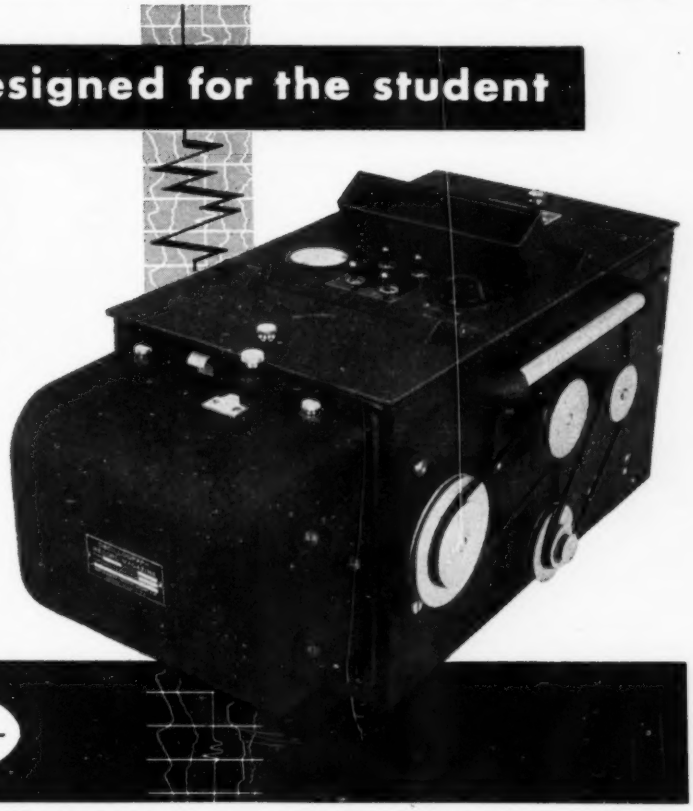

Hathaway
INSTRUMENT COMPANY
1315 SO. CLARKSON STREET • DENVER 10, COLORADO

INDEX TO ADVERTISERS

Name	*Page*
American Instrument Co., Inc.	xxiv
The Arnold Engineering Company	ii
Atomic Instrument Company	xvii
Bell Telephone Laboratories	v
Bendix Aviation Corporation	xxx
Beta Electric Corporation	xxxi
Browning Laboratories, Inc.	iv
Cambridge Instrument Company	xxvii
Capehart-Farnsworth Corporation	xxvi
Central Research Laboratories, Inc.	x
Central Scientific Company	C–4
Consolidated Engineering Corp.	xv
Cyclotron Specialties Company	viii
The Daven Company	xiii
Distillation Products, Inc.	iii
Eastman Kodak Company	xxi
The Eppley Laboratories, Inc.	xxii
Fairchild Camera & Instrument Corporation	xvi
Fenwal, Inc.	xxvii
The Gaertner Scientific Corp.	xxviii
General Electric Company	vii
General Radio Company	C–3
G. M. Giannini & Company, Inc.	xxiv
Hathaway Instrument Company	xxxi
High Voltage Engineering Corp.	xii
Hughes Aircraft Company	xxvii
Jacobs Instrument Company	xxvi
Leeds & Northrup Company	i
Libbey-Owens-Ford Glass Company	vi
The Linde Air Products Company, Unit of Union Carbide and Carbon Corp.	xxvi
McGraw-Hill Book Company	xiv
National Research Corporation	xxiii
North American Aviation, Inc.	xxiv, xxx
Phillips Petroleum Company	xxv
Plummer & Kershaw	xxii
Radio Corporation of America	xix, xxv
Rex Rheostat Company	xxix
Shallcross Manufacturing Company	ix
Society of Exploration Geophysicists	xxx
Statham Laboratories	xi
Tracerlab, Inc.	xx
Union Carbide and Carbon Corp., The Linde Air Products Company	xxvi
W. M. Welch Scientific Company	xviii
The S. S. White Dental Mfg. Co.	xxix

INDEX—*Continued*

PHYSICIST

Ph. D. or equivalent in Physics or Physical Metallurgy, X-Ray Diffraction experience, and good background in solid state physics. For Research Program in residual stresses.

International Harvester
Manufacturing Research
5225 So. Western Blvd.
Chicago 9, Illinois

POSITION OPEN

SEMI-CONDUCTOR RESEARCH

Physicists, chemists or EE's with Ph.D. or equivalent and experience in the field of solid state physics for research work on semi-conductor devices employing germanium and silicon. An excellent opportunity in a research laboratory of a leading manufacturer with laboratories in New York State. Send complete resume. Our employees have been notified. Write Box 1250A, 57 East 55 Street, New York 22, New York.

PHYSICIST, B.S. or M.S., young man, preferably with industrial experience in physics of solids (semi-conductors) for laboratory research, medium size electrical manufacturer, North Jersey. State qualifications and expected salary. Box 1250B, 57 East 55 Street, New York 22, New York.

POSITION WANTED

Physicist, B.S., equivalent M.A., 14 years of broad experience and increasing responsibility in fields of physical, x-ray, magnetic and general testing and research, preferably east. Write Box 1250D, 57 East 55 Street, New York 22, New York.

for R-F Capacitance Measurements . . .

. . . at One Megacycle

THIS instrument offers a very simple means for making measurements of capacitance from 0 to 1200 micromicrofarads, at a frequency of one megacycle.

It is completely self-contained, requiring only a 115-volt a-c or d-c power source. Its operation is extremely simple, the capacitance of the unknown being read directly after a calibrated dial has been set to give the proper meter indication.

The instrument consists of a one megacycle oscillator whose output is loosely coupled to a resonant detector circuit. The resonance indicator includes a crystal rectifier and a d-c microammeter loosely coupled to a resonant circuit.

Substitution method of measurement is used. The capacitance of the calibrated condenser is reduced to restore resonance after the unknown is placed across the terminals. Resonance is indicated by maximum deflection of the microammeter.

A panel trimmer condenser is provided both to standardize the circuit at zero capacitance and to balance out the capacitance of leads to the unknown. About 5 $\mu\mu$f can be balanced out on the low range, and about 120 $\mu\mu$f on the high range.

For production testing of a number of capacitors of approximately the same value, a simple jig can be used to permit very rapid operation. The accuracy of measurement is sufficient for a large number of capacitance measurements.

SPECIFICATIONS

DIRECT READING in two ranges of 0 to 80$\mu\mu$f and 0 to 1200 μf. Ranges are switched automatically as dial is rotated

GOOD ACCURACY: Low range: from 0 to 50 $\mu\mu$f, $\pm(3\% + 0.3\ \mu\mu f)$; between 50 and 80 $\mu\mu$f, $\pm$ 6%. High range: $\pm(3\% + 5\ \mu\mu f)$

APPROXIMATELY LOGARITHMIC SCALE on low capacitance range, makes readings easy

COMPARES DIELECTRIC LOSSES in the unknown where they show as lower resonance indicator readings; useful for intercomparison of relative losses

A-C OR D-C OPERATION: instrument is self-contained and operates from either a-c or d-c lines at 115-volts

TYPE 1612-A

R-F CAPACITANCE METER: $155

GENERAL RADIO COMPANY

Cambridge 39, Massachusetts

90 West St., New York 6 920 S. Michigan Ave., Chicago 5 1000 N. Seward St., Los Angeles 38

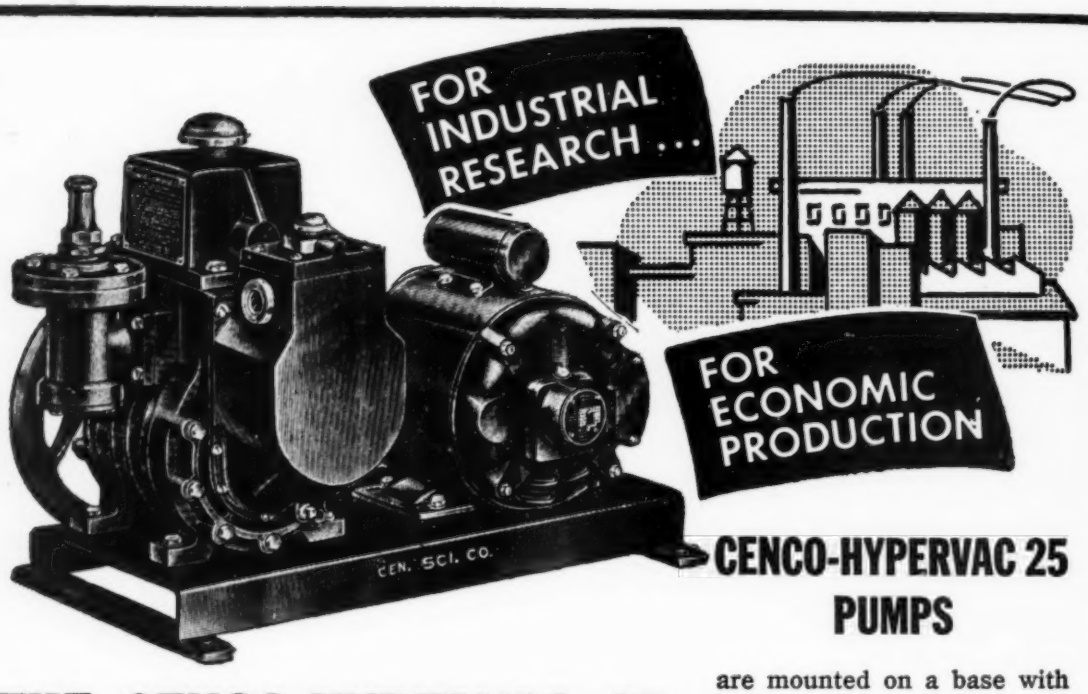

CENCO-HYPERVAC 25 PUMPS

THE CENCO-HYPERVAC 25

Manufactured as carefully as a precision watch, this new high speed, high vacuum pump provides fast initial evacuation for research or production. It combines in a single mechanical unit, ability to pump at a speed of 264 liters per minute of free air or 120 liters per minute at 1 micron pressure and attains an ultimate pressure well below 0.1 micron. Here is a pump that will perform reliably with or without a second stage diffusion pump. Quiet operation and long service are assured.

are mounted on a base with motor as follows:

93020A, for 115/230 volts, 60 cycles, A.C.

93020G, for 115/230 volts, 50 cycles, A.C.

93020S, for 220/440 volts, 60 cycles, A.C. 3 phase

93020Y, without motor

Prices on units with motors for other voltages and frequencies are available on request.

Write Dept. Y.A. for Engineering Bulletin 10 describing Cenco High Vacuum Pumps, Gages and accessory equipment.

SERVING SCIENCE CENCO

CENTRAL SCIENTIFIC COMPANY

Scientific Apparatus · Instruments · Chemicals

1700 IRVING PARK ROAD, CHICAGO 13

NEW YORK BOSTON SAN FRANCISCO NEWARK LOS ANGELES TORONTO MONTREAL

LANCASTER PRESS, INC., LANCASTER, PA.